REPORT DOCUMENTATION PAGE

Form Approved OMB No. 0704-0188

1. REPORT DATE *(DD-MM-YYYY)*	2. REPORT TYPE	3. DATES COVERED *(From – To)*
9 September 2013	Conference Proceedings	25 July 2012 – 7 September 2013

4. TITLE AND SUBTITLE

53rd Course Molecular Physics and Plasmas in Hypersonics II

5a. CONTRACT NUMBER

FA8655-12-1-2121

5b. GRANT NUMBER

CSP 12-2121

5c. PROGRAM ELEMENT NUMBER

61102F

6. AUTHOR(S)

PROF MARIO CAPITELLI

5d. PROJECT NUMBER

5d. TASK NUMBER

5e. WORK UNIT NUMBER

7. PERFORMING ORGANIZATION NAME(S) AND ADDRESS(ES)

UNIVERSITY OF BARI
VIA ORABONA 4
BARI 70125 ITALY

8. PERFORMING ORGANIZATION REPORT NUMBER

N/A

9. SPONSORING/MONITORING AGENCY NAME(S) AND ADDRESS(ES)

EOARD
Unit 4515
APO AE 09421-4515

10. SPONSOR/MONITOR'S ACRONYM(S)

AFRL/AFOSR/IOE (EOARD)

11. SPONSOR/MONITOR'S REPORT NUMBER(S)

AFRL-AFOSR-UK-PC-2013-0016

12. DISTRIBUTION/AVAILABILITY STATEMENT

Distribution A: Approved for public release; distribution is unlimited.

13. SUPPLEMENTARY NOTES

14. ABSTRACT

This Course will deal with subjects of relevance to aerospace engineering, such as (re)entry into planetary atmospheres and experimental methods in high-enthalpy wind tunnels, offering an updated view of the advances made in these fields. In this regard, lectures will consider the physical phenomenology relative to the coupling among fluid dynamics, plasmas and electromagnetism. Such phenomenology has recently attracted renewed interest for the possibility to mitigate through the presence of electromagnetic fields the thermal environment that a spacecraft has to withstand during the entry phase in a planetary atmosphere. The topics of this conference include: molecular dynamics of elementary processes, chemical and physical non-equilibrium kinetics in hypersonic flows, fluid dynamics of reacting flows, plasma chemistry and plasma physics.

The papers collected in this report offer a comprehensive view of the advances recently made in the investigation of different aspects connected to the predictive simulation of hypersonic flows in aerospace applications, emphasizing the role of non-equilibrium effects and the importance of state to state (StS) approaches and representing a roadmap for the future of the research in this field.

15. SUBJECT TERMS

EOARD, Hypersonics, Molecular Physics, Plasma

16. SECURITY CLASSIFICATION OF:			17. LIMITATION OF ABSTRACT	18, NUMBER OF PAGES	19a. NAME OF RESPONSIBLE PERSON
a. REPORT	b. ABSTRACT	c. THIS PAGE			Gregg Abate
UNCLAS	UNCLAS	UNCLAS	SAR	258	19b. TELEPHONE NUMBER *(Include area code)* +44 (0)1895 616021

Molecular Physics and Plasmas in Hypersonics
Special Issue of the Open Plasma Physics Journal

Preface

In the aerospace scientific community, conventional macroscopic chemical-physical models are routinely used in CFD simulations of hypersonic flows. These models assume thermal (if not chemical) equilibrium on the belief that non-equilibrium effects play a minor role in every realistic case of interest but also to the requirement of computational efficiency. Non-equilibrium effects (vibrationally and electronically excited states, free electrons) have been considered by developing multi-temperature approaches, however under strong non-equilibrium conditions temperature is not a significant quantity to describe the distribution of particles over internal energy levels. Moreover the concept of temperature hides all the non equilibrium effects present in the tails of the relevant distributions which play an important role in promoting chemical reactions. Attempts to use state-to-state (StS) kinetics for the study of hypersonic flows are being considered by an increasing number of international groups and preliminary results are indeed encouraging. A strong effort however is required to transform these preliminary studies into a predictive tool.

This Special Issue is intended to give an up-to-date overview of the recent advances made, in the framework of the Phys4Entry EU project, in the simulation of hypersonic flows, from fundamental issues, as the molecular dynamics of elementary processes, to the development of state-to-state and new-concept macroscopic kinetic models to be included in detailed computational fluid dynamic codes for the rebuilding of experiments. Contributions focus also on more applicative subjects of relevance to aerospace engineering, such as (re)entry into planetary atmospheres and experimental methods in high-enthalpy wind tunnels, considering the physical phenomenology relative to the coupling among fluid dynamics, plasmas and electromagnetism.

Starting from the characterization of elementary processes, the challenging objective is the creation of a consistent state-selected cross section databases for the description of the elementary processes relevant to the modeling of planetary atmospheres in the dissociation and ionization regimes, thus including electron-impact induced, heavy particle collision and heterogeneous processes. Quantum, semi- and quasi-classical approaches are exploited for the derivation of complete sets of cross sections resolved on internal (ro-vibrational and electronic) degrees of freedom moving to the treatment of triatomic molecular targets, with special attention to CO_2 molecule.

Dynamical data are of paramount importance in the description of the non-equilibrium state-to-state kinetics and advanced models are presented that self-consistently coupled the kinetic equations with the Boltzmann equation for free electrons energy distribution function. However the high-computational cost required by the full vibrational StS approach actually stimulated the renewed interest in new-concept macroscopic approaches, integrating the information of a detailed kinetics in different strategies, as global rate coefficients in non-equilibrium thermodynamics or a two-level distribution model, hybridizing a multi-temperature model with a kinetic equation for the last vibrational level, or finally a multi-internal temperature model grouping levels in order to associate a temperature to different groups and to give an accurate description of the vibrational distribution. Furthermore the kinetic theory methods for the modeling of reacting flows are used for the simulation of the gas dynamic parameters and the heat transfer to the surface in a boundary layer near spacecraft non-catalytic surface entering the Mars atmosphere, accounting for the complexity of the kinetic model when the non-equilibrium CO_2 internal level distributions are investigated with StS and quasi-stationary multi-temperature models.

Reliable estimates of radiative heat fluxes as well as of the radiation-induced changes in the fluid dynamic field around the vehicle are of paramount importance for the reduction of the uncertainty margin in the design of the thermal protection system. Again, conventional approaches are based on thermal equilibrium assumptions and on the optically thin plasma model that simplifies significantly the radiation transport model. On the one hand, StS models provide a consistent description of the radiation-hot gas interaction by modeling explicitly the excited state populations: synthetic emission spectra are therefore a direct output of the model to be compared with experimental measurements. The improvements in radiation models for the entry conditions in planetary atmosphere, with extended and accurate database of elementary radiative processes, are shown and an advanced collisional-radiative model for Jupiter atmosphere, that coupled self-consistently the kinetic equations for chemical processes, the Boltzmann equation for free electrons and the radiation transfer equation, is also presented. Modern problems of radiative aerothermodynamics of entering space vehicles, concerning the coupling of non-equilibrium processes with radiation heat transfer in shock layers are demonstrated and analyzed, giving a brief account on innovative magneto-hydrodynamic (MHD) technologies.

Again dealing with kinetic modeling, the significant progress achieved with Monte Carlo methods, i.e. PIC (Particle in Cell) and DSMC (Direct Simulation Monte Carlo), in the description of non-equilibrium in steep shock wave fronts is demonstrated, with numerical tools for CFD solvers able to correctly account of effects due to plasma-matter

interaction and to rarefaction.

The ultimate example, integrating the concept of state-to-state models, deals with accurate CFD simulations in the design of hypersonic vehicles, allowing the estimation of error bars and nominal values of the design parameters and emphasizing the potential advantages of the detailed kinetic modules in the code validation with wind tunnel test cases. Moreover the relative importance of the implementation of the computationally expensive state-kinetic (non equilibrium) transport coefficients in CFD simulations of flow conditions is quantified

New experimental tests are reported explicitly designed to address the non-equilibrium character of plasmas generated in four different systems, including the post-shock air plasma in high-enthalpy shock tube, the shock wave generated by an acoustic shock tube, the subsonic nitrogen plasma jet produced by DC-Plasmatron facility and supersonic air plasma jets produced by Plasmatron facility.

The papers collected in this Special Issue offer a comprehensive view of the advances recently made in the investigation of different aspects connected to the predictive simulation of hypersonic flows in aerospace applications, emphasizing the role of non-equilibrium effects and the importance of StS approaches and representing a roadmap for the future of the research in this field.

As Guest Editors we would like to express our sincere appreciation to all invited authors. The relevant papers have been inspired by the invited topical talks presented during the 53rd Course "Molecular Physics and Plasmas in Hypersonics" of the International School of Quantum Electronics of the Ettore Majorana Centre, held in Erice, Sicily (Italy) on September 8-15 2012. I wish to thank the European Office of Aerospace Research and Development (EOARD) Air Force Office of Scientific Research - United States Air Force Research Laboratory and the Italian Centre for Aerospace Research (CIRA) for their contribution to the success of the 53rd Course.

Mario Capitelli
Annarita Laricchiuta
Guest Editors

Table of Contents

Molecular Physics of Elementary Processes relevant to Hypersonics: electron-molecule collisions

R. Celiberto [1,2], V. Laporta[3,2], A. Laricchiuta[2], J. Tennyson[3] and J.M. Wadehra[4]
[1] *Dipartimento di Ingegneria Civile, Ambientale, del Territorio, Edile e di Chimica, Politecnico di Bari, Bari, Italy**
[2] *Istituto di Metodologie Inorganiche e Plasmi, CNR, 70125 Bari, Italy*
[3] *Department of Physics and Astronomy, University College London, London WC1E 6BT, UK and*
[4] *Physics Department, Wayne State University, Detroit, MI, 48202 USA*

Non-resonant, electron-impact, vibro-electronic excitation cross sections, involving vibrationally excited N_2 molecules, to the mixed valence-Rydberg $b, c, o\ ^1\Pi_u$ and $b\ ',c',e'\ ^1\Sigma_u^+$ singlet states are presented. These cross sections are calculated using the so-called *similarity approach*, accounting for the vibronic coupling among excited states, and compared with the experiments and different theoretical calculations.

New cross sections for the electron-impact resonant vibrational excitation of CO_2 molecule are calculated, for the symmetric stretching mode, as a function of the incident electron energy and for the transitions $(0,0,0) \rightarrow (v_f,0,0)$ with $v_f = 0,1,2,5,10$. A resonance potential curve and associated widths are calculated using the R-matrix method. The theoretical cross sections for $v_f = 0,1,2$ are compared with the available experimental data. Rate coefficients, calculated by assuming a Maxwellian electron energy distribution function, are also presented for the cases $v_f = 0,1,5,10$.

Electron-impact cross sections and rate coefficients for resonant vibrational excitations involving the diatomic species N_2, NO, CO, O_2 and H_2, for multi-quantic and mono-quantic transitions, are reviewed along with the cross sections and rates for the process of the dissociative electron attachment to H_2 molecule, involving a Rydberg excited resonant state of the H_2^- ion.

PACS numbers:

I. INTRODUCTION

The presence of molecular species in gaseous systems gives rise to a large variety of collisional and radiative processes, which involve the internal degrees of freedom of the molecules. In non-equilibrium conditions, these processes play a role of fundamental importance in redistributing the energy, and while the rotational population, due to the quasi-continuum structure of the rotation levels, can be considered in many situations as thermalized, vibrational distributions can largely deviate from the equilibrium state, so that the collisional processes may involve highly-excited vibrational levels [1].

In low-temperatures plasmas, which can be characterized by a non-negligible molecular and electronic densities, the impact of electrons on vibrationally excited molecules may assume a role of paramount importance in affecting the plasma properties. With this in view, we roughly classify electron-molecule collisions in two categories represented by the *non-resonant* collisions, where only exchange of energy or momentum may occur, and which include vibrationally elastic and inelastic processes and ionization, and *resonant collisions*, where the incident electron can be momentarily captured by the target molecule with formation of a negative ion in a resonant state [2]. In this latter case, the resonant state is characterized by a finite lifetime and can either give rise to dissociative electron attachment (DEA), where the molecule can be broken in fragments, one of which carries the additional negative charge, or to the resonant vibrational excitation (RVE) occurring through emission of the extra electron back to the continuum, which usually leaves the molecule in a final excited vibrational level. Excited electronic states can also be involved in both the above resonant and non-resonant processes, so that combined vibro-electronic excitations become possible. In addition, when the excited levels fall in a vibrational continuum, molecular dissociation can also take place.

A theoretical kinetic model of a non-equilibrium molecular plasma, aimed at a realistic and predictive description of the system, must take into account all the possible collisional and radiative processes involving both electrons as well as heavy particles in their ground or excited states [1]. This is usually implemented by resorting to the so-called state-to-state approach to plasma kinetic modeling, according to which each molecule, in a given internal quantum state, is considered as an independent chemical species [3]. This requires, in principle, the knowledge of the cross

*Corresponding author: r.celiberto@poliba.it

sections for all the scattering processes starting from each molecular quantum state accessible in the system. Examples of application of the state-to-state approach are provided, in space explorations, by the plasma arising during the re-entry conditions of space shuttles which, entering the atmosphere of a planet, are exposed to gas friction and their kinetic energy is then transferred to the internal motions of the atmospheric molecules, so that the level population assumes a non-equilibrium distribution [4].

In this article, which is part of a series of papers by our collaboration devoted to the study of planetary atmospheric molecules, we present electron-molecule cross sections for vibrationally excited molecules relevant for re-entry problems. In particular, we will discuss the cross sections for processes involving the N_2, O_2 and NO molecules, components of the Earth's atmosphere, CO and CO_2 important for Venus and Mars atmospheres, and H_2 which is the main component of the gas giant planets. The article is divided in two parts. In Part I we will focus on electron-impact non-resonant collisions leading to vibro-electronic excitation of diatomic nitrogen molecules. The cross sections are calculated for excitation to the $b, c, o\ ^1\Pi$ and $b\ ', c', e'\ ^1\Sigma_u^+$ electronic states of the N_2 molecules. In Part II, we present new resonant cross section and rate coefficient calculations for vibrational excitations of the symmetric streching mode of the CO_2 molecule. We also briefly review cross sections and rate coefficients for the vibrational excitation and dissociative attachment for the diatomic molecules mentioned above [5–10]. In particular in Part I, section II, we introduce the non-resonant electron-N_2 molecule excitation processes, and in section III and IV we will illustrate the *similarity approach* for cross section calculations and discuss the obtained results respectively. In Part II, section V, we will briefly outline the theory for resonant collisions for polyatomic molecules, and in Section VI we will present the original results for CO_2 molecule. In Section VII cross sections and rates for diatomic molecules will be reviewed and, finally, in Section VIII we will give our conclusions.

Part I
Non-resonant collisions

II. N_2 MOLECULE DISSOCIATION: EXTREME ULTRA-VIOLET SYSTEMS

Excitation to the lowest three electronic states of the $^1\Sigma$ and $^1\Pi$ spectroscopic series for N_2 system, being dipole-coupled to the ground state and representing the dominant contribution to the extreme ultraviolet spectrum of N_2 plasmas, has received considerable attention since the 1980s [11, 12]. These states, usually denoted as $b, c, o\ ^1\Pi_u$ and $b\,',c',e'\ ^1\Sigma_u^+$ exhibit a strong inter-state coupling, due to their mixed valence-Rydberg character, resulting in significant perturbation of vibronic bands. Moreover, the vibrational levels are strongly predissociated [13, 14], therefore vibronic excitation channels contribute to the formation of atoms in electronically excited, affecting the atomic concentration in the gas phase.

Among the previous works on the subject, special mention should be made of the pioneering work by Ermler *et al.* [11], who computed *ab-initio* potential energy curves and transition dipole moments for the singlet terms of the N_2 spectrum, and the work of Stahel *et al.* [12], who considered for the first time the electronic coupling and provided a complete quantitative vibrational analysis. Spelsberg and Meyer [15] performed new *ab-initio* calculations, within a multi-reference configuration interaction (MRCI) framework, giving accurate potential energy curves of singlet terms, both adiabatic and diabatic representations, and also for the R-dependent coupling terms in the region of effective interaction, while recently Khakoo *et al.* and Malone *et al.* [16, 17] have investigated experimentally the electron-impact excitation of these states, deriving differential cross sections from energy-loss spectra. Finally, very recently Little and Tennyson [18] have calculated a comprehensive set of curves for both singlet and triplet states of N_2.

Here we present excitation cross sections for the processes

$$\mathrm{N_2(X\ ^1\Sigma_g^+}, \upsilon'') + e^- \rightarrow \mathrm{N_2(^1\Sigma_u^+}, \upsilon') + e^-, \tag{1}$$

$$\mathrm{N_2(X\ ^1\Sigma_g^+}, \upsilon'') + e^- \rightarrow \mathrm{N_2(^1\Pi_u}, \upsilon') + e^-, \tag{2}$$

obtained in the framework of the phenomenological *similarity approach*, as discussed in the next section, modified to include the effects of vibronic coupling.

III. THEORETICAL APPROACH

Electron-impact excitation to these states has been considered in different theoretical approaches. Vibrationally-resolved cross sections are also derived in Ref. [19], where however the vibronic coupling was not accounted for. The main consequence of vibronic coupling is that different electronic terms of the same symmetry lose their identity and should be treated as a complex of states.

The treatment of the vibronic coupling entails the numerical solution of a system of coupled radial Schrödinger equations [20],

$$\left[\hat{I}T + \hat{V}^d(R) - \hat{I}E\right]\hat{\chi}^d(R) = 0, \tag{3}$$

where $\hat{V}^d(R)$, depending on the internuclear distance R, is the symmetric interaction matrix, whose diagonal elements are represented by the diabatic potentials, while off-diagonal elements are the non-adiabatic coupling terms. The solution $\hat{\chi}^d(R)$ is a normalized vector of final-state radial wave functions, having a mixed character and containing information about all the coupled a, b and c electronic states, *i.e.*

$$\hat{\chi}^d(R) \equiv \begin{pmatrix} \chi_a^d(R) \\ \chi_b^d(R) \\ \chi_c^d(R) \end{pmatrix}. \tag{4}$$

Equation (3) was solved using a numerical code for a system of coupled second-order differential equations, based on a second-order finite difference method [21], using the diabatic potentials and coupling terms calculated using an accurate MRCI approach in Ref. [15].

The electron-impact induced vibronic transitions were calculated in the frame of the *similarity approach* [22], that allows a simplified expression for the state-to-state cross section, *i.e.*

$$\sigma_{\upsilon'\upsilon''} = \frac{2\pi e^4}{(\Delta E_{\upsilon'\upsilon''})^2} f_{\upsilon'\upsilon''}\varphi(x), \tag{5}$$

where $\Delta E_{\upsilon'\upsilon''}$ is the transition energy, $f_{\upsilon'\upsilon''}$ is the oscillator strength for the vibronic transition, φ is the so-called *similarity function*, a universal function of the reduced incident electron energy $x = E/\Delta E_{\upsilon'\upsilon''}$, describing the collision dynamics,

$$\varphi(x) = \frac{\ln\left[1 + a\sqrt{x-1}\,\right]}{x+b}, \tag{6}$$

whose parameters $a \sim 0.5$ and $b \sim 3.0$ have been optimized so as to fit experimental data for a large number of atomic and molecular systems [22]. Like in other semi-classical approaches, the state-to-state cross section of Eq. (5) is factorized as the product of the oscillator strength of the transition, containing information on the molecular target structure, and the universal function $\varphi(x)$ of the reduced incident electron energy, describing the collision dynamics. The extension of the approach to the treatment of vibronic coupled states goes through the re-definition of the oscillator strength

$$f_{\upsilon'\upsilon''} = \frac{2}{3}\frac{g_{\rm e}}{g_{\rm g}}\Delta E_{\upsilon'\upsilon''}|\langle\chi^d_a|M^d_a(R)|\chi_{\rm ground}\rangle + \langle\chi^d_b|M^d_b(R)|\chi_{\rm ground}\rangle + \langle\chi^d_c|M^d_c(R)|\chi_{\rm ground}\rangle|^2, \tag{7}$$

where g_e and g_g are the statistical weights of the excited and ground electronic terms respectively [23]. $\chi_{\rm ground}(R)$ and $\chi^d_{a,b,c}(R)$ are the ground and excited state vibrational wave functions, and $M^d_{a,b,c}(R)$ are the transition dipole moments coupling the ground and the *a,b,c* excited electronic states. The diabatic transition dipole moments for the $^1\Sigma^+_g$ and $^1\Pi_u$ states were calculated in Ref. [15].

The total cross section for excitation from the different vibrational levels, υ'', of the ground state, to the complex of the excited states results from the summation of state-resolved cross sections over the final vibrational levels

$$\sigma_{\upsilon''}(E) = \sum_{\upsilon'}\sigma_{\upsilon'\upsilon''}(E), \tag{8}$$

The summation runs over levels lying below the lowest dissociation limit. Above this threshold the continuum of the dissociating state is coupled to the bound levels of the other electronic terms in the complex, and the dissociation character of the cross section should be estimated.

IV. VIBRONIC EXCITATION CROSS SECTIONS

Total vibronic excitation cross sections are derived for the transitions to the singlet terms of the nitrogen spectrum. In order to compare the present calculations with different theoretical results, obtained in an *independent-state* description, each term in the summation is multiplied by the vibrational-dependent quantity $P^{\upsilon'}_a = \langle\chi^d_a|\chi^d_a\rangle$, which weights the state-character of the vibrational wave function with respect to the three coupled terms. For example in the case of the $b\ ^1\Pi_u$ state one has,

$$\sigma^b_{\upsilon''}(E) = \sum_{\upsilon'}\sigma_{\upsilon'\upsilon''}(E)P^{\upsilon'}_b, \tag{9}$$

Fig. 1 displays the total cross section for excitation to the $^1\Pi_u$ complex from the υ''=0 level. The vibronic excitation to the *b* state dominates, while the contributions to the *c* and *o* states are considerably smaller. The comparison with theoretical results of Ref. [19], obtained using the Gryzinski approach, is reported in Fig. 1 (a). Though a fairly good agreement in found for the *b* state, for the *c* and *o* states the similarity approach seems to give much lower cross sections. However it should be stressed that in the coupled frame the number of final vibrational levels included in the calculations is lowered with respect to the decoupled description. In fact, as already stressed above, high-lying *c* and *o* vibrational levels are actually coupled to the *b*-state continuum, thus contributing to the direct dissociation.

Integral excitation cross sections have been derived from recent accurate experimental differential total cross sections by Khakoo *et al.* [16], the angular integration being carried out under the assumption of constant $\sigma(\theta, E)$ for the low [$\theta < 3°$] and high [$\theta > 130°$] scattering angles. In comparing the experiments with the theoretical results, it should be considered that the spectral energy window explored in the measurements is 12-13.82 eV, thus collecting emission from a finite number of υ' levels, *i.e.* *b* [υ' 0-14], *c* [υ' 0-3] and *o* [υ' 0-3]; furthermore, in the experimental paper [16] the vibrational analysis was performed assigning the emission intensity in a decoupled frame, i.e. considering each transition belonging only to one member of the coupled system, while in the present theoretical approach vibrational levels have a mixed character, the weight of each member being represented by P. Accounting properly for both

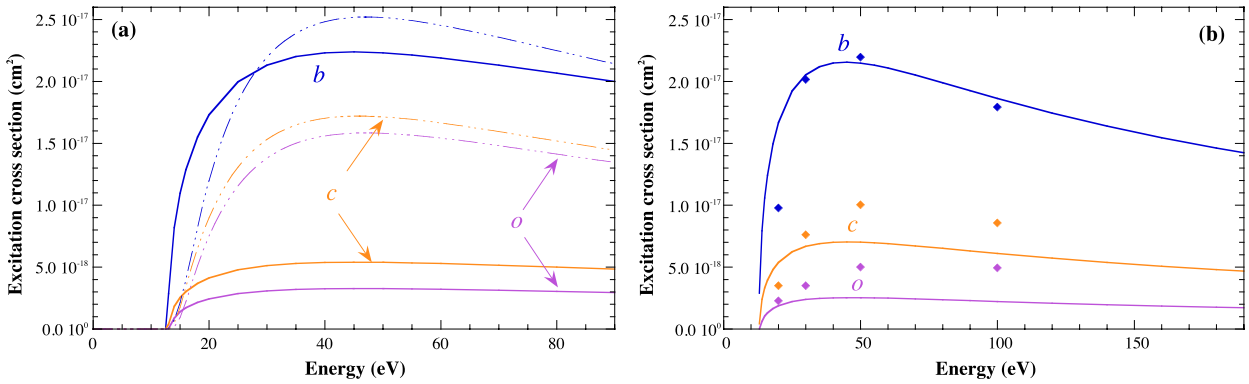

FIG. 1: Total cross section (*solid lines*) for excitation to the $^1\Pi_u$ states from the v''=0 level of the ground state of N_2 molecule as a function of collision energy, compared with (a) theoretical [19] (*dashed-dotted lines*) and (b) experimental [16] (*close diamonds*) results in literature. In (b) total cross sections have been obtained using a de-coupled scheme for assigment (see text for details).

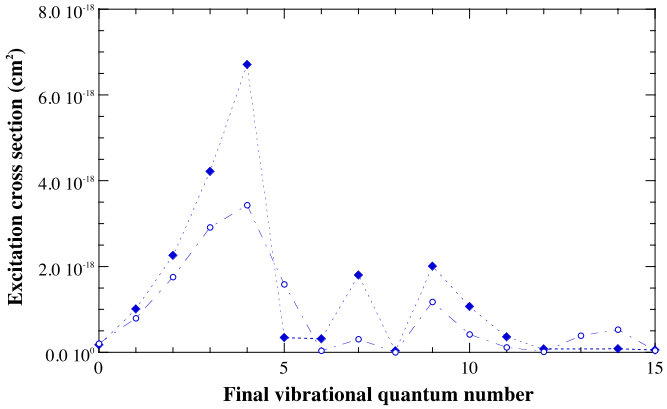

FIG. 2: Excitation cross section (*open circles*) from the v''=0 level of the ground state to the $b\ ^1\Pi_u$ state of N_2 molecule, as a function of final vibrational quantum number v', at collision energy E=200 eV, compared with experimental results (*closed diamonds*) of Ref. [24].

effects, and using a level-character $P_a^{v'}$ switching from 0 to 1, cross sections have been corrected and theoretical and experimental results in Fig. 1 (b) are thus found in good agreement.

An interesting point is the investigation of the role of vibronic coupling in changing the dependence of the excitation on vibrational quantum states. In Fig. 2 the state-to-state cross section for a transition from the v''=0 level to the vibrational levels of the b state, at the collision energy of 200 eV, is shown. The pattern of the final vibrational profile is strongly irregular, due to the coupling perturbation, and far from the expected bell-shape behavior, usually observed for transitions from the fundamental vibrational level. In this case the experimental state-to-state cross sections by Zipf [24] confirm the vibrational pattern. In particular the coincidence of cross section peaks for specific v' levels is observed, though the theoretical calculations predicts lower absolute values.

For the $^1\Sigma_u^+$ complex, the cross sections for the b' and c' components are comparable, while those for the e' state are considerably lower (Fig. 3(a)). In Fig. 3(b) the excitation to the b' state from v''=0 level is compared with experimental integral cross sections in Ref. [17] obtained by electron-energy loss spectroscopy allowing for the detection of a limited number of vibrational levels (v' [0-10]), and with the estimated full-integral cross section, equivalent to v' [0-16]. The large discrepancy is attributed to the inclusion in the theoretical cross section of excitations to higher vibrational levels lying outside the spectral energy range explored by experiments. In fact, the theoretical cross sections of Fig. 3, obtained by including in the summation of Eq. (8) a reduced number of final vibrational levels (dashed lines), are found to be in better agreement with the experiments.

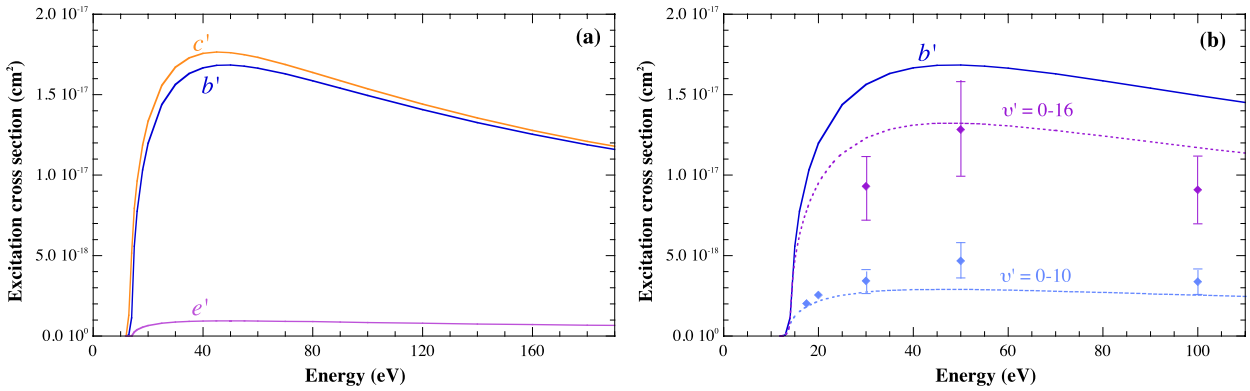

FIG. 3: (a) Total cross section for excitation to the $^1\Sigma_u^+$ states from the v''=0 level of the ground state of N_2 molecule as a function of collision energy. (b) Cross section for excitation to the $b\,'\,^1\Sigma_u^+$ state from the v''=0 level (*solid line*), compared with experimental results in Ref. [17] (close diamonds). Cross sections obtained considering a variable number of final vibrational levels are also shown (dashed lines).

Part II
Resonant collisions

V. ELECTRON-IMPACT VIBRATIONAL EXCITATIONS FOR CO_2 MOLECULE: THEORETICAL MODEL

The low energy integrated cross section, for electron-CO_2 scattering, shows two distinctive features: a $^2\Pi_u$ shape resonance around 3.8 eV (see for example Refs. [25–28]) and, at energies below 2 eV, an enhancement due to the presence of the $^2\Sigma_g^+$ symmetry virtual state [29–32]. Both phenomena give rise to a temporary CO_2^- system. For a general review see Ref. [33] and references therein. In this section we report the electron-CO_2 resonant vibrational-excitation process, via $^2\Pi_u$ shape resonance,

$$e^- + CO_2(X\ ^1\Sigma_g^+, v_i) \rightarrow CO_2^-(^2\Pi_u) \rightarrow e^- + CO_2(X\ ^1\Sigma_g^+, v_f), \tag{10}$$

where $v_i(v_f)$ represents the initial (final) vibrational level of the ground state of CO_2. In its ground electronic state the CO_2 molecule has a linear geometry (D_{2h}) and it has three vibrational normal modes: symmetric stretching, bending mode and asymmetric stretching. The doubly degenerate $^2\Pi_u$ symmetry of CO_2^- splits the bending mode into two (Renner-Teller) non-degenerate $^2A_1$ and $^2B_1$ components (C_{2v} symmetry) [34]. In principle, as the CO_2 is a polyatomic molecule, the scattering cannot be described by a simple one-dimensional model, but it needs a multidimensional treatment of the nuclear motion. Under the usual assumptions for mono-dimensional local complex potential model it is possible to extend the formalism to the case of multidimensional space and to many interacting resonances in a straightforward manner. For the case of two interacting resonances, as the CO_2 case is, the nuclear wave equation can be written, in a matrix form, as [27]:

$$(H - E)\,\vec{\xi}(R) = -\vec{V}_{dk}(\epsilon, R)\,\chi_i(R)\,, \tag{11}$$

where R denotes collectively the nuclear coordinates, k is the incident electron momentum and

$$H = \begin{pmatrix} T_N + V_1 & W_{1,2} \\ W_{2,1} & T_N + V_2 \end{pmatrix}, \tag{12}$$

in which T_N denotes the nuclear kinetic operator; V_a, with $a = 1, 2$, denotes the complex potential surface of each of the two resonances; and the off-diagonal matrix elements $W_{a,b}$ denote the couplings between the resonance states. In Eq. (11) the nuclear wave function is a two-component vector,

$$\vec{\xi}(R) = \begin{pmatrix} \xi_1(R) \\ \xi_2(R) \end{pmatrix}, \tag{13}$$

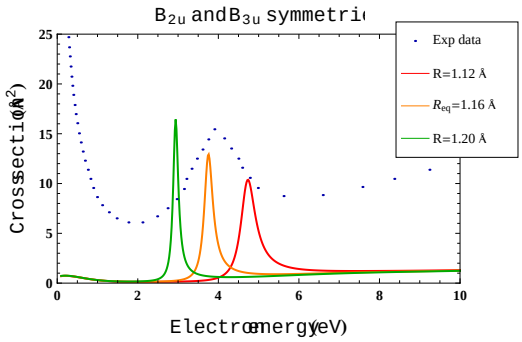

FIG. 4: Electron-CO_2 total cross section for the degenerate B_{2u} and B_{3u} symmetries of D_{2h}, calculated at three different internuclear distances. The experimental data are taken from Ref. [33].

$\vec{V}_{dk}$ contains the discrete-state–continuum couplings for the two resonances,

$$\vec{V}_{dk} = \begin{pmatrix} V_{d_1 k} \\ V_{d_2 k} \end{pmatrix} , \tag{14}$$

, and $\chi_i(R)$ is the initial vibrational state of the neutral molecule potential. The T-matrix can be now rewritten as:

$$\begin{aligned} T_{if}(E) &= \langle \chi_f^* | \vec{V}_{dk}(\epsilon', R) | \vec{\xi} \rangle \\ &= \int dR\, \chi_f^*(R)\, \vec{V}_{dk}(\epsilon', R)\, \vec{\xi}(R) \\ &= \int dR\, \chi_f^*(R)\, \vec{V}_{dk}(\epsilon', R)\, (H - E)^{-1}\, \vec{V}_{dk}(\epsilon, R)\, \chi_i(R) . \end{aligned} \tag{15}$$

Once the T-matrix is known, the total cross section can be finally calculated by [27]

$$\sigma_{v_i, v_f} = \frac{4\pi^3}{k^2} |T_{if}|^2 . \tag{16}$$

VI. ELECTRON-CO_2 RESULTS

A common feature of polyatomic molecules, which is consequence of the multidimensional nature of the system, is the so-called stretch-bend 'Fermi resonance', which refers to an accidental degeneracy between certain vibrational modes. In the case of CO_2, the first Fermi resonance is between the pure symmetric stretching mode $\eta_{100} = (1, 0, 0)$ and pure bending mode $\eta_{020} = (0, 2, 0)$ which are nearly degenerate (Fermi dyad) and they mix, about 50%, to form two physical state [28, 34]:

$$\begin{aligned} \eta_I &= a\, \eta_{100} - b\, \eta_{020} \qquad \text{(lower Fermi)} , \\ \eta_{II} &= b\, \eta_{100} + a\, \eta_{020} \qquad \text{(upper Fermi)} . \end{aligned} \tag{17}$$

Below we ignore this mixing and only address the symmetric stretching mode.

The CO_2 potential energy curve was calculated using MOLPRO [35], an aug-cc-pVQZ basis and the coupled-cluster model. The UK polyatomic R-matrix code of UK-R-matrix code [36, 37] was used for the scattering calculations. A Static Exchange plus Polarization (SEP) model, and the same basis used for CO_2, was used to calculate the complex potential energy curve for CO_2^-. The R-matrix calculations were performed on a grid of fixed internuclear distances. The position and width of the resonant state was then calculated by fitting the corresponding eigenphases sum with a Breit-Wigner function [38].The resonance curve for the symmetric stretch was obtained by changing the internuclear C-O separation. Fig. 4 shows the total cross sections, corresponding to the eigenphases calculated at three different geometries and for two degenerate symmetries, B_{2u} and B_{3u}, of D_{2h} group. The position of the theoretical peak at equilibrium distance is close to the maximum in the experimental data and the peak position shifts as the internuclear distance changes.

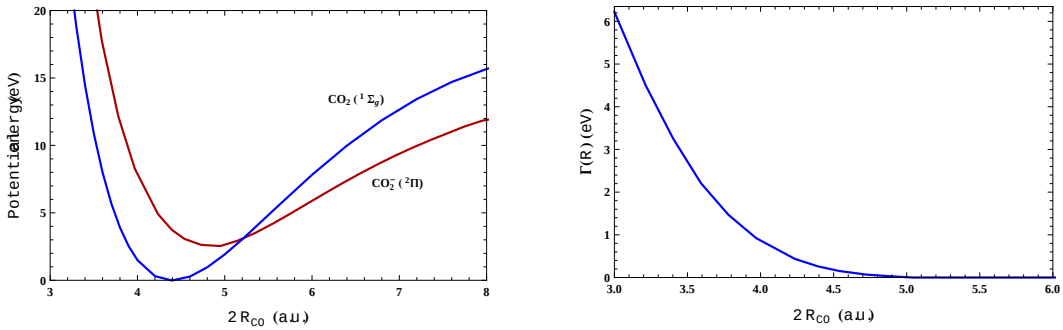

FIG. 5: Curves for the symmetric stretching mode: Left, potential energy curves for CO_2 and CO_2^-; Right, the corresponding resonance width. Both quantities are shown as a function of the O-O distance, which is twice the C-O bond length.

The computed potential energy curves for CO_2 and CO_2^- are reported in Fig. 5 with the resonance width $\Gamma(R)$.

Accidentally the 'boomerang effect' indicates that the resonance lifetime is about equal to the period of the linear symmetrical-stretching oscillation; using this observation it is justified, in a first approximation, to reduce the multidimensional problem of vibrational excitation in CO_2 to a simpler problem in one dimension involving only the linear symmetric-stretch coordinate [26]. Figs. 6, 7 and 8 show some preliminary results for symmetric stretching cross sections calculated for the first few vibrational levels compared with other approaches and experimental data. In particular Fig. 7 compares the calculated pure $(0,0,0) \rightarrow (1,0,0)$ transition with the results of Allan [28] for the Fermi dyad. As proposed by Allan, the FRII component refers predominantly to excitation of the symmetric stretch and the smaller FRI cross section predominantly to bending excitation.

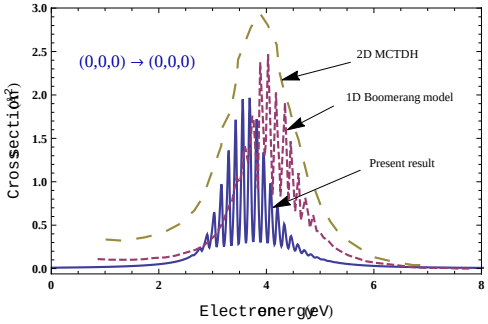

FIG. 6: Elastic electron–CO_2 resonant cross section: solid line refers to the present 1D results, short-dashed line is a 1D boomerang model and the long-dashed line is a multidimensional calculation (MCTDH) [34].

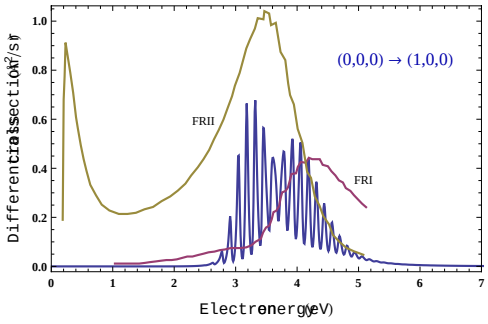

FIG. 7: The pure linear symmetric stretching $(0,0,0) \rightarrow (1,0,0)$ transition (blue line) compared with the experimental result of Allan [28], denoted by FRI and FRII, which refer to the Fermi dyad components as described in Eq. (17).

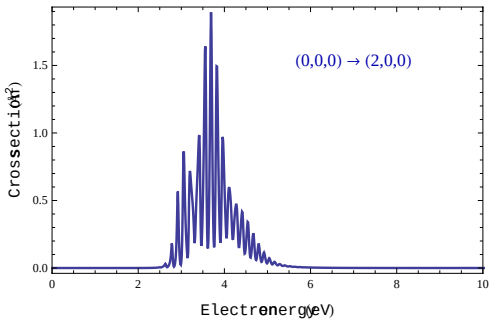

FIG. 8: Electron–CO_2 pure linear symmetric stretching $(0,0,0) \rightarrow (2,0,0)$ transition.

Fig. 9 shows the cross sections (left panel) and the corresponding rate coefficients (right panel) as a function of the electron energy, for the vibrational transitions $(0,0,0) \rightarrow (v_f,0,0)$, where $v_f = 0,1,5,10$. The rate coefficients were calculated by assuming a Maxwellian electron energy distribution function. The typical decreasing trend with the final vibrational levels is observed in both the figures.

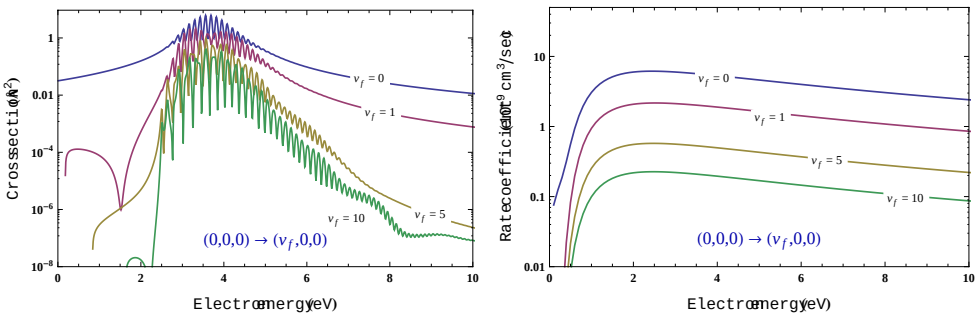

FIG. 9: Electron–CO_2 cross sections (left panel) and rate coefficients (right panel) are shown for the transition $(0,0,0) \rightarrow (v_f,0,0)$ where $v_f = 0,1,5,10$.

VII. ELECTRON-DIATOMIC MOLECULES RESONANT COLLISIONS

A. N_2, NO and O_2 molecules

Electron-impact cross sections and rate coefficients have also been calculated for diatomic nitrogen, nitric oxide and oxygen molecules, relevant for terrestrial atmosphere. The calculations were performed for the following RVE processes, linking different ground state vibrational levels [5, 10],

$$e^- + \mathrm{N_2}(\mathrm{X}\ ^1\Sigma_g^+, v_i = 0-64, J) \rightarrow \mathrm{N_2^-}(\mathrm{X}\ ^2\Pi_g) \rightarrow e^- + \mathrm{N_2}(\mathrm{X}\ ^1\Sigma_g^+, v_f = 0-64, J), \tag{18}$$

$$e^- + \mathrm{NO}(\mathrm{X}\ ^2\Pi, v_i = 0-54, J) \rightarrow \mathrm{NO^-}(^3\Sigma^-, ^1\Delta, ^1\Sigma^+) \rightarrow e^- + \mathrm{NO}(\mathrm{X}\ ^2\Pi, v_f = 0-54, J), \tag{19}$$

$$e^- + \mathrm{O_2}(\mathrm{X}\ ^3\Sigma_g^-, v_i = 0-41, J) \longrightarrow \mathrm{O_2^-}(^2\Pi_g, ^2\Pi_u, ^4\Sigma_u^-, ^2\Sigma_u^-) \longrightarrow e^- + \mathrm{O_2}(\mathrm{X}\ ^3\Sigma_g^-, v_f = 0-41, J)\,, \tag{20}$$

where, in all cases, the molecule, initially in the (v_i, J) ro-vibrational level, is excited by electron-impact to the final level (v_f, J). The range of the vibrational quantum numbers is shown in parenthesis. The process for N_2 occurs through the formation of the resonant state $N_2^-(^2\Pi_g)$, while in the case of NO and O_2 multiple contributions come from the three states $^3\Sigma^-, ^1\Delta, ^1\Sigma^+$ for NO and from the four resonant states $^2\Pi_g, ^2\Pi_u, ^4\Sigma_u^-, ^2\Sigma_u^-$ for O_2. A complete account of the calculations is reported in Refs. [5, 10]. Here we limit ourselves only to the discussion of some relevant result.

The RVE calculations were extended to all the possible transitions $(v_i, J) \rightarrow (v_f, J)$ among all the vibrational levels, and for fixed different J values (rotationally elastic processes) running from 0 to 150 for N_2 and NO and from 1 to 151 for O_2 as allowed by nuclear symmetry considerations [10]. Examples of cross sections for process (18) are shown in Fig. 10a-b, for some elastic and inelastic transitions respectively. An evident feature is the strong oscillations present in all the curves which reproduce the vibrational structures of the resonant state $N_2^-(\mathrm{X}\ ^2\Pi_g)$. The cross section peaks, in fact, are placed at an energy corresponding to the resonant vibrational eigenvalues of N_2^- [9]. These structures disappear abruptly at the energy threshold of the vibrational continuum of the resonant state. Correspondingly, Fig. 10c-d shows the rate coefficients for the transitions given in Fig. 10a-b, calculated by adopting a Maxwellian electron energy distribution function. The rates show a very smooth behavior and no memory is retained of the vibrational oscillations in the cross sections. The trend with respect to the vibrational quantum number is that expected for

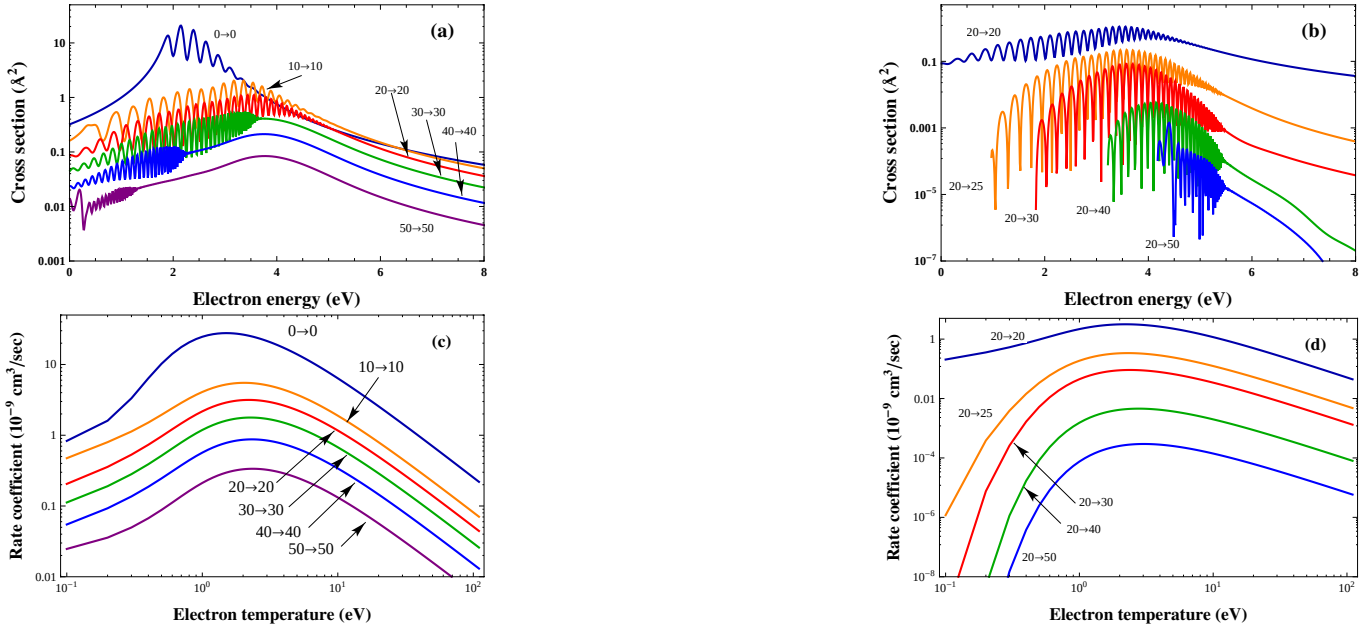

FIG. 10: Resonant e-N_2 vibrational excitation cross sections (a, b) and corresponding rate coefficients (c, d) for $v_i = v_f$ and $v_i = 20 \rightarrow v_f \geq v_i$, respectively. The rotational quantum number is set to $J = 0$.

resonant collisions. In fact, the rates and the cross sections decrease as the vibrational level is increased. This, in a

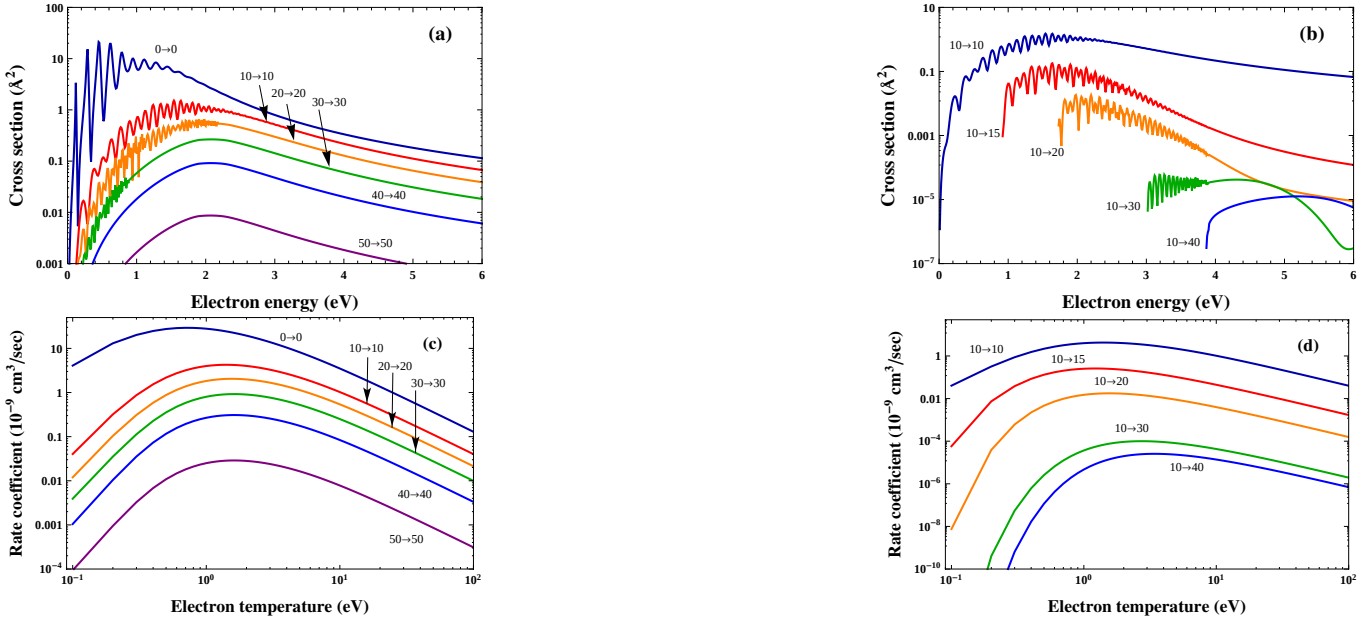

FIG. 11: Same as Fig. 10 for NO molecule.

simplified model for resonant collisions [39], is probably due to the product of the Franck-Condon factors for the two transitions $v_i \to v_r$ and $v_r \to v_f$, (v_r is the resonance vibrational level) involved in the process. The Franck-Condon overlap, in fact, is expected to reduce as the v_i or v_f vibrational levels increase, due to the increasingly rapid wave function oscillations.

Analogous comments hold for the cross sections and rates for RVE process (19) involving NO molecules, shown in Fig 11a-d.

The RVE process (20) for the O_2 molecule gives the cross sections shown in Fig. 12. These display fast oscillations below ∼4 eV which are strongly reduced, but still present, for energies above this value. These structures are due to the different contributions, in different energy ranges, coming from the four resonant states involved in the process. For this molecule the rates for the excitation of low v_i states also show some structure.

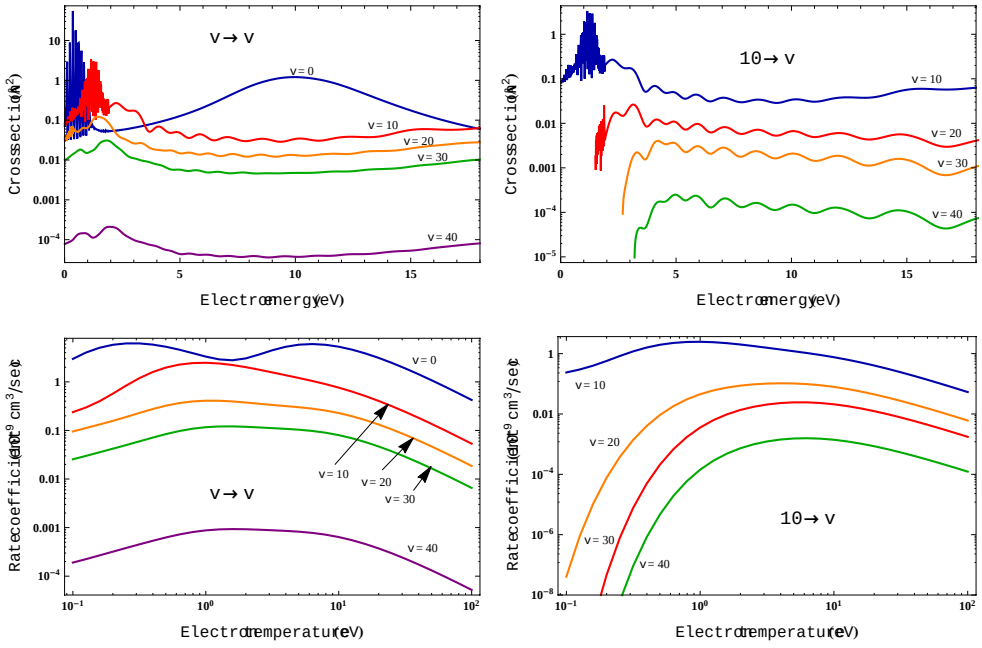

FIG. 12: Same as Fig. 10 for O_2 molecule with $J = 1$ allowed by nuclear symmetry [10].

B. CO molecule

Cross sections and rate coefficients were calculated also for the resonant vibrational excitations involving the vibrationally excited CO molecule. This species, together with carbon dioxide, is the main component of the Venusian and Martian atmospheres. The process considered is,

$$e^- + \mathrm{CO}(\mathrm{X}\ ^1\Sigma^+, v_i = 0-80) \rightarrow \mathrm{CO}^-(^2\Pi) \rightarrow e^- + \mathrm{CO}(\mathrm{X}\ ^1\Sigma^+, v_f = 0-80)\,, \tag{21}$$

occurring through the resonant state $\mathrm{CO}^-(^2\Pi)$ and involving 81 vibrational levels. Cross sections and rates, shown in Fig. 13, are quite similar to the previous cases, except for the appearance of sharp peaks just below the vibrational continuum of the resonant state for some transitions.

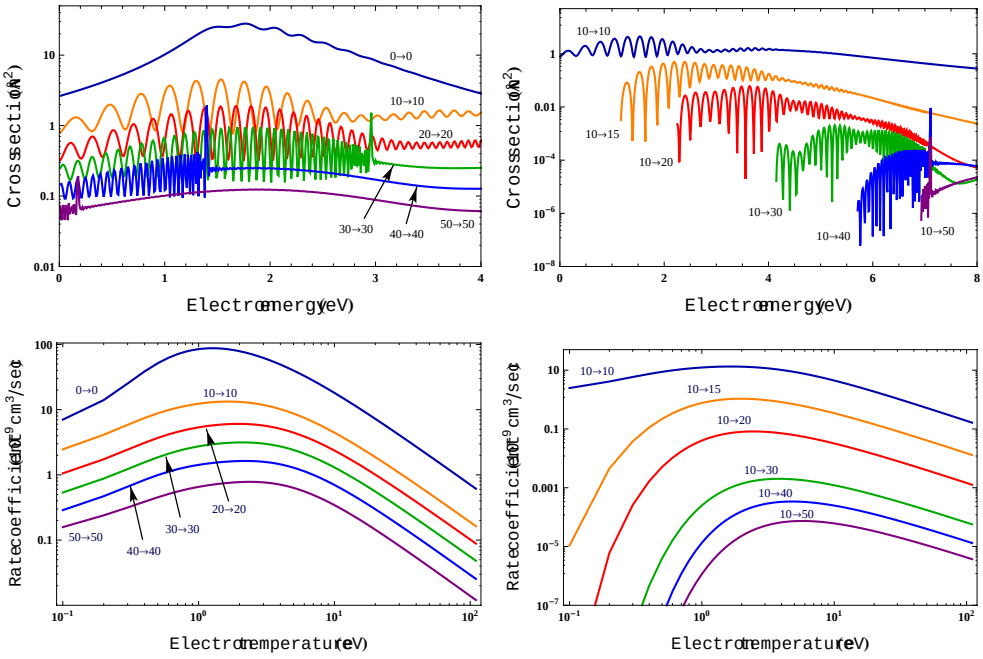

FIG. 13: Same as Fig. 10 for CO molecule with $J = 0$.

C. Single quantum transitions

The RVE elastic transitions show the largest cross sections and rates. However they play no role in redistributing energy among the internal degrees of freedom of the molecular species. The major role, in this case, is played by transitions which change the vibrational state by just one quantum, $v_i \rightarrow v_i \pm 1$, whose cross sections are comparable with the elastic ones. Figs. 14 and 15 show the cross sections and the corresponding rates coefficients for the transitions $v_i \rightarrow v_i + 1$ for the RVE processes involving the diatomic molecules.

D. H_2 molecule

Resonant processes for H_2 molecule, the main component of the giant planets, have been studied over a long period. This has resulted in a vast theoretical and experimental literature on the topic, stimulated by the importance of hydrogen plasmas for both astrophysical and technological research. Sets of cross sections and rate coefficients have been calculated for $H_2(v_i)$ by different authors [40–44] for dissociative attachment and vibrational excitations according to the reactions,

$$e^- + \mathrm{H}_2(\mathrm{X}\ ^1\Sigma_g^+, v_i = 0-14) \rightarrow \mathrm{H}_2^-(\mathrm{X}\ ^2\Sigma_u^+) \rightarrow \mathrm{H}(1s) + \mathrm{H}^-(1s^2), \tag{22}$$

$$e^- + \mathrm{H}_2(\mathrm{X}\ ^1\Sigma_g^+, v_i = 0-14) \rightarrow \mathrm{H}_2^-(\mathrm{X}\ ^2\Sigma_u^+) \rightarrow e^- + \mathrm{H}_2(X\ ^1\Sigma_g^+, v_f = 0-15), \tag{23}$$

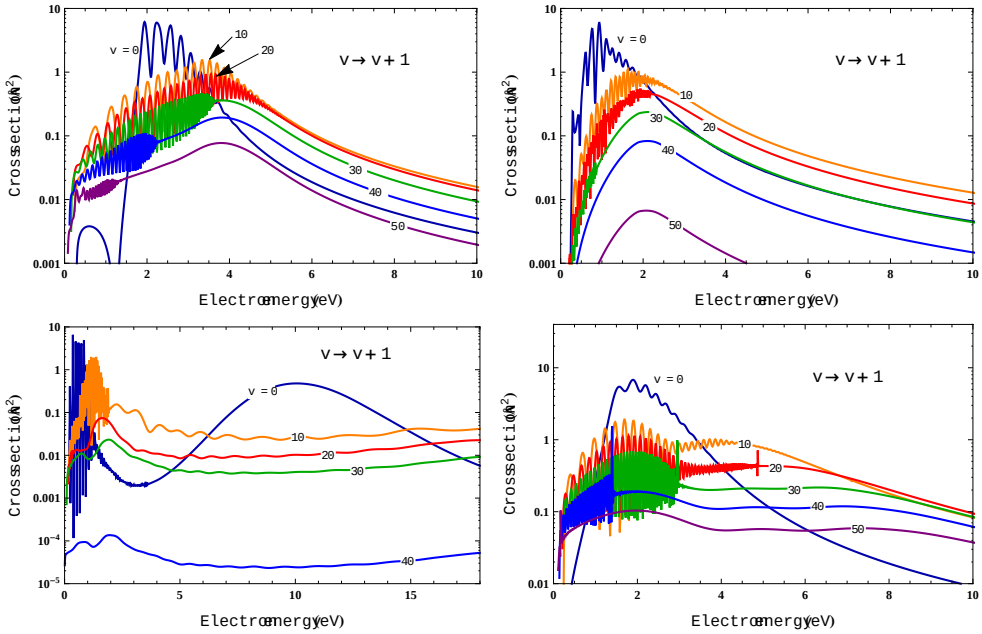

FIG. 14: RVE cross sections for the single quantum excitations ($\Delta v = 1$) in N_2 (upper-left panel), NO (upper-right panel), O_2 (lower-left panel), CO (lower-right panel).

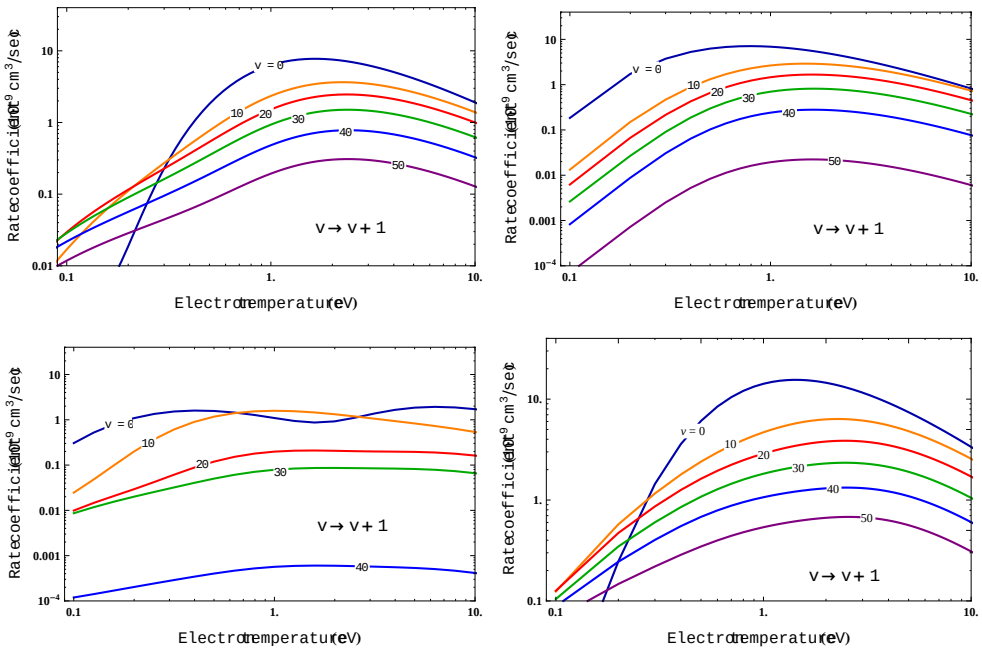

FIG. 15: Same as Fig. 14 for the rate coefficients.

both occurring through the ground resonant electronic state $X\ ^2\Sigma_u^+$ of the H_2^- ion. Calculations have also been extended to the process involving the first excited valence state $B\ ^2\Sigma_g^+$ [45] and to RVE leading to electron impact dissociation of H_2 [42, 46–48].

More recently, cross sections for DEA and RVE processes, involving a Rydberg excited resonance, were calculated in Refs. [7–9]. Complete sets of *ab initio* cross sections and rate coefficients were obtained for the process

$$e^- + H_2(X\ ^1\Sigma_g^+, v_i = 0 - 14) \rightarrow H_2^-(^2\Sigma_g^+) \rightarrow H(n = 2) + H^-(1s^2), \tag{24}$$

occurring through the Rydberg excited $H_2^-(^2\Sigma_g^+)$, and yielding to the production of a negative ion and an excited

atom. Cross sections and rates are shown in Fig. 16. In this case the cross sections for $v_i = 0$ shows the smallest values. For high levels ($v_i > 5$) oscillations start to appear in the cross sections mainly determined by the vibrational continuum of the Rydberg state [9]. The variation of the rates with the vibrational quantum number is contained, at the peaks, within a factor of 100. This behavior is quite different for the case of the shape resonance in process (22) where, as is well-known, the rates increase with the initial vibrational levels by several orders of magnitude [45].

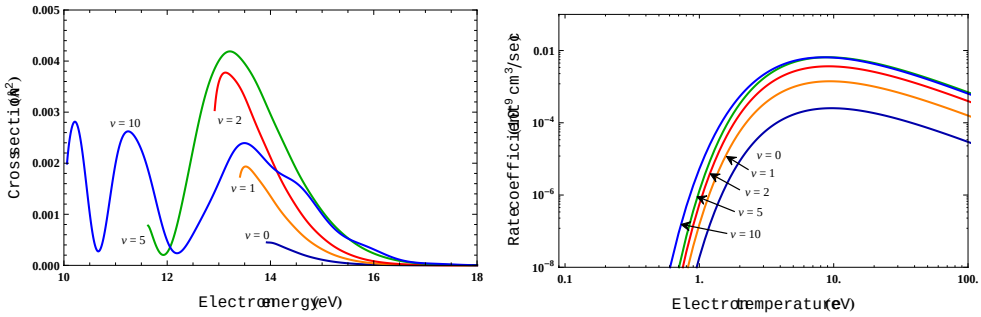

FIG. 16: Resonant e-H_2 dissociative attachment cross sections (left panel) and corresponding rate coefficients (right panel) for process (24). For clarity, the cross sections and rates are shown for some of the vibrational levels, as indicated in the figure.

Differential cross sections were calculated also for RVE process occurring via the Rydberg resonance [7], namely,

$$e^- + \mathrm{H}_2(\mathrm{X}\ ^1\Sigma_g^+, v_i = 0) \rightarrow \mathrm{H}_2^-(^2\Sigma_g^+) \rightarrow e^- + \mathrm{H}_2(\mathrm{X}\ ^1\Sigma_g^+, v_i = 0 - 14). \tag{25}$$

The cross sections have been obtained only for the transition $0 \rightarrow v_f = 0 - 14$. In Fig. 17 the differential RVE cross sections are shown for $v_i = 4$, 5, 6, 7, at a scattering angle of 85 degrees. The theoretical calculations are in satisfactory agreement with the experimental data [39]. Extension to all the vibrational transitions ($v_i, v_f > 0$) is in progress [49].

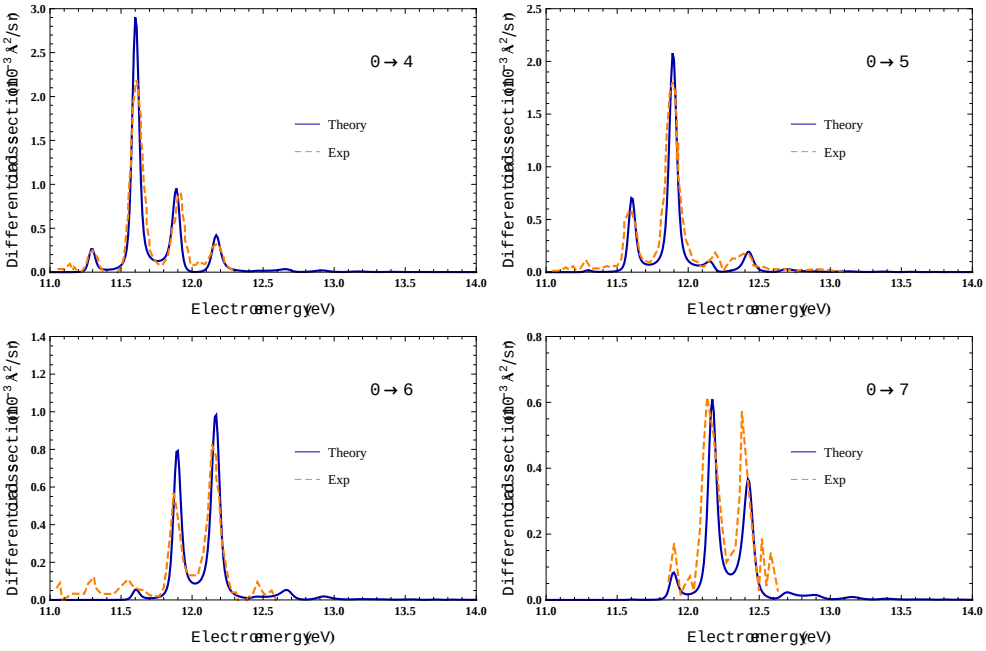

FIG. 17: Differential cross sections at a scattering angle of 85° for the resonant vibrational excitation of H_2 molecule through the process (25) for the transition $0 \rightarrow v_f = 4, 5, 6, 7$. The theoretical calculations (*solid lines*) [7] are compared with the experimental data (*dashed lines*) [39].

VIII. CONCLUSIONS

Non-resonant electron-impact total cross sections are presented for the vibro-electronic excitation of the $N_2(X\ ^1\Sigma_g^+)$ molecule to the electronic states $b, c, o\ ^1\Pi_u$ and $b', c', e'\ ^1\Sigma_u^+$, taking into account the coupling among the three states for each symmetry. The results obtained are compared with previous (uncoupled) calculations and with experiment. For the $^1\Pi_u$ symmetry, good agreement for cross sections is found for the b state with the results obtained by the Gryzinski method. Some discrepancy is observed however for the c and o states. This is attributed to the lower number of vibrational levels included in the present calculations, which recognize that higher levels lead to dissociation through a predissociation mechanism involving the continuum of the b states. Any comparison with experiments must take into account both the limited number of vibrational levels observed in the measurements and the emission intensity assignment which, as reported in literature, has been applied within a state-decoupled frame. Once these two restrictions are implemented in the preset theoretical calculations, the resulting cross sections are to be found in good agreement with the experimental data.

Good agreement with the experiments is found also for the excitation to the $^1\Sigma_u^+$ state of N_2. However, the comparison with the measurements again required the inclusion of a lower number of vibrational levels in the calculations, in order to make the theoretical results consistent with the experiments.

Electron-impact theoretical cross sections and rate coefficients, for the resonant vibration excitation, for the symmetric stretching mode of the CO_2 molecule only, are calculated using the *local complex-potential* model for resonant collisions. The potential curves for both $CO_2(X\ ^1\Sigma_g^+)$ molecule and $CO_2^-(^2\Pi_u)$ resonant state are calculated using the MOLPRO electronic structure code. Resonance positions and widths are calculated by using the R-matrix method. The cross sections obtained are found to be in good agreement with previous theoretical calculations and with experiment. Rate coefficients are also calculated for the transition $(0,0,0) \rightarrow (v_f,0,0)$ with $v_f = 0, 1, 5, 10$, for electron temperatures below 10 eV. No experimental or theoretical data are available for comparison with these rates.

The calculations presented in this work aim to provide input data (cross sections and rate coefficients) for models of planetary atmospheres and, in particular, are intended to acquire knowledge and information useful for (re)-entry problems in space exploration. It is with this perspective that we review all the recent calculations performed by our collaboration for different molecules. In particular we have considered the resonant vibrational excitation of N_2, O_2 and NO by electron impact, important for the Earth re-entry conditions, and of CO molecule, which, together with carbon dioxide, is the main component of the atmospheres of Mars and Venus. Finally, we also review the resonant vibrational excitations and dissociative electron attachment processes for H_2 molecule, the main component of gaseous planets, occurring through the $^2\Sigma_g^+$ Rydberg-excited electronic state of H_2^- molecular ion. The RVE cross section calculations, for this system, are presently limited to transitions starting from the $v_i = 0$ only. Extension of calculations to the other levels ($v_i > 0$) is in progress [49].

The full set of numerical cross sections and rate coefficients, presented in this paper, is available at the website: `http://users.ba.cnr.it/imip/cscpal38/phys4entry/database.html`

Acknowledgements

The present research has received funding from the European Community's Seventh Framework Programme (FP7/2007-2013) under grant agreement number 242311. One of the authors (AL) would also like to thank support from contract C505-IMIP under ESA Contract 21029.

[1] M. Capitelli, R. Celiberto, F. Esposito, and A. Laricchiuta, Plasma Process. Polym. **6**, 279 (2009).
[2] I. Shimamura and K. Takayanagi, eds., *Electron-molecule collisions*, (Plenum Press - New York and London, 1984).
[3] R. Celiberto, *"Electron-molecule collision processes in non-equilibrium molecular plasmas"*, in ESCAMPIG XXI, Viana do Castelo, Portugal, July 10-14 (2012).
[4] M. Capitelli, R. Celiberto, G. Colonna, G. D'Ammando, O. D. Pascale, P. Diomede, F. Esposito, C. Gorse, A. Laricchiuta, S. Longo, et al., Plasma Phys. Control. Fusion **53**, 124007 (2011).
[5] V. Laporta, R. Celiberto, and J. M. Wadehra, Plasma Sources Sci. Technol. **21**, 055018 (2012).
[6] V. Laporta, C. M. Cassidy, J. Tennyson, and R. Celiberto, Plasma Sources Sci. Technol. **21**, 045005 (2012).
[7] R. Celiberto, R. K. Janev, J. M. Wadehra, and A. Laricchiuta, Phys. Rev. A **77**, 012714 (2008).
[8] R. Celiberto, R. K. Janev, J. M. Wadehra, and A. Laricchiuta, Phys. Rev. A **80**, 012712 (2009).
[9] R. Celiberto, R. K. Janev, J. M. Wadehra, and J. Tennyson, Chem. Phys. **398**, 206 (2012), in *Chemical Physics of Low-Temperature Plasmas* (special issue in honour of Prof Mario Capitelli).

[10] V. Laporta, R. Celiberto, and J. Tennyson, Plasma Sources Sci. Technol. **22**, 025001 (2013).
[11] W. C. Ermler, A. D. McLean, and R. S. Mulliken, J. Phys. Chem. **86**, 1305 (1982).
[12] D. Stahel, M. Leoni, and K. Dressler, J. Chem. Phys. **79**, 2541 (1983).
[13] P. C. Cosby, J. Chem. Phys. **98**, 9544 (1993).
[14] B. R. Lewis, S. T. Gibson, W. Zhang, H. Lefebvre-Brion, and J.-M. Robbe, J. Chem. Phys. **122**, 144302 (2005).
[15] D. Spelsberg and W. Meyer, J. Chem. Phys. **115**, 6438 (2001).
[16] M. A. Khakoo, C. P. Malone, P. V. Johnson, B. R. Lewis, R. Laher, S. Wang, V. Swaminathan, D. Nuyujukian, and I. Kanik, Phys. Rev. A **77**, 012704 (2008).
[17] C. P. Malone, P. V. Johnson, X. Liu, B. Ajdari, I. Kanik, and M. A. Khakoo, Phys. Rev. A **85**, 062704 (2012).
[18] D. A. Little and J. Tennyson, J. Phys. B: At. Mol. Opt. Phys. (2013), submitted.
[19] M. Capitelli and R. Celiberto, in "Novel Aspects of Electron-Molecule Collisions", edited by K.H. Becker p. 283 (1998).
[20] B. R. Lewis, S. S. Banerjee, and S. T. Gibson, J. Chem. Phys. **102**, 6631 (1995).
[21] A. G. Abrashkevich and D. G. Abrashkevich, Comput. Phys. Comm. **113**, 105 (1998).
[22] S. Adamson, V. Astapenko, M. Deminskii, A. Eletskii, B. Potapkin, L. Sukhanov, and A. Zaitsevskii, Chem. Phys. Lett. **436**, 308 (2007).
[23] S. T. Gibson and B. R. Lewis, J. Electron Spectrosc. Relat. Phenom. **80**, 9 (1996).
[24] E. C. Zipf and M. R. Gorman, J. Chem. Phys. **73**, 813 (1980).
[25] M. A. Morrison, N. F. Lane, and L. A. Collins, Phys. Rev. A **15**, 2186 (1977).
[26] I. Cadez, F. Gresteau, M. Tronc, and R. I. Hall, J. Phys. B: At. Mol. Opt. Phys. **10**, 3821 (1977).
[27] C. W. McCurdy, W. A. Isaacs, H.-D. Meyer, and T. N. Rescigno, Phys. Rev. A **67**, 042708 (2003).
[28] M. Allan, Phys. Rev. Lett. **87**, 033201 (2001).
[29] L. A. Morgan, Phys. Rev. Lett. **80**, 1873 (1998).
[30] J. Tennyson and L. A. Morgan, Phil. Trans. A **357**, 1161 (1999).
[31] S. Mazevet, M. A. Morrison, L. A. Morgan, and R. K. Nesbet, Phys. Rev. A **64**, 040701 (2001).
[32] M. Allan, J. Phys. B: At. Mol. Opt. Phys. **35**, L387 (2002).
[33] Y. Itikawa, J. Phys. Chem. Ref. Data **31**, 749 (2002).
[34] T. N. Rescigno, W. A. Isaacs, A. E. Orel, H.-D. Meyer, and C. W. McCurdy, Phys. Rev. A **65**, 032716 (2002).
[35] H.-J. Werner, P. J. Knowles, G. Knizia, F. R. Manby, M. Schütz, et al., *Molpro, version 2010.1, a package of ab initio programs* (2010).
[36] J. Tennyson, Phys. Rep. **491**, 29 (2010).
[37] J. M. Carr, P. G. Galiatsatos, J. D. Gorfinkiel, A. G. Harvey, M. A. Lysaght, D. Madden, Z. Masin, M. Plummer, and J. Tennyson, Euro. J. Phys. D **66**, 58 (2012).
[38] J. Tennyson and C. J. Noble, Comput. Phys. Comm. **33**, 421 (1984).
[39] J. Comer and F. H. Read, J. Phys. B: At. Mol. Opt. Phys. **4**, 1055 (1971).
[40] J. M. Wadehra and J. N. Bardsley, Phys. Rev. Lett. **41**, 1795 (1978).
[41] J. N. Bardsley and J. M. Wadehra, Phys. Rev. A **20**, 1398 (1979).
[42] D. E. Atems and J. M. Wadehra, J. Phys. B: At. Mol. Opt. Phys. **26**, L759 (1993).
[43] J. Horáček, M. Čížek, K. Houfek, P. Kolorenč, and W. Domcke, Phys. Rev. A **73**, 022701 (2006).
[44] J. Horáček, M. Čížek, K. Houfek, P. Kolorenč, and W. Domcke, Phys. Rev. A **70**, 052712 (2004).
[45] J. M. Wadehra, Appl. Phys. Lett. **35**, 917 (1979).
[46] D. T. Stibbe and J. Tennyson, New J. Phys. **1**, 2 (1998).
[47] D. T. Stibbe and J. Tennyson, Astrophys. J. **513**, L147 (1999).
[48] C. S. Trevisan and J. Tennyson, Plasma Phys. Control. Fusion **44**, 1263 (2002).
[49] R. Celiberto, R. K. Janev, J. Tennyson, J. M. Wadehra, and V. Laporta, Phys. Rev. A, submitted (2013).

Molecular Physics of Elementary Processes relevant to Hypersonics: atom-molecule, molecule-molecule and atoms-surface processes

A. Laganà, A. Lombardi, and F. Pirani
Dipartimento di Chimica, Università di Perugia, 06100 Perugia, Italy

P. Gamallo and R. Sayós
Departament de Química Física and Institut de Química Teórica i Computacional, Universitat de Barcelona, C. Martí i Franqués 1, 08028 Barcelona, Spain

I. Armenise, M. Cacciatore, F. Esposito and M. Rutigliano
CNR-IMIP (Institute of Inorganic Methodologies and Plasmas), Via Amendola 122/D, 70126 Bari, Italy

In the present chapter some prototype gas and gas-surface processes occurring within the hypersonic flow layer surrounding spacecrafts at planetary entry are discussed. The discussion is based on microscopic dynamical calculations of the detailed cross sections and rate coefficients performed using classical mechanics treatments for atoms, molecules and surfaces. Such treatment allows the evaluation of the efficiency of thermal processes (both at equilibrium and non equilibrium distributions) based on state-to-state and state specific calculations properly averaged over the population of the initial states. The dependence of the efficiency of the considered processes on the initial partitioning of energy among the various degrees of freedom is discussed.

I. INTRODUCTION

The dissociated species produced in the hypersonic flows during a spacecraft planetary entry [1, 2] may significantly alter both the heat content of the surrounding gas layer and the heat load put on the thermal protection system (TPS) of the vehicle. This is due to both homogeneous [3, 4] and heterogeneous [5, 6] processes occurring around and at the surface of the vehicle, respectively. Such processes may be reactive (with production of new species and exchange of energy) or non reactive (with exchange of energy only). Typically, they may involve either collisions of atoms (or molecules) with molecules or collisions of atoms with surfaces.

Depending on the re-entry planet (or satellite) the involved gas phase chemical systems may vary significantly and, in the case of Earth, nitrogen (atom-diatom and diatom-diatom) systems have been, as expected, the most investigated ones [7–9]. Similar calculations have been performed also for hydrogen and oxygen systems [10–14]. As to gas surface processes, because of the fact that the characteristics of the actually used TPS materials are usually undisclosed, modeling has been performed on simpler materials like α- and β-quartz or β-cristobalite.

Traditionally, this kind of dynamical calculations are performed to the end of evaluating fully thermalized rate coefficients $k(T)$. More recently, however, rate coefficients have also been calculated for distinct internal (initial i and final f) states to evaluate the corresponding detailed rate coefficients $k_{i,f}(T_{\rm col})$ (thermalized only for the collision energy $E_{\rm col}$ distribution associated with the chosen collision temperature $T_{\rm col}$). If only a subset of internal states i' (say vibrations) is explicitly considered, the remaining degrees (say rotations) can be thermalized using a separate rotational temperature $T_{\rm rot}$ or the same as the collision one [7, 8, 10, 11, 13]. Such detailed computational studies bear rich information about energy disposal and state population (and as a consequence about microscopic mechanisms) especially when non equilibrium distributions are considered and rate coefficients are linked to the $\sigma_{i,f}(E_{\rm col})$ state-to-state cross section function of the $E_{\rm col}$ collision energy.

In order to carry out accurately such detailed dynamical calculations, properly formulated atomic and molecular interactions have to be used. This makes the cost of the related massive computational campaigns feasible only by exploiting the High Performance Computing (HPC) power of the new generation of supercomputers (see PRACE [15]). However, because of the difficulty of getting timely grants able to allow a continuous and systematic performing of computational campaigns, it is expedient to exploit grid computing. Through the affiliation to the Virtual Organization (VO) COMPCHEM [16] (that gathers together several scientists operating in the field of Chemistry, Molecular and Materials Sciences and Technologies (CMMST)) it is, in fact, possible to run massive calculations of the dynamical properties of the chemical systems of interest. The mentioned VO, in fact, is part of the European Grid Infrastructure (EGI) [17] and supports the use of the European grid in building collaborative computational endeavours for the study of complex molecular systems. This is grounded on the use of the various sections of the so called Grid Empowered Molecular Simulator (GEMS) [18, 19] that coordinates in a single workflow the construction of potential energy surfaces, the integration of dynamical equations and the statistical averaging of their outcomes to evaluate in a full *ab initio* fashion rate coefficients.

Accordingly the paper is organized as follows: The basic theoretical and computational ingredients of such calculations are sketched in section 2. Three typical applications of such approach to systems relevant to the modeling of spacecraft re-entry (atom-molecule, molecule-molecule and atom-surface) are discussed in sections 3, 4 and 5, respectively.

II. THEORETICAL AND COMPUTATIONAL OUTLINES

Kinetic models of use in gas dynamics and plasma chemistry applications usually rely on a database of thermal rate coefficients. However, in order to link them to detailed properties of both theoretical and experimental origin, $k(T)$ is better decomposed into the state-to-state rate coefficients of the intervening processes as follows

$$k(T) = \sum_i \sum_f \frac{g_i e^{-\varepsilon_i/k_B T_{\rm int}}}{Q_{\rm int}(T_{\rm int})} k_{i,f}(T_{\rm col}) \tag{1}$$

In Eq. 1 g_i is the multiplicity of the initial eigenstate i of energy ε_i, k_B is the Boltzmann constant and $Q_{\rm int}(T_{\rm int})$ is the partition function of the internal energy at the temperature $T_{\rm int}$. In the case of atom-diatom processes, the roto-vibrational state vj of the initial diatom to the roto-vibrational state $v'j'$ of the final diatom detailed rate coefficient $k_{vj,v'j'}(T_{\rm col})$ (i.e., $k_{i,f}(T_{\rm col})$ term in Eq. 1) is formulated as

$$k_{vj,v'j'}(T_{\rm col}) = \sqrt{8/k_B^3 T_{\rm col}^3 \pi \mu} \int_0^\infty E_{\rm col} \sigma_{vj,v'j'}(E_{\rm col}) e^{-E_{\rm col}/k_B T_{\rm col}} dE_{\rm col} \tag{2}$$

In Eq. 2 μ is the reduced mass of the reactants, $E_{\rm col}$ is the collision energy of the system and $\sigma_{vj,v'j'}(E_{\rm col})$ is the corresponding detailed state-to-state cross section. Detailed state-to-state cross sections are then related to the state-to-state partial (fixed value of the total angular momentum quantum number J) probabilities $P^J_{vj,v'j'}(E_{\rm col})$ as follows

$$\sigma_{vj,v'j'}(E_{\rm col}) = \frac{\pi}{{\rm k}^2_{vj}} \sum_{J=0}^{\infty} (2J+1) P^J_{vj,v'j'}(E_{\rm col}) \tag{3}$$

in which ${\rm k}^2_{vj}$ is the reactant wavenumber while $P^J_{vj,v'j'}(E_{\rm col})$ can be derived from the exact quantum $\mathbf{S}$ matrix elements (calculated at fixed value of J by integrating related exact quantum scattering equations [20] using a fully *ab initio* potential energy surface (PES)) by means of the following relationship:

$$P^J_{vj,v'j'}(E_{\rm col}) = \frac{1}{2j+1} \sum_{\Lambda=-\Lambda_{\rm max}}^{\Lambda_{\rm max}} \sum_{\Lambda'=-\Lambda'_{\rm max}}^{\Lambda'_{\rm max}} \left| S^J_{vj\Lambda,v'j'\Lambda'}(E_{\rm col}) \right|^2 \tag{4}$$

with Λ (Λ') being the initial (final) body fixed projection of the total angular momentum $\mathbf{J}$ and $\Lambda_{\rm max} = \min(j, J)$. To carry out an exact calculation of the $\mathbf{S}$ matrix elements the nuclear Hamiltonian $\hat{H}_{\rm N}$ is applied to the Λ component of the time dependent partial wave $\Psi^{J\Lambda}(R, r, \Theta, t)$ (or similarly to the time independent analogue $\Psi^{J\Lambda}(R, r, \Theta)$). Most often, in order to evaluate cross sections and rate coefficients use is made of classical (cl) methods, which approximate the state-to-state probability as the fraction of the trajectories starting from state vj and ending in state $v'j'$, after all, trajectory calculations fully exploit the characteristic features of the High Throughput Computing technologies of EGI including the low level bridging of HTC with HPC [21]. This has allowed a straightforward use of the basic GEMS scheme because, as specified below in more detail, related PESs are also formulated as empirical functional forms fitted to *ab initio* data [22]. As commented in the next sections, additional approximations are needed when moving towards more complex systems (like molecule-molecule and atom/molecule-surface systems [23]).

III. ATOM-DIATOM SYSTEMS

As atom-diatom case we consider here the O + $N_2(vj)$ and N + $O_2(vj)$ reactions for which the quasi-classical trajectory (QCT) method was adopted. Despite the scarcity of detailed (vibrational and rotational) experimental data to compare with, the theoretical interest for these reactions has been kept high because of their relevance in air kinetics [24]. Here we report on a systematic scan of the whole vibrational ladder in collision processes. As to the first system, the following reactive channels were considered:

$$\mathrm{O} + \mathrm{N_2}(vj) \rightarrow \mathrm{N} + \mathrm{NO}(v'j') \qquad \textit{reactive channel} \tag{5}$$

$$\mathrm{O} + \mathrm{N_2}(vj) \rightarrow \mathrm{O} + \mathrm{N} + \mathrm{N} \qquad \textit{dissociation} \tag{6}$$

though also non-reactive events (not reported here) were investigated. In the roto-vibrational energy exchange computational study, final rotation contributions are summed up, while initial rotational ones are averaged over Boltzmann distributions so as to mimic the dependence of the calculated quantities on the rotational temperature for a wide range of values. The target of such calculations were the computation of cross section values and their averaging in order to provide an estimate of the rate coefficients (inversion from rate coefficients to cross sections has shown neither to be reliable nor to be of general application [25]).

This allowed us to provide rate coefficient estimates also for non-equilibrium distributions and three body recombination rates [26], which in the case of fairly heavy species like oxygen and nitrogen are also likely to be the only contributions to recombination, because of the likely negligibility of resonant processes [26]. Concerning the O + N_2 reaction, the PESs adopted are those of Ref. [27] which are believed to be the best currently available for this system. The dynamics is calculated adiabatically on two PESs ($^3A''$ ground state, $^3A'$ first excited state). Then the results are summed up by weighting the two contributions with an electronic factor value of 1/3 [28]. For the N + O_2 reaction the PESs used are those of Ref. [29], with the ground state being $^2A'$ and the first excited one being a $^4A'$ state. Also in this case independent sets of results have been obtained on the two PESs which are then summed with 1/6 and 1/3 electronic factors respectively.

The software used for such calculations has been entirely developed by some of us [30], and then specifically adapted for distributed computations on the grid [17]. At each time step of the trajectory, a second integration is performed using a smaller step in order to check the accuracy of the integration (as discussed in Ref. [31] in this way a good

balance of accuracy and computational effort is achieved, due to the possibility of efficiently adapting the timestep on the run). In order to carry out the analysis, the center of mass translational energy was binned in 1000 intervals of 10 meV in the interval of values ranging from 1 meV to 10 eV so as to cover temperature intervals ranging from 300 to 10000 K. A uniform density of 5000 trajectories per Å of impact parameter and per eV of translational energy has been used in the calculations leading to a total number of integrated trajectories higher than 400 millions for each chemical system. Stratified sampling has been used in all these calculations, with typical maximum impact parameters in the range 4 to 7 Å. The whole ladder of initial vibrational states has been scanned together with a sufficient number of rotational states in order to reliably reconstruct the whole rotational distribution by interpolation. As a consequence, one can estimate the value of the rate coefficient at all accessible rotational temperatures. The roto-vibrational ladder of levels has been calculated using the WKB approximation directly from the asymptotes of the three body potential. Related results well compare with those of more accurate calculations.

As to the accuracy and reliability of the calculations, a comparison is given in Ref. [28], where quasi-classical and wave packet results concerning the reactive channels of O + N_2 reaction are shown together. The comparison is always excellent but at very low energies for the excited PES. A comparison of our results for the reaction channel with the well known quasi-classical results of Bose and Candler obtained on their PES [32] and with the Baulch et al. ones fitted to experimental data [33] is given in Fig. 1. From the figure it is apparent the good agreement of our results with the latter data while the agreement with the former (the theoretical ones) is not as good because they are quite lower in the whole temperature range. This, however, can be rationalized in terms of the significant differences of the two PESs and in particular by the presence in the newer surfaces of a C_{2v} minimum, as discussed in Ref. [28], that lacks in the older PESs. As to dissociation, a comparison between our results and those obtained from the fit of experimental data of Shatalov [34] is given in Fig. 2. In the Figure our results appear to closely follow the latter on the whole temperature range going from 2000 to 10000 K confirming the reliability of the PESs used. An analogous calculation has been performed for the N + O_2 collision, considering both abstraction reaction and dissociation channels. Also in this case the comparison is quite good, as can be seen in the following figures. In Fig. 3 the thermal reaction rate coefficient obtained in this work for the reaction:

$$N + O_2 \rightarrow NO + O \tag{7}$$

is shown as a red curve and compared with that of Sayós et al. obtained on the same PESs [35] (blue curve) and experimental data of Ref. [36] (green curve). The agreement looks quite satisfactory especially at intermediate temperatures. Concerning the comparison at high temperature, it is worth noting that there is a factor two error in the experimental result [36], while the theoretical result has been calculated with an approximate method [25]. As a consequence, the agreement is satisfactory. As to dissociation, literature data appears to be quite scattered. However, our results appear to be in good accord with the Shatalov results shown in Fig. 4.

Atom diatom calculations were also performed for the H_2 + He collision process that, in addition to its relevance to the study of the space vehicle entry into Jovian atmosphere [37], is one of the most important collision processes in molecular clouds [38]. The whole set of cross sections for non-reactive roto-vibrational energy exchange and dissociation, including quasi-bound states of reactants and products, has been calculated in the translational energy range 0.001-10 eV, with a density of 50000 trajectories per eV and per Angstrom of impact parameter (with maximum value 7 Å). For this work the PES of Muchnick and Russek (MR PES) [39] has been used. Indeed, the BMP PES [40] of Boothroyd et al. is the more recently published one for the considered system and is based on a large number of *ab initio* points (much larger than that used for the MR PES). However, comparisons by Lee et al. [41] with experimental data have shown some problems about the fitting of the surface, while similar comparisons on the MR PES confirm its reliability.

The above mentioned density of calculated trajectories is based on the integration of about 6 billions of trajectories needing approximately 9.5 years of cpu time. Again such a huge calculation has been made possible by the grid implementation of the already mentioned distributed code that runs efficiently on several serial machines even if networked on slow connections.

In order to assess the validity of the calculations, a comparison of vibrational energy exchange and dissociation are given in Fig. 5 and Fig. 6, respectively. The close coupling calculation of Orlikowsky [42] concerned with vibrational relaxation (from v=1 to v'=0, including thermalized rotation) are compared in the first of them. The agreement is excellent starting from about 2000 K. As shown in Ref. [43], in this system there is a strong correlation between rotation and vibration, and this correlation extends also to very low translational energy ranges, where the changes in roto-vibrational actions can be less than one quantum, resulting in no roto-vibrational transition in the framework of quasi-classical method. This explains the failure of the method at low energy, as evidenced by Fig. 5. Concerning dissociation, on the contrary, this effect is obviously lacking. As a consequence, the agreement with approximate quantum method estimates reported in Ref. [44] is much better, as shown in Fig. 6, where the two results differ mainly in the temperature region around 10000 K for at most a factor two. On that ground by considering the discretization of the continuum (as well as the coupled states approximation used in Ref. [44]) and taking into

account the high initial vibrational level considered, it would be not surprising to find that quasi-classical results reproduce the (not yet available) experimental data. However, it is interesting to note that, at least for this system, quasi-classical roto-vibrational energy transfer results clearly fail to provide an adequate final analysis of product properties at low translational energy (<0.1 eV), while they well reproduce quantum mechanical dissociation in the same range.

IV. A MOLECULE-MOLECULE SYSTEM

For the case of the CO_2-CO_2 collisions, which have been to some extent already illustrated in Ref. [45] and are of fundamental importance because of the widespread presence of the carbon dioxide molecule on Earth and in planetary atmospheres (such as the Martian one), the effect of vibrations and rotations of the involved molecules has to be included in the kinetic model because it strongly affects polarizabilities, charge distributions and modify the interaction, accordingly. This is particularly true for collisions occurring at critical temperature and plasma conditions in which high internal energy levels can be significantly populated and strong excitation of the colliding molecules can be induced by an energy exchange between different degrees of freedom. Such effects are taken into account by using the so called bond-bond approach [46], a method for the description of the intermolecular interactions, illustrated in detail for some specific applications in Refs [45, 47–50]. This approach apart from associating the interaction with physically meaningful properties of the collision partners, offers the advantage of allowing its flexible analytical formulation that includes explicitly the dependence of the potential functional on the internal degrees of freedom (stretching and/or bending) of the monomers and is suitable for application to even more complex cases [51, 52]. To further refine the formulation of the interaction, the PES must also depend on the orientation of the molecular polarizability and on the molecular charge distribution. For the CO_2 dimer case such dependence was derived in Ref. [45] where the obtained PES was also improved thanks to a comparison with *ab initio* data and the measured second virial coefficients. The dependence on the orientation has been treated by adopting a hyperspherical representation of the potential energy surface, by expanding the parameters of the interaction in terms of harmonic functions, a very useful practice in dealing with interaction anisotropies and disentangling some of the most subtle aspects of the stereodynamics of the collisions (see, e.g, [53, 54]). It is worth to point out here that such representation indirectly takes into account also three body effects and is specifically tailored to describe two interacting CO_2 molecules at high internal and rotational excitation.

The developed intermolecular potential energy function was merged with an intramolecular potential energy function, which accounts for the energy of the two isolated molecules [55]. The resulting interaction energy function was used to carry out extended calculations of state-to-state collision cross sections using the QCT method. As already mentioned, QCT techniques are, up to date, the only viable approach to full dimensional dynamics and to the calculation of the collisional cross sections for systems having more than four atoms especially when extended data bases of state-to-state properties are needed. The combined use of the above mentioned complete PES and QCT techniques makes up a versatile computational tool for extended studies of CO_2-CO_2 collision dynamics, which has been being ported on high performance computing facilities and implemented in the European Grid Infrastricture, through the COMPCHEM VO [16], while a similar procedure is being adopted to get efficient tools to study also reactive processes (see, e.g., Refs. [56, 57]). The processes considered here are:

$$CO_2(v_{a1}, v_{a2}, v_{a3}) + CO_2(v_{b1}, v_{b2}, v_{b3}) \rightarrow CO_2(v'_{a1}, v'_{a2}, v'_{a3}) + CO_2(v'_{b1}, v'_{b2}, v'_{b3}) \quad (8)$$

where the $v_{a(b)i}$ $(i = 1, 2, 3)$ are the quantum labels of a normal-mode model for symmetric stretching (1350 cm^{-1}), bending (678 cm^{-1}) and asymmetric stretching (2388 cm^{-1}) respectively, before (unprimed) and after (primed) the collision event. At equilibrium CO_2 is a linear molecule, with degenerate (ground) bending states. Bending excitation generates rotation around the O–C–O molecular axis and an additional quantum number, l, is needed to label the discretized total molecular angular momentum projection on the quantization axis z (yet the associated energy is neglected because its magnitude is often smaller than the typical statistical error of massive QCT calculations (nearly 5%)). Indeed, the huge amount of calculations required to build a significant set of state-to-state cross sections to be used in kinetic models to cover a sufficiently wide range of conditions, suggests to adopt an even simpler model, imposing separability between rotations and vibrations. Accordingly, the CO_2 molecule is approximated as a linear rigid rotor (though dynamical effects induced by the modification of the molecular shape occurring during the collision are in any case properly taken into account by computing the true intermolecular potential). The most efficient scheme for calculations, that fully exploits the intrinsic parallelism of the QCT method, consists in setting the initial conditions of each batch of trajectories in the following way: the collision energy E_{col} is given a fixed value; the initial rotational angular momentum of the two molecules is selected randomly by a uniform sampling of the Boltzmann distribution corresponding to the rotational temperature. The most obvious option for a rotational temperature value is to set this temperature equal to the translational one (a typical choice for this type of massive

computational campaigns [45]); the initial vibrational states of the two molecules were defined by choosing two triples of integer numbers (one for each molecule) corresponding to the $v_{a(b)1}, v_{a(b)2}, v_{a(b)3}$ quantum numbers. Then initial coordinates and momenta for the relative motion are set by assigning a random value to the impact parameter b in the range [0,b_{max}], where b_{max}, the maximum impact parameter, was taken as a truncation limit. The molecules are then randomly oriented and the initial distance between their molecular centres of mass are set large enough to make the related interaction negligible and the rotation of each of them that of a linear rigid rotor with rotations and vibrations being uncoupled. As typical of QCT methods, the final states of the two product molecules are discretized using a binning procedure. The corresponding cross sections, which can be thought of as a target area, are directly obtained by multiplying probabilities by a factor πb_{max}^2. In the calculation presented here, we adopted $b_{max} = 20$ Å, in order to take full account of long range force effects.

The problem of calculating state-to-state cross sections by the QCT method rises, as a side issue, the problem of separating the internal degrees of freedom of a triatomic molecule. The energy content of each vibrational degrees of freedom must be be subsequently discretized (quantized) using a binning procedure. Quantization can be achieved using a separable normal mode harmonic model because the energies corresponding to each normal mode can be directly calculated by projecting the classical phase-space vector of the system final states onto the normal mode vector basis. The rotational compontent of the energy stored in the two bending degrees of freedom can then be extracted by giving the two corresponding normal coordinates a representation in terms of polar coordinates (as stated above, this rotationa component is neglected in our calculations) [58]. Although this simple method may lead to an inaccurate labeling of the vibrational states for highly excited molecules, this is usually of negligible impact when the quantum states lie well below the strong anharmonic region of the potential. An approximate estimate of the deviation of the harmonic model from the actual behavior of the system, can be indeed made by comparing the harmonic vibrational energy levels of CO_2, for a single mode of vibration, with the ones associated with the same vibrational state of the corresponding standard Morse potential (for example, the energy difference for the symmetric stretching $v_{a1} = 11$ is about 10% [45]). Moreover, such deviations have negligible impact on final thermalized results. In fact, the assignment of the final classical state to a quantum one is actually only instrumental to the setting of an integration energy grid for the evaluation of the thermal average. In other words, a difference in the labeling of the states on which the thermal average is performed changes only the location on the energy grid of the integration points without affecting the final estimate of the integral. Attention has only to be paid when dealing with the evaluation of detailed properties in which a rigorous correspondence between states and energy values need to be adopted. There are situations in which the internal dynamics of colliding molecule is strongly anharmonic, so that the harmonic binning approximation breaks down. This is the case, for example, of high rotational temperatures, when the rotation-vibration energy exchange can highly internally excite the molecules, in which a full separation of vibrational degrees of freedom makes no longer sense and a binning based on the total molecular vibrational energy would be preferable.

Examples of the calculated QCT cross sections and probabilities for CO_2+CO_2 inelastic collisions at a collision energy of 3.47 eV and a rotational temperature of 40000 K are shown in Table I and II for colliding molecules initially set either in a ground or in an excited vibrational state. Such a high collision energy and rotational excitation of molecules, although might appear as too severe conditions, are not infrequent when modeling, for example, shock waves in re-entry studies. It can be seen that, due to the quite high amount of energy available, a large number of vibrational states are populated as an effect of the collisions, and consequently there are not dominant vibrational transitions. This behaviour of the cross sections and probabilities, consisting in a slowly decreasing trend, is quite common for collision probabilities at higher energies and rotational temperatures (the opposite would be found at low energies), and it has been also encooutered in previous calculations [45].

V. ATOMS RECOMBINATION ON A SURFACE

The atom recombination on a silica surface, as already mentioned, is also a process strongly related to the vehicle surface temperature and to the flow conditions of the surrounding gas phase. In TPSs two classes of materials are used: reusable and ablative ones [59]. The first type of materials are characterized by the fact that after atmospheric entry no property or mass changes are expected and high emissivity, low thermal conductivity and low surface catalytic efficiency are related requirements. On the contrary, the second type of materials are, instead, expected to accommodate high heating loads and rates by means of mass losses and phase changes. Two coefficients (i.e., γ_i and β_i) are used to suitably quantify the wall catalytic efficiency in typical computer fluid dynamics (CFD) simulations of the aerothermodynamics of these hypersonic flights [5]. The catalytic recombination coefficient (γ_i) is usually obtained from the recombination probability of the ith atomic species to form diatomic molecules on the surface while the chemical energy accommodation coefficient (β_i) represents the ratio of energy released to the surface per atomic recombination with respect to the maximum energy transferable. The values of these coefficients fall within the range

$0 \leq \gamma_i$, $\beta_i \leq 1$ and depend on temperature and total/partial pressures (i.e., γ_i(T, P)). Although some experiments have been carried out to measure such coefficients [6], some of the related publications quote the only effective catalytic efficiency values ($\gamma_{eff,i} = \gamma_i' = \gamma_i \cdot \beta_i$) and only a few of them quote β_i coefficients that in CFD simulations are frequently assumed to be 1 (i.e., fully energy accommodation assumption). On the contrary, theoretical investigations developed at molecular dynamics level [60] have shown that only a fraction of the total exothermicity delivered in the Eley-Rideal (E-R) recombination processes of O and N on silica surfaces is transferred to the substrate as heat flux and that the main part of that energy is disposed into rotation, vibration or translation motions of the newly formed molecules. Therefore, the energy accommodation coefficient β_i associated with the recombination reaction can hardly be taken as a unit. Despite the availability of results of ground-based tests, flight tests and numerical calculations play a key role in investigating the characteristics of hypersonic flights. In particular, theoretical calculations are needed to understand the catalytic effects of TPS materials. A typical rather known TPS is the reaction-cured glass (RCG) coating used in the Shuttle high-temperature reusable surface insulation (HRSI) tiles (94% of SiO_2, 4% of B_2O_3 and 2% of SiB_4). Silicon based-materials are usually modeled as silica surfaces (such as α- or β-quartz and β-cristobalite). The latter (a polymorph of silica stable at high T similar to those of the amorphous silica used in TPSs) has been considered in previous related theoretical studies. Frequently, microkinetic models are used to simulate the heterogeneous chemical kinetics of dissociated airflow impinging on different kinds of surfaces [61–63]. Related results are in quite good agreement with experimental data and allow the calculation of γ_i and β_i coefficients along with their dependence on both temperature and pressure. Due to the importance of atomic adsorption, E-R reactions become usually the main step of the parametric microkinetic models. Accordingly, in the present work, a comparative study of atomic hydrogen and atomic oxygen E-R recombination over a β-cristobalite surface is discussed. To this end an analysis of the corresponding cross sections and the γ_{E-R} contribution to the global γ coefficient is carried out. β-cristobalite is the most stable silica polymorph at the high temperatures involved during the space vehicle re-entry. In order to analyze the behavior of this material during the re-entry conditions in terrestrial and jovian atmospheres, we have considered a surface model of this polymorph to study the chemical processes occurring in hypersonic conditions due to the interaction of H or O atoms with the shuttle tiles since atomic and molecular oxygen or hydrogen are the main components of terrestrial and jovian atmospheres, respectively. Therefore, this contribution presents an analysis of the catalytic effect of silica with respect to the recombination of these atomic species. In particular, we have focused on the H and O recombination occurring via the so-called E-R mechanism, according to which an impinging atom from the gas-phase recombines with an atom already adsorbed on the surface:

$$\mathrm{A}_{gas} + \mathrm{silica} \rightarrow \mathrm{A}_{ad} * \mathrm{silica} + \Delta E_{(1)} \tag{9}$$

$$\mathrm{A}_{gas} + \mathrm{A}_{ad} * \mathrm{silica} \rightarrow \mathrm{A}_{2,gas}(v, j) + \mathrm{silica} + \Delta E_{(2)} \tag{10}$$

where, in our case, A=O (or H) and $\Delta E_{(i)}$ is the reaction exothermicity of the considered elementary process that can be transferred to the surface by the ith process. Obviously, the adsorption of an atom over the surface (i.e., process 9) is a necessary step to produce the E-R reaction (i.e., process 10). The dynamical results reported throughout this work have been obtained using different methodologies: the already mentioned *scl* [64, 65] and *cl* collisional methods with a Generalized Langevin Oscillator (GLO) [66]. As previously mentioned the most critical step in molecular dynamics studies is the determination of a sufficiently accurate PES able to describe correctly the process under investigation. For the case of H, H_2 interaction over β-cristobalite some of us have recently developed a multidimensional PES based on electronic structure DFT calculations [67] whereas for the case of the O, O_2 interaction over β-cristobalite two different PESs have been developed by the two groups: a first one based on DFT cluster calculations [68] and another one based on DFT periodic boundary conditions calculations [69].

As far as the PESs of the O, O_2/β-cristobalite system is concerned, the results of Ref. [68] and Ref. [69] are in substantial agreement between them. In practice, in both studies the most active site over the silica surface with respect to the O atom chemisorption was found to be that on top of a Si surface atom at an equilibrium distance of 1.54 Å and with a chemisorption energy of nearly 5.5 eV. In the case of the PES for H adsorption on β-cristobalite, the most active site presents the same structure as the one found for O adsorption over β-cristobalite but with a shorter equilibrium distance of 1.50 Å and with a weaker interaction energy of 2.1 eV [67]. An independent and detailed description and discussion of the reaction probabilities obtained for the two heterogeneous processes considered here can be found in Refs. [63, 70, 71]. Here we focus on the calculation of the reactive cross sections for the two E-R recombination reactions:

$$\mathrm{O}_{gas} + \mathrm{O}_{ad} * \mathrm{silica} \rightarrow \mathrm{O}_{2,gas}(v, j) + \mathrm{silica} \tag{11}$$

and

$$\mathrm{H}_{gas} + \mathrm{H}_{ad} * \mathrm{silica} \rightarrow \mathrm{H}_{2,gas}(v, j) + \mathrm{silica} \tag{12}$$

In the dynamics simulations of both reactions, the pre-adsorbed atom (i.e., O_{ad} or H_{ad}) is located over the central Si atom (the most important adsorption site), while the initial (x,y) coordinates of the impinging gas atom (i.e., O_{gas} or H_{gas}) are chosen randomly over all available positions inside the surface unit cell. Incoming O_{gas} atoms impinge on the surface at $E_{\rm col}$ values falling in the range (0.008-3.8) eV, while for the H_{gas} atoms this occurs in the range (0.04-3.0) eV. Despite the fact that the surface temperature (T_S) in the case of semiclassical calculations (*scl*) is T_S = 1000 K and in the case of *cl* calculations is T_S=1100 K, the reported cross sections can still be directly compared because the dependence of the reactivity on T_S is small. An important parameter of the process of a gas-phase atom impinging on a solid substrate are the orientation angles (θ_v,ϕ_v), with θ_v being the angle between the incoming atom velocity vector and the normal to the surface plane and ϕ_v being the azimuthal orientation angle over the surface plane. For our calculations, we have considered the normal incidence angle (i.e., θ_v=0^o). At this incidence angle, the ϕ_v angle is undefined. From a theoretical point of view, for an E-R reaction, the reactive cross section (σ_{E-R}) is usually defined as

$$\sigma_{E-R} = \int_0^{2\pi} \int_0^{b_{max}} P(b,\phi) b \; db \; d\phi \tag{13}$$

where b is the impact parameter, $P(b,\phi)$ is the opacity function and ϕ is the orientation angle of the impinging particle. Such expression becomes simpler in the case of axial symmetry,

$$\sigma_{E-R} = \int_0^{b_{max}} P(b) b \; db \tag{14}$$

though, due to the usual cell symmetries of the solid surface, it is possible that P depends on the angle. At the same time, in order to sample correctly the impact parameter b (b = 0 for the initial position of A_{ad} on the cell), according to the standard Monte Carlo method its value should be taken from a b^2 uniform distribution between 0 and b^2_{max}. Frequently, due to the fact that we are interested not only in the E-R process but also in the different competitive processes, a uniform cell sampling is carried out for the incoming atom. This allows to calculate all reaction probabilities P_i (for the ith channel) with a comparable quality. Therefore, for each process in the case of an orthogonal unit cell (*i.e.*, as is the case of the β-cristobalite surface discussed in this paper),

$$\sigma_i = \int_0^{a_x} \int_0^{a_y} P_i(x,y) \; dx \; dy \approx \frac{A}{N} \sum_{j=1}^{N} w_i(\chi_1,\chi_2)_j \tag{15}$$

where a_x and a_y are the lattice parameters, A is the unit cell area ($A = a \cdot b$), N is the total number of selections made and $w_i(\chi_1,\chi_2)$ is either equal to 1 or 0 for all the j-initial selection (i.e., trajectory) depending on whether the i-channel is reached or not. The two random numbers χ_1 and χ_2 are selected in a way that $0 \leq \chi_1, \chi_2 \leq 1$, with $x = \chi_1 \cdot a_x$ and $y = \chi_2 \cdot a_y$. Finally, the probability of each P_i channel is taken equal to the N_i/N fraction of trajectories assigned to the ith-channel.

If the surface corresponds to a periodic structure, only a minimum unrepeated unit cell should be sampled. This is entirely correct for a clean surface while some corrections should be introduced for a pre-covered one. Thus, if only one atom is adsorbed into the unit cell, the previous expressions holds. However, for higher coverages, alternative targets (i.e., *ad* atoms) are introduced. Therefore, if the same total unit cell is used, the calculated cross section (*e.g.*, for the E-R reaction) should be divided by the number of equivalent targets. Likewise an atomic adsorption process, the corresponding cross section should be divided by the number of equivalent adsorption sites.

In Fig. 7 the cross sections σ_{E-R} calculated for the oxygen atom recombination (i.e., reaction 11) using both *scl* (semiclassical [64, 65]) and *cl* (classical [66]) dynamics methods are plotted together with the ones obtained for the hydrogen atom recombination (i.e., reaction 12) using the *scl* technique. In the following, σ_{E-Rscl} refers to the calculated cross section using the *scl* approach, while σ_{E-Rcl} refers to the cross section obtained using the *cl* approach. In the case of oxygen atom recombination (see Fig. 7), there is a good agreement between the *scl* and *cl* cross sections at low collision energies (¡ 0.1 eV). At intermediate energies ($\simeq$ 0.1–0.5 eV) the agreement seems to be much worse, improving again at higher energies ($\simeq$ 1 eV). However, additional *cl* and *scl* cross sections would be necessary to compare appropriately this behaviour (see, eqs. 11 and 12, respectively). Using only the *scl* method we can infer that the energy threshold for the two processes is different. In particular, the recombination reaction for H is more efficient than that for O. This depends on the fact that the pre-adsorbed H atom is more weakly bound than the O atom and is therefore more prone to recombine. The two reactions exhibit also a different trend with collision energy. In fact, while in the case of oxygen recombination, σ_{E-Rscl} decreases as $E_{\rm col}$ increases, the opposite is true for hydrogen recombination whose σ_{E-Rscl} increases with $E_{\rm col}$ up to a maximum value of 5.0 $Å^2$ at collision energies around 0.4 eV. Another important aspect of the recombination reactions, of relevance for the TPS problem, is the

reaction exothermicity partitioning between the internal degrees of freedom of the new-formed O_2 and H_2 molecules and the surface. In Fig. 8 we compare the percentage of energy transferred to the internal degrees of freedom and to the surface phonons using the *scl* approach. The comparison is made at two collision energies ($E_{\rm col}$= 0.06 and 0.1eV). From Fig. 8 it can be inferred that, in the case of the formation of the O_2 molecules, the largest fraction of available energy is disposed into rotation, whereas in the case of the formation of H_2 it is disposed into vibration. Besides, the coupling with the surface silica atoms is more active in the case of oxygen recombination because of the different molecular masses of O and H. In fact, in the formation of the O_2 molecules, the percentage of energy exchanged with the surface phonons reaches a value of 15%, about three times larger than the energy transferred to the surface in the case of H_2 formation. The vibrational energy of the newly formed molecules is higher for H_2 than for O_2. This can also be inferred from the vibrational distributions, $P(v)$, reported in Fig. 9. The two distributions were obtained at low energy. In particular, the O_2 distribution (see Fig. 9a) is obtained for a thermal condition ($T = T_{gas} = T_S$ =1000 K that could well correspond to an $E_{\rm col}$ of 0.12 eV if $3/2{\rm k}_B T$ is assumed for this kind of condition) and using the *cl* method on the CRP PES [66]. On the contrary, the H_2 distribution (Fig. 9) is obtained for $E_{\rm col}$= 0.06 eV using the *scl* approach on the recently reported PES of Ref. [67]. The main difference between the two distributions is that for the O_2 molecules it is thermal while for the H_2 ones it is inverted. Moreover, the number of vibrational states implied is larger in the case of H_2 distribution ($0 \leq v \leq 12$) than in the case of the O_2 one ($0 \leq v \leq 8$) although the collision energy of the incoming H atoms is lower than that of the O atoms. One has also to take into account that the vibrational levels present a higher separation in the case of H_2 molecule due to a lighter mass. These distributions agree as well with the shape of the PESs. Thus, for the case of the O_2 distribution the uppermost populated level $v = 8$ corresponds to an internal energy of $\mathrm{E}(v = 8, j = 0) \approx 1.5$ eV (under harmonic oscillator and rigid rotor approximations) that agrees perfectly with the exothermicity of E-R process (11) on the CRP PES [66] (ΔE_{E-R}= 1.4 eV) the extra contribution from the initial $E_{\rm col}$ close to 0.12 eV. For the case of the H_2 distribution the highest populated vibrational level $v = 12$ corresponds to an internal energy of $\mathrm{E}(v = 12, j = 0) \approx 2.44$ eV that agrees also perfectly with the exothermicity of E-R reaction (12) in the recently published PES [67] (ΔE_{E-R}= 2.4 eV) and the extra initial $E_{\rm col} = 0.06$ eV.

VI. CONCLUSIONS

In the present paper we report on the exploitation of the computing power made available by the European Grid infrastructure to carry out massive trajectory computations of the detailed cross sections of gas phase and gas surface collision processes for systems relevant to the modeling of planetary entries. The rigorous detailed quantum treatments has been recalled though for practical purposes (memory size and computing time) trajectory approaches have been preferred. For similar reasons semi-empirical formulations of the PESs have been adopted even if their parameters have been regularly used to tune their main features to that of rigorous electronic structure calculations. At the same time trajectory outcomes have been compared with those of other theoretical treatments and experimental data in order estimate their accuracy and support their validation.

The picture emerging from our work is that computational approaches to the microscopic modeling of the processes occurring during the atmospheric entry of spacecrafts is deemed to be successful if inserted into more global model treatments. The success of such approach is clearly ascribable to the use of Grid technologies which allow a detailed investigation of the efficiency of state-to-state processes through the use of the so called Grid Empowered Molecular Simulator without depending on large scale facilities.

ACKNOWLEDGMENTS

The authors acknowledge financial support from the Phys4entry FP7/2007-2013 project (Contract 242311), ARPA Umbria, INSTM, the EGI-Inspire project (Contract 261323), MIUR PRIN 2008 (2008KJX4SN 003), MIUR PRIN 2010-2011 (contract 2010ERFKXL_002), the ESA-ESTEC contract 21790/08/NL/HE and the Spanish CTQ2009-07647 and 2009SGR1041 projects. Computations have been supported by the use of Grid resources and services provided by the European Grid Infrastructure (EGI) and the Italian Grid Infrastructure (IGI) through the COMPCHEM Virtual Organization. Thanks are also due to the COST CMST European Cooperative Project CHEMGRID

(Action D37). A. Lombardi thanks the Italia CINECA for the allocated computing time.

---

[1] Sarma GSR. Relevance of aerothermochemistry for hypersonic technology. In: Capitelli M Ed. Molecular Physics and Hypersonic Flows NATO ASI Series C, vol. 482. Dordrecht: Kluwer Academic Publishers 1996; pp. 1-20.

[2] Bertin JJ, Cummings RM. Critical hypersonic aerothermodynamics phenomena. Ann Rev Fluid Mech 2006; 38: 129-157.

[3] Capitelli M. Non equilibrium vibrational kinetics, Springer, Berlin 1986.

[4] Capitelli M, Barsdley JN. Non equilibrium processes in partially ionized gases, Plenum, New York 1990.

[5] Kovalev VL, Kolesnikov AF. Experimental and theoretical simulations of heterogeneous catalysis in aerothermochemistry. Fluid Dyn 2005; 40: 669-693.

[6] Cacciatore M, Rutigliano M. Molecular dynamics simulation of surface processes: oxygen recombination on silica surfaces at high temperatures. In: Chazot O Ed. Experiments, Modeling and Simulation of Gas-Surface Interactions of Reactive Flows in Hypersonic Flights. RTO-EN-AVT-142 2007; paper 5.

[7] Laganà A, Ochoa de Aspuru G, Garcia E. Quasi-classical and quantum rate coefficients for the N + N_2 reaction. Stamperia Università di Perugia, Perugia 1996.

[8] Verdicchio M, Pacifici L, Laganà A. Grid enabled high level *ab initio* electronic structure calculations for the N + N_2 reaction. Lecture Notes in Computer Science 2012; 7333: 371-386.

[9] Esposito F, Armenise I, Capitelli M. N-N_2 state to state vibrational-relaxation and dissociation rates based on quasiclassical calculations. Chem Phys 2006; 331: 1-8.

[10] Laganà A, Garcia E. Quasi-classical rate coefficients for the H + H_2 reaction. Stamperia Università di Perugia, Perugia 1996.

[11] Ceballos A, Garcia E, Rodriguez A, Laganà A. Quasi-classical rate coefficients for the H_2 + H_2 reaction and dissociation. J Phys Chem Ref Data 2002; 31: 371-385.

[12] Esposito F, Gorse C, Capitelli M. Quasi-classical dynamics calculations and state-selected rate coefficients for H+$H_2(v,j)$→3H processes: application to the global dissociation rate under thermal conditions. Chem Phys Lett 1999; 303: 636-640.

[13] Laganà A, Garcia E, Martinez T. Quasi-classical and quantum rate coefficients for the O + O_2 reaction. Stamperia Università di Perugia, Perugia 1996.

[14] Esposito F, Armenise I, Capitta G, Capitelli M. O-O_2 state-to-state vibrational relaxation and dissociation rates based on quasiclassical calculations. Chem Phys 2008; 351: 91-98.

[15] http://www.prace-ri.eu/

[16] Laganà A, Riganelli A, Gervasi O. On the Structuring of the Computational Chemistry Virtual Organization COMPCHEM. Lecture Notes in Computer Science 2006; 3980: 665-674. (URL http://compchem.unipg.it/)

[17] The European Grid Initiative (EGI). URL http://web.eu-egi.eu/documents/other/egi-blueprint/.

[18] Gervasi O, Dittamo C, Laganà A. A Grid Molecular Simulator for E-Science. Lecture Notes in Computer Science 2005; 3470: 16-22.

[19] Laganà A, Gervasi O. A Priori Molecular Virtual Reality on EGEE Grid. Int J Quantum Chemistry 2009; 110: 446-453.

[20] Laganà A, Crocchianti S, Piermarini V. Towards a full dimensional exact quantum calculation of the Li + HF reactive cross section. Lecture Notes in Computer Science 2004; 3044: 422-431. Garcia E, Sánchez C, Saracibar A, Laganà A, Skouteris D. A detailed comparison of centrifugal sudden and J-shift estimates of the reactive properties of the N + N_2 reaction. Phys Chem Chem Phys 2009; 11: 11456-11462. Rampino S, Skouteris D, Laganà A. Microscopic branching processes: The O + O_2 reaction and its relaxed potential representations. Int J Quantum Chem 2010; 110: 358.

[21] Manuali C, Costantini A, Laganà A, Cecchi M, Ghiselli A, Carpené M, Rossi E. Efficient Workload Distribution bridging HTC and HPC in Scientific Computing. Lecture Notes in Computer Science 2012; 7333: 345-357.

[22] Freire E, Simon A, Lopez J, Fernandez C, Diez R, Diaz S, Manuali C, Laganà A. Application Domain Accounting for EGI, 5th EGEE User Forum, Uppsala (SW) 2010. URL http://egee-uf5.eu-egee.org/.

[23] Laganà A, Riganelli A. Reaction and Molecular Dynamics. Springer Verlag, Berlin 2000.

[24] Armenise I, Esposito F, Capitelli M. Dissociation-recombination models in hypersonic boundary layer flows. Chem Phys 2007; 336: 83-90. Armenise I, Esposito F. Dissociation-recombination models in hypersonic boundary layer O_2/O flows. Chem Phys 2012; 398: 104-110. Capitelli M, Celiberto R, Esposito F, Laricchiuta A. Molecular Dynamics for State-to-State Kinetics of Non-Equilibrium Molecular Plasmas: State of Art and Perspectives. Plasma Processes and Polymers 2009; 6: 279-294.

[25] Minelli P, Esposito F, Bruno D, Capitelli M, Longo S. Extracting Cross Sections from Rate Coefficients: Application to Molecular Gas Dissociation. J Thermophys Heat Transfer 2011; 25: 374.

[26] Esposito F, Capitelli M. Selective Vibrational Pumping of Molecular Hydrogen via Gas Phase Atomic Recombination. J Phys Chem A 2009; 113: 15307-15314.

[27] Gamallo P, González M, Sayós R. Ab initio derived analytical fits of the two lowest triplet potential energy surfaces and theoretical rate constants for the N(^4S)+NO($X^2\Pi$) system. J Chem Phys 2003; 119: 2545.

[28] Akpinar S, Armenise I, Defazio P, Esposito F, Gamallo P, Petrongolo C, Sayós R. Quantum mechanical and quasiclassical BornOppenheimer dynamics of the reaction $N_2(X^1\Sigma_g^+)$ + O(^3P) → N(^4S) + NO($X^2\Pi$) on the N_2O $\tilde{a}^3A$" and $\tilde{b}^3A$ surfaces. Chem Phys 2012; 398: 81-89.

[29] Sayós R, Oliva C, González M. New analytical ($^2A'$, $^4A'$) surfaces and theoretical rate constants for the N(^4S)+O_2 reaction. J Chem Phys 2002; 117: 670.

[30] Esposito F. Dinamica Quasiclassical di Processi Collisionali Inelastici e Reattivi in Sistemi H + H_2 e N + N_2 rotovibrazionalmente risolti. PhD Thesis. Università degli Studi di Bari 1999.

[31] Esposito F, Capitelli M. Quasi-classical trajectory calculations of vibrationally specific dissociation cross sections and rate constants for the reaction O + $O_2(v) \rightarrow$ 3O. Chem Phys Lett 2002; 364: 180-187.

[32] Bose D, Candler GV. Thermal rate constants of the N_2 + O $\rightarrow$ NO + N reaction using *ab initio* ^3A" and ^3A potential energy surfaces. J Chem Phys 1996; 104: 2825.

[33] Baulch DL, Bowman CT, Cobos CJ, Cox RA, Just T, Kerr JA, Pilling MJ, Stocker D, Troe J, Tsang W, Walker RW, Warnatz J. Evaluated Kinetic Data for Combustion Modeling: Supplement II. J Phys Chem Ref Data 2005; 34: 757-1397.

[34] Shatalov OP. Recommended Data on Rate Constants of Physical and Chemical Processes in NO Atoms System. Technical report 1987, Moscow State University Russia, Inst. of Mechanics Avogadro Center.

[35] Gamallo P, González M, Sayós R. *Ab initio* study of the two lowest triplet potential energy surfaces involved in the N(^4S)+NO ($X^2\Pi$) reaction. J Chem Phys 2003; 118: 10602.

[36] Baulch D, Cobos C, Cox R, Frank P, Hayman G, Just Th, Kerr JA, Murrells T, Pilling MJ, Troe J, Walker RW, Warnatz J. Evaluated kinetic data for combustion modeling. Supplement 1. J Phys Chem Ref Data 1994; 23: 847.

[37] Gnoffo PA. Planetary entry gas dynamics. Ann Rev Fluid Mech 1999; 31: 459-494.

[38] Balakrishnan N, Vieira M, Babb J, Dalgarno A, Forrey R, Lepp S. Rate coefficients for ro-vibrational transitions in H_2 due to collisions with He. Astrophys J 1999; 524: 1122.

[39] Muchnick P, Russek A. The HeH_2 energy surface. J Chem Phys 1994; 100: 4336.

[40] Boothroyd AI, Martin PG, Peterson MR. Accurate analytic HeH_2 potential energy surface from a greatly expanded set of *ab initio* energies. J Chem Phys 2003; 119: 3187.

[41] Lee T-G, Rochow C, Martin R, Clark TK, Forrey RC, Balakrishnan N, Stancil PC, Schultz DR, Dalgarno A, Ferland, GJ. Close-coupling calculations of low-energy inelastic and elastic processes in ^{4}He collisions with H_2: A comparative study of two potential energy surfaces. J Chem Phys 2005; 122: 024307.

[42] Orlikowski T. Close-coupling calculations of the cross sections and relaxation rates for ro-vibrational transitions in H_2 colliding with He. Chem Phys 1981; 61: 405-413.

[43] Forrey RC, Balakrishnan N, Dalgarno A, Haggerty MR, Heller EJ. Quasi-resonant energy transfer in ultracold atom-diatom collisions. Phys Rev Lett 1999; 82: 2657-2660.

[44] Paolini S, Ohlinger L, Forrey R. Hydrogen recombination due to collisions with He and Ar. Phys Rev A 2011; 83: 042713.

[45] Bartolomei M, Pirani F, Laganà A, Lombardi A. A full dimensional Grid empowered simulation of the CO_2 + CO_2 processes. J Comp Chem 2012; 33: 1806-1819.

[46] Cappelletti D, Pirani F, Bussery-Honvault B, Gomez L, Bartolomei M. A bond-bond description of the intermolecular interaction energy: the case of weakly bound N_2-H_2 and N_2-N_2 complexes. Phys Chem Chem Phys 2008; 10: 4281-93.

[47] Lombardi A, Faginas Lago N, Laganà A, Pirani F, Falcinelli S. A Bond-Bond Portable Approach to Intermolecular Interactions: Simulations for N-methylacetamide and Carbon Dioxide Dimers. In: Murgante, B, Gervasi, O, Misra, S, Nedjah, N, Rocha, AMAC, Taniar, D, Apduhan, BO (eds.) ICCSA 2012, Part I. LNCS, vol. 7333, pp. 387-400. Springer, Heidelberg.

[48] Lombardi A, Laganà A, Pirani F, Faginas Lago N, Palazzetti F. Carbon oxides in gas flows and earth and planetary atmospheres: State-to-state simulations of energy transfer and dissociation reactions. In: Murgante B, Misra S, Carlini M, Torre CM, Nguyen H-Q, Taniar D, Apduhan BO, Gervasi O (eds.). ICCSA 2013, Part II. LNCS, vol. 7972, pp. 17-31. Springer, Heidelberg.

[49] Faginas Lago N, Albertí M, Laganà A, Lombardi A. Water $(H_2O)_m$ or Benzene $(C_6H_6)_n$ Aggregates to Solvate the K^+? In: Murgante B, Misra S, Carlini M, Torre CM, Nguyen H-Q, Taniar D, Apduhan BO, Gervasi O (eds.). ICCSA 2013, Part I. LNCS, vol. 7971, pp. 1-15. Springer, Heidelberg.

[50] Falcinelli S, Rosi M, Candori P, Vecchiocattivi F, Bartocci A, Lombardi A, Faginas Lago N, Pirani F. Modeling the intermolecular interactions and characterization of the dynamics of collisional autoionization processes. In: Murgante B, Misra S, Carlini MT, Nguyen H-Q, Taniar D, Apduhan BO, Gervasi O (eds.) ICCSA 2013. LNCS, vol. 7971, pp. 69-83. Springer, Heidelberg.

[51] Albertí M, Faginas Lago N, Laganà A, Pirani F. A portable intermolecular potential for molecular dynamics studies of NMA-NMA and NMA-H_2O aggregates. Phys Chem Chem Phys 2011; 13: 8422-8432.

[52] Faginas Lago N, Albertí M, Lombardi A, Pacifici L, Costantini A. Implementation of a distributed version on the grid: molecular dynamics simulation of the NMA-NMA dimer. J Comp Chem 2013; submitted

[53] Su, T-M, Palazzetti, F, Grossi, G, Aquilanti, V. Molecular alignment and chirality in gaseous streams and vortices. Rendiconti Lincei 2013; in press.

[54] Palazzetti, F, Tsai, P-Y, Lombardi, A, Nakamura, M, Che, D-C, Kasai, T, Lin, K-C, Aquilanti, V. Rendiconti Lincei 2013; in press.

[55] Carter, S, Murrell, JN. Analytical Two-valued Potential Energy Functions for the Ground State Surfaces of $CO_2(\tilde{X}^1\ \Sigma_g^+)$ and CS_2 $(\tilde{X}^1\ \Sigma_g^+)$. Croat Chem Acta 1984; 57: 355-365.

[56] Faginas Lago N, Lombardi A, Pacifici L, Costantini A. Design and Implementation of a Grid Application for Direct Calculations of Reactive Rates J Phys Chem 2013; submitted

[57] Pacifici L, Verdicchio M, Faginas Lago N, Costantini A. A high level ab initio study of the N_2 + N_2 reaction channel. J Comp Chem 2013; submitted

[58] Lombardi, A, Faginas Lago, N, Costantini, A, Pacifici, L. J Comp Chem 2013; Submitted.

[59] Laub B, Venkatapathy E. Thermal protection system technology and facility needs for demanding future planetary missions. International workshop on planetary probe atmospheric entry and descent trajectory analysis and science. Lisbon: Portugal 2003.
[60] Cacciatore M, Rutigliano M, Billing GD. EleyRideal and LangmuirHinshelwood recombination coefficients for oxygen on silica surfaces. J Thermophys Heat Trans 1999; 13: 195-203.
[61] Barbato M, Reggiani S, Bruno C, Muylaert J. Model for heterogeneous catalysis on metal surfaces with application to hypersonic flows. J Thermophys Heat Trans 2000; 14: 412-420.
[62] Morón V, Gamallo P, Sayós R. DFT and kinetics study of O/O_2 mixtures reacting over a graphite (0001) basal surface. Theor Chem Acc 2011; 128: 683-694.
[63] Morón V, Gamallo P, Martin-Gondre L, Crespos C, Larregaray P, Sayós R. Recombination and chemical energy accommodation coefficients from chemical dynamics simulations: O/O_2 mixtures reacting over a β-cristobalite (001) surface. Phys Chem Chem Phys 2011; 13: 17494-17504.
[64] Dynamics of Molecule-Surface Interactions. In: Billing GD. (New York, 2000). Ed. John Wiley&Sons.
[65] Cacciatore M, Billing GD. Dynamical relaxation of $H_2(vj)$ on a copper surface. Surf Sci 1990; 232: 35-50.
[66] Arasa C, Morón V, Busnengo HF, Sayós R. Eley-Rideal reaction dynamics between O atoms on β-cristobalite (100) surface: A new interpolated potential energy surface and classical trajectory study. Surf Sci 2009; 603: 2742-2751.
[67] Gamallo P, Rutigliano M, Orlandini S, Cacciatore M, Sayós R. Molecular dynamics study of hydrogen atom recombination over silica, based on a new analytical DFT potential energy surface. AIP Conference Proceedings 2012; 1501: 1129-1136.
[68] Rutigliano M, Zazza C, Sanna N, Pieretti A, Mancini G, Barone V, Cacciatore M. Oxygen adsorption on β-cristobalite polymorph: *ab initio* modeling and semiclassical time-dependent dynamics. J Phys Chem A 2009; 113: 15366-15375.
[69] Arasa C, Gamallo P, Sayós R. Adsorption of atomic oxygen and nitrogen at β-cristobalite (100): a density functional theory study. J Phys Chem B 2005; 109: 14954-14964.
[70] Rutigliano M, Zazza C, Orlandini S, Sanna N, Barone V, Cacciatore M. Oxygen Atoms and Molecules on Silica Surfaces: collisional data relevant to aerospace In: Catalytic Gas-Surface Interactions, NATO Applied Vehicle Technology Panel AVT-199, STO-MP-AV-T199 2012; pp. 5-1- 5-28.
[71] Sayós R, Morón V, Arasa C, Busnengo HF. Theoretical dynamics study of several atomic and molecular oxygen processes over a silica surface. Proceedings of the 6th European Symposium on Aerothermodynamics for Space Vehicles (ESA SP-659), Versailles, France 2009.

TABLE I. Final states, cross sections and probabilities for the process CO_2(0,0,0) + CO_2(0,0,0) at collision energy $E_{\rm col}$ = 3.47 eV and molecular angular momentum randomly selected from a Boltzmann distribution at 40000 K

$v'_{a1}, v'_{a2}, v'_{a3}$	$v'_{b1}, v'_{b2}, v'_{b3}$	Prob.	Cross section (Å^2)
1 0 0	0 0 0	0.07426	103.0
1 1 0	1 0 0	0.06706	95.0
1 0 0	1 0 0	0.06179	86.0
1 0 0	0 1 0	0.04790	65.0
1 1 0	0 0 0	0.03779	53.0
0 1 0	0 0 0	0.02961	39.0
1 2 0	1 0 0	0.02781	39.0
1 1 0	0 1 0	0.02631	36.0
0 0 0	0 0 0	0.02258	32.0
1 0 0	0 2 0	0.02164	29.0
1 1 0	1 1 0	0.02078	29.0
1 2 0	0 0 0	0.01847	26.0
1 0 0	0 3 0	0.01898	26.0
1 2 0	1 1 0	0.01650	23.0
0 2 0	0 0 0	0.01448	20.0
1 0 0	0 4 0	0.01281	18.1
1 1 0	0 2 0	0.01213	17.2
0 1 0	0 1 0	0.01204	15.4
1 2 0	0 1 0	0.01157	15.2
1 3 0	1 0 0	0.01063	15.0
1 1 0	0 3 0	0.01028	14.7
0 3 0	0 0 0	0.01101	14.5
1 0 0	0 5 0	0.00844	12.1
0 3 0	0 1 0	0.00883	11.9
0 2 0	0 1 0	0.00810	10.7
0 4 0	0 0 0	0.00758	10.4
1 1 0	0 4 0	0.00698	10.3
1 3 0	0 0 0	0.00724	9.8
1 4 0	1 0 0	0.00617	9.1
1 3 0	1 1 0	0.00604	8.5

TABLE II. Final states, cross sections and probabilities for collisions the process CO_2(1,0,0) + CO_2(1,0,0) at collision energy $E_{\rm col}$ = 3.47 eV and molecular angular momentum randomly selected from a Boltzmann distribution at 40000 K

$v'_{a1}, v'_{a2}, v'_{a3}$	$v'_{b1}, v'_{b2}, v'_{b3}$	Prob.	Cross section (Å^2)
1 1 0	1 1 0	0.05323	72.0
1 2 0	1 1 0	0.04945	67.0
1 1 0	0 1 0	0.04061	55.0
2 1 0	1 1 0	0.02649	36.0
2 0 0	1 1 0	0.02507	35.0
1 3 0	1 1 0	0.02527	34.0
1 1 0	0 2 0	0.02101	29.0
1 2 0	0 1 0	0.01700	24.0
2 0 0	1 2 0	0.01363	20.0
2 1 0	1 2 0	0.01318	18.0
1 4 0	1 1 0	0.01266	17.8
1 3 0	1 2 0	0.01274	17.5
1 1 0	0 3 0	0.01229	17.1
1 2 0	1 2 0	0.01233	16.6
1 2 0	0 2 0	0.01132	16.0
2 0 0	0 1 0	0.01140	15.6
1 3 0	0 1 0	0.00974	13.7
2 1 0	0 1 0	0.00945	13.4
0 2 0	0 1 0	0.00876	12.6
3 0 0	1 1 0	0.00872	11.7
0 1 0	0 1 0	0.00795	11.3
2 2 0	1 1 0	0.00791	10.7
1 1 0	0 4 0	0.00815	10.6
1 5 0	1 1 0	0.00763	10.5
2 1 0	1 3 0	0.00722	10.0
2 1 0	2 0 0	0.00682	10.0
2 1 0	0 2 0	0.00677	9.6
1 4 0	1 2 0	0.00665	9.5
2 0 0	1 3 0	0.00665	9.0

VII. FIGURE CAPTIONS

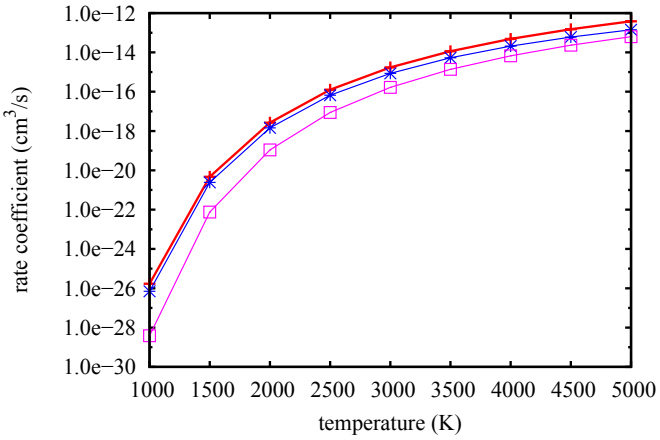

FIG. 1. Thermal rate coefficients for $N_2 + O \rightarrow NO + N$ reaction compared with results in literature. (plus markers) this work; (asterisks) Baulch et al. [33]; (squares) Bose and Candler [32].

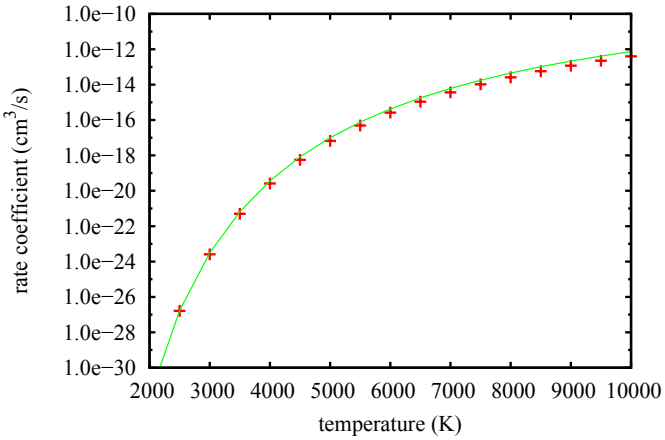

FIG. 2. Thermal rate coefficient for dissociation in $N_2 + O$ collisions compared results in literature. (plus markers) this work; (solid line) Shatalov [34].

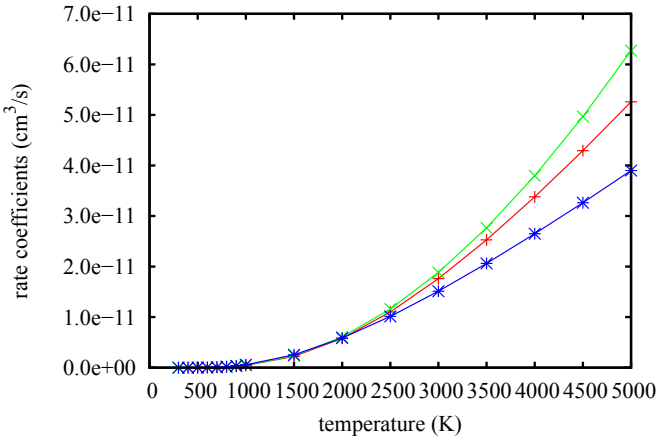

FIG. 3. Thermal rate coefficients for N + O_2 → NO + O reaction compared with results in literature. (plus markers) this work; (cross markers) Sayós et al. [29]; (asterisks) Baulch et al. [36].

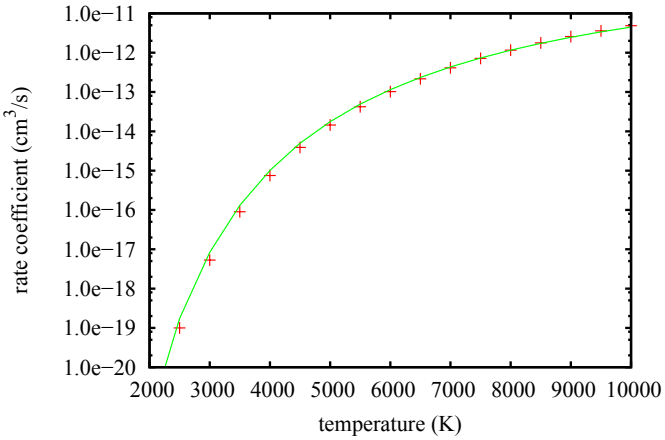

FIG. 4. Thermal rate coefficient for dissociation in N + O_2 collisions compared results in literature. (plus markers) this work; (solid line) Shatalov [34].

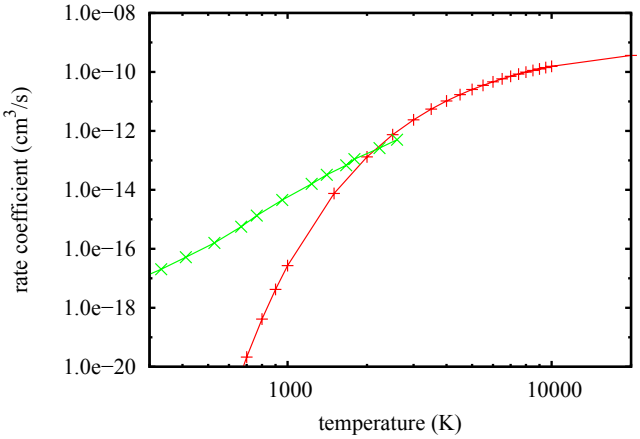

FIG. 5. Vibrational relaxation rate coefficient obtained in this work (plus markers) compared with results by Orlikowski [42] by close coupling calculations (cross markers).

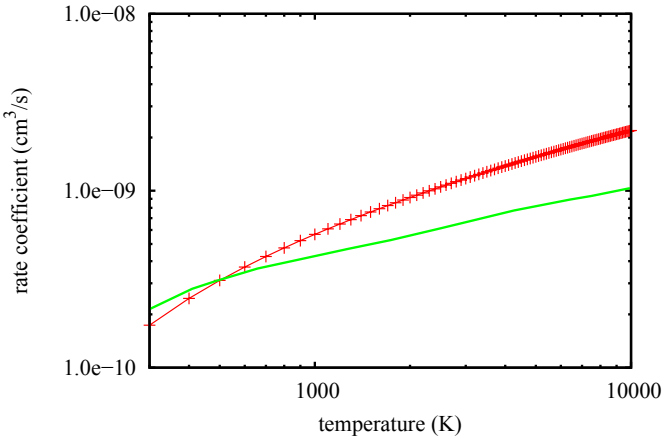

FIG. 6. Dissociation rate coefficient for He + $H_2(v = 14, j = 0)$ collision obtained in this work (plus markers) compared with results by Paolini et al. [44] by quantum method (solid line).

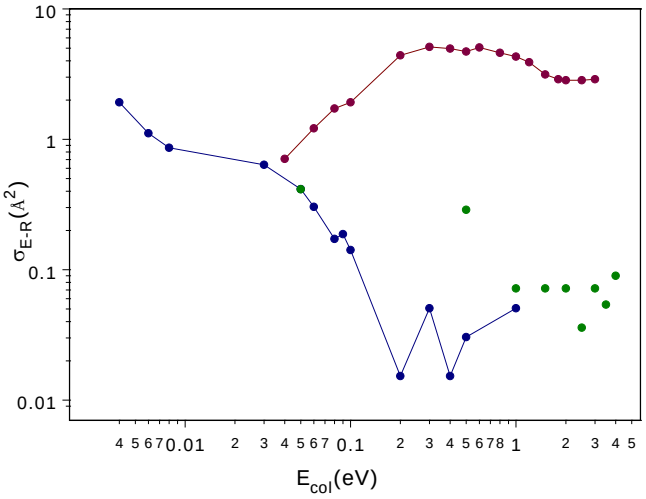

FIG. 7. σ_{E-R} values calculated on the on β-cristobalite PES using semiclassical approaches for oxygen (blue dots and lines) and hydrogen (red dots and lines) atoms recombination. The σ_{E-R} values calculated for the oxygen atom (green dots) recombination using the classical approach is also shown.

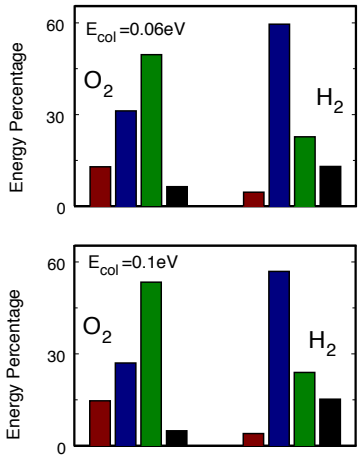

FIG. 8. Reaction exothermicity percentage transferred to vibrational (blue bar), rotational (green bar), translational (black bar) motion of he formed O_2 and H_2 molecules and to the phonons surface (red bar), using the semiclassical approach for $E_{\rm col}$ = 0.06 and 0.1 eV and T_S = 1000 K.

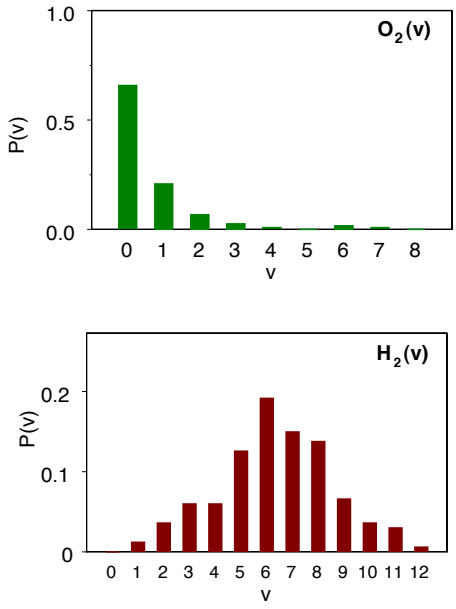

FIG. 9. Vibrational population distributions (normalized to unit) for O_2 and H_2 molecules formed by E-R reaction at $E_{\rm col}$ = 0.13 eV for the classical approach and 0.06 eV for semiclassical approach, respectively.

Reduction of State-to-State to macroscopic models for hypersonics

A. Bourdon [1,2], J. Annaloro[3], A. Bultel[3], M. Capitelli[4], G. Colonna[5], A. Guy[1,2], T.E. Magin[6], A. Munafó[6], M.Y. Perrin[1,2] and L.D. Pietanza[5]

[1] CNRS, UPR 288 "Laboratoire d'Energétique Moléculaire et Macroscopique, Combustion" (EM2C), Grande voie des vignes, 92295 Châtenay-Malabry, France
[2] Ecole Centrale Paris, Grande voie des vignes, 92295 Châtenay-Malabry, France
[3] CORIA, UMR CNRS 6614, Université de Rouen, BP 12, Avenue de l'Université, 76801 Saint-Etienne du Rouvray Cedex, France
[4] Dip. di Chimica, Universitá di Bari, Via Orabona, 4, 70126, Italy
[5] CNR-IMIP, sede di Bari, Via Amendola 122/D, 70126, Italy
[6] Aeronautics and Aerospace Department, von Karman Institute for Fluid Dynamics, Chaussée de Waterloo 72, 1640 Rhode-Saint-Genèse, Belgium

E-mail: `anne.bourdon@ecp.fr`

Keywords: Nonequilibrium flows, vibration-chemistry coupling, state-to-state models, macroscopic models, re-entry applications

1 July 2013

Abstract. Four different types of macroscopic models developed for the vibration-chemistry coupling in nonequilibrium flows for reentry applications are presented. First, using an approach based on nonequilibrium thermodynamics, global rate coefficients of dissociation of N_2 and O_2 under parent molecular or atomic impact and backward molecular recombination are determined. Then a Two-Level Distribution (TLD) model is developed, in which a relaxation equation for vibrational temperature is solved as in the case of multi-temperature models but with the simultaneous solution of a kinetic equation, as in the case of state-to-state models, but only for the last vibrational level. In a third approach, a multi-internal temperature model is presented to describe accurately the vibrational distribution function in using several groups of levels, within which the levels are assumed to follow a Boltzmann distribution at an internal temperature of the group. This multi-internal temperature model allows us to describe accurately the vibrational energy relaxation and dissociation processes behind a strong shock wave. Finally, a rovibrational collisional coarse-grain model is developed to reduce a detailed rovibrational mechanism for the internal energy excitation and dissociation processes behind a strong shockwave in a nitrogen flow.

1. Introduction

The planetary atmospheric entry phase of a moving body (spacecraft, probe, meteorite, etc.) involves a complex chemistry mainly due the weak values of the hydrodynamic characteristic time scale with respect to the characteristic time scales required to reach chemical equilibrium. The most accurate way to simulate non equilibrium flows for re-entry applications is to use State-to-State models (StS), in which a system of master equations is solved, with one equation for each internal energy level of each species. This approach allows a self consistent calculation of chemistry and energy source terms without any assumption on the internal distribution. In the last years, StS vibrational kinetics have been developed and applied to 1-D high enthalpy flows, such as boundary layer [1; 2], nozzle expansion [3; 4; 5; 6] and shock wave [3; 4; 5; 7; 8; 9; 10; 11]. These models give a very accurate insight of the behavior of chemical processes and predict, for example, in recombination regimes, the overpopulation of the tail of vibrational distributions due to preferential pumping of high-lying vibrational levels [12]. Unfortunately, the systematic implementation of STS is difficult due to both the lack of data for rate coefficients for each internal level and to long computational times, preventing the use of these models in higher (2D-3D) dimensional codes. For these reasons, one of the most commonly used approach, especially in the case of 2D or 3D high enthalpy flow simulations for re-entry applications, is the Multi-Temperature (MT) approach [13; 14; 15; 16; 17; 18; 19]. In MT, each degree of freedom is described by a Boltzmann distribution at a different temperature. As an example, for diatomic molecules, the rotational degree of freedom is generally assumed to be in equilibrium with the translational temperature while the vibrational temperature is determined solving a linear relaxation equation. Vibrational temperatures affect the rate coefficients for chemical reactions, such as molecular dissociation, which can be accelerated by vibrational excited distributions. One of the most widely used

multitemperature model has been proposed by Park [13; 14; 15]. In this model, the rate coefficients are calculated using an Arrhenius function depending on an effective temperature calculated as the geometric average of the translational and vibrational temperatures. However, as discussed by Park [16; 20], even if very efficient from a computational point of view, the use of multitemperature models can only be justified when the departure from the Boltzmann population is small (i.e., for low velocity and high pressure reentry conditions). Moreover, multitemperature rate coefficients have been obtained heuristically, to reproduce experimental data obtained in shock tube facilities.

To overcome this problem, the group of St Petersburg proposed to approximate the vibrational distribution by a piecewise function dividing the vibrational ladder in three regions [21]. The low energy region is approximated by a Treanor distribution, the middle energy range by a constant function and the distribution tail by a Boltzmann function. This approximation is based on the idea that the low and middle levels are determined mainly by mono-quantum Vibration-Vibration (VV) processes and high energy levels by mono-quantum Vibration-Translation (VT) processes. These assumptions are based on the general hierarchy of relaxation times for the different processes. It is interesting to note that recently, significant efforts have been done by different research groups at NASA Ames [22; 23], University of Barcelona [24] and Plasma Institute in Bari [25; 26; 27] to calculate rovibrational rate coefficients for processes of importance for re-entry applications. In these new databases, the importance of multi-quantum VT and dissociation/recombination processes has been clearly put forward. Then there is the need to derive new macroscopic models to carry out 1D, 2D and 3D simulations of high enthalpy flows for re-entry applications which allow to better describe nonequilibrium flows and which are based on most recent state-to-state rate coefficients. In this paper, we discuss the derivation of different types of macroscopic models and we focus on the modeling of the vibration-chemistry coupling. In Section 2, we first present global dissociation and recombination rate coefficients, very easy to implement in multi-dimensional flow codes. In Section 3, we present a Two-Level Distribution (TLD) model, in which a relaxation equation for vibrational temperature is solved as in the case of MT but with the simultaneous solution of a kinetic equation, as in the case of STS, but only for the last vibrational level. In Section 4, we propose to better represent the vibrational nonequilibrium of a molecular flow, in using several internal vibrational temperatures. Finally in Section 5, we discuss the derivation of a coarse-grain model from a detailed rovibrational database.

2. Global dissociation and recombination rate coefficients

In this section, we propose to study global rate coefficients. We illustrate their determination for N_2 and O_2 dissociation under heavy particle impact. The developed method is also applied to recombination. The relation between these rate coefficients and the equilibrium constant is discussed.

2.1. Global rate coefficient definition

The balance equation for a species X_n ($n = 1$ for atoms and $n = 2$ for diatomic molecules) in its excited state i in a volume V without inner swirls and without radiative phenomena can be written under the form

$$\frac{1}{V}\frac{dN_{X_{n,i}}}{dt} = [\dot{X_{n,i}}]_C \tag{1}$$

where $N_{X_{n,i}} = [X_{n,i}]\,V$ is the number of particles $X_{n,i}$ and $[X_{n,i}]$ their number density. Inside V, elementary processes occur which can be generally written as

$$X_{n,i} + P \rightleftarrows X^{\beta+}_{n-\alpha,j} + \alpha X_{1,m} + \beta e^- + P \tag{2}$$

where P is the collision partner and (n, α, β) defines the type of the elementary process. The process is called elementary since it refers to excited states only. If initially the total number of X_n is higher than its value at equilibrium ($N_{X_n} > (N_{X_n})_{eq}$), the system globally evolves according to the process

$$X_n + P \xrightarrow{f} X^{\beta+}_{n-\alpha} + \alpha X_1 + \beta e^- + P \tag{3}$$

This global process is denoted *f*. The temporal evolution of N_{X_n} is therefore governed by

$$\frac{1}{V}\left(\frac{dN_{X_n}}{dt}\right)_f = \frac{1}{V}\sum_i \frac{dN_{X_{n,i}}}{dt} = [\dot{X_n}]_C \tag{4}$$

which is similar to equation (1), but for the species X_n for all excited states. The global rate coefficient k_f is then defined as the parameter depending on T_P the kinetic temperature of P, such as

$$\frac{1}{V}\left(\frac{dN_{X_n}}{dt}\right)_f = -k_f[X_n][P]. \tag{5}$$

The global rate coefficient is therefore the equivalent or effective rate coefficient reflecting the behaviour of the species X_n [12; 28; 29; 30; 31; 32; 33]. This rate coefficient is a measurement of the net variation rate of X_n due to the complex behaviour of the excited states.

If $N_{X_n} < (N_{X_n})_{eq}$, elementary processes lead to the global process of type r

$$X^{\beta+}_{n-\alpha} + \alpha X_1 + \beta e^- + P \xrightarrow{r} X_n + P \tag{6}$$

with

$$\frac{1}{V}\left(\frac{dN_{X_n}}{dt}\right)_r = \frac{1}{V}\sum_i \frac{dN_{X_{n,i}}}{dt} = k_r[X^{\beta+}_{n-\alpha}][X_1]^\alpha[e^-]^\beta[P] \tag{7}$$

Owing to the value of T_P and the initial conditions, the values of

$$k_f^* = -\frac{1}{[X_n][P]}\frac{1}{V}\sum_i \frac{dN_{X_{n,i}}}{dt} \tag{8}$$

for a process of type f or

$$k_r^* = \frac{1}{[X_{n-\alpha}^{\beta+}][X_1]^\alpha[e^-]^\beta[P]} \frac{1}{V} \sum_i \frac{dN_{X_{n,i}}}{dt} \tag{9}$$

for a process of type r are time-dependent. The simplest proof is given by the fact that $k_{f,r}^* \neq 0$ during the evolution and $k_{f,r}^* = 0$ when equilibrium is reached since $\frac{dN_{X_{n,i}}}{dt} = 0$ $\forall i$. When we follow k_f^* or k_r^* in time, a quasi-steady state (QSS) is observed. This behaviour is illustrated in section 2.3. However, experimental determinations of the global rate coefficients show that they are time-independent provided the temperature is steady. The QSS is therefore the only duration for which the concept of global rate coefficient is relevant. As a result, k_f and k_r are then identified as the values of k_f^* and k_r^* during the QSS, respectively.

2.2. Global rate coefficients and equilibrium constant

It is worth noticing that $\sum_i \frac{1}{V} \frac{dN_{X_{n,i}}}{dt}$ refers to irreversible processes in (8) and (9). In addition, they depend on initial conditions. In the general case, k_f and k_r are therefore independent from each other. However, they are often assumed linked by the corresponding equilibrium constant. This peculiarity can be observed only for weak departure from equilibrium. Indeed, during a global process, when (p, T_P) are maintained constant, the time variation of the free enthalpy of the mixture is governed by

$$\begin{aligned}
\left(\frac{dG}{dt}\right)_{f,r} = {} & \mu_{X_{n-\alpha}^{\beta+}}(p, T_P) \frac{dN_{X_{n-\alpha}^{\beta+}}}{dt} \\
& + \alpha\, \mu_{X_1}(p, T_P) \frac{dN_{X_1}}{dt} + \beta\, \mu_{e^-}(p, T_P) \frac{dN_{e^-}}{dt} \\
& + \mu_{X_n}(p, T_P) \frac{dN_{X_n}}{dt} + \frac{dN_{X_{n-\alpha,j}^{\beta+}}}{dt} k_B T_P \ln x_{X_{n-\alpha,j}^{\beta+}} \\
& + \alpha \frac{dN_{X_1}}{dt} k_B T_P \ln x_{X_1} + \beta \frac{dN_{e^-}}{dt} k_B T_P \ln x_{e^-} \\
& + \frac{dN_{X_n}}{dt} k_B T_P \ln x_{X_n}
\end{aligned} \tag{10}$$

where μ_l is the chemical potential (free enthalpy) per particle of type l, x_l the mole fraction of the species l, and $\mu_l(p, T_P) = \mu_l(p, T_P, x_l) - k_B T_P \ln x_l$ the pure species chemical potential assuming a dilute gas-like behaviour (see [34]) with k_B the Boltzmann constant. Defining the extent of reaction $\xi_{f,r}$, $K_{f,r}$, $\delta = 1$ for a reaction of type f, $\delta = -1$ for a reaction of type r, and $\Delta\mu(p, T_P)$ such as

$$\left(\frac{d\xi}{dt}\right)_{f,r} = \delta \left(\frac{dN_{X_{n-\alpha}^{\beta+}}}{dt}\right)_{f,r} = \delta \left(\frac{dN_{X_1}}{dt}\right)_{f,r} = \delta \left(\frac{dN_{e^-}}{dt}\right)_{f,r} = -\delta \left(\frac{dN_{X_n}}{dt}\right)_{f,r}, \tag{11}$$

$$K_{f,r} = \frac{[X_{n-\alpha}^{\beta+}][X_1]^\alpha[e^-]^\beta}{[X_n]}, \tag{12}$$

$$\Delta\mu(p,T_P) = \mu_{X_{n-\alpha}^{\beta+}}(p,T_P) + \alpha\,\mu_{X_1}(p,T_P) + \beta\,\mu_{e^-}(p,T_P) - \mu_{X_n}(p,T_P)\,, \tag{13}$$

$K_{f,r}$ finally writes as

$$K_{f,r} = e^{\frac{1}{k_B T_P}\left[\delta\left(\frac{\frac{dG}{dt}}{\frac{d\xi}{dt}}\right)_{f,r} - \Delta\mu(p,T_P)\right]}. \tag{14}$$

When equilibrium is reached, G does not vary anymore, even if a fluctuation of the extent ξ is observed. As a result, $K_{eq} = e^{\frac{1}{k_B T_P}[-\Delta\mu(p,T_P)]}$ and

$$K_{f,r} = K_{eq}\, e^{\frac{\delta}{k_B T_P}\left(\frac{\frac{dG}{dt}}{\frac{d\xi}{dt}}\right)_{f,r}}. \tag{15}$$

The global reaction is irreversible which leads to $\left(\frac{dG}{dt}\right)_{f,r} < 0$ and $\left(\frac{d\xi}{dt}\right)_{f,r} > 0$ (see [34]). Therefore $K_f < K_{eq}$ and $K_r > K_{eq}$. Let us assume the system close to equilibrium such as $N_{X_n} > (N_{X_n})_{eq}$ in a first part and $N_{X_n} < (N_{X_n})_{eq}$, the total number being the same as at equilibrium for the complete system. Owing to the weak departure from equilibrium, N_{X_n} evolves in each part such as

$$\left(\frac{dN_{X_n}}{dt}\right)_f + \left(\frac{dN_{X_n}}{dt}\right)_r = 0 \tag{16}$$

From the product $K_f K_r$, the ratio $\frac{k_f}{k_r}$ can be deduced

$$\frac{k_f}{k_r} = -\frac{\left(\frac{dN_{X_n}}{dt}\right)_f}{\left(\frac{dN_{X_n}}{dt}\right)_r}\frac{K_{eq}^2}{\frac{[X_{n-\alpha}^{\beta+}][X_1]^\alpha[e^-]^\beta}{[X_n]}} e^{\frac{1}{k_B T_P}\left[\frac{\left(\frac{dG}{dt}\right)_f}{\left(\frac{d\xi}{dt}\right)_f} - \frac{\left(\frac{dG}{dt}\right)_r}{\left(\frac{d\xi}{dt}\right)_r}\right]}. \tag{17}$$

Equilibrium being stable with respect to fluctuations,

$$\frac{dG}{dt} = \left(\frac{dG}{dt}\right)_f + \left(\frac{dG}{dt}\right)_r \equiv 0 \tag{18}$$

is obvious and using (11) and (16), we obtain, since the system is close to equilibrium

$$\frac{k_f}{k_r} = \frac{K_{eq}^2}{\frac{[X_{n-\alpha}^{\beta+}][X_1]^\alpha[e^-]^\beta}{[X_n]}} \simeq \frac{K_{eq}^2}{\left(\frac{[X_{n-\alpha}^{\beta+}][X_1]^\alpha[e^-]^\beta}{[X_n]}\right)_{eq}} = K_{eq}. \tag{19}$$

It is worth noticing that $k_f/k_r \simeq K_{eq}$ is only valid close to equilibrium. Indeed, equations (16) and (18) are not fulfilled in case of strong nonequilibrium.

2.3. Global rate coefficients for N_2 and O_2 dissociation and recombination

These cases correspond to $X \equiv$ N or O, $n = 2$, $\alpha = 1$ and $\beta = 0$. The vibrational energy diagram of the molecules is taken from [26] and [35]. The cases $P \equiv N_2$ or N for the dissociation of N_2 and $P \equiv O_2$ or O for the dissociation of O_2 are treated. Elementary processes (2) correspond to vibration-translation (when $P \equiv N_2$, O_2, N

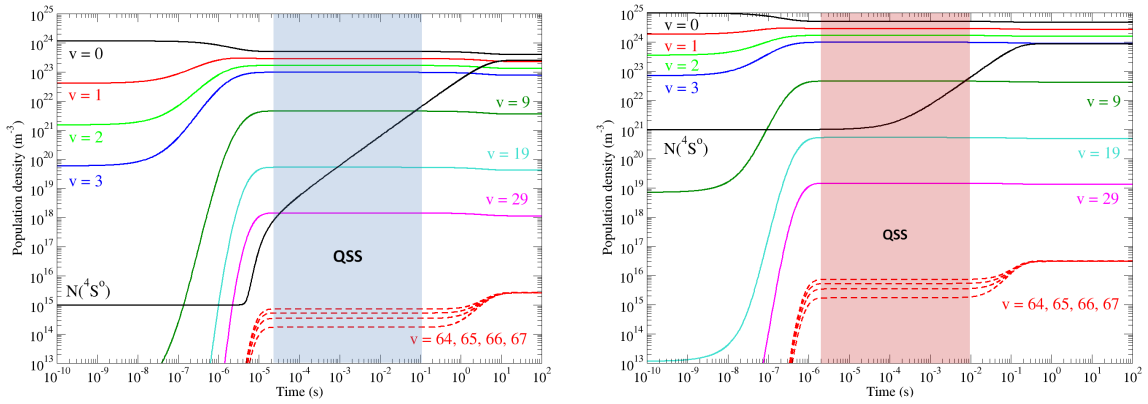

Figure 1. Time evolution of the population density of excited states of N and N_2 under $P \equiv N_2$ impact at $T_A = 6\ 000\ K$ in dissociation situations for arbitrary initial conditions with (a) $p = 10^5\ Pa$ and (b) $p = 10^6\ Pa$.

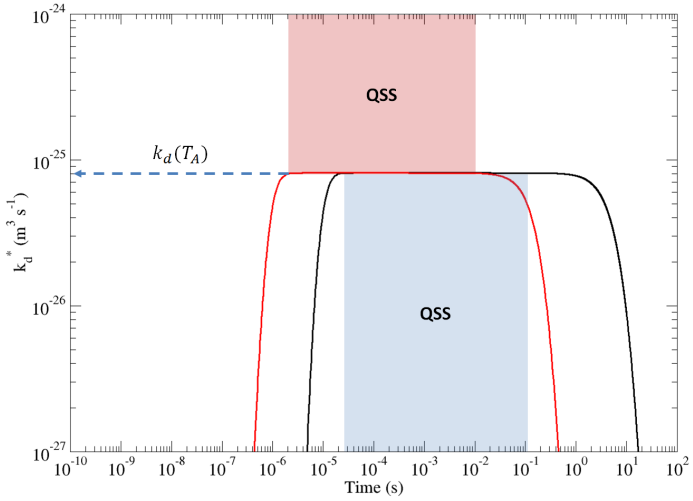

Figure 2. Evolution of k_d^* defined as k_f^* by equation (8) in the conditions of figure 1(a) in black and of figure 1(b) in red. The QSS corresponding to figures 1(a) and 1(b) are indicated.

or O) and vibration-vibration (when $P \equiv N_2$ or O_2) processes. Multi-quanta jumps are taken into account only when $P \equiv$ N or O: for molecule-induced collisions, the rate coefficients for $\Delta v = \pm 1$ transitions are indeed largely higher ([2], [26], [27] and [36]). Figures 1(a) and 1(b) illustrate the time evolution of the species densities in the case of the dissociation of N_2 ($K_f < K_{eq}$) under $P \equiv N_2$ impact when $T_P \equiv T_A = 6\ 000\ K$ for $p = 10^5\ Pa$ and $p = 10^6\ Pa$, respectively. Before the final equilibrium state, the mixture reaches an intermediate quasi-steady state characterized by constant population densities for excited states. One can see that this QSS is not the same. It therefore depends on the initial conditions and particularly on the pressure level, a magnification of one order of magnitude of the pressure leading to characteristic time

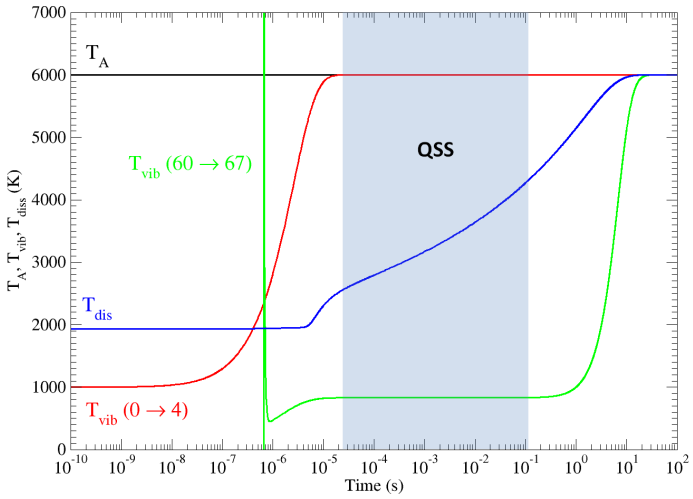

Figure 3. Evolution of T_{dis}, $T_{vib}(0 \rightarrow 4)$ and $T_{vib}(60 \rightarrow 67)$ in the conditions of figure 1(a).

scales ten times shorter. We can observe that states close to the dissociation limit are underpopulated with respect to equilibrium with higher values for the case at higher pressure. Figure 2 displays the parameter k_d^* similar to k_f^* of equation (8) for the present case of dissociation. We observe the same QSS as the one previously observed on excited states. Although the cases are different, the value obtained for k_d^* is the same whatever the initial conditions and the pressure level. Since the common parameter between 1(a) and 1(b) is only T_A (6 000 K in the present case), we deduce that the final value of the global rate coefficient is $k_d \equiv k_d^*(QSS)$ which depends on T_A only. In order to further characterize the global process, we calculated two vibrational temperatures defined as the excitation temperature

$$T_{vib}(i \rightarrow j) = -\frac{1}{k_B \left[\frac{d}{dE_v}\left(\ln[N_2^v]\right)\right]_{lsl}} \tag{20}$$

of the groups corresponding to the first 5 ($i = 0$, $j = 4$) and to the last 8 ($i = 60$, $j = 67$) vibrational levels. lsl means that the derivative is the slope of the least square line. On figure 3, the different T_{vib} values (equal to 1 000 K at $t = 0$) are compared with T_A and the dissociation temperature defined as

$$T_{dis} = \frac{E_{dis}}{k_B \ln\left\{\frac{[N_2^{v=0}]}{[N]^2}\frac{g_N^2}{Z_r(v=0)}\left(\frac{2\pi\mu k_B T_A}{h^2}\right)^{3/2}\right\}} \tag{21}$$

with usual notations. T_{dis} is close to the temperature of the mixture at equilibrium having the same dissociation degree. We can see that the coupling between translation and low lying levels is very rapid contrary to the case of high-lying levels. The evolution of the high-lying levels is so rapid that $T_{vib}(60 \rightarrow 67)$ is quite different from its initial value for $t > 10^{-10}s$. This is due to the chosen initial conditions which correspond to a

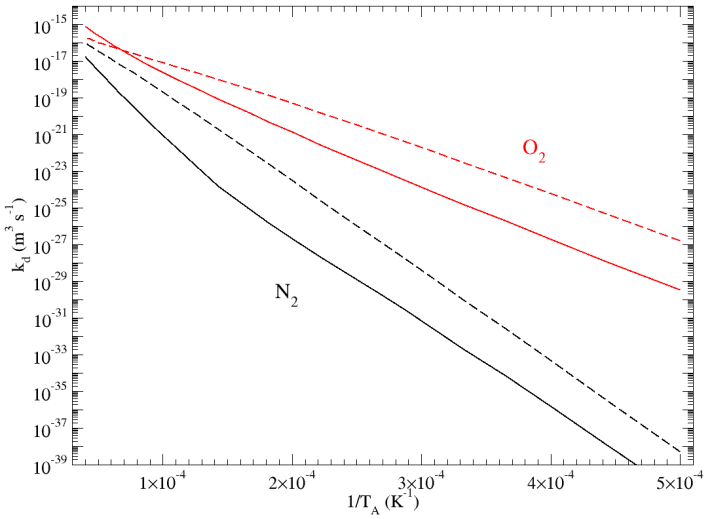

Figure 4. Global rate coefficient of N_2 (in black) and O_2 (in red) dissociation for molecular collision partner (continuous lines for $P \equiv N_2$ or $P \equiv O_2$, respectively) and for atomic collision partner (dashed lines for $P \equiv N$ or $P \equiv O$, respectively) as a function of $1/T_A$.

very strong nonequilibrium. Vibrational temperatures are steady during the QSS and T_{dis} increases since the mixture globally dissociates. The discrepancy between the two vibrational temperatures previously defined illustrates the vibrational nonequilibrium during dissociation, therefore the inequality $K_f < K_{eq}$. Dissociation occurs through the last vibrational level since multi-quanta jumps are not taken into account. This level is approximately ten times underpopulated with respect to equilibrium during dissociation. Changing the T_{vib} initial values leads to a modification of the dynamics of the excited states, but the value of k_d^* remains unchanged during the QSS and basically depends on T_A only. In the present case, the pressure p has no influence on k_d^* since the plasma is ideal. The previous procedure is repeated for 2 000 $K \leq T_A \leq$ 25 000 K for $P \equiv N_2$ and N. The O_2 dissociation is also treated with $P \equiv O_2$ or O. The results are displayed on figure 4. The quasi-linear form of the curves of figure 4 suggests an Arrhenius interpolation

$$k_{f,r}(T_A) = A_{f,r}\, T_A^{\alpha_{f,r}}\, e^{-\frac{T_{f,r}}{T_A}}, \tag{22}$$

the parameters A_f, α_f and T_f of which are listed in table 1. The resulting rate coefficients can be compared to reference data. Figure 5 illustrates this comparison for the N_2 dissociation under N impact with the values of [37], [38], [39], [40], [41] and [27]. The agreement is fairly good. The previous approach is applied to the recombination (here performed for 2 000 $K \leq T_A \leq$ 6 000 K only because a clear QSS identification is not systematic for higher temperature). The evolution of k_r with T_A is satisfactorily interpolated by the Arrhenius form (22). The coefficients A_r, α_r and T_r are listed in table 1. Significant discrepancies are found with literature for the recombination due to molecular impact. For atomic impact, the agreement between our 3 O $\rightarrow$ O_2 + O recombination rate coefficient and the ones due to [37], [41] and [42] is very good. Since

Table 1. $A_{f,r}$, $\alpha_{f,r}$, $T_{f,r}$ values for Arrhenius interpolations (22) of the global rate coefficients.

Arrhenius interpolation	$k_f = A_f\, T_A^{\alpha_f}\, e^{-T_f/T_A}$ $(m^3\, s^{-1})$			$k_r = A_r\, T_A^{\alpha_r}\, e^{-T_r/T_A}$ $(m^6\, s^{-1})$		
Global process	A_f	α_f	T_f (K)	A_r	α_r	T_r (K)
$N_2 + N_2 \underset{k_r}{\overset{k_f}{\rightleftarrows}} 2\,N + N_2$	7.61×10^{-34}	4.085	96 068	2.41×10^{-41}	-2.111	1 430
$N_2 + N \underset{k_r}{\overset{k_f}{\rightleftarrows}} 3\,N$	2.62×10^{-11}	-0.780	115 657	1.32×10^{-45}	0.048	143
$O_2 + O_2 \underset{k_r}{\overset{k_f}{\rightleftarrows}} 2\,O + O_2$	1.23×10^{-25}	2.458	58 450	1.30×10^{-39}	-2.140	7 448
$O_2 + O \underset{k_r}{\overset{k_f}{\rightleftarrows}} 3\,O$	2.88×10^{-13}	-0.474	58 688	5.19×10^{-41}	-1.141	-2 226

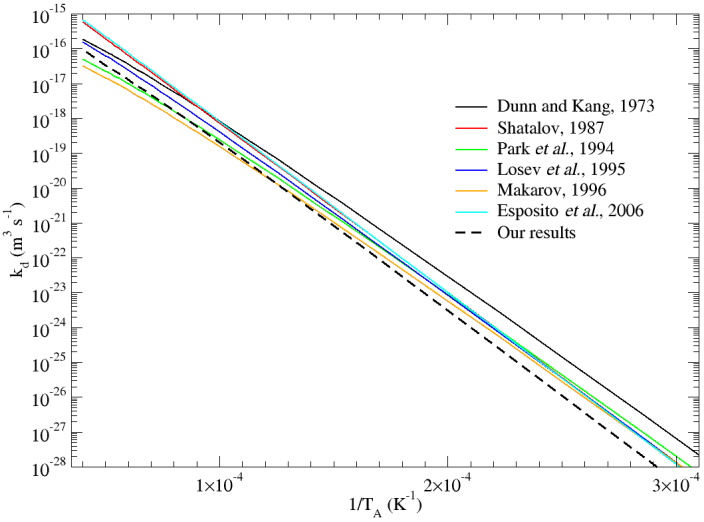

Figure 5. Comparison between the present results and some reference data for the global rate coefficient of N_2 dissociation under N impact as a function of $1/T_A$.

$k_f \equiv k_d$ and k_r are independently determined, k_d/k_r is calculated and compared with the equilibrium (Guldberg & Waage) constant (see figure 6). The discrepancy between k_d/k_r and K_{eq} remains weak in the case of atomic impact. We have shown in section 2.2 that the ratio is close to K_{eq} when the mixture is close to equilibrium. For $T_A = 6\ 000\ K$, figures 1(a), 1(b) and 3 show that the vibrational distribution is far from equilibrium when $P \equiv N_2$. The ratio k_d/k_r is therefore far from K_{eq} at 6 000 K on figure 6. It is interesting to note that in Kustova *et al.* [21; 43], similar results on global dissociation rates and relations with equilibrium constants have been obtained based on the kinetic theory approach.

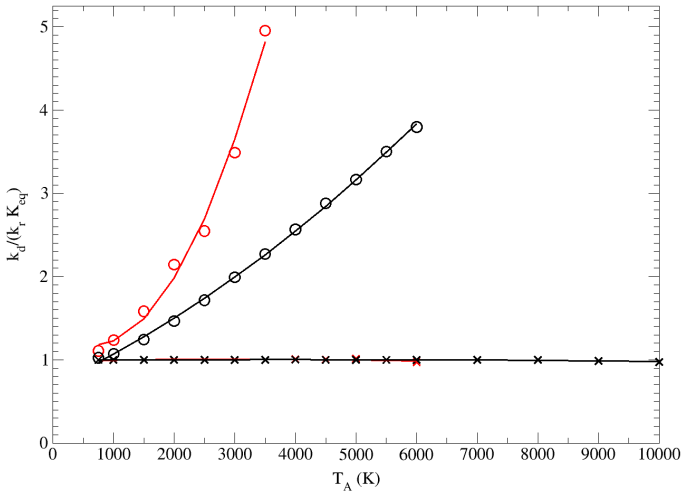

Figure 6. Evolution with T_A of the ratio $k_f/(k_r K_{eq})$ for nitrogen (in black) and oxygen (in red) under atomic (crosses) or molecular (circles) impact. The lines correspond to polynomial interpolations of the second order.

3. Two level Distribution (TLD) Model

In this section, an innovative reduced kinetic model is presented and firstly applied to pure N_2 and O_2 system [12; 44] and to NO formation in air in recombination conditions [45; 46]. To build this model we have applied an inductive approach, starting from a detailed analysis of the StS time evolution of the vibrational distributions and gas composition in conditions similar to those met in different fluid dynamic systems. The basic assumptions are: whatever the initial distribution, the system reaches a quasi-steady-state (QSS) solution obtained as the balance of different processes; the QSS state obtained in the homogeneous calculations are encountered also in fluid dynamic conditions. Different behaviors have been observed [12] for the low energy and the high energy distribution. As a general behavior, the low energy distribution follows a Boltzmann function, while the distribution tail presents a plateau or a strong depletion respectively in recombination and dissociation regime. In recombination regime (see for example ref. [4]) the global rates of endo–thermal chemical processes are influenced mainly by the distribution tail, also in presence of multi–quantum transitions, while the low energy distribution have a small influence, except close to equilibrium conditions. Therefore the Two-Level Distribution (TLD) model has been proposed, where the vibrational temperature is the parameter describing the low energy distribution, where anharmonic correction is negligible, and the population of the last vibrational level is representative of the distribution tail. Other quantities can be representative of the distribution tail, such as the total density of levels with $v > v_{lim}$, but it is more difficult to write the evolution equation for this quantity than for the last vibrational level.
To determine the dependence of the global rates on the relevant quantities, the evolution of the distribution relaxing from T_v to T, with $T_v > T$ and with atomic density higher

than equilibrium value (recombination regime) is calculated, using the state-to-state model, considering one chemical process at a time. Then, we correlate the population of the last level with the global rate of the process considered, even if multi–quantum transitions are considered. This approach gives the so called *first order* rates. In case of diatomic dissociation, the first order rates gives a good accuracy. In other cases, complex interplay between different processes makes the first order rates inaccurate and then higher order corrections are necessary. This is the case of NO formation where there is a strong influence of intermediate vibrational states of oxygen and nitrogen molecules, that cannot be accounted in the TLD model as it was developed in previous papers [12; 44].

3.1. Model description

In this paper the TLD approach has been applied to a 5 species air mixture (N_2, N, O_2, O, NO) and the kinetic processes included into the state-to-state model are [12; 44; 45; 46]

- vTa and vTm for N_2 and O_2

$$N_2(v) + N \rightleftharpoons N_2(v - \Delta v) + N \tag{23}$$

$$N_2(v) + N_2 \rightleftharpoons N_2(v - 1) + N_2 \tag{24}$$

$$O_2(v) + O \rightleftharpoons O_2(v - \Delta v) + O \tag{25}$$

$$O_2(v) + O_2 \rightleftharpoons O_2(v - 1) + O_2 \tag{26}$$

- vv for N_2 and O_2

$$N_2(v) + N_2(w - 1) \rightleftharpoons N_2(v - 1) + N_2(w) \tag{27}$$

$$O_2(v) + O_2(w - 1) \rightleftharpoons O_2(v - 1) + O_2(w) \tag{28}$$

- dissociation by atoms and molecules

$$N_2(v) + N \rightleftharpoons 2N + N \tag{29}$$

$$N_2(v) + N_2 \rightleftharpoons 2N + N_2 \tag{30}$$

$$O_2(v) + O \rightleftharpoons 2O + O \tag{31}$$

$$O_2(v) + O_2 \rightleftharpoons 2O + O_2 \tag{32}$$

- first (Z_1) and second (Z_2) Zel'dovich reactions

$$N_2(v) + O \rightleftharpoons NO + N \tag{33}$$

$$O_2(v) + N \rightleftharpoons NO + O \tag{34}$$

The rates of vT and of dissociation by atoms are those calculated by Esposito [26; 27] and include multi–quantum transitions. The dissociation rates by molecules have been calculated by considering the same dependence on the vibrational quantum number of the dissociation by atoms, normalized to reproduce the thermal rates reported by Shalatov [47]. As a consequence, also the dissociation induced by molecular collisions includes multi-quantum transitions. For the first (Z_1, see eq. 33) and second (Z_2, see eq. 34) Zel'dovich reactions of NO formation, the rate coefficients have been taken from the work of Bose and Candler [48; 49]. The kinetic model is not complete because the mixed processes, as vT for O_2 by N or N_2, have been neglected, even if their contribution can be important. Moreover, the vibrational levels of NO have been neglected because the state-selective rates of NO formation consider only the ground state.

In the TLD approach, plasma composition is obtained by solving a system of macroscopic kinetic equations describing each specie density and, for each molecular specie, two other kinetic equations, one for the vibrational energy relaxation and one for the last vibrational level population. In this approach, chemical rates of dissociation are expressed as the sum of two terms: one as a function of gas and vibrational temperature, as in the MT approach, and the other as a function of gas temperature and of the last vibrational level population (α_S)

$$K_S^{diss} = K_S^0(T, T_{v,S}) + K_S^1(T, \alpha_S) \tag{35}$$

where K^0 is the two–temperature rate used in MT models [12; 44; 45] and $K_S^1(T, \alpha_S)$ is determined from the state–to–state calculations, with the requirement that it goes to zero when α_S approaches the $n_{S,v}^B(T_{v,S})$. It should be emphasized that with eq. 35 we also model processes involving states with $v < v_{last}$, but influenced mainly by highly excited vibrational states.

The dependence on α_S is the innovative point introduced by this model. In this way, chemical rates depend both on the low vibrational energy distribution through the vibrational temperature and on the high vibrational energy distribution through the last vibrational level population. The idea of the TLD model has been developed after accurate analysis of the vibrational distribution behavior [12; 44]. It has been observed [12; 44; 45], from STS calculations that, in recombination regime, the vibrational distribution reaches a quasi-stationary condition in a time interval of approximately t=10^{-8} s. After that, dissociation rates shows a regular dependence on the population of the last vibrational level of the molecule involved into the process.

As an example, fig. 7 shows the dependence of $N_2 + N$ global dissociation rates as a function of last level population obtained from STS time dependence calculations at constant pressure for different gas temperature ($T_g = 1000K, 2000K, 5000K$) [44]. These calculations have been performed by considering the pure gas N_2/N and choosing an initial condition in which recombination should dominate the kinetics, i.e. initial vibrational temperature of N_2 greater than gas temperature ($T_{v0} = 8000K > T_g$) and initial gas composition with molar fractions $\chi_N = 0.9$ and $\chi_{N_2} = 0.1$. As observed, $N_2 + N$ dissociation rate shows a linear dependence from last level population, with the

only exception of short time behavior corresponding to the time interval necessary to reach quasi-steady state conditions.

For the relaxation of the vibrational energy of the s-th molecular specie, the following equation is used

$$\frac{dE_{v,S}}{dt} = G_{vT,S}(T, T_{v,S}) - L_{vT,S}(T, T_{v,S}) \tag{36}$$

in which the gain (G) and the losses (L) are due to vT processes and have been calculated summing up the state-to-state over a Boltzmann vibrational distribution multiplied by the variation of internal energy in the given transition. This strategy is different from MT model approach in which the relaxation depends on $p\tau$ values [13; 14; 15]. In any case, the internal energy is related to the vibrational distributions considering the anharmonic energy levels of the diatomic species [26; 27]. It must be pointed out that in the TLD the contribution of the vibrational energy to the chemical kinetics is very weak, except when the system approaches the chemical equilibrium.

The master equation of the last vibrational level population (α_S) of the s-th molecular specie is obtained by considering gains and losses coming from chemical processes of dissociation by vTa and vTm, NO formation reactions (first second Zel'dovich reaction Z_1 in the case of N_2 and second Zel'dovich reaction Z_2 in the case of O_2), and only losses due to vTa and vTm processes towards lower level ($v < v_{last}$), since, in recombination regime [12; 44], the vv and the vT up-pumping can be considered negligible.

$$\begin{aligned}\frac{d\alpha_S}{dt} = G_S - L_S\alpha_S = K^{r\_vTa}N^3 + K^{r\_vTm}N^2N_2 + K^{r\_Z_i}NON - (K^{d\_vTa}N \\ + K^{d\_vTm}N_2 + K^{d\_Z_i}O + K^{vTa}_{v_{last}\to v}N + K^{vTm}_{v_{last}\to v}N_2)\end{aligned} \tag{37}$$

3.2. Results

In this section, results of the implementation of TLD model and the comparison with STS and MT model are presented. Fig. 8 shows the time evolution of molar fractions of (a) N_2 and (b) O_2 calculated with the three models in the condition in which an air mixture is relaxing at atmospheric pressure to T=1000 K, starting with initial vibrational temperatures $T_{v,N_2} = T_{v,O_2} = 10000K$ and with the following initial molar fractions: $N_2 = 8\ 10^{-4}$, $N = 0.7992$, $O_2 = 2\ 10^{-4}$, $N = 0.1998$, $NO = 0$ [45; 46]. As it can be seen, the TLD model determines molar fractions of N_2 and O_2 molecules in a very good agreement with STS in all the time interval while MT agrees with the other models only for $t > 10^{-5}$ s. In this case, the MT model underestimates the contribution of the overpopulated distribution tails to the chemical processes. As a consequence, for N_2 this behavior results in lower dissociation rates, speeding up the recombination kinetics. The same behavior is observed for O_2, where MT does not detect the decreasing of the molar fraction starting around $t = 10^{-8}$ s, because does not consider the contribution of the last level and, as for nitrogen, anticipate the oxygen recombination with respect to STS. To calculate the time evolution of NO molecules, as a first attempt, the same approach

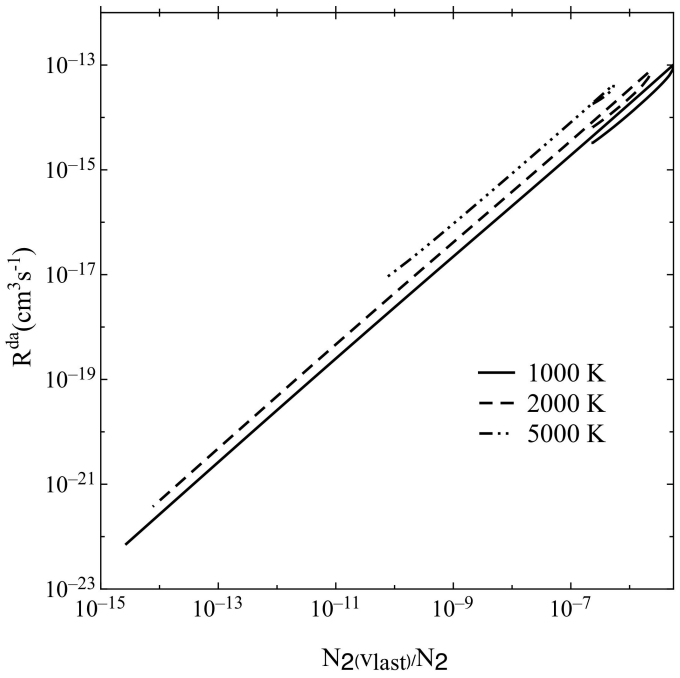

Figure 7. N_2+N dissociation rates calculated from state-to-state kinetic as a function of the last level population of N_2 ($\alpha = N_2(v_{last})/N_2$) for initial conditions $T_{v0} = 8000K$ and $\chi_N = 0.9$.

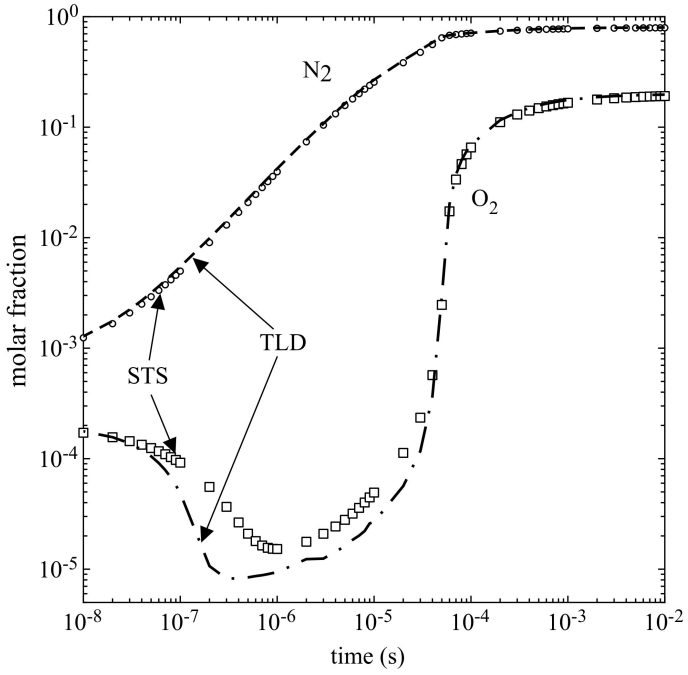

Figure 8. Molar fraction time evolution of N_2 and O_2 for STS and TLD kinetic models in recombination regime.

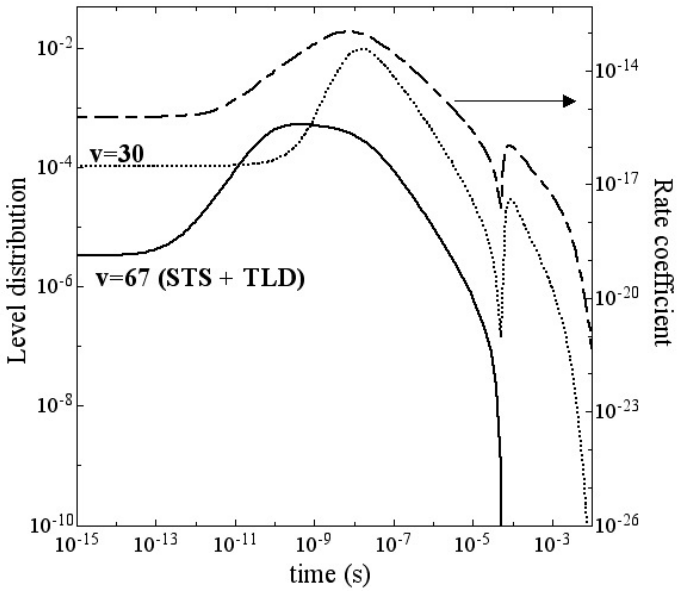

Figure 9. Time evolution of N_2(v=67) and N_2(v=30) vibrational level distribution and of the first Zel'dovich rate coefficient (right axis) calculated in the complete STS model, in recombination regime.

of the TLD model used for pure N_2/N and O_2/O has been applied also to the two Zel'dovich reactions [45; 46]. Thus, to determine the dependence of the rate of the first and second Zel'dovich reactions on the last vibrational level of N_2 and O_2, respectively, STS calculations have been performed in recombination regime by considering both the kinetics of pure N_2/N and O_2/O mixture, but adding only the process under study, i.e. N_2+O, in the first case and O_2+N, in the second one. In this way, the two corresponding rate coefficients were written as a function of the last vibrational level of N_2 for the N_2+O process and of O_2 for the O_2+N process (see Eq. 35). Unfortunately, the corresponding TLD results showed a bad reproduction of STS results for O, NO and N molar fractions for $t > 10^{-4}$ s [45; 46]. The reason of this failure can be found by observing that a strong and complex correlation between the two Zel'dovich reactions occurs. Thus, the dependence of the rate should be analyzed by including the complete kinetics in the calculations. Fig. 9 reproduces the time evolution of N_2+O rate coefficient (right axis) and of the N_2(v=30) and N_2(v=67) level population (one intermediate and the last vibrational level of N_2, respectively) obtained by performing complete kinetics STS calculations. As it can be seen, N_2+O rate coefficient looses the correlation with the last vibrational level and seems to be influenced by the time evolution of the intermediate part of the level distribution population (v=30). The second Zel'dovich reaction O_2+N strongly affects the vibrational distribution of N_2, even if it is not directly involved in the process by creating a channel which produces N_2 molecules in intermediate levels. This channel is created by the following chain processes between the two Zel'dovich

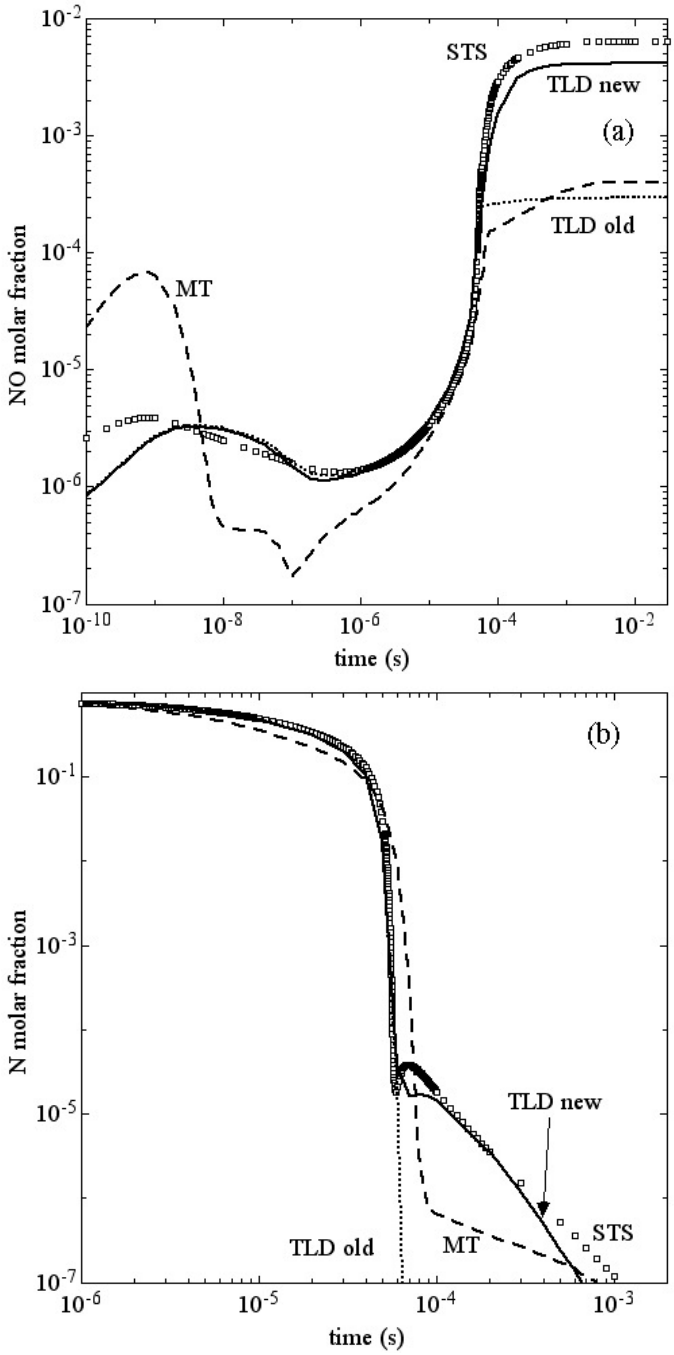

Figure 10. Comparison between STS, MT and new and old TLD results obtained for (a) NO and (b) N molar fraction time evolution is shown. The old TLD corresponds to $N_2 + O$ rate fitting performed using Eq. 35, while the new one using eq. 40.

reactions

$$\begin{array}{rlll} O_2 + N \rightarrow & NO & +O & \\ & \downarrow & & \\ & NO & +N \rightarrow N_2(v_{med}) + O & \end{array} \tag{38}$$

$$\begin{array}{rlll} O + NO \rightarrow & N & +O_2 & \\ & \downarrow & & \\ & N & +NO \rightarrow N_2(v_{med}) + O & \end{array} \tag{39}$$

These chain reactions are the preferential channel to N_2 formation, reducing the contribution of N+N direct recombination in high energy states and resulting in the depletion of the tail of the vibrational distribution of N_2 [50]. In this case the NO formation comes mainly from intermediate levels of N_2. To appreciate this behavior, we have to consider the full state-to-state kinetics and we have to add a *second order correction* K^2. To take into account the dependence of the rate of the first Zel'dovich reaction on intermediate level population, the second order correction should be constructed considering the channels in eqs. 38 and 39 and therefore it should depend on the reactant of the reactions, i.e. N, N_2, NO and O and thus be proportional to the population of intermediate state $N_2(v_m)$:

$$K_{N_2+O\rightarrow NO+O} = K^{TLD}(T, \alpha_{N_2}) + K^2(T, N, N_2, NO, O) \tag{40}$$

New TLD results obtained by applying eq. 40 for $N_2 + O$ rate coefficient are shown in fig. 10 where comparison between STS, MT and new and old TLD results obtained for (a) NO and (b) N molar fraction time evolution is shown. The old TLD corresponds to $N_2 + O$ rate fitting performed by using eq. 35. As it can be observed, new approach of rate fitting gives much more better agreement with STS, respect to old TLD. Again, we want to stress that the state-to-state model used to calculate the results presented in this section includes multiquantum transitions for VT processes with atoms and for dissociation by both atoms and molecules and includes also VV processes.

4. Multi-internal-temperature models

In classical multitemperature models, a unique vibrational temperature is used to describe the vibrational distribution function. In this section, we propose to use several internal vibrational temperatures to better represent the vibrational nonequilibrium of a molecular flow. In the macroscopic model obtained, energy exchange terms and macroscopic rate coefficients are derived self-consistently from a state to state database [51; 54]. Recently, this model was successfully applied to FIRE 2 flight conditions where relaxation and dissociation processes are relatively fast due to a very high translational temperature [51]. In this work, we apply this model to a low earth orbit return condition where the translational temperature is lower and nonequilibrium processes dominate in the entire shock layer.

Table 2. Free stream and post shock conditions used.

	Velocity $(m.s^{-1})$	Pressure (Pa)	Temperature (K)
Free stream	7181	2.5	205.3
Post shock	1206	1762	24324

4.1. Model description

In this work we consider a vibrational state to state model for N_2, using the $v_{max} = 61$ vibrational energy levels of Leroy [55]. The reaction rate constants for multiquanta VT transitions are computed by means of the Forced Harmonic Oscillator (FHO) model, as used by Adamovich et al. [56]. The state dependent dissociation rate constants are also estimated thanks to the FHO model. As demonstrated by Adamovich et al. [57], VV processes have only a little effect on the dissociation behind a shock wave in N_2 and then we have neglected them in this work. We then performed the simulation of relaxation of the flow behind a shock wave. The reactive Euler equations are solved in an ODE form, using the Rankine-Hugoniot relations to compute the initial condition just behind the shock. The simulation is performed for conditions derived from the Hermes H1 test case, given in table 2. For all computations, an effective vibrational temperature T_V is extracted from the energy of the vibrational distribution function (VDF), according to:

$$\frac{\sum_{v=0}^{v_{max}-1} e^{-\frac{E_v}{k_B \cdot T_V}} \cdot e_v}{\sum_{v=0}^{v_{max}-1} e^{-\frac{E_v}{k_B \cdot T_V}}} = \frac{\sum_{v=0}^{v_{max}-1} N_2^v \cdot e_v}{\sum_{v=0}^{v_{max}-1} N_2^v} \tag{41}$$

where e_v and E_v are the energies of the vibrational level v and k_B is the Boltzmann constant.

Figure 11(a) shows that T_V quickly increases as a consequence of the VT processes and reaches a maximum 4 mm after the shock where the dissociation processes are more efficient than VT processes and then deplete the vibrational energy. This distance depends on the test-case but corresponds to the zone of incubation of the vibrational energy behind a shock wave [16]. Then T_V decreases and equilibrates with the translational temperature T, without overshooting it because of the depletion of vibrational energy by dissociation. Figure 11(b) shows the chemical dynamics which starts slowly in the incubation zone, where only the low-lying levels are populated. Dissociation becomes fast at $x = 4$ mm where the high lying vibrational levels are populated. The dissociation phenomenon is slow: after 10 cm, which is the typical thickness of the shock layer, N_2 is still dissociating. As dissociation processes are endothermic, Figure 11(a) shows that the temperatures decrease as the flow dissociates.

In this work, to take into account the vibrational nonequilibrium we choose to model the vibrational distribution function (VDF) by several groups of levels, within which the levels are assumed to follow a Boltzmann distribution at the temperature of the group T_V^i. Hence, each group i is described by its density $\rho_{N_2^i}$ (and the corresponding mass

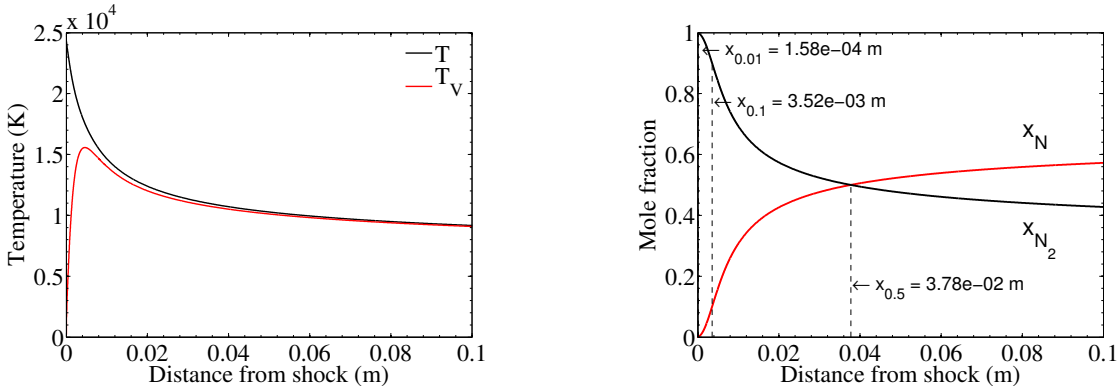

(a) Evolution of temperatures T and T_V

(b) Evolution of composition

Figure 11. Flowfield behind the shock wave computed with the vibrational collisional model for the conditions given in Table 2.

fraction $y_{N_2^i}$) and its vibrational temperature T_V^i (and the corresponding vibrational energy e_{Vib}^i). This leads to a continuity equation and an energy equation for each group:

$$\begin{aligned}\partial_t(\rho_{N_2^i}) + \partial_x(\rho_{N_2^i} u) &= \omega^i_{diss/rec} + \omega^i_{VT}\\ \partial_t(\rho \cdot y_{N_2^i} \cdot e^i_{Vib}(T_V^i)) + \partial_x(\rho u \cdot y_{N_2^i} \cdot e^i_{Vib}(T_V^i)) &= \Omega^i_{CV} + \Omega^i_{VT}\end{aligned}$$

where u is the velocity of the flow and ρ is the density. $\omega^i_{diss/rec}$, resp. ω^i_{VT} are the chemical source terms resulting from dissociation and recombination, respectively from VT excitation. Ω^i_{CV}, resp. Ω^i_{VT} are the vibrational energy source terms resulting from dissociation and recombination, respectively from VT excitation. These equations are derived from the equations of continuity for the vibrational levels. For example, the rate of dissociation and recombination for the group i is obtained by summing the continuity equations over the vibrational levels v in group i:

$$\omega^i_{diss/rec} = m_{N_2} \sum_{M=N,N_2} \sum_{v\in i} (k_v^{d,M} \cdot N_2^v \cdot M - k_v^{r,M} \cdot N^2 \cdot M) \tag{42}$$

where m_{N_2} is the molar mass of N_2, $k_v^{d,M}$ and $k_v^{r,M}$ are the dissociation and recombination rate constants for the level v known from the database. N_2^v and N are the molar density of the corresponding species.

Assuming that the VDF is Boltzmann within a group, we get

$$\omega^i_{diss/rec} = m_{N_2} \sum_{M=N,N_2} \left[\sum_{v\in i} k_v^{d,M} \cdot f_i(v, T_V^i) \cdot N_2^i \cdot M - \sum_{v\in i} k_v^{r,M} \cdot N^2 \cdot M \right] \tag{43}$$

and then the rate of dissociation and recombination for the group i is a function of T, T_V^i and the densities N_2^i and of N_2 and N. The other source terms can be derived self-consistently using the same procedure [54].

4.2. Results

In this section, the reduced model is applied on the H1 test case given in Table 2 with one group to assess the Boltzmann assumption. Then it is applied with two groups to take into account the different behavior of low lying and high lying levels. The respective results are compared with the detailed vibrational model.

Figure 12(a) shows that both the model with one group (in red) and with two groups (in blue) predict a vibrational temperature T_V that reaches a maximum value at the same location, then decreases without overshooting T. However the relaxation predicted by the one group model is too fast, which leads to a temperature too low by several hundreds of Kelvin at a distance representative of the shock layer thickness (10 cm). The two group model (in blue) overlaps the detailed model (in black), so the vibrational energy is well predicted. The one group model slightly overestimates the dissociation rate as shown in fig. 12(b). Though small, this difference explains the more rapid cooling of T and T_V, due to the conversion of translational and vibrational energy into formation energy. We also note a slowing of equilibration between the translational and the vibrational modes. The two-group model (in blue) reproduces the results of the detailed collisional model with a very good agreement. These results indicate that

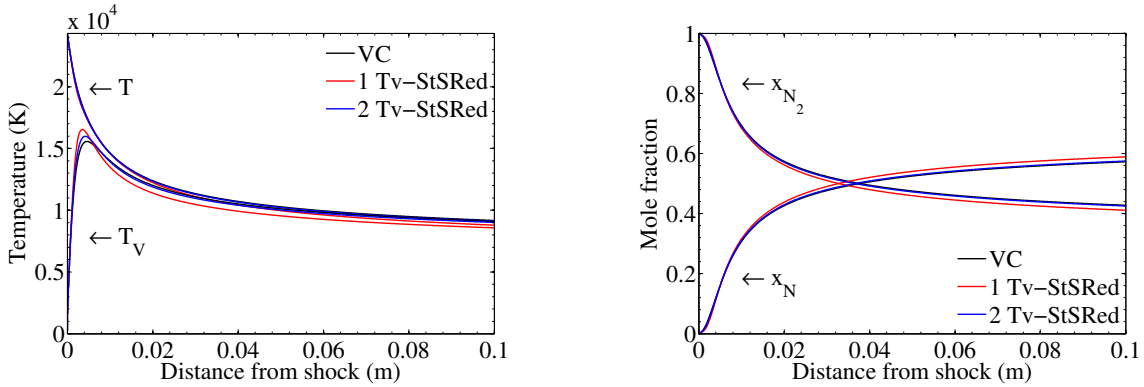

(a) Evolution of temperatures T and T_V

(b) Evolution of composition

Figure 12. Flowfield behind the shock wave computed with the detailed collisional model and with the reduced model with 1 and with 2 groups for the conditions given in Table 2.

nonequilibrium effects affect the flow. To investigate these nonequilibrium effects on the coupling between vibrational excitation and kinetics, we plot the VDF at several significant locations represented on fig. 11(b):

- $x = x_{0.01}$ where the mass fraction $x_N = 0.01$: in the incubation zone.
- $x = x_{0.1}$ where the mass fraction $x_N = 0.1$: where dissociation starts to be significant.
- $x = x_{0.5}$ where the mass fraction $x_N = 0.5$: where half dissociation is achieved.
- $x = 1$ m : at the end of the simulation domain.

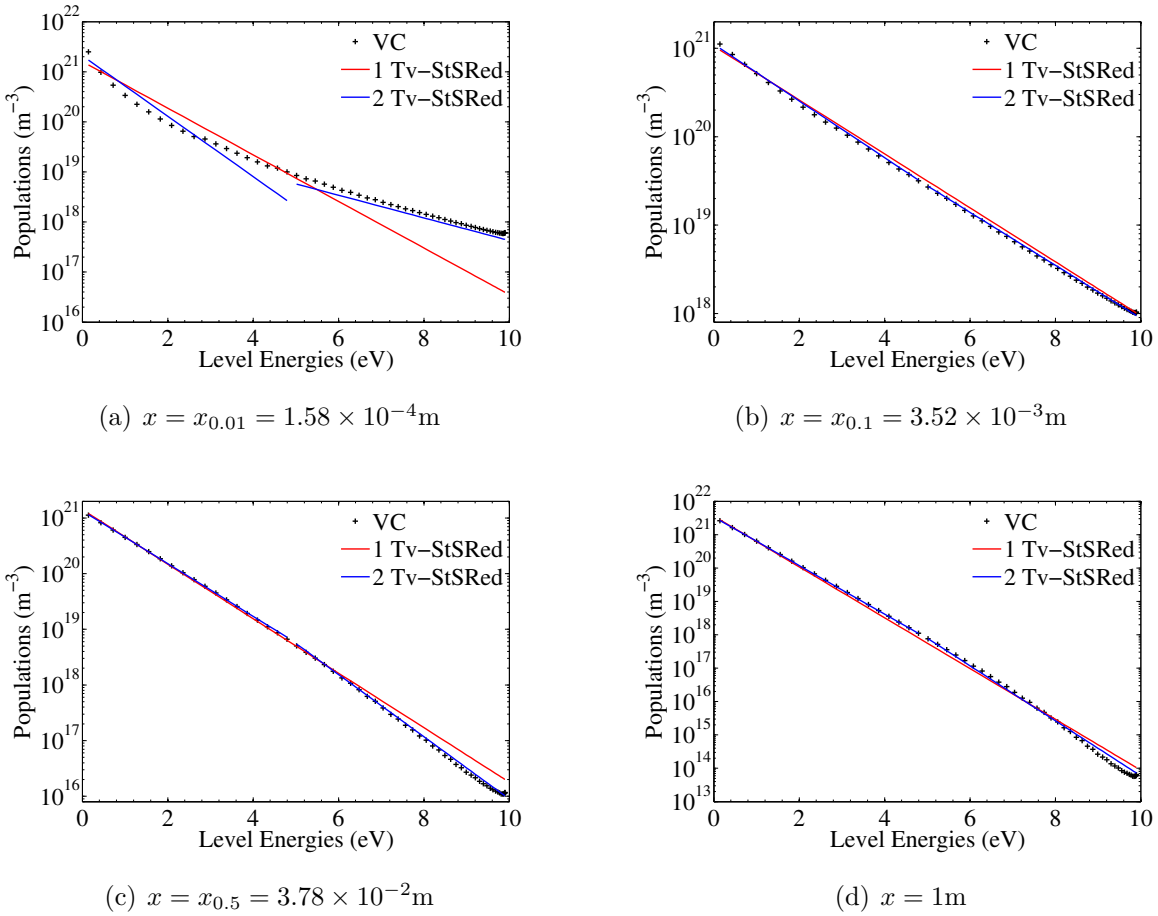

(a) $x = x_{0.01} = 1.58 \times 10^{-4}$m

(b) $x = x_{0.1} = 3.52 \times 10^{-3}$m

(c) $x = x_{0.5} = 3.78 \times 10^{-2}$m

(d) $x = 1$m

Figure 13. VDF computed with the detailed vibrational collisional model and the 1 group and 2 groups models.

Figure 13(a) shows the rapid vibrational excitation that happens just after the shock and populates the high levels. At this location there is a significant nonequilibrium and a 2 group model is required to accurately model it. It can be observed that the vibrational temperature based on the vibrational energy gives a much better representation of the VDF than the one obtained using a vibrational temperature based on the population of the two first vibrational levels. When dissociation begins to be significant (fig. 13(b)) the VDF is almost Boltzmann. But after that, as half of the dissociation is achieved, we observe a depletion of high vibrational levels on fig. 13(c). The translational temperature T has decreased below $15000K$ so that dissociation happens from higher vibrational levels. This leads to a depletion of the high lying levels that are populated by VT processes and depopulated by dissociation. This depletion remains up to 1 m after the shock where equilibrium is still not reached as shown on fig. 13(d).

Except in the incubation zone just after the shock front, the one group model is quite close to the VDF computed with the state-to-state model. However this approximation is obviously not sufficient here: as seen in fig. 12(b) the flow predicted by the one-group model 10 cm after the shock is too much dissociated, and correspondingly the

temperatures are too low. Conversely, the two-group model is able to predict dissociation and thus gives the right evolution of temperatures. This is because it allows to predict more accurately the evolution of the high lying levels (fig. 13(c)) than the one-group model.

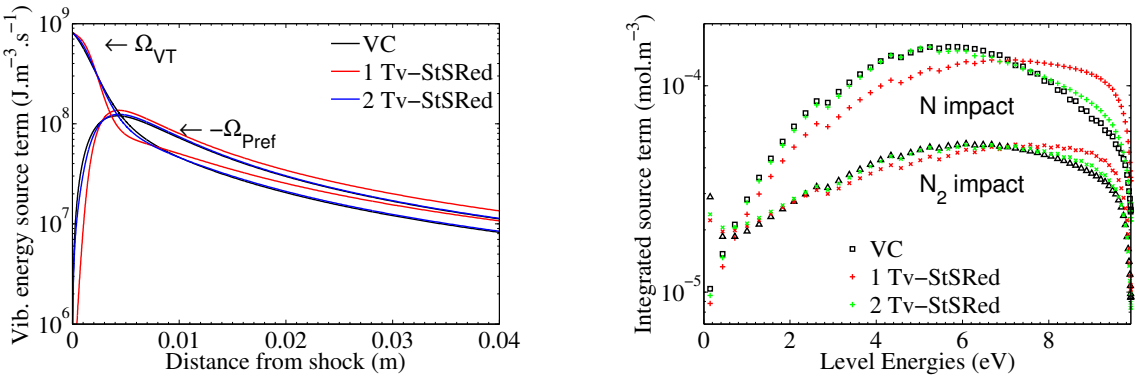

Figure 14. (a) Post-shock evolution of sources terms of vibrational energy Ω_{VT} and Ω_{Pref} and (b) Contribution of each level to the dissociation process over the whole simulation time.

To explain the difference between the two models, we investigate the source terms. The first source term that influences the vibrational temperature is Ω_{VT}. Concerning the coupling with chemistry, a molecule that dissociates will change the vibrational temperature only if its energy is different from the average vibrational energy. Thus the relevant source term is not Ω_{CV} but Ω_{Pref}, defined as:

$$\Omega_{Pref} = \Omega_{CV} - \omega_{N_2} \cdot e_{Vib}^{N_2} \tag{44}$$

where Ω_{CV} is the total chemistry-vibration source term for N_2, ω_{N_2} the total chemical source term and $e_{Vib}^{N_2}$ is the average vibrational energy of N_2.
Figure 14 shows these two source terms as a function of the distance from the shock for the detailed vibrational model and the 1 group and 2 group reduced model. We note that the reduced model with one group qualitatively reproduces the behavior of both source terms. However, a two-group model is needed to have a correct prediction of both source terms. On fig. 14(b) is plotted the contribution to dissociation of each vibrational level I^v, integrated over the whole simulation time as follows:

$$I^v = \int_{t=0}^{t_f} (k_d^{M,v} \cdot N_2^v - k_r^{M,v} \cdot N^2) \cdot M \cdot dt \tag{45}$$

Fig. 14(b) shows that the one-group model overestimates the dissociation from high-lying levels. First this induces in an overprediction of the dissociation rate, resulting in a decrease of the temperatures. Secondly, this induces an overestimation of the vibrational energy lost during dissociation, which decreases T_V. By improving the representation of these high levels, the two-group model better describes the level-dependent dissociation,

which eventually leads to a better prediction of the nonequilibrium flow.
Finally, the H1 test case studied in this section presents a different behavior from the FIRE 2 test case investigated in [51]: the high-lying levels are depleted slowly contrary to the FIRE 2 test case where the VDF quickly reaches Boltzmann equilibrium. However, the reduced model with two temperatures is able to predict the VDF, and then allows to predict the nonequilibrium of the flow for the H1 test-case.

5. Coarse-grain models

The most detailed databases developed in the literature are rovibrational databases [22; 23; 24; 25]. In [58], a 0D rovibrational collisional model has been developed for the 9390 rovibrational energy levels of the electronic ground state of the nitrogen molecule with the reaction rate coefficients of the *ab initio* database developed at NASA Ames Research Center for the $N_2 + N$ system [22; 23]. Then different reduced models have been developed based on this rovibrational database. In particular, as an alternative to vibrational-collisional models, in [10], the 9390 rovibrational energy levels of N_2 have been lumped into a smaller number of bins as a function of the total internal energy, independently of their vibrational and rotational contributions. This approach is more general since the assumptions on the rotational energy mode are relaxed. The rate coefficients are averaged for each bin based on a uniform distribution of the energy levels within a bin. The Master equation for the reduced mechanism has been coupled with a one-dimensional flow solver to study excitation and dissociation processes behind a strong shock wave in a nitrogen flow for conditions expected for reentry into Earth's atmosphere. For the conditions of Table 2, Figures 15 and 16 show the influence of the number of bins on the evolution of the composition and of the translational and internal temperatures behind the shock. The solid line corresponds to the solution for 200 bins which is very close to the reference solution with the detailed rovibrational model.

We point out that a rovibrational collisional coarse-grain model based on a uniform distribution of the internal energy levels into bins allows to describe accurately the internal energy relaxation and dissociation processes based on a reduced number of equations (of the order of 50). Furthermore, in [10], it is shown that the induction times for thermal relaxation and dissociation with a coarse-grain model are larger than the ones obtained by means of vibrational collisional and multitemperature models assuming thermal equilibrium between the rotational and translational energy modes.

6. Conclusions

In the present work we have presented the derivation of different types of macroscopic models by increasing order of complexity for the vibration-chemistry coupling in nonequilibrium flows for reentry applications.
First, using an approach based on nonequilibrium thermodynamics, we have determined the global rate coefficients of (a) dissociation of N_2 and O_2 under parent molecular or

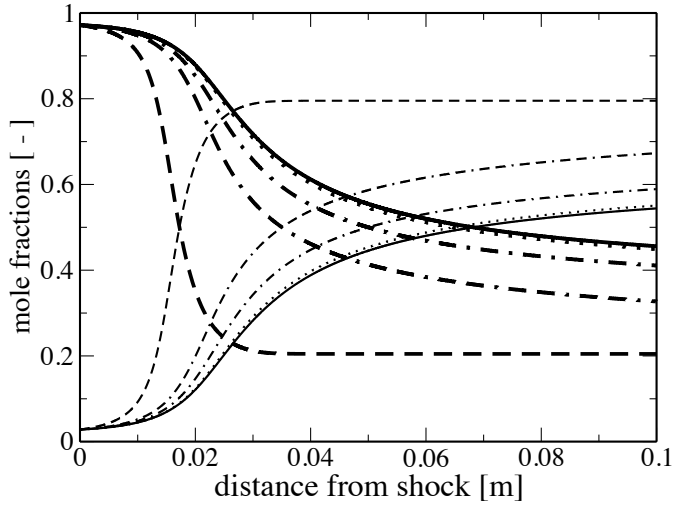

Figure 15. Post-shock nitrogen atom mole fraction (thin lines) and nitrogen molecule mole fraction (thick lines) as a function of the distance from the shock based on the post-shock nonequilibrium conditions given in Table 2. Uniform RoVibrational Collisional (URVC) coarse-grain model with various numbers of bins for the coarse-grain model (– – – 5, · – –· 10, · – · 20, – ·· – 50, ··· 50 bins, —— 200 bins).

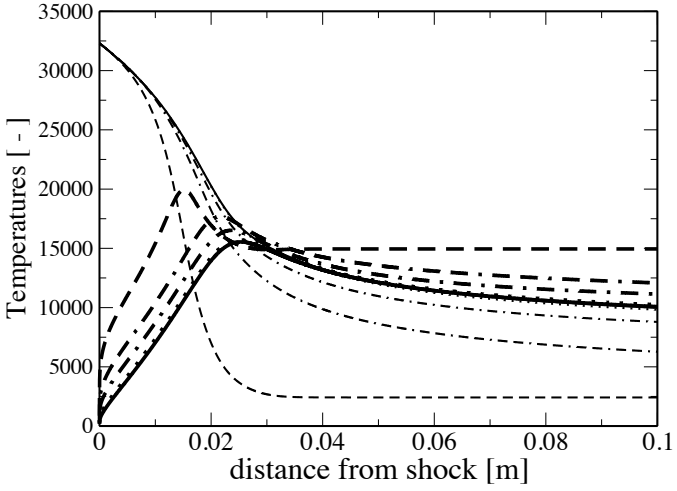

Figure 16. Post-shock translational temperature (thin lines) and rovibrational temperature (thick lines) as a function of the distance from the shock based on the post-shock nonequilibrium conditions given in Table 2. Uniform RoVibrational Collisional (URVC) coarse-grain model with various numbers of bins for the coarse-grain model (– – – 5, · – –· 10, · – · 20, – ·· – 50, ··· 50 bins, —— 200 bins).

atomic impact and (b) backward molecular recombination. Although the elementary forward and backward rate coefficients have a ratio equal to the corresponding equilibrium constant, this property is not observed for global rate coefficients unless the departure from equilibrium is weak. We have demonstrated this basic property which results from the nonequilibrium distribution of excited states during a global process. Such a study has also been performed for (c) ionization [$n = 1$, $\alpha = 0$, $\beta = 1$ in (2)] of $X \equiv$ C, N, O, and Ar under $P \equiv e^-$ impact and (d) ionic three-body recombination (see [59]). Then we have presented a Two-Level Distribution (TLD) model, in which a relaxation equation for vibrational temperature is solved as in the case of multi-temperature models but with the simultaneous solution of a kinetic equation, as in the case of state-to-state models, but only for the last vibrational level. Then we have presented the self-consistent derivation of a multi-internal temperature model from a vibrational state-to-state model. The objective of the multi-internal temperature model is to describe accurately the vibrational distribution function in using several groups of levels, within which the levels are assumed to follow a Boltzmann distribution at an internal temperature of the group. This multi-internal temperature model has been applied to the simulation of the nonequilibrium coupling between vibration and dissociation behind a shock wave. We have studied the influence of the number of groups on the results and compared, as a reference, with the results obtained with the vibrational state-to-state model. First, using one group, we have shown that assuming a single Boltzmann distribution for all vibrational levels leads to an overestimation of dissociation and consequently to underestimation of temperatures compared with the reference vibrational model. We have shown that the use of a two-internal temperature model was a good compromise between accuracy and complexity for the studied test-case. A thorough study of source terms confirmed that the improvement of the prediction using two groups results from a better prediction first of the global source term Ω_{VC} and Ω_{VT}, and second of the level-dependence of dissociation, which is required for a good prediction of the chemistry-vibration coupling. Finally, a rovibrational collisional coarse-grain model has been developed to reduce a detailed rovibrational mechanism the $N_2(v, J) + N$ system to study the internal energy excitation and dissociation processes behind a strong shockwave in a nitrogen flow. It is interesting to note that lessons learned from studying the $N_2(v, J) + N$ system by means of a coarse-grain model should help to derive in the near future, a reduced mechanism for more complex systems as for example, the $N_2(v, J) + N_2(v', J')$ system studied in [60].

Acknowledgments

The research leading to these results has received funding from the European Community's Seventh Framework Programme [FP7/2007/2013] under grant agreement n° 242311.

References

[1] I. Armenise, M. Capitelli, G. Colonna, N. Koudriavtsev, and V. Smetanin (1995), Nonequilibrium vibrational kinetics during hypersonic flow of a solid body in nitrogen and its influence on the surface heat-flux, *Plasma Chem Plasma Process* **15**, 501–528.

[2] Armenise I., Capitelli M., Colonna G. and Gorse C. (1996), Nonequilibrium vibrational kinetics in the boundary layer of re-entering bodies, *J. Thermophys. Heat Transfer*, **106**, 397.

[3] D. J. Kewley (1975), Numerical study of anharmonic diatomic relaxation rates in shock waves and nozzles, *J. Phys. B: At. Mol. Opt. Phys.* **8**, 2565.

[4] G. Colonna, M. Tuttafesta, M. Capitelli, and D. Giordano (1999), Non-Arrhenius NO Formation Rate in One-Dimensional Nozzle Airflow, *J. Thermophys. Heat Transfer* **13**, 372–375.

[5] G. Colonna, F. Esposito, and M. Capitelli (2003), The role of state-selected recombination rates in supersonic nozzle expansion, *36th AIAA Thermophysics Conference*, , AIAA Paper 2003-3645.

[6] A. Munafo, M. Panesi, R.L. Jaffe, G. Colonna, A. Bourdon, and T.E. Magin (2012), QCT-based vibrational collisional models applied to nonequilibrium nozzle flows, *Eur. Phys. J. D*, **66**, 188.

[7] D. Bruno, M. Capitelli, F. Esposito, S. Longo, and P. Minelli (2002), Direct simulation of non-equilibrium kinetics under shock conditions in nitrogen, *Chem. Phys. Lett.* **360**, 31–37.

[8] M. Panesi, T. Magin, A. Bourdon, A. Bultel, and O. Chazot (2009), Analysis of the FIRE II Flight Experiment by Means of a Collisional Radiative Model, *J. Thermophys. Heat Transfer* **23**, 236.

[9] M. Panesi, T. Magin, A. Bourdon, A. Bultel, and O. Chazot (2011), Electronic Excitation of Atoms and Molecules for the FIRE II Flight Experiment, *J. Thermophys. Heat Transfer* **25**, 361.

[10] T. Magin, M. Panesi, A. Bourdon, R.L. Jaffe and D.W. Schwenke (2012), Coarse-grain model for internal energy excitation and dissociation of molecular nitrogen, *Chem. Phys.* **398**, 90.

[11] A. Bultel and J. Annaloro (2013), Elaboration of collisional-radiative models for flows related to planetary entries into the Earth and Mars Atmospheres, *Plasma Sources Sci. Technol.*, **22**, 025008

[12] G. Colonna, I. Armenise, D. Bruno, and M. Capitelli (2006), Reduction of state-to-state kinetics to macroscopic models in hypersonic flows, *J. Thermophys. Heat Transfer* **20**, 477–486.

[13] C. Park (1989), A review of reaction rates in high temperature air, AIAA paper 89-1740.

[14] C. Park (1993), Review of Chemical-Kinetic Problems of Future NASA mission, I: Earth Entries, *J. Thermophys. Heat Transfer* **7**, 385–398.

[15] S. P. Sharma, W. M. Huo, and C. Park (1992), Rate Parameters for Coupled Vibration-Dissociation in a Generalized SSH Approximation, *J. Thermophys. Heat Transfer* **6**, 9–21.

[16] C. Park (1989), *Nonequilibrium Hypersonic Aerothermodynamics.* John Wiley and Sons, New York.

[17] O. Knab, H.H. Frühauf, and E.W. Messerschmid (1995), URANUS/CVCV model validation by means of thermochemical nonequilibrium nozzle airflow calculations. *Proceeding of the 2nd European Symposium on Aerothermodynamics for Space Vehicles, ESA Publication Div., Noordwijk, The Netherlands*, 129.

[18] S. Surzhikov, I. Sharikov, M. Capitelli, and G. Colonna (2006), Kinetic model of nonequilibrium radiation of strong air shock waves, *AIAA* paper 2006–586.

[19] S. Surzhikov, O. Rouzaud, T. Soubrie, V. Gorelov, and A. Kireev (2006), Prediction of nonequilibrium and equilibrium radiation for reentry conditions, *AIAA* paper 2006–1188.

[20] C. Park (2006), Thermochemical relaxation in shock tunnels. *J. Thermophys. Heat Transfer*, **20**, 689.

[21] E.V. Kustova, E.A. Nagnibeda, T.Yu. Alexandrova, A. Chikhaoui (2002), On the non-equilibrium kinetics and heat transfer in nozzle flows *Chem. Phys.* **276**, 139.

[22] R. Jaffe, D. Schwenke, and G. Chaban (2009), Theoretical analysis of N_2 collisional dissociation and rotation-vibration energy transfer. *47th AIAA Aerospace Sciences Meeting and Exhibit, Orlando, Florida*, AIAA Paper 2009-1569.

[23] D. Schwenke. Dissociation cross-sections and rates for nitrogen. *RTO-EN-AVT-162, Nonequilibrium Gas Dynamics, from Physical Models to Hypersonic Flights, Rhode-Saint-Genèse, Belgium*, 2008.

[24] P. Gamallo, R. Martínez, R. Sayós, and M. Gonzáles (2010), Quasiclassical dynamics and kinetics of the $N + NO \rightarrow N_2 + O, NO + N$ atmospheric reactions, *J. Chem. Phys.*, **132**, 144304.

[25] F. Esposito and M. Capitelli (2006), QCT calculations for the process $N_2(v)+N \rightarrow N_2(v') + N$ in the whole vibrational range, *Chem. Phys. Lett.*, **418**, 581.

[26] F. Esposito, I. Armenise, G. Capitta and M. Capitelli (2008), O_2-O state-to-state vibrational relaxation and dissociation rates based on quasiclassical calculations, *Chem. Phys.*, **351**, 91

[27] F. Esposito, I. Armenise and M. Capitelli (2006), N_2-N state-to-state vibrational relaxation and dissociation rates based on quasiclassical calculations, *Chem. Phys.*, **331**, 1.

[28] J.A. Kunc and W.H. Soon (1989), Collisional-radiative nonequilibrium in partially ionized atomic nitrogen, *Phys. Rev.* A, **40**, 5822.

[29] W.H. Soon and J.A. Kunc (1990), Thermal nonequilibrium in partially ionized oxygen, *Phys. Rev.* A, **41**, 825.

[30] A. Bourdon and P. Vervisch (1996), Three-body recombination rate of atomic nitrogen in low-pressure plasma flows, *Phys. Rev.* E, **54**, 1888.

[31] A. Bourdon, Y. Tereziak and P. Vervisch (1996), Ionization and recombination rates of atomic oxygen in high-temperature air plasma flows, *Phys. Rev.* E, **57**, 4684.

[32] K. Sawada and T. Fujimoto (1994), Temporal relaxation of excited-level population of atoms and ions in a plasma: validity range of the quasi-steady-state solution of coupled rate equations, *Phys. Rev.* E, **49**, 5565.

[33] A. Bultel, B. van Ootegem, A. Bourdon and P. Vervisch (2002), Influence of Ar_2^+ in an argon collisional-radiative model, *Phys. Rev.* E, **65**, 046406.

[34] K. Denbigh (1981), The principles of chemical equilibrium, *Cambridge University Press*

[35] I. Armenise, F. Esposito and M. Capitelli (2007), Dissociation-recombination models in hypersonic boundary layer, *J. Chem. Phys.*, **336**, 83.

[36] M. Capitelli, I. Armenise and C. Gorse (1997), State-to-state approach in the kinetics of air components under re-entry conditions, *J. Thermophys. Heat Transfer*, **11**, 570.

[37] M.G. Dunn and S.-W. Kang (1973), Theoretical and experimental studies of reentry plasmas, *NASA CR-2232*

[38] O.P. Shatalov (1987), Recommended data on rate constants of physical and chemical processes in N-O atoms systems, *Institute of Mechanics, AVOGADRO Center, Moscow State University, Russia*

[39] C. Park, J.T. Howe, R.L. Jaffe and G.V. Candler (1994), Review of chemical-kinetic problems of future NASA missions, II. Mars entries, *J. Thermophys. Heat Transfer*, **8**, 9.

[40] S.A. Losev, V.N. Makarov and M.Y. Pogosbekyan (1995), Model of the physico-chemical kinetics behind the front of a very intense shock wave in air, *Fluid Dynamics*, **30**, 299.

[41] V.N. Makarov (1996), Determination of the mechanism of physicochemical processes in high-temperature air, *J. Appl. Mech. Tech. Phys.*, **37**, 206.

[42] O.E. Krivonosova, S.A. Losev, V.P. Nalivaiko, Yu.K. Mukoseev and O.P. Shatalov (1987), Recommended data on the rate constants of chemical reactions among molecules consisting of N and O atoms, *Plasma Chemistry, Energoizdat, Moscow*, 1.

[43] E.V. Kustova and E.A. Nagnibeda (2005), Deviations from the mass action law in non-equilibrium gas flows, *AIP Conference Proceedings*, **762**, 908.

[44] G. Colonna, L. D. Pietanza, and M. Capitelli (2008), Recombination-assisted nitrogen dissociation rates under nonequilibrium conditions, *J. Thermophys. Heat Transfer* **22**, 399–406.

[45] G. Colonna, L. D. Pietanza, and M. Capitelli (2011), Reduced two-level approach for air kinetics in recombination regime, in *AIP Conference Proceedings*, **1333**, 1365–1370.

[46] G. Colonna, L. D. Pietanza, and M. Capitelli (2012), Macroscopic Kinetic Model for Air in Nozzle Flow, in *Proceedings of the 28th international symposium on rarefied gas dynamics*, edited by M. Mareschal and A. Santos, **2**, 1501.

[47] O. E. Krivonosova, and O. P. Shatalov (1999), *Chemical physics reports c/c of Khimicheskaia fizika* **18**, 1621–1630.

[48] D. Bose, and G. Candler (1997), Thermal rate constants of the $O_2 + N \rightarrow NO + O$ reaction based on the $^2A'$ and ^4A" potential energy surfaces *J. Chem. Phys.* **107**, 6136–6145.

[49] D. Bose, and G. Candler (1996), Thermal rate constants of the $N_2 + O \rightarrow NO + N$ reaction using ab initio ^3A" and $^3A'$ potential energy surfaces, *J. Chem. Phys.* **104**, 2825–2833.

[50] G. Colonna, M. Tuttafesta, M. Capitelli, and D. Giordano (1999), Influence of $O_2(v) + N \rightleftharpoons$NO+O on NO Formation Rate in One-Dimensional Air Nozzle Flow, *J. Thermophys. Heat Transfer* **14**, 455–456.

[51] A. Guy, A. Bourdon, and M. Y. Perrin (2013), Derivation of a consistent multi-internal-temperature model for vibrational energy excitation and dissociation of molecular nitrogen in hypersonic flows, AIAA paper 2013-0194.

[52] G. S. R. Sarma (1958) Physico-chemical modeling in hypersonic flow simulation, *Progress in Aerospace Sciences*, 281–349.

[53] P. Domingo A. Bourdon, A. Leroux and P. Vervisch (1999), Experiment-modeling comparison in a nonequilibrium supersonic air nozzle flow, *J. Thermophys. Heat Transfer*, **13**, 68–75.

[54] A. Guy, A. Bourdon, and M. Y. Perrin (2013), Consistent multi-internal-temperatures models for nonequilibrium nozzle flows, *Chem. Phys., in press.*

[55] R. J. Le Roy, Y. Huang, and C. Jary (2006), An accurate analytic potential function for ground state N_2 from a direct potential fit analysis of spectroscopic data, *J. Chem. Phys.*, **125**, 164310.

[56] V. I. Adamovich, S. O. Macheret, W. J. Rich, and C. E. Treanor (1995), Vibrational relaxation and dissociation behind shock waves. 1: Kinetic rates model, *AIAA J.*, **33(6)**, 1064.

[57] V. I. Adamovich, S. O. Macheret, W. J. Rich, and C. E. Treanor (1995), Vibrational relaxation and dissociation behind shock waves. 2: Master equation modeling, *AIAA J.*, **33(6)**, 1070.

[58] M. Panesi, R.L. Jaffe, D.W. Schwenke and T.E. Magin (2013) Rovibrational internal energy transfer and dissociation of $N_2(^1\Sigma_g^+) - N(^4S_u)$ system in hypersonic flows, *J. Chem. Phys.*, **138**, 044312.

[59] J. Annaloro, V. Morel, A. Bultel and P. Omaly (2012), Global rate coefficients for ionization and recombination of carbon, nitrogen, oxygen, and argon, *Phys. Plasmas*, **19**, 073515.

[60] R. Jaffe, D. Schwenke, and G. Chaban (2010), Vibration-rotation excitation and dissociation in $N_2 - N_2$ collisions from accurate theoretical calculations, *10th AIAA/ASME Joint Thermophysics and Heat Transfer Conference, Chicago, Illinois*, AIAA Paper 2010-4517.

Vibrational-Chemical Kinetics in Mars Entry Problems

E.V. Kustova [1], E.A. Nagnibeda [2]

Saint Petersburg State University, Department of Mathematics and Mechanics
28 Universitetsky pr, 198504 Saint Petersburg, Russia

I. Armenise[3]

CNR-IMIP (Consiglio Nazionale delle Ricerche, Istituto di Metodologie Inorganiche e dei Plasmi), Via Amendola 122/D, 70126 Bari, Italy

Abstract

The paper deals with kinetic theory methods modelling of reacting gas flows near spacecrafts entering the Mars atmosphere. For mixtures containing CO_2 molecules, the complete kinetic scheme including all vibrational energy transitions, dissociation, recombination and exchange chemical reactions is proposed. For the prediction of gas dynamic parameters and heat transfer to the surface of a spacecraft, a detailed approach taking into account state-to-state CO_2 vibrational and chemical kinetics as well as multi-temperature approaches based on quasi-stationary vibrational distributions are used. A more accurate but complicated and time consuming state-to-state model is applied for the numerical simulation of a one dimensional flow in a boundary layer near the entering body surface. More simple quasi-stationary three-temperature, two-temperature and one-temperature approaches are used for the numerical study of a 2-D viscous shock layer under entry conditions. The vibrational distributions near the surface are far from the local vibrational and chemical equilibrium and a noticeable difference is found between the values of CO_2 vibrational-specific energies at the surface obtained by means of the state-to-state and quasi-stationary approaches. At the same time, for all considered approaches, the kinetic model for vibrational distributions and chemical reactions has a weak influence on the heat transfer to the non-catalytic vehicle surface.

Keywords: vibrational kinetics, transport properties, non-equilibrium CO_2 flows, state-to-state model, multi-temperature model

1. Introduction

For the accurate prediction of gas dynamic parameters on the trajectory of nonexpendable space vehicles in their entry into the Mars atmosphere and heat transfer to the vehicle surfaces, non-equilibrium vibrational and chemical kinetics in mixtures containing CO_2 should be taken into account. For a large part of the descending trajectory at the altitudes about 40-60 km, the relaxation times of kinetic processes become comparable to the mean time of variation of

[1]Email: kustova@math.spbu.ru
[2]Email: e_nagnibeda@mail.ru
[3]Email: iole.armenise@ba.imip.cnr.it

gas dynamic parameters. Therefore, for mathematical modeling of a flow, the gas dynamic equations should be coupled to the equations for non-equilibrium CO_2 kinetics. The important up-to-date problem is the development of adequate CO_2 kinetics models and their incorporation into the computational fluid dynamics (CFD) schemes.

The kinetic theory makes it possible to derive closed sets of governing equations of a flow under different non-equilibrium conditions and elaborate calculation procedures for transport coefficients and reaction rates which are included in equations. However, till now, only simplified one-temperature or two-temperature CO_2 models [1, 2, 3, 4] have been used in numerical simulations. These models do not describe the complex CO_2 kinetics well and can lead to considerable errors in predicted values of flow parameters. Indeed, in the one-temperature approach the gas is assumed to be in the thermal equilibrium, and only non-equilibrium chemical reactions take place in a mixture. The two-temperature CO_2 model is based on introducing a single vibrational temperature for all three vibrational modes of CO_2 molecules.

More rigorous multi-temperature [5, 6, 7, 8, 9] and state-to-state [10, 11] models of CO_2 kinetics take into account real structure of carbon dioxide molecules and include to the kinetic scheme intra- and inter-mode vibrational energy exchanges as well as VT vibrational-translational energy transitions. Based on the rigorous kinetic theory algorithms proposed in [7, 10], transport properties in dissociating CO_2 flows behind shock waves have been evaluated [9]. In these studies, calculations have been performed for the flow parameters found previously from simplified fluid dynamic equations. The most accurate state-to-state models are very detailed and computationally expensive for the numerical simulations of viscous non-equilibrium flows, especially for the transport terms evaluation because a huge number of equations for vibrational level populations of various CO_2 modes and state dependent transport coefficients which should be considered. And even simpler multi-temperature models can be complicated for applications, if the vibrational temperatures are introduced for each mode of anharmonic CO_2 vibrations and several test cases are needed.

A self-consistent three-temperature description of the three-component $CO_2/CO/O$ mixture suitable for applications and providing satisfactory accuracy has been proposed in [12] on the basis of the kinetic theory methods using the relations between relaxation times of different CO_2 vibrational energy exchanges; its generalization for the five-component five-temperature $CO_2/CO/O_2/C/O$ mixture is proposed in [13]. The model takes into account various mechanisms of CO_2 vibrational relaxation and gives the expressions for transport coefficients which may be implemented into the viscous flow solvers. In [14, 15], the five-component reacting mixture $CO_2/CO/O_2/C/O$ was studied and the accurate transport algorithms were implemented directly into CFD solver for simulation of a 2-D flow in a viscous shock layer near spacecrafts entering the Mars atmosphere. The flows near space vehicles Mars Sample Return Orbiter (MSRO), Mars Express and blunt bodies of different shape for various free stream conditions in the cases of fully-catalytic and non-catalytic vehicle surfaces were studied on the basis of this model.

The objectives of the paper are the following. The first goal is to propose a complete kinetic scheme for a five-component $CO_2/CO/O_2/C/O$ mixture flow taking into account all vibrational energy transitions and main chemical reactions. This general scheme can be applied for any non-equilibrium CO_2 flow, and can be simplified under various flow conditions. The second task is to specify the rate coefficients of non-equilibrium processes included to the reduced kinetic scheme used for flow simulations discussed in the paper. The next objective is to elaborate

closed self-consistent macroscopic flow descriptions in the state-to-state and multi-temperature approaches and to derive corresponding governing equations. Finally, we aim to study 1D and 2D non-equilibrium CO_2 flows using different models and to analyze the influence of the kinetic model on gas dynamic parameters and transport properties on the descending trajectory under the Mars entry conditions.

The originality of the present paper is in comparison of non-equilibrium vibrational-chemical CO_2 kinetics and heat transfer evaluated on the basis of the state-to-state and multi-temperature approximations. It is worth mentioning that the vibrational specific state-to-state mechanism for a carbon dioxide mixture has been developed in our previous work [11], and here it is applied for the specific test case. Existing multi-temperature 2D shock layer flow results [14, 15] are used to define the boundary layer edge conditions for the state-to-state simulations performed in this study.

2. Mechanisms of vibrational and chemical relaxation

Mars atmosphere consists of 95.32% carbon dioxide, 2.7% nitrogen, 1.6% argon, and small amount of admixtures: oxygen, carbon monoxide, water vapor. For Mars entry problems, there is a considerable increase in the amount of CO_2 dissociation products, CO and O.

CO_2 is a linear triatomic molecule. In the ground electronic state it has three vibrational modes: symmetric stretching mode with frequency ν_1, doubly degenerated bending mode (ν_2), and asymmetric stretching mode (ν_3). Its vibrational energy can be described as [16]

$$\varepsilon_{v_1 v_2^l v_3} = \sum_{k=1}^{3} \omega_k^e \left(v_k + \frac{d_k}{2} \right) + \sum_{k=1}^{3} \sum_{j \geq k}^{3} x_{kj}^e \left(v_k + \frac{d_k}{2} \right) \left(v_j + \frac{d_j}{2} \right) + x_{ll}^e l^2 + ...$$

where v_m, $m = 1, 2, 3$ are the vibrational levels of CO_2 symmetric, bending and asymmetric modes respectively, l is the additional quantum number describing the projection of the momentum of bending vibrations onto the axis of the molecule, d_k characterize the degeneration ($d_1 = d_3 = 1$ whereas $d_2 = 2$). The terms of higher order in the above expansion are small and can be neglected in this study. The vibrational energy of diatomic molecules is modelled by Morse anharmonic oscillator.

In the present work, we do not take into account electronic excitation of atoms and molecules as well as ionization. Moreover, we do not include processes involving nitrogen to the kinetic scheme. These assumptions certainly lead to noticeable limitations of the proposed model, and we plan to incorporate these missing processes at the next step of our work.

For diatomic molecules, there are two main mechanisms of vibrational relaxation, namely, VV exchanges of vibrational quanta and VT transitions of vibrational energy to the translational one. Since CO_2 molecule has multiple vibrational modes, there are several additional relaxation channels. To present the kinetic scheme, we first introduce intra-mode vibrational transitions VV_m:

$$\mathbf{VV_1}: CO_2(v_1, v_2^l, v_3) + CO_2(w_1, w_2^m, w_3) \rightleftharpoons CO_2(v_1 \pm 1, v_2^l, v_3) + CO_2(w_1 \mp 1, w_2^m, w_3), \quad (1)$$

$$\mathbf{VV_2}: CO_2(v_1, v_2^l, v_3) + CO_2(w_1, w_2^m, w_3) \rightleftharpoons CO_2(v_1, v_2^{l \pm 1} \pm 1, v_3) + CO_2(w_1, w_2^{m \mp 1} \mp 1, w_3), \quad (2)$$

$$\mathbf{VV_3}: CO_2(v_1, v_2^l, v_3) + CO_2(w_1, w_2^m, w_3) \rightleftharpoons CO_2(v_1, v_2^l, v_3 \pm 1) + CO_2(w_1, w_2^m, w_3 \mp 1), \quad (3)$$

$$\mathbf{VV}_{\mathrm{O2}} : O_2(v) + O_2(w) \rightleftharpoons O_2(v \pm 1) + O_2(w \mp 1), \tag{4}$$

$$\mathbf{VV}_{\mathrm{CO}} : CO(v) + CO(w) \rightleftharpoons CO(v \pm 1) + CO(w \mp 1). \tag{5}$$

The next relaxation mechanism is due to vibrational-translational transitions in each mode VT_m:

$$\mathbf{VT_1} : \quad CO_2(v_1, v_2^l, v_3) + M \rightleftharpoons CO_2(v_1 \pm 1, v_2^l, v_3) + M, \tag{6}$$

$$\mathbf{VT_2} : \quad CO_2(v_1, v_2^l, v_3) + M \rightleftharpoons CO_2(v_1, v_2^{l\pm1} \pm 1, v_3) + M, \tag{7}$$

$$\mathbf{VT_3} : \quad CO_2(v_1, v_2^l, v_3) + M \rightleftharpoons CO_2(v_1, v_2^l, v_3 \pm 1) + M, \tag{8}$$

$$\mathbf{VT}_{\mathrm{O2}} : \quad O_2(v) + M \rightleftharpoons O_2(v \pm 1) + M, \tag{9}$$

$$\mathbf{VT}_{\mathrm{CO}} : \quad CO(v) + M \rightleftharpoons CO(v \pm 1) + M, \tag{10}$$

M stands for the partner in a collision

A particular feature of polyatomic molecules relaxation is the existence of inter-mode VV_{m-k} exchanges, in our case within CO_2 molecule:

$$\mathbf{VV_{1-2}} : \quad CO_2(v_1, v_2^l, v_3) + M \rightleftharpoons CO_2(v_1 \pm 1, v_2^l \mp 2, v_3) + M, \tag{11}$$

$$\mathbf{VV_{2-3}} : \quad CO_2(v_1, v_2^l, v_3) + M \rightleftharpoons CO_2(v_1, v_2^{l\pm1} \pm 3, v_3 \mp 1) + M, \tag{12}$$

$$\mathbf{VV_{1-2-3}} : \quad CO_2(v_1, v_2^l, v_3) + M \rightleftharpoons CO_2(v_1 \pm 1, v_2^{l\pm1} \pm 1, v_3 \mp 1) + M, \tag{13}$$

and between molecules of different chemical species:

$$\mathbf{VV_{3-CO}} : \quad CO_2(v_1, v_2^l, v_3) + CO(w) \rightleftharpoons CO_2(v_1, v_2^l, v_3 \mp 1) + CO(w \pm 1), \tag{14}$$

$$\mathbf{VV_{2-CO}} : \quad CO_2(v_1, v_2^l, v_3) + CO(w) \rightleftharpoons CO_2(v_1, v_2^{l\pm1} \mp 3, v_3) + CO(w \pm 1), \tag{15}$$

$$\mathbf{VV_{1-2-CO}} : \quad CO_2(v_1, v_2^l, v_3) + CO(w) \rightleftharpoons CO_2(v_1 \pm 1, v_2^{l\pm1} \pm 1, v_3) + CO(w \mp 1), \tag{16}$$

$$\mathbf{VV_{1-O_2}} : \quad CO_2(v_1, v_2^l, v_3) + O_2(w) \rightleftharpoons CO_2(v_1 \mp 1, v_2^l, v_3) + O_2(w \pm 1), \tag{17}$$

$$\mathbf{VV_{CO-O_2}} : \quad CO(v) + O_2(w) \rightleftharpoons CO(v \mp 1) + O_2(w \pm 1). \tag{18}$$

Finally, among state-specific chemical reactions we consider dissociation–recombination:

$$CO_2(v_1, v_2, v_3) + M \rightleftharpoons CO(w) + O + M, \tag{19}$$

$$CO(v) + M \rightleftharpoons C + O + M, \tag{20}$$

$$O_2(v) + M \rightleftharpoons O + O + M \tag{21}$$

and exchange reactions:

$$CO_2(v_1, v_2, v_3) + O \rightleftharpoons CO(v) + O_2(w), \tag{22}$$

$$CO(v) + O \rightleftharpoons O_2(w) + C, \tag{23}$$

$$CO(v) + CO(w) \rightleftharpoons CO_2(v_1, v_2, v_3) + C. \tag{24}$$

Processes (1)–(24) represent the complete kinetic scheme for a five-component $CO_2/CO/O_2/C/O$ mixture without electronic excitation and ionization. The rates of these processes may differ by several orders of magnitude, which allows neglecting some transitions under particular physical conditions and provides a basis for the development of multi-temperature models.

3. Rate coefficients for vibrational transitions and chemical reactions

In this section, we introduce the rate coefficients for the processes included to reduced kinetic scheme used further for the flow simulations.

One of the problems arising in the modelling of vibrational kinetics for polyatomic molecules is the lack of data on the rate coefficients of different kinds of vibrational energy transitions within and between modes. The diverse experimental results describe only several vibrational transitions between the lowest states (see [1, 17, 18, 19, 20]). Unfortunately these data are not sufficient for the description of transitions between highly located states and for the modelling of VV transitions. The majority of theoretical models are based on the so called SSH-theory [21, 22] which gives only qualitative behaviour of transition probabilities and can be applied for the moderate temperature range. To have confidence on the choice of a model, the rate coefficients should be validated against corresponding experimentally measured values or semi-classical and quantum mechanical trajectory calculations (see [23, 24, 25, 26]). We propose the following procedure for the calculation of the transition rates [12]: the rate coefficients of vibrational energy transitions between the lowest vibrational states are computed using the experimental data [20], the remaining rate coefficients (for higher states) are calculated on the basis of the SSH theory [21] modified for polyatomic molecules.

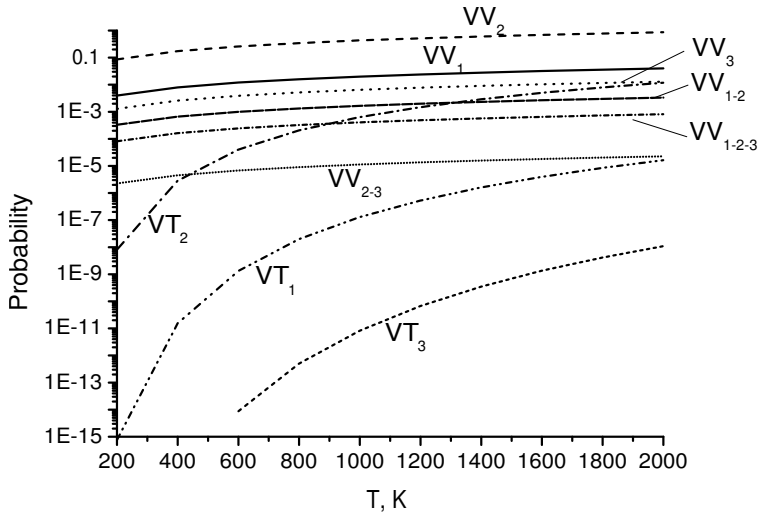

Figure 1: Probabilities of vibrational energy transitions between the lowest states, the SSH theory.

In Fig. 1, probabilities of vibrational energy transitions between the lowest states calculated on the basis of the SSH theory are reported. One can notice that whereas the probabilities of intra-mode transitions are close to each other, other probabilities differ significantly. Moreover, it is seen that the symmetric mode relax mainly through VV_{1-2} exchanges and not through

VT_1 processes. The asymmetric mode relax through inter-mode VV_{2-3}, VV_{1-2-3} transitions since the probability of VT_3 transitions is low. Therefore, we keep only VT_2 transitions as the main channel of VT relaxation in CO_2.

On the basis of the SSH theory, we obtain the following expressions for the rate coefficients of the most relevant vibrational transitions:

$$\mathbf{VT_2}: \quad k^M_{v_2+1\to v_2} = k^M_{010\to000}(v_2+1), \tag{25}$$

$$\mathbf{VT_{CO,O_2}}: \quad k^M_{v+1\to v} = k^M_{1\to0}(v+1), \tag{26}$$

$$\mathbf{VV_{2-3}}: \quad k^M_{v_2+3,v_3\to v_2,v_3+1} = k^M_{030\to001}\frac{(v_2+1)(v_2+2)(v_2+3)(v_3+1)}{3!}, \tag{27}$$

$$\mathbf{VV_{1-2-3}}: \quad k^M_{v_1+1,v_2+1,v_3\to v_1,v_2,v_3+1} = k^M_{110\to001}(v_1+1)(v_2+1)(v_3+1), \tag{28}$$

$$\mathbf{VV_{3-CO}}: \quad k^{w\to w+1}_{v_3+1\to v_3} = k^{0\to1}_{001\to000}(v_3+1)(w+1), \tag{29}$$

$$\mathbf{VV_{2-CO}}: \quad k^{w\to w+1}_{v_2+3\to v_2} = k^{0\to1}_{030\to000}\frac{(v_2+1)(v_2+2)(v_2+3)(w+1)}{3!}, \tag{30}$$

$$\mathbf{VV_{1-2-CO}}: \quad k^{w\to w+1}_{v_1+1,v_2+1\to v_1,v_2} = k^{0\to1}_{110\to000}(v_1+1)(v_2+1)(w+1). \tag{31}$$

For the more accurate calculation of the rate coefficients $k^M_{010\to000}$, $k^M_{1\to0}$, $k^M_{030\to001}$, and so on, we propose to use experimental data from Ref. [20]. The rate coefficient for a transition γ can be connected to the corresponding relaxation time by an approximate expression

$$k_\gamma = \frac{kT}{p\tau_\gamma},$$

where k is the Boltzmann constant, T is the temperature, p is the pressure in atmospheres, and τ_γ is the characteristic time of the process γ. In [20], τ_γ is calculated as

$$\log_{10}(p\tau_\gamma) = A_0 + A_1T^{-1/3} + A_2T^{-2/3}.$$

Coefficients A_n for the different processes and M=CO_2 are reported in Table 1.

Table 1: Coefficients A_n for various transitions.

Process	A_0	A_1	A_2
VT_2	-10.327	57.31	-156.7
VT_{CO}	-12.820	155.91	-450.5
VV_{2-3}, VV_{1-2-3}	-12.662	88.87	-272.5
VV_{1-2-CO}, VV_{2-CO}	-10.708	69.94	-203.3
VV_{3-CO}	-9.144	31.91	-103.5

The rate coefficients of backward transitions are connected to the rate coefficients of forward transitions by the detailed balance principle. For vibrational-translational transitions in each mode VT_m or inter-mode VV_{m-k} exchanges, it reads:

$$k^M_{v_1',v_2',v_3'\to v_1,v_2,v_3} = k^M_{v_1,v_2,v_3\to v_1',v_2',v_3'}\,\frac{v_2+1}{v_2'+1}\exp\left(\frac{\varepsilon_{v_1'v_2'v_3'} - \varepsilon_{v_1v_2v_3}}{kT}\right). \tag{32}$$

For inter-molecular VV transitions we have:

$$k^{w'\to w}_{v_1',v_2',v_3'\to v_1,v_2,v_3} = k^{w\to w'}_{v_1,v_2,v_3\to v_1',v_2',v_3'} \frac{v_2+1}{v_2'+1} \exp\left(\frac{\varepsilon_{v_1'v_2'v_3'} + \varepsilon^c_{w'} - \varepsilon_{v_1v_2v_3} - \varepsilon^c_w}{kT}\right). \tag{33}$$

In these expressions, v_2+1 is the statistical weight connected to the degeneration of the bending mode, ε^c_w is the vibrational energy of diatomic species c.

Let us consider the rate coefficients of state-specific chemical reactions. For the dissociation rate coefficient of CO_2 in reaction (19) we use the generalization of the Treanor–Marrone model [27] for three-atomic molecules:

$$k^M_{v_1v_2v_3,\,diss} = \frac{Z^{CO_2}_{vibr}(T)}{Z^{CO_2}_{vibr}(-U)} \exp\left(\frac{\varepsilon_{v_1v_2v_3}}{k}\left(\frac{1}{T}+\frac{1}{U}\right)\right) k^{eq,\,M}_{diss}. \tag{34}$$

Here

$$Z^{CO_2}_{vibr}(T) = \sum_{v_1v_2v_3} (v_2+1)\exp\left(-\frac{\varepsilon_{v_1v_2v_3}}{kT}\right)$$

is the equilibrium vibrational partition function of CO_2, $k^{eq,\,M}_{diss}$ is the thermal equilibrium dissociation rate coefficient of CO_2, U is the parameter describing preferential character of dissociation. The rate coefficient for recombination can be expressed with the use of the detailed balance principle:

$$k^M_{rec,\,v_1v_2v_3}(T) = k^M_{v_1v_2v_3,\,diss}\left(\frac{m_{CO_2}}{m_{CO}m_O}\right)^{3/2}(2\pi kT)^{-3/2}h^3(v_2+1)\frac{Z^{CO_2}_{rot}(T)}{Z^{CO}_{rot}}\times$$
$$\times\exp\left(-\frac{\varepsilon_{v_1v_2v_3}+\varepsilon^{CO_2}-\varepsilon^{CO}_w-\varepsilon^{CO}-\varepsilon^O}{kT}\right), \tag{35}$$

h is the Planck constant, $Z^{CO_2}_{rot}$, Z^{CO}_{rot} are the rotational partition functions for CO_2 and CO molecules, ε^c is the formation energy for c species (for homonuclear molecules like O_2, $\varepsilon^c = 0$).

For the dissociation and recombination rate coefficients of diatomic molecules, using the Treanor–Marrone model we obtain

$$k^{c,M}_{v,\,diss} = \frac{Z^c_{vibr}(T)}{Z^c_{vibr}(-U)}\exp\left(\frac{\varepsilon^c_v}{k}\left(\frac{1}{T}+\frac{1}{U}\right)\right)k^{eq,\,c,M}_{diss}, \qquad c = CO, O_2 \tag{36}$$

$$k^{CO,M}_{rec,\,v}(T) = k^{CO,M}_{v,\,diss}\left(\frac{m_{CO}}{m_Cm_O}\right)^{3/2}(2\pi kT)^{-3/2}h^3Z^{CO}_{rot}(T)\exp\left(-\frac{\varepsilon^{CO}_v+\varepsilon^{CO}-\varepsilon^C-\varepsilon^O}{kT}\right), \tag{37}$$

$$k^{O_2,M}_{rec,\,v}(T) = k^{O_2,M}_{v,\,diss}\left(\frac{2}{m_O}\right)^{3/2}(2\pi kT)^{-3/2}h^3Z^{O_2}_{rot}(T)\exp\left(-\frac{\varepsilon^{O_2}_v-2\varepsilon^O}{kT}\right) \tag{38}$$

with the vibrational partition function for diatomic species

$$Z^c_{vibr}(T) = \sum_v \exp\left(-\frac{\varepsilon_{v^c}}{kT}\right).$$

The state-to-state rate coefficients of forward exchange reactions also can be related to the equilibrium Arrhenius rate coefficients using the non-equilibrium factor, see Ref. [28]. In this

paper the following expression is proposed for $k_{v,f,r}$ ("r" denotes one of the reactions (22)–(24); "f" corresponds to the forward reaction; for CO_2, v stands for the set of quantum numbers (v_1, v_2, v_3)):

$$k_{v,f,r} = k^{eq}_{f,r}(T)\mathcal{Z}_v(T,U) \tag{39}$$

$\mathcal{Z}_v(T,U)$ is the non-equilibrium factor specified by the activation energy of r-th reaction, $E_{a,r}$

$$\mathcal{Z}_v(T,U) = \begin{cases} F(T,U)\exp\left(-\dfrac{E_{a,r}}{kU}\right)\exp\left(\dfrac{\varepsilon^c_v}{k}\left(\dfrac{1}{T}+\dfrac{1}{U}\right)\right), & \varepsilon^c_v < E_{a,r}, \\ F(T,U)\exp\left(\dfrac{E_{a,r}}{kT}\right), & \varepsilon^c_v > E_{a,r}, \end{cases} \tag{40}$$

normalizing function $F(T,U)$ is given by

$$F(T,U) = Z^c_{vibr}(T)\left[\sum_{v,\,\varepsilon^c_v<E_{a\ r}} \exp\left(-\frac{E_{a,r}-\varepsilon^c_v}{kU}\right) + \sum_{v,\,\varepsilon^c_v>E_{a\ r}} \exp\left(-\frac{E_{a,r}-\varepsilon^c_v}{kT}\right)\right]^{-1}. \tag{41}$$

Note that if $E_{a,r}$ approaches to the dissociation energy, the rate coefficients for exchange reactions (39) reduce to the dissociation rate coefficients (34) or (36).

The backward reaction rate coefficients for the reactions (22)–(24) $k_{v,b,r}$ are found applying the detailed balance principle:

$$k_{v,b,\,22} = k_{f,\,22}\left(\frac{m_{CO_2}m_O}{m_{CO}m_{O_2}}\right)^{3/2}\frac{Z^{CO_2}_{rot}}{Z^{CO}_{rot}Z^{O_2}_{rot}}\exp\left(-\frac{\varepsilon_{v_1v_2v_3}-\varepsilon^{CO}_v-\varepsilon^{O_2}_w+\varepsilon^{CO_2}+\varepsilon^O-\varepsilon^{CO}}{kT}\right), \tag{42}$$

$$k_{v,b,\,23} = k_{f,\,23}\left(\frac{m_{CO}m_O}{m_{O_2}m_C}\right)^{3/2}\frac{Z^{CO}_{rot}}{Z^{O_2}_{rot}}\exp\left(-\frac{\varepsilon^{CO}_v-\varepsilon^{O_2}_w+\varepsilon^{CO}+\varepsilon^O-\varepsilon^C}{kT}\right), \tag{43}$$

$$k_{v,b,\,24} = k_{f,\,24}\left(\frac{m^2_{CO}}{m_{CO_2}m_C}\right)^{3/2}\frac{\left(Z^{CO}_{rot}\right)^2}{Z^{CO_2}_{rot}}\exp\left(-\frac{\varepsilon^{CO}_v+\varepsilon^{CO}_w-\varepsilon_{v_1v_2v_3}+2\varepsilon^{CO}-\varepsilon^{CO_2}-\varepsilon^C}{kT}\right). \tag{44}$$

Thermal equilibrium rate coefficients of chemical reactions can be found using various models. In Tables 2,3 the rate coefficients are given according to the Mc-Kenzie [29] and Park [30] models. For dissociation reactions M =CO_2. More recent experimental data on dissociation rate coefficients in CO_2 mixtures can be found in [31, 32]

Table 2: Thermal equilibrium rate coefficients for reactions (19)–(22). Mc-Kenzie model.

Reaction	$k_{f,r}$ cm^{3}mole^{-1}s^{-1}
(19)	$7.2\cdot10^{11}T^{1/2}\exp(-36850/T)$
(20)	$3.5\cdot10^{12}T^{1/2}\exp(-92800/T)$
(21)	$0.77\cdot10^{17}T^{-1/2}\exp(-59400/T)$
(22)	$0.61\cdot10^{12}\exp(-17600/T)$

Thus we have all required information on the rate coefficients for vibrational transitions and chemical reactions contributing to the simplified kinetic mechanism applied in the Results section.

Table 3: Thermal equilibrium rate coefficients for reactions (19)–(24). Park model.

Reaction	$k_{f,r}$, $\mathrm{m^3 mole^{-1} s^{-1}}$
(19)	$6.9 \cdot 10^{15} T^{-1.5} \exp(-63275/T)$
(20)	$2.3 \cdot 10^{14} T^{-1} \exp(-129000/T)$
(21)	$2.0 \cdot 10^{15} T^{-1.5} \exp(-59500/T)$
(22)	$2.1 \cdot 10^{7} \exp(-27800/T)$
(23)	$3.9 \cdot 10^{7} T^{-0.18} \exp(-69200/T)$
(24)	$2.33 \cdot 10^{3} T^{0.5} \exp(-65710/T)$

4. State-to-state description of vibrational-chemical kinetics

The most detailed state-to-state model of vibration-chemical kinetics and transport properties is needed under the condition of strong vibrational and chemical coupling:

$$\tau_{tr} < \tau_{rot} \ll \tau_{vibr} < \tau_{react} \sim \theta, \tag{45}$$

where τ_{tr}, τ_{rot}, τ_{vibr}, and τ_{react} are respectively the characteristic times of translational, rotational, vibrational and chemical relaxation, θ is the time of gas-dynamic parameters variation. The closed set of macroscopic parameters consists of vibrational level populations of CO_2 $n_{v_1 v_2^l v_3}$ and diatomic species n_w^c, number densities of atoms n_c, macroscopic flow velocity $\mathbf{v}$, and gas temperature T.

The general set of governing equations has the form

$$\frac{d\rho}{dt} + \rho \nabla \cdot \mathbf{v} = 0, \tag{46}$$

$$\rho \frac{d\mathbf{v}}{dt} + \nabla \cdot \mathbf{P} = 0, \tag{47}$$

$$\rho \frac{du}{dt} + \nabla \cdot \mathbf{q} + \mathbf{P} : \nabla \mathbf{v} = 0, \tag{48}$$

$$\frac{dn_{v_1 v_2^l v_3}}{dt} + n_{v_1 v_2^l v_3} \nabla \cdot \mathbf{v} + \nabla \cdot (n_{v_1 v_2^l v_3} \mathbf{V}_{v_1 v_2^l v_3}) = R^{vibr}_{v_1 v_2^l v_3} + R^{react}_{v_1 v_2^l v_3}, \; v_m = 0, ..., L_m, \tag{49}$$

$$\frac{dn_w^c}{dt} + n_w^c \nabla \cdot \mathbf{v} + \nabla \cdot (n_w^c \mathbf{V}_{cw}) = R^{vibr}_{cw} + R^{react}_{cw}, \quad w = 0, ..., L_c, \quad c = CO, O_2, \tag{50}$$

$$\frac{dn_c}{dt} + n_c \nabla \cdot \mathbf{v} + \nabla \cdot (n_c \mathbf{V}_c) = R^{react}_c, \quad c = O, C \tag{51}$$

where $\rho = \sum_c m_c n_c$ is the density, m_c and n_c are the mass and number density of species c, $\mathbf{P}$ is the stress tensor, u is the specific mixture energy, $\mathbf{q}$ is the total heat flux, $\mathbf{V}_{v_1 v_2^l v_3}$, $\mathbf{V}_{cw}$ are the diffusion velocities of vibrational states $(v_1 v_2^l v_3)$ and w, $R^{vibr}_{v_1 v_2^l v_3}$, $R^{react}_{v_1 v_2^l v_3}$, R^{vibr}_{cw}, R^{react}_{cw} are the state-to-state production terms due to vibrational transitions and chemical reactions, R^{react}_c are the production rates of atoms c, L_m is the number of excited vibrational levels in the mth vibrational mode.

The production terms in Eqs. (46)–(51) depend on the vibrational levels populations, number densities of species and rate coefficients of corresponding processes. The expressions for all production terms are given in [13]. The state-to-state transport theory for diatomic molecules was developed in [33] and generalized for polyatomic molecules in [10, 11]. A particular feature of the heat transfer in the state-to-state approach is that the heat flux consists of four terms [34]

$$\mathbf{q} = \mathbf{q}^{HC} + \mathbf{q}^{MD} + \mathbf{q}^{TD} + \mathbf{q}^{DVE} \tag{52}$$

where the corresponding terms are responsible for heat conduction, mass and thermal diffusion, and diffusion of vibrational energy. Whereas the first three terms appear in the heat flux in all models (multi-temperature and one-temperature), the term $\mathbf{q}^{DVE}$ is specified only for the state-to-state kinetics. The heat conductivity in this case does not include the term connected to the vibrational energy, and the transport of vibrational energy is completely defined by the diffusion of vibrational states.

Since we are going to apply the state-to-state model to a 1D boundary layer problem, we simplify the fluid dynamics equations (46)–(51) using the boundary layer assumptions and Dorodnitsyn-Lees co-ordinate transformation in the vicinity of the stagnation point [35, 36]. Thus we obtain a 1D boundary layer equation system in the state-to-state approach:

$$\frac{\partial^2 c_v}{\partial \eta^2} + f\mathrm{Sc}\frac{\partial c_v}{\partial \eta} = S_v, \qquad v = 1, ..., NumSp \tag{53}$$

$$\frac{\partial^2 \theta}{\partial \eta^2} + f\mathrm{Pr}\frac{\partial \theta}{\partial \eta} = S_T. \tag{54}$$

The direction η corresponds to the normal to the surface in the self-similar coordinate system. The first $NumSp$ equations are the species continuity equations whereas the last equation is the temperature one. As species we mean either molecules on the v-th vibrational level (for CO_2, $v = (v_1, v_2, v_3)$, for diatomic species v is the vibrational state) or atoms (v = C or O). $c_v = \rho_v/\rho$ is the mass fraction of the v-species; $\theta = T/T_e$ is the ratio of the gas temperatures inside and at the external edge of the boundary layer; f is the stream function, and Sc and Pr are the Schmidt and Prandtl numbers, respectively. The production terms S_v and S_T are given by expressions

$$S_v = -\sum_{i=1}^{NumSp} B(v,i)c_i \tag{55}$$

$$S_T = \sum_{v=1}^{NumSp} \frac{\mathrm{Le}}{C_p T_e}\varepsilon_v \sum_{i=1}^{NumSp} B(v,i)c_i \tag{56}$$

where C_p is the gas specific heat at constant pressure including, in the present model, only rotational and translational contributions, Le is the Lewis number, and the matrix $B(v,i)$ containing the kinetic terms is given in Ref. [11].

The implementation of the state-to-state description of mixtures containing CO_2 to CFD is very computationally expensive. First, the number of equations for the vibrational level populations and number densities of atoms is equal to $N = L_1 \times L_2 \times L_3 + L_{CO} + L_{O_2} + 2 = L_{CO_2} + L_{CO} + L_{O_2} + 2$. For the CO_2 molecule, the dissociation energy is $8.83859{\cdot}10^{-19}$ J, which leads to the maximum vibrational quantum numbers 34, 67 and 20 for the symmetric, bending

and asymmetric modes respectively, and the total number of CO_2 states is 9018. Next problem is the calculation of transport coefficients. Thus the number of diffusion coefficients about N^2, and the dimension of transport linear systems which should be solved at each step of numerical solution is of the order of N.

Based on the above arguments, we propose to use in the fluid dynamic equations a simplified transport model with constant Prandtl and Schmidt numbers to obtain preliminary results on CO_2 vibrational kinetics. Then, in order to evaluate the influence of vibrational kinetics on the transport terms, we use the macroscopic gas parameters obtained numerically solving the fluid dynamics equations and the rigorous transport model for the calculation of the transport coefficients and heat flux. Such a post-processing procedure is certainly approximate, however, the main trends and contributions of various processes to the heat transfer can be qualitatively estimated.

Another way of studying vibrational non-equilibrium in polyatomic viscous gases is to use advanced multi-temperature models for kinetics and transport properties taking into account real gas effects and different rates of vibrational exchanges.

5. Multi-temperature models for CO_2 mixtures

In this section we consider multi-temperature models for the flows of the five-component reacting mixture $CO_2/CO/O_2/C/O$ near spacecrafts entering the Mars atmosphere. The multi temperature description of non-equilibrium kinetics in reacting mixtures is much simpler compared to the state-to-state model considered in the previous section and therefore more suitable for applications in computational fluid dynamics. Actually, in multi-temperature approaches fluid dynamic equations are coupled to relaxation equations for vibrational temperatures of different molecular species instead of equations for vibrational level populations of different molecular components. The multi-temperature models are based on the experimental and theoretical data on relaxation times of different processes in the considered mixtures. The analysis of these data for CO_2 containing mixtures under high temperature condition shows that the translational and rotational relaxation as well as CO_2 intra-mode vibrational energy exchanges proceed much faster compared to other vibrational energy transitions and chemical reactions. Such relations between characteristic times make it possible to introduce vibrational temperatures T_m $(m = 1, 2, 3)$ for three vibrational CO_2 modes and express vibrational level populations in terms of these temperatures. Consequently, the number of governing equations is essentially reduced: instead of L_{CO2} equations for level populations one may consider only three equations for vibrational temperatures.

Experimental data also show that the inter-mode exchange between CO_2 symmetric and bending modes (11) proceeds fast due to the Fermi resonance between the frequencies of these modes and can be considered as a rapid process along with the intra-mode energy exchanges. The remaining kinetic process are slow and have relaxation times of the same order as the mean time of the gas-dynamic parameters variation. In this case the relaxation times of different processes in the considered mixture satisfy the following conditions:

$$\tau_{tr} < \tau_{rot} < \tau_{VV_m} \sim \tau_{VV_{1-2}} \ll \tau_{VT_2} \sim \tau_{VV_{2-3}} \sim \tau_{VV_{1-2-3}} < \tau_{react} \sim \theta, \quad m = 1, 2, 3. \tag{57}$$

The rapid VV_{1-2} exchange makes it possible to consider the coupled (symmetric-bending) mode with a single vibrational temperature T_{12}. For the case of harmonic oscillators we represent

the vibrational distributions of CO_2 molecules as a combination of two non-equilibrium Boltzmann distributions with the vibrational temperature T_{12} in the coupled mode and T_3 in the asymmetric mode.

$$n_{v_1v_2v_3}(T_{12},T_3) = \frac{n_{CO_2}(v_2+1)}{Z_{vibr}^{CO_2}(T_{12},T_3)} \exp\left(-\frac{(2v_1+v_2)\varepsilon_{010}}{kT_{12}} - \frac{v_3\varepsilon_{001}}{kT_3}\right), \tag{58}$$

where $Z_{vibr}^{CO_2}(T_{12},T_3)$ is the non-equilibrium CO_2 vibrational partition function. In the present study, the diatomic species CO and O_2 are supposed to equilibrate faster than CO_2 and are considered in thermal equilibrium. The vibrational non-equilibrium excitation of CO and O_2 species in considered mixture is taken into account in Ref. [13].

The governing equations are derived in [15] from the kinetic equations for distribution functions and include the conservation equations of mass, momentum and total energy coupled to the equations of chemical kinetics and two relaxation equations for vibrational energies of coupled and asymmetric modes:

$$\frac{d\rho}{dt} + \rho\,\nabla\cdot\mathbf{v} = 0, \tag{59}$$

$$\rho\frac{d\mathbf{v}}{dt} + \nabla\cdot\mathbf{P} = 0, \tag{60}$$

$$\rho\frac{du}{dt} + \nabla\cdot\mathbf{q} + \mathbf{P}:\nabla\mathbf{v} = 0, \tag{61}$$

$$\frac{dn_c}{dt} + n_c\nabla\cdot\mathbf{v} + \nabla\cdot(n_c\mathbf{V}_c) = R_c^{react}, \quad c = CO_2,\ CO,\ O_2,\ C,\ O, \tag{62}$$

$$\rho_{CO_2}\frac{dE_{12}}{dt} + \nabla\cdot\mathbf{q}_{12} = R_{12} - m_{CO_2}E_{12}R_{CO_2}^{react} + E_{12}\,\nabla\cdot(\rho_{CO_2}\mathbf{V}_{CO_2}), \tag{63}$$

$$\rho_{CO_2}\frac{dE_3}{dt} + \nabla\cdot\mathbf{q}_3 = R_3 - m_{CO_2}E_3R_{CO_2}^{react} + E_3\,\nabla\cdot(\rho_{CO_2}\mathbf{V}_{CO_2}). \tag{64}$$

Here $E_{12}(T_{12})$, $E_3(T_3)$ are the specific vibrational energies of the coupled and asymmetric modes, respectively, $\mathbf{q}_{12}$, $\mathbf{q}_3$ are the fluxes of vibrational energy in the corresponding modes. The relaxation terms R_c^{react} , R_{12}, R_3 describe slow processes which include dissociation, recombination, exchange reactions, inter-mode CO_2 exchanges except VV_{12} exchange and VT_2 transitions.

The transport and relaxation terms in Eqs. (59)-(64) are reported in details in [13] on the basis of the generalized Chapman–Enskog method. All transport coefficients are found from linear transport systems given in [12, 13], elements of these systems depend on the cross sections of the most often collisions with inelastic non-resonant energy transitions. The expressions for heat fluxes $\mathbf{q}$, $\mathbf{q}_{12}$, and $\mathbf{q}_3$ contain gradients of temperatures T, T_{12}, T_3 and heat conductivity coefficients for transfer of total energy and vibrational energies of coupled and asymmetric CO_2 modes.

The relaxation terms R_c^{react} specify processes (19)–(24). These expressions involve three-temperature rate coefficients for CO_2 dissociation $k_{CO_2,diss}^M(T,T_{12},T_3)$ and exchange reactions as well as thermal equilibrium reaction rate coefficients for diatomic molecules that depend only on the gas temperature. The expressions for three-temperature CO_2 reaction rate coefficients are obtained by averaging the state-depending rate coefficients considered in Section 3 with

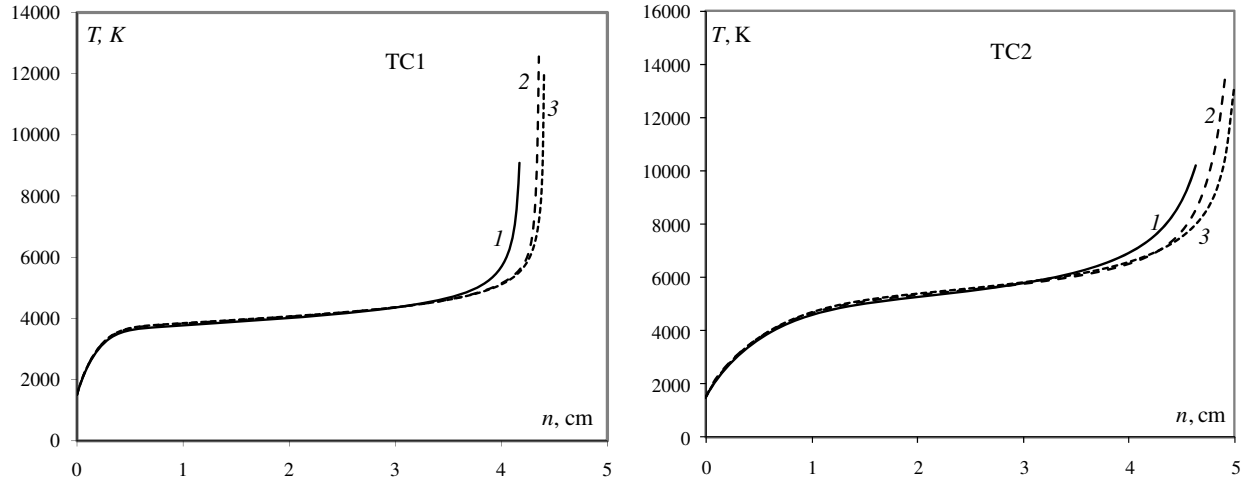

Figure 2: Gas temperature along the stagnation line. (a) TC1: $V_\infty = 5223$ m/s, $\rho_\infty = 2.93 \cdot 10^{-4}$ kg/m^3, $T_\infty = 140$ K, (b) TC2: $V_\infty = 5687$ m/s, $\rho_\infty = 3.141 \cdot 10^{-5}$ kg/m^3, $T_\infty = 140$ K. Curve 1: one-temperature model; curve 2: three-temperature model; curve 3: two-temperature model [1].

vibrational distributions (58). The rate coefficient for CO_2 dissociation is written in the form derived in [12] using the generalization of the Treanor–Marrone model [27]:

$$k^M_{CO_2,\,diss}(T, T_{12}, T_3) = k^{eq,\,M}_{diss} \frac{Z^{CO_2}_{vibr}(T)}{Z^{CO_2}_{vibr}(-U) Z^{CO_2}_{vibr}(T_{12}, T_3)} \times$$

$$\times \sum_{v_1, v_2, v_3} (v_2 + 1) \exp\left(\frac{v_1 \varepsilon_{100} + v_2 \varepsilon_{010}}{k} \left(\frac{1}{T} - \frac{1}{T_{12}} \right) + \frac{v_3 \varepsilon_{001}}{k} \left(\frac{1}{T} - \frac{1}{T_3} \right) + \frac{\varepsilon_{v_1 v_2 v_3}}{kU} \right). \qquad (65)$$

Rate coefficients for backward reactions are found using the detailed balance principle. The approximate expressions for production terms of slow processes (7), (12) and (13) via relaxation times which can be measured experimentally are proposed in [13].

Thus we derived self-consistent macroscopic flow descriptions in the state-to-state and multi-temperature approaches. These governing equations are solved numerically in the next section for particular test cases.

6. Results and discussion

Let us consider first the results of multi-temperature modelling. Equations (59)-(64) with rigorous kinetic schemes for transport coefficients have been solved numerically for a flow in a 2D viscous shock layer near the blunt bodies imitating the form of the spacecrafts MSRO (Mars Sample Return Orbiter) and Mars Express for two test cases: $V_\infty = 5223$ m/s, $\rho_\infty = 2.93 \cdot 10^{-4}$ kg/m^3, $T_\infty = 140$ K (TC1) and $V_\infty = 5687$ m/s, $\rho_\infty = 3.141 \cdot 10^{-5}$ kg/m^3, $T_\infty = 140$ K (TC2). The orthogonal system of co-ordinates (s, n) is used, where s is counted from the stagnation point along the body surface while n is normal to the surface. The free stream is supposed to be consisted of pure CO_2, the body surface is assumed to be either non-catalytic or fully catalytic. The results are presented in Refs. [14, 15] and show the behaviour of flow parameters in a shock layer and heat transfer to the vehicle surfaces.

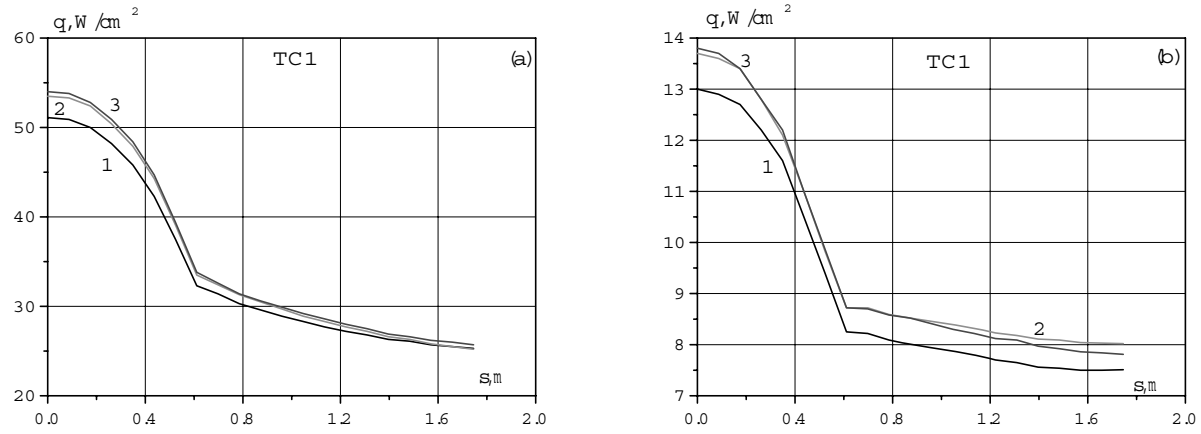

Figure 3: Heat flux along the body surface, TC1: $V_\infty = 5223$ m/s, $\rho_\infty = 2.93 \cdot 10^{-4}$ kg/m^3, $T_\infty = 140$ K. (a) Catalytic surface; (b) Non-catalytic surface.

In order to understand the influence of a kinetic model on macroscopic flow parameters and heat transfer to the body surface, we solved in Refs. [14, 15] the system of governing equations not only in the three-temperature approximation but also the two-temperature and one-temperature approaches. In the first case, a single vibrational temperature for all three CO_2 modes $T_v = T_{12} = T_3$ is introduced; and in the second model $T_{12} = T_3 = T$.

The profiles of the gas temperature along the stream line orthogonal to the surface in the shock layer and the heat flux values on the body surface obtained in [14, 15] for the spacecraft MSRO are presented in Figs. 2, 3. The values $n = 0$ and $s = 0$ correspond to the stagnation point. Curves 1 correspond to the one-temperature approach, 2 to the three-temperature approach, and 3 to the two-temperature approach.

The results show that the profiles of gas temperature corresponding to the two- and three-temperature models (curves 2,3) differ rather weakly, the discrepancy does not exceed 5%. This justifies the validity of the approximate two-temperature model under the entry conditions. On the other hand, far from the surface ($n > 3$ cm) one can notice considerable difference between the results obtained for thermal equilibrium (one-temperature) and non-equilibrium (multi-temperature) flows. The vibrational temperatures T_{12} and T_3 equilibrate coming to the surface as well as the specific vibrational energies. The difference between the values of the total vibrational energy found in the three-temperature, two-temperature and one-temperature approaches is very small near the surface. Non-equilibrium vibrational CO_2 excitation leads to a slight increase in distance between the shock wave and body surface, noticeable rising (up to 30%) of the gas temperature near the shock front and weakly affects the gas temperature near the surface. Vibrational non-equilibrium of CO_2 molecules also leads to the increase of the surface heat flux up to 10%. The results were obtained using three models for thermal equilibrium reaction rates [29, 30, 32]. While only the slight influence of chemical reaction model on the heat transfer to the non-catalytic surface was found, near the fully catalytic surface this effect occurs more essential [15]. Recently a strong influence of a body shape on the gas parameters in a shock layer and heat fluxes to the surface was found in [37].

Now let us consider the state-to-state solution of a 1D boundary layer problem (see Eqs. (53)–(54)). In the test cases considered below, we use as external edge boundary conditions the macroscopic gas flow parameters obtained in the frame of the TC2 multi-temperature test case discussed above. We choose the conditions corresponding to the region where thermal equilibrium establishes in the shock layer, i.e. about n =3 cm (see Fig. 2b). Note that at this distance the mixture composition is still far from chemical equilibrium. Thus we set $(c_{CO_2})_e$= 10.4%, $(c_{CO})_e$ = 57.6%, $(c_C)_e$ = 0.3%, $(c_{O_2})_e + (c_O)_e$ = 31.7%, T_e = 6000 K, p_e = 888 Nm^{-2}, and β= 2708 s^{-1}, where T_e and p_e are temperature and pressure at the boundary layer edge, and β is the gradient of the free stream velocity with respect to the coordinate along the surface (its physical meaning is the inverse of the residence time of a fluid element in a particular point of the boundary layer). The vibrational distributions at the external edge are Boltzmann at $T = T_e$ since we consider thermal equilibrium region. At the surface, the temperature T_w = 1500 K, and the surface is assumed non-catalytic, so that the gradients of species molar fractions are zero.

Two test cases are considered with simplified kinetic schemes. In the first test case (TC2-st.to.st1), the following processes are taken into account: (7), (11), (13), (15), (16), (19). In the second test case (TC2-st.to.st2), only vibrational exchanges (7), (11), (13) in CO_2 molecules are included; dissociation, recombination and inter-molecular transitions are neglected. Although simplified, these kinetic schemes describe the most important channels of vibrational relaxation and thus can describe the main features of CO_2 kinetics. Moreover, in order to minimize computational costs, a reduced number of CO_2 vibrational levels is considered by setting the CO_2 dissociation energy to $4.8065{\cdot}10^{-19}$ J (see [11] for details); in this way the maximum vibrational quantum numbers become 17, 33 and 9 in the symmetric, bending and asymmetric modes respectively, resulting in the total number of CO_2 states of 1224, which is much less than in the full model. In [11] it is shown that such a reduced model practically does not affect the flow parameters for a non-catalytic surface.

In Fig. 4 the temperature profile (Fig. 4a) and the total vibrational energy per mass unit (Fig. 4b) across the boundary layer are shown. Curve 1 corresponds to the solution of the energy equation (54) without the production term. Solving equation (54) with $S_T = 0$ we find the temperature at each grid step, and then assume that the vibrational distributions are Boltzmann with the local temperature. Curve 2 corresponds to the TC2-st.to.st1 test case and curve 3 to the TC2-st.to.st2 test case. One can see that vibrational transitions do not affect the temperature, whereas dissociation and recombination processes slightly modify the temperature profile at $1 < \eta < 7$. The total vibrational energy strongly depends on the vibrational distribution, especially close to the surface. Assuming Boltzmann vibrational distributions in the flow leads to considerable underestimation of the vibrational energy at the surface. This effect can be of importance near the catalytic wall, where the transport of vibrational energy gives noticeable contribution to the energy flux.

The vibrational distributions versus quantum numbers of each mode, at fixed values of the other two modes, are plotted on Figs. 5a-c. Curve 1 corresponds to the equilibrium Boltzmann distribution at $T = T_w$, curve 2 corresponds to the distribution on the surface ($\eta = 0$) obtained

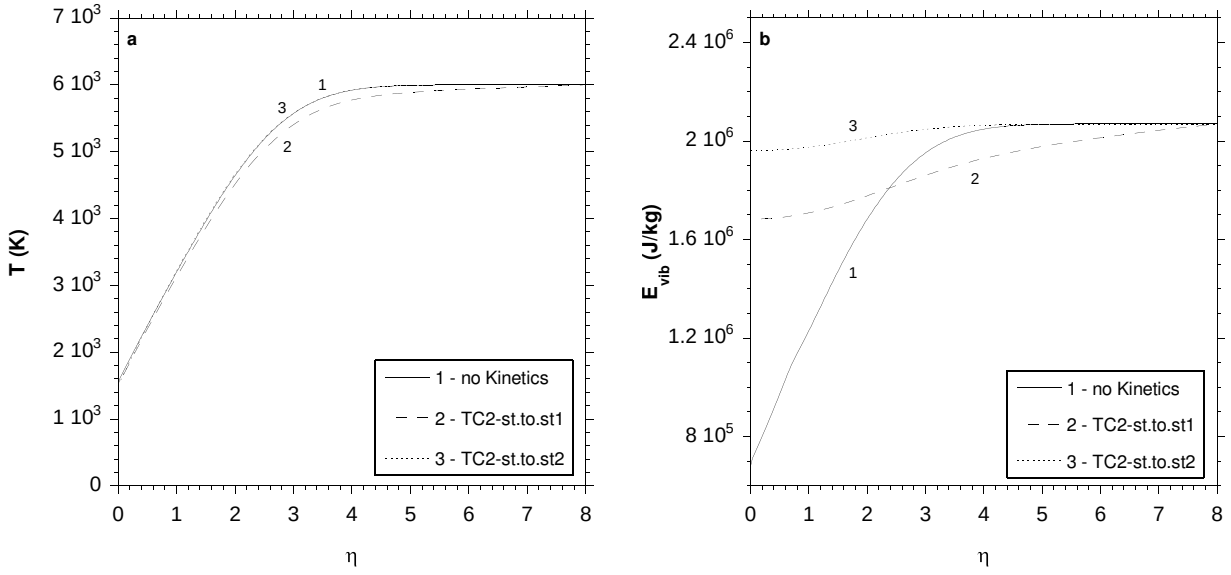

Figure 4: Temperature profile (a) and total vibrational energy per mass unit (b) across the boundary layer. Comparison of different kinetic schemes: no kinetics (curve 1); processes (7), (11), (13), (15), (16), and (19) are included (curve 2); processes (7), (11), and (13) are included (curve 3).

under conditions of TC2-st.to.st1, curve 3 corresponds to the distribution on the surface ($\eta = 0$) obtained in the TC2-st.to.st2 case, finally curve 4 is the external edge vibrational distribution (the Boltzmann distribution at T_e). The considered processes influence the flow, which does not remain frozen in the boundary layer; however the flight conditions do not give to the kinetic processes the time to thermalize the flow, so that it reaches the surface far from local equilibrium: curves 2 and 3 of Figs. 5a-c do not coincide with curve 1. The statement that the flow does not remain frozen in the boundary layer is also evident in Fig. 5d, that gives an idea of the vibrational distributions as functions of vibrational energy (and not fixed quantum numbers) on the surface and at the external edge for the TC2-st.to.st1 test case: the two distributions do not coincide. It is worth mentioning that the multi-temperature models give thermal equilibrium vibrational distributions near the surface (see also Fig. 2).

In Fig. 6 the heat flux normal to the surface is reported. Curve 1 corresponds to the calculation neglecting kinetics, curve 2 to the TC2-st.to.st1 test case, and curve 3 to the TC2-st.to.st2 test case. When no kinetics is included in the calculation, the heat flux on the surface is slightly higher. Comparing curves 2 and 3 corresponding to more adequate calculations we conclude that including dissociation, recombination and inter-molecular transitions does not influence noticeably the heat flux; however it would be important to include all the state-to-state kinetic processes (1)-(24) to give more accurate evaluations. Besides that we expect more important effect of vibrational kinetics in the case of a catalytic wall, when recombination pumps vibrationally excited states, and contributions of mass and vibrational energy diffusion to the heat flux become greater.

Now let us compare the vibrational energy and the heat flux on the surface obtained in the multi-temperature and state-to-state approaches for the TC2. In Table 4 the specific vibrational energy and the total heat flux calculated at $\eta = 0$ are given. The specific vibrational energy

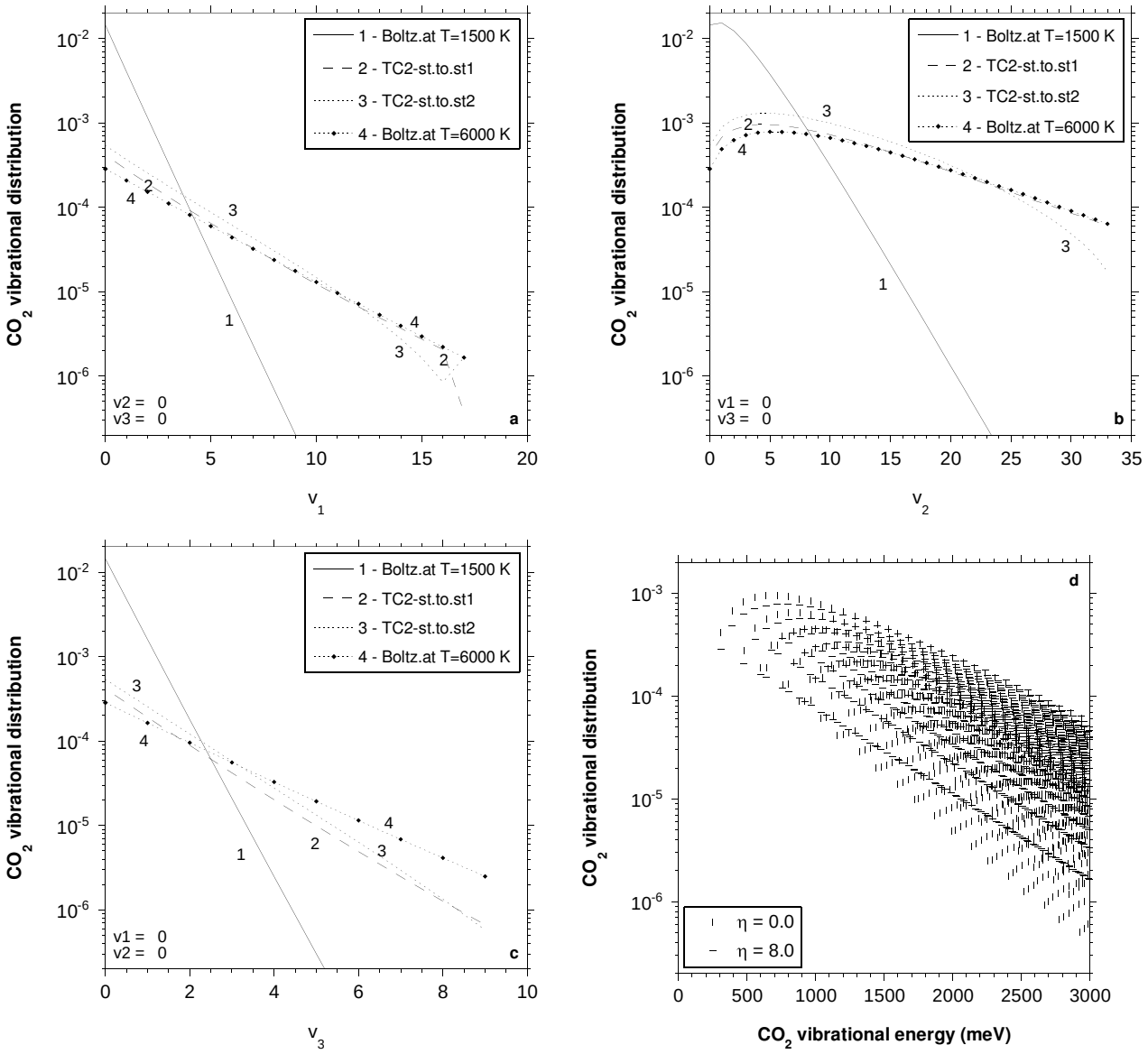

Figure 5: Vibrational distributions versus each mode quantum number at fixed values of the other two modes quantum numbers (a-c); whole distributions versus the vibrational energy for the TC2-st.to.st1 test case (d). Case TC2-st.to.st1: processes (7), (11), (13), (15), (16), and (19) are included; Case TC2-st.to.st2: processes (7), (11), and (13) are included.

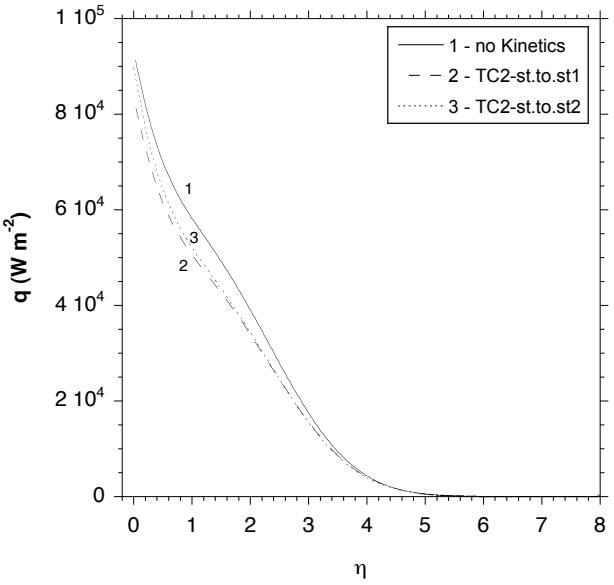

Figure 6: Heat flux versus the normal to the surface. Comparison of different kinetic schemes: no kinetics (curve 1); processes (7), (11), (13), (15), (16), and (19) are included (curve 2); processes (7), (11), and (13) are included (curve 3).

Table 4: Specific vibrational energy and heat flux at $\eta = 0$ for TC2 case: $V_\infty = 5687$ m/s, $\rho_\infty = 3.141 \cdot 10^{-5}$ kg/m^3, $T_\infty = 140$ K. Case TC2-st.to.st1: processes (7), (11), (13), (15), (16), and (19) are included; Case TC2-st.to.st2: processes (7), (11), and (13) are included.

	MT, TC2	STS, TC2-st.to.st1	STS, TC2-st.to.st2	no kinetics
E_{vibr}, MJ/kg	0.65	1.66	1.93	0.71
q, kW/m^2	71.1 [30] 96.0 [29] 80.5 [32]	83.54	89.68	91.3

obtained in the state-to-state approach is considerably higher than that found using the multi-temperature or one-temperature model, which is rather close to E_{vibr} calculated neglecting vibrational kinetics. This confirms again that the state-to-state flow is not in vibrational equilibrium close to the surface, and the store of vibrational energy is higher than in the multi-temperature flows. Nevertheless, it does not affect the total heat flux. In the multi-temperature model, the heat flux was calculated using three chemical reaction models. In the state-to-state simulation, the McKenzie model [29] was applied for the thermal equilibrium dissociation rate coefficients. One can see that the heat fluxes calculated in the multi-temperature and state-to-state models using the same chemical reaction rates agree very well. The influence of the detailed kinetics on the energy transfer is found to be negligible for a non-catalytic surface. Once again, it is worth mentioning that for a catalytic surface, the contribution of state-to-state kinetics to the heat flux can be much more important. These effects are the subject of our future study.

7. Conclusions

A comprehensive kinetic scheme indicating all possible mechanisms of vibrational relaxation and chemical reactions is proposed for CO_2 flows. Detailed information on the rate coefficients of processes characteristic for Mars entry problems is presented. State-to-state and multi-temperature approaches are developed for the prediction of non-equilibrium gas flow parameters and heat transfer. The accurate state-to-state model is applied for modelling of a 1D boundary layer near the spacecraft entering the Mars atmosphere whereas the quasi-stationary approach is used to study a 2D shock layer between the shock front and MSRO surface. The state specific model is unfortunately very time consuming. Even reducing the number of vibrational states, we obtain 1224 equations for CO_2 vibrational level populations coupled to fluid dynamic equations.

The results obtained on the basis of multi-temperature and one-temperature models show the strong influence of non-equilibrium vibrational excitation just behind a shock on the gas temperature and specific vibrational energy. However, near the surface non-equilibrium effects diminish, the difference between the values of gas temperature and vibrational temperature found in three-temperature and two-temperature non-equilibrium models becomes very small. Thus we conclude that multi-temperature models give thermal equilibrium reacting flows near the surface.

This is not the case for the state-resolved vibrational mechanism. The results show that vibrational distributions near the surface are far from the local vibrational and chemical equilibrium, and a noticeable difference between the values of CO_2 surface specific vibrational energies obtained in the state-to-state and quasi-stationary approaches is found. At the same time, a weak influence of a kinetic model on the heat transfer to the non-catalytic vehicle surface is shown for all considered approaches. For the catalytic surface, we expect more important effects of non-equilibrium kinetics on the heat flux.

Acknowledgements

The research leading to these results has received funding from the European Community's Seventh Framework Programme (FP7/2007-2013) under grant agreement n°242311 and Russian foundation for basic research (projects 11-01-00408 and 12-08-00826). The authors are grateful to Dr. N. G. Syzranova for providing data on the used thermal equilibrium reaction rates and numerical results obtained in the quasi-stationary approaches.

[1] R. Taylor, S. Bitterman, Survey of vibrational relaxation data for process important in the CO_2–N_2 laser system, Rev. Mod. Phys. 41 (1) (1969) 26.

[2] R. Thomson, The thermal conductivity of gases with vibrational internal energy, J. Phys. D: Appl. Phys. 11 (1978) 2509.

[3] R. Brun, Transport properties in reactive gas flows, AIAA Paper 88-2655.

[4] M. Capitelli, D. Bruno, A. Laricchiuta, Fundamental Aspects of Plasma Chemical Physics: Transport, Vol. 74 of Springer Series on Atomic, Optical, and Plasma Physics, Springer Verlag, Berlin, 2013.

[5] A. Likalter, On the vibrational distribution of polyatomic molecules, Prikl. Mekh. Tekn. Fiz. 4 (1976) 3, (in Russian).

[6] A. Cenian, Study of nonequilibrium vibrational relaxation of CO_2 molecules during adiabatic expansion in a supersonic nozzle. The Treanor distribution — existence and generation, Chem. Phys. 132 (1989) 41–48.

[7] E. Kustova, E. Nagnibeda, Nonequilibrium distributions in CO_2 and their influence on the transport and thermodynamic properties, in: Rarefied Gas Dynamics 21, Vol. 2, CEPADUES, Toulouse, France, 1999, pp. 289–296.

[8] A. Chikhaoui, E. Kustova, Effect of strong excitation of CO_2 asymmetric mode on transport properties, Chem. Phys. 216 (1997) 297–315.

[9] E. Kustova, E. Nagnibeda, A. Chikhaoui, Heat transfer and diffusion in mixtures containing CO_2, in: A. Ketsdever, E. P. Muntz (Eds.), Rarefied Gas Dynamics, Vol. 663 of AIP Conference Proceedings, 2003, pp. 100–105.

[10] E. Kustova, E. Nagnibeda, State-to-state theory of vibrational kinetics and dissociation in three-atomic gases, in: T. Bartel, M. Gallis (Eds.), Rarefied Gas Dynamics, Vol. 585 of AIP Conference Proceedings, 2001, pp. 620–627.

[11] I. Armenise, E. Kustova, State-to-state models for CO_2 molecules: from the theory to an application to hypersonic boundary layers, Chem. Phys. 415 (2013) 269–281.

[12] E. Kustova, E. Nagnibeda, On a correct description of a multi-temperature dissociating CO_2 flow, Chem. Phys. 321 (2006) 293–310.

[13] E. Kustova, E. Nagnibeda, Kinetic model for multi-temperature flows of reacting carbon dioxide mixture, Chem. Phys. 398 (2012) 111–117.

[14] E. Kustova, E. Nagnibeda, Y. Shevelev, N. Syzranova, Non-equilibrium supersonic CO_2 flows with real gas effects near a blunt body, in: T. Abe (Ed.), Rarefied Gas Dynamics: 26-th International Symposium, Vol. 1084 of AIP Conference Proceedings, 2009, pp. 831–836.

[15] E. Kustova, E. Nagnibeda, Y. Shevelev, N. Syzranova, Different models for CO_2 flows in a shock layer, Shock Waves 21 (3) (2011) 273–287.

[16] G. Herzberg, Infrared and Raman Spectra of Polyatomic Molecules, D.Van Nostrand Company, Inc., New York, 1951.

[17] V. Makarov, S. Losev, Application of the database of physical-chemical processes for the creation of the equations set for gases with chemical reactions and vibrational relaxation, Khim. Phizika 16 (5) (1997) 29–43, (In Russian).

[18] P. Borrel, G. Millward, Vibrational energy transfer process in shock-heated binary gas mixtures of CO with CO_2, N_2O and COS, J. Chem. Phys. 57 (1972) 462.

[19] V. Salnikov, A. Starik, Numerical analysis of energetic characteristics of gas-dynamic lasers on the hydrocarbon fuels combustion products, Teplofizika Vysokikh Temperatur 33 (1) (1995) 121, (in Russian).

[20] O. Achasov, D. Ragosin, Rate constants of V-V exchange for CO_2-GDL, Preprint 16, Institute of Heat and Mass Transfer, Minsk, Bielarus (1986).

[21] R. Schwartz, Z. Slawsky, K. Herzfeld, Calculation of vibrational relaxation times in gases, J. Chem. Phys. 20 (1952) 1591.

[22] J. Blauer, G. Nickerson, A survey of vibrational relaxation rate data for processes important to CO_2-N_2-H_2O infrared plume radiation, AIAA Paper 74-536.

[23] C. Billing, Semiclassical calculation of energy transfer in polyatomic molecules. II. The effect of anharmonic coupling terms, Chem. Phys. 46 (1980) 123–131.

[24] D. Clary, Ab initio calculations of vibrational relaxation rate coefficients for the collisions of CO_2 with helium and neon atoms, Chem. Phys. 65 (1982) 247–257.

[25] C. Wickham-Jones, C. Simpson, D. Clary, Experimental and theoretical determination of rate constants for vibrational relaxation of CO_2 and CH_3F by He, Chem. Phys. 117 (1987) 9–16.

[26] M. Bartolomei, F. Pirani, A. Laganà, A. Lombardi, A full dimensional grid empowered simulation of the CO_2 + CO_2 processes, Journ. Comp. Chemistry 33 (2012) 1806–1819.

[27] P. Marrone, C. Treanor, Chemical relaxation with preferential dissociation from excited vibrational levels, Phys. Fluids 6 (9) (1963) 1215.

[28] A. Aliat, State-to-state dissociation–recombination and chemical exchange rate coefficients in excited diatomic gas flows, Physica A 387 (2008) 4163–4182.

[29] R. Mc Kenzie, J. Arnold, Experimental and theoretical investigation of the chemical kinetics and non-equilibrium CN radiation behind shock waves in CO_2-N_2-mixtures, AIAA Paper 67-322.

[30] C. Park, J. Howe, R. Howe, R. Jaffe, G. Candler, Review of chemical-kinetic problems of future NASA missions, II: Mars entries, J. Thermophys. Heat Transfer 8 (1) (1994) 9–23.

[31] L. Ibragimova, G. Smekhov, O. Shatalov, Dissociation rate constants of diatomic molecules under thermal equilibrium conditions, Fluid Dynamics 34 (1) (1999) 153–157.

[32] L. Ibragimova, Rate coefficients of chemical reactions in the high-temperature gas CO_2, Math. Modelling 12 (4) (2000) 3–19.

[33] E. Kustova, E. Nagnibeda, Transport properties of a reacting gas mixture with strong vibrational and chemical nonequilibrium, Chem. Phys. 233 (1998) 57–75.

[34] E. Kustova, E. Nagnibeda, T. Alexandrova, A. Chikhaoui, On the non-equilibrium kinetics and heat transfer in nozzle flows, Chem. Phys. 276 (2) (2002) 139–154.

[35] J. Anderson, Hypersonic and High Temperature Gas Dynamics, McGraw-Hill, New York, 1989.

[36] M. Capitelli, I. Armenise, C. Gorse, State-to-state approach in the kinetics of air components under re-entry conditions, J. Thermophys. Heat Transfer 11 (4) (1997) 570–578.

[37] E. Kustova, E. Nagnibeda, Y. Shevelev, N. Syzranova, The influence of CO_2 kinetics on the hypersonic flow near blunt bodies, in: M. Mareschal, A. Santos (Eds.), Rarefied Gas Dynamics, Vol. 1501 of AIP Conference Proceedings, 2012, pp. 1102–1109.

Particle methods for nonequilibrium hypersonic and plasma flows

D. Bruno[b], A. Panarese[a], S. Longo[a,b], F. Taccogna[b], P. Minelli[b], S. T. Surzhikov[c], A. S. Dikaljuk[c], P. De Palma[d], M. D. de Tullio[d]

[a]*Department of Chemistry, University of Bari, via E. Orabona 4, 70126 Bari, Italy*
[b]*Istituto di Metodologie Inorganiche e dei Plasmi, Consiglio Nazionale delle Ricerche, via G. Amendola 122/D, 70126 Bari, Italy*
[c]*Institute for Problems in Mechanics, Russian Academy of Sciences, Pr. Vernadskogo 101-1, 119526 Moscow, Russia*
[d]*Dipartimento di Ingegneria Meccanica e Gestionale & Centro di Eccellenza in Meccanica Computazionale, Politecnico di Bari, via Re David 200, 70125 Bari, Italy*

Abstract

Kinetic modelling of nonequilibrium flows is described as it applies to hypersonic phenomenology. A Monte Carlo method is described for the study of species separation on shock wave fronts; a Particle in Cell with Monte Carlo Collisions (PIC/MCC) technique is described for the simulation of dust in plasma flows; modelling of nonequilibrium radiation in shock heated gases; implementation of slip models for the description of separation zones occurring in shock-boudary layer interactions.

1. Introduction

The study of high-speed reacting gas flows, as it arises in aerospace applications, involve the consideration of nonequilibrium effects. Current research on nonequilibrium modelling in Computational Fluid Dynamics (CFD) solvers has progressed substantially in including many nonequilibrium effects in the flow description. Still, there are flow conditions where the degree of nonequilibrium is such that the hydrodynamic description fails and kinetic methods are required for the correct description of the flowfield. In this cases, new methods must be used to solve the governing equations at the kinetic level. In this study we report on a number of situations where kinetic nonequilibrium effects have a large impact on the overall flowfield and we introduce the kinetic models used to tackle them.

In section 2, the problem of diffusion in shock wave fronts in analyzed. Here, large temperature and density gradients prevent the Navier-Stokes description from being accurate. A particle (i.e. Monte Carlo) method is devised to solve the relevant Boltzmann transport equations both for the bulk gas and for a trace species. It is shown, in particular, how the proposed method can successfully describe the transport of the seed species to any desired level of accuracy, thus overcoming a major limitation of standard Monte Carlo methods for flow simulation (like, e.g. Direct Simulation Monte Carlo, DSMC).

In section 3, a Particle-in-Cell (PIC) technique is described for the simulation of dust grains inside a plasma. This is relevant for the study of dust grains effects in complex plasmas, but it is also interesting for aerospace applications in that it shows how charged particle kinetic effects affect the boundary layer of macroscopic objects flying through a partially ionised gas.

In section 4, a theoretical framework is presented for the simulation of the nonequilibrium radiation emitted by shock heated gas mixtures. While the gas flowfield is here described by hydrodynamic equations, with due account of thermal and chemical nonequilibrium effects, a detailed kinetic framework is developed for the description of the radiation field. This is required when comparing simulation results to detailed experimental spectral measurements.

Finally, in sec. 5 a approach is proposed for the description of separation zones in CFD simulations. The Immersed Boundary (IB) method [] has been shown to be a promising technique to include boundary conditions in CFD solvers without requiring a body-fitted mesh, thus providing a significant gain in flexibility and computational requirements. In separation zones, however, rarefied gas effects make their appearance and standard boundary conditions fail to describe the flow accurately. In this study we show that rarefied gas effects (velocity slip and temperature jump) can effectively be described in a IB framework. Predictions of the model are assessed by comparison to accurate DSMC simulations for a hypersonic ramp flow in Nitrogen.

2. Neutral separation in shock waves

2.1. Monte Carlo model

The Test Particle Monte Carlo (TPMC) method has been used to determine separation effects in seeded atomic gas flows, in fact it has been applied, in a first stage, to solve the main component, and, in a second stage, to solve each separate component in a flow field which is preliminarily calculated in the first stage.

In the first stage, the following non linear Boltzmann equation has been solved for the main component to calculate the bulk flow field:

$$\frac{\partial f_a}{\partial t} + \mathbf{v} \cdot \frac{\partial f_a}{\partial \mathbf{r}} = \int d\Omega d^3 v_1 g \sigma_{aa} (g, \vartheta) \left(f'_a f'_{0a} (f'_a) - f_a f_{0a} (f_a) \right). \tag{1}$$

Here g is the relative speed, $\sigma_{aa} (g, \vartheta)$ is the differential elastic cross section, f_a is the unknown translational distribution of the main species, whereas f_{0a} is the corresponding local equilibrium distribution based on local macroscopic variables, i.e.

$$\begin{aligned} f_{0a} &= n_a (\mathbf{r}, t) \left(\frac{m_a}{2\pi k T_a (\mathbf{r}, t)} \right)^{\frac{3}{2}} exp \left(-m_a \frac{(\mathbf{v} - \mathbf{v}_a (\mathbf{r}, t))^2}{2\pi k T_a (\mathbf{r}, t)} \right), \\ n_a (\mathbf{r}, t) &= \int d^3 v f_a, \\ \mathbf{v}_a (\mathbf{r}, t) &= n_a^{-1} \int d^3 v \mathbf{v} f_a, \\ k T_a (\mathbf{r}, t) &= \frac{1}{3} m_a n_a^{-1} \int d^3 v v^2 f_a - \frac{1}{3} m_a v_a^2. \end{aligned} \tag{2}$$

$f_{0a} (\mathbf{r}, \mathbf{v})$ is not given but determined from the simulation.
Eqs. (1) and (2) are solved by employing a nonlinear self-consistent version of TPMC method (see [1]), in which the collision treatment is based on the sampling of a "virtual" target particle from a local equilibrium distribution. The particle handling and storage is much closer to Monte Carlo methods for the Bhatnagar-Gross-Krook model equation (BKG/MC) [2, 3, 4] than to Direct Simulation Monte Carlo (DSMC). For simplicity a fixed number of particles is used. When a particle leaves the simulation domain, it is injected back from the inlet. Three dimensional velocity vectors, $\mathbf{v} (t)$, are chosen to match the exact specific heat ratio γ ($\gamma = 5/3$ for atoms).
During a time step Δt, particles are moved according to their velocity:

$$\mathbf{r} (t + \Delta t) = \mathbf{r} (t) + \mathbf{v} (t) \Delta t. \tag{3}$$

Solid obstacles (diagnostic devices, reactor walls) are included in the model by mapping the mesh onto a logical matrix. Solid-filled mesh elements are easily detected during the particle motion. Adiabatic isotropic diffusion is simply implemented by replacing the particle into the previous position and selecting a random rotation of the particle velocity until the advance step ends outside the solid. The solid surface model can easily be extended to describe partial or total thermal equilibration of the particles with the surface, when appropriate.
Every particle contributes to the local average of a generic quantity a:

$$\langle a \rangle_c = \frac{\sum_p S_c \left(\mathbf{r}_p \right) a_p}{\sum_p S_c \left(\mathbf{r}_p \right)}, \tag{4}$$

where c is the cell index, p is the particle index, $S_c (\mathbf{r})$ is the characteristic function of the c-th cell, and a_p is a single particle quantity (e.g. v_p^2). For example, the average number density is

$$\langle n (\mathbf{r}, t) \rangle_c = \frac{w}{V_c} \sum_p S_c \left(\mathbf{r}_p \right), \tag{5}$$

where $n (\mathbf{r}, t)$ is the local number density at the time t, V_c is the cell volume, and w, which is fixed in order to fit the requested physical conditions, is the real to simulated particle ratio.

Every particle interacts with a virtual target particle by means of binary collisions. The collision probability is given by

$$P_{\mathbf{v}\mathbf{v}_1} = 1 - exp\left(-g\sigma\left(g\right) n\left(\mathbf{r}, t\right) \Delta t\right), \tag{6}$$

where $\mathbf{v}$, $\mathbf{v}_1$, and $g = |\mathbf{v} - \mathbf{v}_1|$ are the particle velocity, the virtual particle velocity, and the relative speed, respectively. Finally σ is the scattering cross section and $n\left(\mathbf{r}, t\right)$ is the local number density of the target species at the time t.
$\mathbf{v}_1$ is a stochastic variable distributed according to the distribution $f_{0a}\left(\mathbf{r}, \mathbf{v}_1, t\right)$. The i-th Cartesian component of v_1 can be produced by the following formula:

$$v_{1i} = h\sqrt{\frac{2}{3}\left\langle\left(\mathbf{v} - \langle v\rangle\right)^2\right\rangle} + \langle v_i\rangle, \tag{7}$$

where the averages, denoted by $\langle\ldots\rangle$, are calculated as in Eq. 4, and h is a random number extracted from an ensemble with a $exp\left(-h^2\right)$ distribution. This last ensemble is conveniently generated by the von Neumann rejection method and stored in a vector variable to increase the calculation speed.
Let η be a random number from a uniform distribution, $0 < \eta \leq 1$, then the collision occurs if $P_{\mathbf{v}\mathbf{v}_1} > \eta$. The particle velocity after the collision $\mathbf{v}'$ is calculated as

$$\mathbf{v}' = \frac{m\mathbf{v} + m_1\mathbf{v}_1}{m + m_1} + \frac{m_1}{m + m_1}\mathbf{g}', \tag{8}$$

where the new relative velocity $\mathbf{g}'$ is produced as a random vector sampled from an appropriate distribution. If the momentum transfer cross section is used, the isotropic distribution is the appropriate one.
A new sampling to the grid is performed, without canceling results of the previous one, to enforce the energy and momentum conservation. Then the particle velocities are scaled in any cell in order to match the previous sampling results by using the following procedure:

$$\mathbf{v} \leftarrow \left(\mathbf{v} - \mathbf{a}'\right)\sqrt{b/b'} + \mathbf{a}, \tag{9}$$

where $\mathbf{a} = \langle\mathbf{v}\rangle$, $\mathbf{a}' = \langle\mathbf{v}'\rangle$, $b = \left\langle\mathbf{v}^2\right\rangle - a^2$, $b' = \left\langle\mathbf{v}'^2\right\rangle - a'^2$. The superscript refers to the post collision sampling results, and the averages are on the mesh cell. The described procedure is applied only to particles not alone in their cell.
In the developed model it is not necessary to build a dynamic list of particles present in any cell like in DSMC, because any particle communicates only with the cell and not with other particles directly.
The cycle composed by the procedures of the first stage is iterated and run until a steady state condition is reached. Only after the steady state is reached, the space resolved number density, temperature and velocity components of the main species are calculated and cast into vectors for the separation calculations, which are performed in the following stage. The transport equation proposed is not strictly the Boltzmann equation, but a nonlinear equation obtained generalizing the linear transport method and requires the local energy conservation to be enforced. The approach proposed presents elements of novelty. As such, its accuracy is to be verified: such check has been performed in [9] by comparing the flow field calculated with this approach for a transition regime flow on a cylinder with a finite element solution of the Boltzmann equation, obtaining very close results.

In the second stage, TPMC method has been used to solve the following linear transport equation for i-th species:

$$\frac{\partial f_i}{\partial t} + \mathbf{v}\cdot\frac{\partial f_i}{\partial \mathbf{r}} = \int d\Omega d^3 v_1 g\sigma_{ia}\left(g, \vartheta\right)\left(f_i' f_{0a}' - f_i f_{0a}\right), \tag{10}$$

which has been obtained by setting the target distribution f_{0a} to the solution of Eqs. (1) and (2). Moreover f_i is the translational distribution of the i-th component, including the main one, and σ_{ia} is the differential cross section for the elastic scattering between the i-th and the main species.
In this way we finally determine the physical quantities of both the main component and the impurity components by mean of a TPMC technique analogous to those used for thermal neutron transport [5, 6]. Furthermore the particle-thermal background collision term is sampled as in [1], where a formal proof that Eq. (10) is solved exactly by this procedure is produced (see Appendix 2).
The transport equation is rewritten in an integral form and its solution is expanded as a convergent Neumann series. The terms in the series are shown to be estimated systematically and exactly using suitably chosen stochastic processes. These processes can be interpreted as particle trajectories. The demonstration is fully general under the only

hypothesis that the transport equation is linear.
The particles of the i-th component collide with the main species particles with a frequency preliminarily estimated as

$$v_i(\mathbf{r}) = C \cdot n(\mathbf{r})\, \sigma_i(kT(\mathbf{r}))\, \sqrt{\frac{kT(\mathbf{r})}{\pi \mu_i}}, \tag{11}$$

where $n(\mathbf{r})$ and $T(\mathbf{r})$ are the local number density and temperature of the target species, respectively. $\sigma(kT(\mathbf{r}))$ is the temperature corrected average cross section for the process (for rigid spheres this is a constant) and $\mu_i = m_i m_a/(m_i + m_a)$ is the reduced mass. A suitable global value for the proportionality constant C, which is usually about 10, is selected following the rule described later in this section.
The random free time between two collisions, t_c, which is different for all particles and for all flights, is calculated by the usual relation

$$t_c = -\frac{\ln \eta}{v_i(\mathbf{r})}, \tag{12}$$

where η is a random number from a uniform distribution, $0 < \eta \leq 1$. Excess collisions are removed using the null collision method in order to match the real collision frequency, which takes into account the thermal velocity distribution of target particles. The particle motion for the stochastic time t_c, and the treatment of boundary conditions are the same as in the first stage. After any free flight the candidate collision partner, a main component atom, is sampled as in the previous stage, too. In this cse the collision probability is given by

$$P_{\mathbf{vv}_1} = \frac{n(\mathbf{r})\, \sigma_i(g)\, g}{v_i(\mathbf{r})}. \tag{13}$$

When $P_{\mathbf{vv}_1} > \eta$, where η is a random number $0 < \eta < 1$ sampled from a uniform distribution, the collision is effective and the post collision velocity is calculated using Eq. (8). Clearly $P_{\mathbf{vv}_1}$ must be always < 1 in view of its physical meaning. The use of local maximization of the collision frequency given by Eq. (11) allows a strong reduction of the computational cost and it is verified a posteriori by checking that the fraction of computed collisions with $P_{\mathbf{vv}_1} > 1$ is insignificant, e.g. $< 10^{-3}$. Otherwise, C needs to be increased until the condition is satisfied.
This second stage is exact and totally free of numerical diffusion, in fact no information is propagated along the grid, which is only used to detect obstacles and to store values of the quantities calculated in the previous stage and their functions. This stage peculiarity allows us to reapply the same calculation stage to evaluate enrichment effects.

The flow field of the main component is calculated twice, the differences between the preliminary calculation through the non linear equation and the linear refinement provide an estimate of the precision of the approximations made in the first stage, which is not exact. Therefore this method can be used to evaluate the precision of other kinds of flow calculations.

2.2. Neutral separation

We have applied the method to a transonic flow of He with Ar as impurity component. The corresponding mass ratio of about 10 is rather high and leads to distinct separation phenomena. For hydrodynamic calculation of quantities is assumed rigid sphere scattering with the momentum transfer total cross sections for He/He and He/Ar reported in ref [7]. This solution has been also selected for a simpler comparison of test case results with those obtained by using other models in the next future. Of course for technical applications the Variable Soft Sphere (VSS) model cross section [8] or even better cross sections based on quantum calculations are to be preferred. In ref. [9] the reader can find a comparison between results obtained using different cross sections in an expanding atomic beam based on a preliminary version of the code presented in the same ref. [9].

We have considered a flow around a cylindrical obstacle, where the surface of the cylinder is an adiabatic diffuser. In the unperturbed free flow the Mach number is $M = 3$ and the Knudsen number is $Kn_\infty = 0.5$ ($Kn_\infty = \lambda_\infty/R$). The w coefficient is fixed by the following formula valid for a supersonic injection with $M \geq 3$ and based on the equivalence of numerical and physical particle fluxes:

$$w = n_0 M \frac{\sqrt{\gamma k T_0/m}}{\Phi_p}, \tag{14}$$

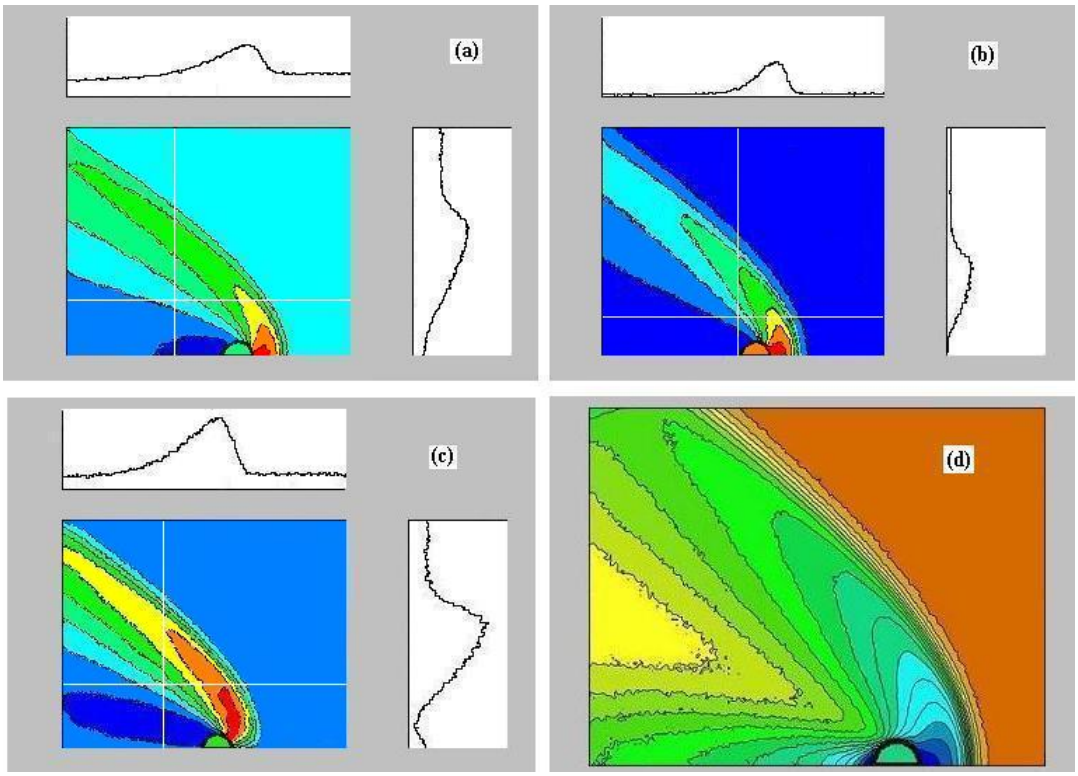

Figure 1: Bulk flow field results for a supersonic flow ($M = 3$) of He seeded with Ar on a cylinder, calculated by rigid sphere scattering. Fig.(a): number density. Fig.(b): temperature. Fig.(c): x component of the velocity. Fig.(d): Mach number.

where Φ_p is the flux of injected numerical particles, evaluated in the course of the simulation by a time average and $\gamma = 5/3$ is the specific heat ratio. The grid for the full domain is uniform with 200×150 cells. The number of simulated particles is 2×10^4 in both the first and second stage. In the first stage 4000 time steps are needed to reach the steady state and the dynamic quantities are collected for further 4000 time steps. In the second stage, a total of 1.3×10^9 events is sampled.

2.3. Results

The results for these test cases are reported in the following figures.
Fig. 1 is the result for the main component calculated by the nonlinear test particle method. In particular Fig. 1 (a) is the number density, Fig. 1 (b) is the the temperature, Fig. 1 (c) is the x component of the velocity and Fig. 1 (d) is the Mach number. These results which have the function to establish a bulk flow field have been calculated by assuming rigid sphere scattering. The results for the density of the main component (He) are close to those reported in ref. [10] and obtained by deterministic numerical solution of the Boltzmann equation for an atomic gas with adaptive grid equation and in the same conditions. The shock structure is clearly visible and it is better outlined by the side plots which reports the corresponding quantites along the white horizontal and vertical lines shown in the color plot. The next figures show results related to the impurity component which is calculated by the linear test particle. In particular Fig. 2 (a) report the ratio of the impurity particle density with respect to the bulk one, whereas Fig. 2 (b) report the impurity particle density.

The distributions represented in Fig. 1, and Fig. 2 are in agreement with expected theoretical distribution [11]. As expected, separation effects are more relevant in the higher Kn case. The flow is impoverished of the more massive impurity (Ar) entering the shock front, and it is enriched just after the shock. This effect is essentially due to the fact that momentum relaxation of a higher mass impurity is slower than that in the main gas: therefore Ar atoms move faster in the shock than He ones and consequently their relative density decreases because of mass conservation.

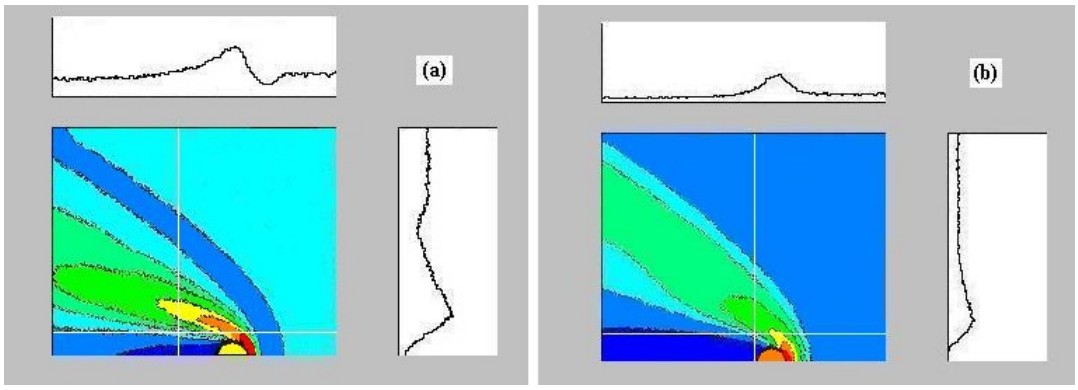

Figure 2: Impurity component results for a supersonic flow ($M = 3$) of He seeded with Ar on a cylinder, calculated by rigid sphere scattering. Fig.(a): ratio of the impurity particle density with respect to the bulk one. Fig.(b): impurity particle density.

Another separation region is observed in the wake, which is impoverished in Ar. This last effect can be explained by the different thermal speed of the two particle species: He is faster in filling a vacuum.

Let us discuss briefly the computational cost of the results. The computational cost when including anisotropic scattering, is about 21 hours on a 3.6 GHz Intel Xeon processor, most of the time spent in the calculation of the deflection angle by the interfaced module, while in the case of rigid sphere approach the time falls down to 14 minutes. Much of the computational time is spent after the steady state is reached, in order to collect a satisfactory statistics. Under such conditions, the computational cost is determined by the desired relative variance and is controlled by changing the number of particles and sampling steps.

In this context, the use of linear transport methods well developed for thermal neutrons offers the possibility to borrow standard variance reduction techniques from this field ref. [5, 6]. For example, if an estimate of the separation effect is needed in the front shock, it is possible to inject particles in the flow just before the shock and remove them just after it. In this way a drastic reduction of the computational cost is possible. A more advanced treatment can employ the adjoint equation in order to provide local solutions for a few space positions of interest.

2.4. Test case conclusions

A practical method is proposed for the calculation of seeded atomic flows in the transition regime. The basic idea is that the nonlinear fluid dynamics of the main component is treated first, while the final determination of all components is made by using the linear TPMC method which is totally free of numerical diffusion being based on the accurate implementation of the free flight time (or length).

The method proposed is actually of simpler implementation than DSMC recipes in spite of its obvious advantages for the treatment of seeded atomic flows, namely the variance reduction in the treatment of the impurities and the expected good reliability of the calculated atomic separation in view of the lack of numerical diffusion. The transport of more complex and structured seed species (e.g. molecules) should be possible by straightforward extensions of the linear part of the model.

3. Absorbing dust in stationary plasma

3.1. Introduction

The study of particle-plasma interaction is still an open issue in plasma physics [12, 13, 14, 15] . In particular, a self-consistent calculation of the plasma dynamics around a particle and its dependence on particle and ambient plasma parameters is an unsolved problem in complex plasmas. Of particular importance are basic processes like particle charging and electric potential distribution around a charged particle in plasmas. The traditional and most frequently used approach to study the particle-plasma interaction is the Orbital Motion Limited (OML) theory [16, 17], which predicts: (a) the same floating potential for all sizes of dust particle and gas pressures; (b) a linear dependence of the dust charge Q_d from the dust radius r_d; (c) the same dust charge for all gas pressures P. Concerning the electric potential distribution around the particle, the most accepted behaviour is the Debye-Hückel (DH) form:

$$\phi_{DH}(r) = \phi_d \frac{r_d}{r} e^{-(r-r_d)/\lambda} \tag{15}$$

where $\lambda = \lambda_{De}\lambda_{Di}/\sqrt{\lambda_{De}^{-2} + \lambda_{Di}^{-2}}$ is the linearized Debye length.

This work is aimed to study deviations from OML predictions and of electric potential from the DH form (15) for an isolated absorbing spherical particle immersed in stationary, isotropic, non-flowing plasma under the influence of ion-neutral collisions for different particle radius and gas pressures.

3.2. Numerical model

The model consists of a Particle-in-Cell (PIC) technique [18, 19, 20, 21, 22, 23] of the dynamics of plasma (electrons and ions) around a particle. The numerical model is one-dimensional radial (spherical symmetry due to the isotropy of the problem, motion in a central field of forces), and self-consistent in relation to the Poisson equation solution. The plasma system is represented as a collection of macro-particles (about 10^6) moved by solving the equations of motion using the electric field generating from their dynamics. Every macro-particle represents $w = 14$ real plasma particles. The radial domain simulated ($\approx 40\lambda$) is limited on the inner edge by the grain surface, while the outer edge represents the unperturbed neutral plasma. The domain is divided in 300 cells smaller than the Debye length, while the time evolution is processed using a time step smaller than the characteristic time of plasma oscillation $\omega_p \Delta t < 0.3$. The input data used are those typical of Argon ($\mu = 39.95 \times 1836$) gas discharge: plasma density $n_p = 6 \cdot 10^{15} m^{-3}$; electron/ion temperature $T_e = 1\ eV$ and $T_i = 0.2\ eV$ ($\tau = 5$); grain radius $r_d = 0.8$–$200\ \mu m$, corresponding to $\rho_d = r_d/\lambda = 0.02$–$5$; gas pressure $P = 0$–$1000\ Pa$, corresponding to a Knudsen number $Kn = 5 \cdot 10^{-3}$–∞; gas temperature $T_g = 1000\ K$. The equations of motion are integrated through the leapfrog technique [19], while the particles plasma charge is deposited on the grid points taking into account the spherical metrics [24]. After that, the Poisson equation with the following boundary conditions:

$$\left.\frac{d\phi}{dr}\right|_{r_d} = -\frac{Q_d}{4\pi\epsilon_0 r_d^2} \tag{16}$$

$$\left.\phi\right|_{r_\infty} = 0 \tag{17}$$

is solved by using the Thomas tridiagonal algorithm [25]. Ion-atom collisions (momentum MT and charge CT transfers) are processed through a detailed Test-Particle Monte Carlo technique [26] based on a Langevin polarization potential between the ion and the parent atom corresponding to a charge-induced dipole interaction.

3.3. Results and discussion

3.3.1. Ionic flux, dust charge and surface potential

Figure 3 shows the ion flux $j_i = I_i/q$ collected on the particle as a function of the gas pressure for different particle radius. It is evident that ion-neutral collisions start to affect the ion dynamics already at pressure of the order of few Pa. Increasing the pressure, the ion current collected on the surface increases reaching a maximum value and then dramatically decreases. In fact, collisions of ions with neutrals produce an increase of the ion current collected by the particle at lower pressures due to the destruction of the orbital motion and a decrease at higher pressures due

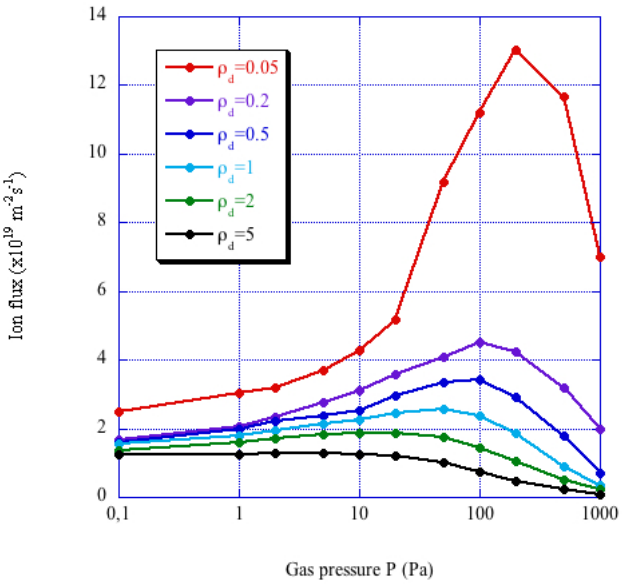

Figure 3: Ion collection flux to the particle as a function of the gas pressure for different particle size.

to the scattering effect. A single ion-atom collision may leave the ion with insufficient total energy to escape from the potential well surrounding the dust particle (orbital motion destruction): the ion is then collected by the particle. While, for a very large number of collisions, the ion dynamic enters in a diffusion-dominated regime leading to a drastic reduction of ion flux collected on the grain surface. Situations in which collisions enhance the ion collection are ones in which the particle radius is smaller than the screening length (as a demonstration of the fact that is an orbital motion destruction effect) and for $\rho_d > 5$ this effect completely disappears and the ion flux collected becomes a simple monotonic decreasing function of the gas pressure (thin sheath limit).

Figure 4(a) shows the surface potential ϕ_d as a function of gas pressure for different particle size. The surface potential follows the same behaviour of the ion current collected on the particle showing a peak, which is absent for large particles. Figure 4(b) shows the size-dependence of the surface dust potential for different collisional regimes. Collisions cause the surface potential of the particle to depend more strongly from the particle size, while OML theory predicts no-dependence at all. For very weak collisional regimes ($P < 10\ Pa$) the size-dependence becomes important only at small dust particles ($\rho_d < 0.5$), while for intermediate collisional regimes the surface potential becomes strongly dependent from the particle size. This is again a proof of the importance of the destruction of the orbital motion in the unscreened region around the particle. Figures 4(c) and 4(d) show the charge number of the dust particle as a function of gas pressure for different particle size and as a function of dust radius for different collisional regimes, respectively. Particle charge follows the ion flux behaviour: for intermediate collisional regime, a first increasing of the ion flow with increasing pressure results in a lower particle charge number, while the decrease of the ion flow for high collisional regime results in a larger particle charge number.

3.3.2. Ionic flux, dust charge and surface potential

Figure 5(a) shows the radial profiles of electric potential around a particle of radius $\rho_d = 1$ for three different collisional regime. The main results can be formulated as follows:

1. the power law scale decay of the far asymptote has been confirmed: $\phi \propto r^{-2}$ in the collisionless case (dashed violet line), while $\phi \propto r^{-1}$ in the strong collisional case (dashed light blue line);

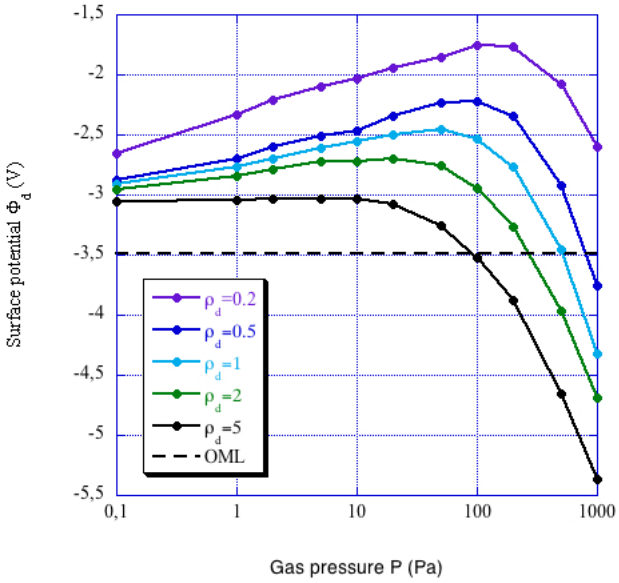

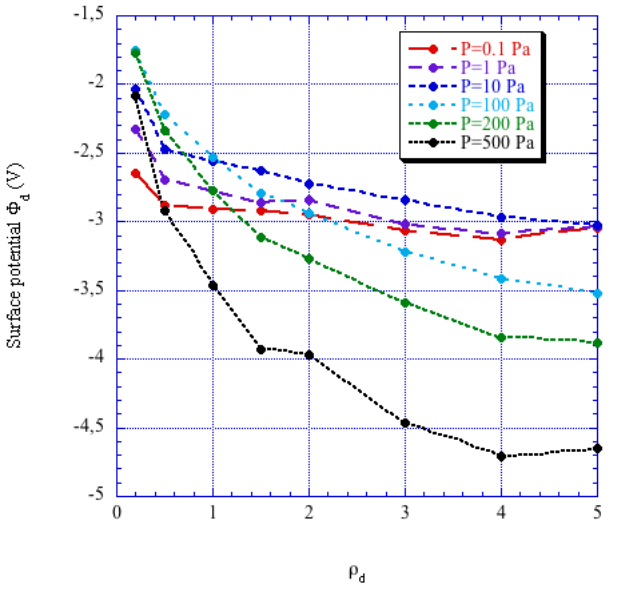

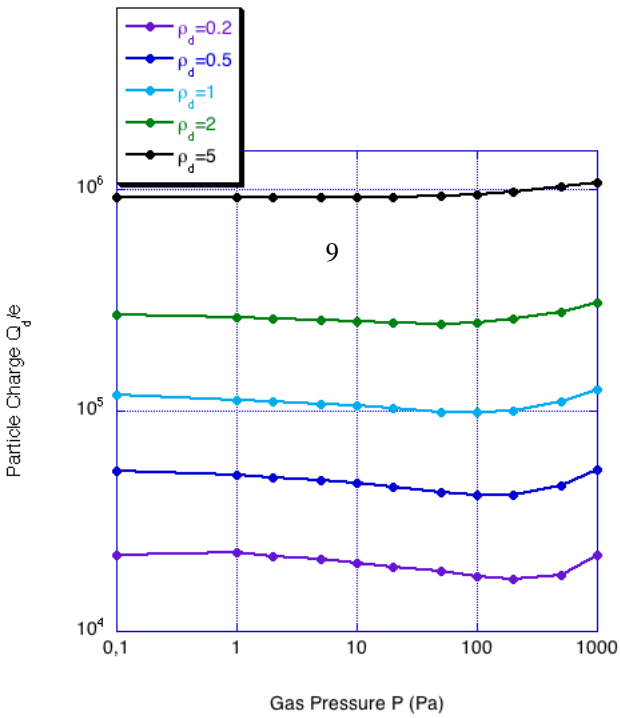

2. for the entire radial domain, the actual potential can be quite well fitted with a Yukawa form (15), but with an effective screening length λ_{eff} which depends on the particle size: for small particles ($\rho_d << 1$), λ_{eff} is close to the ion Debye radius λ_{Di}, while for larger particles ($\rho_d >> 1$), λ_{eff} increases reaching values comparable to several λ_{De}.

In figure 5(b) we have reported the radial profile of the potential for $P = 100\ Pa$ for four different particle sizes. Based on this analysis we can conclude that in the intermediate collisional regime ($Kn \approx 0.1$), the ion-neutral collisions reduces the screening length due to an increased ion flux toward the grain surface that reduces the absolute value of the grain charge. This effect is present for small particles ($\rho_d < 0.4$), while for large particles the screening length monotonically increases with P.

Figure 5(c) shows the radial profiles of electron (red lines) and ion (black lines) density around the particle for two different particle size $\rho_d = 0.5$ and $\rho_d = 5$, both at $P = 100\ Pa$. The most striking aspect is that the ion density increases rapidly near the particle surface. This is due to the spherical geometry and to the ion angular motion. In fact, most of the ions orbiting around the particle have significant angular momentum and these ions do not strike the particle. This makes this situation different from the usual planar sheath behaviour (monotonic decreasing density), where all the ions that enter the sheath are continuously accelerated until hitting the surface. In fact, the local ion rise decreases with the increasing of the particle size due to the fact that as ρ_d becomes large, we begin to see the transition to a planar sheath. In the case shown here, the ions still possess enough orbital angular momentum to cause a local rise in the ion density near the particle, but the maximum at the particle surface is decreased and the behaviour is no more monotonic increasing. Concerning the electron density behaviour, it has to be pointed out that the Boltzmann representation (dashed red lines) is a rude approximation and it overestimates n_e along the entire domain by a factor up to 5 close to the particle. Finally, as already shown in figure 5(b), the characteristic size of the sheath grows from λ_{Di} to a size of order of several λ_{De} with ρ_d. The potential perturbation caused by the particle extends much farther from the particle surface.

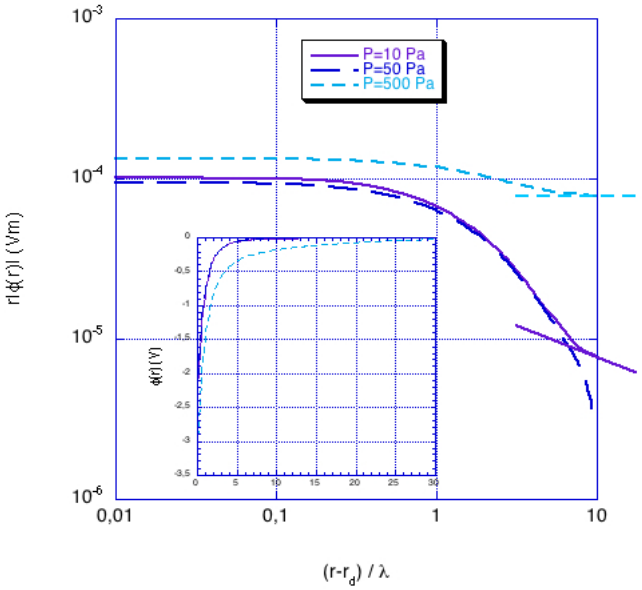

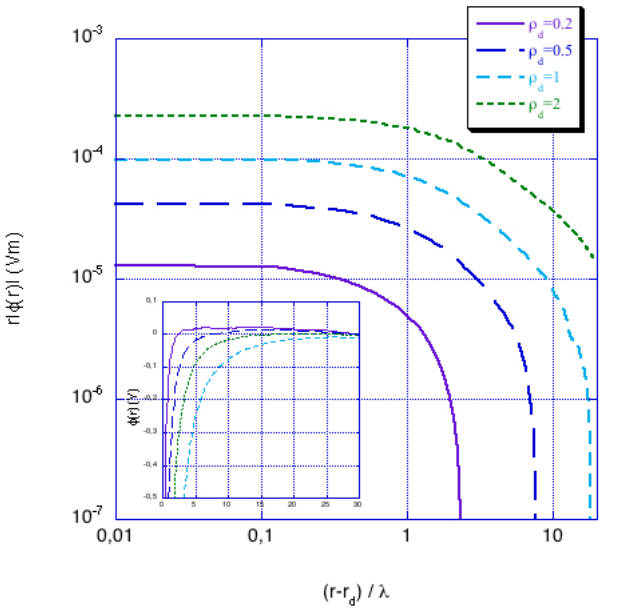

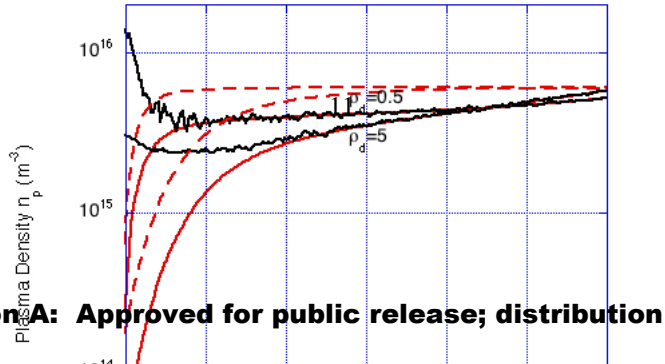

4. Advanced Models in Shock-Waves

The first investigation in the Laboratory of Radiative Gas Dynamics dedicated to the calculation of nonequilibrium spectral intensity of radiation emitted by the shock-heated gases was performed and presented in 1997 [27]. Since then our group is involved in this area of scientific researches [28, 29, 30]. Two parts of activities are distinguished in this area. The first one is connected with the development and investigation of properties of hybrid radiative-collisional model. In our opinion hybrid and full radiative-collisional models differ in the following way. In the full radiative-collisional models all electronic excited states of particles presented in the gas mixture and processes relevant for the transitions among these states are taken into account. The problem with this approach is that there is limited amount of reliable data in the temperature region of interest regarding the rates (or cross sections) of processes accounted for in the model (due to the fact that there are a lot of processes generally because of the number of states included in the full model). Another problem is the extreme computational cost of these models [31]. Consequence of it is inability of inclusion of them into high fidelity Computational Fluid Dynamics (CFD) codes. However, in the hybrid radiative-collisonal models not all but only those of electronic excited states of particles (and processes responsible for transitions among them) are accounted for that are important from the point of view of radiation. It should significantly reduce cost of computations and uncertainty in the obtained results. The hybrid radiative-collisional model developed in our group consists of the following parts:

- Euler system of equations for the determination of parameters of the flow in the relaxation zone behind the shock front. The equation of energy is modified in order to take into account the fact that the considered gas mixture is multicomponent and chemically reacting:

$$\frac{d}{dx}(\rho u) = 0; \quad \frac{d}{dx}(p + \rho u^2) = 0; \quad \frac{d}{dx}(h + \frac{u^2}{2}) = 0 \tag{18}$$

$$p = \frac{\rho R_0 T}{M_\Sigma}; \quad M_\Sigma = \sum_{i=1}^{N_s} \mu_i x_i; \quad \mu_i = m_i N_A \tag{19}$$

$$h = \left[(T - T^0)(\frac{5}{2} + \sum_{i=1}^{N_M} x_i) + \sum_{i=1}^{N_M} x_i \sum_{j=1}^{N_{V,i}} g_{i,j} \frac{\theta_{i,j}}{\exp(\theta_{i,j}/T_{V,i,j}) - 1} \right] \tag{20}$$

  Here p, ρ, u, T - pressure, density, velocity and translational temperature; x_i, m_i - molar fraction and mass of i-th chemical component (atom or molecule); $T_{V,i,j}, \theta_{i,j}, g_{i,j}$ - vibrational temperature, characteristic vibrational temperature and degeneracy of j-th vibrational mode of i-th molecule, N_s - number of chemically reacting components; N_M - number of diatomic and triatomic molecules; $N_{V,i}$ - number of vibrational modes of i-th molecule.

- the system of chemical kinetic equations:

$$\frac{dX_k}{dx} = \sum_{j=1}^{N_r} \left[(b_{kj} - a_{kj}) k_j^f \prod_{i=1}^{N_s} X_i^{a_{ij}} + (a_{kj} - b_{kj}) k_j^r \prod_{i=1}^{N_s} X_i^{b_{ij}} \right], \quad k = 1, \ldots, N_s \tag{21}$$

  Here X_k - molar volume concentration, a_{kj}, b_{kj} - stoichiometric coefficients of the j-th forward and backward reactions for the k-th chemical component, k_j^f, k_j^r - forward and backward rate coefficient of j-th reaction. The system of chemical equations can be written in the following form:

$$\sum_{i=1}^{N_s} a_{ij} [X_i] \underset{k_j^r}{\overset{k_j^f}{\rightleftharpoons}} \sum_{i=1}^{N_s} b_{ij} [X_i] \tag{22}$$

Here $[X_i]$ - symbol that correspond to the i-th chemical component, N_r - total number of reactions. It is worth noticing that for the chosen electronic excited states of molecules the relevant set of *chemical* equations formulated and kinetic equations are solved in order to determine populations of these states.

- equations for the determination of temperature of vibrational modes of molecules:

$$\frac{de_m}{dt} = Q^m_{VT} + Q^m_{CV} \tag{23}$$

The relaxation times are usually estimated using the Millikan-White approximations combined with Park correction. The mutual influence of chemical kinetic and vibrational relaxation is taken into account in the model (CVDV interaction).

- equation for the determination of temperature of electron gas:

$$\frac{d}{dx}\left(\frac{3}{2}T_e X_e u\right) + T_e X_e \frac{du}{dx} = Q_{ei} + Q_{ea} + Q_{ai} + Q_{ion} + Q_{ev} \tag{24}$$

The processes responsible for the heating/cooling of the electron gas are as follows: elastic electron-ion and electron-atom collisions; associative ionization/dissociative recombination; ionization; interaction of electron gas and vibrational modes of molecules.

- The *just-overlapping* line model is used for the spectral intensity of radiation calculations. The equations of the model are as follows:

$$j_\lambda = 3.202 \cdot 10^{-10} \frac{N_{eel}}{Q_{VR}\lambda^6} \sum_{V}^{'} \sum_{V}^{''} \frac{S_{V'V''}}{|\Delta B_V|} \exp\left[-\frac{hc}{kT_V}E_{eel}(V')\right] \exp\left[-\frac{hc}{kT_R}\frac{B_{V'}}{\Delta B_V}(\omega - \omega_{V'V''} + B_{V'})\right] \tag{25}$$

The most important value here is $S_{V'V''}$ which is the strength of vibronic transition. It is connected with the square of moment of vibronic transition in accordance with the following relation:

$$S_{V'V''} = (2 - \delta_{0,\Lambda'+\Lambda''})(2S + 1)|R_{V'V''}|^2 \tag{26}$$

$$|R_{V'V''}|^2 = \frac{3h}{64\pi^4 a_0^2 e^2} \frac{2 - \delta_{0,\Lambda'}}{2 - \delta_{0,\Lambda'+\Lambda''}} \frac{1}{\omega^3_{V'V''}} \cdot A_{V'V''} \tag{27}$$

Here $A_{V'V''}$ is the Einstein coefficient of vibronic transition. One can obtain the $A_{V'V''}$ as a result of solution of quantum mechanical problem of the calculation of vibronic wave functions.

The full description of the model can be found in refs. [28, 29, 30]. It is worth noting that what is presented here is actually a framework. Using it different gas mixtures and chemical kinetics models can be studied. Using the method it is possible to study nonequilibrium and equilibrium spectral intensities of radiation emitted by shock-heated gases. The second part of activity in our group is dedicated to the systematic processing of experimental data obtained on different shock tube facilities all around the world by means of the model developed in our group. Up to the moment we have performed the analysis of results obtained on the shock tubes of NASA Ames Research Center (EAST facility) [32, 33], Chofu Aerospace Center [34], Queensland University (X2 facility) [35], Institute of Mechanics MSU [36]. By means of our model we have studied spectral intensity of radiation of shock-heated $N_2 - O_2$, $CO_2 - N_2$, $CH_4 - N_2$ gas mixtures. Examples of comparison of numerical and experimental results are presented in Figs. 6 and 7.

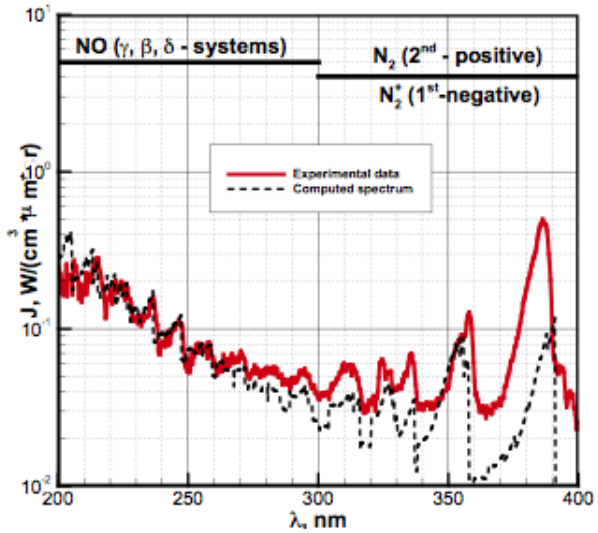

Figure 6: Nonequilibrium spectral emissivity of the relaxation zone behind the shock wave initiated in $80\%N_2 - 20\%O_2$ gas mixtures at $P = 1\ Torr, V_{sh} = 5.56\ km/s$.

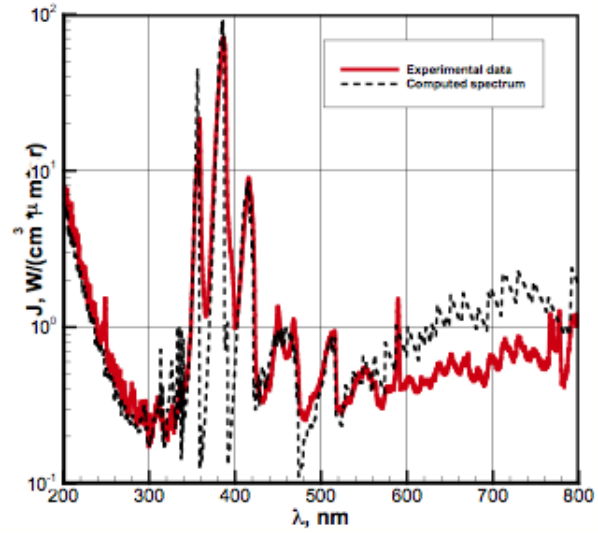

Figure 7: Nonequilibrium spectral emissivity of the relaxation zone behind the shock wave initiated in $30\%N_2 - 70\%CO_2$ gas mixtures at $P = 0.3\ Torr, V_{sh} = 6.76\ km/s$.

5. Simulation of hypersonic rarefied flows with the immersed-boundary method

5.1. Introduction

In recent years the Immersed Boundary (IB) method is emerging as a very appealing approach for solving flows past very complex geometries, like those occurring in most industrial applications. Its main, very significant, feature is the use of a Cartesian grid embodying the complex boundaries of the flow domain, which allows one to generate the computational mesh within a few minutes, whereas a very complicated body fitted grid may require several hours or even days. In the IB approach, the presence of a solid boundary is replaced by suitable forcing conditions modeling the effect of the body on the flow. The IB technique was originally developed for incompressible flows [37, 38, 39, 40, 41] using non-uniform Cartesian grids to take advantage of simple numerical algorithms. Two of the authors have contributed to the extension of the IB method to the preconditioned compressible Navier–Stokes (NS) equations in order to solve complex flows at any value of the Mach number [42], and equipped it with a local mesh refinement procedure to resolve boundary layers and regions with high flow gradients (e.g., shocks) [43]. In this work, the IB method is extended to the solution of flows with rarefaction effects and is validated against DSMC simulations of a shock wave-boundary layer interaction.

5.2. Immersed-boundary Navier–Stokes (IBNS) equation solver

The preconditioned Navier–Stokes (NS) equations for a steady laminar flow of a perfect gas are solved [43]. The Prandtl number is equal to 0.71 and a temperature exponent for the viscosity coefficient equal to 0.75 has been employed.

A pseudo-time derivative is added to the NS equations in order to use a time marching approach to compute the steady-state solution. The preconditioning matrix proposed in [44] is used to pre-multiply such a pseudo-time derivative to enhance the efficiency of the solution at all values of the Mach number. The equations are discretized by an implicit Euler scheme in the pseudo-time. The space discretization is based on a cell-centred finite volume approach. The convective terms are discretized using a second-order-accurate upwind flux-difference-splitting scheme. The viscous terms are discretized by second-order-accurate centred differences. The resulting discrete system is solved direction-by-direction using a BiCGStab [45] approach, the boundary conditions being treated explicitly (see [43] for details).

An efficient local grid refinement technique is employed for clustering cells near the immersed boundary and at other high-flow-gradient regions. For each face, the contributions of the neighbor cells are collected to build the corresponding convective and diffusive operators for the cell, the maximum number of neighbors being limited to two for the present two-dimensional computations [43].

The IB technique used in this work is based on that proposed in [39, 40]. In a preliminary step, the geometry under consideration, which is described by a closed polygon in two dimensions (a closed surface in three dimensions), is overlapped onto a Cartesian grid. Using the ray tracing technique based on the geometrical algorithms reported in [46], the computational cells occupied entirely by the flow are tagged as *fluid cells*; those whose centres lie within the immersed body are tagged as *solid cells*. Furthermore, the *fluid cells* neighboring *solid* ones are tagged as *interface fluid cells*, and the *solid cells* neighboring *fluid* ones are tagged as *interface solid cells*. Interface cells are used to enforce the boundary conditions between the solid body and the fluid.

In the present implementation, starting from a grid with uniform mesh size, a locally refined grid is generated by recursively halving the mesh size at the immersed boundary region, until an assigned target value is reached [47]. This automatic refinement is based on the following strategy. A tag function, generated using the ray tracing technique, is used to mark the cells inside and outside the immersed body: an integer value ± 1 is assigned to "fluid" and "solid" cells, respectively. The gradient of this function is different from zero only at the immersed boundary and depends on the local grid size. The components of this gradient in the x and y directions are used to select the cells to be refined. The grid is refined until a user specified resolution is achieved at the boundary. One can define other regions of the computational domain to be refined, selecting the local resolution of the mesh, like the wake or wall regions and, finally, it is possible to refine on *void* surfaces, namely, surfaces without solid or interface points, like bow-shock regions. An anisotropic local grid refinement is allowed, namely, each cell can be refined independently in each Cartesian direction. This feature complicates the grid topology but renders the approach more flexible to handle complex geometries with a remarkable reduction of the memory requirement with respect to a standard OCTREE data structure. Then, employing the software METIS [48], the obtained mesh is divided into a number of blocks defined

by the user, balancing the number of computational cells among them. Following a domain decomposition approach, each block is assigned to a CPU which performs the integration of the NS equations in parallel, exchanging the needed information with neighboring processors. Finally, all the necessary information about the grid (coordinates, metrics, pointers for the communications among cells and among processors, etc.) are allocated according to an edge-based data structure and the data are provided in output files to be read by each processor. All these operations are performed automatically and the user needs only to establish the number of processors employed for the computation. The code has been parallelized implementing the communication exchange among the processors based on the MPI protocol.

Concerning the boundary conditions at the solid surfaces, a linear reconstruction is employed near the wall to determine the flow variables at the interface cells imposing the values of the velocity and of the temperature at the solid surface [43]. Slip velocity conditions are computed using the first-order relation provided in [49], which allows one to capture the bulk flow-field away from the walls.

5.3. DSMC method

IBNS results have been compared to DSMC simulations. The latter use a standard DSMC implementation [50]. In the present case, a model with continuous internal energy is used. Energy in collision is distributed according to the Larsen-Borgnakke scheme with unitary collision relaxation number in order to simulate the constant-γ behavior. The code implements a two-dimensional geometry with a bulti-block, stretched grid approach. Parallel computations, based on a domain decomposition approach and coded with MPI standard have been performed for the hypersonic ramp flow on a 16-cpu Linux cluster.

5.4. Slip model validation

As a first step, the slip flow model has been validated in a simple configuration. The gas is a Hard Sphere gas with the following properties:

mass: m=28.9641 amu

specific heat ratio: $\gamma = 1.4$

viscosity: $\eta = 5.6853 \cdot 10^{-6} \sqrt{\frac{T}{80}}\ Pa \cdot s$

Prandtl number: $Pr = 0.71$

The domain is a two-dimensional channel, $4 \cdot 10^{-3}\ m$ wide and periodic in the other direction. The walls are perfectly diffusing with wall temperature set to 150 K. The average density in the channel is $n = 9.13 \cdot 10^{21}\ m^{-3}$. The gas is subject to a volume acceleration in the longitudinal direction equal to $a_x = 5 \cdot 10^6\ m/s^2$.

The Knudsen number, based on the average density and the channel half-length, is $Kn = 0.05$. The local Knudsen number, instead, based on the local density and on the velocity gradient can reach the value 0.9 near the wall. The flow is highly rarefied, in fact.

For the NS simulations, uniform grids with 32 and 64 mesh points in the normal direction to the boundary provide the same results within plotting accuracy. Computations have been performed in a two-dimensional domain with periodic boundary-conditions in the streamwise direction, slip-velocity boundary conditions at the bottom wall, and symmetry conditions at the top boundary corresponding to mid-channel height.

DSMC simulations have been performed on a simulation domain $8 \cdot 10^{-3}\ m$ long with periodic boundary conditions in the streamwise direction and $2 \cdot 10^{-3}\ m$ wide with a diffuse wall at $y = 0$ and symmetry condition at the upper limit. The simulation space has been discretized in 256x64 square cells $3.125 \cdot 120^{-5}\ m$ in length. The time step is $dt = 5 \cdot 10^{-9}\ s$ and the number of simulated particles is about $3.25 \cdot 10^5$. Time averaging has been performed in order to decrease the statistical error.

The velocity profiles obtained by DSMC and IBNS with and without slip are reported in Fig. 8. In this plot, the position in the channel is divided by the channel half-length and the flow speed is divided by the maximum value at the center of the channel. The first-order slip model therefore allows to accurately reproduce DSMC results in this case even in conditions of strong rarefaction.

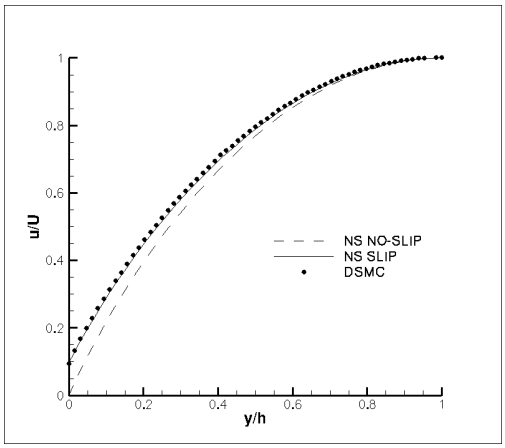

Figure 8: Channel flow: velocity profiles.

5.5. Hypersonic ramp flow

In order to validate the IBNS approach on a more complex test case, simulations are performed for the hypersonic flow over a compression ramp [51]. The ramp geometry is employed to study the effects of flap deflection on the flow past a space vehicle. This configuration shows the typical features of shock wave-boundary layer interaction with flow separation and re-attachment.

The distance x_c, between the leading edge of the flat plate and the ramp corner is equal to 71.4 *mm*. The ramp angle is 35-deg and also its length is equal to 71.4 *mm*. Further details of the ramp geometry are provided in [51].

The gas is Nitrogen with $\gamma = 1.4$. The Prandtl number is equal to 0.71 and a temperature exponent for the viscosity coefficient equal to 0.75 has been employed. In the present work, steady flow simulations have been performed.

The flow of nitrogen gas is considered with the following free-stream conditions [51]: $\rho_\infty = 1.401 \times 10^{-4}\ kg/m^3$, $V_\infty = 1521\ m/s$, $T_\infty = 9.06\ K$. The corresponding free-stream Mach number and Reynolds number are 24.8 and 12,020, respectively. The wall is perfectly diffusing with wall temperature set to 403.2 K.

Two-dimensional IBNS computations have been performed using a locally refined grid with about 80000 cells clustered at the leading edge of the plate and in the recirculation region. The height of the first cell along the wall is 0.02 *mm*. About 20 minutes wall-clock CPU time are needed using 16 cores of a Linux cluster with 8-core Intel Xeon @2.80Ghz processors to obtain the numerical solution, including the grid generation process.

DSMC simulations used 16 cpus on a Linux cluster. The mesh is made of 5 blocks with 1.7 million cells. The timestep is $dt = 10^{-8}\ s$ and the number of simulated particles is 22 millions.

Figure 9 shows the pressure and skin friction coefficients as obtained by DSMC and by IBNS method with slip conditions. Moss's results [51] are also reported for comparison. The IBNS results have been smoothed to avoid the typical small oscillations of the data at wall due to the linear reconstruction near the boundary. Concerning the DSMC results, a small residual statistical scatter is still visible after the time averaging procedure.

At the leading edge, the strong velocity gradient that induces nonlinear transport terms in the stress tensor is the likely cause of discrepancy between the particle methods on one side and the Navier-Stokes equation solver on the other.

Apart from this, the results compare favorably. A better agreement is found when using the slip conditions than when the standard no-slip conditions are considered (not shown in the figures). The skin friction plot shows that the separation zone is overestimated by the IBNS method. As a result, the flow velocity following re-attachment is underestimated. One possible reason for the discrepancy might be the use of slip coefficients for the Hard Sphere gas. Although, on general grounds, first-order slip coefficients are considered insensitive to the gas model [49], in the present case the position and the extent of the separation zone are found to be very sensitive to the slip coefficients. Further investigations are in progress in order to clarify this point.

Figures 10 and 11 provide the non-dimensional density contours, ρ/ρ_∞, obtained by the IBNS and DSMC methods, respectively. The peak value of density is found about in the same region and is equal to 12.4 for the IBNS

approach and to 14.3 for the DSMC, whereas the value reported in [51] is 14.8. Finally, figures 12 and 13 report the streamlines (superposed to the density contours) obtained by the IBNS and DSMC methods, respectively. The agreement is satisfactory both qualitatively and quantitatively apart from the small discrepancy in the separation zone already discussed.

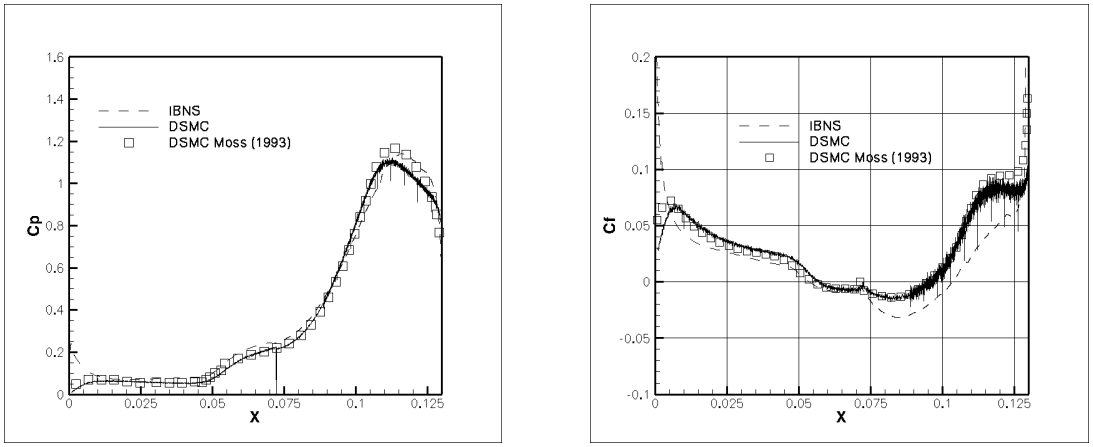

Figure 9: Hypersonic ramp flow: pressure coefficient (left); skin-friction coefficient (right).

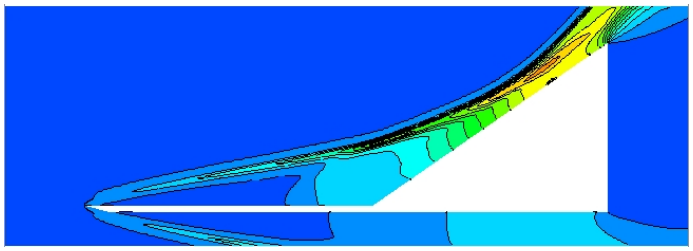

Figure 10: Hypersonic ramp flow; Navier–Stokes equations: density contours (ρ/ρ_∞; $\Delta = 1$).

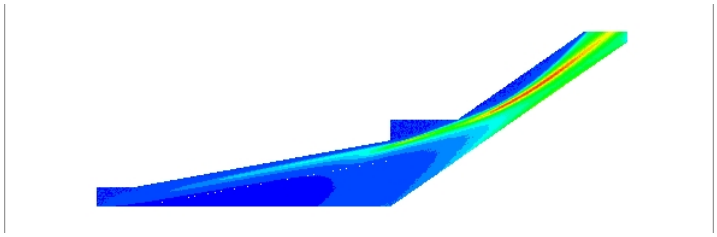

Figure 11: Hypersonic ramp flow; DSMC: density contours (ρ/ρ_∞; $\Delta = 1$).

5.6. Conclusions

This paper provides a validation of a very efficient immersed boundary method based on the solution of the Navier–Stokes equations for computing hypersonic rarefied gas flows. First-order slip-velocity boundary conditions are employed and tested for taking into account rarefied gas effects. The method employs a flexible local grid refinement technique and is implemented on parallel machines using a domain-decomposition approach. The comparison with the results obtained with DSMC simulations is satisfactory. Some discrepancies are found is the prediction of the separation bubble extension which need further investigations to be fully explained.

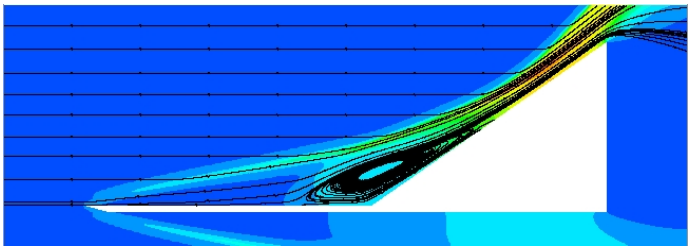

Figure 12: Hypersonic ramp flow; Navier–Stokes equations: streamlines.

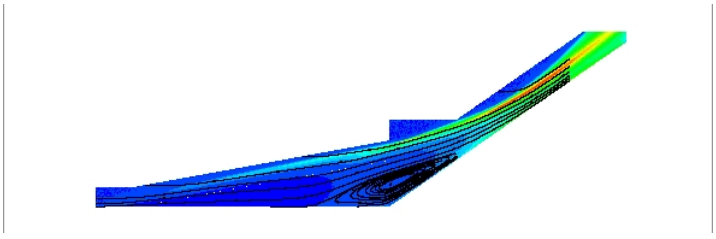

Figure 13: Hypersonic ramp flow; DSMC: streamlines.

6. Conclusions

A number of studies are reported that show the importance of kinetic simulation tools, in particular Monte Carlo methods, for the description of nonequilibrium effects in hypersonic flows. Mass diffusion in steep shock wave fronts can therefore be analysed, which is not possible in the frame of a Navier-Stokes description of the fluid mixture. Plasma kinetic effects, arising in the interaction of macroscopic objects within a plasma environment, have been studied with a PIC technique. Finally, gas rarefaction effects have been studied with a DSMC simulation tool and the results used to build a IB method for CFD solvers that takes these effects correctly into account. In addition, these results demonstrate that based on the results of such accurate kinetic models, significant progress has been achieved in devising nonequilibrium models for CFD solvers.

Acknowledgments

The research leading to these results has received funding from the European Community's Seventh Framework Programme (FP7/2007–2013) under grant agreement n^{o} 242311.

References

[1] S. Longo, P. Diomede, Monte Carlo modeling of gas phase ion transport under thermal gradients and external fields, Eur. Phys. J. Appl. Phys. 26 (3) (2004) 177.

[2] M. N. Macrossan, A particle simulation method for the BGK equation, in: Proceedings of the 22nd International Symposium on Rarefied Gas Dynamics, Vol. 585 of AIP Conference Proceedings, 2001, pp. 426–433.

[3] D. Bruno, S. Longo, Monte Carlo simulation of nearly kinematic shock fronts in rarefied gases, Eur. Phys. J. Appl. Phys. 17 (3) (2002) 233–241.

[4] D. Bruno, S. Longo, M. Capitelli, A BGK/MC method for the simulation of shock waves in binary mixtures, AIAA paper 2002-2895.

[5] J. Spanier, E. M. Gelbard, Monte Carlo Principles and Neutron Transport Problems, Addison Wesley, 1969.

[6] S. A. Dupree, S. K. Fraley, A Monte Carlo primer: practical approach to radiation transport, Kluwer, 2002.

[7] M. A. Lieberman, A. J. Lichtenberg, Principles of Plasmas Discharges and Material Processing, Wiley, 2005.

[8] G. A. Bird, Molecular Gas Dynamics and the Direct Simulation of Gas Flows, Clarendon, Oxford, 1994.

[9] S. Longo, P. Diomede, A Monte Carlo model for seeded atomic flows in the transition regime, Journal of Computational Physics 228 (10) (2009) 3851–3857.

[10] V. I. Kolobov, R. R. Arslanbekov, V. V. Aristov, A. A. Frolova, Unified solver for rarefied and continuum flows with adaptive mesh and algorithm refinement, Journal of Computational Physics 223 (2) (2007) 589–608.

[11] Y. B. Zel'dovich, Y. P. Raizer, Physics of Shock Waves and High-Temperature Hydrodynamic Phenomena, Dover, New York, 2002.

[12] V. E. Fortov, I. A. V., K. S. A., K. A. G., G. E. Morfill, Complex (dusty) plasmas: Current status, open issues, perspectives, Physics Reports 421 (2005) 1–103.

[13] O. Ishihara, Complex plasma: dusts in plasma, Journal of Physics D: Applied Physics 40 (8) (2007) R121–R147.

[14] S. P. K., B. Eliasson, Fundamentals of dust-plasma interactions, Rev. Mod. Phys. 81 (2009) 25–44.

[15] K. S. A., G. E. Morfill, Basic processes in complex (dusty) plasmas: Charging, interactions, and ion drag force, Contr. Plasma Phys. 49 (3) (2009) 148–168.

[16] J. E. Allen, Probe theory - the orbital motion approach, Physica Scripta 45 (1992) 497–503.

[17] M. Lampe, Limits of validity for orbital-motion-limited theory for a small floating collector, Journal of Plasma Physics 65 (3) (2001) 171–180.

[18] D. Tskhakaya, K. Matyash, R. Schneider, F. Taccogna, The Particle-in-Cell method, Contr. Plasma Phys. 47 (8-9) (2007) 549–594.

[19] F. Taccogna, S. Longo, M. Capitelli, A Particle-in-Cell/Monte Carlo Model of the Ar^{+} Ion Collection in He Gas by a Cylindrical Langmuir Probe in the Transition Regime, Eur. Phys. J. Appl. Phys. 22 (2003) 29–39.

[20] F. Taccogna, S. Longo, M. Capitelli, PIC model of the ion collection by a Langmuir probe, Contr. Plasma Phys. 44 (7-8) (2004) 594–600.

[21] F. Taccogna, S. Longo, M. Capitelli, Ion orbits in a cylindrical Langmuir probe, Physics of Plasmas 13 (2006) 043501.

[22] F. Taccogna, S. Longo, M. Capitelli, Ion-neutral collision effects in Langmuir probe theory, Contr. Plasma Phys. 48 (5-7) (2008) 509–514.

[23] F. Taccogna, Dust in plasma I. Particle size and ion-neutral collision effects, Contr. Plasma Phys. 52 (9) (2012) 744–755.

[24] J. P. Verboncoeur, Symmetric spline weighting for charge and current density in particle simulation, Journal of Computational Physics 174 (2001) 421–427.

[25] W. H. Press, S. A. Teukolsky, W. T. Vetterling, B. P. Flannery, Numerical Recipes in Fortran 77: The Art of Scientific Computing, Cambridge University Press, New York, 2001.

[26] K. Nanbu, Y. Kitatani, An ion-neutral species collision model for particle simulation of glow discharge, Journal of Physics D: Applied Physics 28 (2) (1995) 324–330.

[27] L. A. Kuznetsova, S. T. Surzhikov, Spectral radiation of shock waves and radiative models of diatomic molecules, AIAA paper 97-2564.

[28] N. N. Kudryavtsev, L. A. Kuznetsova, S. T. Surzhikov, Kinetics and nonequilibrium radiation of $CO_2 - N_2$ shock waves, AIAA paper 2001-2728.

[29] S. T. Surzhikov, I. Sharikov, M. Capitelli, G. Colonna, Kinetic models of non-equilibrium radiation of strong air shock waves, AIAA paper 2006-0586.

[30] A. S. Dikalyuk, S. T. Surzhikov, O. P. Shatalov, P. V. Kozlov, Y. V. Romanenko, Nonequilibrium radiation behind the strong shock waves in martian and titan atmospheres: Numerical rebuilding of experimental data, AIAA paper 2012-0795.
[31] M. Panesi, T. Magin, A. Bourdon, A. Bultel, O. Chazot, Fire II Flight Experiment Analysis by Means of a Collisional-Radiative Model, Journal of Thermophysics and Heat Transfer 23 (2) (2009) 236–248.
[32] J. H. Grinstead, M. C. Wilder, M. J. Wright, D. W. Bogdanoff, G. A. Allen, K. Dang, M. J. Forrest, Shock radiation measurements for mars aerocapture radiative heating analysis, AIAA paper 2008-1272.
[33] B. A. Cruden, D. Prabhu, R. Martinez, H. Le, D. Bose, J. H. Grinstead, Absolute radiation measurement in venus and mars entry conditions, AIAA paper 2010-4508.
[34] H. Takayanagi, K. Fujita, Absolute radiation measurements behind strong shock wave in carbon dioxide flow for mars aerocapture missions, AIAA paper 2012-2744.
[35] A. M. Brandis, R. G. Morgan, T. J. McIntyre, P. A. Jacobs, Nonequilibrium radiation intensity measurements in simulated titan atmospheres, Journal of Thermophysics and Heat Transfer 24 (2) (2010) 291–300.
[36] P. V. Kozlov, Y. V. Romanenko, O. P. Shatalov, Radiation intensity measurement in simulated Martian atmospheres on the double diaphragm shock tube, in: Proceedings of the 4th International Workshop on Radiation of High Temperature Gases in Atmospheric Entry, ESA SP-689, Lausanne, Swiss, 2010.
[37] C. S. Peskin, Flow patterns around heart valves: A numerical method, Journal of Computational Physics 10 (1972) 252.
[38] J. Mohd-Yusof, Combined Immersed Boundaries/B-Splines Methods for Simulations of Flows in Complex Geometries, CTR Annual Research Briefs, NASA Ames - Stanford University (1997).
[39] E. A. Fadlun, R. Verzicco, P. Orlandi, J. Mohd-Yusof, Combined Immersed-Boundary Finite-Difference Methods for Three-Dimensional Complex Flow Simulations, Journal of Computational Physics 161 (2000) 35.
[40] G. Iaccarino, R. Verzicco, Immersed Boundary Technique for Turbulent Flow Simulations, Appl. Mech. Rev. 56 (2003) 331–347.
[41] R. Mittal, G. Iaccarino, Immersed Boundary Methods, Annu. Rev. Fluid Mech. 37 (2005) 239.
[42] P. De Palma, M. D. de Tullio, G. Pascazio, M. Napolitano, An immersed boundary method for compressible viscous flows, Comput. Fluids 35 (2006) 693.
[43] M. D. de Tullio, P. De Palma, G. Iaccarino, G. Pascazio, M. Napolitano, An immersed boundary method for compressible flows using local grid refinement, Journal of Computational Physics 225 (2007) 2098–2117.
[44] C. L. Merkle, Preconditioning methods for viscous flow calculations, in: M. Hafez, K. Oshima (Eds.), Computational Fluid Dynamics Review 1995, Wiley, New York, 1995, p. 419.
[45] H. van der Vorst, Bi-CGSTAB: a fast and smoothly converging variant of Bi-CG for the solution of non-symmetric linear systems, SIAM J. Sci. Statist. Comput. 13 (1992) 361.
[46] J. O'Rourke, Computational Geometry in C, Cambridge University Press, Cambridge, 1998.
[47] S. Kang, G. Iaccarino, F. Ham, DNS of buoyancy-dominated turbulent flows on a bluff body using the immersed boundary method, Journal of Computational Physics 228 (2009) 3189.
[48] G. Karypis, V. Kumar, A fast and high quality multilevel scheme for partitioning irregular graphs, SIAM J. Sci. Comput. 20 (1998) 359.
[49] N. G. Hadjiconstantinou, The limits of Navier-Stokes theory and kinetic extensions for describing small-scale gaseous hydrodynamics, Physics of Fluids 18 (2006) 111301.
[50] D. Bruno, M. Capitelli, F. Esposito, S. Longo, P. Minelli, Direct simulation of non-equilibrium kinetics under shock conditions in nitrogen, Chemical Physics Letters 360 (2002) 31.
[51] J. N. Moss, D. F. G. Rault, J. M. Price, Direct Monte Carlo simulations of hypersonic viscous interactions including separation, in: B. D. Shizgal, D. P. Weaver (Eds.), Rarefied Gas Dynamics: Space Science and Engineering, Vol. 160 of Progress in Aeronautics and Aeronautics, AIAA, Washington, 1993, pp. 209–220.

Advanced Models in Shock Waves

G. Colonna *[1], G. D'Ammando[2], A. S. Dikalyuk[3], M. Panesi[4], L. D. Pietanza[1], and S. T. Surzhikov[3]

[1]CNR-IMIP, Via Amendola 122/D, 70126 Bari, Italy
[2]Dipartimento di Chimica, Universitá degli studi di Bari, Via Orabona 4, 70125 Bari, Italy
[3]A. Ishlinsky Institute for Problems in Mechanics, Russian Academy of Sciences, Prospect Vernadskogo 101-1, Moscow 119526, Russia
[4]University of Illinois at Urbana-Champaign, Urbana, 104 S. Wright street, 61801 IL, USA

Abstract

The paper presents three collisional-radiative models developed to investigate non-equilibrium chemistry and radiation in hypersonic shock tubes operating with different planetary atmospheres. An hybrid collisional radiative model, employing the state-to-state kinetics of electronically excited states of molecules and the multi-temperature approximation for the vibrational degree of freedom is presented first, and applied to the numerical rebuilding of experimental shock tube emission spectra. Next, an hybrid collisional-radiative model for ionized air is presented. This model consider the state-to-state approach for electronic states of atoms and the multi-temperature model for the vibrational populations of diatomic molecules in their ground electronic state. A radiative transport equation is also solved to determine radiative source terms in the kinetic scheme and the enthalpy production due to radiation. The third model considers the state-to-state collisional-radiative model of Jupiter's atmosphere, self-consistently coupled with the Boltzmann equation for free electrons and the radiative transfer equation for the radiation transport in one-dimensional slab geometry.

Keywords: Collisional-radiative model, Radiative transfer, Re-entry flows

1 Introduction

The radiation emitted by the shock-heated gas during the entry of a space vehicle in planetary atmospheres can give a relevant contribution to the heat load of the Thermal Protection System (TPS). In some conditions, the radiative heat flux is effective when the convective and conductive contributions are negligible [1–3].

The flow region downstream a shock wave formed during high-speed atmospheric entry is characterized by a relaxation layer where the gas is far from chemical and thermal equilibrium. The width of this region, ranging from few millimeters to some centimeters, depends on the entry conditions and on the rates of elementary processes acting during the relaxation phase.

Shock tubes [4–8] are devices commonly used to validate the chemical model and the relaxation coefficients of internal degrees of freedom, based on optical emission spectroscopy [9, 10]. Modeling shock tubes is a fundamental tool for rebuilding experiments. Different approaches are possible to describe the relaxation of internal degrees of freedom and their influence on the chemical processes.

*Corresponding author. E-mail: gianpiero.colonna@ba.imip.cnr.it

In this work we are reporting three non-equilibrium models describing also the radiation emission. The first model, devoted to the study of non-equilibrium spectral intensity of radiation emitted by the shock-heated gases for comparison with available shock tube experimental data, has been developed in the Laboratory of Radiative Gas Dynamics in Moscow [11–13]. After an hybrid collisional-radiative (CR) model coupled to an Euler solver and a radiative transfer equation (RTE) used to analyze the behavior of the electronically excited states of atomic species behind a strong shock, has been developed in a joint collaboration between research groups in France and Belgium [14–16]. The third model, a full CR model coupled to an Euler solver, a radiative transfer equation and a Boltzmann equation for the free electrons has been developed in the Plasma Group of CNR in Bari [17, 18].

2 Numerical Model

In this paper we will limit our calculations to stationary shock tubes, which can be described with good accuracy by the 1D Steady Euler equations

$$\begin{aligned} &\frac{d\rho u}{dx} = 0 \\ &\frac{d}{dx}(p + \rho u^2) = 0 \\ &\frac{d}{dx}\left(h + \frac{u^2}{2}\right) = \dot{h} \end{aligned} \tag{1}$$

where ρ is the mass density, u the flow speed, p the static pressure, h is specific enthalpy. The source term $\dot{h}$ is the enthalpy production rate. Possible contributions can come from electrical discharges (Joule effect), from radiative losses or laser heating. The Euler equations need to be coupled with the ideal gas equation of state

$$\begin{aligned} p &= \frac{\rho R T}{\bar{M}} \\ \bar{M} &= \sum_{i=1}^{N_s} M_i \chi_i \end{aligned} \tag{2}$$

where T is the gas temperature, R is the ideal gas constant, $\bar{M}$ is the mean molar mass and $\chi_i = n_i/n$ is the molar fraction of the ith species of mass M_i and molar density n_i ($n = \sum_i n_i$ is the total mole density).

The system of equations listed above is not closed because need to define the specific enthalpy. Under Local Thermodynamic Equilibrium (LTE) conditions, the specific enthalpy is a function of the temperature and pressure, $h(T, p)$ [19–21]. In shock waves, there is a region, just behind the shock front, in which the LTE assumption is not valid and both chemical and thermal non-equilibrium must be considered. It is necessary to add a kinetic equation for each species

$$\frac{d\rho_i u}{dx} = \dot{\rho}_i \tag{3}$$

where $\dot{\rho}_i$ is a source term due to chemical reactions. For the following reaction set ($j = 1 \dots N_r$)

$$\sum_k^{N_s} a_{kj} X_k \rightleftharpoons \sum_k^{N_s} b_{kj} X_k \tag{4}$$

where X_k is the kth species and a_{jk} and b_{jk} are the stoichiometric coefficients of the direct and reverse j-th reaction.

The chemical reaction source term is given by

$$\dot{\rho}_i = M_i \sum_{j=1}^{N_r} \left[(b_{ji} - a_{ji}) k_j^f \prod_{k=1}^{N_s} \left(\frac{\rho_k}{M_k} \right)^{a_{kj}} + (a_{ji} - b_{ji}) k_j^r \prod_{k=1}^{N_s} \left(\frac{\rho_k}{M_k} \right)^{b_{kj}} \right] \tag{5}$$

The enthalpy per unit mass is given by

$$h = \frac{1}{\bar{M}} \sum_{i}^{N_s} \chi_i \bar{H}_i \tag{6}$$

being $\bar{H}_i$ the molar enthalpy of the ith species. Under thermal non-equilibrium conditions it is convenient to express the species molar enthalpy as the sum of three contributions

$$\bar{H}_i = \bar{H}_i^T(T) + \bar{H}_i^{int} + \bar{H}_i^f \tag{7}$$

where the $\bar{H}_i^T(T)$ term includes translation and those internal degrees of freedom which are assumed in equilibrium with translation. On the other hand $\bar{H}_i^{int}$ is the contribution of internal degrees of freedom which are out of thermal equilibrium and $\bar{H}_i^f$ is the molar formation energy of the i-th species, including the excitation energy of electronically excited states. As a general rule, in evaluating $\bar{H}_i^T(T)$, only the translational energy is considered for atomic species, while for molecules the rotational degrees of freedom are considered in equilibrium with the translation according to

$$\bar{H}_i^T = \frac{5}{2} RT + \frac{n_{rot}}{2} RT \tag{8}$$

where n_{rot} is the number of rotational degrees of freedom of the species, e.g. $n_{rot} = 0$ for atoms, 2 for linear molecules and 3 for non-linear molecules.

An important aspect of thermal non-equilibrium kinetics is the dependence of the rate coefficients (k^f and k^r) in eq. (5) on the electronic energy states of atoms, and on the electronic and rovibronic energy states of molecules as well as on the temperature of free electrons (for electron impact processes). Selected models, reported in literature [13, 15, 17, 22] and briefly discussed in the next sections, differ mainly in the way they consider the influence of internal distributions on the chemical rates [23] . These differences reflect also on the radiation model, since the calculated emissivity and absorption coefficients are directly related to the adopted model for the distribution of population over the available atomic and molecular quantum states, i.e. the internal state distribution (isd) of each species. For the purposes of this paper, it is useful to distinguish between two approaches which can be used to introduce the effect of excited states in radiative gas dynamics: full and hybrid collisional-radiative models.

In the full collisional-radiative models, all relevant internal states of the species present in the gas mixture and the individual processes linking such states are taken into account. The main difficulties of the full model are the need of large datasets of level-specific cross sections or rate coefficients which, especially for excited states, are not always available, and its high computational cost [15], limiting their application to 1D or 2D situations. As a consequence, the full models can hardly be inserted into the 3D CFD codes for complex geometries used in engineering applications.

On the other hand, the hybrid collisional-radiative models attempt to reduce the computational burden using a state-specific description of the electronically excited states which are more important from the point of view of radiation transport and

non-equilibrium, while the other degrees of freedom are described by an equilibrium Boltzmann distribution at a given temperature. The multi-temperature approach to thermal non-equilibrium results from associating a different temperature to individual degrees of freedom. A more general multi-internal-temperature approach [24], using several temperatures to describe different energy ranges of the isd of a single degree of freedom, is also possible but it is not considered in this paper.

3 Multi-temperature kinetics and just-overlapping line model

The first investigation in the Laboratory of Radiative Gas Dynamics dedicated to the calculation of non-equilibrium spectral intensity of radiation emitted by the shock-heated gases was presented in 1997 [25]. Since then our group is involved in this area of scientific research [11–13]. In this section, an hybrid collisional-radiative model for the relaxation zone behind a shock is presented. The model solves the Euler system of equations for the determination of flow parameters (see eqs. (1) and (2)). The equations have been modified in order to take into account reacting gas mixtures following eqs. (3) to (6). In the calculations presented here, we have neglected in the Euler equations the energy lost by radiation, i.e. $\dot{h} = 0$ in eq. (1). The populations of vibrational degrees of freedom of molecules are calculated introducing a vibrational temperature for each vibrational mode of diatomic and triatomic molecules. The electron gas temperature T_e is determined by a separate equation containing different source terms, accounting for the most important electron impact processes.

The following chemical components were accounted in the model: e, N, C, O, C_2, N_2, O_2, CN, CO, NO, CO_2, NCO, C^+, N^+, O^+, C_2^+, N_2^+, O_2^+, CN^+, CO^+, NO^+. The description of the transformations among the chosen chemical species was performed according to the chemical kinetic mechanism based on the results of the studies [26–32]. The populations of the radiating electronic states of molecules, which are considered as independent chemical species in the model [33], are calculated by solving the corresponding kinetic equations. The following molecular electronically excited states have been considered: $CN(A^2\Pi)$, $CN(B^2\Sigma^+)$, $C_2(d^3\Pi)$, $CO(A^1\Pi)$, $NO(A^2\Sigma^+)$, $NO(B^2\Pi)$, $NO(C^2\Pi)$, $N_2(A^3\Sigma)$, $N_2(B^3\Pi)$, $N_2(C^3\Pi)$, $N_2^+(B^2\Sigma)$. The mechanism of population of these states includes the following processes: excitation/de-excitation of the electronic states of molecules by electron impact, spontaneous emission, excitation/de-excitation of the electronic states of molecules in collisions with heavy particles. The data needed to model these processes were partially taken from [30, 34–36]. The effect of the nonequilibrium dissociation was accounted using the Kuznetsov model [37]. It is worth noticing that the results of the experimental measurements of the nonequilibrium radiation of the shock heated CO_2-N_2 and N_2-O_2 gas mixtures were successfully reconstructed using the same set of parameters of the model without any special adjustment (it means the same set of chemical reactions rates and rates of the processes of population of electronic excited states of molecules).

In the calculation of enthalpy, molecular rotation is considered in equilibrium with the translation, therefore the ro-translational contribution to the energy is that given in eq. (8) while the internal enthalpy considers the vibrational contribution of each electronic state

$$\bar{H}_i^{int} = \sum_{j=1}^{N_{v,i}} g_{i,j} \frac{R\theta_{i,j}}{exp(\theta_{i,j}/T_{v,i,j}) - 1} = \sum_{j=1}^{N_{v,i}} M_i g_{i,j} e_{i,j}(T_{v,i,j}) \tag{9}$$

Here $T_{v,i,j}$, $\theta_{i,j}$, $g_{i,j}$ are respectively the vibrational temperature, the characteristic vi-

brational temperature and the degeneracy of j-th vibrational mode of i-th molecule (which can be an electronically excited state), $N_{v,i}$ is the number of vibrational modes of i-th molecule and $e_{i,j}(T_{v,i,j})$ is the vibrational energy per unit mass at the given vibrational temperature.

To determine the vibrational temperatures, we consider the following relaxation equation

$$\frac{due_{s,j}(T_{v,s,j})}{dx} = Q_{s,j}^{VT} + Q_{s,j}^{CV} \tag{10}$$

where $Q_{s,j}^{VT}$ takes into account the vibration-translation energy transfer and $Q_{s,j}^{CV}$ the influence of chemical processes on the vibrational energy. On the other hand, the $Q_{s,j}^{VV'}$ term, modeling the vibration-vibration energy exchange has been neglected in the present radiation model, for the following reason. In Ref. [29] it was shown that in relatively strong shock wave the $V-V$ exchange influences only on the relative values of the vibrational temperatures. Under the present conditions ($p \sim 1$ torr, $v_{sh} \sim 5-8$ km/s) it is very unlikely that the multitemperature approach could correctly determine the vibrational distribution function of the molecules at each point behind the shock front. On the other hand, if the aim is the calculation of the radiation of shock-heated gases, then in our opinion the most important factor is the correct modeling of the kinetics of electronically excited states: the influence of the vibrational temperature on the radiation a second order effect. CV processes have a very important effect on the vibrational temperature, and accounting for that process could change significantly (several thousand K) the profile of the vibrational temperature behind the shock front. Clearly, in the absence of intensive chemical transformations it is necessary to include the $V-V\prime$ mechanism in the model.

The $Q_{s,j}^{VT}$ source terms are calculated in the Landau-Teller approximation as

$$Q_{s,j}^{VT} = \frac{e_{s,j}(T) - e_{s,j}(T_{v,s,j})}{\tau_{s,j}} \tag{11}$$

where the relaxation times $\tau_{s,j}$ are usually estimated using the Millikan-White approximations combined with Park's correction. The influence of chemical kinetics and vibrational relaxation is taken into account in the model (CVDV interaction). The following equation is used for the determination of the temperature of electron gas

$$\frac{d}{dx}\left(\frac{3}{2}T_e X_e u\right) + \frac{3}{2}T_e X_e \frac{du}{dx} = Q_{ei} + Q_{ea} + Q_{ai} + Q_{ion} + Q_{ev} \tag{12}$$

The rates of the processes responsible for the variation of the free electron temperature T_e are described by the following Q-terms: elastic electron-ion (ei) and electron-atom (ea) collisions; associative ionization/dissociative recombination (ai); ionization (ion); interaction of electron gas and vibrational modes of molecules (ev). The term Q_{ee}, corresponding to electron impact excitation/de-excitation of molecules and ions, has been omitted in eq. (12), since in the moderate intensity shock waves investigated by the present model (the degree of ionization is less than 0.2% in air at $v_{sh} \leq 8$ km/s), the population of excited state of molecules is much less than the density of free electrons, resulting in a negligible effect of electron impact excitation processes on T_e.

The *just-overlapping* line model [38] is used for the spectral intensity of radiation calculations. The equations of the model are as follows (W cm^{-3} μm^{-1} sr^{-1})

$$\begin{aligned} j_\lambda = 3.202\ 10^{-10} \frac{N_{eel}}{Q_{VR}\lambda^6} \sum_{V',V''} \frac{S_{V'V''}}{|\Delta B_V|} \exp\left[-\frac{hc}{kT_v} E_{eel}(V') \right. \\ \left. -\frac{hc}{kT_R}\frac{B_{V'}}{\Delta B_V}(\omega - \omega_{V'V''} + B_{V'}) \right] \end{aligned} \tag{13}$$

where N_{eel} (cm^{-3}) is the population of the electronic excited state of the molecule; ω (cm^{-1}) is the wave number; λ (nm) is the wavelength; $\omega_{V'V''}$ (cm^{-1}) is the wavenumber of a vibronic transition; $\Delta B_V = B_{V'} - B_{V''}$ and $B_{V'}$, $B_{V''}$ are the rotational constants of the upper and lower molecular electronic states respectively; Q_{VR} is the rovibrational partition function of the electronic excited state of the molecule; $S_{V'V''}$ the strength of the vibronic transition; $E_{eel}(V')$ is the energy of the vibrational level V' of the electronic excited state; T_V, T_R are the vibrational and rotational temperatures. $S_{V'V''}$ is determined from the square of the moment of the electronic transition by the following formulas

$$\begin{aligned} S_{V',V''} &= (2 - \delta_{0,\Lambda'+\Lambda''})(2S+1)|R_{V',V''}|^2 \\ |R_{V',V''}|^2 &= \frac{3h}{64\pi^4 a_0^2 q_e^2} \frac{2 - \delta_{0,\Lambda'}}{2 - \delta_{0,\Lambda'+\Lambda''}} \frac{1}{\omega^3_{V',V''}} A_{V',V''} \end{aligned} \tag{14}$$

where $A_{V',V''}$ is the Einstein coefficient of vibronic transition that can be obtained as a result of solution of quantum mechanical problem of the calculation of vibronic wave functions.

The full description of the model can be found in [11–13, 25]. It is worth noting that what is presented here is actually a framework: different gas mixtures and chemical kinetics models can be studied by this code, with the possibility of studying both nonequilibrium and equilibrium spectral intensities of radiation emitted by shock-heated gases.

The second part of activity in our group is dedicated to the systematic processing of experimental data obtained on different shock tube facilities all around the world by means of the model developed in our group. Up to now we have performed the analysis of results obtained on the shock tubes of NASA Ames Research Center (EAST facility [4, 5], Chofu Aerospace Center [6], Queensland University (X2 facility) [7], Institute of Mechanics Moscow State University [8]. By means of our model we have studied spectral intensity of radiation of shock-heated N_2-O_2, CO_2-N_2, CH_4-N_2 gas mixtures.

Figures 1 and 2 report a comparison between numerical results calculated by the present model (dashed line) and experimental data (solid line). In fig. 1 the nonequilibrium spectral intensity of the radiation of an 80% N_2-20% O_2 gas mixture at $p = 1$ torr heated by a shock wave with velocity $v_{sh} = 5.56$ km/s. The most important electronic band systems generating the observed radiation in this spectral region are: N_2 2^{nd} positive ($C^3\Pi - B^3\Pi$), N_2^+ 1^{st} negative ($B^2\Sigma - X^2\Sigma$), NO γ-system ($A^2\Sigma - X^2\Pi$), NO β-system ($B^2\Pi - X^2\Pi$) and NO δ-system ($C^2\Pi - X^2\Pi$).

For the N_2-O_2 gas mixture, the reported spectral distribution is typical in the 200-400 nm spectral region at shock wave speeds 5 km/s$\leq v_{sh} \leq$8 km/s. As the shock wave speed increases, the intensity of nonequilibrium radiation in the spectral range 300-400 nm, mainly produced by the N_2 2^{nd} positive and N_2^+ 1^{st} negative band system systems, increases faster than the spectral intensity of radiation in the 200-300 nm range generated by the NO γ, β and δ-systems. On the other hand, in the whole spectral range (200-400 nm) the radiation intensity increases with the shock velocity. The model successfully describes the above discussed trends in the experimental data.

In fig. 2 the nonequilibrium spectral intensity of the radiation of 70% CO_2-30% N_2 gas mixture at pressure $p = 0.3$ torr heated by the shock wave with velocity $v_{sh} = 6.76$ km/s is reported. The main radiative electronic band systems in this case are CO 4^{th} positive ($A^1\Pi - X^1\Sigma^+$), NO γ-system ($A^2\Sigma^+ - X^2\Pi$), NO β-system ($B^2\Pi - X^2\Pi$), NO δ-system ($C^2\Pi - X^2\Pi$, active between 200 and 340 nm), CN violet ($B^2\Sigma^+ - X^2\Sigma^+$, active between 340 and 440 nm), C_2 Swan ($d^3\pi - a^3\Pi$, active between 440 and 560 nm) and CN red ($A^2\Pi - X^2\Sigma^+$, active between 560 and 800 nm). NO molecules play a more important role in the formation of the radiation in ultraviolet part of the spectrum

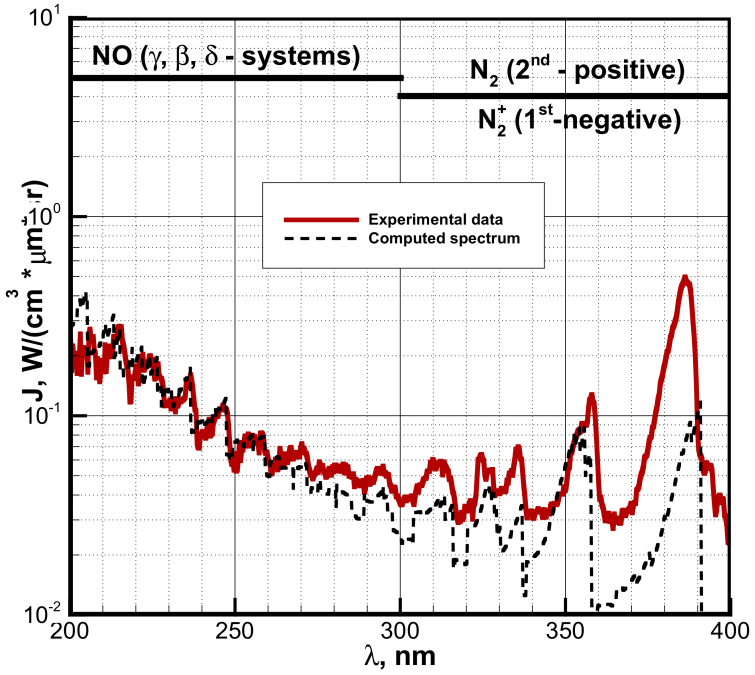

Figure 1: Nonequilibrium spectral emissivity of the relaxation zone behind the shock wave initiated in 80% N_2 - 20% O_2 gas mixtures at P=1 Torr, V_{sh}=5.56 km/s

due the higher amount of N_2 molecules in the test gas mixture compared to the actual composition of the Mars atmosphere, which is 96% CO_2-4% N_2.

In Ref. [39] the error in the measured spectral intensity of radiation was estimated to be 90%. Taking into account this value agreement between experimental and numerical data should be regarded as acceptable.

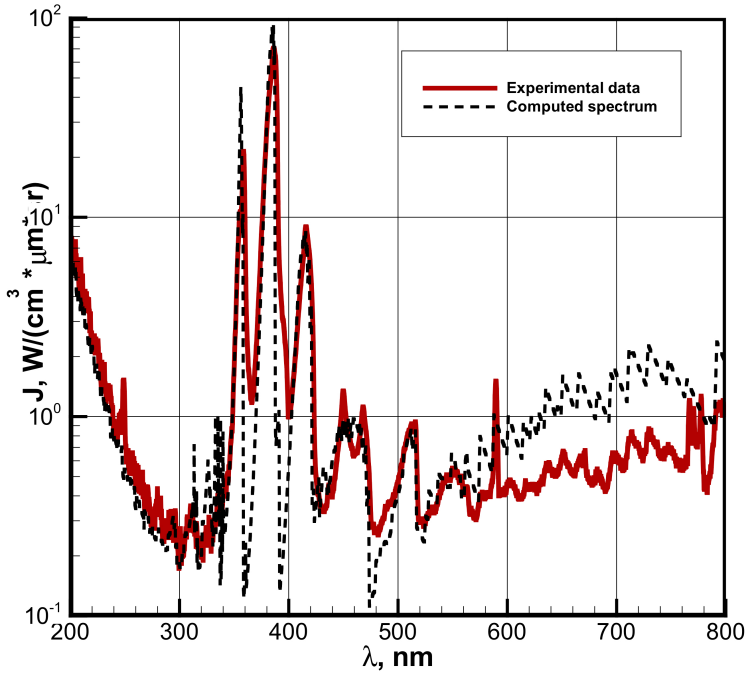

Figure 2: Nonequilibrium spectral emissivity of the relaxation zone behind the shock wave initiated in 30% N_2 - 70% CO_2 gas mixtures at P=0.3 Torr, V_{sh}=6.76 km/s

4 Hybrid collisional radiative modeling of the FIRE II Flight Experiment

Modeling of the collisional and radiative processes and analysis of available experimental and in-flight data put forward the importance of ionization processes in shock heated air [15, 40]. The radiative and convective heat loads generated during Earth entry are also shown to be strongly dependent on the degree of ionization in the gas. In ionizing air, the formation of the first electrons is due to the association of N and O atoms into NO^+ [41, 42]. This is the first step in a two-step ionization process, favored by the relatively low activation energy. Also the reaction does not require the presence of charged particles. Thus it is well suited as the initialization step. In a second step, when the number of electrons is sufficiently large, the high-speed electrons at the tail end of the Maxwellian distribution can ionize the neutral atoms, rapidly increasing the electron density. The accurate modeling of this two-step process requires the correct modeling of the thermo-chemical relaxation leading to the formation of the atomic species (e.g. dissociation [43–45]), as well as a detailed modeling of the excitation and ionization of the atomic species, contributing to the production of electrons in the hypersonic regimes. One important aspect in the present discussion is the explicit coupling of the species conservation equations with radiation by solving the radiative transfer equation, instead of employing an escape factor to approximately account for the effect of the radiative processes on the population of the excited states. This results in a consistent modeling of the radiative processes.

4.1 Transport equations

In this section, consideration is given to the model used to describe the dynamics of multi-component, multi-temperature, chemically reacting, relaxing and emitting flows.

The air mixture used in this work comprises 95 species (11 chemical components), including some of the electronic energy levels of atomic nitrogen and oxygen listed in Ref. [46]. The populations of the vibrational energy levels of the molecules (N_2, NO, O_2, N_2^+, NO^+, O_2^+) are assumed to follow Boltzmann distributions and share a common vibrational temperature T_v. The rotational energy level populations are assumed to follow Boltzmann distributions at the translational temperature T of the gas. The CR model provides the electronic state populations of the N and O atoms.

4.1.1 Thermodynamics

In this study, air is considered as a mixture of nitrogen and oxygen and their products. It is composed of neutral species (N_2, O_2, NO, N(1-46), and O(1-40)) and charged species (N_2^+ , O_2^+ , NO^+, N^+, O^+, and e^-). Forty-six electronic energy levels for N and forty levels for O are employed. The levels used are a combination of real physical states and lumped states, obtained by averaging over the energies and by summing over the degeneracies of the states that are lumped together. The final reduced atomic model obtained allows one to accurately calculate with manageable effort 1) ionization of the N and O atoms by electron impact and 2) the net population of the excited states resulting from the collisional and radiative processes. The number of electronic levels used to compute the energy of the ions and molecules is tuned to yield the best matching agreement between values of the computed energies and the reference tables of Gurvich [47]. Molecular energy is computed assuming the rigid rotor and harmonic oscillator approximations. Spectroscopic constants are taken from Gurvich [47]. The vibrational and rotational data for the molecules are specific to their electronic states.

4.1.2 Shock Tube flow solver

A one-dimensional flow solver, SHOCKING, was developed to simulate air plasmas obtained in shock-tube facilities, details about the solver and the physical model used are given in several publications [14–16]. This model has been modified to simulate re-entries at speeds higher than 10 km/s. First, a radiative source term Q_{Rad} has been added in the equation that expresses conservation of the total energy. The inclusion of this term is important as radiative transitions influence the redistribution of the energy of the system (e.g. radiative cooling). Second, a separate source term in the species continuity equation has been added to account for the effect of radiation on the population of electronic states. Post-shock conditions are derived from the jump relations (Rankine-Hugoniot equations) assuming frozen-gas composition and frozen vibrational and electronic energy modes. The rotational mode is assumed to be in equilibrium with the translational mode. The downstream flow-field is determined by solving a set of continuity equations for each chemical component, including its electronic structure in the case of the atoms, complemented by the Euler system of equations, namely mass, momentum and energy conservation, which allow one to retrieve the remaining characteristic flow quantities, such as pressure, temperature and flow speed. Also, the relaxation of the vibrational and free-electron energy is modeled using separate conservation equations accounting for the energy exchanges with other modes and chemistry. Finally, the characterization of the radiative field is modeled solving the radiative transfer equation.

Compared to the general formulation of section 2, the present model has the following characteristics:

- the enthalpy production term $\dot{h}$ of eq. (1) is modified to explicitly include the contributions of radiation as

$$\dot{h} = -\frac{\partial Q_{rad}}{\partial x} \tag{15}$$

- additional vibrational energy conservation equations including the radiative losses from each vibrational mode are solved

$$\frac{\partial}{\partial x}(\rho u e_m) = \Omega^m - \frac{\partial}{\partial x} Q^m_{Rad} + \cdots, \qquad [m \in \mathcal{U}] \tag{16}$$

- the following radiative transfer equation in slab geometry is solved

$$\frac{\mu}{\kappa_\lambda}\frac{dI_\lambda}{dx} + I_\lambda(x) = \frac{\eta_\lambda}{\kappa_\lambda}(x) = S_\lambda(x) \tag{17}$$

where the advection velocity is indicated with u and the radiative energy fluxes are indicated with Q_{rad}. In eq. (16), e_m refers to the energy of the internal energy modes (e.g. vibration, kinetic energy of free electrons ...). In the particular case, the kinetic energy of the free electrons and all the internal energy modes with the exception of the rotational structure of the molecular species and the internal energy of the atomic species are included in e_m. The energy exchanged by the internal energy modes with chemistry (e.g. vibration-dissociation coupling ...), and the translational energy modes are indicated with Ω^m. In eq. (17), I_λ is the spectral intensity, μ is the cosine of the angle between the direction of radiation and the axis x, κ_λ indicates spectral absorption coefficient and η_λ the spectral emissivity. The ratio between emissivity and absorption coefficient is indicated with S_λ, and it is referred to as the source function.

4.2 Kinetic and radiative processes included in the model

The closure of the complex non-linear set of equations previously discussed requires the knowledge of rate parameters governing the dynamics of the particles and photons. Recently, Bultel *et al.* [48] compiled an electronic specific kinetic mechanism for air, which was applied to the study of compressing and expanding flow situations using a 0D model. In Bultel's model, also referred to as ABBA model, 13 species in their ground states and numerous electronic excited states were taken into account. Although similar models have already been proposed by Teulet *et al.* [49] and Sarrette *et al.* [50], none are valid for pressures between 1 kPa and the atmospheric pressure. Furthermore, numerous recent experiments and *ab-initio* calculations have been carried out to improve the accuracy of excitation cross sections by electron impact, dissociative recombination rates of NO^+, O_2^+ and N_2^+ and their branching fractions as well as vibrational processes. In the present study the more recent data are incorporated in Bultel's database.

The system under study is composed of molecules, atoms, ions, and electrons interacting with each other and with the radiation field. This system is modeled with the photons regarded simply as another species of particles. This simplifying assumption is appropriate for the description of the chaotic light characterizing the re-entry environment. Under these assumptions, the kinetic theory of particles and photons is thus reduced to the set of kinetic equations for the material particle (e.g. the Euler eq. (1)), complemented by conservation equations for energy and the various chemical components, eq. (16), and the well-known RTE, eq. (17). The theory governing the dynamics of such systems in non-equilibrium is well established and is discussed in detail in Huo *et al.* [14].

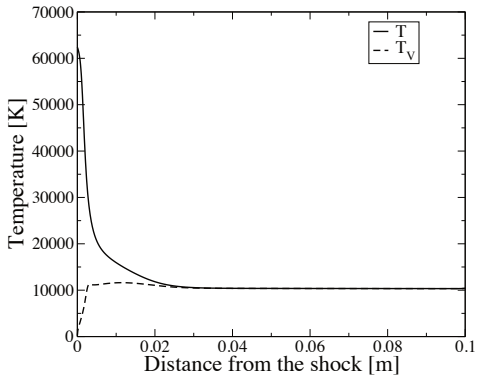

(a) Post shock temperature profile.

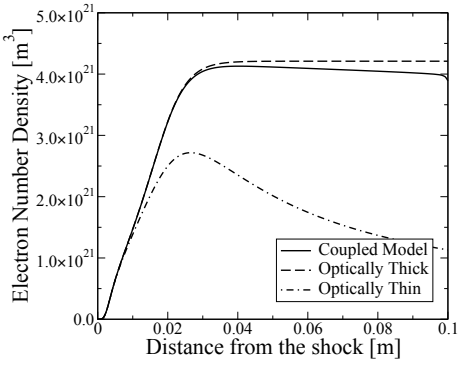

(b) Electron density as a function of the optical thickness.

Figure 3: Temperature and electron density profiles in the post shock.

4.2.1 FIRE II Flight experiment

One of the primary objectives of the FIRE project was to define the radiative heating environment associated with the re-entry of an Apollo vehicle at a velocity of 11.4 km/s. The aim of the present work is to test the CR model for different physico-chemical conditions, from electronic energy level populations in strong non-equilibrium to populations following Boltzmann distributions. The shock-tube operating conditions corresponding to the trajectory point investigated here are presented in Huo *et al*[14].

4.2.2 Chemistry and flow field energy distribution

The characterization of the physical-chemical state of the plasma in the shock layer requires knowledge of its chemical composition as well as the internal energies of the particles. To this aim, fig. 3(a) shows the evolution of the rotational and translational temperature and the vibrational/free-electron temperature. After a jump in the translational temperature across the shock (located on the left at $x = 0$), the gas redistributes energy through activation of the internal energy modes as well as the onset of chemical reactions, until the flow eventually reaches its post-shock equilibrium state. The internal temperature profile, indicated by T_v, shows a rapid initial increase due to the excitation of the vibrational energy states, but then flattens out due to the eventual onset of chemical reactions (see fig. 3(a)). In this picture, radiative processes play a fundamental role, since they influence the dynamics of the thermal and chemical relaxation. The influence of the optical thickness of the gas on the chemistry is clear when observing the electron density profiles, shown in fig. 3(b). When the medium is assumed optically thick, all of the radiation emitted is immediately self-absorbed and the electron density quickly reaches its equilibrium value. In the case of optically thin gas case, the ionization rate is considerably slower; this is due to the fact that radiative processes (when only emissive processes are considered) tend to deplete the excited states, resulting in a delay of the excitation as well as the ionization processes. In fig. 3(b), the density plot exhibits a maximum and is monotonically decreasing due to the radiative energy losses, which work to consume energy, thereby preventing the gas from reaching the desired equilibrium electron density. The result of the coupled calculation is in close agreement with the optically thick case. This is the first time a rigorous modeling of the radiative processes and their interaction with the surrounding matter is used to test the escape factor approximation.

In the electron temperature regime under consideration, the average electron energy

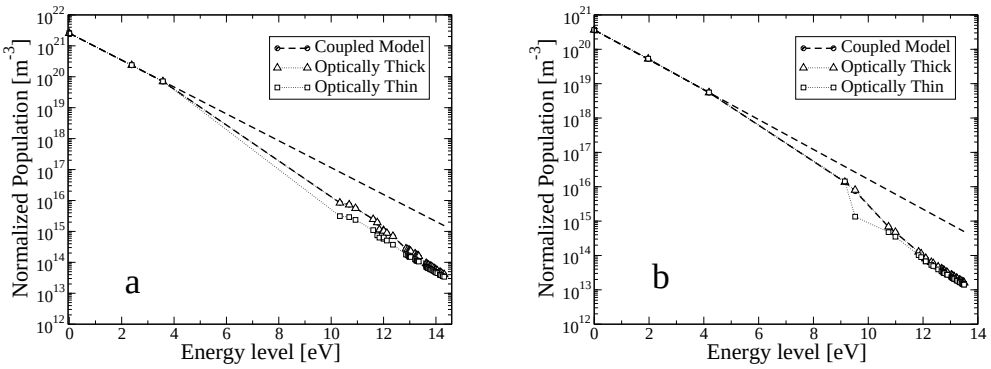

(a) Electronic distribution of nitrogen.

(b) Electronic distribution of oxygen.

Figure 4: Population distributions of atomic species at 1 cm from the shock. The Equilibrium distribution of the electronic levels is indicated in dashed line. The self-consistent model is indicated in circles, while the triangles and the square symbols refers to optically thick and optically thin approximation respectively.

is insufficient to ionize the N and O atoms in their ground states and low-lying meta-stable states. The ionization of the atomic species follows a ladder-climbing dynamic, in that it requires the excitation of the atomic species before ionizing. Thus, an atom needs to "climb" the electronic ladder before ionizing. Hence, in order to characterize non-equilibrium ionization processes, it is necessary to characterize the distribution of the electronic states of atomic nitrogen and oxygen. To this aim, the Boltzmann distribution (at T_e) in the post-shock area is compared with the distribution of the atomic species at 1 cm from the shock front, fig. 4. These results demonstrate how the dynamics of upper and lower excited states are significantly different: while the excitation from the lower to the upper states as well as the ionization processes take place at relatively slow rates for the lower energy levels (e.g. ground and meta-stable), the higher levels exhibit the opposite behavior, as the rates for these processes are very rapid. As a consequence the lower states are very likely to follow a Boltzmann distribution (at T_e), while the higher states are more likely to be in Saha equilibrium at T_e with the free electrons, as shown in figs. 4(a) and 4(b).

5 Collisional-radiative model of H_2/He plasma for entry in Jupiter atmosphere

The non-equilibrium models based on multi-temperature approach assume that the internal states are described by a Boltzmann distribution and the free electrons follow the Maxwell-Boltzmann distribution function. In order to evaluate the energy content of the different degrees of freedom, the multi-temperature approach gives good accuracy, because, in most practical cases, the low energy distribution follow the Boltzmann function. However it frequently occurs that the high-energy tail of the distributions strongly departs from equilibrium as a consequence of the coupling between internal states and chemical processes. This is a crucial aspect because exothermic processes are strongly favored from excited states and, as a consequence, the rate coefficients depart from the Arrhenius trend.

These aspects can be investigated using the full state-to-state model presented in this section. This model solves the master equation for chemical kinetics considering transi-

tions between internal states and chemical processes involving excited levels. The main differences between the model presented in this section and the previously presented models are

- the population distribution over excited states of atoms and molecules are determined solving a kinetic master equation system including the most significant populating/depopulating processes for each internal state. The multi-temperature approximation is not invoked for any internal degree of freedom.
- due to the strong coupling between free electrons and excited states of heavy particles, it is not assumed that free electrons follow a Maxwell-Boltzmann distribution function. Instead, to properly describe the time dependence of the electron energy distribution (eedf), the Boltzmann equation for free electron must be solved.

In this case, strongly non-equilibrium eedf can be obtained, characterized by a rich structure (peaks, bumps, rapid change of slope, plateaux), due to electron collisions with atoms and molecules, reflecting the structure of the corresponding cross sections. An important contribution comes from superelastic collisions, where the energy is transferred from excited states of atoms and molecules to electrons, increasing the high-energy tail of the distribution. There is a strict correlation between internal level populations and the eedf: the distribution of internal level is input data for the Boltzmann distribution, while the rate coefficients of electron impact induced processes enter in the master equation for the plasma composition. These rates are calculated as

$$K_e = \int_0^\infty \sqrt{\epsilon} f_e(\epsilon)\sigma(\epsilon)v_e(\epsilon)d\epsilon \tag{18}$$

where ϵ is the electron energy, f_e is the eedf normalized in the energy space , v_e is the relative velocity and σ is the process cross section.

To complete the kinetic model, the interaction with radiation should be considered, accounting for photon emission and absorption. This problem require to couple the kinetic equation with the radiation (collisional-radiative model) considering also an equation for the photon transport, to determine the absorption coefficients. The strict connection between chemical kinetics, electron kinetics, radiation transport and fluid dynamics makes this problem strongly non-linear, and requires a self-consistent approach which solves at the same time all the equations, as schematized in fig. 5.

The self-consistent approach, without radiation transport, has been applied to nozzle expansion for different mixtures [51–53], also in presence of applied electric and magnetic fields [54, 55], in the boundary layer of hypersonic vehicle [56, 57], a 2D flow around a cylinder [58] and in gas discharges [59], neglecting the radiation. Recently, a full model also including radiation transfer is being developed and applied to 1D shock waves in hydrogen [17] and hydrogen-helium (Jupiter atmosphere) mixtures [18].

5.1 State-to-State Kinetics

To calculate the internal energy as given in eq. (6) we have to solve a continuity equation for each species in each internal state analogous to eq. (3) where $\dot{\rho}_i$ is the source term accounting for the production/consumption of an internal level of a chemical specie due to internal transitions and chemical reactions [51, 53].

The present CR model for atomic H/He considers electron induced transition and ionization/three body recombination

$$\begin{aligned} A(n) + e^- &\rightleftharpoons A(m) + e^- \\ A(n) + e^- &\rightleftharpoons A^+ + 2e^- \end{aligned} \tag{19}$$

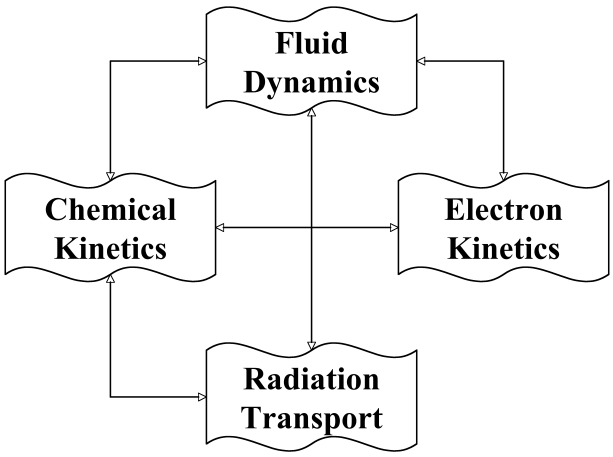

Figure 5: Schematic plot of the self-consistent approach coupling fluid dynamics, chemical and electron kinetics and radiation transport.

the radiative losses

$$\begin{aligned} &A(n) \rightarrow A(m<n) + h\nu_{mn} \\ &A(m<n) + h\nu_{mn} \rightarrow A(n) \\ &A^+ + e^- \rightarrow A(n) + \rightsquigarrow \end{aligned} \tag{20}$$

where $A = H,\ He$. Details of the CR model for H atom and corresponding cross sections can be found in ref. [60], while He atom has recently been introduced to study atmospheric entry in Jupiter atmosphere [18], closely following refs. [61, 62] for the construction of the level energies, and using state-specific electron impact cross sections reported in Ref. [63]. The transition probabilities of He have been taken from NIST's online database [64] while radiative-recombination cross sections have been calculated from Opacity Project's [65] theoretical photoionization cross-section using Milne's [66] relation.

For H atoms we also include the atom-atom excitation and ionization processes [67, 68]

$$\begin{aligned} &H(n) + H(1) \rightleftharpoons H(m) + H(1) \\ &H(n) + H(1) \rightleftharpoons H^+ + H(1) + e^- \end{aligned} \tag{21}$$

which are fundamental in the region just behind the shock front to produce the first electrons, so that the electron induced transitions become effective. Differently from traditional CR models, where the radiation absorption was considered by the way of the escape factor, we include separately photon emission, both spontaneous and stimulated, and absorption, calculated by the radiation transport module.

The model has been completed by adding the vibrational, dissociation and ionization kinetics of hydrogen molecules in the ground electronic state, induced either by molecule-molecule and atom-molecule collisions

$$\begin{aligned} &H_2(v) + H_2(w) \rightleftharpoons H_2(v+1) + H_2(w-1) \\ &H_2(v) + H_2 \rightleftharpoons H_2(w) + H_2 \\ &H_2(v) + H \rightleftharpoons H_2(w) + H \\ &H_2(v) + H_2 \rightleftharpoons 2H + H_2 \\ &H_2(v) + H \rightleftharpoons 2H + H \end{aligned} \tag{22}$$

The considered electron impact processes are: resonant vibrational excitation, ionization and dissociation for H_2 and ionization, dissociation and dissociative recombination

for H_2^+

$$\begin{aligned}
&H_2(v) + e^- \rightleftharpoons H_2(w) + e^- \\
&H_2(v) + e^- \rightleftharpoons e^- + H(n=1) + H(n=1,2,3) \\
&H_2(v) + e^- \rightleftharpoons H + H^+ + 2e^- \\
&H_2^+ + e^- \rightleftharpoons 2H^+ + 2e^- \\
&H_2^+ + e^- \rightleftharpoons H + H^+ + e^- \\
&H_2^+ + e^- \rightleftharpoons 2H
\end{aligned} \tag{23}$$

In the next subsection we report typical results of our self-consistent model simulating entry conditions in Jupiter atmosphere and comparing these results with those obtained assuming thin and thick plasmas and considering an entry speed of $M = 20$.

5.2 Mach 20

In this case we consider the Jupiter atmosphere ($H_2 : He = 89 : 11$) initially at $T_0 = 160$ K and $P_0 = 10$ Pa, corresponding to a free stream gas flow speed $v_0 \approx 18.4$ Km/s. After the shock front the gas temperature suddenly jumps to $T_g = 13,000$ K ($P = 4.6\,10^3$ Pa) promoting chemistry and excitation of internal states of both molecules and atoms. Figure 6(a) reports the behavior of the concentration of the different species as a function of the distance from the shock. We can see that in the range $0.1 \div 1$ m a plasma is produced with an high degree of dissociation and a modest ionization degree.

The behavior of the different temperatures, translational ones for the gas and the electrons, internal ones for the molecules and atoms is reported in fig. 6(b) as a function of the distance from the shock. The gas temperature T_g is directly obtained from the translational enthalpy, as a part of the solution algorithm of the Euler equations, while the electron temperature is calculated as $T_e = \frac{2\bar{E}_e}{3k}$ where $\bar{E}_e$ is the average translational electron energy associated to the non-equilibrium eedf. On the other hand, the internal temperatures T_H and T_{He} are determined interpolating with a Boltzmann distribution the populations of the ground and first excited state of the atoms, and of the $v = 0$ and $v = 1$ vibrational level populations for H_2 as obtained from the CR model. Internal temperatures, which essentially provide an estimate of the energy stored in the low energy part of the internal state distributions of atoms and molecules, are useful to perform comparison between the results of the present detailed state-to-state models and the multi-temperature models.

Again we note that in the distance range $0.1 \div 1$ m T_g, T_e and T_{H_2} converge to the same values as a result of the strong coupling between translation and vibrational temperatures, while the internal atom temperatures of both H and He present a non-monotone behavior. Figure 7(a) presents the distribution function of atomic H electronic levels as a function of level energy at different distances from the shock. We can see that the initial Boltzmann character of the distribution function is lost at small distances from the shock, becoming again Boltzmann at large distances.

More interesting is the behavior of the electron energy distribution function at different distances reported in fig. 7(b). In this case the non Maxwell character of eedf is well evident for both small and high distances from the shock. The plateaux present in eedf are due to superelastic collisions from cold electrons and the first excited state of atomic hydrogen, this action being more evident when the electron temperature is small. At high electron temperature (i.e. at 10 cm) the superelastic collisions are well evident even in the absence of the plateau.

To better understand the role of radiation, we compare the results obtained by the self-consistent approach (SC) with the corresponding ones obtained by decoupling the radiation transport from the kinetics i.e. by considering optically thin and thick

conditions for photon reabsorption. Figure 8(a) reports the molar fraction of the first excited state of hydrogen atom (principal quantum number $n = 2$) as a function of the distance from the shock calculated according to the three models (SC, thick, thin). We can see that SC and thick $H(n = 2)$ concentration tend to the same values for $x \geq 3$ cm their values being much higher compared to the thin case. On the other hand, at smaller distances the $H(n = 2)$ population predicted by the SC model is larger than the thick case due to the absorption of Lyman-α radiation generated in the emissive plasma region near the ionization maximum and moving towards the shock front. This effect, not present in both the plasma thick an thin cases, provides an additional excitation channel which can be important when the excitation by electron impact is slow due to very small electron concentrations. A similar behavior is presented by the molar fraction of electrons, fig. 8(b), that in any case keeps very small values.

Figure 9 reports the distribution functions of atomic hydrogen excited states calculated with the three models at different distances from the shock. Already at $d = 10$ cm thick and self-consistent concentrations coincide, being much higher than the corresponding thin concentrations. It should be also noted that in any case the internal state distributions thermalize only at $x = 20.7$ cm for thick and SC cases i.e. only when the concentration of electrons is high enough to promote electron collisions processes. The observed differences in the excited state concentrations are responsible of the structures appearing in the eedf at various distances as reported in fig. 10. These structures are much more pronounced in the thick and SC cases as a consequence of the higher concentrations of excited states in comparison to the thin case.

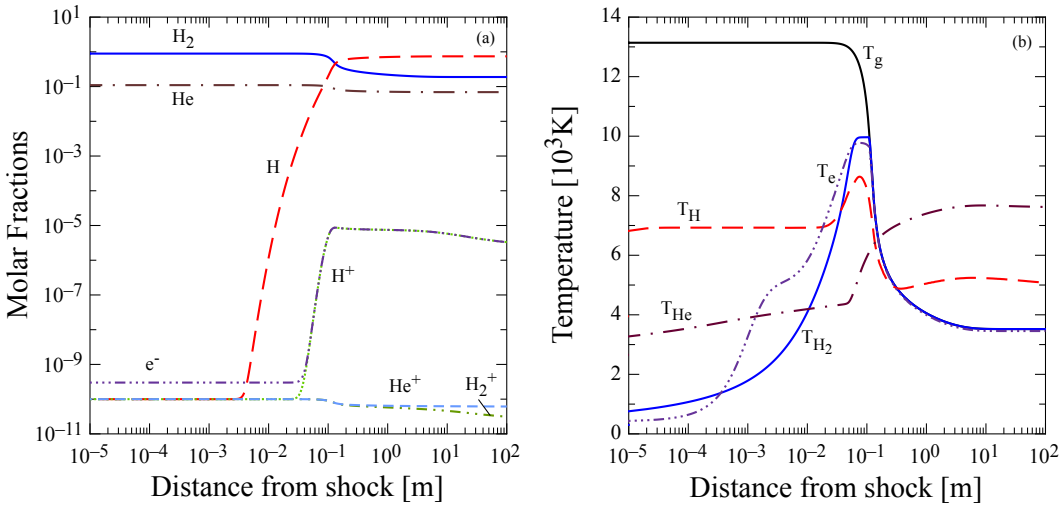

Figure 6: Post-shock molar fraction and temperature profiles as a function of the distance d from the shock front for $M = 20$.

6 Conclusions

In this paper we have summarized the main features and possible applications of our collisional-radiative models for the study of shock waves and its radiation in hypersonic flows and atmospheric entry plasmas.

A description of an hybrid collisional-radiative model developed in the Laboratory of Radiative Gas Dynamics, Moscow has been presented. The model combines a state-to-state description of molecular electronic states with a multi-temperature description of the remaining degrees of freedom, and solves the reactive Euler equations to determine flow parameters in the relaxation zone behind the shock front. The code can be applied to different gas mixtures, such as N_2-O_2, CO_2-N_2 and CH_4-N_2, using different kinetic models to study both nonequilibrium and equilibrium spectral intensities of radiation emitted by shock-heated gases. The code has already been used to analyze experimental shock tube results from different facilities around the world.

Next, an hybrid collisional-radiative model for ionized air, including a detailed scheme of electronically excited states of neutral N and O atoms has been described. Modeling of the partially ionized flow is carried out using a one-dimensional flow solver coupled with kinetic processes described by the collisional-radiative model and the radiative transfer equation. Explicit calculations of the population of the atomic electronic states are carried out using state-to-state gas kinetics and treating the quantum states of the atoms as separate pseudo-species. It was found that the electronic energy level populations of the N and O atoms depart from Boltzmann distributions because the high-lying bound electronic states are depleted. Another important factor in a realistic simulation of the ionized flow is the coupling of the kinetic equations with the radiative transfer equation, resulting in a fully consistent treatment of the radiation processes. Differences are found between the fully coupled result and uncoupled calculations using escape factors based on optically thick or optically thin models. Generally, the coupled result is closer to the optically thick model.

Finally, a one-dimensional steady shock wave model coupling a comprehensive CR model of a H_2/He plasma, a Boltzmann solver for the eedf and an RTE solver has been described. The model solves the steady state shock continuity equations, using the

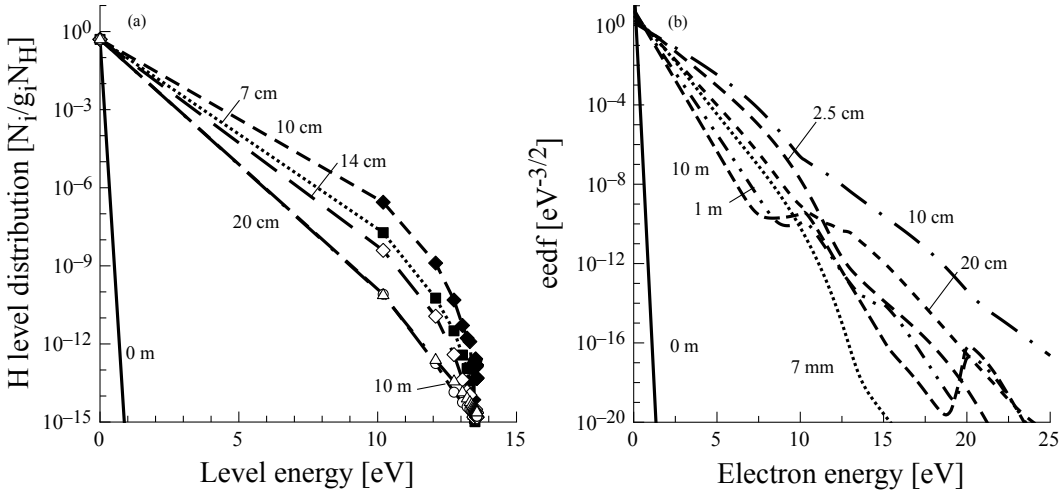

Figure 7: (a) isd of H atom and (b) eedf in the H_2/He plasma for $M = 20$.

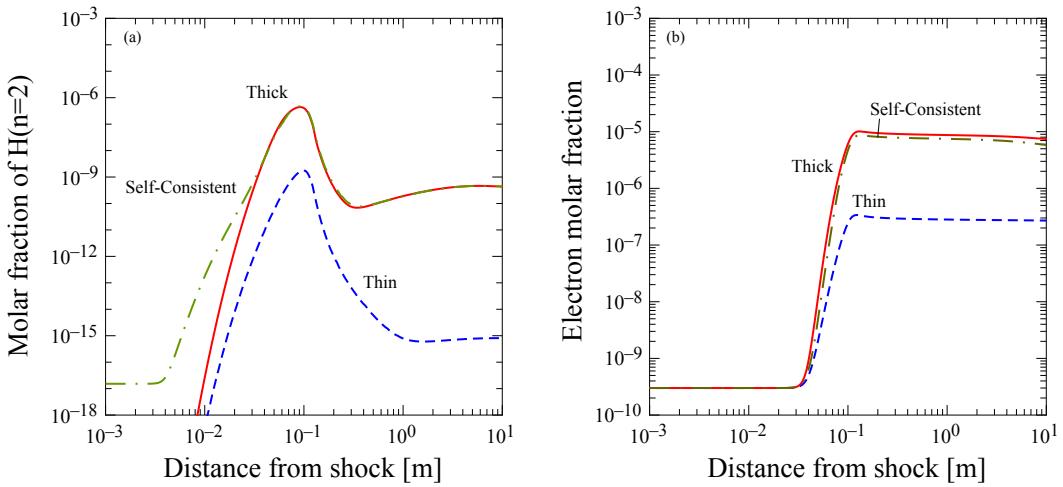

Figure 8: (a) Molar fraction profiles of the first excited state of the H atom and (b) electron molar fraction profiles for the $M = 20$ case.

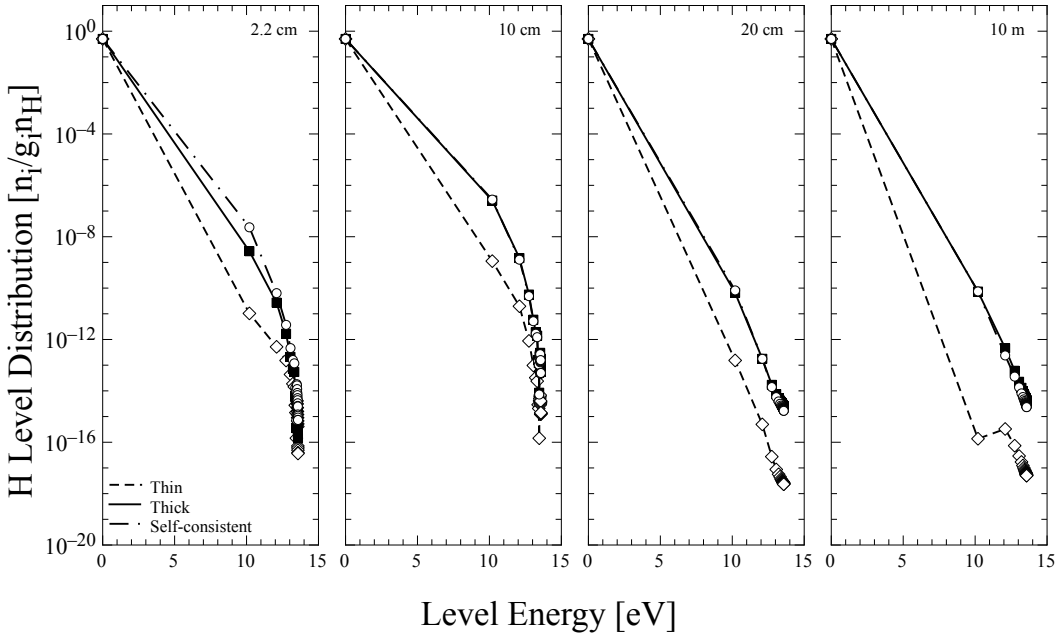

Figure 9: isd of the H atom in the post-shock region for the $M = 20$ case: comparison between optically thin, optically thick and self-consistent calculations.

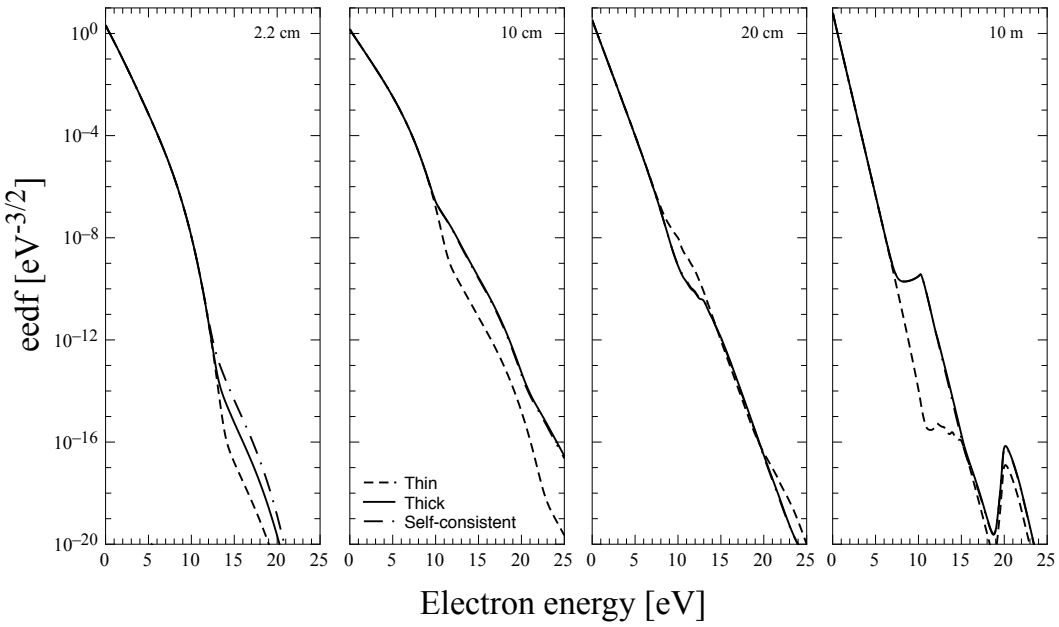

Figure 10: eedf in the post-shock region for the $M = 20$ case: comparison between optically thin, optically thick and self-consistent calculations.

CR model to determine the non-equilibrium chemical composition and the distribution of atomic and molecular excited states. Electron-impact rate coefficients are directly calculated integrating the relevant cross-section over the actual eedf determined by the Boltzmann solver, while radiative rate coefficients are self-consistently calculated using the local spectral intensity determined by the RTE solver. The model has been applied to study an high speed shock wave under conditions typical of a planetary entry in Jupiter's atmosphere. Dissipation of the shock energy happens mainly through dissociation of H_2 molecules and ionization of the resulting H atoms, while He atoms are scarcely excited/ionized.

Acknowledgements

The research leading to these results has received funding from the European Community's Seventh Framework Programme [FP7/2007/2013] under grant agreement n ° 242311.

References

[1] S. T. Surzhikov. Coupled radiation–gasdynamic model for sturdust aerothermodynamic data. *AIAA Paper*, AIAA 2010-4521.

[2] S. T. Surzhikov. Radiative–gasdynamic model of martian descent space vehicle. *AIAA Paper*, AIAA 2004-1355.

[3] S. T. Surzhikov. A study of the influence of kinetic models on calculations of the radiation-convective heating of a space vehicle in fire–II flight experiment. *Russian Journal of Physical Chemistry B*, 2(5):814–826, 2008.

[4] J.H. Grinstead, M.C. Wilder, M.J. Wright, D.W. Bogdanoff, G.A. Allen, K. Dang, and M.J. Forrest. Shock radiation measurements for mars aerocapture radiative heating analysis. *AIAA Paper*, AIAA 2008-1272.

[5] B.A. Cruden, D. Prabhu, R. Martinez, H. Le, D. Bose, and J.H. Grinstead. Shock radiation measurements for mars aerocapture radiative heating analysis. *AIAA Paper*, AIAA 2010-4508.

[6] H. Takayanagi and K. Fujita. Absolute radiation measurements behind strong shock wave in carbon dioxide flow for mars aerocaprure missions. *AIAA Paper*, AIAA 2012-2744.

[7] A.M. Brandis, R.G. Morgan, T.J. McIntyre, and P.A. Jacobs. Nonequilibrium radiation intensity measurements in simulated titan atmospheres. *J. Thermophys. Heat Transfer*, 24(2):291–300, 2012.

[8] P.V. Kozlov, Yu.V. Romanenko, and O.P. Shatalov. Radiation intensity measurement in simulated martian atmospheres on the double diaphragm shock tube. In ESA, editor, *Proc. of 4th International Workshop on Radiation of High Temperature Gases in Atmospheric Entry*, volume SP-689. ESA, 2010.

[9] S. P. Sharma, S. M. Ruffin, W. D. Gillespie, and S. A. Meyer. Vibrational relaxation measurements in an expanding flow using spontaneous raman scattering. *J. Thermophys. Heat Transfer*, 7(4):697–703, 1993.

[10] N. Siefert and G. Hebner. Shock velocity in a decaying nitrogen plasma shock velocity in a decaying nitrogen plasma. *AIAA Paper*, AIAA 2005-5381.

[11] N N Kudryavtsev, L A Kuznetsova, and S T Surzhikov. Kinetics and nonequilibrium radiation of CO_2-N_2 shock waves. *AIAA Paper*, AIAA 2001-2728.

[12] S T Surzhikov, I Sharikov, M Capitelli, and G Colonna. Nonequilibrium Radiation behind the Strong Shock Waves in Martian and Titan Atmospheres: Numerical Rebuilding of Experimental Data. *AIAA Paper*, AIAA 2006-0586.

[13] A S Dikalyuk, S T Surzhikov, O P Shatalov, P V Kozlov, and Yu V Romanenko. Nonequilibrium Radiation behind the Strong Shock Waves in Martian and Titan Atmospheres: Numerical Rebuilding of Experimental Data. *AIAA Paper*, AIAA 2012-0795.

[14] M. W. Huo, M. Panesi, and E. T. Magin. Ionization Phenomena behind Shock Waves. *Physical Phenomena in Shock Waves - Shock waves Springer*, 2011.

[15] M Panesi, T Magin, A Bourdon, A Bultel, and O Chazot. Analysis of the Fire II Flight Experiment by means of a Collisional Radiative ModelI Flight Experiment by means of a Collisional Radiative Model. *J. Thermophys. Heat Transfer*, 23(2): 236–248, April-June 2009.

[16] M Panesi, T Magin, A Bourdon, A Bultel, and O Chazot. Electronic Excitation of atoms and molecules for the Fire II Flight Experiment. *J. Thermophys. Heat Transfer*, 25(3):361–374, 2011.

[17] G. Colonna, L. D. Pietanza, and G. D'Ammando. Self-consistent collisional-radiative model for hydrogen atoms: Atom-atom interaction and radiation transport. *Chem. Phys.*, 398:37–45, 2012.

[18] G Colonna, G D'Ammando, L D Pietanza, and M Capitelli. Self-consistent coupling of chemical, electron and radiation models for shock wave in jupiter atmosphere. In *AIP Conference Proceedings*, volume 1501, pages 1400–1407, 2012.

[19] M. Capitelli, G. Colonna, and A. D'Angola. *Fundamental Aspects of Plasma Chemical Physics: Thermodynamics*, volume 66 of *Atomic, Optical, and Plasma Physics*. Springer, New York, 1st edition, 2011.

[20] G. Colonna, A. D'Angola, A. Laricchiuta, D. Bruno, and M. Capitelli. Analytical Expressions of Thermodynamic and Transport Properties of the Martian Atmosphere in a Wide Temperature and Pressure Range. *Plasma Chem. Plasma Process.*, 33(1):401–431, 2013. doi: 10.1007/s11090-012-9418-4.

[21] A. D'Angola, G. Colonna, C. Gorse, and M. Capitelli. Thermodynamic and transport properties in equilibrium air plasmas in a wide pressure and temperature range. *Eur. Phys. J. D*, 46(1):129–150, 2008.

[22] A S Dikalyuk and S T Surzhikov. Numerical Investigation of a Model of Nonequilibrium Radiation behind a Shock Front in the Martian Atmosphere. *Fluid Dyn.*, 48(1):123–140, 2013.

[23] I. V. Arsentiev, B. I. Loukhovitski, and A. M. Starik. Application of state-to-state approach in estimation of thermally nonequilibrium reaction rate constants in mode approximation. *Chem. Phys.*, 398:73–80, 2012.

[24] Aurélien Guy, Anne Bourdon, and Marie-Yvonne Perrin. Derivation of a consistent multi-internal-temperature model for vibrational energy excitation and dissociation of molecular nitrogen in hypersonic flows. AIAA 2013-0194, 2013.

[25] L A Kuznetsova and S T Surzhikov. Spectral radiation of shock waves and radiative models of diatomic molecules. *AIAA Paper*, AIAA 97-2564.

[26] C Park. *Nonequilibrium Hypersonic Aerothermodynamics*. Wiley, 1990.

[27] C Park. Review of Chemical-Kinetic Problems of Future NASA Missions, I: Earth Entries. *J. Thermophys. Heat Transfer*, 7(3):385–398, 1993.

[28] C Park, J T Howe, R L Jaffe, and G V Candler. Review of Chemical Kinetic Problems of Future NASA Mission. II Mars Entries. *J. Thermophys. Heat Transfer*, 8(1):9–23, 1994.

[29] S A Losev, V N Makarov, and M Yu Pogosbekyan. Model of the physico-chemical kinetics behind the front of a very intense shock wave in air. *Fluid Dyn.*, 20(2): 299–309, 1995.

[30] P. Teulet, J.-P. Sarrette, and A.-M. Gomes. Calculation of electron impact inelastic cross sections and rate coefficients for diatomic molecules. Application to air molecules. *J. Quant. Spectrosc. Ra.*, 62:549–569, 1999.

[31] C Park. Rate Parameters for Electronic Excitation of Diatomic Molecules I. Electron-Impact Processes. *AIAA Paper*, AIAA 2008-1206.

[32] A. M. Starik, N S Titova, and I. V. Arsentiev. Comprehensive analysis of the effect of atomic and molecular metastable state excitation on air plasma composition behind strong shock waves. *Plasma Sources Sci. Technol.*, 19:015007, 2010.

[33] A. S. Sharipov and A. M. Starik. Kinetic mechanism of CO-H_2 system oxidation promoted by excited singlet oxygen molecules. *Combust. Flame*, 159(1):16–29, 2012.

[34] D C Cartwright. Rate coefficients and inelastic momentum transfer cross sections for electronic excitation of N_2 by electrons. *J. Appl. Phys.*, 49(7):3855–3862, 1978.

[35] C Park. Rate Parameters for Electronic Excitation of Diatomic Molecules II. Heavy Particle Impact Processes. *AIAA Paper*, AIAA 2008-1446.

[36] S Harrison and J Tennyson. Electron collisions with CN radical: bound states and resonances. *J. Phys. B: At. Mol. Opt. Phys.*, 45:035204, 2012.

[37] G G Cherniy and S A Losev. *Physical-chemical processes in gas dynamics: reference book*. MSU publishing, Moscow, 1995.

[38] K T Zeidler and D Koester. On the "Just Overlapping Line Approximation" for Molecular Absorption. *Astron. Astrophys.*, 113:173–175, 1982.

[39] G N Zalogin, P V Kozlov, L A Kuznetsova, S A Losev, V N Makarov, Yu V Romanenko, and S T Surzhikov. Radiation Excited by Shock Waves in a CO_2-N_2-Ar Mixture: Experiment and Theory. *Tech. Phys.*, 46(6):654–661, 2001.

[40] C.-O. Johnston. *Nonequilibrium Shock-Layer Radiative Heating for Earth and Titan Entry*. PhD thesis, Virginia Polytechnic Institute and State University , Virginia, 2006.

[41] Y. Zeldovich and Y Raizer. *Physics of Shock Waves and High Temperature Hydrodynamic Phenomena*. Academic Press Inc., Berkley Square House, London, 1966.

[42] C. Park. *Nonequilibrium Hypersonic Aerothermodynamics*. John Wiley and Sons, New York, 1990.

[43] M. Panesi, R. L. Jaffe, D. Schwenke, and E. T. Magin. Rovibrational internal energy transfer and dissociation of N_2-N system in hypersonic flows. *J. Chem. Phys.*, 138: 044312, 2013.

[44] T. E. Magin, M Panesi, A. Bourdon, R. Jaffe, and D. Schwenke. Uniform rovibrational collisional coarse-grain model for internal energy excitation and dissociation of molecular nitrogen. *J. Chem. Phys.*, 2011.

[45] D. Schwenke. Dissociation cross-sections and rates for nitrogen. *VKI LS 2008, Nonequilibrium Gas Dynamics, from Physical Models to Hypersonic Flights* - Rhode-Saint-Genése, Belgium, 2008.

[46] W. C. Martin, J. R. Fuhr, D. R. Kelleher, A. Masgrove, J. Sugar, and W. L. Wiese. Nist atomic spectra database (version 2.0). *Avaliable from: http://physics.nist.gov/asd2 Gaihersburg*, 1999.

[47] L.V. Gurvich, I.V. Veyts, and C.B. Alcock. Thermodynamic properties of individual substances. *Hemisphere Publishing Corporation*, 1, 1989.

[48] A Bultel, B G Chéron, A Bourdon, O Motapon, and I F Schneider. Collisional-radiative model in air for earth re-entry problems. *Phys. Plasmas*, 13(4):11, 2006.

[49] P Teulet, J P Sarrette, and A M Gomes. Collision-radiative modeling of one- and two- temperature air and air-sodium plasmas at atmospheric pressure with temperatures of 2000 - 12000 K. *J. Quant. Spectrosc. Ra.*, 1:70–159, 2001.

[50] J P Sarrette, A M Gomes, J Bacri, C O Laux, and C H Kruger. Collisional-radiative modelling of quasi-thermal air plasmas with electronic temperatures between 2000 and 13,000 K–I. $\Theta_e > 4000$ K. *J. Quant. Spectrosc. Ra.*, 53(2):125–141, 1995.

[51] G Colonna and M Capitelli. The influence of atomic and molecular metastable states in high-enthalpy nozzle expansion nitrogen flows. *J. Phys. D: Appl. Phys.*, 34:1812, 2001.

[52] G Colonna, M Tuttafesta, M Capitelli, and D Giordano. Non-arrhenius NO formation rate in one-dimensional nozzle airflow. *J. Thermophys. Heat Transfer*, 13(3): 372–375, 1999.

[53] G Colonna and M Capitelli. Self-consistent model of chemical, vibrational, electron kinetics in nozzle expansion. *J. Thermophys. Heat Transfer*, 15(3):308–316, 2001.

[54] Carlo A. Borghi, Mario R. Carraro, Andrea Cristofolini, Abraham Veefkind, Leonardo Biagioni, Gabriele Fantoni, Andrea Passaro, Mario Capitelli, and Gianpiero Colonna. Magnetohydrodynamic interaction in the shock layer of a wedge in a hypersonic flow. *IEEE Trans. Plasma Sci.*, 34:2450–2463, 2006.

[55] Gianpiero Colonna and Mario Capitelli. Boltzmann and master equations for magnetohydrodynamics in weakly ionized gases. *J. Thermophys. Heat Transfer*, 22(3): 414–423, 2008.

[56] I Armenise, M Capitelli, G Colonna, N Koudriavtsev, and V Smetanin. Nonequilibrium vibrational kinetics during hypersonic flow of a solid body in nitrogen and its influence on the surface heat-flux. *Plasma Chem. Plasma Process.*, 15(3):501–528, 1995.

[57] G Colonna and M Capitelli. Electron and vibrational kinetics in the boundary layer of hypersonic flow. *J. Thermophys. Heat Transfer*, 10(3):406–412, 1996.

[58] D Giordano, V Bellucci, G Colonna, M Capitelli, I Armenise, and C Bruno. Vibrationally relaxing flow of N_2 past an infinite cylinder. *J. Thermophys. Heat Transfer*, 11(1):27–35, 1997.

[59] M. Capitelli, I. Armenise, D. Bruno, M. Cacciatore, R. Celiberto, G. Colonna, O. De Pascale, P. Diomede, F. Esposito, C. Gorse, K. Hassouni, A. Laricchiuta, S. Longo, D. Pagano, D. Pietanza, and M. Rutigliano. Non-equilibrium plasma kinetics: a state-to-state approach. *Plasma Sources Sci. Technol.*, 16:S30–S44, 2007.

[60] G Colonna, L D Pietanza, and M Capitelli. Coupled solution of a time-dependent collisional-radiative model and boltzmann equation for atomic hydrogen plasmas: possible implications with LIBS plasmas. *Spectrochim. Acta, Part B*, 56:587–598, 2001.

[61] T Fujimoto. A collisional-radiative model for helium and its application to a discharge plasma. *J. Quant. Spectrosc. Ra.*, 21:439–455, 1979.

[62] M Goto. Collisional-radiative model for neutral helium in plasma revisited. *J. Quant. Spectrosc. Ra.*, 76(3-4):331–344, 2003.

[63] Yu Ralchenko, R K Janev, T Kato, D V Fursa, I Bray, and F J de Heer. Electron-impact excitation and ionization cross sections for ground state and excited helium atoms. *Atom. Data Nucl. Data*, 94:603–622, 2008.

[64] A Kramida, Yu Ralchenko, J Reader, and NIST ASD Team. *NIST Atomic Spectra Database (version 5.0)*. National Institute of Standards and Technology, Gaithersburg, MD, 2012.

[65] OP Team. *The Iron Project - The Opacity Project*, 2012. URL http://cdsweb.u-strasbg.fr/topbase/topbase.html.

[66] D Mihalas and B W Mihalas. *Foundations of Radiation Hydrodynamics*. Dover Publications, 1999.

[67] H W Drawin. Influence of atom–atom collisions on the collisional-radiative ionization and recombination coefficients of hydrogen plasmas. *Zeitschrift fur Physik*, 225 (5):483–493, 1969.

[68] H W Drawin and F Emard. Atom-atom excitation and ionization in shock waves of the noble gases. *Phys. Lett. A*, 43(4):333–335, 1973.

Radiation Models and Radiation Transfer in Hypersonics

M.Y. Perrin *[1], G. Colonna[2], G. D'Ammando[3], L. D. Pietanza[2], Ph. Riviere[1], A. Soufiani[1], and S. Surzhikov[4]

[1]CNRS, UPR 288 Laboratoire d'Energétique Moléculaire et Macroscopique, Combustion (EM2C), Grande Voie des Vignes, 92295 Châtenay-Malabry, France
[2]CNR-IMIP, Via Amendola 122/D, 70126 Bari, Italy
[3]Dipartimento di Chimica, Universitá degli studi di Bari, Via Orabona 4, 70125 Bari, Italy
[4]A. Ishlinsky Institute for Problems in Mechanics, Russian Academy of Sciences, Prospect Vernadskogo 101-1, Moscow 119526, Russia

Abstract

The paper presents radiation models developed to investigate radiation in entry in earth, Mars and Jupiter atmospheres. The capacity of ASTEROID computing code to simulate elementary radiative processes, calculate spectral and groups optical properties, and also solve simple radiative heat transfer problems is presented for earth entry. The large number of radiative processes involved in the radiative flux is put forward. The contributions of the different radiative processes encountered in Mars entry are studied using the HTGR spectroscopic database. The accuracy of this database with respect to diatomic molecules systems and CO_2 infrared radiation is illustrated through experimental validations. The accuracy of statistical narrow-band model to predict radiative flux is illustrated for an afterbody. Finally recent improvements of the model developed for the calculation of radiative properties of high-temperature H_2/He mixtures representative of Jupiter atmosphere is presented. The model takes into account the most important radiative processes.
Keywords: Spectroscopic databases, Radiative transfer, Re-entry flows

*Corresponding author. E-mail: marie-yvonne.perrin@ecp.fr

1 Introduction

During an atmospheric entry, a shock layer is created in front of the vehicle. The hot gases in this shock layer emit a radiation that contribute to the incident flux at the vehicle surface. A correct evaluation of this flux is needed to design the thermal protection shield of the vehicle, especially at very high entry speed. The present paper describes recent advancements and associated numerical codes used for evaluation of radiation in hypersonic flows encountered in earth, Mars and Jupiter atmospheric entries. Several radiative mechanisms are involved, which give rise to a complex structure of the emission and absorption spectra. Bound-bound transitions in atoms and molecules give line spectra. Free-free transitions contribute to a continuous spectrum. Bound-free transitions result in a continuous spectrum with eventually some structures. The selection of the radiative mechanisms and associated spectroscopic data is a critical issue. All the processes which may contribute to emission and absorption have to be considered. Due to the wide temperature range that can be encountered (up to 80 000 K for entry applications), the spectral range has to cover Infrared (IR) to Vacuum Ultra-Violet (VUV). Ideally, the monochromatic local emission and absorptions coefficients, which depends on the the internal sates of the gas in the non-equilibrium shock layer, have to be known to determine the radiative flux. However, models of radiative properties may be of interest for practical applications. It should be noted that radiation may also modify the gas dynamics. The emitted photons can either leave the flow or can be re-absorbed, contributing to the transport of energy. Under some conditions, the processes of emission and absorption of photons have to be included in the equations describing the evolution of atomic and molecular internal states. Modeling radiation in hypersonics is not an easy task, which explains the development of several computer codes and spectral databases in the last decades : NEQUAIR [1], LORAN [2], SPRADIAN [3], MONSTER [4], SPECAIR [5], PARADE [6], HARA [7], GPRD [8].
The paper presents recents efforts of three groups to progress in the field. Section 2 gives a brief description of the ASTEROID computing code developed in Russia for the numerical simulation of elementary radiative processes, calculation of spectral and groups optical properties, and also for solving simple radiative heat transfer problems. As an example, the calculated half-spherical emissivity of high temperature air, which can be used to estimate radiative heating of space vehicles entering into atmospheric dense layers, is presented. Section 3 presents the HTGR spectroscopic database developed in France which aims at modelling high resolution radiation. Applications to CO_2/N_2 mixtures representative of Mars atmosphere are presented. Section 4 presents recent improvements of the model developed in Italy for the calculation of radiative properties of high-temperature H_2/He mixtures representative of Jupiter atmosphere, taking into account the most important radiative processes.

2 ASTEROID and Earth Atmosphere Entry Plasma

Notwithstanding the fact that the theory and the practice for the calculation of elementary and statistical radiative properties of low temperature plasma and hot gases have been developing for more than a half century [9–13], the devel-

opment of reliable spectral optical models for radiative gas dynamics and heat transfer application is still an issue. Modern computing technologies give new methods for improvement of calculations [14, 15]. The ASTEROID computing code has been developed for solving a wide class of problems that are linked with radiation heat transfer in hot gases and low-temperature plasmas namely :

1. numerical simulation of elementary radiation processes cross-sections;
2. creation of spectral, multi-group, integral and combined models of absorption and emission coefficients;
3. creation of the optimum multi-group radiative models for low-temperature plasma and hot gases;
4. numerical simulation of spectral radiative heat transfer in simple cases i.e of plane, cylindrical and spherical volumes.

The following sections give a brief description of this code and a few examples of application.

2.1 Brief description of models and code

The optical and radiative models can be created for temperatures T ranging from 300 K to 20 000 K and more, for pressures p up to 100 atm and for wavenumbers in the range 1000÷500 000 cm^{-1}. Presently, the ASTEROID code contains spectroscopic information and numerical simulation models for the following chemical elements: H, He, C, N, O, Si, Ar, Na, Mg, Al, K, Ca. The ASTEROID code is available in two versions.
The first one is actually the computing platform intended for comparative investigation of different quantum mechanical and quasi-classical models of elementary radiative processes. It is well known that a specific property of radiative gas dynamics is the necessity to take into account a large number of elementary radiative processes in a wide temperature region. To describe each of individual radiative processes a set of theoretical and computational models have been developed, from detailed ab-initio models down to approximate quasi-classical and half-empirical ones. Each of the models has a defined field of application. Most universal ab-initio quantum mechanical Hartree-Fock models of multi-channel interactions are intended for description of the fine structure of absorption and emission spectra. These models are very time-consuming, and therefore could not be included into complex radiative gas dynamic codes. On the other side, simplified semi-empirical and quasi-classical models can be used together with gasdynamic and kinetic codes, because of their high computational efficiency, but, unfortunately, they could not describe several significant peculiarities of radiative processes. Consequently the creation of integrated radiative gas dynamic codes, which include models of gasdynamics, chemical and physical kinetics, as well as radiation heat transfer models and models of spectral (or group) optical properties, always conjugates with choice of alternative approaches.
The second version of ASTEROID, which is called ABSORB, is a significantly simplified version of the first one. ABSORB is intended for calculation of spectral and group optical models in the frame of radiative gas dynamic codes. It is assumed that models included into the code have been tested by comparison

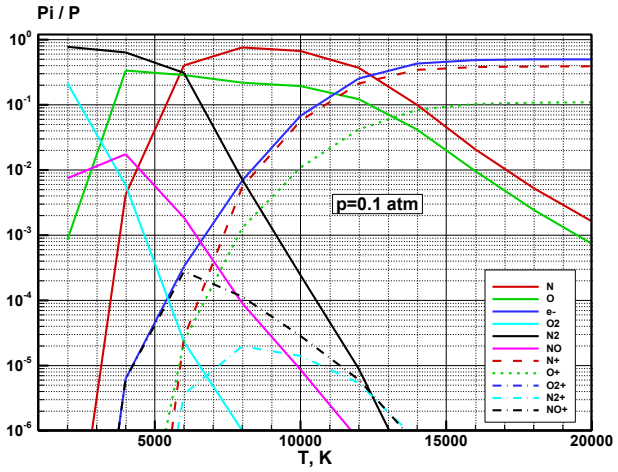

Figure 1: Molar fractions of air species ($x_i = \frac{p_i}{p}$) at pressure p=0.1 atm.

with other alternative models of ASTEROID code, as well as with available experimental data. Initial data for ABSORB (temperature, species concentrations, total pressure) are prepared after solution of gasdynamic equations, species and energy conservation equations. As for initial conditions for ASTEROID code, three files for the initial data are accordingly available. The first one contains initial data, specifying chemical composition of the considered mixture of gases and a scale of temperatures; the second file contains initial data, specifying number and the sizes of each spectral group, and also number of points on wavenumber in limits of each spectral group; and the third file contains initial data, specifying geometry of volume, and also distribution of temperature in this volume.
The principles of fundamental spectroscopy form the basis of the ASTEROID code. Therefore a database of energy levels of atoms and ions [16, 17], as well as a database of energy levels of diatomic molecules and ions [18], also used for the calculation of probabilities of elementary radiative processes, and the atomic and molecular lines parameters are included.

The ASTEROID code creates data files containing the information for the equilibrium chemical composition, optical group models, and also group and integrated characteristics of radiation transfer. Figure 1 shows an example of calculations of equilibrium chemical composition of high temperature air at pressure p=0.1 (double ionization of atoms is not taken into account).

The ASTEROID computing platform contains several auxiliary programs, which cannot be integrated in the computing system because they are highly laborious or cumbersome to use. The results obtained by these programs are used to create local databases, or to compare with results obtained by any alternate programs. These programs are dedicated to the calculation of :

1. Franck-Condon-factors;

2. parameters of RKR-potential of diatomic molecules;

3. rotational lines parameters of diatomic molecules;
4. vibrational wave functions of diatomic molecules;
5. radial wave functions of atoms and ions;
6. parameters for atoms and ions lines;
7. fine structure for the absorption and emission spectrum of diatomic molecules;
8. absorption coefficients for diatomic molecules averaged on rotational and vibrational structures;
9. absorption coefficients averaged on the rotational structure of multi-atomic molecules in the infrared area of a spectrum;
10. absorptivity (or transmissivity) of non-uniform gas layers assuming thin rotational structure of a spectrum of diatomic molecules. These codes use "line-by-line" methods, and also various random models;
11. absorptivity (or transmissivity) of non-uniform layers of low-temperature plasma based on atomic lines. These codes use "line-by-line" methods, and also various random models.

The ASTEROID computing platform allows to investigate not only basic models of elementary radiative processes but also to conjugate its simplified version (code ABSORB) with other models of radiative gas dynamics.

2.2 Use of integral half-spherical emissivities to estimate radiative heating

When solving applied problems of aerophysics, there is often a need of fast estimations of radiative heating of entering space vehicles without solving the full system of radiative gas dynamic equations. This can be done for 'standard' mixtures like air, CO_2-N_2 (97%-3%), etc. The method includes a few simple steps. On a first step, an estimation of shock wave stand-off distance δ is calculated with the approximate formula [19]:

$$\delta = \frac{\epsilon R}{1+\sqrt{8\epsilon/3}}, \epsilon = \frac{\rho_\infty}{\rho_w}, \tag{1}$$

where ρ_∞ and ρ_w are the densities in the free stream flow and at the surface. R is the blunt body nose radius.
On a second step, temperature and pressure are calculated in the equilibrium zone of the shock layer behind the shock wave. A model of thermodynamic equilibrium can be used for this purpose. Assuming an homogeneous volume, the half-spherical integral emissivity ϵ_0 of the corresponding 'standard' mixture is calculated from the shock layer depth, approximated by δ, its temperature and pressure according to :

$$\epsilon_0 = \frac{\pi}{\tilde{\sigma}T^4}\int_{\sigma_{min}}^{\sigma_{max}}(1-\exp(-\kappa_\sigma\delta))I_\sigma^b d\omega, \tag{2}$$

where κ_σ is the spectral absorption coefficient and σ_{min} and σ_{max} are the wave numbers corresponding to the boundaries of the heat radiation spectral region.

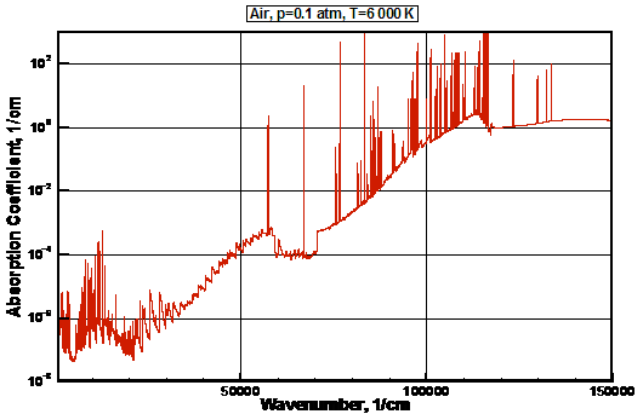

Figure 2: Spectral absorption coefficient of air at p=0.1 atm and T=6 000 K.

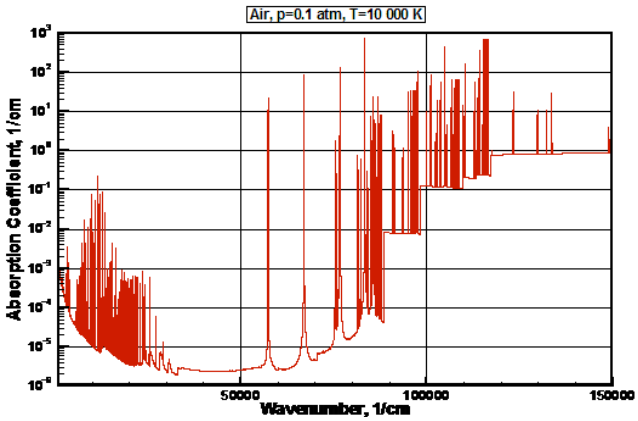

Figure 3: Spectral absorption coefficient of air at p=0.1 atm and T=1 0000 K.

I_σ^b is the equilibrium intensity given by the Planck's law and $\tilde{\sigma}$ is the Stephan-Boltzmann constant.
The radiative flux can be determined by:

$$q_{rad} = \epsilon_0 \tilde{\sigma} T^4 \tag{3}$$

Spectral absorption coefficients κ_σ of high temperature air, calculated with the code ASTEROID in 10^6 spectral points, are presented in Figs. 2 and 3 for two temperatures. These thermodynamic points are quite typical for problems of radiative heating of entering space vehicles. Half-spherical emissivities of high temperature air are presented in Figs. 4-6. Each of the figures shows half-spherical emissivity at three pressures calculated with and without atomic lines structure. It should be noted that taking into account the line structure of emission and absorption spectra is one of unsolved problems of radiative gas dynamics with strong radiative-gasdynamic interaction.

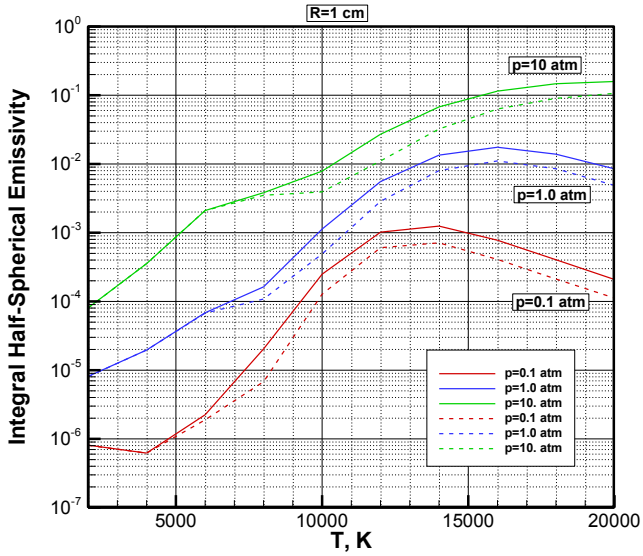

Figure 4: Half-spherical integral emissivity of high temperature air with (solid lines) and without (dashed lines) atomic lines at R=1 cm.

Figures 7- 9 show cumulative distributions defined by

$$Q(\sigma) = \frac{\pi}{\tilde{\sigma} T^4} \int_{\sigma_{min}}^{\sigma} (1 - \exp(-\kappa_\sigma \delta)) I^b_\sigma d\omega \tag{4}$$

where σ_{min}=1000 cm^{-1} is the minimal wavenumber for integration. These cumulative functions allow to demonstrate the most significant spectral subregions contributing to the integral emissivity. For example, at temperature T=6 000 K and pressure p=0.1 atm (see cumulative function in Fig. 7) radiative processes in the spectral subregion 10 000÷55 000 cm^{-1} give general contribution to integral emissivity, while at T=12 000 K radiative processes located in spectral subregion 60 000÷120 000 cm^{-1} become most significant. The spectral distributions of individual radiation processes, shown in Figs. 10 and 11 , allow to identify the most significant radiative processes. In the case under consideration photoionization from bound states of atoms N and O, as well as resonant atomic lines are most significant at T=12 000 K. At T=6 000 K, the electronic bands of diatomic molecules and radicals (N_2, O_2, NO) are most significant.

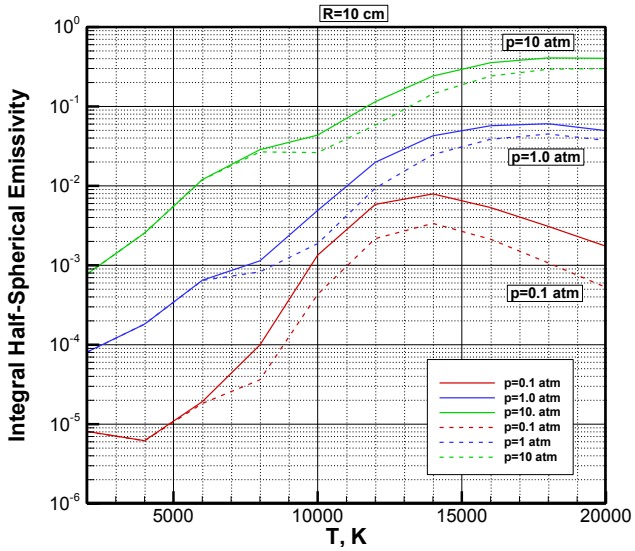

Figure 5: Half-spherical integral emissivity of high temperature air with (solid lines) and without (dashed lines) atomic lines at R=10 cm.

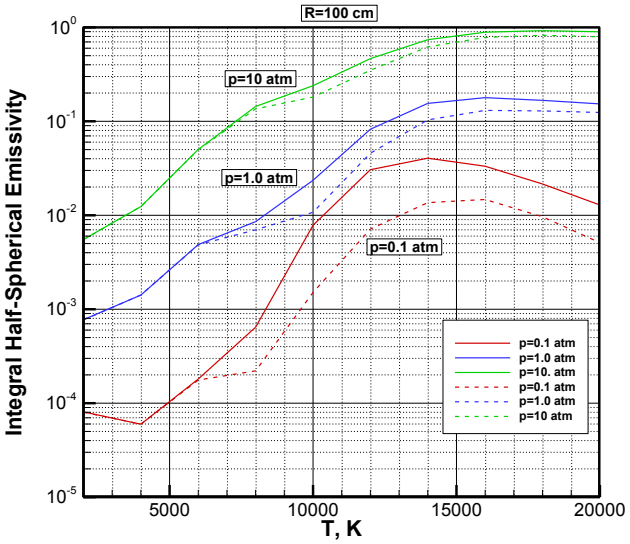

Figure 6: Half-spherical integral emissivity of high temperature air with (solid lines) and without (dashed lines) atomic lines at R=100 cm.

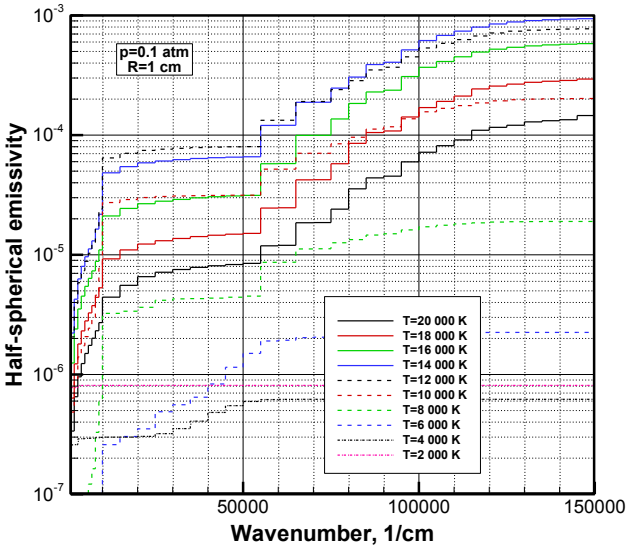

Figure 7: Cumulative functions of spectral half-spherical emissivity at p=0.1 atm and R=1 cm.

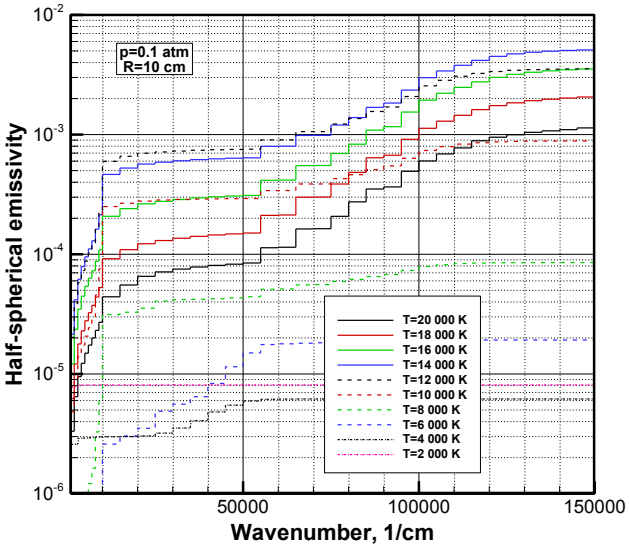

Figure 8: Cumulative functions of spectral half-spherical emissivity at p=0.1 atm and R=10 cm.

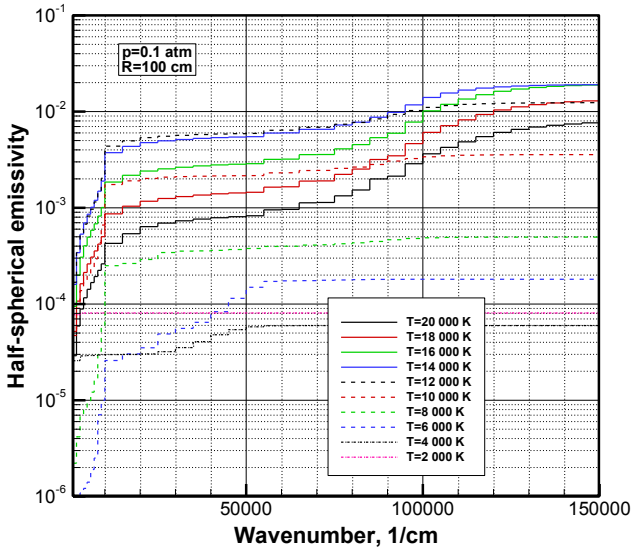

Figure 9: Cumulative functions of spectral half-spherical emissivity at p=0.1 atm and R=100 cm.

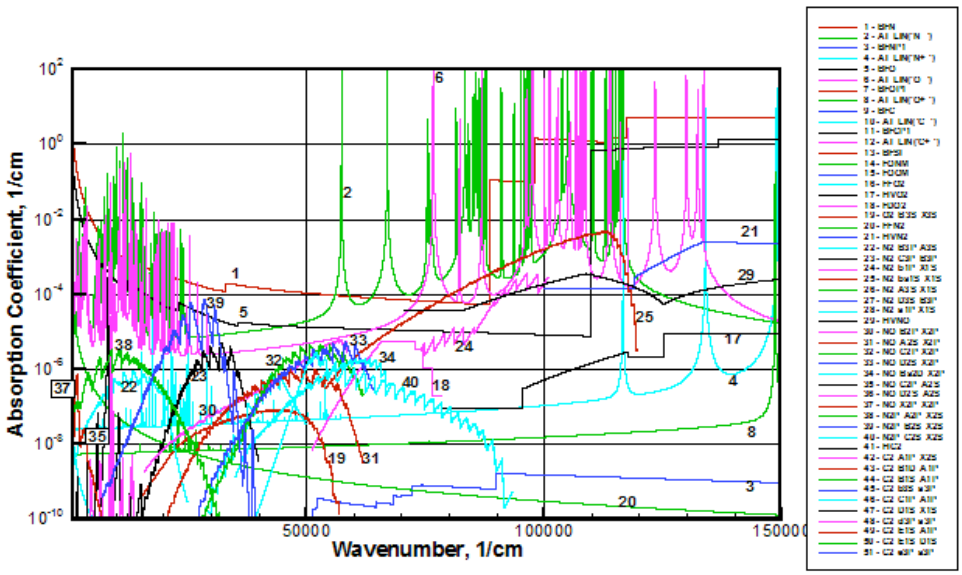

Figure 10: Partial contribution of individual radiative processes to the total absorption coefficient of high temperature air at p=1 atm, T=12000 K.

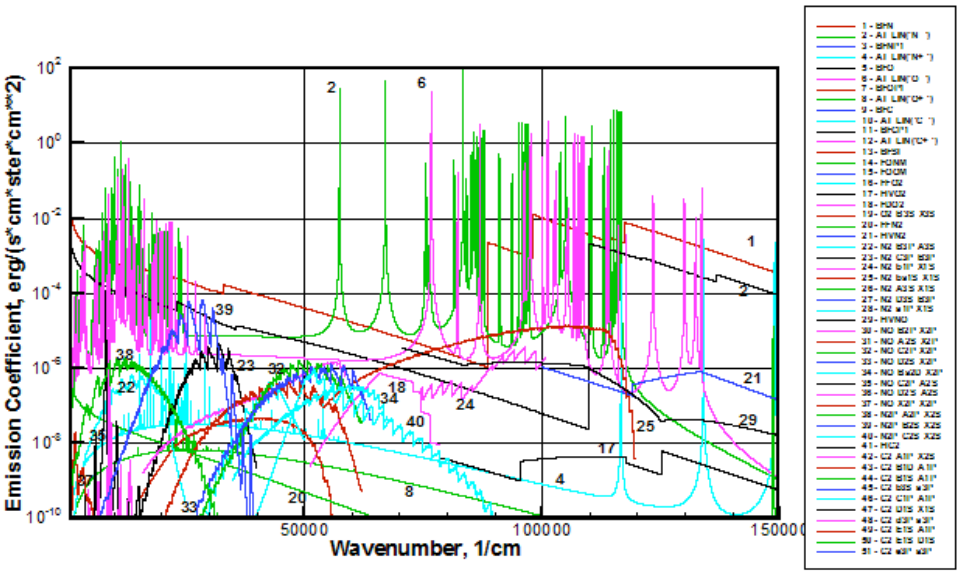

Figure 11: Partial contribution of individual radiative processes to the total emission coefficient of high temperature air at p=1 atm, T=12000 K .

3 HTGR and Mars Atmosphere Entry Plasma

3.1 HTGR radiation database

The HTGR spectroscopic database have been originally developed to describe radiative processes in air [20, 21]. Later, it has been extended to include radiative processes observed in CO_2-N_2 plasma [22] and is continuously complemented with new species and radiative processes. Atomic species line-strengths and line-positions are taken from the NIST database [17]. As many atomic lines can be optically thick in the considered applications, their line shapes have to be carefully determined. Systematic calculations have been performed in the impact approximation to account for the different collisional broadening mechanisms [23].The database includes 35 electronic systems of N_2, O_2, NO, N_2^+, CO, CO^+, C_2 and CN molecules. A systematic approach is used to calculate diatomic spectroscopic data [20]. Line positions are taken from the literature in order to have a good accuracy. The RKR procedure is used to reconstruct the intramolecular potential. The radial Schrodinger equation is solved to get rotationless-vibrational wavefunctions which are combined to critically selected ab-initio or experimental electronic transition moment functions to obtain the line strengths. The atomic species photoionization cross sections are taken from the Opacity Project (OP) [24]. Molecular photoionization, molecular photodissociation and negative atomic ions photodetachment are modelled pragmatically [21, 22]. Free-free transitions are included. The knowledge of very high temperature absorption and emission spectra of triatomic molecules like CO_2 remains a challenge. The recent CDSD-4000 database [25] has been selected.
The HTGR database allows to calculate the spectral characteristics, in particular the spectral emission and absorption coefficients, η_σ and κ_σ, on a wide spectral range, 1000 - 200 000 cm^{-1}, by a line-by-line approach from local thermochemical state and level populations. Figure 12 shows the absorption spectrum of equilibrium CO_2(97%)-N_2(3%) plasma, which composition is representative of Mars atmosphere, at 1 atm and 5000K. Fig 13 shows the optically thin emission defined by:

$$S_R = \int \kappa_\sigma I_\sigma^b d\sigma \tag{5}$$

Are also shown in Fig 13 the contributions due to atomic bound-bound processes, diatomic bound-bound processes, continuum processes and CO_2 infrared radiation. In the backside of a capsule entering Mars atmosphere, the temperature is limited to 4000K, the radiation will be due mainly to CO_2 In the front side, the temperature in the shock layer is typically in the range [2000 -7000] K. The contribution of CO_2 infrared radiation is important up to 4000K; the radiation is due to diatomic bound-bound processes above. These two types of radiative processes are more thoroughly discussed in the following sections.

3.2 Carbonaceous diatomic mole-cules

The spectra of carbonaceous diatomic molecular sytems have been studied both theoretically and experimentally. The most important electronic systems for e.g. Martian entries are those of CO (Infrared, fourth posistive $A^1\Pi - X^1\Sigma^+$, Hopfield-Birge $B^1\Sigma^+ - X^1\Sigma^+$, and third Positive $b^3\Sigma^+ - a^3\Pi$), of CN (Red $A^2\Pi_i - X^2\Sigma^+$, Violet $B^2\Sigma^+ - X^2\Sigma^+$, and LeBlanc $B^2\Sigma^+ - A^2\Pi_i$), of CO^+

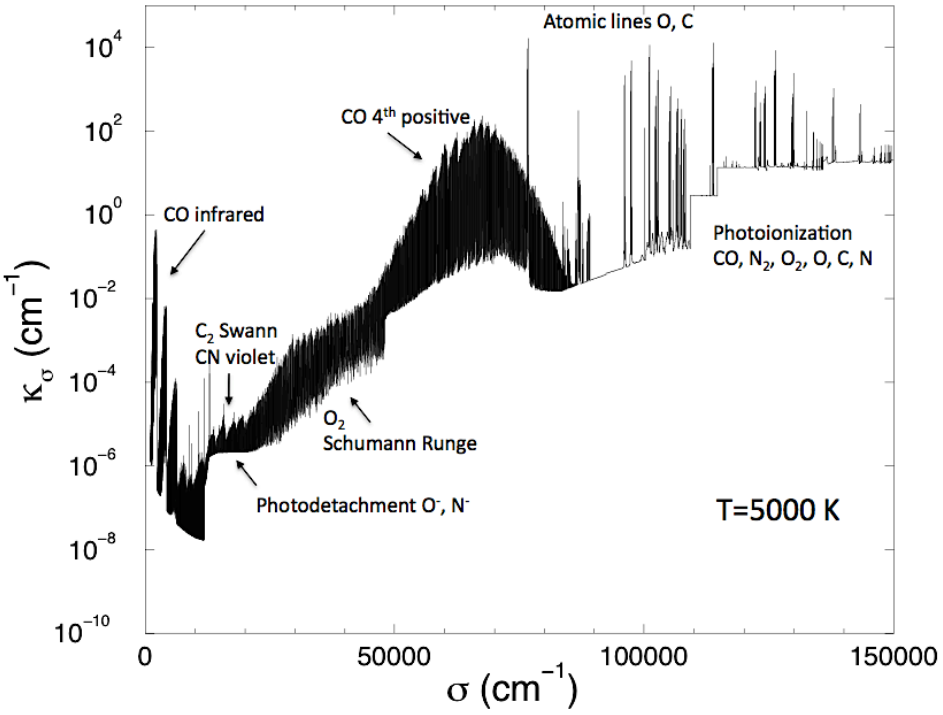

Figure 12: Absorption spectrum of equilibrium CO_2(97%)-N_2(3%) plasma at 1 atm and 5000K.

(Comet-tail $A^2\Pi_i - X^2\Sigma^+$, Baldet-Johnson $B^2\Sigma^+ - A^2\Pi_i$, and First Negative $B^2\Sigma^+ - X^2\Sigma^+$), and of C_2 (Philips $A^1\Pi_u - X^1\Sigma_g^+$, Mulliken $D^1\Sigma_u^+ - X^1\Sigma_g^+$, Deslandres-D'Azambuja $C^1\Pi_g - A^1\Pi_u$, Swann $d^3\Pi_g - a^3\Pi_u$, Ballik-Ramsay $b^3\Sigma_g^- - a^3\Pi_u$, and Fox-Herzberg $e^3\Pi_g - a^3\Pi_u$). Theoretical calculations have been carried out using the RKR method for internuclear potential reconstruction, a spectral Chebyshev method for the determinantion of vibrational wave functions from the radial Schrödinger equation, and using up-to-date available electronic transition moment functions [22].

Some of these systems have been studied experimentally using optical emission spectroscopy and a microwave plasma flow confined in a quartz tube [26]. Figure 14 shows an example of comparison between absolute local (Abel inverted) measured emission coefficient and the predicted coefficient from HTGR databse for the C_2 Swan system. The spectral range in this figure corresponds to vibrational bands characterized by $\Delta v = v' - v'' = 1$. The agreement between the predictions and the experimental calibrated spectrum is very satisfactory. The HTGR database possesses a spectroscopic accuracy which allows its use in optical diagnostics. Figure 15 shows an example of comparisons between normalized spectra in the spectral range corresponding to the CN violet $\Delta v = -1$ vibrational bands. The adjustment of the measured spectrum enables quite accurate determination of vibrational and rotational temperatures.

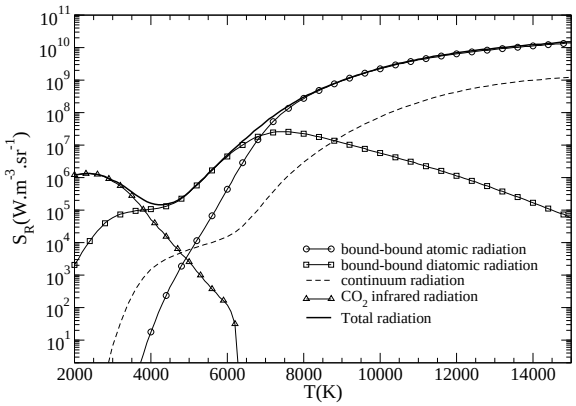

Figure 13: Optically thin emission of bound-bound atomic, bound-bound diatomic, continuum and CO_2 infrared mechanisms for a CO2(97%)-N_2(3%) plasma at 1 atm.

3.3 CO_2 infrared radiation

As shown above in Fig.13, CO_2 IR radiation remains very important at temperatures as high as 4000 K although its concentration is quite small. Its contribution is then expected to be important for high velocity entries in planetary atmospheres containing CO_2. We have studied the accuracy of various available CO_2 databanks by comparing their predictions to measurements [27, 28]. To this end, an experimental setup combining a microwave plasma torch and a high resolution Fourier transform spectrometer has been designed. CO_2 and CO_2-N_2 flows were excited by a microwave discharge inside quartz or sapphire tubes and temperature and concentration distributions were inferred from CO overtone emission in the spectral range [4000 – 4360 cm^{-1}]. The line of sigh integrated emission spectra were then compared to the predictions from CDSD4000 [25] and HITELOR [29] spectroscopic databases in the 4.3 and 2.7 μm regions. A comparison between measurements and predictions is shown in Fig. 16 for a pure CO_2 plasma confined in a saphire tube and 20 mm above the exit of the microwave discharge. It appears that the recent CDSD-4000 database is more accurate than HITELOR, especially in the 2.7 μm region. The high experimental uncertainties in the range [2200 – 2400 cm^{-1}] are due to important uncertainties on the temperature distribution in the cold peripheral regions of the flow.

The CDSD-4000 gathers 573,881,316 rovibrational transitions, when considering only the main isotopologue $^{12}C^{16}O_2$. A correct description of each spectral line profile associated to these transitions requires about 10^6 spectral points to predict accurately the radiative transfer in the IR spectral range, at atmospheric pressure. At lower pressures such as encountered in Martian entry problems, spectral line profiles are dominated by Doppler broadening, and become therefore much narrower, requiring about 10 times more spectral points.

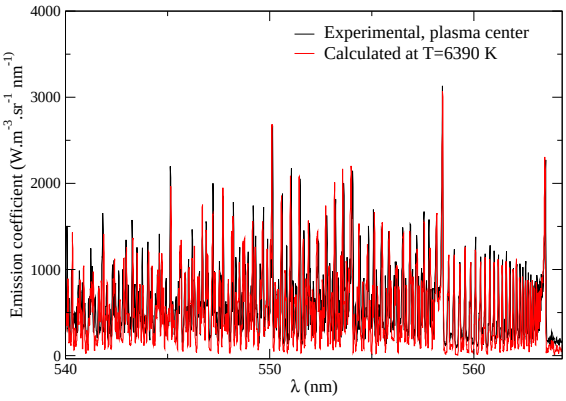

Figure 14: Comparison between the absolute levels of emission coefficient at the center of a CO_2 plasma and 6 mm above the exit of the microwave cavity, and the calculated one, for the C_2 Swan system, $\Delta v = 1$ region. The experimental setup is described in Ref. [26].

Such spectral high resolution predictions of radiative transfer will therefore require a large amount of CPU time, in particular when complex 3D geometries are considered.

Statistical Narrow Band (SNB) models [30] enable to easily calculate the mean transmissivities of an optical path, averaged over spectral narrow-bands, whose widths are a few 10 cm^{-1}, from only a few parameters: the mean absorption coefficient inside each narrow-band, and a parameter characterizing the overlapping of absorption lines within the narrow-band. Such models enable to drastically reduce the required number of "spectral" resolution of the radiative transfer equation — about 300 narrow-bands of width 25 cm^{-1} are sufficient to cover the IR spectral range where CO_2 is active. We have recently obtained updated SNB parameters for CO_2, based on the CDSD-4000 database at atmospheric pressure [31], and also in pure Doppler broadening regime [32]. These parameters have been calculated from least square adjustments between CDSD-4000 based line-by-line and SNB predictions of mean transmissivities of columns for various optical thicknesses, and tabulated in a wide range of temperature between 300 and 5000 K.

As an example of application, these SNB parameters have been used to calculate the incident radiative flux at some locations of the afterbody of the Viking capsule during its entry in Mars atmosphere [33]. 3D aerothermal fields used to perform these radiative transfer calculations were provided from Ref. [34]. No coupling with radiative transfer was considered. Radiative transfer calculations were carried out, assuming local thermal equilibrium at the rotation-translation temperature, and only considering Doppler broadening of spectral lines. Figure 17 shows the spectral distribution in the 4.3 μm region of the radiative flux at the thermocouple location on the outer aluminum cone of the Viking after-

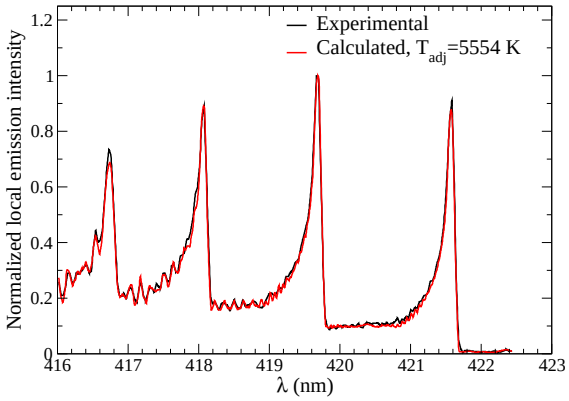

Figure 15: Normalized experimental and adjusted local emission coefficient in a CO_2-N_2 plasma. The peaks correspond to vibrational bands $\Delta v = -1$ of the CN violet system.

body (see details in Ref. [33]). Three flight times are considered. SNB model results compare successfully with the reference results obtained from a spectral high resolution approach of radiative transfer and line-by-line calculations (LBL). Figure 17 shows also results obtained from the SNB model, under the weak limit approximation (SNB weak), which consists in neglecting the spectral correlation of gaseous radiative properties within each narrow-band, and thus in just using a mean absorption coefficient (box model); such simplification introduces large discrepancies in this case, confirming the need of using a full correlated model like SNB. More details on these calculations and discussions on the retained approximations may be found in Ref. [33].

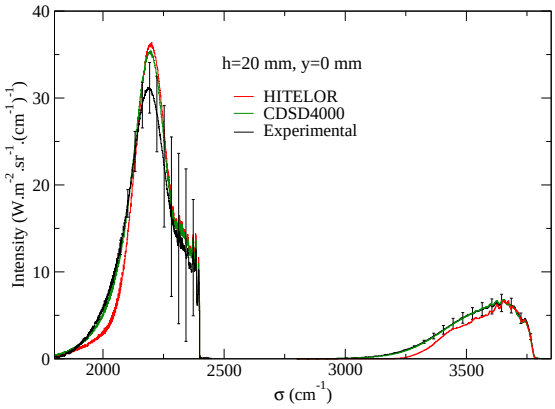

Figure 16: Comparison between experimental and calculated line-of-sight integrated intensity emitted by a CO_2 plasma in the infrared. For legibility, the high resolution spectra are convolved with a rectangular function of width 10 cm^{-1}. Adapted from Ref. [28].

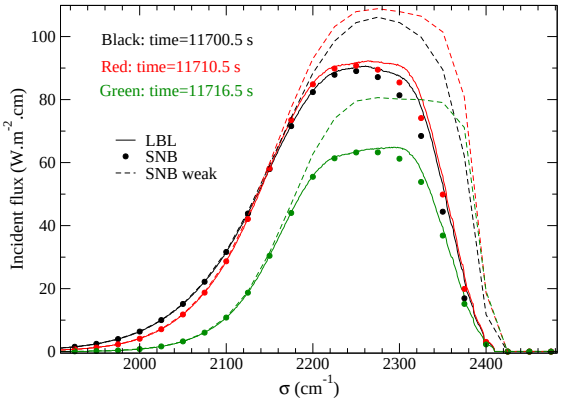

Figure 17: Low spectral resolution incident flux on a wall point of the outer aluminum cone of the Viking afterbody, calculated using line by line (LBL), SNB model (SNB), and SNB in the weak absorption limit (SNB weak). The three colors refer to three trajectory times. Adapted from Ref. [33].

4 Radiative Properties for Jupiter Atmosphere Entry Plasma

In this section the model used for the calculation of the spectral radiative properties of the Jupiter atmosphere under high speed shock conditions is described. An important property of the proposed model is that it can be easily coupled to collisional-radiative models (CRM) for the calculation of non-equilibrium spectral coefficients using the actual population of atomic and molecular levels, to determine the absorption coefficient and emissivity entering the radiative transfer equation (RTE). Solving the RTE allows for a self-consistent determination of both the radiative rate coefficients entering the master equations of the CRM and the contribution of radiation to the internal energy of the flow, which could be important in the case of low-pressure, high-speed entry trajectories in atmospheric entry problems [35].

4.1 Spectral properties of Jupiter plasmas

The present spectral model for the H_2/He plasma is based on a previous model for pure hydrogen plasma, extended to include the helium atom and molecular hydrogen. The following radiative processes are included

- Absorption and emission due to transitions between atomic or molecular bound levels (bound-bound transitions) of H, He and H_2 species.
- Transition of the optical electron from a bound state towards the continuum (photoionization) and the reverse process of capture of a free electron by the corresponding ion (radiative recombination, bound-free transitions) of H and He.
- Bremsstrahlung emission from free electrons in the electric field of the H^+ ions and inverse Bremsstrahlung absorption (free-free transitions).

The reader is referred to Ref [36] for a full account of the model limited to atomic hydrogen species. Tab. 1 reports the radiative processes considered in the full model. In the next sections, the implementation of the new radiative processes R_2, R_3 and R_5 is described.

Table 1: Radiative processes considered in the calculation of the spectral radiative properties of H_2/He plasma.

	Reaction	Ref.
R_1	$H(n) \rightleftharpoons H(m<n) + \rightsquigarrow$	[37]
R_2	$H_2(B^1\Sigma_u^+, C^1\Pi_u) \rightleftharpoons H_2(X^1\Sigma_g^+) + \rightsquigarrow$	[38]
R_3	$He(n) \rightleftharpoons He(m<n) + \rightsquigarrow$	[17]
R_4	$H^+ + e^-(\varepsilon) \rightleftharpoons H(n) + \rightsquigarrow$	[39]
R_5	$He^+ + e^-(\varepsilon) \rightleftharpoons He(n) + \rightsquigarrow$	[40]
R_6	$H^+ + e^-(\varepsilon) \rightleftharpoons H^+ + e^-(\varepsilon' < \varepsilon) + \rightsquigarrow$	[41]

4.1.1 Bound-bound transitions of H_2

Modeling of H_2 Lyman ($H_2(B^1\Sigma_u^+ \leftrightarrow X^1\Sigma_g^+)$) and Werner ($H_2(C^1\Pi_u \leftrightarrow X^1\Sigma_g^+)$) radiation is performed at the level of rational lines (including λ-doubling for the C state) using Einstein coefficients $A^{e',v',J'}_{e'',v'',J''}$ and corresponding transition energies calculated by Abgrall *et al.* in a series of papers [see 42, and references therein]. Abgrall's *et al.* calculations fully account for the non-adiabatic couplings between H_2 electronically excited states up to $n = 3$, and have been validated by comparison with high-resolution spectroscopic measurements [43]. These data are available online as a part of Paris-Meudon Observatory MOLAT database [38]. This data set is recommended for the calculation of high-resolution bound-bound spectra of H_2.

The calculation of equilibrium spectra, and of non-equilibrium spectra using vibrational populations calculated by a CRM needs accurate partition functions to distribute the total H_2 number density (equilibrium) or the vibrational population of the ground and electronically excited states $H_2(Y, v)$ (CRM) over the rotational manifold. The partition function of H_2 has been calculated using spectroscopic Dunham coefficients from Ref. [44] for the X state and from Ref. [45] for the B and C states. It is worth noting that the population of a rotational J-level of an homonuclear diatomic molecule depends also on the symmetry of the electronic wave function due to nuclear statistics considerations [44, 46].

Individual rotational line profiles $(e', v', J') - (e'', v'', J'')$ have been modeled with an approximate Voigt line shape function [47], using the following expression to determine the Doppler and collisional half-widths [48]

$$\begin{aligned} \gamma_D &= \frac{\bar{\nu}_0}{c}\sqrt{\frac{2\ln 2 k T_g}{M}} \\ \gamma_{\text{coll}} &= 0.1\left(\frac{273}{T_g}\right)^{0.7} \quad \text{cm}^{-1} \end{aligned} \tag{6}$$

4.1.2 Bound-bound transitions of He

The recent comprensive tabulation by Wiese and Fuhr [49] includes transition probability data for about 2400 transitions with principal quantum number $n \leq 10$ and orbital argular momentum quantum number $\ell \leq 7$, taking fully into account the fine structure. The data set also includes transition probabilities for several intercombinations lines, and is available in NIST's atomic spectral database [17].

The few lines missing from NIST's tables, namely the lines involving the excited states with $n = 9, \ell = 8$ and $n = 10, \ell = 8, 9$, have been estimated as follows. The dipolar transition probability is given by

$$A(J', J) = \frac{64\pi^4 (e a_0)^2}{3h(4\pi\varepsilon_0)} \bar{\nu}^3 \frac{S(J', J)}{2J' + 1} \tag{7}$$

The transition strength $S(J', J)$ (a.u.) can be written as [50]

$$S(J', J) = R^2_{\text{line}} R^2_{\text{multiplet}} \mathcal{I}^2 \tag{8}$$

where the line and multiplet factors are defined as

$$R_{\rm line} = (-1)^{S+J+L'+1} \times \sqrt{(2J+1)(2J'+1)} \left\{ \begin{array}{ccc} S & J & L \\ 1 & L' & J' \end{array} \right\} \tag{9}$$

$$R_{\rm multiplet} = G \times (-1)^{L_c+L+\ell'+1} \times \sqrt{(2L+1)(2L'+1)} \left\{ \begin{array}{ccc} L_c & L & \ell \\ 1 & \ell' & L' \end{array} \right\} \tag{10}$$

In the latter equation the L, S, J are the spin, orbital and total angular momentum quantum numbers, L_c is the orbital angular momentum quantum number of the core, the primed quantities refer to the upper state of the transition, ℓ is the orbital quantum number of the "optical" electron and G is a coefficient (fractional parentage coefficient) that assumes value $G = 1$ for transitions of the kind $I\ell - I\ell'$ and $G = \sqrt{2}$ for transitions $\ell^2 - \ell\ell'$, where I is a ionic core. In the case of atomic helium, only transitions of the kind $1s^2 - 1s.np$ and $1s.n\ell - 1s.n\ell \pm 1$ have been considered for calculation with the approximate method. Finally, the radial factor is defined as [51]

$$\mathcal{I} = (-1)^{\ell_> - \ell} \sqrt{\ell_>} \int_0^\infty P_{\nu\ell}(r) r P_{\nu'\ell'}(r) dr \tag{11}$$

where $P_{\nu\ell}(r)$ is a radial function and $\ell_> = \max(\ell, \ell')$. In the Coulomb approximation, the radial functions are replaced by the asymptotically accurate expression $P_{\nu\ell}(r) \sim K W_{\nu, l+\frac{1}{2}}(r)$ where K is an approximate normalization factor and W is the Wittaker function. In the above equations, ν is a generally non-integral effective quantum number, calculated from the experimental level energy E_i as

$$\nu = \zeta \sqrt{\frac{\rm Ryd}{I_{ion} - E_i}} \tag{12}$$

where $\zeta = 1, 2, \ldots$ for neutral atoms, first ions etc., Ryd is the Rydberg constant and I_{ion} is the experimental ionization energy of the Rydberg series to which the given excited level belongs. The radial integrals have been evaluated according to the method described in section III of Ref. [52]. This paper improves over the previous work [36] implementing a method for the calculation of quadratic Stark widths of neutral He lines following Ref. [53]. The electron impact Stark half-width w_e and shift d_e in $\rm cm^{-1}$ are calculated using

$$\begin{aligned} w_e + i d_e = \frac{2}{3c} n_e \left(\frac{\hbar}{m}\right)^2 \int \frac{dv}{v} f_e(v) \Bigg\{ \frac{3}{4} \left(\frac{mv}{\hbar}\right)^2 \rho_{\rm min}^2 \\ + \sum_{i'} \mathbf{R}_{ii'}^2 [a_{ii'}(z_{ii'}^{\rm min}) - i\epsilon_{ii'} b_{ii'}(\tilde{z}_{ii'}^{\rm min})] \\ + \sum_{f'} \mathbf{R}_{ff'}^2 [a_{ff'}(z_{ff'}^{\rm min}) + i\epsilon_{ff'} b_{ff'}(\tilde{z}_{ff'}^{\rm min})] \Bigg\} \end{aligned} \tag{13}$$

where n_e is the electron density $f_e(v)$ is the eedf, $\rho_{\rm min}$ is a threshold impact parameter and $R_{jj'}$ are coordinate matrix elements that have been calculated from available Einstein coefficients, while the summations on i' and f' represent

the contribution to the broadening of the dipole interaction of the lower and upper states of the line with nearby energy levels and the other quantities are defined as in Ref. [53]. The total Stark half-width of a line has been calculated according to Ref. [54]

$$w = w_e + 1.75A(1 - 0.75R)w_e \tag{14}$$

where A is the ion-broadening parameter calculated according using Eq. (224) of Ref. [55] and R is the ratio between the the Debye length and the average ion-ion distance, calculated according to Ref. [54].

4.1.3 Bound-free transitions of He

The most reliable atomic photoionization cross sections (and radiative recombination) calculations up to date are based on the close-coupling (CC) approximation and the R-matrix method as implemented by the Opacity Project (OP) [24]. Very recently, the cross section data for He in the OP database have been superseded by the calculations reported in Ref. [56], which are based on the same CC method as the OP database, but using an improved theoretical approach accounting for photoionization and dielectronic recombination in a unified manner. These data include both the total photoionization cross section, leaving the ion He^+ in various excited core states as well as level-specific photoionization cross sections leaving the ionic core in its ground electronic state. The cross sections are given on a photon energy mesh of a few thousand points, where the lower energy point corresponds to energy difference between the level i and the core ground state. Cross sections are provided for excited states with $n \leq 10$ and $\ell \leq 6$ for both the singlet and triplet systems of He. The cross sections are calculated in the LS coupling scheme and are not resolved over the fine structure, which is not big issue for He since the fine splittings are anyway very small. This latter dataset has been employed in the present work for the calculation of photoionization/recombination spectra of He atom.

4.2 Results

In this section we present calculated spectra of a Jupiter-like plasma of initial molar composition H_2:He=89:11. In Fig. 18 absorption spectra of an equilibrium plasma at $p = 1$ atm and different temperatures are reported. It is clearly observed that with increasing temperature, molecular absorption lines in the region $60000 \div 110000$ cm^{-1} are progressively overcome by atomic H Lyman absorption. At very high temperature, absorption from atomic H and He excited states and Bremsstrahlung below 50000 cm^{-1} starts to be significant compared to absorption from the ground states of atoms.

In Fig. 19 absorption spectra calculated at different points in the post-shock region of an hypersonic shock wave propagating in a Jovian plasma (H_2 :He=89:11) initially at $T_0 = 160$ K and $P_0 = 10$ Pa and a free stream gas flow speed $v_0 \approx 46$ Km/s. Downstream the shock the gas temperatures suddenly jumps to $T_g = 81,000$ K and the pressure to $P = 2.9\,10^4$ Pa (≈ 0.3 atm). The post-shock relaxation of the generated plasma is studied using a CRM [57], which recently has been extended with a reasonably complete set of elementary processes for the He atom [58]. In Fig. 19, absorption spectra corresponding to the two limiting cases of optically thin (the emitted radiation escapes the plasma

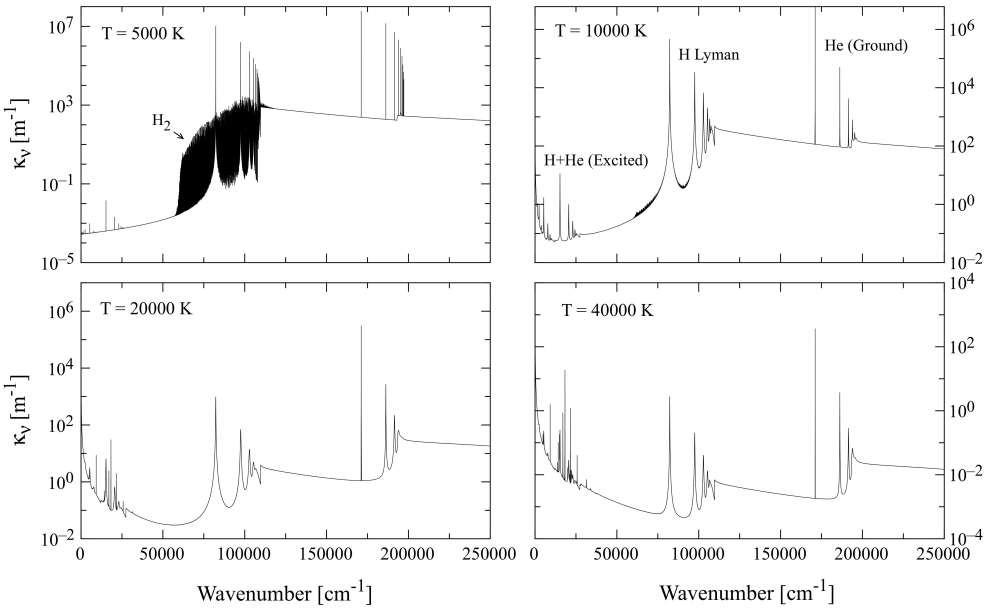

Figure 18: Calculated absorption spectra of an equilibrium H_2/He Jovian plasma at p=1 atm at different temperatures.

volume without being reabsorbed) and optically thick (the emitted radiation is completely reabsorbed locally) are reported. At small distances from the shock front (Fig 19-a) most of the absorption is due to undissociated H_2 molecules and He, while at about 20 cm from the shock front (Fig 19-b), corresponding to the maximum of the electron molar fraction, absorption features of atomic H Lyman lines are increased due to formation of hydrogen atoms by dissociation of H_2 molecules. The thin plasma is characterized by a slightly smaller dissociation degree of H_2 and a lower ionization degree, resulting in stronger absorption in H_2 bands and smaller Stark widths of atomic lines. At large distances from the shock front (Fig 19-c) the thin and thick cases are not very different, being both the plasma composition and internal distributions nearly equilibrium at this distance, but the thick case is characterized by stronger absorption below 50000 cm^{-1} due to the higher number densities of excited states resulting from neglecting radiative the decay process.

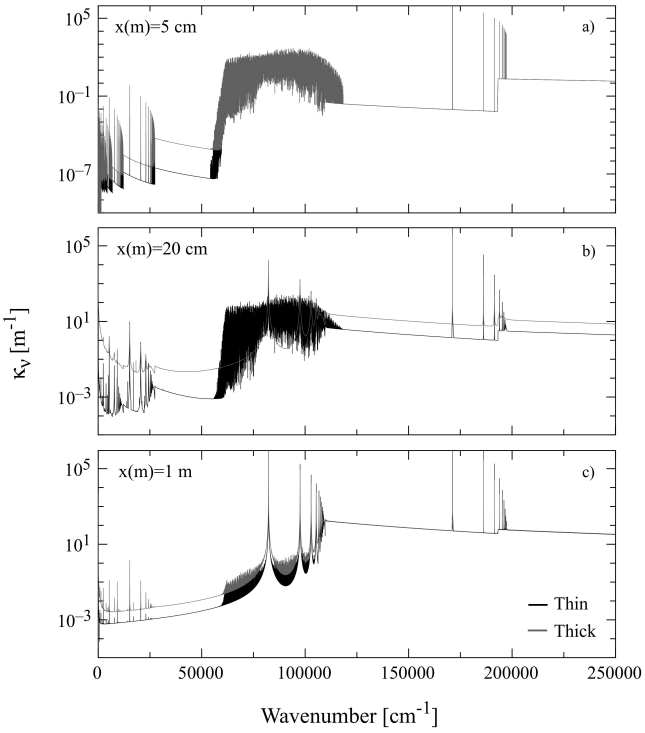

Figure 19: Calculated absorption spectra of a Jovian plasma at different positions in the post shock region of a shock wave. The initial free stream condition is defined by $T_0 = 160$ K, $P_0 = 10$ Pa and free flow speed $v_0 \approx 46$ Km/s, corresponding to a Mach number $M \approx 50$. Optically thin (solid black line) and optically thick (solid gray line) are compared.

5 Conclusion

Many advances and improvements have been recently achieved in the field of radiation properties of low temperature plasmas and hypersonic flows. These achievements have been illustrated in this paper with regard to radiation in atmospheric entries, including earth, Mars, and Jupiter like atmospheres.
A description of the computing code ASTEROID has been presented. This code is applicable to many different kinds of spectral and group optical models for hot gases and low-temperature plasmas. The half-spherical emissivity which is of practical interest for estimation of the radiative heating of space vehicles surface, has been shown to involve a large number of different elementary radiative processes for air plasma.
Using the HTGR database, it has been shown that for entry in Mars atmosphere, two types of radiative processes are predominant. Up to 4000 K, the contribution of CO_2 IR radiation is important. Above and up to 7000K, the radiation due to diatomic bound-bound transitions dominates. For these two types of processes, an experimental validation has been performed. An example of spectral distribution of the radiative flux on an afterbody has been presented based on line-by-line calculations and on statistical narrow band model whose parameters have been deduced from line-by-line calculations.
Finally, recent improvements of a model for the calculation of radiative properties of high-temperature H_2/He mixtures, taking into account the most important radiative processes have been presented. It can be used to determine emissivity and absorption coefficient needed in the solution of the radiative transfer equation for hypersonic entry flows, and can be easily coupled to a collisional-radiative model to compute rate coefficients of radiative processes self-consistently with the radiation field, which can be important in the state-to-state chemical kinetic description of non-equilibrium atmospheric entry plasmas.
To increase the reliability of radiative heating prediction, there is a need for further verification and validation of the presented radiative data. Some additional elementary radiation processes require further investigation. This is the case for instance of processes involving ablation products (when ablative materials are used) which may contain many exotic molecules that can contribute to radiation shielding. Future work should also include the modeling of resonance broadening of He atoms, which is important to predict line widths in low-temperature He-rich plasmas, and the modeling of photodissociation and photoionization of H_2 molecules, which could be important to model the chemistry of the precursor region just before a shock front.
The prediction of radiative transfer in entry problems and in hypersonic flows is closely related to the knowledge of the thermodynamic state of the gas surrounding the vehicle. Level populations of the various species must be known with accuracy compatible with the searched accuracy for radiative transfer. These level populations may also be influenced by radiation. Therefore, a consistent treatment of coupled radiation and collision processes is sometimes necessary, though not easy to implement. As an example, the full model on H_2/He is currently being incorporated in an advanced collisional-radiative model, including a Boltzmann solver for the non-equilibrium electron energy distribution function [59].

Acknowledgments

The research leading to these results has received funding from the European Community's Seventh Framework Programme [FP7/2007/2013] under grant agreement n ° 242311.

References

[1] E.E. Whiting, C. Park, Y. Liu, J.O. Arnold, and J.A. Paterson. NEQAIR96, Nonequilibrium and Equilibrium Radiative Transport and Spectra Program: User's Manual. Reference Publication 1389, NASA, Ames Research Center, Moffet Field, California, Dec 1996.

[2] L.C. Hartung. Predicting radiative heat transfer in thermo-chemical nonequilibrium flowfields: theory and user's manual for the LORAN code. Technical Memorandum 4564, NASA Langley Research Center, Hampton, VA 23681-0001, September 1994.

[3] K. Fujita and T. Abe. SPRADIAN, structural package for radiation analysis: theory and application. Technical report, ISAS Report No 669, 1997.

[4] L.A. Kuznetsova and S.T. Surzhikov. Absorption cross sections of diatomic molecules for problems of radiative heat transfer in low-temperature plasma. *High Temperature*, 37(3):374–385, 1999.

[5] C.O. Laux. Radiation and nonequilibrium collisinal-radiative models. In *VKI special course on physico-chemical models for high enthalpy and plasma flows modeling*, June, 4-7 2002.

[6] A. Smith, A. Wood, J. Dubois, M. Fertig, and B. Pfeiffer. Plasma radiation database parade v22 final report. Technical Paper 3, ESTEC contract11148/94/NL/FG, FGE TR28/96, Oct 2006.

[7] C. Johnston, B. Hollis, and K. Sutton. Non-Boltzmann Modeling for Air Shock-Layer Radiation at Lunar-Return Conditions. *Journal of Spacecraft and Rockets*, 45:865–878, 2008.

[8] P. Passarinho and M. Lino da Silva. GPRD, a database for the spectral properties of diatomic molecules of atmospheric interest. *Journal of Molecular Spectroscopy*, 236(1):148–149, 2006. URL http://www.sciencedirect.com/science/article/B6WK8-4J625WX-1/2/8ed0df3b71e3410a8accb6372088d6c4.

[9] Armstrong, B.H. and Nicholls, R.W. *Emission, absorption and transfer of radiation in heated atmospheres.* Pergamon Press, Oxford, 1972.

[10] D.R. Bates and A. Damgaard. The calculation of absolute strengths of spectral lines. *Phil. Trans. Roy. Soc.*, 242:101–111, 1949.

[11] Hartree, D.R. *The Calculation of Atomic Structures.* John Wiley Sons, Inc, New York, 1957.

[12] Levinson, I.B. and Nikitin, A.A. *Handbook for Theoretical Computation of Line Intensities in Atomic Spectra*. Daniel Davey Co., Inc., 257 Park Ave. South, New York, 1965.

[13] Park, C. *Nonequilibrium Hypersonic Aerothermo-dynamics*. Willey-Interscience Publication, New-York, 1990.

[14] S.T. Surzhikov. Computational Radiation Models for Low-Temperature Plasma. AIAA 96-2313, 1996.

[15] S.T. Surzhikov. Computing System for Mathematical Simulation of Selective Radiation Transfer. AIAA 00-2369, 2000.

[16] C.E Moore. Atomic energy levels). NBS Circular 467, Washington D.C, Vol.1, 1949; Vol.2, 1952; Vol.3, 1958.

[17] A Kramida, Yu Ralchenko, J Reader, and NIST ASD Team. *NIST Atomic Spectra Database (version 5.0)*. National Institute of Standards and Technology, Gaithersburg, MD, 2012.

[18] Huber, K.P. and Herzberg, G. *Molecular Spectra and Molecular Structure. IV. Constants of Diatomic Molecules*. Van-Nostrand-Reinhold Company, New-York, 1979.

[19] Hayes, W.D. and Probstein, R.F. . *Hypersonic Flow Theory*. Hypersonic Flow Theory, New York and London, 1959.

[20] S. Chauveau, M.-Y. Perrin, Ph. Rivière, and A. Soufiani. Contributions of diatomic molecular electronic systems to heated air radiation. *Journal of Quantitative Spectroscopy and Radiative Transfer*, 72:503–530, 2002. ISSN 0022-4073. doi: {10.1016/S0022-4073(01)00141-8}.

[21] S. Chauveau, Ch. Deron, M.-Y. Perrin, Ph. Rivière, and A. Soufiani. Radiative transfer in LTE air plasmas for temperatures up to 15000 K. *Journal of Quantitative Spectroscopy and Radiative Transfer*, 77:113–130, 2003. ISSN 0022-4073. doi: {10.1016/S0022-4073(02)00080-8}.

[22] Yacine Babou, Philippe Rivière, Marie-Yvonne Perrin, and Anouar Soufiani. Spectroscopic data for the prediction of radiative transfer in CO2-N2 plasmas. *J. Quant. Spectrosc. Radiat. Transfer*, 110:89 – 108, 2009.

[23] M.Y.. Perrin, Ph.. Riviere, and A.. Soufiani. Radiation phenomena behind shock waves. In R. Brun, editor, *High Temperature Phenomena in Shock Waves*, pages 193–230. Springer-Verlag, 2012.

[24] OP Team. *The Iron Project - The Opacity Project*, 2012. URL http://cdsweb.u-strasbg.fr/topbase/topbase.html.

[25] S. A. Tashkun, V. I. Perevalov, and L. H. Coudert. Cdsd-4000: High-resolution, high-temperature carbon dioxide spectroscopic databank. *J. Quant. Spectrosc. Radiat. Transfer*, 112(9):1403–1410, 2011.

[26] Yacine Babou, Philippe Rivière, Marie-Yvonne Perrin, and Anouar Soufiani. Spectroscopic study of microwave plasmas of CO_2 and CO_2–N_2 mixtures at atmospheric pressure. *Plasma Sources Science and Technology*, 17 (4):045010, 2008. URL http://stacks.iop.org/0963-0252/17/i=4/a=045010.

[27] S. Depraz and A. Perrin, M.-Y. Soufiani. Infrared emission spectroscopy of CO2 at high temperature. Part I: Experimental setup and source characterization. *J. Quant. Spectrosc. Radiat. Transfer*, 113:1–13, 2012.

[28] S. Depraz, M.-Y. Perrin, Ph. Rivière, and A. Soufiani. Infrared emission spectroscopy of CO2 at high temperature. Part II: Experimental results and comparisons with spectroscopic databases. *J. Quant. Spectrosc. Radiat. Transfer*, 113:14–25, 2012.

[29] D. Scutaru, L. Rosenmann, and J. Taine. Approximate intensities of hot CO_2 hot bands at 2.7, 4.3 and 12 μm for high temperature and medium applications. *J. Quant. Spectrosc. Radiat. Transfer*, 52:765–781, 1994.

[30] R.M. Goody and Y.L. Yung. *Atmospheric radiation*. Oxford University Press, 2 edition, 1989.

[31] Ph. Rivière and A. Soufiani. Updated band model parameters for H2O, CO2, CH4 and CO radiation at high temperature. *Int. J. Heat Mass Transfer*, 55:3349–3358, 2012.

[32] Ph. Rivière, M. Y. Perrin, and A. Soufiani. New developments for CO_2 IR radiation: comparison between experiments and spectroscopic database predictions, and updated band model parameters. In *International Workshop on Radiation of High Temperature Gases in Atmospheric Entry, Barcelona, October 16-19*, 2012.

[33] Ph. Rivière and A. Soufiani. Contribution to test case TC7: line-by-line and SNB calculations of the incident radiative flux on two points on the afterbody. In *Proceedings of the International Workshop on Radiation of High Temperature Gases in Atmospheric Entry, Barcelona, October 16-19, ESA SP-714*, December 2012.

[34] J. Beck and J. Merrifield. Viking radiation heat flux computation, Test Case 7. In *Proceedings of the International Workshop on Radiation of High Temperature Gases in Atmospheric Entry, Barcelona, October 16-19, ESA SP-714*, December 2012.

[35] G Colonna, L D Pietanza, and G D'Ammando. Self-consistent collisional-radiative model for hydrogen atoms: Atom–atom interaction and radiation transport. *Chem. Phys.*, 398:37–45, 2012.

[36] G. D'Ammando, L. D. Pietanza, G. Colonna, S. Longo, and M. Capitelli. Modelling spectral properties of nonequilibrium atomic hydrogen plasma. *Spectrochim. Acta, Part B*, 65(2):120–129, 2010.

[37] M Bautista-Moedano and J Lopez-Bonilla. Matrix elements $\langle n_2\ell_2|r^k|n_1\ell_1\rangle$ for the Coulomb interaction. *Apeiron*, 13(1):34–42, 2006.

[38] Paris-Meudon Observatory. *MOLAT–Atomic and Molecular Data*, 2012 (accessed June 2, 2012). URL http://molat.obspm.fr/index.php?page=accueil.php.

[39] P J Storey and D G Hummer. Fast computer evaluation of radiative properties of hydrogenic systems. *Comp. Phys. Comm.*, 66(1):129–141, 1991.

[40] Sultana N Nahar. *NORAD-Atomic-Data (Nahar-OSU-Radiative-Atomic-Data)*, 2012 (accessed June 2, 2012). URL http://www.astronomy.ohio-state.edu/~nahar/nahar_radiativeatomicdata/index.html.

[41] W J Karzas and R Latter. Electron radiative transitions in a coulomb field. *ApJS*, 6:167–212, 1961.

[42] H Abgrall, E Roueff, F Launay, J-Y Roncin, and J-L Subtil. The Lyman and Werner Band Systems of Molecular Hydrogen. *Journal of Molecular Spectroscopy*, 157:512–523, 1993.

[43] X Liu, S M Ahmed, R A Multari, K J Geoffrey, and J M Ajello. High-resoluton electron-impact study of the far-ultraviolet emission spectrum of molecular hydrogen. *ApJS*, 101:375–399, 1995.

[44] A W Irwin. Refined diatomic partition functions. I - Calculational methods and H2 and CO results. *Astron. Astropys.*, 182(2):348–358, 1987.

[45] I Dabrowski. The Lyman and Werner Bands of H_2. *Can. J. Phys.*, 62: 1639–1664, 1984.

[46] M Capitelli, G Colonna, and A D'Angola. *Fundamental Aspects of Plasma Chemical Physics: Thermodynamics*. Springer, 2012.

[47] R J Wells. Rapid approximation to the Voigt/Faddeeva function and its derivatives. *J. Quant. Spectrosc. Ra.*, 62(1):29–48, 1999.

[48] M.-Y. Perrin, P Riviere, and A Soufiani. Radiation Database for Earth and Mars Entry. In *RTO-EN-AVT-162*. NATO Science and Technology Organization, 2009.

[49] W L Wiese and J R Fuhr. Accurate atomic transition probabilities for hydrogen, helium and litium. *J. Phys. Chem. Ref. Data*, 38(3):565–719, 2009.

[50] W Bruce Shore and Donald H Menzel. Generalized tables for the calculation of Dipole transition probabilities. *ApJS*, 12:187–213, 1965.

[51] G K Oertel and L P Shomo. Tables for the calculation of radial multipole matrix elements by the coulomb approximation. *ApJS*, 16:175–218, 1968.

[52] S Klarsfeld. Alternative forms of the Coulomb approximation for bound-bound multipole transitions. *Phys. Rev. A*, 39(5):2324–2332, 1989.

[53] M S Dimitrijević and N Konjević. Simple formulae for estimating stark widths and shifts of neutral atom lines. *AA*, 163:297–300, 1986.

[54] J Menart, J Heberlein, and E Pfender. Line-by-line method of calculating emission coefficients for thermal plasmas consisting of monoatomic species. *JQSRT*, 56(3):377–398, 1996.

[55] Hans R Griem. *Spectral Line Broadening by Plasmas*. Academic Press, 1974.

[56] Sultana N Nahar. Photoionization and electron-ion recombination of He I. *New Astronomy*, 15:417–426, 2010.

[57] G Colonna, G D'Ammando, L D Pietanza, and M Capitelli. Self-consistent coupling of chemical, electron and radiation models for shock wave in jupiter atmosphere. In *AIP Conference Proceedings*, volume 1501, pages 1400–1407, 2012.

[58] M Capitelli, G Colonna, L D Pietanza, and G D'Ammando. Coupling of radiation, excited states and electron energy distribution function in non equilibrium hydrogen plasmas. *Spectrochim. Acta, Part B*, (In Press), 2013.

[59] L D Pietanza, G Colonna, A De Giacomo, and M Capitelli. Kinetic processes for laser induced plasma diagnostic: A collisional-radiative model approach. *Spectrochim. Acta, Part B*, 65(8):616–626, 2010.

RADIATIVE AEROTHERMODYNAMICS OF ENTERING SPACE VEHICLES: TOWARD THE USE OF STATE-TO-STATE APPROACH

S. Surzhikov[1], P. Reynier[2], G. Seller[3], and F. Taccogna[3]

[1]A. Ishlinsky Institute for Problems in Mechanics Russian Academy of Sciences, prospect Vernadskogo 101-1, Moscow, Russia; surg@ipmnet.ru
[2]IngénierieetSystèmesAvancés, Pessac, France; Philippe.Reynier@isa-space.eu
[3]IMIP-CNR, via Amendola 122/D, 70126 Bari, Italy; francesco.taccogna@ba.imip.cnr.it

Abstract

Modern problems of radiative aerothermodynamics of entering space vehicles are demonstrated and analyzed in the paper.
New radiative gasdynamic problems concerned to coupling processes of non-equilibrium dissociation with radiation heat transfer in shock layers generated above large scale re-entry space vehicles returning from orbital and super orbital space mission are considered in the first part.
Three dimensional numerical simulation data on radiative aerothermodynamics of Martian entry probes Pathfinder, Exomars and Mars Science Laboratory (MSL) are presented and analyzed in the second part. It is shown that integral radiative heating of leeward surface of the entry probes exceeds corresponding convective heating.
The third part is dedicated to consideration preliminary numerical simulation results on radiative gasdynamics of Galileo probes. At first, a review of the available results obtained during the mission preparation and post-flight analyses has been undertaken to select a computational matrix. This matrix has been selected by accounting for previous numerical efforts from the literature to crosscheck the results. Then, a model based on previous efforts has been set up for computing the flow-field around the probe at high altitude. Finally the test case matrix has been computed and crosschecked with existing numerical predictions performed.
Some possibilities of innovative magneto-hydrodynamic (MHD) technologies being applied to solving problems of re-entry vehicles heat protection are discussed in the fourth part.
All presented data demonstrate necessity of further development of the radiative aerothermodynamics based on state-by-state approaches.

1. Introduction

Modern models of computational aerophysics of space vehicles, entering into atmosphere with orbital and super-orbital velocities, are based on gasdynamic models of thermally and chemically non-equilibrium gases. These models use Navier – Stocks (NS) or Reynolds averaged Navier – Stocks (RANS) equations in one-, two-, and three dimensions. Also they take into account radiative and non-equilibrium processes of chemical and physical kinetics, as well as different models of turbulent mixing and radiation transfer. Such models are realized, as a rule, on multi-block inhomogeneous grids, or on unstructured grids. Used models of chemical kinetics are conjugated often with heterogeneous chemical processes on solid surfaces, or with kinetics of ablative processes. Electronic data bases on chemical-physical kinetics, thermodynamic and transport properties, as well as the spectral optical properties are the important components of these computational models. And what is more, there is a common opinion in aerospace community that just in the direction of development of thermo-physical models of non equilibrium high temperature flows should be concentrated significant efforts of scientists and engineers.
Development of such computational models and codes for description of aerothermodynamics of re-entry into Earth atmosphere apace vehicles or entry probes intended for investigation of planets of the Solar system is the important part of scientific and engineering programs which are currently realized in different space agencies.
This paper is dedicated to review of achievements of different scientific groups involved into project Phys4Entry with has a general goal to introduce into the radiative aerothermodynamic CFD practice state-to-state approaches for description thermal non equilibrium flow conditions.
The paper contains four parts. The first two parts are dedicated to consideration of general peculiarities of aerothermodynamics of Earth (the part 1) and Mars entry (the part 2). The third part is dedicated to the Titan entry. Some possibilities of MHD technologies for flow control around entry bodies are discussed in the fourth part.

2. Radiative aerothermodynamics of the Earth and Mart entry

2.1 Earth entry

Space vehicles of new generation, currently considering in space agencies, are characterized by the large sizes (with midship diameters about 5 meters). For example, the Orion International Space Station Crew Exploration Vehicle (ISS CEV)project considers possibility to use re-entry space vehicles with nose radius more than 400 cm [1].This part of the paper contains description of current results of investigation of radiative and convective heating of such space vehicles for orbital trajectory conditions, as well as the urgent problems in the field of physical-chemical kinetics which has to be solved.

Two classes of computational codes are currently used in aerospace community. The first one is the two-dimensional computer codes with different models of chemical and physical kinetics. The computational fluid dynamic codes are based on the following groups of governing equations: (*a*) the Navier-Stokes and continuity equations, (*b*) the equations of mass conservation of separate species, (*c*) the equation of energy conservation, including total and vibrational energy, and (*d*) radiation heat transfer equation in multi-group spectral approximation. As a rule, calculations are performed with using a multi block and multi grid computational technology.

The second one is the three-dimensional computer codes, which realizes the same models of physical and chemical hypersonic gasdynamics, as for the two dimensional case, but allow predict flow field around space vehicles under angles of attack. State of the art of the CFD problems of entry space vehicles is discussed in [2,3].

Spectral optical properties of gases of complex chemical composition are provided by the several computer codes. These are: ASTEROID**,** HARA, LORAN, NEQUAIR, PARADE, SPECAIR, SPRADIAN[4].

Some preliminary quantitative predictions of aerothermodynamics of large scale space vehicles were demonstrated in papers [2,3]. These are:

- The relatively large stand-off distance of bow shock wave front spacecraft surface (~30-40 cm) ,
- The large zone of nonequilibrium flow in shock layer behind shock wave front at altitudes > 75 km (~5 cm),
- High degree of inhomogeneity of convective heating of space vehicle surface at angle of attack.

It was shown [5] that the use of well known models of chemical kinetics [6-8] together with models of non-equilibrium dissociation drastically change distributions of gasdynamic and heat transfer functions in conditions of super-orbital entry. It was demonstrated also, that the entering velocity higher, the role of nonequilibrium processes increase. So, the question is how the radiative heating of space vehicle is sensitive to possible variation of the models due to some uncertainties in their formulation.

General goal of the part is to demonstrate the significant role of nonequilibrium dissociation processes in condition of orbital entry for space vehicles of large sized on their radiative heating. The Park-Jaffe-Partridge [6] model of chemical kinetics was fixed in these calculations. But it should be mentioned that the use of other models of chemical kinetics will probably demonstrate another quantitative correlations.

The role of vibrational relaxation of diatomic molecules in radiative gas dynamics was studied intensively in literature [9-11]. It was found that the use of multi-temperature approach allows describe translational, rotational, vibrational and even electronic relaxation behind leading shock wave with acceptable accuracy for aerospace engineering [11].

Translational and vibrational temperatures being calculated are used for dissociation prediction. Different models of non-equilibrium dissociation are in common use: the Treanor-Marrone [9], the Marrone-Treanor [10], and the Park [11] models. All the models assume possibility to modify dissociation rate constants by multiplying of corresponding one-temperature rate constants on nonequilibrium factor, which is the function of translational and vibrational temperatures $Z(T,T_V)$. This factor, as a rule, less than unit because molecular translational and rotational internal degrees of freedom are excited significantly faster behind shock wave front than vibrational ones.

As it was mentioned above the non equilibrium radiation heat transfer processes can be significant for large-scale spacecraft of the new generation (with blunt radiuses ~ 5 m) even at orbital entry (V_∞ ~ 7 km/s), at least at high altitudes (H~ 80 km) where intensities of radiative and convective heating are not so much as at region of maximal heating load (at altitudes H~ 60-70 km). It was predicted [12,13] and found [2,3] that for high altitudes of such space vehicles the radiative-gas dynamic interaction becomes also significant. It means that taking into account radiation heat processes in energy conservation equation results in significant rebuilding of the gas dynamic fields. The role of dissociation processes is demonstrated in the paper just for these conditions.

First of all we will consider results of two-dimensional calculations for axisymmetric case of zero angle of attack. Two-dimensional radiative aerothermodynamics of Orion International Space Station Crew Exploration Vehicle

(further, for short, Orion) was investigated for several trajectory points presented in Table 1. Note that trajectory points located higher than ~75 km correspond, as expected, to nonequilibrium conditions inside shock layer above front shield, and large depth of vibrational relaxation zone behind shock wave front can be observed here.

Table 1: ISS CEV trajectory parameters [1]

#	t, s	H, km	V_∞, km/s	ρ_∞, erg/см^3	T_∞, K
1	150	83.0	7.7	3.37	187
2	200	78.2	7.7	14.2	202
3	300	65.6	7.0	100.	232
4	400	65.6	6.2	100.	232
5	500	57.1	5.2	324.	255
6	600	42.8	3.0	1980.	258

Figure 1 shows typical distributions of thermal and gasdynamic parameters of flow fields around Orion space vehicle for the first trajectory point. The Treanor-Marrone CVD model [9] was used in the case under consideration. Figure 2 shows axial distributions of the translational and vibrational temperatures along stagnation line for succession trajectory points.

Axial distributions of translational and vibrational temperatures along forward stagnation line at t=150 s are shown in Fig. 3. Different models of nonequilibrium dissociation were used in these calculations. The use of the Local Thermodynamic Equilibrium (LTE) model leads in the case under consideration to increasing of bow shock wave stand-off distance. In the frame of the LTE model rates of the forward and reverse chemical reactions were calculated with the use of the translational temperature. Vibrational temperatures shown for this calculation case were calculated only for comparison purposes. Translational and vibrational temperatures obtained with the use of different models of non-equilibrium dissociation are also shown in Fig. 3. In the last cases these vibrational temperatures were used for modification rates of forward chemical reactions. Taking into account the nonequilibrium dissociation leads to increasing of the translational temperature, because lesser part of initial kinetic energy is spent on dissociation and ionization.

Shock wave stand-off distance is achieved of ~ 25 cm in the case under consideration, while the depth of relaxation zone equal to ~5 cm. Vibrational temperatures of molecules N_2, O_2 and NO increase in this zone from temperature of environment gas up to T_V~10 000 K. Maximal vibrational temperature is achieved for molecules NO, and minimal for molecules N_2. Note that the use models of nonequilibrium dissociation follows to overheating of N_2 vibrational mode above translational temperature at the end of the relaxation zone.

Figures 4 show distributions of the species molar fractions along stagnation line in the shock layer above front shield for different mentioned thermodynamic models. Note that the large molar fractions of molecular N_2 and O_2 and low molar fractions of atomic N and O are observed in the vicinity of the space vehicle surface in full agreement with used assumption of the catalytic surface. Observed differences in species concentration distributions in shock layer have their origin in different rates of dissociation provided by the different models of non-equilibrium dissociation. Let us compare, for example, the species concentration distributions predicted by the LTE model, and the Park model of non-equilibrium dissociation [11] (Figs. 4*a* and *b*). One can see that in the first case the molecular (N_2, O_2) and radicals (NO) species significantly less than in the second case due to higher degree of dissociation rate, while the temperature distributions in shock layer are similar. It means that spectral emissivity by vibronic bands of these diatomic molecules should be significantly lower in the first considered case. Just this effect we can observe at analysis of spectral heat fluxes reaching space vehicle surface at critical point, which are shown in Fig.5. Radiation heat transfer was calculated with the use of 99 multi-group spectral models. Spectral absorption and emission coefficients were averaged inside each of the group. We notice that in the spectral region ω =25000-55000 cm^{-1} there is observable difference in the spectral heat fluxes. If now we will analyze cumulative functions of the radiative heat fluxes (see Figs. 5 and 6), then we determine that the general difference in the heat fluxes is accumulated in this spectral region. And, as a result, the integral radiation heat fluxes on the space vehicle surface become about three times less than in the cases of taking into account the non-equilibrium dissociation (Fig. 6). Note that one can observe in Fig. 6 also the significant differences between intensity of radiative heating for different models of non-equilibrium dissociation.

Numerical simulation results obtained for ORION ISS CEW at angle of attack α =25^0 in the first trajectory point are shown in Fig. 7. Note that for analysis of aerothermodynamics of space vehicles of large sizes there is a necessity to

consider not only flow field above windward surface, but also above leeward surface and wake because radiative heating of the space vehicles has volume nature. Noticeably also that not only temperature distributions should be considered correctly, but also distributions of mass fractions of optically active species.

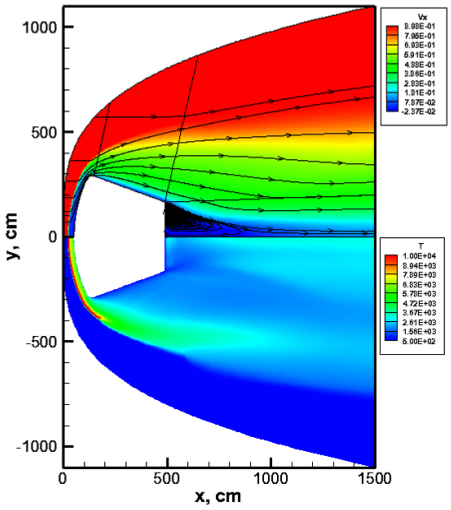

Figure 1: Fields of longitudinal velocity $V_x = u/V_\infty$ (at the top) and translational temperature, in K (at the bottom), at trajectory point t=150 s

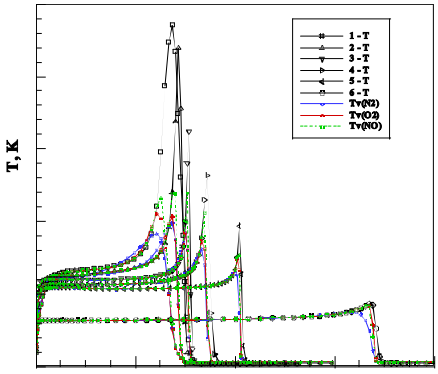

Figure 2: Translational (solid lines) and vibrational (dashed lines) temperatures in shock layer at consecutive trajectory points. The Treanor-Marrone CVD model [9]; 1 – t=150 s, 2 – t=200 s, 3 – t=300 s, 4 – t=400 s, 5 – t=500 s, 6 – t=600 s

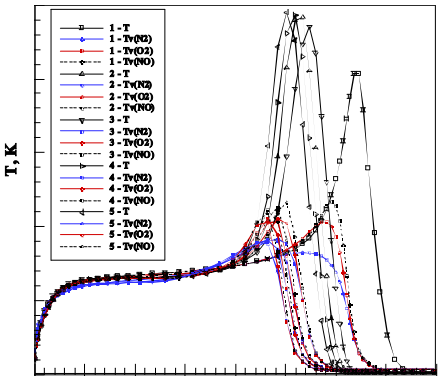

Figure 3: Translational (solid lines) and vibrational (dashed lines) temperatures in shock layer under conditions of LTE (1), and nonequilibrium dissociation at t=150 s: 2 - the Park model of CVD [11], 3 - the Treanor-Marrone model [9], 4 – the Marrone-Treanor model [10] with U=3; 5 – the Marrone-Treanor model [10] with U=6

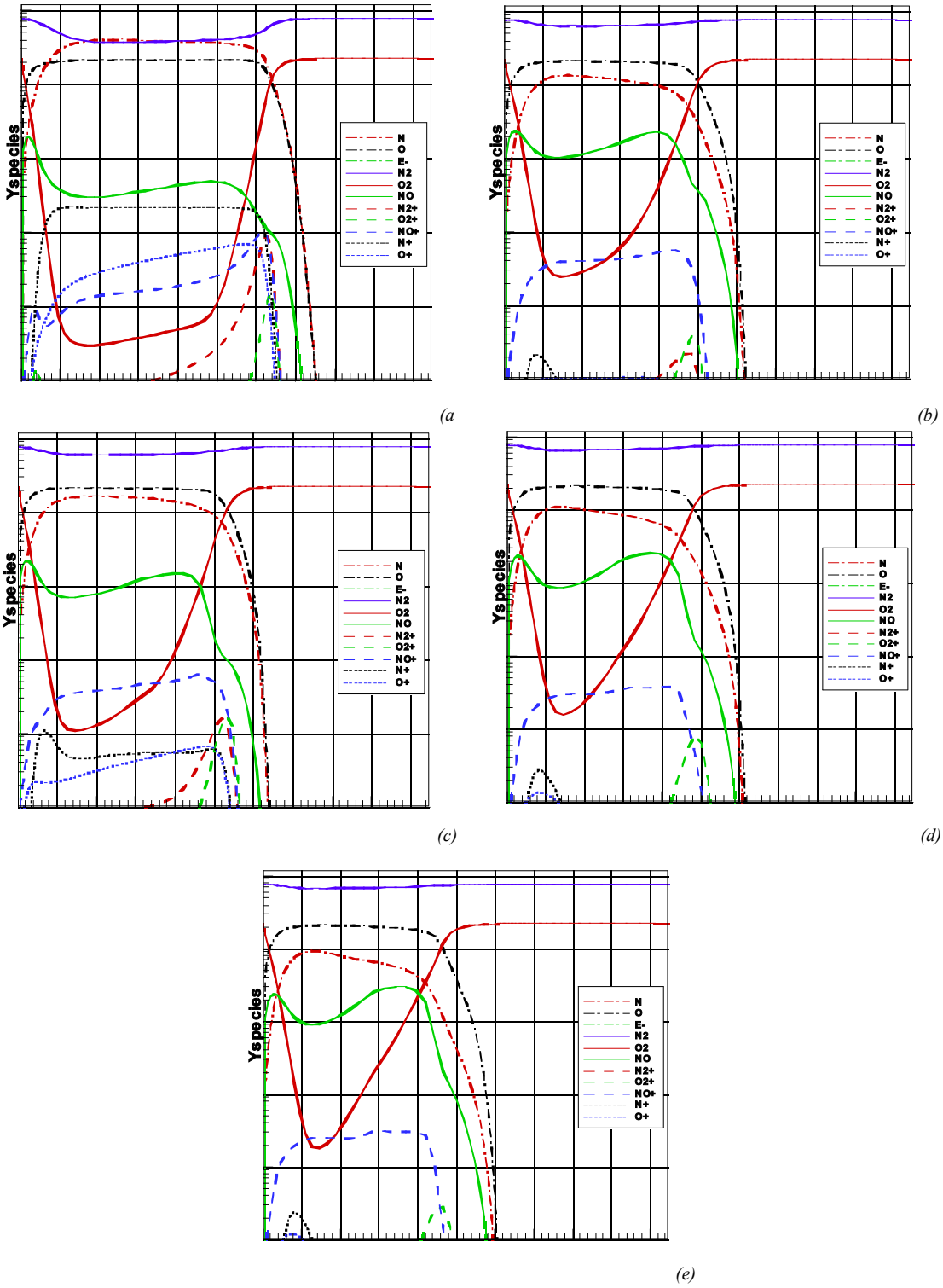

Figures 4: Molar fractions of species along forward stagnation line at t=150 s. Catalytic surface. *a* - LTE model;*b* - the Park model of CVD [11] *c* - the Treanor-Marrone model [9], *d* – the Marrone-Treanor model [10] with U=3; *e* – the Marrone-Treanor model [10] with U=6

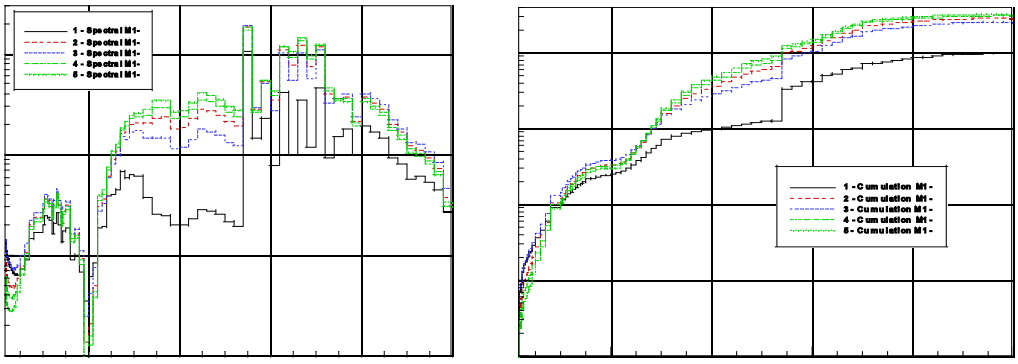

Figure 5: Spectral radiation heat fluxes to stagnation point and corresponding cumulative functions at t=150 s: 1 - LTE model; 2 - the Park model of CVD [11], 3 - the Treanor-Marrone model [9], 4 – the Marrone-Treanor model [10] with U=3; 5 – the Marrone-Treanor model [10] with U=6

Figures 7 show translational temperatures above leeward surface and in near and far wake, as well as distribution of longitudinal projection of the flow velocity. Densities of convective and radiative heat fluxes along surface for this and another trajectory points are shown in Fig. 8. Model of LTE was used in this case. Surface coordinate *S* is counted off from the bottom boundary of the first block (see Fig.9).

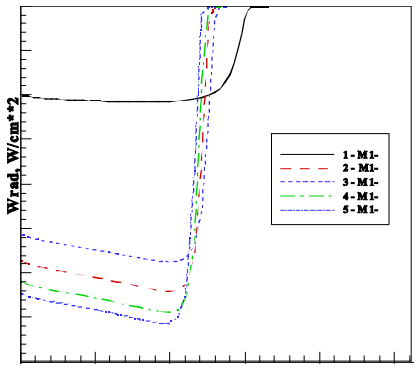

Figure 6: Integral radiation heat fluxes directed to surface along stagnation line in shock layer at t=150 s: 1 - LTE model; 2 - the Park model of CVD [11], 3 - the Treanor-Marrone model [9], 4 – the Marrone-Treanor model [10] with U=3; 5 – the Marrone-Treanor model [10] with U=6

Presented distributions show that at non-equilibrium stage of the trajectory the radiative heating can be significant. Also, presented calculated data clearly indicate that CVD models, being applied for solving coupled radiative gasdynamic problems for large space vehicles, exert noticeable effect on radiative heating of its surface at orbital entry on high altitudes ($h \geq 70$ km).

2.2. Partial conclusion: the challenging problems of Earth entry aerothermodynamics

Observed differences in radiative heating of re-entry space vehicle depending on used CVD models are of great practical interest for aerothermodynamic characterisation of the new generation SV. Unfortunately, the common limitation of investigated CVD models is that there is no way to recommend one or other such the model for trustworthy aerothermodynamic prediction, because each the model contains some heuristic parameters or physical assumptions. The state-by-state radiative collisional approach intensively developing last decades shows promise of increasing plausible predictive properties of coupled radiative gasdynamic models.
Observed large volumes of high temperature shock layers with nonequilibrium gas should motivate additional efforts in investigations of nature and models of relaxation of internal degree of freedoms in emitting gases.

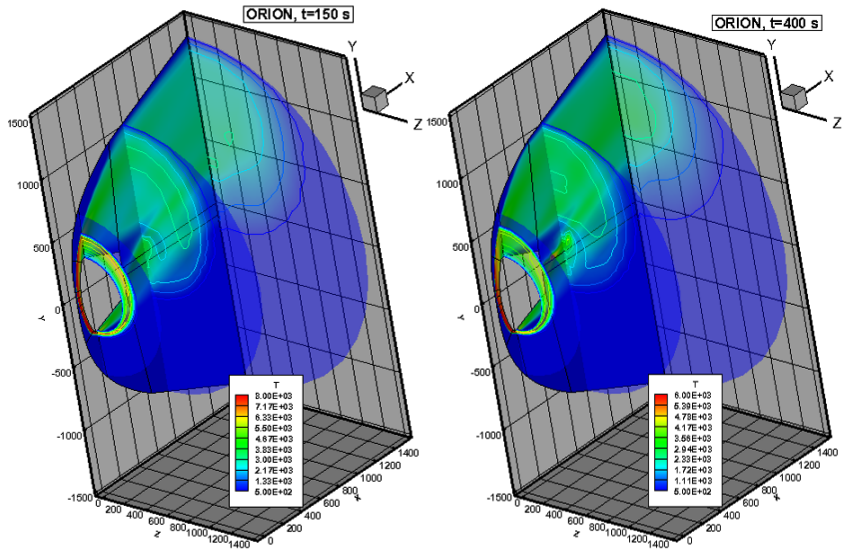

Figure 7. Translational temperature at consecutive trajectory points. Angle of attack α =25^0

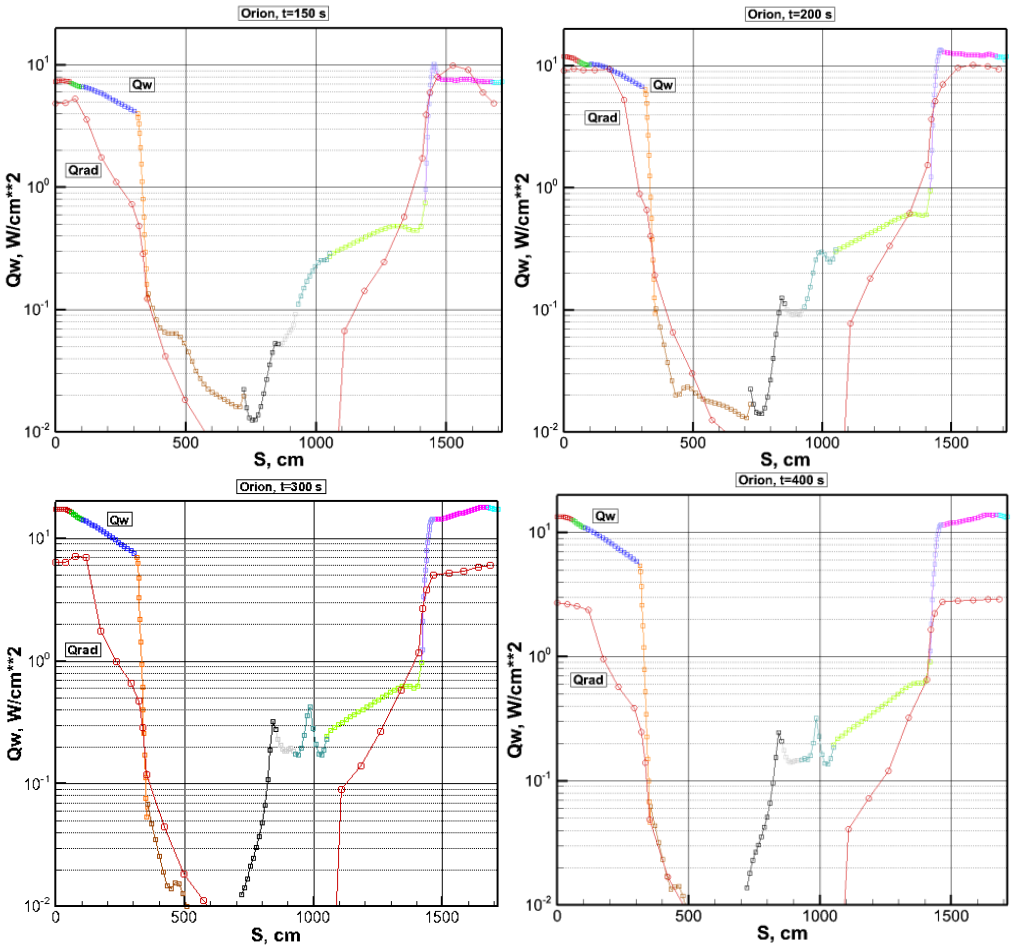

Figure 8. Convective (squares) and integral radiation (circles) heat fluxes on spacecraft surface at t=150 (*a*), 200 (*b*), 300 (*c*) and 400 (*d*) s. α =25^0

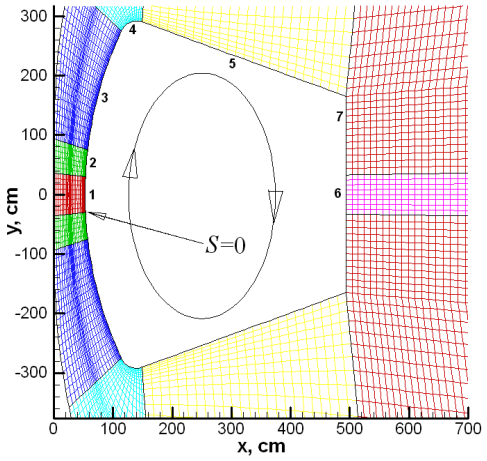

Figure 9: Calculation grid near to space vehicle in three dimensional case

2.3. Martian entry

Aerophysics of Martian entry probes has some characteristic properties in comparison with Earth entry. These are: relatively low velocity of atmospheric entry (~6-7 km/s), relatively rare atmosphere, and significant role of radiative processes in ultraviolet (UV) spectral region, connected with intensive electronic band CO (4+), and in infrared (IR) spectral region, connected with vibrational bands of CO_2 and CO.

Theoretical basis of the Martian entry gasdynamic models which are in common use at the present have been developing about 50 years [14-25]. Conventionally this period can be divided into three parts. The first investigations were dedicated to experimental measurements of real thermo-physical and optical properties of CO_2-N_2 mixtures [15-20]. First theoretical models were also created in 60-th–70-th years of last Century [14,19,20,23].

From the beginning of 90-th large number of investigations were published in AIAA journals which were connected with scientific program of Mars exploration established by NASA [21-35].

A lot of obtained calculation and experimental data [36-42] allow form general representation about aerothermodynamics of Martian entry aerothermodynamics. All these data were undoubtedly used at successfully realized Martian missions.

Development of the Martian radiative gasdynamic models was also the subject of some recently publications. Numerical simulation results on radiative aerothermodynamics of Martian entry probes were presented in [43-50]. These papers contain calculated data obtained with two- and three-dimensional codes. Calculation data for convective heating of front shield and leeward surface of probes [35-37] were used for verification of numerical simulation results of the given paper.

In this part we will show some predictions of conductive and radiative heat fluxes to surface of space vehicles Pathfinder, Exomars and Mars Science Laboratory (MSL) along their entry trajectories. These calculations are complicated by the nonequilibrium character of radiation heat transfer. Attempts to predict radiative heating along the whole surface of space vehicle pose a number of additional problems of radiation heat transfer in shock layer and wake regions.

General ways for verification and validation all of such models and codes are the comparison with available experimental and flight data such as [36,39-42]. Unfortunately, the list of the data, is utterly small. Therefore comparative investigations of aerothermodynamic data obtained with the use of different computational models and codes are also of much current interest.

This part presents results obtained with the use of the three dimensional (3D) multi-physics radiative-gasdynamic model of Martian descent space vehicles, which is realized in NERAT-ASTEROID computer platform. Gasdynamic code NERAT-3D included unto the computing platform uses the time-relaxation method on structured multi-blocks curvilinear calculation grids. On the each time step the following groups of governing equations are integrated successively: the Navier – Stokes (or Reynolds averaged N-S equations, with several turbulence models) and continuity equations, the equations of mass conservation of chemical species, the equation of energy conservation together with equations for vibrational energy conservation for separate vibrational modes, the electron energy conservation, and the radiation heat transfer equation (in multi-group approximation). The energy conservation equation is integrated in the form of the Fourier-Kirchhoff equation, which is formulated relative to translational temperature.

Some computing models, intended for determination of integrated radiative characteristics are included into the codes. These are: the multi-group (line-by-line) models of spectrum, the ray-tracing method for radiative heating prediction of space vehicle surface, the half-moment method for description radiation heat transfer inside inhomogeneous shock layers in multi-group approximation in view of random models of molecular lines [39]. To create different multi-group spectral models of gases of complex chemical composition a computing code ASTEROID [40] is used. Due to relatively small entry velocities of Martian space vehicles the interaction of gasdynamic and radiation heat transfer processes are considered in the frame of the model of weak radiation gasdynamic coupling. Nevertheless, it will be shown that the radiative heating of Martian space vehicles gives significant contribution to total heating of entry capsule.

2.3.1. Initial conditions for numerical simulation

Preliminary results of systematic computational fluid dynamics (CFD) investigations of radiation aerothermodynamics of Martian entry probes were presented in [43-50]. Different kinds of entry probes and different freestream conditions were analyzed with the purpose of determination of intensity of convective and radiative heating along entry trajectories. Investigated freestream conditions are presented in Tables 2-4. The first reference for each the table shows original source for the parameters, while others indicate papers were corresponding calculations were performed.

Detailed description of the base aero-physical model is presented in [44,50]. Numerical simulation results obtained with two-dimensional code NERAT-2D for four trajectory points of Pathfinder (t=42 s, 52 s, 66 s, and 80 s) are presented in [44]. It was demonstrated that front aerodynamic shield is heated generally by ultra-violet radiation with flux q_R ~ 100 W/cm^2, while Pathfinder's leeward surface is heated by infrared radiation due to emissivity of vibrational bands CO_2 (q_R ~ 2-5 W/cm^2). Spectral radiation heat fluxes are presented in that paper in six points along Pathfinder's surface in meridional plane from the forward up to back stagnation points.

Three Exomars' trajectory points were studied also with NERAT-2D code (SC.1, SD.1, SD.2 [44]). It was shown that due to relatively low entry velocities a windward surface of Exomars is subjected by relatively small radiative heating (q_R~50-60 W/cm^2). But radiative heating of its leeward surface remain as for Pathfinder (q_R ~ 2-5 W/cm^2). Also it was demonstrated that radiation heat flux on the front shield increases in 2-3 times from the stagnation point in the direction of its edge.

Results of some three dimensional calculations are presented also in [44]. Only one Exomars' trajectory points (SC.1) was analyzed there. Convective and radiative heating of Exomars at angle of attack α=15^0 were calculated for non-catalytic and catalytic surface. It was demonstrated that catalytic properties of space vehicle surfaces are extremely significant for predicted convective heating but not very significant for radiative heating.

Investigation of radiative aerothermodynamics of the two mentioned space vehicles was continued in [55,56]. Extremely non-equilibrium conditions for Pathfinder entry (t=40s) and two quasi-"equilibrium" Exomars' trajectory points were analyzed there. The paper contains also estimations of turbulent heating of front shield of Exomars.

Comparative analysis of three kinds of Martian descent vehicles (Pathfinder, Exomars and some model representation of the Mars Sample Return Orbiter (MSRO)) is presented in [58]. Studied trajectory points are presented in Table 4. This paper contains numerical prediction of radiative and convective heating of MSRO at angle of attack α=15^0 and V_∞=5.2 km/s. Calculated data for MSRO are compared with predictions for Pathfinder (t=52 s, α=0^0 and V_∞=7.49 km/s), and for Exomars (point SC.1, α=15^0 and V_∞=4.22 km/s). All these calculations confirm high level of radiative heating of leeward surface due to CO_2 emissivity (q_R~1-5 W/cm^2).

Table 2: Trajectory points for MSRO [42,45,47]

No.	Time,s	ρ_∞, g/cm^3	p_∞, erg/cm^3	V_∞, m/s	T_∞, K
1	70	3.14×10^{-8}	8.4	5687	140
2	115	2.93×10^{-7}	78.7	5223	140
3	175	3.07×10^{-7}	82.3	3998	140
4	270	2.82×10^{-8}	7.6	3536	140

Numerous results of methodological investigations concerned to development of computing models of Martian entry probes are presented in [50]. Different topologies of computing meshes are considered there, as well as comparison of two-dimensional and three-dimensional calculations for Exomars at trajectory point SD.1.
First comparison for three-dimensional radiative and convective heating of Pathfinder (trajectory point t=66 s) and MSL (trajectory point t=89 s) are presented in [57]. As before, convective and radiative heat fluxes were calculated along surface, including windward and leeward surfaces. It was shown that the radiative heating of leeward surface of these space vehicles exceed ones convective heating.
Below we will consider typical general results of CFD research which were not demonstrated before, and formulate general conclusion of the numerical modeling.

2.3.2. Radiative gasdynamics of Pathfinder

Figures 10 show flow field about space vehicle Pathfinder under angle of attack $\alpha = 15^\circ$. These calculations were performed for catalytic surface. The distinctive features of the flow field are the following:
- Flow field asymmetry in distributions of longitudinal velocity (*a*), mole fractions of CO (*b*) and CO_2 (*c*), translational temperature (*d*), and anti-symmetric vibrational temperature CO_2 (*e*) is observed due to angle of attack $\alpha = 15^\circ$;
- Shock layer expansion above windward surface from the direction of incident flow is observed, as well as the vortex structure above the top piece of leeward surface;
- The catalytic surface is characterised by high mass fractions of CO_2 and low mass fractions of CO in the vicinity of the surface (Fig. 10*c*). But behind bow shock wave high concentration of molecules CO is observed due to intensive dissociation of molecules CO_2;
- It is not observed significant influence of catalytic properties of Pathfinder's surface on its integral and spectral radiative heating. At the same time, convective heating of catalytic surface is about two times higher than for non-catalytic one;
- Radiative heating of Pathfinder's surface should be taken into account at the leeward part (Fig. 11*a*), because it is exposed by infrared radiation in vibrational bands CO_2 and CO from large volume of heated gas in the wake region. Integral radiation heat fluxes achieve here value about 1 W/cm^2. Emissivity of vibrational bands of CO_2 and CO is easily observable in Figs. 11*b* and *c*;
- Cumulative functions which are shown in Fig. 11*c* indicate two spectral regions only give general contribution into total radiation heat fluxes. These are: $\Delta\omega = 2000 \div 3000\,\text{cm}^{-1}$ and $50000 \div 70000\,\text{cm}^{-1}$. Vibrational molecular bands of CO_2 are located in the first one, while the electronic bands of CO are located in the second spectral region. To determine the locations of grid nodes in equatorial cross section of the space vehicle, where spectral radiation heat fluxes were calculated, one can use Fig 10*f* (see ## 1,36,71,106,141,171).

2.3.3. Radiative gasdynamics of Exomars

This part presents three dimensional numerical simulation results on spectral and integral radiative heating of Exomars' surface in Martian atmosphere for trajectory point SC.1 (see Table 3). Comparison of calculated data for other trajectory points are presented for non-axisymmetric and axisymmetric cases in [44,45]. Current calculations were performed for trajectory point SC.1 at angle of attack α=15^0. Figures 12 show fields of longitudinal velocity, translational and one of vibrational temperature (for anti-symmetric vibrational mode of CO_2), as well as mass fractions of CO_2 and CO in calculation domain.
The following significant peculiarities are observed in the flow field structure:
- General deceleration of incident flow is observed above the lower part of the windward surface. A thickening of the shock layer is also observed here;
- Large scale vortex attached to leeward surface is shifted in the direction of flow. Obviously that spatial structure of the flow becomes more complex, because the vortex structure exists above curvilinear (conical) part of the surface;
- Fluctuations of velocity field are observed in wake region. Calculation field in this part of flow is unsteady, while above the windward surface the full convergence of numerical solution is observed. Figures 12*d,e* illustrate degree of temperature nonequilibrium in the case under consideration. Only one of vibrational modes is characterised here. Other vibrational temperatures also differ significantly from the translational temperature. This fact should be taken into account at prediction of radiative heating of spacecraft surfaces in Martian atmosphere. Figures 12*b,c* show distributions of mass fractions of CO_2 and CO in the calculation domain. One can see, as before, high level of CO_2 mass fractions and low level of CO mass fraction in the vicinity of the surface. Such behaviour of mass fractions is in full agreement with used assumption concerning catalytic properties of the surface.

Investigation of influence of catalytic properties of streamlining surface on its radiative heating should be performed in future. Here we present some numerical simulation results on convective and radiative heating of Exomars under angle of attack, which were obtained for catalytic surface.

Figure 13*a* shows distribution of convective and integral radiation heat fluxes along over all Exomars' surface in the plane z=0. Coordinate along the surface in equatorial plane is counted out from the point #1 showed in Fig. 12*f*. This point is located on the bottom boundary of the first grid block. Presented data demonstrate significant fact of convective heating domination on the windward part of the surface, and of the radiative heating domination on the leeward part of the surface. Note, that such a ratio of levels of convective and radiative heating is very sensitive to initial conditions.

In the case under consideration general contribution into radiation heat flux provides infrared radiative energy. Figure 13*b* shows spectral heat fluxes traceable at different points along surface. Locations of the points on the surface are elucidated in Fig. 12*f*. It is clearly seen from Fig. 13*b* that infrared radiation emitted by vibrational bands of CO_2 and CO is really dominant in the spectrum of heat radiation. Some insignificant contribution into integral heat flux one can observe in the visible and near-ultraviolet part of the spectrum for the points location on the windward surface.

2.3.4. Radiative gasdynamics of MSL

Detail investigation of convective heating of MSL is presented in [38]. Non-axisymmetric nonequilibrium full Navier-Stokes equation solver LAURA (Langley Aerothermodynamic Upwind Relaxation Algorithm) [53] was used in [38]. For Mars flight conditions, LAURA models an 8-species Mars gas (CO_2, CO, N_2, O_2, NO, C, N, O) in chemical and thermal non-equilibrium using the Park'94 reaction rates [54]. A finite-volume approach was used on a structured grid to solve the full Navier – Stokes flowfield equations. The code uses Roe's averaging for inviscid fluxes with second-order corrections using Yee's symmetric total variation diminishing scheme. A super-catalytic wall boundary condition fixes the species mass fractions for CO_2 and N_2 at their freestream values of 0.97 and 0.03, respectively. This boundary condition results in conservative heating rate predictions in flight. A radiative-equilibrium wall temperature was specified as $q_w = \varepsilon\sigma T_{w;rad-eq}^4$, where $\varepsilon = 0.9$ is the surface emissivity.

It was stressed in [38] that all heating results reported there are convective only, and the heat radiation contribution was expected to be small and was therefore excluded from the analysis. Calculation data obtained in [26] were successfully used for verification of 3D flow fields predicted in the given paper. Nevertheless predictions of the given paper show that the radiative heating of MSL's surface should be taken into account.

Figures 14 show flow field about space vehicle MSL with catalytic surface under angle of attack $\alpha = 11°$. As before, a snaking was assumed to be zero therefore the calculations were performed in half of the whole calculation domain (i.e. Y0X is the plane of symmetry). The distinctive features of the flow field are the following:

- Predicted asymmetry of the flow field (longitudinal velocity (*a*), mass fractions (*b,c*), translational and vibrational temperatures (*d,e*)) is formed due to angle of attack $\alpha = 11°$;
- As well for other entry probes, an expansion of shock layer above windward surface from the direction of incident flow is observed. The vortex structure above top piece of leeward surface is also observed;
- Significant differences in distributions of mass fractions of molecules CO_2 and CO are observed for non catalytic and catalytic surface. The non catalytic surface is characterised by increased mass fraction of CO and decreased mass fraction of CO_2 in the vicinity of streamlined surface, while high mass fractions of CO_2 and low mass fractions of CO are characterised for catalytic surface (Figs. 14*b,c*);
- Convective heating of catalytic surface is about two times higher than for non-catalytic one;
- It is not observed significant influence of catalytic properties of MSL's surface on its integral and spectral radiative heating.

The radiative heating of MSL's surface, as is observed, higher than for Pathfinder, and also should be taken into account at the leeward part, where integral radiation heat fluxes achieve values about 2-3 W/cm^2. This part of the surface is exposed by infrared radiation in vibrational bands CO_2 and CO from large volume of heated gas in the wake region. Emissivity of vibrational bands of CO_2 and CO is easily observable in Figs. 15*b,c*;

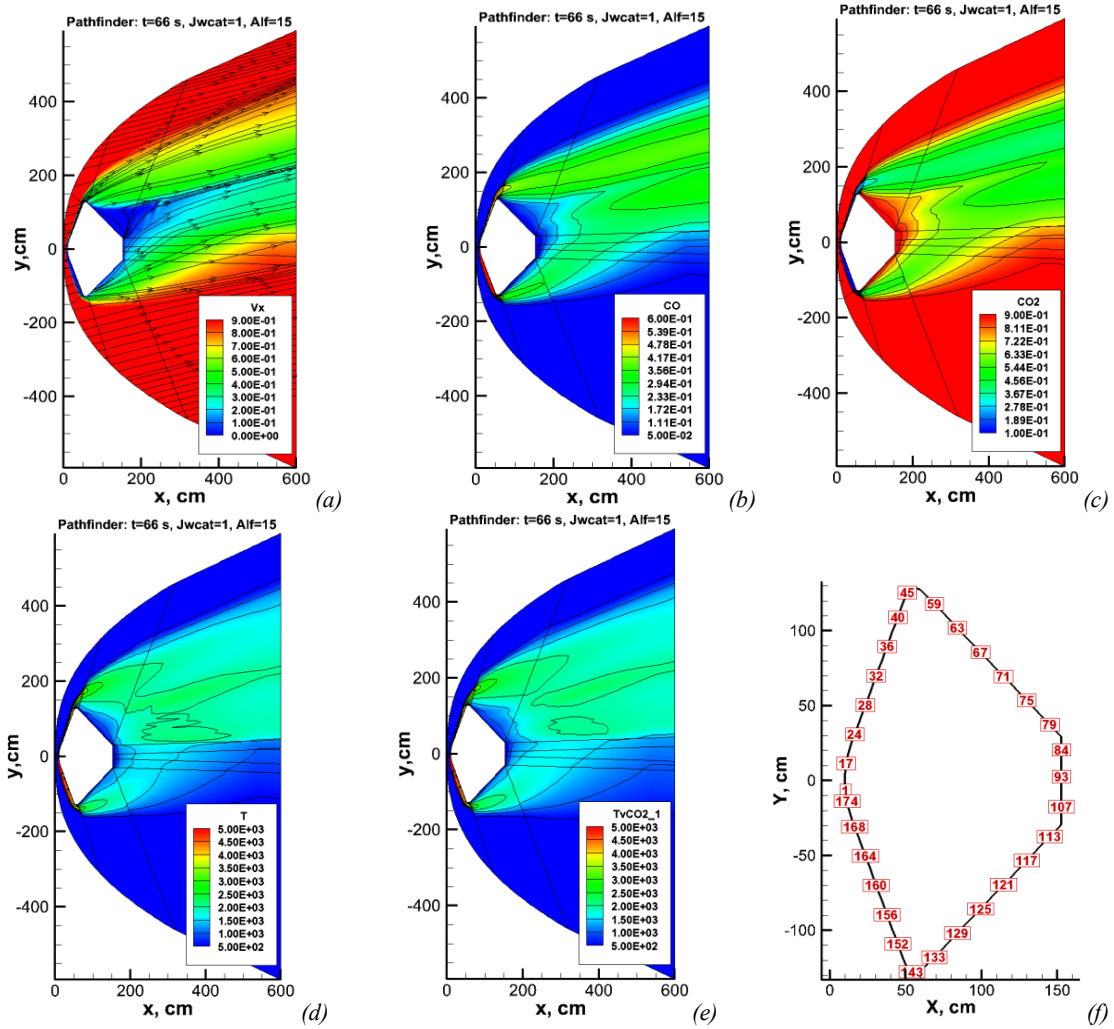

Figure 10: Flow field about Pathfinder at angle of attack $\alpha = 15°$ (trajectory point $t = 66$ s): *a*- longitudinal velocity, molar fractions of CO (*b*) and CO_2 (*c*) for catalytic surface, *d* - translational temperature, e – vibrational temperature of CO_2anti-symmetric mode; *f* - location of grid nodes in equatorial cross section

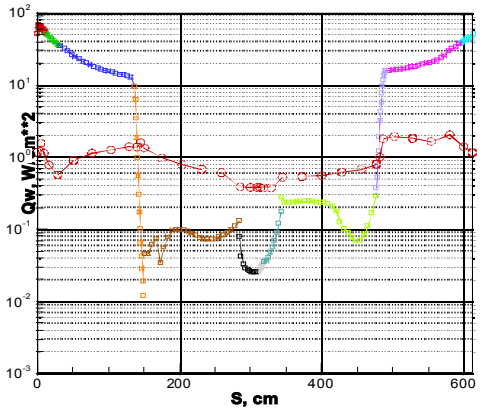

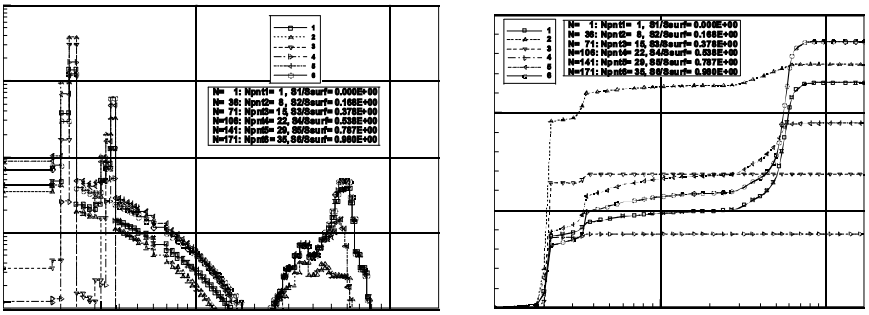

(*b*) (*c*)

Figure 11: Convective (squares) and radiative heating (circles) of Pathfinder's catalytic surface (trajectory point $t = 66$ s) (*a*); spectral heat fluxes (*b*) and cumulative function (*c*) for six points on the non-catalytic surface. Angle of attack $\alpha = 15°$

Table 3: Trajectory points for PATHFINDER[35]

t, s	ρ_∞, g/cm^3	p_∞, erg/cm^3	V_∞, km/s	T_∞, K
40	0.724×10^{-8}	1.660	7.496	122
42	1.01×10^{-8}	2.462	7.490	129
52	5.76×10^{-8}	15.56	7.364	143
66	2.80×10^{-7}	89.41	6.596	169
80	8.54×10^{-7}	282.0	4.717	175

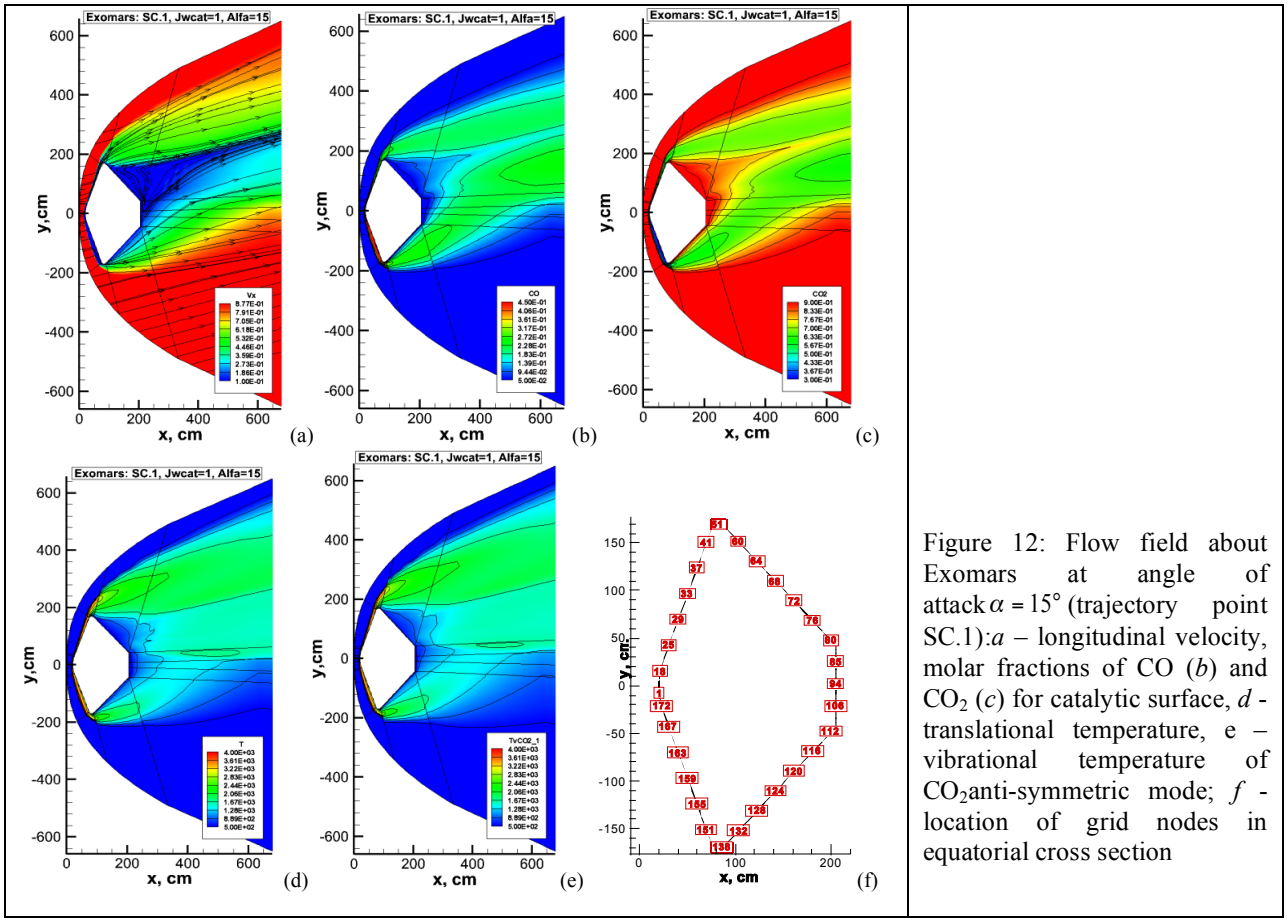

Figure 12: Flow field about Exomars at angle of attack $\alpha = 15°$ (trajectory point SC.1):*a* – longitudinal velocity, molar fractions of CO (*b*) and CO_2 (*c*) for catalytic surface, *d* - translational temperature, e – vibrational temperature of CO_2anti-symmetric mode; *f* - location of grid nodes in equatorial cross section

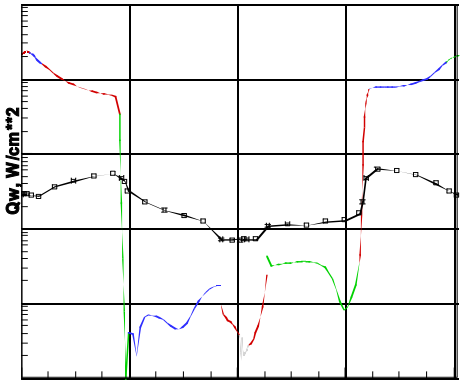

(a)

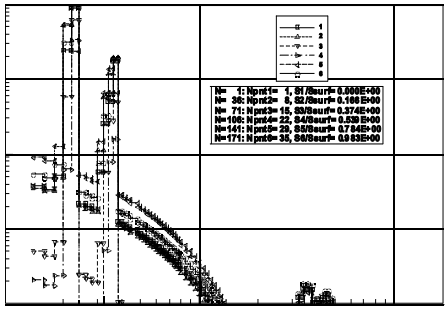

(b

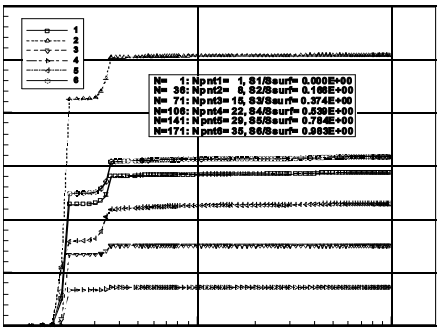

) *(c)*

Figure 13: Convective (squares) and radiative heating (circles) of Exomars' catalytic surface (trajectory point SC.1)(*a*); spectral heat fluxes (*b*) and cumulative function (*c*) for six points on the non-catalytic surface. Angle of attack $\alpha = 15°$

Table 4: Trajectory points for EXOMARS [54]

	ρ_∞, g/cm^3	p_∞, erg/cm^3	V_∞, km/s	T_∞, K
SC.1	6.838×10^{-7}	200.3	4.922	195
SC.2	1.069×10^{-6}	324.6	4.474	194
SD.1	3.708×10^{-7}	137.4	4.878	158
SD.2	5.534×10^{-7}	205.9	4.489	153
Cold94.1	1.186×10^{-6}	352.8	3.842	155
Storm90.1	1.911×10^{-7}	77.3	5.268	211

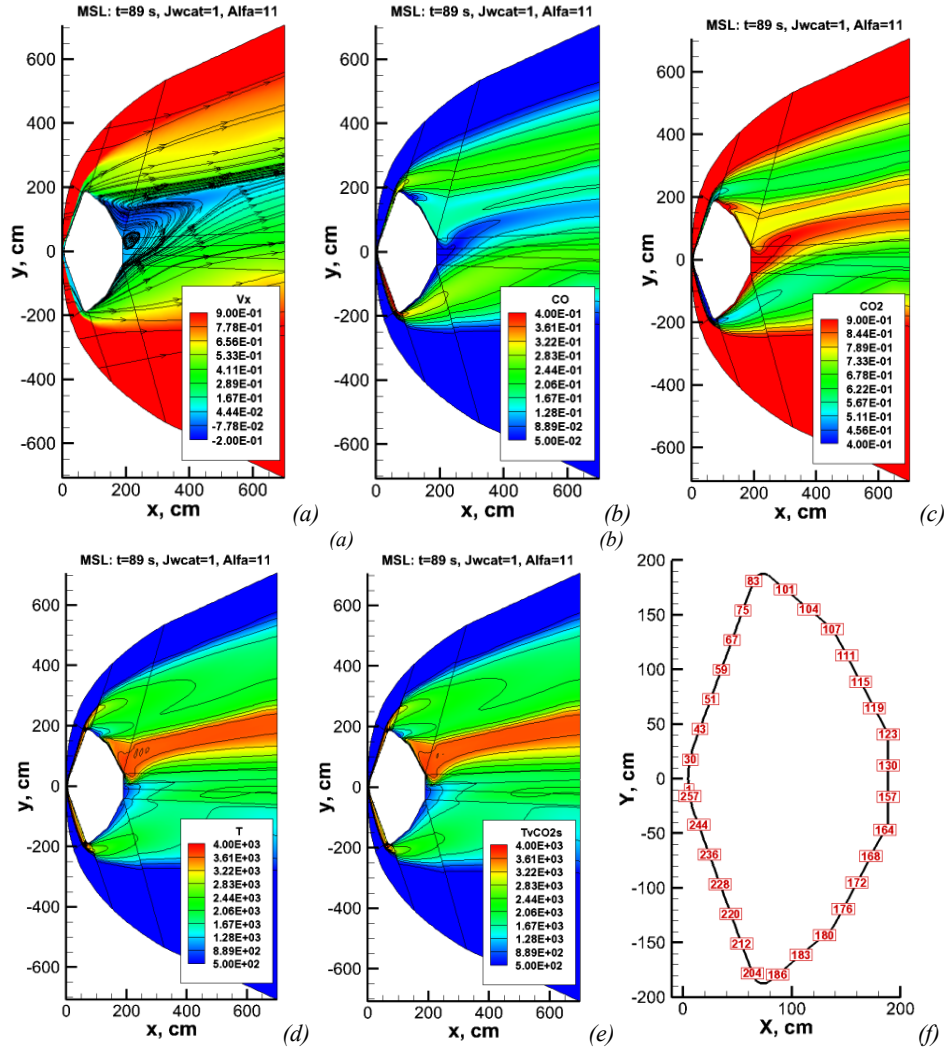

Figure 14: Flow field about MSL at angle of attack $\alpha = 11°$ (trajectory point $t = 80$ s): *a* – longitudinal velocity, molar fractions of CO (*b*) and CO_2 (*c*) for catalytic surface, *d* - translational temperature, e – vibrational temperature of CO_2anti-symmetric mode; *f* - location of grid nodes in equatorial cross section

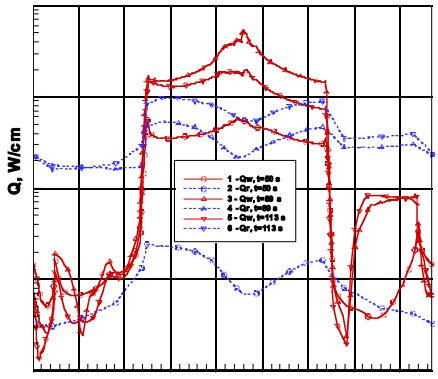

(a)

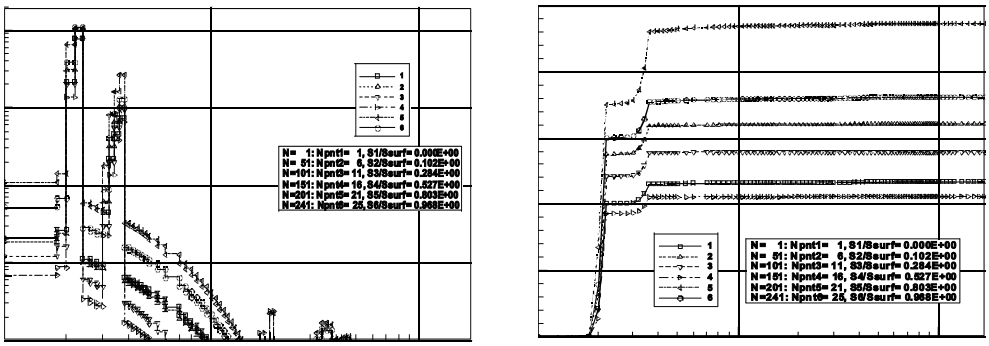

(b) *(c)*

Figure 15: Convective (squares) and radiative (circles) heating of MSL's surface at $t = 80$ s for catalytic surface (*a*); *c*– spectral heat fluxes, and cumulative function (*d*) for six points on the non-catalytic surface. Angle of attack $\alpha = 11°$

Table 5: Freestream conditions for CFD analysis of MSL [37]

Time, s	h, km	ρ_∞, g/cm^3	p_∞, erg/cm^3	V_∞, km/s	T_∞, K
50	68.3	4.71×10^{-9}	1.29	5.54	145
70	47.7	7.63×10^{-8}	21.5	5.48	149
80	38.3	2.10×10^{-7}	64.3	5.31	162
89	31.0	4.74×10^{-7}	150.	4.98	179
103	22.3	1.05×10^{-6}	377.	4.10	189
109	19.6	1.44×10^{-6}	517.	3.63	190
113	18.0	1.48×10^{-6}	534.	3.32	191
137	14.2	2.43×10^{-6}	886.	1.95	193

2.2. Partial conclusion: the challenging problems of the Martian entry aerothermodynamics

Three-dimensional laminar convective and radiative heating predictions have been performed for three Martian entry probes. These are: Pathfinder, Exomars and Mars Science Laboratory. Presented numerical simulation results for convective heating were successfully compared with available calculation data for Pathfinder [24,25] and Mars Science Laboratory [26]. Presented calculation data on radiative heating predict significant contribution of the heat radiation into total heating of leeward surface of the space vehicles. Afterbody radiative heating rates are predicted to be generally one order higher than the laminar convective heating.

It should be taken into account that in this part we analyzed preliminary numerical simulation results which were obtained with assumption of local thermodynamic equilibrium of dissociated mixture of CO_2 and N_2in nearby and far regions of wake. But, at the same time, our calculation data demonstrate significant differences between translational and vibrational temperatures just in the wake. It means that to receive more reliable data concerning radiative heating of leeward surfaces of Martian space vehicles fully non-equilibrium radiative gas dynamic problem should be solved in the future.

3. Radiative aerothermodynamics of the Jupiter

3.1 Introduction

Many studies have been focused on thermal analysis and aerothermodynamics of Galileo probe (shown in Figure 16) from the mid-seventies to the early eighties for the mission preparation [57-58-59-60] and more recently for the post-flight analyses [61-62-63-64]. Due to very high radiative and convective heat-fluxes characterizing a Jupiter entry, the dominant uncertainty factor associated to the heat-shield recession calculations was the radiation absorption within the ablation layer. As a consequence, for this mission, the evaluation of the blockage (convective

and radiative) was a major issue and a thorough effort was carried out for its estimate [65]. Among the different studies, several contributions have provided some estimate of the blockage factors and blowing rates for a Jupiter entry [57,66-67]. Another issue was the turbulence that has been extensively investigated [57,59,66-67]. Rarefied effects were also investigated for the mission preparation [68].

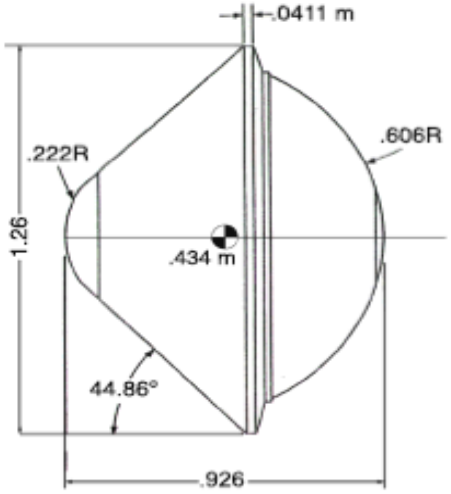

Figure 16: Scheme of Galileo probe[69]

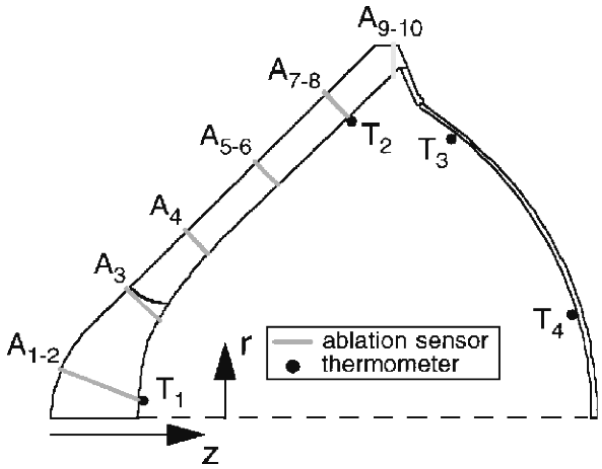

Figure 17: Location of ablation sensors (A1-10) and thermometers (T1-4) on Galileo probe [70]

Galileo probe was equipped with ablation detector sensors (ARAD) for collecting flight data during entry. The in-flight experiments have been well detailed by Milos [70]. Ten ablation sensors were included in the TPS, at 6 different locations, as shown in Figure 17. The descent module was also containing an instrument for measuring temperature, density and pressure profiles along the trajectory. Four resistance thermometers were also bonded inside the aluminium structure as shown in Figure 17. Data from the heat-shield experiments were transmitted from Galileo orbiter to Earth and then analysed [70-71].

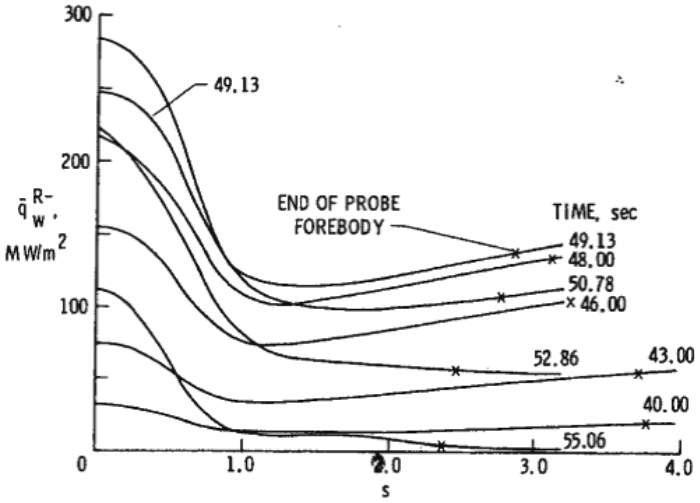

Figure 18: Forebody distributions of radiative heating at different trajectory locations [58]

The different post-flight analysis carried out to reconstruct the thermal protection system (TPS) recession have highlighted different points:

- There are large discrepancies between most of the numerical rebuilding and the flight data;

- Accuracy of chemical kinetics and thermodynamic data for H and H^+ species;
- VUV absorption mechanisms such as photo-ionization and radiation from spalled particles should be considered;
- Since the ionization level is high, the validity of existing models is questionable.

The last point is a key issue since for such entry conditions, ionization can be strong. Additionally, most of the chemical kinetics models have been built for low or moderate levels of ionization and their reliability for such high-enthalpy flows has not been fully established.

In the frame of this study a computational test matrix for the numerical simulations has been selected, based on the numerical, experimental and flight results obtained for Galileo. Then, a chemical kinetics model has been set up accounting from previous efforts. Finally, numerical computations of Galileo flow-field have been performed and comparisons with other data are presented with a focus on the results obtained with some non-equilibrium at high altitude.

3.2. Survey and computational matrix

For the mission preparation, numerical predictions have not only been done using engineering correlations [57] but flow-field solutions have been also computed. First numerical simulations have been done for shock-layer solutions at chemical equilibrium [67,72], later on Navier-Stokes solutions have been calculated [58,60] still at chemical equilibrium.
Most of the available numerical data focused on the evolution during entry of stagnation point heat-flux. Radiative surface heat-flux distributions with and without blowing are available in [57,59-60,67]. These results have been obtained at chemical equilibrium for laminar and turbulent flow conditions. Forebody distributions of radiative heat-flux at different entry times are shown in Figure 18.

Time, s	Altitude, km	Velocity, km/s	Density, kg/m^3	Pressure, bars	Temperature, K
0.00	450	47.406	3.47E-09	7.21E-08	527.8
7.30	400	47.429	9.92E-09	1.45E-07	381.9
14.80	350	47.451	5.65E-08	4.35E-07	210.8
22.50	300	47.468	3.05E-07	2.13E-06	195.9
30.44	250	47.446	2.77E-06	1.60E-05	163.2
34.51	225	47.368	7.73E-06	4.45E-05	162.8
38.67	200	47.135	2.16E-05	1.23E-04	160.4
40.35	190	46.951	3.16E-05	1.84E-04	165.0
42.06	180	46.674	4.81E-05	2.75E-04	161.9
43.79	170	46.256	7.03E-05	4.12E-04	165.8
45.55	160	45.667	1.00E-04	6.06E-04	170.6
47.36	150	44.813	1.49E-04	8.90E-04	168.9
49.21	140	43.531	2.27E-04	1.32E-03	164.3
51.16	130	41.591	3.49E-04	1.99E-03	160.8
53.23	120	38.617	5.56E-04	3.02E-03	153.6
55.52	110	34.296	8.34E-04	4.62E-03	156.6
58.19	100	28.440	1.23E-03	7.00E-03	160.6
61.57	90	21.342	1.85E-03	1.05E-02	160.1
66.35	80	13.544	3.06E-03	1.60E-02	147.8
74.55	70	6.352	5.30E-03	2.57E-02	136.9
89.77	60	2.261	9.48E-03	4.23E-02	126.3
111.02	50	0.833	1.89E-02	7.51E-02	112.4

Table 6: Entry trajectory and reconstructed atmosphere [70]

The flight data have been analysed [70-71] and the entry trajectory, as well as the atmospheric properties have been determined. They are all reported in Table 6. Using the determined trajectory, post-flight analyses have been carried out to reconstruct the TPS recession using numerical simulations. Some of these results are reported in Figure 19. They highlight the point [74] that for Galileo, when comparing the predicted surface recession and the flight data, the measured recession is around half of the calculated value at the stagnation point and twice as large on the frustum. Figure 19 shows that the predicted recession overestimates the flight data by 30% in the stagnation region, while it substantially underestimates the flight data by 50% in the frustum region.

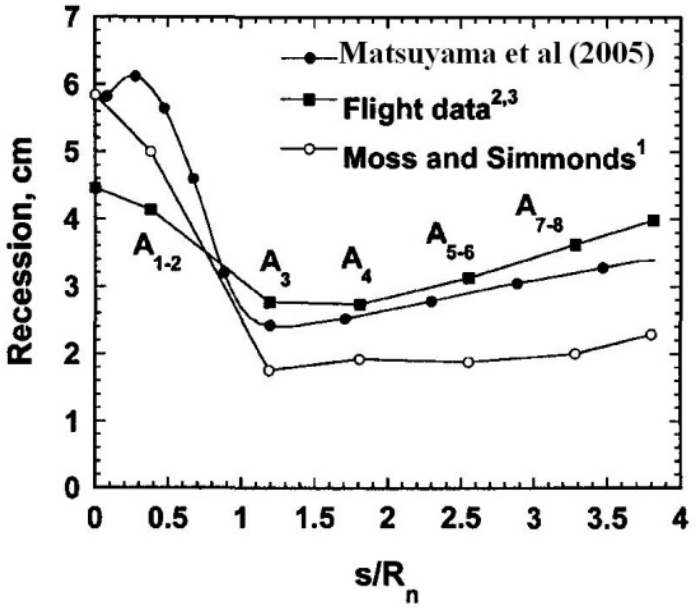

Figure 19: Predicted surface recession and flight data

The discrepancy in the stagnation region might be due to issues related to radiation and high temperature thermodynamic [64]. Concerning the frustum, the standard turbulence models failed to reproduce the anomalously high heating rate in the frustum at the origin of the higher recession. It has been pointed out [73-74] that the promotion of boundary layer turbulence due to injection of pyrolysis gas, not accounted for in standard turbulence models, was the potential source of discrepancy. Accounting for these phenomena leads to a much better agreement between predictions of recession and flight data as reported in [64].

Recently, several contributions have been published focusing on Galileo post-flight reconstruction. Matsuyama et al [61] have performed a set of calculations (8 trajectory points) for computing the gas mixture and the ablation products with an assumption of thermochemical equilibrium. Seven species were considered for the atmosphere model: H_2, H, He, H_2^+, H^+, He^+, e^- and 18 additional species, C, C_2, C_3, C_4, C_5, C^+, CH, C_2H, C_3H, C_4H, C_5H, CH_2, C_2H_2, O, O_2, O^+, CO and CO_2 for the ablation products.

The most recent contributions for rebuilding Galileo data have been carried out by Furudate et al [63] and Park [64]. In the first study, the non-equilibrium influence has been investigated using Euler solutions and a 7 species model, H_2, He, H, H^+, H_2^+, He^+, e^-, for the trajectory points (the same as in [61]). The contours of translational and vibrational temperatures predicted by Furudate et al [63] for an altitude of 170 km are plotted in Figure 18, while Figure 19 shows the contours of mole fractions of atomic hydrogen and electrons. Apparently, the translational temperature reaches 50 000 K in the stagnation region, the non-equilibrium region is one cm width covering half of the shock-layer. If the simulations for 170 km exhibit some non-equilibrium behaviour, at 130 km the equilibrium is nearly reached.

In the literature, the most computed point is the peak heating location. Calculations at this trajectory point have been carried out in [58,61,63,64,75]. Calculations carried out in [61] and [63-64] were performed for the same trajectory points.

A test matrix has been selected based on the different numerical predictions. The velocity and atmosphere parameters along the entry trajectory are available in Table 6. This gives the advantage to have all necessary variables requested for the calculations: velocity, pressure, density and temperature. Since there are contours of variables available for the points at 170 and 130 km, it is useful for future comparisons to have them in the matrix. This is also the case for the trajectory point at 180 km of altitude [75] that has been included (even if the density retained for the calculations does not fit the flight data of Table 6). To these three points, the point at 120 km, considered to be the peak heating in [63] while peak heating is located at 130 km in [74], has been added. A last point included in this list, is the location of the maximum of convective flux occurring at 100 km of altitude according to [64]. The final matrix for the numerical simulations with velocity and atmosphere parameters is shown in Table 7.

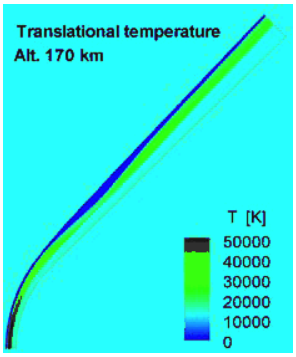

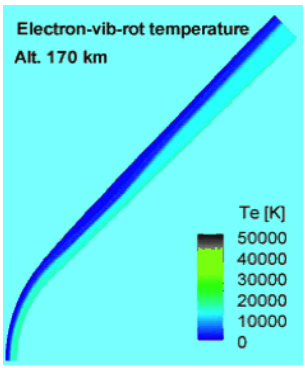

Figure 18: Temperature contours at 130 and 170 km predicted in [63]

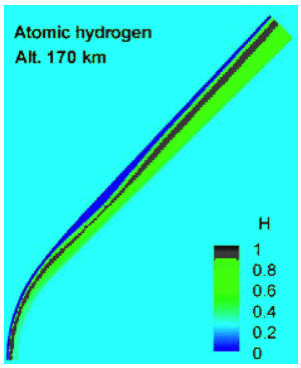

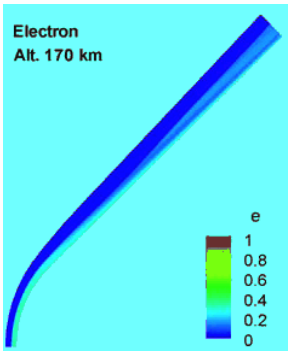

Figure 19: Mole fraction contours of atomic hydrogen and electrons [63]

Entry time (s)	Altitude (km)	Velocity (km/s)	Density kg/m^3	Pres., Pa	T, K
42.06	180	46.674	4.81 e^{-5}	27.5	161.9
43.79	170	46.256	7.03 e^{-5}	41.2	165.8
51.16	130	41.591	3.49 e^{-4}	199.0	160.8
53.23	120	38.617	5.56 e^{-4}	302.0	153.6
58.19	100	28.44	1.23 e^{-3}	700.0	160.6

Table 7: Test matrix for numerical simulations

Reaction	A (cm^3/mol/s)	b	E_f (J)	T_r
R1	2.27e13	0.5	157800.0	Te
R2	1.33e13	0.5	285200.0	Te
R3	6.20e10	0.5	116000.0	Te
R4	4.89e10	0.5	116000.0	T
R5	4.17e18	-1.0	52340.0	T
R6	1.04e19	-1.0	52340.0	T
R7	8.346e19	-1.0	52340.0	T
R8	8.346e19	-1.0	52340.0	T
R9	8.346e19	-1.0	52340.0	T
R10	6.604e14	-0.4	0.0	T

Table 8: Constants and controlling temperature for the kinetic rates

3.3. Kinetic scheme and transport properties

First computations [76] have been carried out to assess the code capabilities [77] for Jovian entry conditions, the computations have been carried out for all trajectory conditions of Table 7. For this purpose, the thermodynamic and kinetic models already used for ESA internal studies [75,78] have been selected. Numerical results have been obtained [76] but they have highlighted the need to perform additional effort for the kinetic model.

As a consequence, a kinetic model has been set up accounting for previous efforts carried out for simulating Jupiter entry. Several chemical kinetics models can be found in the literature related to entry into giant planet atmospheres [79]. Most of them have been developed and used for the Galileo mission [80]. Other models retained for recent studies carried out for Jovian entry [63,75] or Neptune entry [81-82], have been also considered.

Among, the different models, those proposed by Tiwari&Szema [80] and Furudate et al [63] are the most detailed. Tiwari&Szema [80] have proposed a model with 6 species H_2, He, H, H^+, He^+, e^-, and 11 reactions. Furudate et al [63] have published a recent contribution for rebuilding Galileo entry. In this study, the non equilibrium influence has been investigated using Euler solutions and a 7 species model, H_2, He, H, H^+, H_2^+, He^+, e^-, accounting for the non-equilibrium ionization of H and the photo-ionization of H_2. In both models the reaction schemes are based on the measurements of Leibowitz [83]. The different reactions describe the dissociation of molecular hydrogen, excitation of electronic states of hydrogen and helium, and ionization of atomic species by collisions with atoms and electrons.

Using these two models, a chemical kinetics model has been set up by selecting some of the reactions and related chemical rates. The photo-ionization has not been retained since this phenomenon cannot be yet accounted for radiation calculations using PARADE [84]. The discrimination of the rates has been carried out for ensuring the model consistency (from a numerical point of view) and an easy incorporation in TINA [77]. Using this approach a 6 species model H_2, He, H, H^+, He^+, e^-, has been set up with 9 reactions. A variation of this model, with 7 species (H_2, He, H, H^+, H_2^+, He^+, e^-) and 10 reactions, has been also used for the calculations. The chemical reactions retained for the computations are:

$$H + e^- = H^+ + e^- + e^- \quad (R1)$$
$$He + e^- = He^+ + e^- + e^- \quad (R2)$$
$$H + H = H^+ + e^- + H \quad (R3)$$
$$H + He = H^+ + e^- + He \quad (R4)$$
$$H_2 + He = H + H + He \quad (R5)$$
$$H_2 + H_2 = H + H + H_2 \quad (R6)$$
$$H_2 + H = H + H + H \quad (R7)$$
$$H_2 + H^+ = H + H + H^+ \quad (R8)$$
$$H_2 + e^- = H + H + e^- \quad (R9)$$
$$H_2^+ + e^- = H + H \quad (R10)$$

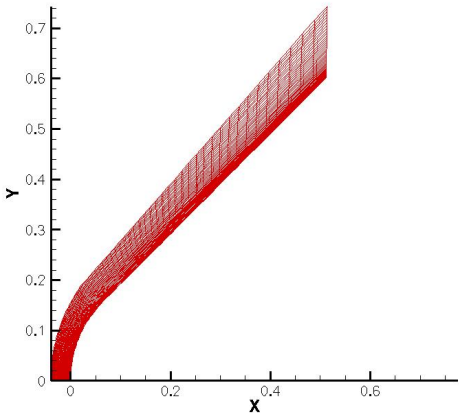

Figure 19: Final mesh used for the calculations

The forward reaction rates are described using the following Arrhenius law,

$$k_f = A T_r^n \exp\left(-\frac{E_f}{RT}\right)$$

The values for the different constants are reported in Table 8. The rates for reaction R1 to R4 are from [80] while those for reaction R5 to R10 are taken from [63]. Concerning the controlling temperature, for the calculations a two-temperature model is used with the assumption that the electronic temperature is equal to the vibrational temperature.

The thermodynamic and transport properties for the chemical species have been taken from CEA [85] (Chemical Equilibrium with Application), as an in-depth study of the model at high temperature, typical of a Jovian entry, has not been yet undertaken but such a task is planed in future efforts.

3.4. A Jupiter entry: numerical simulation results

Calculations have been carried out using TINA [77], a Navier-Stokes solver, accounting for chemical and vibrational non-equilibrium. It is adapted to the simulation of hypersonic flows encountered in high enthalpy nozzles or during entries, where enthalpies and local Mach numbers are high enough to allow non-equilibrium effects. The solver uses a time marching algorithm with the approximate Roe-Riemann solver and the flux limiters proposed by Yee [86] for inviscid flows. The thermo-chemistry is implicitly coupled to the flow-field for computing the non-equilibrium effects.

The computations have been performed for the trajectory points reported in Table 7. However, most of the figures are related to the results obtained for the trajectory point with the highest altitude since it is the point with the highest non-equilibrium effects due to the high velocity and low pressure. Several meshes have been used for the calculations to assess the grid dependence of the results.

The final mesh is 80×80 cells, it is shown in Figure 19. The first cell along the axis is 10 μm, special care has also been given to densify the cells at the shock location. The domain extends over 4 cm along the stagnation line and 15 cm at the leading edge. For the calculations, an isothermal wall at 3 000 K, the temperature of carbon sublimation, has been retained. Calculations with a wall temperature of 4000 K did not show some influence on the flow-field. A non-catalytic wall has been retained for the simulations, at the exception of the ionic species, which recombine at the wall.

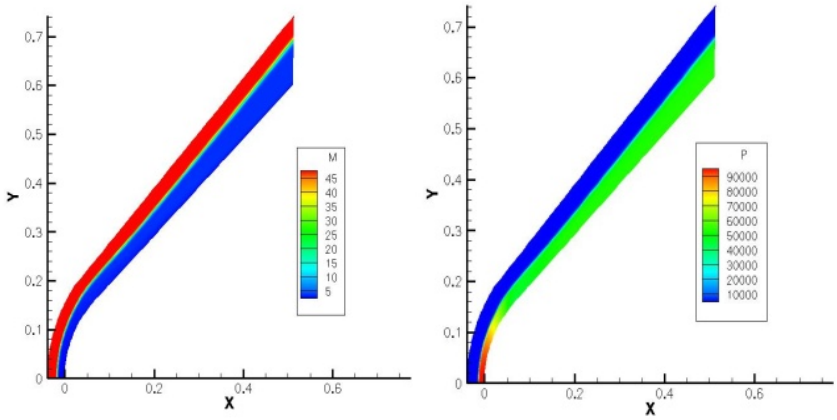

Figure 20: Mach number (left) and pressure (right) distributions obtained with the 6 species model at 180 km of altitude

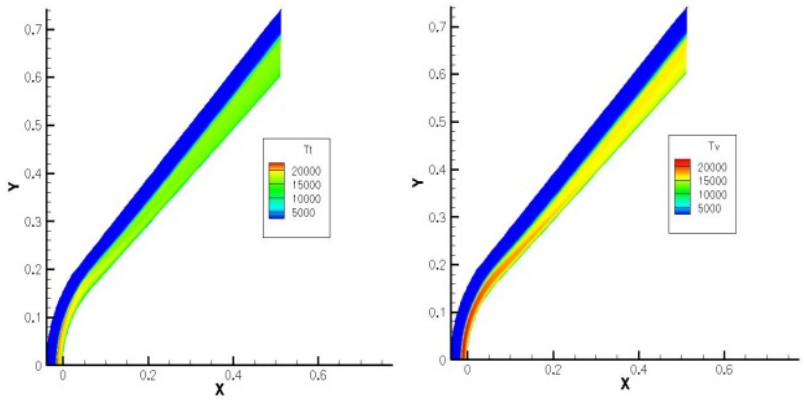

Figure 21: Translational and vibrational temperature distributions predicted with the 6 species model at 180 km of altitude

The free-stream was the nominal Jupiter atmosphere with 76% of H2 and 24% of He in volume fractions. Calculations have been carried out with a CFL of 0.5, one order of magnitude larger than in previous computations [76]. Numerical simulations have been carried out for laminar flows using the 6 and 7 species models presented in the previous section. The convergence was reached after 200 000 iterations and the residual was around 10^{-4}.

The predicted Mach number and pressure distributions are shown in Figs. 20, the translational and vibrational temperatures in Figs. 21. The simulations with the 6 and 7 species models did not show some influence on the flow-field topology and flow variables such as the Mach number, the pressure, and the temperature. The shock standoff predicted numerically is 1.5 cm at the stagnation point for the altitude of 180 km. This value is very close to the predictions obtained by Savajano [75] for the same altitude but with atmosphere conditions slightly different. For the stagnation pressure, its maximum is close to 1bar at the stagnation point, lower than the value of 1.2 bar obtained in [75]. However, in this last study the free-stream density was 20 % higher, with a value of 6.610^{-5} kg/m^3 instead of $4.81\ 10^{-5}$ kg/m^3 in the current simulations.

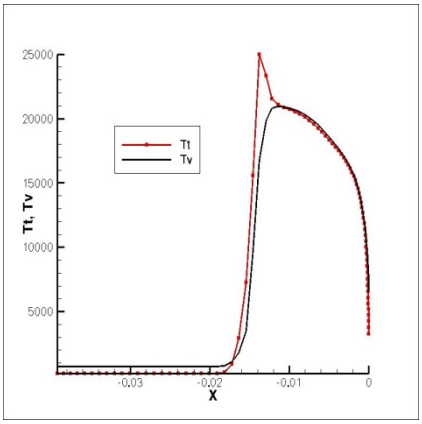

Figure 22: Translational and vibrational temperatures along the stagnation line predicted with the 6 species model at 180 km of altitude

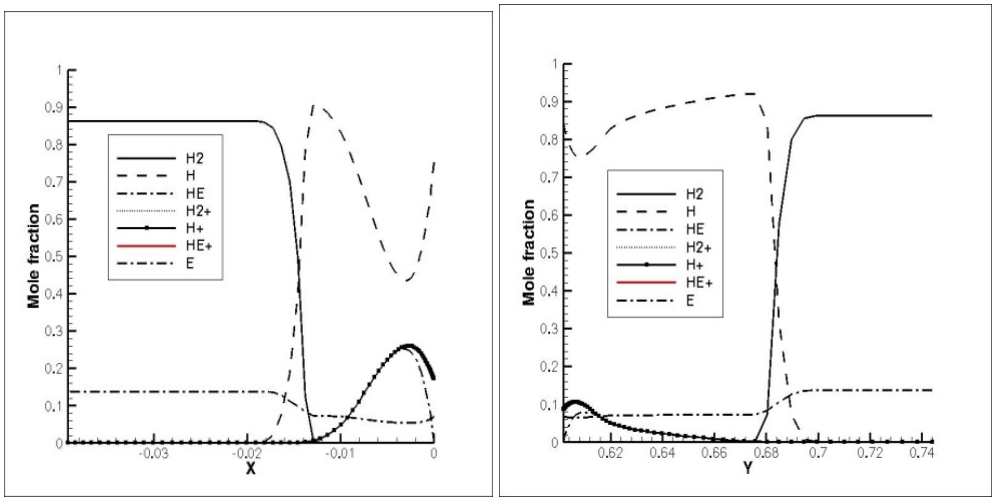

Figure 23: Mole fraction distributions of species along the stagnation line (top) and at the leading edge (bottom) predicted with the 7 species model at 180 km of altitude

The temperature distributions along the stagnation line predicted with 6 species at 180 km of altitude are plotted in Figure 22. The figure puts in evidence a small region of non-equilibrium just behind the shock, according to the calculations this zone extends over 3 mm approximately. The maximum of the vibrational temperature is 20 000 K in the stagnation region while the translational temperature reaches a value of 25 000 K. This is in good agreement with the value predicted for the translational temperature at the same location (also 25 000 K) in [75].

When comparing with the results obtained by Furudate et al [63] shown in Figure 17, the agreement is apparently good for the vibrational temperature but not for the translational one. The results obtained for the same altitude

exhibits the same differences. As a consequence the reason of this discrepancy does not come from the trajectory location but more certainly from the different chemical kinetics and transport properties used in the two studies.

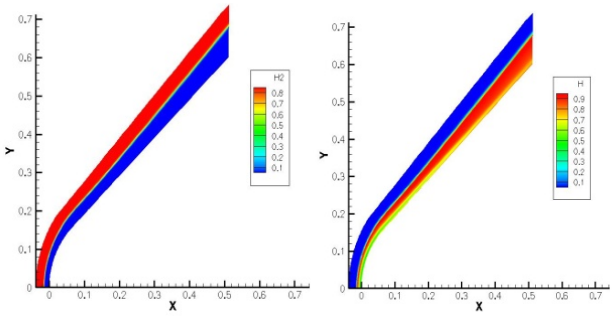

Figure 24: Mole fraction distributions of molecular hydrogen (left) and atomic hydrogen (right) predicted with the 6 species model at 180 km of altitude

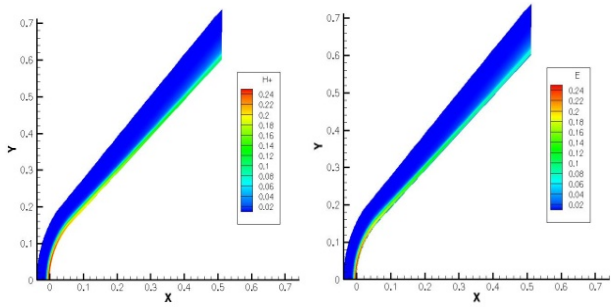

Figure 25: Mole fraction distribution of protons (left) and electrons (right) predicted with the 6 species model at 180 km of altitude

The species mole fraction distributions along the stagnation line and at the leading edge predicted with the 7 species model are plotted in Figure 23. The mole fraction flow-field of molecular and atomic hydrogen, as well as electrons and protons are plotted in Figs. 24-25. These distributions show that most of the hydrogen is dissociated in the shock-layer. In the same figure, the distribution of atomic hydrogen shows the presence of a high fraction of atomic hydrogen in the shock-layer that decreases in a thin band at the vicinity of the wall. This flow-field topology agrees qualitatively with the results shown in Figure 18 where a similar thin band with a lower level of mole fraction of atomic hydrogen. This thin band corresponds of the maximum of hydrogen ionization that can be observed in Figure 25. In this thin band, the level of protons is high since it reaches a local maximum of 0.25 in the stagnation region.

The mole fraction of electrons is plotted in Figure 27. The distribution of electrons is similar to the distribution of protons since the level of ionization of helium is very low. The maximum of ionized helium is of the order of 10^{-5} (in mole fraction) in the stagnation region as shown in Figure 26. The electron mole fraction reaches a maximum of 0.25 in the stagnation region that can be observed in Figure 25 These predictions seem to be close to those obtained by Furudate et al [63] shown in Figure 18.

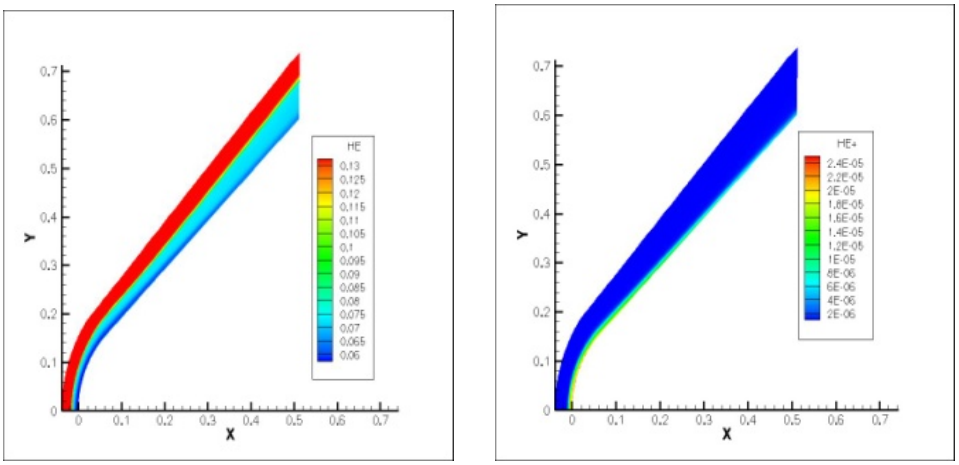

Figure 26: Mole fraction distribution of He (left) and H_e^+ (right) obtained with the 7 species model at 180 km of altitude

The distribution of the mole fraction of He is displayed in Figure 26. The higher values in the shock-layer are due to the massive ionization there that increases the number of species. The mole fraction distribution of H_2^+ predicted using the 7 species model is plotted in Figure 27. However, this specie is not very abundant as demonstrated in Figure 23. The maximum of H_2^+ distributions is located in a band of the shock-layer located over the frustum of the capsule. Apparently, the molecular hydrogen is there ionized and this is the ion H_2^+, which is dissociated in the vicinity of the wall by the collisions with electrons. So far, no element of comparison has been found in the literature

and it is difficult to conclude on this point.

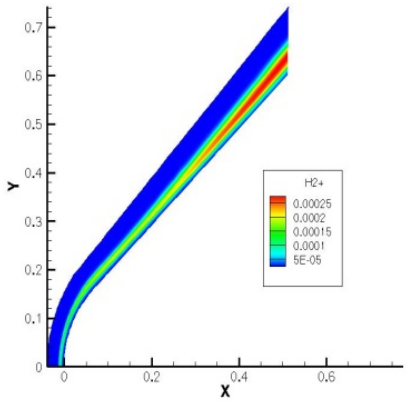

Figure 27: Mole fraction distribution of H_2^+ ions obtained with the 7 species model at 180 km of altitude

The last point concerns the convective heat-flux. Its value is equal to 105 MW/m^2 at the stagnation point, this for both 6 and 7 species models. In a previous communication [87] this value was compared to those predicted in [63] for 170 and 190 km of altitude, unfortunately this was a mistake since these values concerned a radiative flux. However, comparisons with pre-flight predictions [57-59] and with the results of Savajano [75] are possible. This value is in between the predictions of 79 and114 MW/m^2 done by Moss [59] for altitudes of 195 and 170 km respectively; it is higher than other predictions [57-58]. Comparisons with the results of Savajano [75] are interesting since this author obtains a convective stagnation-point heat-flux in between 74 and 158 MW/m^2 as function of the models retained for the thermodynamic and transport properties. This confirms that a certain effort is needed for investigating the chemistry of Jupiter atmosphere at high temperature.

3.5. Partial conclusion: the challenging problems of the Jupiter entry aerothermodynamics

The available data related to Jupiter entry have been gathered and analysed. Using the flight data and the CFD activities performed for the mission preparation and post-flight analyses, a computational matrix has been selected. In a second phase, a chemical kinetic model has been set up based on previous efforts.

Then, the computational matrix has been computed, and the effort of analysis concentrated on the trajectory point with the highest non-equilibrium. The numerical results obtained for 180 km of altitudes how generally a good agreement with other studies. Comparisons have also highlighted some discrepancies for the temperatures and heat-flux that underlines that some additional efforts are necessary for transport properties and thermodynamic. Future efforts will be concentrated for the prediction of radiative heat-flux and computations with a chemical kinetic model based on a state-to-state approach.

4. MHD Effects on Chemical Reacting Flow Past a Blunt-Body

4.1. Introduction

Many aerospace applications are characterized by low magnetic Reynolds number R_m (~1) and the aircraft re-entry problem is one of them. In fact, in the flight regime of interest, static temperature is too low (5000 K) for thermal ionization of air and it does not allow the electrical conductivity σ in hypersonic magneto-hydrodynamics (MHD) devices to be very high [σ<10^3 $(\Omega m)^{-1}$]. Up to now, only few works using upwind methods with a self-consistent, finite and non-homogeneous electrical conductivity have been afforded [88-92]. For this reason, in this work we have developed a two-dimensional MHD model describing a chemically reacting nitrogen hypersonic flow past a blunt-body. The electrical conductivity is obtained self-consistently by transport calculations solving Boltzmann equation with the third order approximation of the Chapman-Enskog method [93]. A four-species (N, N_2, N_2^+, e) reduced to three by plasma neutrality hypothesis, three-reactions scheme for nitrogen chemistry has been used [94]: two gas-induced dissociation channels ($N_2+N_2 \leftrightarrow N+N+N_2$ and $N_2+N \leftrightarrow N+N+N$) and the ionizing recombination

($N+N \leftrightarrow N_2^+ + e$). The system is considered ideal as regards the gas phase (Euler representation) but not ideal as regards the plasma-magnetic field interaction.

4.2. Numerical analysis

Free stream conditions used are density ρ_∞=1.48 gm^{-3}, pressure p_∞=132 Pa and temperature T_∞=300 K, corresponding to air properties of atmosphere at an altitude of 40 km [88]. A blunt-body diameter D=1.6 m has been taken into consideration and in all the cases the imposed initial magnetic field is uniform and perpendicular to the flow direction. Free stream conditions used are density ρ_∞=1.48 gm^{-3}, pressure p_∞=132 Pa and temperature T_∞=300 K, corresponding to air properties of atmosphere at an altitude of 40 km [88]. A blunt-body diameter D=1.6 m has been taken into consideration and in all the cases the imposed initial magnetic field is uniform and perpendicular to the flow direction.

4.3. MHD effect on a chemical frozen gas

First effects of magnetic field on the plasma flow with a fixed uniform electrical conductivity over the entire simulation domain have been studied. Figs. 1 show the two-dimensional pressure contour distributions in acoustic (B=0 in Fig. 28a) and plasma (B=5.2x10^{-3} T in Fig. 28b) fields at Mach number M_∞=3.05 using an electrical conductivity σ=4.9x10^5 (Ωm)$^{-1}$. Results reveal that the magnetic field effectively pushes the bow shock wave further away from the blunt body as already observed by different authors [91,92,95]. For this case, the shock envelope in the plasma field exhibits an outward displacement compared to the gas-dynamic shock by a factor 2 in standoff distance Δ (see Fig. 29b).

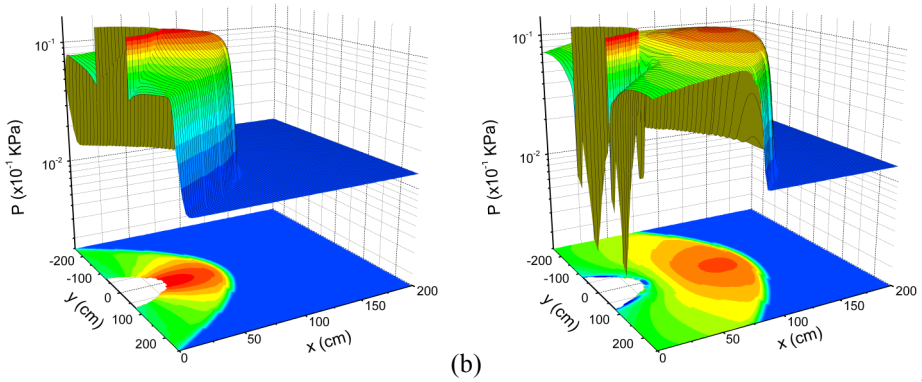

Figure 28: Two-dimensional distribution of pressure for (a) acoustic (B=0) and (b) plasma (B=5.2x10^{-3} T) flow field using a fixed electrical conductivity σ=4.9x10^5 (Ωm)$^{-1}$ for M_∞=3.05.

Numerical results for the acoustic field (B=0) show that pressure jump across the shock wave according to the Rankine-Hugoniot condition. Subsequently, pressure rises monotonically as the flow further compresses to the stagnation point of the blunt-body nose. In contrast, the post-shock pressure distribution along the line of symmetry in the MHD case follows a non-monotonic variation. As the strength of the magnetic field increases, a new secondary wave appears in addition to the main shock wave. The compression across the bow shock is subsequently followed by an expansion across the secondary MHD wave. This wave develops at the body surface and it is the result of the magnetic force $\boldsymbol{F}_m$ opposing to the flow velocity $\boldsymbol{u}$ and then tending to decelerate the flow. This can also explain the increased shock standoff distance observed for the case of imposed magnetic field (see Fig. 29b). In fact, the shock wave location results from a balance between the aerodynamic pressure P ahead of the shock and the total, aerodynamic plus magnetic, pressure, behind the shock. The magnetic pressure increases as B is increased, thus moving the shock wave away from the body. The gradients of the gasdynamic parameters decrease and the gasdynamic force exerted on the body also decreases, as shown by the surface pressure behaviour in Fig. 29a. This trend is completely reversed increasing the Mach number M_∞=5.4 with σ=1x10^3 (Ωm)$^{-1}$. In this case, the surface pressure (Fig. 29a) is an increasing function of the applied magnetic field, while the shock standoff distance (Fig. 29b) is almost unchanged, as already observed by Hoffmann-Damevin-Dietiker [91]. The reason for the reduction of magnetic effectiveness on the plasma flow is ascribed to the fact that the retarding magnetic force $\boldsymbol{F}_m$ is not more able to overcome the accelerating effect, which is larger due to the high Mach number value.

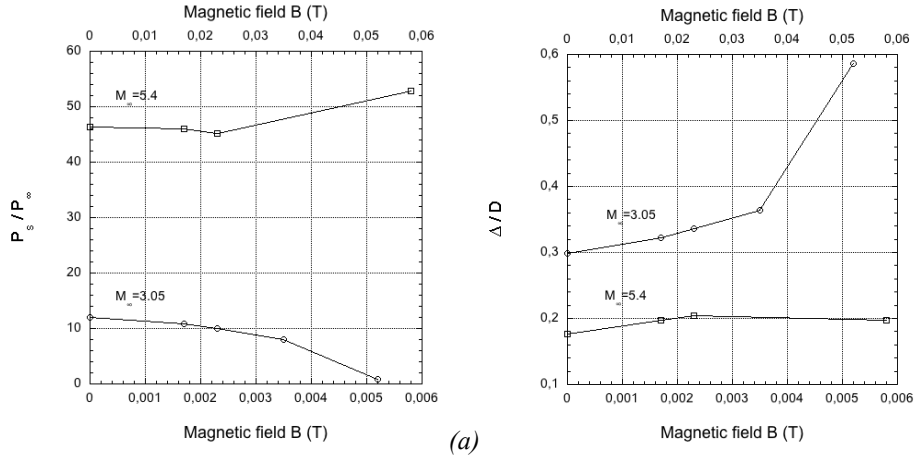

Figure 29: (a) Surface pressure and (b) shock standoff distance Δ as a function of magnetic field for the two flow regimes analyzed, M_∞=3.05 and M_∞=5.4 in the case of chemical frozen gas.

4.4. MHD effect on a chemical reacting gas

With self-consistent calculation of the electrical conductivity, as already observed in the boundary layer theory of Bush [96], the effectiveness of magnetic control is strongly reduced. MHD effects on plasma flow are almost absent for Mach number M_∞<16. The reason is ascribed to a very low ionization degree; electrical conductivity is too small to couple magnetic field with plasma flow. Only for high-hypersonic M_∞>16 conditions (corresponding to a specific enthalpy H of 16.4 MJ/kg), the ionization rate starts to became relevant and the conductivity acquires values enabling a coupling between plasma flow and magnetic field [97-99]. In Fig. 30a, profiles along the x-axis of σ for two different Mach numbers, M_∞=12 and M_∞=18, are reported. Due to the fact that magnetic field effects are important only at high Mach numbers, the effect is an increasing of the surface pressure with applied magnetic field as already seen for the chemically frozen gas case at M_∞=5.4. In Fig. 3b pressure profiles along the x-axis are reported comparing the acoustic case with magnetic cases at M_∞=18.

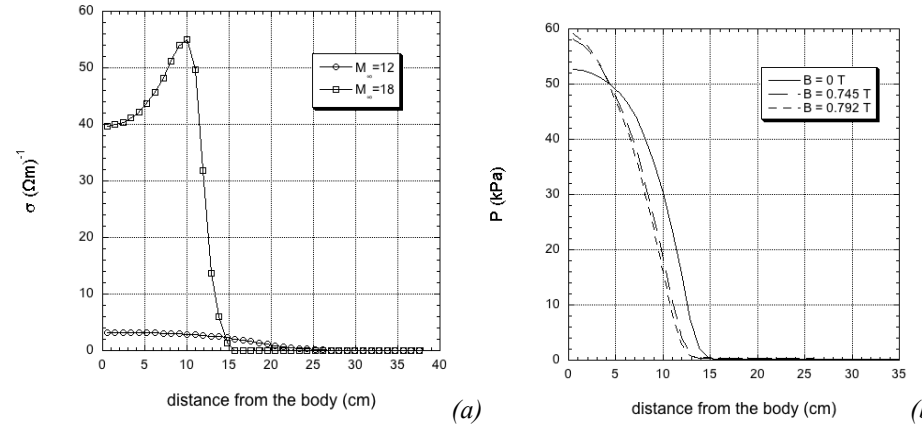

Figure 30: (a) Electrical conductivity profile along the stagnation line for two flow regimes, M_∞=12 and M_∞=18, in the case of chemical reacting gas. (b) Pressure profiles along the stagnation line calculated for three different magnetic fields in the case of chemical reacting gas for M_∞=18.

These results emphasize the usefulness of uncoupling the electrical conductivity (that is the ionization degree) from the flow dependent variables (such as the temperature). It is possible to achieve such as result with a system in which ionization is assisted by using electron beams or Caesium seeding [89,100].

4.5. Partial conclusion: the challenging problems of reactive MHD

Computational studies of supersonic and hypersonic flows over a blunt body were carried out by mean of a numerical tool for magnetohydrodynamic simulation coupled with a chemical reacting gas though the self-consistent calculation of electrical conductivity. The flow was studied in the low magnetic Reynolds regimes with an imposed uniform magnetic field perpendicular to the flow direction. Results indicate that the effect of magnetic field using a variable conductivity are visible only at high Mach number, where the accelerating effect of the pressure gradient is too strong to be balanced by the retarding magnetic force. This conclusion suggests the necessity of introducing extra electrons and superconducting magnets in order to make electromagnetic control effective.
Further developments will include different magnetic field configurations (dipolar, radial, *etc*.), oxygen chemistry and tensorial electrical conductivity with the evaluation of other transport variables (thermal conductivity and viscosity) with the implementation of Navier-Stokes equation coupled with Poisson equation to study anode-cathode configurations [101,102].

Acknowledgements

The research leading to these results has received funding from the European Community's Seventh Framework Program (FP7/2007-2013) under grant agreement n° 242311.
The authors thank Professor M. Capitelli for valuable discussions of all problems presented in the paper.

References

1. NASA's Exploration Systems Architecture. Final Report. NASA-TM-2005-214062. November 2005. 758 p.
2. Surzhikov S.T., Shang J.S. Radiative and Convective Heating of ORION Space Vehicles at Earth Orbital Entries. AIAA paper 2011-0251. 2011. 22 p.
3. Djadkin A., Beloshitsky A., Shuvalov M., Surzhikov S. Nonequilibrium Radiative Gasdynamics of Segmental-Conical Space Vehicle of Large Size. AIAA paper 2011- 0453. 2011. 29 p.
4. Colonna G., D'Ammando G., M.Y.Perrin, Pietanza L.D., Riviere Ph., Soufianu A., Surzhikov S.T. Radiation Models and Radiation Transfer in Hypersonics. The Open Plasma Physics Journal. 2013. Vol. No.
5. Surzhikov S.T. A Study of the Influence of Kinetic Models on Calculations of the Radiation-Convective Heating of a Space Vehicle in Fire-II Flight Experiment. Russian Journal of Physical Chemistry. 2008. Vol.2. No.5. pp.814-826.
6. Park C., Jaffe R.L., Partridge H. Chemical-Kinetic Parameters of Hyperbolic Earth Entry. Journal of Thermophysics and Heat Transfer. 1991. Vol.15. No.1. pp.76-90
7. Dunn, M.G. and Kang, S.W. Theoretical and Experimental Studies of Reentry Plasmas. NASA CR 2232, April 1973.
8. Bond J.W., Watson K.M., Welch J.A.Jr, Atomic Theory of Gas Dynamics. Addison-Wesley Reading. Massachusets. 1964.
9. Treanor C.E., Marrone P.V. Effect of Dissociation on the Rate of Vibrational Relaxation. Phys. of Fluids. 1962. Vol. 5. No. 9 .pp. 1022-1026.
10. Marrone P.V., Treanor C.E. Chemical Relaxation with Preferential Dissociation from Excited Vibrational Levels. The Physics of Fluids. 1963. V. 6. No.9. pp.1215–1221.
11. Park C.NonequilibriumHypersonicAerothermo-dynamics. Willey-Intersc. Publication, J. Wiley & Sons. New-York (1990).
12. Walter R. Recent Advances in Computational Analysis of Hypersonic Vehicles. Combustion, Explosion, and Shock Waves. 1993. Vol.29, No.3. p. 316.
13. Schneider W. Effect of Radiation on Hypersonic Stagnation Flow at Low Density. Z. Flugwiss. 1970. 18. Heft 2/3. Pp.52-58.
14. Martin J. Atmospheric reentry. An Introduction to its Science and Engineering. Prentice-Hall, Inc., Englewood Cliffs N.J. 1962.
15. Gruszczynski J.S., Warren W.R. W.R.,Jr. Experimental Heat-Transfer Studies of Hypervelocity Flight in Planetary Atmospheres. AIAA J. 1964, Vol.2. No. 9. pp.1542-1550.
16. James C.S. Experimental Study of Radiative Transport from Hot Gases Simulating in Composition the Atmospheres of Mars and Venus. AIAA J. 1964, Vol.2. No. 3. pp.470-475.
17. Faibairn A.R. Spectrum of Shock-Heated Gases Simulating the Venus Atmosphere. AIAA J. 1964, Vol.2. No. 6. pp.1004-1007.

18. Thomas G.M., Menard W.A. Experimental Measurements of Nonequilibrium and Equilibrium Radiation from Planetary Atmospheres. AIAA J. 1966. Vol.4. No.2. pp.227-237.
19. Freeman G.N., Oliver C.C. High-Temperature Thermodynamic and Transport Properties of Planetary CO_2-N_2 Atmospheres. AIAA J. 1970. Vol.8. No.9. pp.1687-1693.
20. Kirk D.B., Intrieri P.F., Seiff A. Aerodynamic Behaviour of the Viking Entry Vehicle: Ground Test and Flight Results. J. Spacecraft. 1978. Vol.15. No.4. pp.208-212.
21. Chen Y.K., Henline W.D., Stewart D.A., Candler G.V. Navier-Stokes Solutions with Surface Catalysis for Martian Atmosphere Entry. JSR. 1993. Vol.30. No.1 pp.32-42.
22. Tauber M.E., Yang L., Paterson J. Flat Surface Heat-Transfer Correlations for Martian Entry. JSR. 1993. Vol.30. No.2. pp.164-169.
23. Park,C., Nonequilibrium Hypersonic Aerothermo-d/ynamics. Willey-Interscience Publication, J. Wiley & Sons. New-York, 1990.
24. Tauber M., Sutton K. Stagnation-Point Radiative Heating Relations for Earth and Mars Entries. J. Spacecraft. 1991. Vol.28. No.1. pp.40–42.
25. Hassan B., Candler G., Olynick D. Thermo-Chemical Nonequilibrium Effects on the Aerothermodynamics of Aerobraking Vehicles. JSR. 1993. Vol.30. No.6. pp.647–655.
26. Tauber M., Palmer G., Earth Atmospheric Entry Studies for Manned Mars Mission. JTHT. 1992. Vol.6. No.2. pp.193–199.
27. Chen Y.K., Henline W.D., Tauber M.E. Mart Pathfinder Trajectory Based Heating and Ablation Calculations. JSR. 1995. Vol.32. No.2. pp.225-230.
28. Hartung L. Development of a Nonequilibrium Radiative Heating Prediction Method for Coupled Flowfield Solutions. JTHT. 1992. Vol.6. No.6. pp.618–625.
29. Park C., Yoon S. Fully Coupled Implicit Method for Thermochemical Nonequilibrium Air at Suborbital Flight Speeds. J.Spacecraft. 1992. Vol. 28. No.1. pp.31–39.
30. Henline W., Tauber M. Trajectory-Based Heating Analysis for the European Space Agency/Rosetta Earth Return Vehicle. JSR. 1994. Vol.31. No.3. pp.421–428.
31. Greendyke R., Gnoffo P., Wes Lawrence R. Calculated Electron Number Density Profiles for Aeroassist Flight Experiment. JSR. 1992. Vol.29. No.5. pp.621–626.
32. Gnoffo P., Price J., Braun R. Computation of Near-Wake, AerobrakeFlowfields. JSR. 1992. Vol.29. No.2. pp.182–189.
33. Gupta R., Lee K., Moss J., Sutton K. Viscous Shock-Layer Solution with Coupled Radiation and Ablation for Earth Entry. JSR. 1992. Vol.29. No.2. pp.173–181.
34. Mitcheltree R.A., Gnoffo P.A. Wake Flow About the Mart Pathfinder Entry Vehicle. Journal of Spacecraft and Rockets. 1995. Vol.32. No.5. pp.771-775.
35. Milos F.S., Chen Y.K., Gongdon W.M. et al. Mars Pathfinder Entry Temperature Data, Aerothermal Heating, and Heatshield Material Response. JSR. 1999. Vol.36. No.3. pp.380–391.
36. Paterna D., Monti R., et al. Experimental and numerical investigation of martian atmosphere entry. JSR. 2002. V. 39, N. 2. P. 227-236.
37. Edquist K.T. Afterbody Heating Predictions for a Mars Science Laboratory Entry Vehicle. AIAA paper 2005-4817, 2005, 12 p.
38. Bose D., Wright M. Uncertainty Analysis of Laminar Aeroheating Predictions for Mars Entries. AIAA paper 2005-4682. 2005. 11 p.
39. Hollis B.R., Collier A.S. Turbulent Aeroheating Testing of Mars Science Laboratory Entry Vehicle in Perfect-Gas Nitrogen. AIAA Paper 2007-1208. 2007. 20 p.
40. Hollis B.R., Collier A.S. Turbulent Aeroheating Testing of Mars Science Laboratory Entry Vehicle. JSR. 2008. Vol. 45. No.3. pp.417-427.
41. Grinstead J.H., Wright M.J., Bogdanoff D.W., Allen G.A. Shock Radiation Measurements for Mars Aerocapture Radiation Heating Analysis. JTHT. 2009. Vol.23. No.2. pp.249-255.
42. Surzhikov S., Omaly P. MSRO convective and radiative heating. AIAA Paper 08-1274. 2008. 43 p.
43. Surzhikov S.T., Omaly P. Radiative Gas Dynamics of Martian Space Vehicles. AIAA paper 2011- 0452. 2011. p.28.
44. Surzhikov S.T. Comparative Analysis of Radiative Aerothermodynamics of Martian Entry Probes. AIAA paper 2012-2867. 2012. p. 38.

45. Gromov V.G., Surzhikov S.T., Charbonnier J.-M. Convective and Radiative Heating of a Martian Space Vehicle Base Surface. 4th European Symp. on Aerothermodynamics for Space Vehicles. Capua, Italy. ESA SP-487. 2002. pp. 265-269.
46. Surzhikov S.T. 2D CFD/RGD Model of Space Vehicles. Proc. of the Int. Workshop on Radiation of High Temperature Gases in Atmospheric Entry. October 2003, Lisbon, Portugal. European Space Agency, SP-533, 2003, pp.95–102.
47. Surzhikov S.T. TC3: Convective and Radiative Heating of MSRO For Simplest Kinetic Models. Proc. HTGR Workshop ESA SP-583. 2005. pp.55–62.
48. Surzhikov S.T. TC3: Convective and Radiative Heating of MSRO, Predicted by Different Kinetic Models. Proc. 2nd HTGR Workshop. ESA SP-629. 2006. (CD-ROM).
49. Surzhikov S.T. Three-Dimensional Computer Model of Nonequilibrium Aerophysics of the Spacecraft Entering in the Martian Atmosphere. Fluid Dynamics. 2011. Vol. 46. No.3. pp.490-403.
50. Surzhikov S.T. Random models of Atomic Lines for Calculation of Radiative Heat Transfer in Laser Supported Waves. AIAA paper 97-2367. 1997. 11 p.
51. Surzhikov S.T. Computing System for Mathematical Simulation of Selective Radiation Transfer. AIAA paper 00-2369. 2000. 15 p.
52. Chatwood F.M., Gnoffo P.A. User's Manual for the Langley Aerothermodynamic Upwind Algorithm (LAURA). NASA TM-4674, Apr. 1996.
53. Park C., Howe J.T., Jaffe R.L. and Candler G.V. Review of Chemical-Kinetic Problems of Future NASA Missions, II: Mars Entries. *J. ofThermophysics and Heat Transfer*. 1994. Vol.8, No.1, pp.9–23.
54. Surzhikov S., Omaly P. Radiative Gasdynamics of Exomars at Angle of Attack. Proc. of the 4th European HTGR Workshop. 12-15 October. Lausanne, Switzerland. Available on CD and www-page of European Space Agency.
55. Surzhikov S.T., Shang J.S. Radiative Aerothermodynamics of Entry Probes in Martian and Earth Atmospheres. 7th European Aerothermodynamics Symposium on Space Vehicles. 9-12 May 2011. Bruges, Belgium. 8 p.
56. Surzhikov S.T. Convective and Radiative Heating of Martian Space Vehicles. 4th European Conference for Aerospace Sciences (EUCASS). 2011. 8 p. (Proceedings on CD).
57. Brewer, R. A., &Brant, D. N., Thermal protection system for the Galileo mission atmospheric entry probe, AIAA Paper 80-0358, Jan. 1980.
58. Moss, J. N., & Simmonds, A. L., Galileo probe forebody flowfield predictions during Jupiter entry, AIAA Paper 82-0874, 3rd Joint Thermophysics Fluids, Plasma and Heat Transfer Conference, St Louis, Missouri, June 7-11, 1982.
59. Moss, J. N., A study of the aerothermal entry environment for the Galileo probe, AIAA Paper 79-1081, 1979.
60. Kumar, A., Tiwari, S. N., Graves, R. A., &Weilmuenster, K. J., Laminar and turbulent flow solutions with radiation and ablation injection for Jovian entry, AIAA Paper 80-0299, 1980.
61. Matsuyama, S., Ohnishi, N., Sasoh, A., and Sawada, K., Numerical simulation of Galileo probe entry flowfield with radiation and ablation, Journal of Thermophysics and Heat Transfer, Vol. 19(1), pp. 28-35, Jan.-March 2005.
62. Matsuyama, S., Shimogonya, Y., Ohnishi, N., Sasoh, A., & Sawada, K., Multiband radiation model for simulation of Galileo probe entry flowfield, Journal of Thermophysics and Heat Transfer, Vol. 20(3), pp. 611-613, Sept. 2006.
63. Furudate, M., Jeung, I-S., and Matsuyama, S., Nonequilibrium Calculation of Flowfield over Galileo Probe,AIAA Paper 2006-383, Jan. 2006.
64. Park, C., Stagnation-region heating environment of the Galileo probe, Journal of Thermophysics and Heat Transfer, Vol. 23(3), pp. 417-424, July-Sept. 2009.
65. Reynier, Ph, Survey of convective blockage for planetary entries, ActaAstronautica, Vol. 83, pp. 175-195, 2013.
66. Brewer, R. A., Brant, D. N., and Fogaroli, R. P., Development of a Steady-State Shape Change Ablation Code for the Design of Outer Planet Probes, AIAA Paper 77-95, January 1977.
67. Moss, J. N., Simmonds, A. L., & Anderson, E. C., Turbulent radiating shock-layers with coupled ablation injection, Journal of Spacecraft & Rockets, Vol. 17, pp. 177-183, 1980.
68. Haas, B. L., & Milos, F. S., Simulated rarefied entry of the Galileo probe into the atmosphere of Jupiter, NASA TM-110507, Jan. 1993.
69. Anon., Planetary mission entry vehicles, Quick Reference Guide, NASA SP-3401, Version 3, 2006.
70. Milos, F., S., Galileo probe heat shield ablation experiment, Journal of Spacecraft and Rockets, Vol. 34(6), pp. 705-713, Nov.-Dec. 1997.

71. Milos, F. S., Analysis of Galileo probe heatshield ablation and temperature data, Journal of Spacecraft and Rockets, Vol. 36(3), pp. 298-306, May-June 1999.
72. Moss, J. N., Jones, J. J., & Simmonds, A. L., Radiative flux penetration through a blown shock-layer for Jupiter entry, AIAA Paper 78-908, 2nd AIAA/ASME Thermophysics and Heat Transfer Conference, Palo Alto, California, May 24-26, 1978.
73. Park, C., & Tauber, M. E., Heat shielding problems of planetary entries. A review, AIAA Paper 99-3415, 1999.
74. Park, C., Injection-induced turbulence in stagnation point boundary layers, AIAA Journal, Vol. 22(2), pp. 219-225, 1984.
75. Savajano, R., Modelling of hypersonic flows in Jupiter‘s atmospheric reentry ESA-ESTEC, Projet de fin d’étude de l’ENSMA, Poitiers, France, 2007.
76. Reynier, Ph., CFD computations of Galileo entry, 53rd Course on Molecular Physics and Plasma in Hypersonics, International School of Quantum Electronics, Erice, Italy, Sept. 8-15, 2012.
77. TINA Version 4: Theory and user manual, TN89/96 Issue 7, Fluid Gravity Engineering, Emsworth, UK, March 2008.
78. Jupiter Entry Probe,Concurrent Design Facility Study, CDF-43(A), ESA-ESTEC, Noordwijk, The Netherlands, December 2005.
79. Park, C., Frontiers of aerothermodynamics, Non-Equilibrium Gas Dynamics – From Physical Models to Hypersonic flights, RTO-EN-AVT-162-11, Sept. 2009.
80. Tiwari, S. N., Szema, K. Y., Effects of precursor heating on radiative and chemically reacting viscous flow around a Jovian entry body, NASA CR-3181, Oct. 1979.
81. Park, C., Nonequilibrium ionization and radiation in hydrogen-helium mixtures, Journal of Thermophysics and Heat Transfer, Vol. 26(2), pp. 231-243, April-June 2012.
82. Park, C., Nonequilibrium chemistry and radiation for Neptune entry, Journal of Spacecraft and Rockets, Vol. 48(6), pp. 897-903, Nov.-Dec. 2011.
83. Leibowitz, L. P., Measurements of the structure of an ionizing shock wave in a hydrogen-helium mixture, The Physics of Fluids, Vol. 16(1), pp. 59-68, Jan. 1973.
84. Smith A.J., Gogel T., Vandevelde P. and Marraffa L., PlasmA Radiation DatabasE, final report ESTEC contract 11148/94/NL/FG, Fluid Gravity Engineering, Emsworth, UK, April 1996.
85. McBride, B. J., Zehe, M. J., & Gordon, S., NASA Glenn coefficients for calculating thermodynamic properties of individual species, NASA TP-2002-211556, Sept. 2002.
86. Yee, H. C., Construction of explicit and implicit symmetric TVD schemes and their applications, Journal Comp. Phys, Vol. 68, pp. 151-179, 1987.
87. Reynier, Ph., “Numerical reconstruction of Galileo entry, ESA SP-714, 5th International Workshop on Radiation and High Temperature Gases in Atmospheric Entry, Barcelona, 16-19 Oct. 2012.
88. Fujino T, Ishikawa M. Numerical Simulation of Control of Plasma Flow With Magnetic Field for Thermal Protection in Earth Reentry Flight. IEEE Trans. Plasma Sci. 2006; 34(2): 409-420.
89. MacCormack R W. Numerical Simulation of Aerodynamic Flow Within a Strong Magnetic Field with Hall Current and Ion Slip. AIAA paper 2007-4370.
90. Macheret O S, Shneider M N, Miles R B. Magnetohydrodynamic Control of Hypersonic Flows and Scramjet Inlets Using Electron Beam Ionization. AIAA J. 2002; 40(1): 74-81.
91. Hoffmann K A, Damevin H M, Dietiker J F. Numerical Simulation of Hypersonic Number Magneto-fluid-dynamic Flows. AIAA paper 2000-2259.
92. Poggie J, Gaitonde D. Magnetic control of flow past a blunt body: Numerical validation and exploration. Phys. Fluids 2002; 14(5): 1720-1731.
93. Capitelli M, Gorse C, Longo S, Giordano D. Collision Integrals of High-Temperature Air Species. J. Thermophys. Heat Transfer 2000; 14(2): 259-268.
94. Sarma G S R. Physico–chemical modelling in hypersonic flow simulation. Progr. Aerospace Sci. 2000; 36(3):281-349.
95. Bityurin V A, Bocharov A N. Magnetohydrodynamic Interaction in Hypersonic Air Flow past a Blunt Body. Fluid Dynamics 2006; 41(5): 843-856.
96. Bush W B. Magnetohydrodynamic-Hypersonic Flow Past a Blunt Nose. J. Aero. Sci. 1958; 25(11): 685-690.
97. Cristofolini A, Borghi C A, Neretti G, Schettino A, Trifoni E, Battista F, Passaro A, Baccarella D. Experimental Investigations on the MHD Interaction around a Blunt Body in a Hypersonic Unseeded Air Flows. AIAA paper 2012-2730.
98. Cristofolini A, Borghi C A, Schettino A, Battista F. Numerical Rebuilding of MHD Tests in an Unseeded Mach 10 Air flow around a Blunt Body. AIAA paper 2012-2733.

99. Cristofolini A, Borghi C A, Neretti G, Schettino A, Trifoni E, Battista F, Passaro A, Baccarella D. Experimental investigations on the magneto-hydro-dynamic interaction around a blunt body in a hypersonic unseeded air flow. J. Appl. Phys. Vol. 112, 093304, 2012.
100. MacCormack R W. Solution of Maxwell's Equations Coupled to the Navier-Stokes Equations. AIAA paper 2009-3911.
101. Wan T, Candler G V, Macheret O S, Shneider M N. Three-Dimensional Simulation of the Electric Field and Magnetohydrodynamic Power Generation During Reentry. AIAA J. 2009; 46(6): 1327-1336.
102. Fujino T, Yoshino T, Ishikawa M. Aerodynamic Heating of a Reentry Body Equipped Surface Hall Magnetohydrodynamic Generator. J. Prop. and Power 2010; 26(4): 638-648.

Thermodynamic characterization of high-speed and high-enthalpy plasma flows

Y. Babou[a], D. Lequang[a,h], O. Chazot[a],
S. T. Surzhikov[b], A.S. Dikaljuk[b],
A. Panarese[c], G. Cicala[d], S. Longo[c,d],
J. Hoffman[e], Z. Szymanski[e], A. Kaminska[f], M. Dudeck[g], D. Vacher[h]

[a]*Aeronautics and Aerospace Department, von Kármán Institute for Fluid Dynamics,Chaussée de Waterloo 72, 1640 Rhode-Saint-Genèse, Belgium*
[b]*Institute for Problems in Mechanics Russian Academy of Sciences, 101-1, Vernadskogo prosp. Moscow, 119526, Russia*
[c]*Department of Chemistry, University of Bari, via Orabona 4, 70126 Bari, Italy*
[d]*CNR-IMIP, Bari Section, via Amendola 122/D, 70126 Bari, Italy*
[e]*Institute of Fundamental Technological Research, Polish Academy of Science, Adolfa Pawinskiego 5, 02-106 Warsaw, Poland*
[f]*Institute of Electric Power Engineering, Poznan University of Technology, ul. Piotrowo 3A, 60-965 Poznan, Poland*
[g]*Institut dAlembert, UniversitPierre et Marie Curie (Paris 6), 4 place Jussieu, 75252 Paris, Cedex, France*
[h]*Clermont Université, Université dAuvergne, LAEPT, BP 80026, F-63000, Clermont-Ferrand, France*

Abstract

This contribution proposes a description of selected experimental activities conducted in aerospace sciences and dedicated to generate experimental data to assess atmospheric entry plasma models. In order to provide comprehensive set of experimental data, high enthalpy shock tube facilities have been developed to generate plasma representative of entry plasma for broad range of trajectory entry conditions. The shock-heated plasma is obtained through adiabatic compression and the resulting post-shock plasma flow exhibits thermodynamic state analogous to actual entry plasma. However, significant insight can be obtained through experiments conducted also with non-equilibrium plasma flows obtained with other methods. The typical methodologies adopted to provide experimental data of interest to enhance entry plasma modeling are sketched for four distinct non-equilibrium plasma kinds produced respectively by four specific ground facilities. The contribution firstly will consider experimental campaigns conducted with a high enthalpy shock tube in order to document in absolute radiance the radiative signature in the UV spectral range of an Earth entry plasma. Then, the investigations of the interaction between a shock wave and an electrical discharge will be described. These investigations were performed to identify the role of the internal degrees of freedom of molecular gases on the propagation of the shock. Also, the contribution covers investigations devoted to the thermodynamic state characterizations by means of spectroscopic diagnostics in the cases of the non-equilibrium plasmas flows generated by plasma wind tunnels. The examination of the Saha-Boltzmann equilibrium is proposed in the case of a subsonic plasma flow. And at last, the characterization methods of air supersonic plasma jet are presented and the 2D distributions of the subsequently measured plasma properties are documented for a straight comparisons with non-equilibrium plasma jet computations.

I. Introduction

During a hypersonic reentry into a planetary atmosphere, large amount of the free stream kinetic energy is converted, across a strong bow shock through inelastic collisions, into internal energy of the gas. After the shock, in the relaxing flow, competition between coupled collisional and radiative processes occurring at different time scales rules the energy distribution in the dissociating, ionizing and radiating flow. As a consequence, the post shock plasma, designated as entry plasma, is typically characterized by energy levels no more ruled by the Maxwell-Boltzmann equilibrium distribution. The accurate prediction of non-equilibrium distributions is a decisive task for reliable prediction of the radiative heating, determining the design optimization of the space vehicle heat shield. The validation

of non-equilibrium models developed for entry plasmas should be conducted via measurements performed during real-flight experiments [1]. Due to the elevated cost of these experiments and the difficulty to obtain low uncertainty measurements in such harsh environment, this information is far from being complete today. Therefore, the continuous improvement of advanced chemico-physical and plasma models for entry plasmas is performed on the basis of experiments carried out on ground with dedicated facilities operated with well-suited diagnostics to examine in details non-equilibrium processes. In practice, quantitative characterization of excited states populations, gas temperature and electron densities is made via the standard Optical Emission Spectroscopy (OES) diagnostic due to its moderate cost and easy implementation, conversely to a laser-based optical diagnostic. The present contribution proposes an outline of current research activities conducted in the aerospace sciences by focusing on up-to-date experimental investigations carried out on four specific ground facilities. The objective is to depict the common methodologies employed to produce experimental data of interest to assess thermodynamic state of the investigated plasma. The investigations encompass the characterization of four distinct non-equilibrium plasma kinds with the aim to produce new data which can be directly used to assess the performances of non-equilibrium plasma flow computations.

High enthalpy shock tube experiments aim to investigate the kinetic processes taking place after a pressure discontinuity wave traveling through a gaseous mixture representative of planetary atmosphere conditions (composition and pressure). Such shock wave (SW) is generated by rupturing a diaphragm between high and low pressure regions. To achieve a shock wave representative of the entry plasma requires to generate high energy pulse to dissipate a large amount of energy over hundreds of microseconds to adiabatically compress the gas. Experiments dedicated to the measurements of radiation emitted by the post-shock plasma have started in the second half of twentieth century, triggered by the requirements for space exploration missions. The first attempts of recording radiation in absolute units behind the front of shock waves generated with a shock tube operating with air and CO_2-N_2 mixtures have been reported in [2] and [3] respectively . However the instrumentation available at the time could not provide desirable quality of measurements. Since the last decade, development of high-speed and high-resolution CCD cameras and technology of digital registration of optical signals revitalized high enthalpy shock tube experimental activities dedicated to Earth, Mars, Venus and Titan atmospheric entry (e.g. [4, 5, 6, 7, 8, 9, 10]). The fruitful harvest of experimental spectra has been conducive to assess performances of standard chemical models adopted in aerospace engineering, such as the so-called two-temperatures Park model [11, 12] or detailed kinetic models developed by plasma scientists such as electronic or vibrational specific Collisional-Radiative (CR) models. For instance, the *Tube a Choc Marseille 2* (TCM2) facility which is middle-sized free piston shock tunnel [13] has been employed to document the CN and C_2 absolute intensity behind a strong shock wave in a CO-N_2 mixture for various operating conditions. Significant discrepancies between recorded spectral intensities and those rebuilt with species densities determined with the Park model have pointed out the needs for modeling improvement to reproduce correctly CN and C_2 emission profiles [14]. Also, the *Electric Arc Shock Tube* (EAST) facility at NASA Ames, which operates with an electric arc-heated driver, was recently used to procure spectral intensities emitted by the plasma behind a shock representative of Earth entry [4]. Very good agreement has been obtained between the measured post-shock emission profiles of N and O electronic transitions and those rebuilt with up-to-date electronic specific CR model for N and O species [15], meanwhile pointing out the inadequacy of standard two-temperatures models. Currently, the experimental research efforts are oriented to record intensities in UV and more particularly VUV spectral ranges, both exhibiting moderate and strong self-absorption pending on the contributive radiative systems. Measurement in the VUV spectral domain requires in particular specific arrangement to guarantee optical path under well controlled vacuum. The recent EAST shock tube experiments with carbonaceous mixture, focusing on VUV measurements, provided up-to-date experimental data to validate the CO radiative properties [16]. A typical high enthalpy shock tube experimental campaign conducted at Institute for Problems in Mechanics (Russian Federation) to document the UV radiative signature of a post-shock plasma representative of Earth entry is described in Part II.

In addition to high enthalpy shock tube experiments, significant insight can be obtained through experiments conducted with non-equilibrium plasma flows not necessarily representative of the entry plasma. Indeed, there is a broad range of non-equilibrium plasma situations that can be considered, in order to examine independently some specific mechanisms or to identify limitations of adopted entry plasma descriptions. For example an interesting and still open question is the role of the internal degrees of freedom of molecular gases on the propagation of the shock. This problem can be tackled through a campaign of comparative experiments involving an atomic and a molecular plasma, e.g.

Ar and N_2 (respectively the most important atomic and molecular gas in aerospace studies) under the same experimental conditions [17]. Until now, such comparative measurements have only been performed at University of Bari. Several research groups have found and observed that the propagation velocity of SW in ionized gas is higher than that in nonionized gas and also the shock shapes differ in plasma with respect to neutral gas because they broaden, split and attenuate. Many researchers [18, 19] believed that the broadening, splitting and acceleration of shock in gas discharges are due to conventional thermal phenomena: gas heating and temperature inhomogeneity. From a theoretical point of view Aital and Subramaniam [20] predicted that the splitting of the signal as well as the spread and attenuation of weak SW, as revealed by laser deflection measurements, are due to a temperature gradient along the axis and radius of the discharge tube, as well as to a wall shear that causes a marked curvature of the shock front (near-wall regions). Subsequently, the same authors [21] showed that the measurements of the laser deflection signal recovery dependent on the direction of discharge electric field are further evidence of plasma effects. The recovery distance measured in the afterglow when the SW travels from the anode to the cathode is indeed longer than that from the cathode to the anode in glow discharge because of the cathode (i.e. the hot electrode) proximity. For example Macheret et al. [19] obtained a direct proof of the thermal mechanism by pulsing the discharge and demonstrated experimentally and numerically that the changes in SW velocity and broadening are explained by a heating of the gas and a radial temperature gradient, respectively. However, several other authors argued that the transformations of SW (such as the splitting in two waves, the significant broadening of SW front and the average velocity increase) are due to various plasma-specific effects such as electric double layer, ion-acoustic waves and long range interaction [22, 23, 24]. Thus, for the above cited phenomena two kinds of interaction have been invoked and consequently two disparate explanations have been proposed. Whether or not the SW velocity is enhanced for a thermal [18, 19] or a non thermal (i.e. electrostatic interaction with the plasma) [22, 24] mechanism; SW propagation in plasma is still a contentious issue being addressed in Part III.

In the field of aerospace science, in addition to shock tube experiments, diverse Plasma Wind Tunnel (PWT) facilities have been constructed for Heat Protective Material (HPM) testing purpose to support the development of Thermal Protection System (TPS) for space mission. PWTs are employed to provide a steady axisymmetric subsonic or supersonic plasma flow of large diameter ($\gtrsim 10$ cm) in order to test insulating performance of material samples, candidates for TPS applications, undergoing thermal heat fluxes representative of those encountered during the entry trajectory into planetary atmosphere ($\sim 1-20$ MW.m^{-2}). Different methods based on electric discharge heating are used to generate high enthalpy plasmas. PWTs based on Direct-Current (DC) discharge are so-called arc-jets or DC-Plasmatron [25, 26]. PWTs using Inductively Coupled Plasma (ICP) torch, based on Radio-Frequency (RF) discharge, are so-called RF-Plasmatron [25, 26]. Both types are employed to test HPM under duplicated flight conditions, nevertheless it might be stressed that currently higher enthalpy range is covered with DC-Plasmatrons, making them well appropriate to test HPM undergoing heat fluxes beyond ~15 kW·m^{-2}. PWTs are still under exploited nowadays for the task of non-equilibrium plasma description assessment, despite their ability to offer a steady plasma flow jet with varied thermodynamic situations and their practical advantages in comparison with shock tube flows of shorter runtime. For example in subsonic plasma flows the thermodynamic equilibrium is rarely achieved since the elevated temperature of electrons produced in the DC or RF discharge region, plasma jet radiative losses, velocity and temperature gradients can result in significant departure from chemical and thermal equilibrium. Electron density determination on the basis of OES diagnostics in air subsonic plasma jet produced at low pressure with the VKI-Plasmatron facility were reported in [29]. Differences between electron density estimations at equilibrium and measurements evidenced for a non negligible departure from Saha-Boltzmann equilibrium similarly to plasma undergoing recombination. Subsonic plasma jets generated with ICP torch of more modest size than PWT facilities can be smartly exploited for the specific task of experimental assessment of Collisional-Radiative models. As reported in [30], OES characterisation of an atmospheric pressure nitrogen/argon plasma flowing at high velocity through a water-cooled test-section, to control its recombination time, have permitted to assess a vibrational specific CR model of N_2 excited states. The Part IV of the contribution proposes a detailed examination of the thermodynamic state by means of OES of a low pressure subsonic plasma flow generated with nitrogen mixture by the DC-Plasmatron facility at Poznan University of Technology (Poland).

Plasma flows presenting considerable departure from equilibrium can be achieved with PWTs by using a convergent or convergent-divergent nozzle to generate a supersonic plasma jet. Many aspects of supersonic expanding

plasma flows are of major interest for fundamental plasma physics and chemical-kinetics investigations. Because electrons and heavy species have important mass difference, a charge separation might occur, inducing then a self-consistent electromagnetic field that can influence transport of charged species. Also, a short flow residence time (due to its high velocity) is conducive for detailed investigations of the coupling between the ionization-recombination processes and the transport, and even for rebuilding rates for electronic kinetic processes [31]. In addition to the strictly expanding plasma, underexpanded supersonic plasma jets offer successive shocks structures. They typically exhibit various stages: in the supersonic expansion the plasma flow tends to be chemically frozen while in the post shock regions the plasma flow is subsonic. Comprehensive theoretical and numerical studies of the entire underexpanded jet are still scarce due to the wide range of flow regimes with more or less pronounced departure from equilibrium for the electronic, vibrational, rotational, and translational degrees of freedom (especially in shock regions). Besides the difficulties to predict supersonic plasma jet, inherent to the complexity of the flow, the reliability of standard OES methods used to rebuild plasma flow properties might be questioned. For instance OES investigations of a supersonic plasma jet generated with argon mixtures by an ICP torch have shown complete disagreement between electron temperature profiles obtained on the basis of two distinct rebuilding methods [32]. OES diagnostics applied to air underexpanded plasma jet generated by VKI-Plasmatron facility, available at von Karman institute (Belgium), are presented and discussed in Part V. The plasma parameters (electronic excitation temperature and electron density) were rebuilt adopting conventional approaches to characterized radially and axially the jet. The resulting 2D distributions of plasma parameters can be straightly employed to assess prediction of supersonic plasma flow coupled with detailed description of kinetic processes.

II. High enthalpy shock tube plasma

II.1. Experiments

The scheme of the shock tube facility developed at Institute of Mechanics of Moscow State University by P.V. Kozlov, Yu.V. Romanenko, O.P. Shatalov is presented in Fig. II.1. Inner diameter of all 3 seamless tubes which are the sections of tube is 50 mm. Use of seamless stainless steel tubes allowed to exclude jumps of temperature and density on the junctions of tube in the registration section. High Pressure Chamber (HPC) is filled with $0.5(H_2+1/2O_2)+0.5He$ gas mixture and operated in detonation regime. Mixing of the mixture is performed in HPC. Hydrogen is added to preliminary prepared mixture of helium and oxygen. Stability of HPC operation in detonation regime substantially depends on the duration of mixing of explosive (combustible) mixture. Spark-plug is used at the rear end of the chamber for burning of this mixture. Spark-plug operates in the self-breakdown regime. Energy stored on the discharge high-voltage capacitors is less than 100 mJ, duration of the discharge is 300-400 ns. Capacitors and spark-plug are low-inductance circuit which provide nanosecond duration time of discharge. Antechamber is situated between blind flange with the spark-plug and HPC section. It promotes the rapid development of plane combustion front in HPC. Cassettes with copper diaphragms and cross-like cutters are situated between the sections of the tube. The width of the diaphragm between HPC and intermediate section (filled with helium) is 130 μm and the width of diaphragm between intermediate section and low-pressure chamber (LPC) is 80 μm. Configuration of the double-diaphragm shock-tube described above when HPC filled with mixture H_2:O_2:He=2:1:3 at pressure 438 kPa and LPC is filled with air (78% of N_2 and 21% of O_2) at pressure 133 Pa allows to reach the shock velocity equal to 7 km/s. Reproducibility of gas parameters behind the shock wave is about 2% and in general depend on the quality of mixing of explosive mixture in HPC. Buffer tank and low pressure chamber are evacuated to the pressure 10^{-4} Pa using the dry pump system with leakage lower than 0.001 Pa/min. Pure gases of AGA company are used in order to produce the gas mixtures for the experiments.

Resulting spectral resolution, due to the ICCD camera and spectrograph combination, is about 0.33 nm for the diffraction grating of 150 groves per millimeter. The sensitivity region of ICCD camera is within the range of wavelengths 170-870 nm. The measurements are performed within the wavelength region 200-850 nm. Four overlapping sub-regions were chosen for the whole region 200-850 nm. In order to eliminate influence of the spectra of radiation from second-order of grating on the measured spectra in the wavelength region 400-750 nm filters are installed in front of the spectrograph. Spectral radiation emitted by shock-heated gases is registered by ICCD-camera. From the

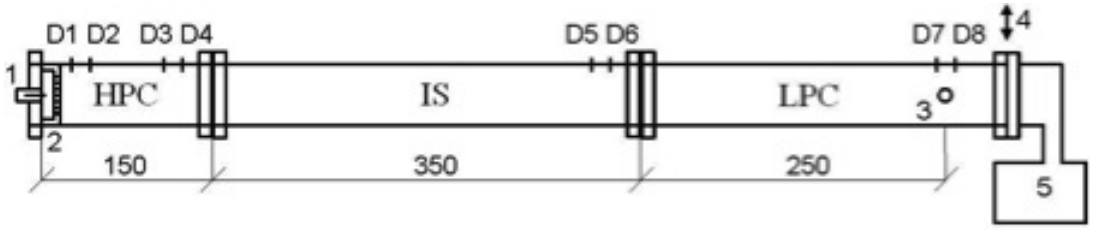

Figure II.1: The scheme of double-diaphragm shock tube. 1-spark-plug; 2-antechamber; 3-quartz window; 4-vent damper; 5-buffer tank. HPC – high-pressure chamber; IS – intermediate section; LPC – low-pressure chamber.

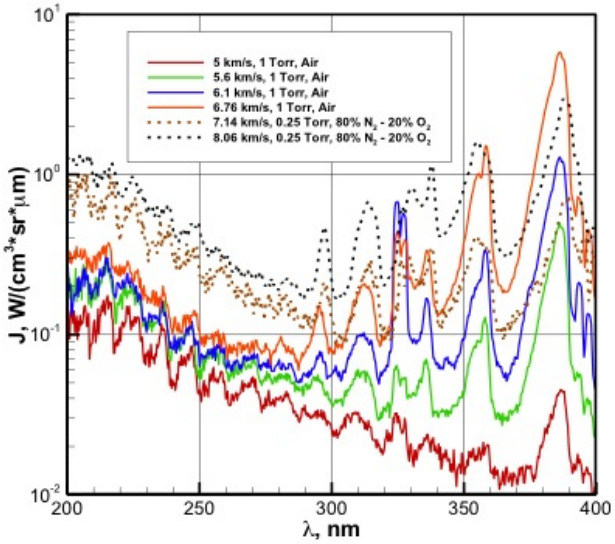

Figure II.2: Nonequilibrium spectral emissivity of the shock-heated ambient air solid lines; 80% N_2 - 20% O_2 gas mixture dashed line.

opposite window the temporal dependence of integral signal through the quartz optical fiber is registered by means of photoelectric multiplier FEU-100. The signal from electric photomultiplier is registered using the digital oscilloscope. The spectral region of such scheme is 200-850 nm due to the transmissivity of optical fiber and the sensitivity region of photomultiplier. It is possible to install monochromator between the FEU-100 and optical fiber in order to register the temporal behavior of radiation in given regions of a spectrum. Temporal resolution of such scheme is 1 μs due to the geometry of optical scheme, can be improved up to 0.1 μs. The typical radiative signature recorded in UV spectral range for various operating conditions, presented in Fig. II.2, point out the rise of emission with the shock velocity for a given working gas. An augmentation of 60 percent of the shock velocity leads to an increase of two order of magnitudes the N_2^+ peak intensity located at approximatively 380 nm.

III. Shockwave-electrical discharge interaction

III.1. Experiments

The investigations described here below consider shock waves, generated by the Bari acoustic shock tube, propagating in weakly ionized discharge. The aim of such experiment is to compare and contrast the results of direct current discharge in atomic Ar and in molecular N_2 and to uncover the role of thermal and non thermal effect in heat transfer. The characteristics of DC discharge, i.e. voltage, resistance and power of discharge, are obtained by electrical characterization of the plasma. The laser deflection technique is used to measure the structure and velocity of shock

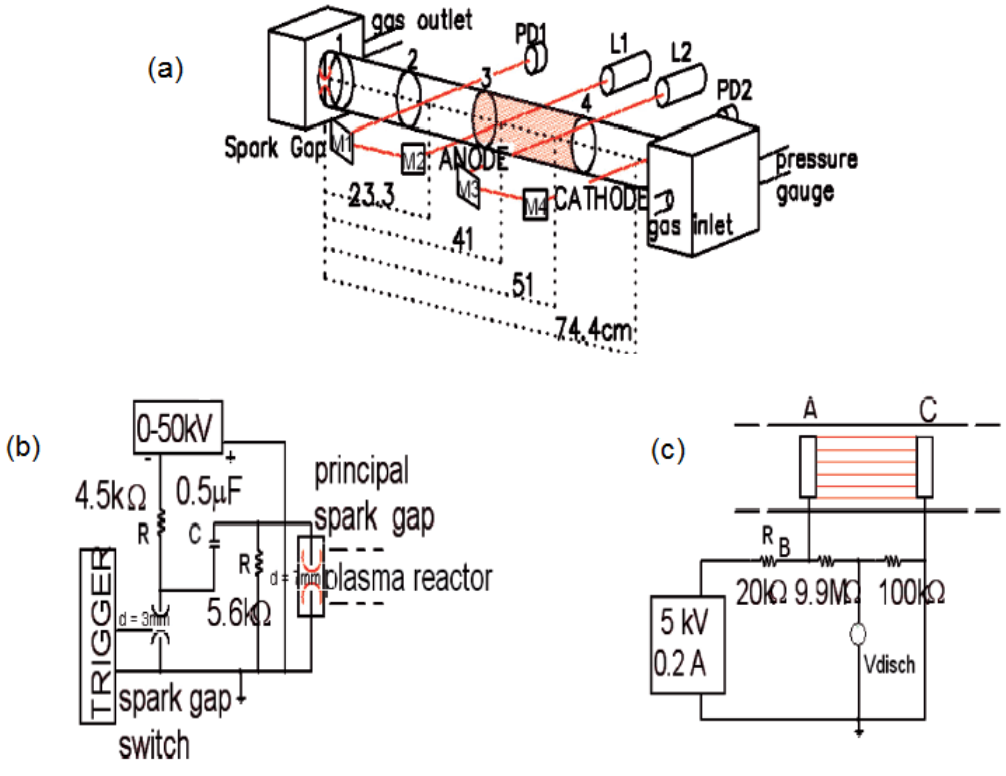

Figure III.1: Experimental set-up of the version of the Bari plasma shock tube used for the preliminary campaign of measurements (adapted from [17]): (a) schematic of the apparatus; (b) circuit diagram of spark gap; (c) circuit diagram of DC discharge.

wave. The passage of shock wave creates a density gradient that permits to evaluate the propagation velocity of SW and to monitor the SW evolution. In Fig. III.1 (a) the schematic of the experimental set-up is shown. The apparatus essentially consists of a Pyrex discharge tube, whose length and inner diameter are 8 cm and 4.3 cm, respectively, and a spark gap which generate the shock wave. A DC supply ignites a non equilibrium discharge in the discharge tube between a pair of stainless steel annular electrodes. The spark gap is made by a pair of stainless steel cylindrical electrodes separated by 7 mm, as sketched in the circuit diagram of spark gap of Fig. III.1 (b). The acoustic shock wave is produced by the spark gap driven by a triggered home-made spark switch, a high voltage capacitor (0.5 μF), and a DC supply (50 KV). The stored pulse energy is about 25 J, as a voltage of 10 KV is applied to the spark gap electrodes. The circuit diagram of DC discharge of Fig. III.1 (c) shows that a ballast resistance, R_B = 20 KΩ, is connected in series with plasma resistance, R_{pl}. This resistive ballast provides a positive resistance that limits the current through the tube and, therefore, prevents the DC supply to be destroyed or to fail. Besides R_B makes the discharge stable at contemplated current range. In the circuit diagram of DC discharge is also shown the voltage divider that allows us to measure the discharge voltage. By varying the discharge current in the range (0 - 90 mA), it is possible to study the effects of the discharge current on the electrical characteristics and on the SW. The gas flow is fixed at 200 sccm (Standard Cubic Centimeter per Minute), whereas the gas pressure is constant and equal to 399 Pa. Preliminary results obtained by using the Bari plasma facility with atomic and molecular gases are consistent with a thermal effect. At the same time, the shock initiation device in the present version of the tube has a low energy, therefore shock with Mach number only slightly larger than 1 has been obtained [17]. Besides, the absence of Langmuir probe and molecular spectroscopy as part of the diagnostics strongly limits the possibility to detect plasma effects. The work in progress is now aimed at redesigning and rebuilding the plasma tube, in order to increase the Mach number achievable by reducing the tube section and modifying the shock initiation device, while the implementation of more advanced diagnostic facilities will be performed afterwards.

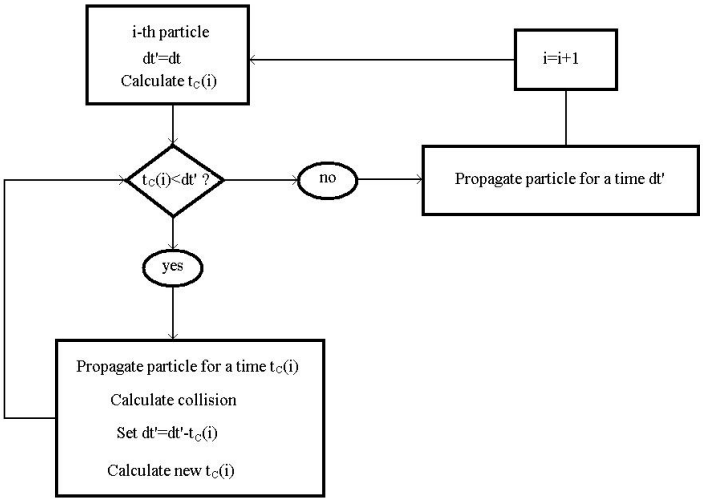

Figure III.2: Modified time step flow chart.

III.2. Plasma tube modeling

A Particle in Cell - Monte Carlo (PIC-MC) program has been developed to treat the problem of charge separation under the conditions of plasma shock tubes, in order to evaluate the electric potential and field which arise due to the non-zero space charge across the shock in a weakly ionized gas. A practical method is proposed for the calculation of component separation since these tubes operate in the transition regime. The basic idea is that the nonlinear fluid dynamics of the main component is treated first, while the final determination of all components is made by using the linear Test Particle Monte Carlo (TPMC) method. The TPMC method has been used to solve the linear transport equation for minor species (including electrons and ions), which is obtained by setting the target distribution $f_0(\mathbf{r})$ to match locally the fluid dynamics results for the main component shock. This method is totally free of numerical diffusion and is of simpler implementation than DSMC approach in spite of its obvious advantages for the treatment of seeded atomic flows, namely the variance reduction in the treatment of the impurities and the expected good reliability of the calculated atomic separation in view of the lack of numerical diffusion.

The transport of more complex and structured seed species (e.g. molecules) should be possible by straightforward extensions of the linear part of the model. The use of linear transport methods well developed for thermal neutrons offers the possibility to borrow standard variance reduction techniques from this field ref. [33, 34]. For example, if an estimate of the separation effect is needed in the front shock, it is possible to inject particles in the flow just before the shock and remove them just after it. In this way a drastic reduction of the computational cost is possible. A more advanced treatment can employ the adjoint equation in order to provide local solutions for a few space positions of interest.

Argon has been considered as discharge feed. The electric potential is the unknown of the Poisson equation on the numerical grid on which particles are sampled, coherently with the PIC-MC methodology, i.e.

$$\nabla^2\phi = -4\pi\rho$$

$$\rho = e\int f_{ion}(\mathbf{r},\mathbf{v})d^3v - en_e(\mathbf{r}), \tag{III.1}$$

where f_{ion} is the kinetic distribution of ions which is the result of the sampling of MC particles.

In the case of normal shocks a 1D model is to be developed (2D is expected for the case of plasma boundary layer); furthermore, in a first evaluation of the 1D code we concentrated on ion kinetics, since ions are mostly responsible for the plasma contribution to viscosity. The solution for electrons has been according strongly simplified as $n_e(x) = \alpha\, n_{Ar}(x)$.

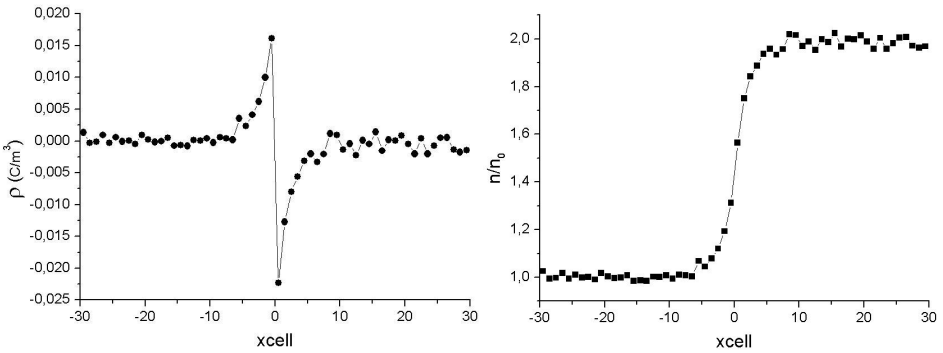

Figure III.3: MC simulation: (a) space charge density, (b) density.

To calculate $\rho(x)$ we have to know the position of charged particles at every time, but the particle dynamics evolves in time through an appropriate time step dt, whereas the free flight times t_c are random and vary for every particle. So to harmonize this different time period we have used the *modified time step technique* of Hockney and Eastwood. In a generic time iteration dt, the $i-th$ particle undergoes a definite number of collisions. We introduce the residual of the time step dt', which we set initially equal to dt, and we select randomly the free flight times $t_c(i)$. If $t_c(i) \leq dt'$, the particle propagates freely and collides, then dt' is updated to $dt' - t_c(i)$. Now a new value for $t_c(i)$ is selected, and the procedure begins again until $t_c(i) \geq dt'$. In this case the collision do not occurs, but the i-esim particle undergoes a free propagation during the residual time dt'. This algorithm is schematized in Fig. III.2.

A first series of runs has been performed under the following conditions: $M = 1.73$, $n_{Ar} = 3.22 \cdot 10^{23} m^{-3}$, $\alpha = 10^6$, and $T = 300K$. The result of this first series of run are shown in Fig. III.3 to III.5. Fig. III.3 (a) shows that a net charge density appears in the shock region, with a change of sign across the shock, and an apparent zero average across the whole shock. This behavior in our simple model is due to the diffusion of positive charges ahead of the shock, since the electrons are considered as a steady term. In real conditions the diffusion of electrons cannot be neglected, but our method can be still used with a much higher consumption of computer resources. This interpretation of the phenomenon is confirmed by Fig. III.3 (b) and in Fig. III.4 reporting the ion density and average speed respectively. In Fig. III.5 the self-generated electric field is plotted.

As can be seen in Fig. III.5, the pure collisional dynamics of ions in a shock front lead to the development of a residual electric field after the shock. This result of course is not physical and show that the ions and the electrons will be subjected to a self-generated field and consequently accelerated until the residual field is removed: this happens when the total charge across the shock is exactly neutralized. Therefore it is of interest to establish and study the effect of an electric field on the ion kinetics in a shock. Furthermore, in an experiment of shock propagation in a partially ionized gas, an electric field is already present, and such field can also be transversal i.e. not directed along the mean velocity in the flow. In view of the interest of such information, we have performed numerical experiments of ion propagation in the shock including either transversal or longitudinal electric fields.

The electric field effect is accounted during the free flight time based on the electric potential evaluated using the modified time step technique [35], where the particle dynamics of a simulated ensemble evolves in time with an appropriate time step while the time-to-next collision is an independent variable for any particle, which is gradually reduced during the free-flight. New free-flight time are generated after collision events. For the same reason, the inclusion of electric field gradients adds no special difficulty.

The effects are shown in Fig. III.6 and III.7 where relative ion concentration, ion temperature, and longitudinal component of ion velocity are represented. In Fig. III.6 (b) we see that longitudinal and transversal electric field produce precursor heating of the ions ahead of the shock. Both the fields also produce a sharp increase in the ion temperature behind the shock. Much interesting, a temperature overshoot is observed which was absent in without the electric field. This overshoot is due to the fact that the ion directed speed is essentially determined from the reduced electric field E/N, which leads to a decrease of the electric heating in the post shock. The directed speed of the ions is changed to thermal energy when the neutral density increases, thereby producing a transient overheating. The effect

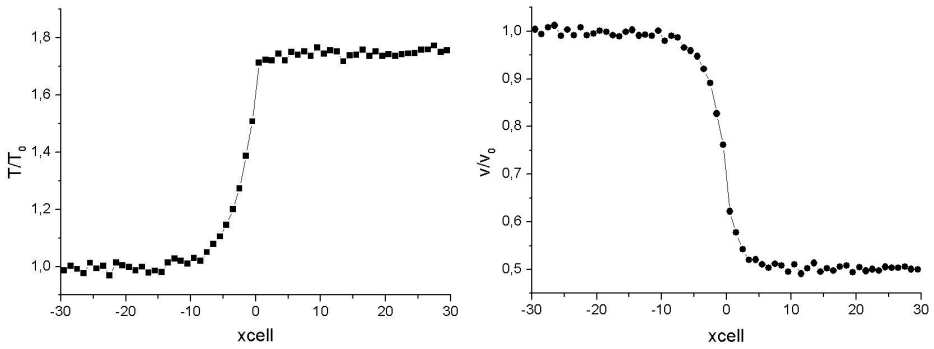

Figure III.4: MC simulation: (a) temperature, (b) velocity.

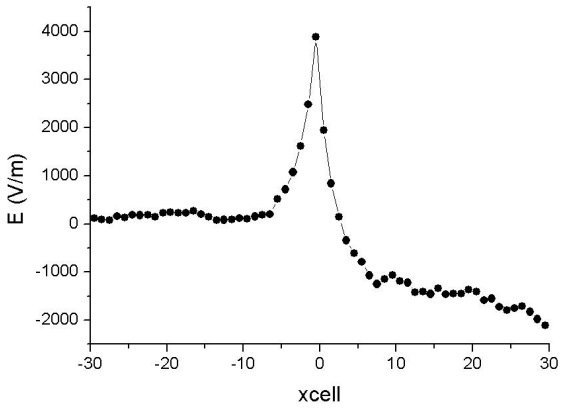

Figure III.5: Electric field intensity computed by MC simulation.

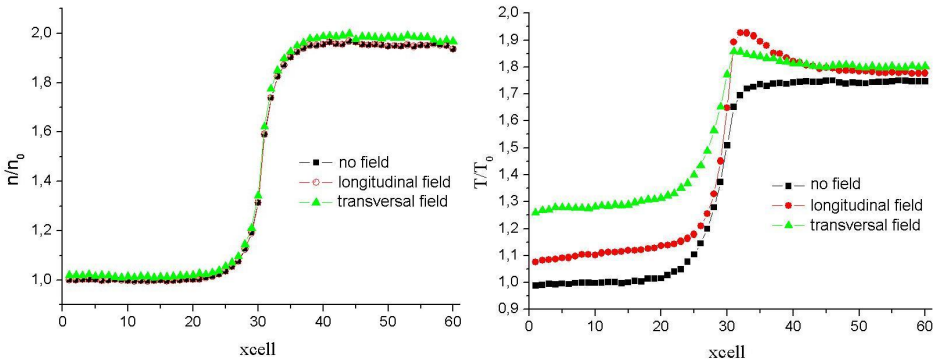

Figure III.6: MC simulation: (a) relative ion concentration, (b) ion temperature.

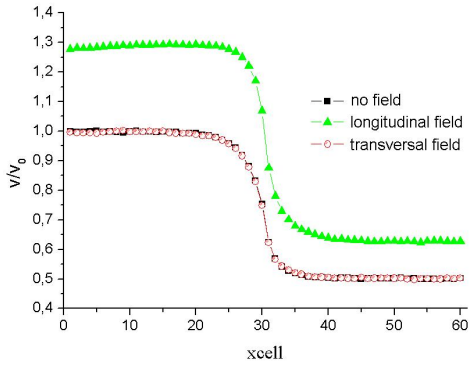

Figure III.7: Longitudinal component of ion velocity computed by the PIC-MC simulation.

is observed in both cases when the E field is added. However, the effects produced by the two orientations of the field with the shock propagation directions are sensibly different in details. When the field E is transversal, the temperature overshoot is higher: this effect cannot be separated from the clear higher temperature of the ions ahead of the shock, which is higher in the case of the transversal field. In the case of the longitudinal field this is directed towards the shock, and particles which are moving opposite to the flow have a much different translational distribution $f_{ion}(\mathbf{v})$. When the particles cross the shock boundary, they not only find themselves in a denser environment, but also the flow speed is reduced. The consequent relaxation of $f_{ion}(\mathbf{v})$ accounts for the stronger T overshoot. These preliminary results provide theoretical basis for limited but detectable plasma effects on shock propagation via electrical diagnostics and molecular spectroscopy, based on the electric field produced by the shock, the ion-molecule energy transfer and the excitation of internal levels. However, it must be noted that these calculations describe shock conditions which are not presently accessible, although they should be achieved using the improved version of the Bari plasma tube under design.

IV. DC-Plasmatron subsonic plasma jet

IV.1. Experiments

The DC-Plasmatron facility, built at the Institute of Electric Power Engineering at Poznan University of Technology and schemed in Fig IV.1, consists of a thoriated tungsten rod cathode of 6 mm diameter, placed in a water-cooled housing and copper cylindrical sections with the internal diameter of 12 mm and 30 mm long. The sections are in-

2. Experiment

The D.C. plasmatron schematically shown in Fig. 1 consists of a thoriated tungs
mm diameter, placed in a water-cooled housing and copper cylindrical sections with the in
mm and 30 mm long.

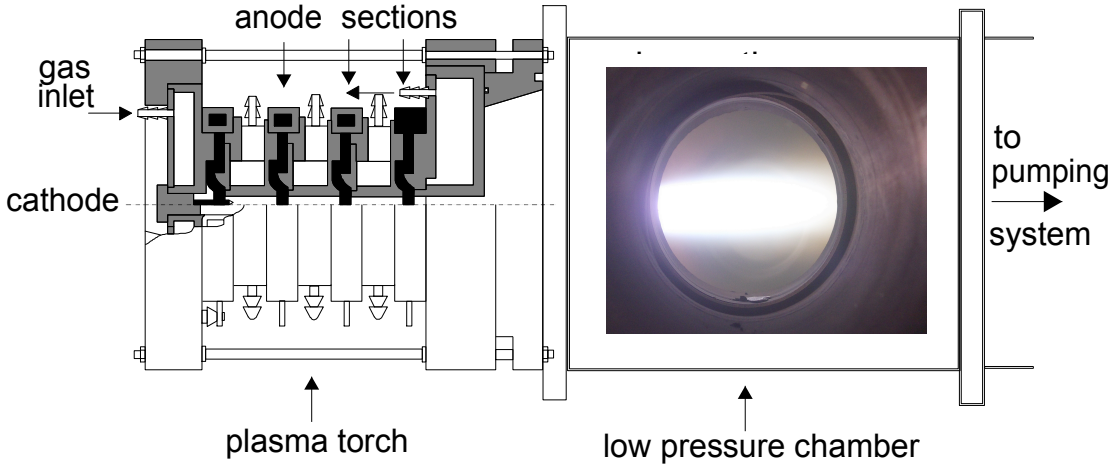

Fig.1. Segmented plasma torch Figure IV.1: Segmented plasma torch.

sulated by means of rings used to inject gas in such a way that a vortex develops in the plasma torch channel. This vortex movement is necessary to stabilize the plasma and to avoid a destruction of sections. Cathode, anode and other sections have a separated water cooling circuits, thus allowing evaluation of the energy exchanges. The plasmatron is mounted on a low pressure chamber 780 mm long with diameter of 100 mm. The chamber is equipped with observation windows. The reduced pressure inside the chamber is achieved by two rotary vane pumps with electric power 1.5 kW each and Roots vacuum pump with a power of 4 kW. The arc is ignited between the cathode and the first section serving as an anode using a high voltage-high frequency discharge. There is a possibility to add a second arc between two other segments in order to increase the electric input power. Two welding power sources connected in series are used to supply an electric arc. The experiments aim to study the emission of N and C atoms, CN, N_2, N_2^+ molecules in N_2-CO_2 mixture. For this study the nitrogen is injected into the arc, and behind the arc into the plasma jet nitrogen or CO_2 is introduced. In this paper the measurements in pure nitrogen plasma flow are described therefore both in arc and plasma jet nitrogen gas is injected. Since the arc cannot be sustained in CO_2 gas due to the torch construction in the next experiments with N_2-CO_2 mixture CO_2 gas will be introduced into the plasma jet region. In this experiment the plasmatron consisted of single section as anode and only one after anode. During the experiment the plasmatron was working with arc current of 347A and mean arc voltage about 50 V giving a delivered power of 17.4 kW. The static pressure inside chamber was 55 mbar, gas flow rate injected into arc 0.8 g/s and injected into plasma jet 0.6 g/s. Assuming the temperature of heavy particles 6500 K (see characterization hereafter), it gives the Mach number 0.6 (flow velocity was about 920 m/s).The emission spectra of the plasma jet are registered with the use of a spectrograph/monochromator (Acton, model SpectraPro2500i) and an ICCD camera (Andor, iStar). The spectrograph is equipped with three gratings 2400, 1800, and 600 grooves/mm. In the case of 2400 g/mm, the reciprocal dispersion in the visible region is 0.005-0.008 nm/pixel depending on the wavelength. The width of the entrance slit was 20-50 μm. The plasma is imaged on the entrance slit either using 180 mm achromatic lens (or fused silica 300 mm lens) mounted on a movable table. The entrance slit of the spectrograph is perpendicular to the direction of plasma expansion and its width and magnification determine the spatial resolution of the imaging system in this direction. The reduction of the plasma size on the entrance slit of the spectrograph is 6.25 (in the case of 180 mm lens). The spatial resolution along the slit is given by the CCD camera track width which was 260 μm, i.e. 1.6 mm including magnification. Such a configuration enables the Abel inversion of axially symmetric jet. The whole optical system was calibrated with the use of DH-2000-CAL Deuterium Tungsten Halogen Calibration Standard and in some spectral regions also with the use of a tungsten ribbon lamp. The spectra were registered at a distance of 65-95 mm from the anode.

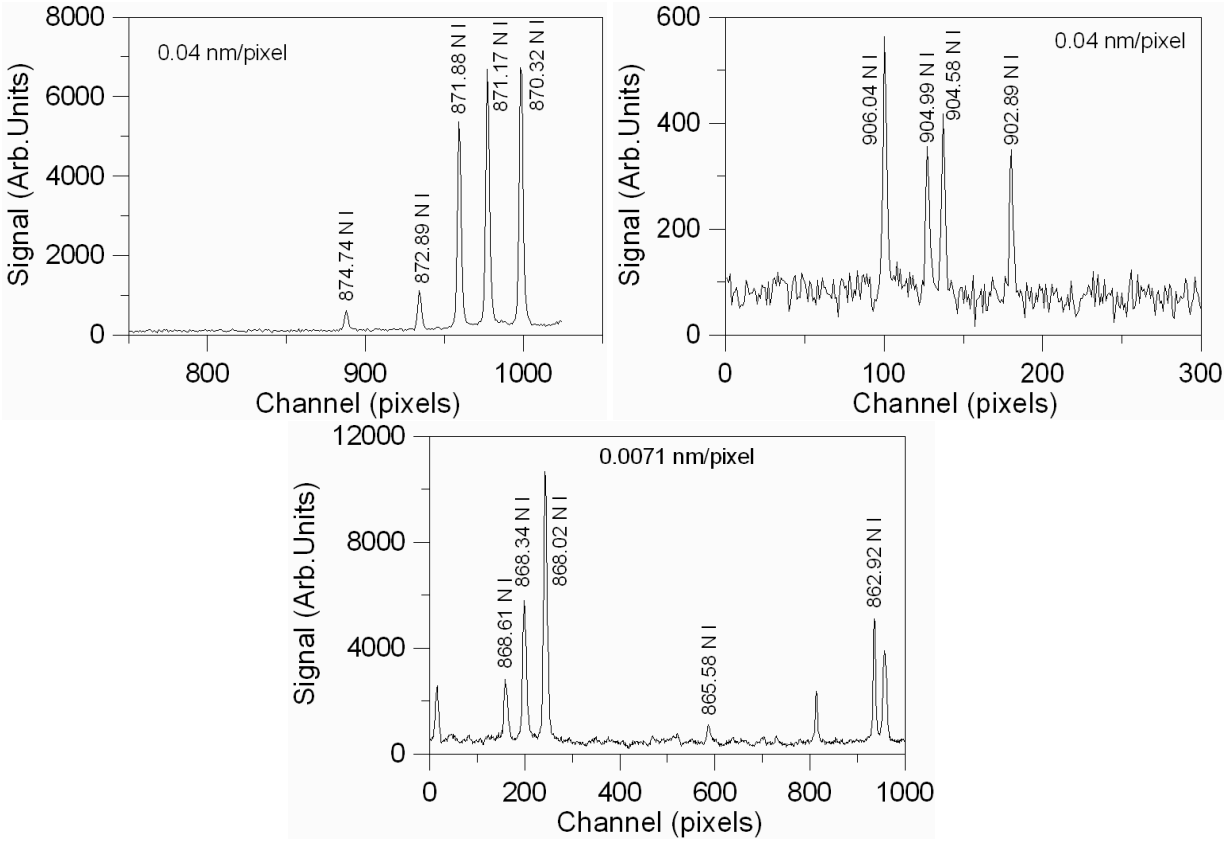

Figure IV.2: Spectral lines of atomic nitrogen in infrared region.

IV.2. Results

IV.2.1. Atomic lines

The emission spectra of nitrogen plasma consisted of atomic nitrogen lines and N_2^+ molecular bands. The lines of nitrogen were clearly distinguishable only in the infrared region. In other spectral region weak nitrogen lines were often overshadowed by the impurity W I lines. Although it was determined that the level of impurities usually did not exceed 0.001 % of nitrogen, due to low excitation energy tungsten lines seriously affected the observed spectra in some regions. No lines were broadened over the measured apparatus broadening so determination of the electron density from the Stark broadening of spectral lines was not possible. Therefore only relative and absolute population densities could be determined from intensities of spectral lines. Some characteristic spectra of the atomic lines of nitrogen are shown in Fig. IV.2.

The excitation temperature T_{exc} was determined from the relative intensities of the following N I lines: 870.32, 871.17, 871.88, 872.89, 874.74, 902.89, 904.58, 904.99, 906.04 nm (see Fig. IV.2). The upper levels of these lines have energy 11.75 eV, 12.97 eV and 13.72 eV. The energy gap between the levels is wide enough to determine T_{exc} with good accuracy and all these lines could be registered together with the grating 600 g/mm. The Boltzmann plot from intensities integrated along the central plasma chord 95 mm from the anode is shown in IV.3. The estimated accuracy is ~15 %. Unfortunately the lines originating from the transitions from highly excited levels (902.89 906.04 nm) are very weak which results in poor accuracy of Abel inversion. As a result the radial distribution of the electron temperature is flat with T_{exc} about 8000 K. The absolute calibration allows the determination of population densities of the upper levels of measured lines. It seems that all levels with energy 11.75 eV or higher are in equilibrium with a T_{exc} of about 8000 K. The population density of upper level of 746.83 nm N I line is shown in Fig. IV.3.

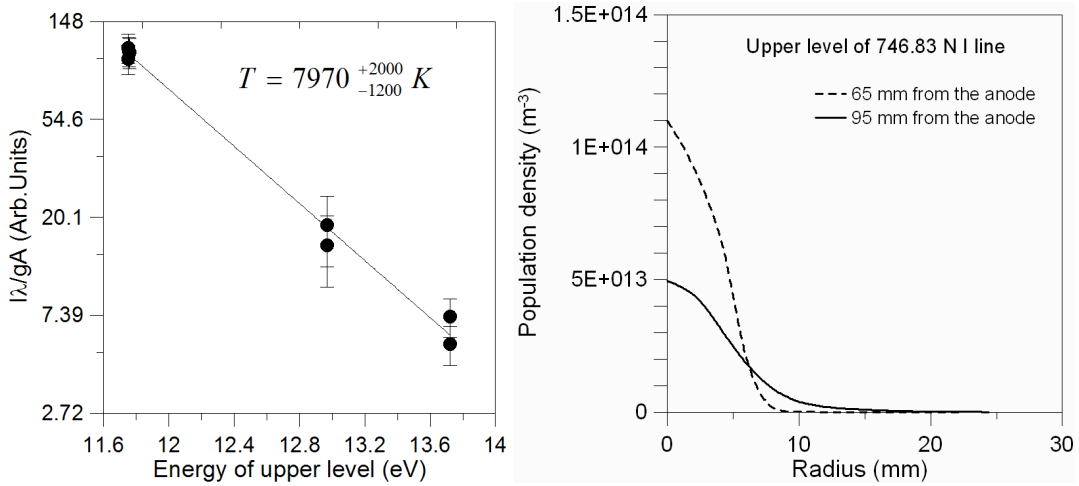

Figure IV.3: At left, Boltzmann plot from relative N I lines intensities. At right, population density of upper level of 746.83 nm N I line.

The measured lines were checked to be free from self-absorption by examining the plasma optical depth for a spectral line using the formula [36] (in SI units)

$$\tau_{ki} = 8.85 \times 10^{-15} f_{ik} \times \lambda^2 n_{z,i} d \times [1 - \exp(-hc/\lambda k T_e)]\, P_i(\lambda_0), \tag{IV.1}$$

where τ_{ki} denotes the optical depth in a line centre, f_{ik} the absorption oscillator strength, λ the wavelength, $n_{z,i}$ the population density of the lower level, d the plasma dimension, h the Planck constant, k Boltzmann constant, c the speed of light in vacuum, T_e the electron temperature and $P_{ki}(\lambda_0)$ the line profile in a line centre. For Gaussian profile $P_{ki}(\lambda_0) = \sqrt{\frac{\ln 2}{\pi}} \frac{1}{\Delta\lambda_{1/2}}$, where $\Delta\lambda_{1/2}$ is half-width at half-maximum (HWHM).

For a given line profile, the relation between the optical depth in a line centre and the total line absorption can be easily evaluated [36]. The absorption can be neglected when the optical depth in a line centre is lower than 0.1. The spectrometer was calibrated with the use of a tungsten ribbon lamp placed at the same distance as the plasma. The calibration allowed us to determine the population densities of the upper levels of spectral lines used in the experiment. Next, the population densities of the lower levels were obtained assuming the Boltzmann distribution between upper and lower level. The half-widths of the lines were determined mainly by the Doppler broadening. The results showed that the lines used for the electron temperature determination were not influenced by self-absorption.

IV.2.2. Continuum radiation

Since the Stark broadening of spectral lines was too small the electron density was determined from the continuum radiation. The method does not require thermodynamic equilibrium to be valid. The total continuum emission coefficient can be written as

$$\epsilon_{total} = \epsilon_{ei}^{fb}(\lambda) + \epsilon_{ei}^{ff}(\lambda) + \epsilon_{ea}^{ff}(\lambda), \tag{IV.2}$$

where fb and ff indices denote free-bound and free-free transitions i.e., the emission due to the recombination and the Bremsstrahlung respectively and *ei* and *ea* denote electron-ion and electron-atom collisions. Formulas for $\epsilon(\lambda)$ are written below (in SI units).

$$\epsilon^{fb}(\lambda) = 1.632 \times 10^{-43}\, N_e T_e^{-1/2} \lambda^{-2} \frac{g_{z,1}}{U_z} \left(1 - \exp\left\{\frac{hc}{\lambda k T_e}\right\}\right) \cdot \sum_z N_z z^2 \xi(T_e, \lambda) \tag{IV.3}$$

$$\epsilon^{fb}(\lambda) = 1.632 \times 10^{-43}\, N_e T_e^{-1/2} \lambda^{-2} \frac{g_{z,1}}{U_z} \exp\left\{-\frac{hc}{\lambda k T_e}\right\} \cdot \sum_z N_z z^2 G^{ff}(T_e, \lambda) \tag{IV.4}$$

$$\epsilon_{ea,\lambda)} = 1.026 \times 10^{-34}\, N_a N_e \lambda^{-2} T_e^{3/2} \sigma_{ea}(T) \left[1 + \left(1 + \frac{hc}{\lambda k T_e}\right)^2\right] \exp\left(-\frac{hc}{\lambda k T}\right) \tag{IV.5}$$

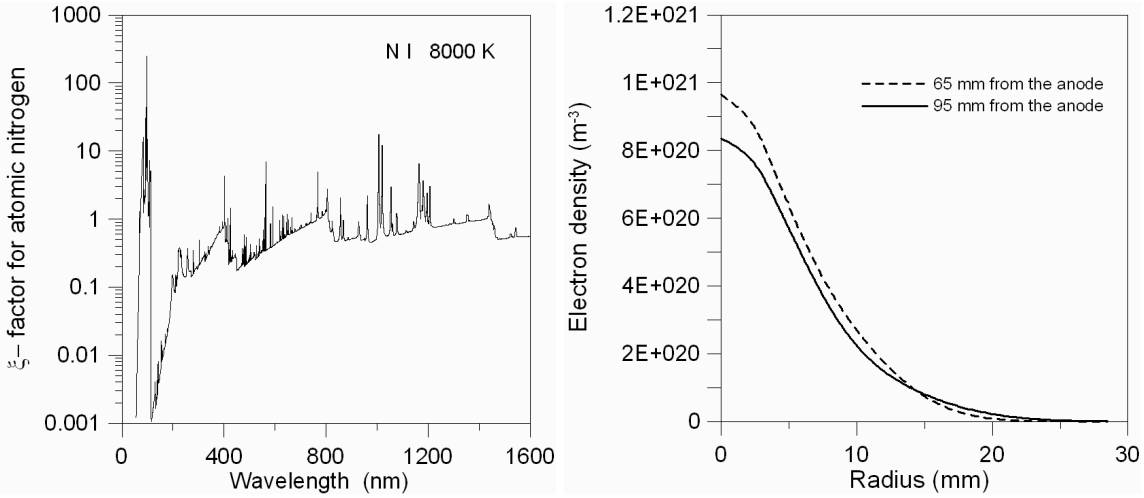

Figure IV.4: At left, ξ factor for atomic nitrogen at T_e = 8000 K. At right, radial distributions of the electron density at two different distances from the anode.

where N_e, N_z and N_a is the electron, ion and atom density, respectively, z denotes ion charge seen by free electron, U_z is the ion partition function, g_z is the statistical weight of the ion, G^{ff} the Gaunt factor, ξ is a correction (Biberman) factor [37], and σ_{ea} is the cross section for electron-atom collisions. The formula IV.3 with $\xi = 1$ has been derived for hydrogen-like atoms and the ξ-factor introduces the edge structure of the real coefficients [37]. The ξ factor for nitrogen atom was calculated with the use of photoionization cross sections taken from [38]. It has been assumed that $T_e = T_{exc}$. The Gaunt factor was taken from [39]. The formulas IV.3 and IV.4 were taken from [37] and formula IV.5 from [40]. All above formulas can be found in [41]. The formula IV.5 was also used for electron-N_2 collisions. The cross sections for e-N and e-N_2 collisions were taken from [42]. It has been found that in present experiment the continuum radiation due to recombination is dominant, other processes did not exceed 8% of total radiation. The radial distributions of the electron density calculated from the continuum radiation at ~ 430 nm are shown in Fig. IV.4.

IV.2.3. Molecular spectra

The observed molecular spectra consisted mainly from the 1st negative system of N_2^+. The rotational and vibrational temperatures were determined by comparing synthetic spectra issued from the SPARTAN code of M. Lino daSilva [43] with spectroscopic measurements. Both spectra are shown in IV.5. The best fit is obtained for rotational temperature T_R = 6500 K and vibrational temperature T_V = 10000 K indicating a non-equilibrium plasma flow. Assuming that T_R is equal to the atom temperature and taking into account that the flow velocity was about 920 m/s we get the flow Mach number of about 0.6.

IV.3. Concluding remarks

The results show that the plasma produced by the segmented plasmatron is in non-equilibrium. This is what can be expected. The criterion for local thermodynamic equilibrium (LTE) has the form [44]:

$$N_e \geq N_e^{cr} = 1.6 \times 10^{18} T_e^{\frac{1}{2}} (\Delta E)^3 \tag{IV.6}$$

where N_e^{cr} is the critical electron density (in m^{-3}) necessary to fulfil LTE conditions and ΔE is the largest energy gap of atomic (ionic) energy level system (in eV). Since such energy gap for N I is 10.33 eV (the level with energy 3.55 eV has been neglected in these considerations because the transition rate to this level is weak) the electron density necessary to fulfill the above criterion is $\sim 1.6 \times 10^{23}$ m^{-3} at a temperature of 8000 K. Even taking into account that in practice this criterion can be lowered one order of magnitude because of the absorption of resonance lines the electron density necessary to fulfill LTE conditions is still 10 times higher than that observed in the experiment. In addition

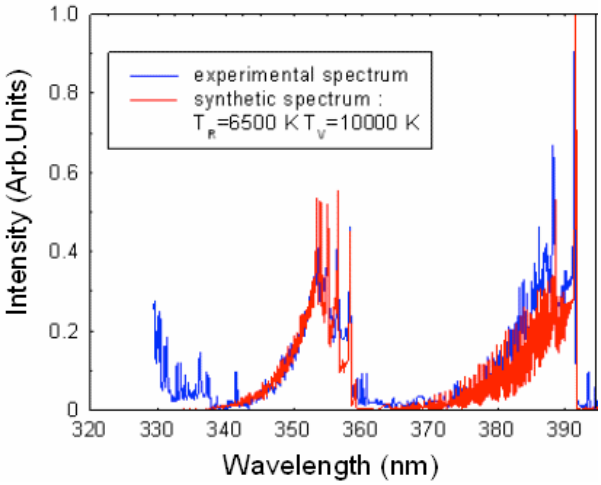

Figure IV.5: Experimental and synthetic spectra of N_2^+ molecular bands at a distance 95 mm from the anode.

the transport of particles can also influence the Saha balance. To summarize, the results represent subsonic nitrogen plasma in strong non-equillibrium which can be used to test the validity of collisional-radiative models.

V. RF-Plasmatron supersonic plasma jet

V.1. Experiments

The experiments described hereafter have been performed with the PWT facility so-called VKI-Plasmatron. The Plasmatron facility includes an Inductively Coupled Plasma torch using a single-turn inductor powered by a high frequency, high power, and high voltage (400 kHz, 1.2 MW, 2 kV) solid state (MOS technology) generator. The discharge is generated inside the torch composed of a quartz tube with an internal diameter of 200 mm and 5 mm thickness, and also a cold cage of 160 mm internal diameter, made of water-cooled copper segments, inserted inside to prevent from severe overheating. The test gas, which is ambient air in the experiments reported here, is injected inside the torch with an annular injection. Once the plasma is started, the electric discharge is enhanced mainly by induced azimuthal electronic currents. The ionized flow is steadily heated by Joule effect, due to efficient electron-neutral energy transfers, absorbing RF power penetrating the plasma over the resistive skin depth, also called the Kelvin length. In the present experiments, the Plasmatron is operated at 490 kW power and 4.5 g/s mass flow rate settings. Supersonic plasma jet is obtained by expanding the plasma through a strictly convergent nozzle (sonic nozzle) of 35 mm throat exit diameter into the test chamber where a low pressure is maintained. The pressure in the reservoir P_{res} was set to 120 mbar and the supersonic plasma jet was investigated with chamber pressure P_c set to 12 mbar and to 6 mbar, corresponding respectively to moderately and highly underexpanded plasma jet cases. Images of the plasma jet acquired with a High Speed Camera (HSC) are displayed in Fig. V.1 to visualize the general aspect of the supersonic jet. The underexpanding jet is typically characterized by a pressure at the nozzle exit higher than in the chamber. In order to equilibrate the pressure difference at the nozzle exit, expansion waves originating from the Prandtl-Meyer expansion are directed towards the jet axis and then reflected toward plasma jet boundaries. The edges of the expansion zone are bright consequently to the reflection of the expanding flow by the cold dense surrounding gas, giving rise to the so-called Barrel shocks. In our conditions, a well distinguishable Mach disk takes place downstream of the first expansion cell. The post Mach disk region is characterized by subsonic velocities together with an increase of the local temperature and pressure typical of post shock relaxing flows. Abel transformation applied to HSC image, also evinced in Fig. V.1 gives insight into actual flow peculiarities such as the significant lack of emission in central regions of the jet consequently to the expansion (well pronounced at P_c = 6 mbar).

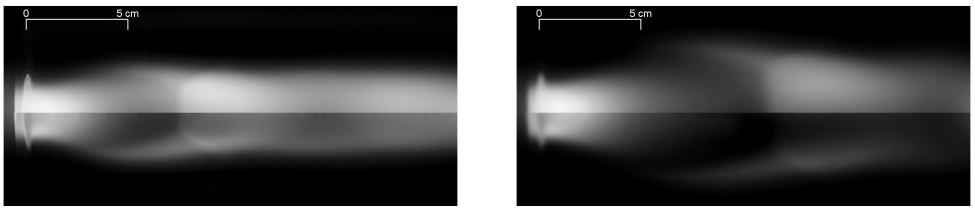

Figure V.1: HSC images for P_c = 12 mbar (on left) and for P_c = 6 mbar (on right) cases. The upper half is the actual record and the lower half is the one processed with Abel transform.

The plasma jet is characterized in terms of excitation temperature of atomic electronic states and electron density by means of Optical Emission Spectroscopy. The plasma jet line-of-sight emission is collected through an aperture and imaged with a fused silica lens onto the entrance slit of an Acton Series monochromator of 750 mm focal length. The spectrometer is combined with a ICCD PI-MAX camera, well-suited to deal with low intensity levels emitted by the rarefied region and offering a large recording frame of 1024 × 1024 pixels of 12.8 μm side. The optical arrangement sketched in Fig. V.2 was designed to obtain a radial slice of about 19 cm height optically conjugated with the CCD height with a magnification factor of 0.07 (the monochromator magnification being 1), in such a way the whole radial emission profile is recorded with the CCD frame with a spatial resolution of about 180 μm. Plasma radiative signatures recorded in the range 400-900 nm are principally constituted of atomic nitrogen and oxygen lines as illustrated in Fig. V.2. Atomic line emission was recorded using a 150 groves/mm grating. The presence of trace of water vapor in the initial cold air mixture resulted in the presence of hydrogen Balmer lines H_α and H_β that have been recorded with a 1200 groves/mm grating in order to resolve the Stark broadening. The spectral resolutions corresponding to both gratings were measured to be respectively of 0.5 nm and 0.06 nm, with the monochromator entrance slit width set to 3 μm. The overall experimental setup is schemed in Fig. V.2. The spectra recorded in the visible spectral range were calibrated in absolute intensity with a ribbon tungsten lamp and its documented absolute radiance (note that only relative intensity are reported in Fig. V.3).

Measured intensities were spatially filtered with a Butterworth-like digital filter. We checked that the plasma is fairly axisymmetric and the considered atomic transitions are optically thin within covered pressure and temperature ranges. Before performing the plasma characterization, the line of sight intensities I_λ (W.cm^{-2}.nm^{-1}.sr^{-1}) have been processed by mean of the Abel transformation to rebuild spectral distribution of local emission ϵ_λ (W.cm^{-3}.nm^{-1}.sr^{-1}).

The optical arrangement was set on a translational stage in order to record radial plasma jet line-of-sight intensity at various positions along the jet z-axis. Intensity measurements started at z = 2.5 cm away from the nozzle exit, corresponding to the nearest axial location accessible by the optical access. Translating the optical arrangement along z-axis, radial distribution of plasma spectral intensity was measured at a dozen of axial locations to cover the first expansion, the Mach disk and the post shock regions. For moderately underexpanded jet (P_{res} = 120 mbar, P_c = 12 mbar), OES measurements were taken after nozzle exit at 2.5, 3.5, 4.5, 6.5, 7.5, 8.5, 9.5, 10.5, 11.5 and 12.5 cm. For highly underexpanded jet (P_{res} = 120 mbar, P_c = 6 mbar), OES measurements were taken after nozzle exit at 2.5, 3.5, 4.5, 8.5, 10.5, 11.5, 12.5, 13.5, 15.5 and 17.5 cm

V.2. Characterization methods

V.2.1. Electronic excitation temperature

The characterization in terms of excitation temperature T_{ex} is performed using measured local emission values ϵ_{ul} associated to atomic radiative transition due to spontaneous emission from an upper (emitting) level u to a lower level l. Knowing the emission ϵ_{ul} allows a straight probing of the upper (emitting) level u population density through the relation:

$$\epsilon_{ul} = n_u \frac{A_{ul}}{4\pi} \frac{hc}{\lambda_{ul}} \quad (\text{W.m}^{-3}.\text{sr}^{-1}), \tag{V.1}$$

where A_{ul} (s^{-1}) is the Einstein coefficient associated to spontaneous emission from level u to level l, respectively of energy E_u and E_l (cm^{-1}) and λ_{ul} (nm) designates the line spectral position. The population of a given emitting level

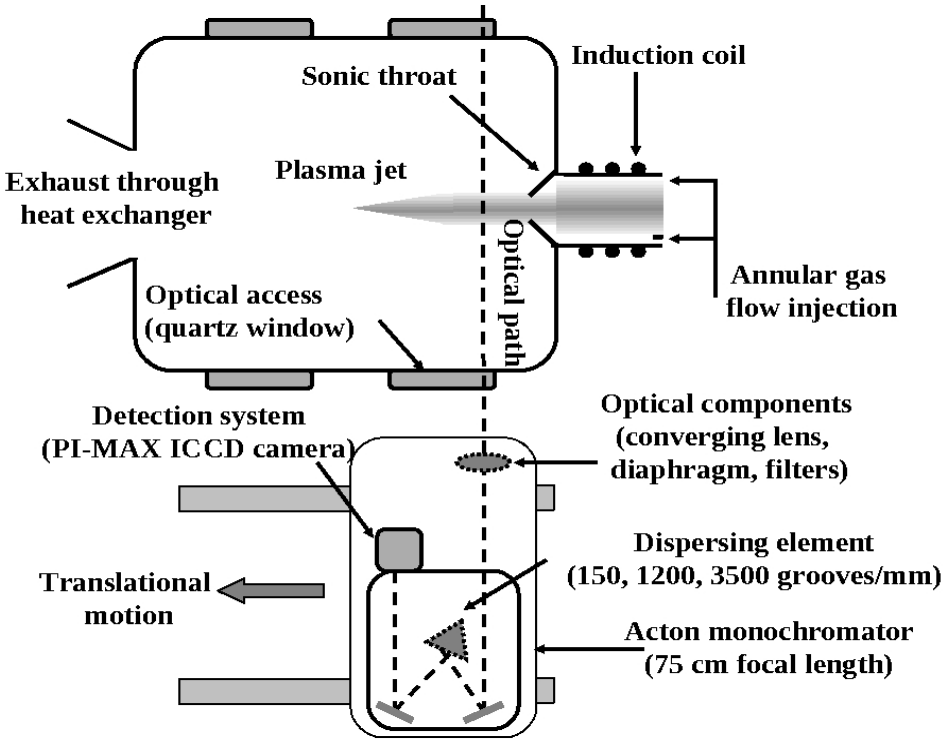

Figure V.2: Top view scheme of the experimental arrangement.

n_u is determined through the spectral integration of its associated emission profile: $\epsilon_{ul} = \int \epsilon_\lambda \mathrm{d}\lambda$, with ϵ_λ referring to the spectral line profile of local emission corrected from a linear background adjusted on the line profile edges.

The excitation temperature T_{ex} is evaluated on the basis of the Boltzmann diagram method, assuming that population of excited states n_i is ruled by the Boltzmann distribution expressed as:

$$n_i(T_{ex}) = \frac{N}{Q_{int}} g_i \exp\left(\frac{hcE_i}{k_B T_{ex}}\right) \quad (\mathrm{m}^{-3}), \tag{V.2}$$

with N (m^{-3}), Q_{int} and g_i designating respectively the species concentration, the internal partition function and the degeneracy of level i. Starting from Eqs. V.1 and V.2, the measured density population versus energy E_u can be expressed as:

$$\ln\left(\frac{n_u}{g_u}\right) = -\left(\frac{hc}{k_b T_{ex}}\right) E_u + \ln\left(\frac{N}{Q_{int}}\right). \tag{V.3}$$

T_{ex} is then simply obtained by mean of a straight line fitting on distribution of measured population densities. Required spectroscopic data for T_{ex} determination were taken from NIST [45]. Uncertainties associated to this approach might be roughly evaluated as $\frac{\Delta T_{ex}}{T_{ex}} \approx 20 T_{ex}/(1.44 \times \Delta E_{max})$, where a critical error of 20 % on local emission is assumed and ΔE_{max} (expressed in cm^{-1}) is the difference between upper energy level extrema. Hence, for a typical ΔE_{max} of $\sim$25000 cm^{-1} and temperature of 10000 K the uncertainty is of $\sim$ 5%.

For brevity, the present study considers only oxygen lines to evaluate the plasma excitation temperature, nitrogen lines are fewer and cover a more reduced energy range making them less reliable than oxygen lines. The numerous atomic oxygen lines, taken into account in the T_{ex} determination method, belong to three groups of transitions. Transitions $3p \rightarrow 3s$ of upper energy level below 90000 cm^{-1}, including the triplet oxygen lines located at roughly 777 nm, the group of transitions $7s, 6s, 5d, 4d, 5s \rightarrow 3p$ characterized by upper energy level E_u ranging from 98000 to 107000 cm^{-1}, and the transition located at 715.67 nm of upper energy level E_u = 116631.094 cm^{-1} above the first ionization energy E_i = 109837.02 cm^{-1}.

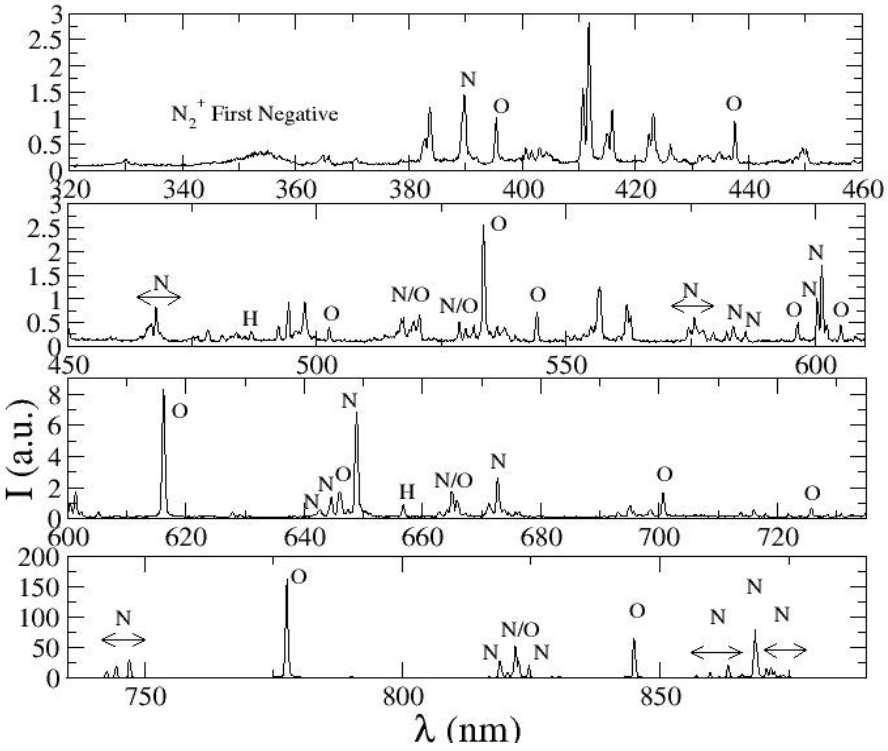

Figure V.3: Typical radiative signature for supersonic air plasma jet in the expansion region (case P_c = 12 mbar).

Typical Boltzmann diagram plots, presented in Fig. V.4, show that at the early expansion, excited state population densities are slightly scattered and fairly distributed along a straight line. However their distribution might deviate significantly from a strict Boltzmann distribution in shock regions. In particular the population of the highest upper energy levels, located beyond the first ionization energy, was found to be systematically slightly underpopulated. In regions of low intensity, the temperature reliability is affected by the rise of the signal to noise ratio and the vanishing of lines of higher upper energy level.

V.2.2. Electron density

The determination of the electron density n_e is performed in a conventional manner by means of recorded hydrogen line profile fits with computed Stark broadened profiles. We used the up-to-date database proposed in [46] to model hydrogen H_α and H_β line profile, located respectively at 656.279 nm and 486.135 nm, undergoing broadening due to coulombian collisions. The database contains intensity profiles tabulated against wavelengths for several values of electron temperature T_e and electron density n_e, covering respectively the range $10^3 \lesssim T_e \lesssim 10^6$ K and $10^{14} \leq n_e \leq 10^{19}$ cm^{-3}. The computation of hydrogen line profile at any electron temperature T_e and electron density n_e is performed by mean of a bilinear interpolation of tabulated data. The computed Stark profile is then convoluted with the instrumental apparatus function.

Systematic computations have shown that computed line profile shapes exhibit a very weak sensitivity to the electron temperature in the range covered by the present experiments (~ 5000-15000 K), while a slight electron density variation induces detectable modifications of the profile at our spectral resolution. Hence, the fitting procedure was performed with the electron density being the only unknown variable, the electron temperature being set to 8000 K. The electron density n_e is then obtained through minimization of the functional expressed as the Root Mean Square

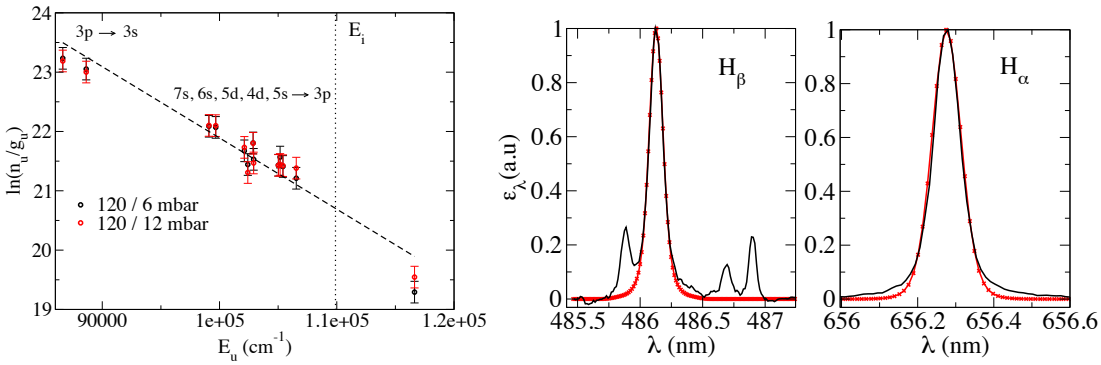

Figure V.4: Typical Boltzmann diagram plot at $z = 2.5$ cm: black-$P_c = 6$ mbar; red-$P_c = 12$ mbar (on left). Typical best fits obtained with H_α and H_β experimental line profiles (on right).

Error (RMSE) between the experimental and computed profiles:

$$RMS\,E(n_e) = \sqrt{\frac{1}{N}\sum_{i}^{N}\left(\overline{\epsilon_{\lambda_i}} - \overline{\epsilon_{\lambda_i}}^{sim}(n_e)\right)^2}, \tag{V.4}$$

where N is the number of spectral grid points, $\overline{\epsilon_{\lambda_i}}^{sim}$ and $\overline{\epsilon_{\lambda_i}}$ are the values at λ_i of simulated and experimental line profiles scaled to unity. Typical H_α and H_β measured spectral profiles are plotted in Fig. V.4 together with their respective best fitted profiles, the one minimizing the RMSE value as defined above. Although the actual H_β profile can be strongly overlapped with various other contributions, the fitting demonstrates a good tolerance and typically yields squared correlation coefficient value of $R^2 \sim 0.98$.

V.3. Results and discussions

Resulting n_e and T_{ex} radial profiles, obtained scanning axially the jet, have been appropriately arranged and processed to yield two dimensional distribution by means of bicubic spline interpolation under MATLAB environment. The 2D distribution of plasma emission in the visible spectral range is considered first. In Fig. V.5, are displayed the resulting interpolations of the emission rebuilt by mean of Abel transform and integrated in the spectral range 400-900 nm (largely dominated by atomic emission).

The black lines correspond to the actual emission profiles taken into account by the interpolation procedure. Starting from the resulting emission 2D distribution, the Mach disk location is roughly gauged as the location at the end of the first expansion where the centerline emission starts rising. The estimated Mach disk position is $z_M \approx 7.6$ cm at $p_c \approx 12$ mbar and $z_M \approx 11.5$ cm at 6 mbar. Using the well-known empirical correlation proposed in [47] in the case of an ideal gas expansion, the Mach disk position is expressed as:

$$\frac{z_M}{D_0} = 0.67\sqrt{\frac{P_c}{P_{res}}}, \tag{V.5}$$

yielding in our experimental conditions $z_M = 7.4$ cm at $P_c = 12$ mbar and $z_M = 10.5$ cm at $P_c = 6$ mbar, with nozzle diameter $D_0 = 3.5$ cm. Although the experimental estimations and the empirical values are in satisfactory agreement, the discrepancies could be attributed to the non ideal gas effects.

The interpolated distributions for n_e are presented in Fig. V.6. The black lines indicate the actual radial extent of n_e measurements derived from H_β line profiles. Density lower than 1.10^{14} cm^{-3} were not measured with respect to the validity domain of Stark broadening prediction [46]. After the first expansion region, the n_e distribution is greatly influenced by the chamber pressure, while the electron density range is slighter affected after the nozzle exit. The electron density drops rapidly after the nozzle exit consequently to rarefaction taken place with the supersonic expansion. In the region of highest expansion, $z = 8.5$ cm, it was possible to determine n_e only over a limited radial

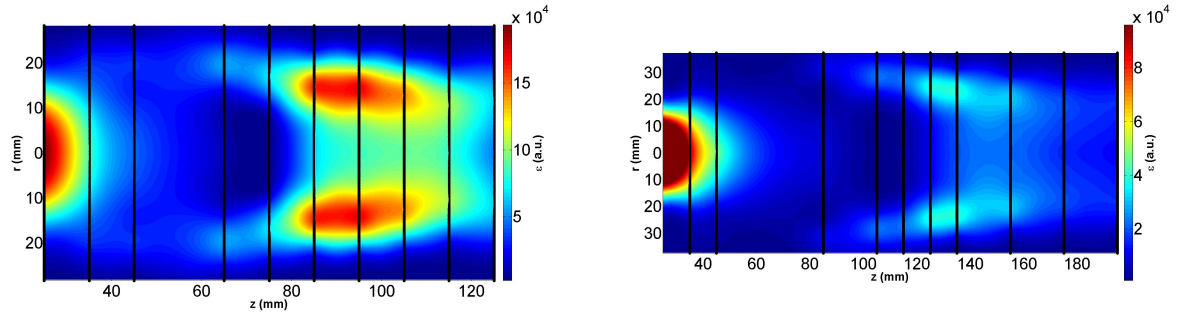

Figure V.5: ϵ distributions with $P_c = 12$ mbar (on left) and $P_c = 6$ mbar (on right).

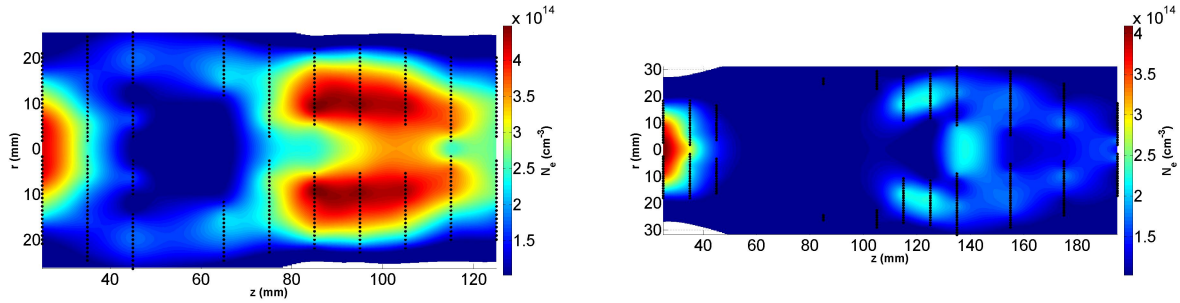

Figure V.6: n_e distributions with $P_c = 12$ mbar (on left) and $P_c = 6$ mbar (on right).

extent. At 6 mbar, measurements are critically limited to the radial range $24 \lesssim r \lesssim 28$ mm. The lack of measurements induces some undesirable numerical artifacts when rebuilding the interpolated distribution with incomplete radial information. For instance, in the case $P_c = 12$ mbar, it is clear that the electron density increases at the jet edges at the proximity of the first compression, but its rise at centerline does not appear plausible, otherwise it would have been measured. That stands too for the 6 mbar case, preventing from the reliable characterization of the structure of the rarefaction cell after the Mach disk.

The resulting interpolated distributions for T_{ex} are given in Fig. V.7. The black lines indicate the actual radial extent of T_{ex} measurements which ranges from ~ 5000 to ~ 14000 K. Temperature determination with Eq. V.3 is not tractable in regions of lowest emission where, as consequence of the rarefaction local emission nearly fully vanished. Similarly to n_e distribution situations, interpolation of measured T_{ex} profiles suffers from the lack of data in the central part of the jet, generating unreliable distribution in regions of weakest emission. In spite of such inconvenient artifacts, the rebuilt distributions remain fully reliable in regions of actual measurements. The resulting distributions stand as a valuable data to serve as a test case to assess compressible plasma flow computations.

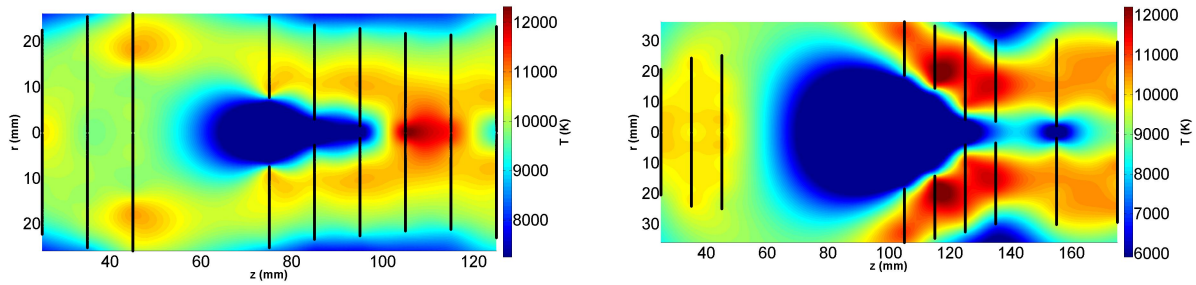

Figure V.7: T_{ex} distributions with $P_c = 12$ mbar (on left) and $P_c = 6$ mbar (on right).

VI. Conclusions and perspectives

The reported investigations address the characterization of four distinct non-equilibrium plasma kinds to produce new data valuable to assess the performances of non-equilibrium plasma flow descriptions.

High enthalpy shock tube experiments are well suited to procure critical data to assess the sophisticated descriptions developed to predict kinetic processes taking place behind the shock. The measurements of the emission of air post-shock plasma generated with the high enthalpy shock tube at Institute for Problems in Mechanics (Russian Federation) have been documented and shortly analyzed. The radiative signatures measured in absolute radiance in the UV spectral range for an extended range of shock velocity stands as the most relevant data to validate post-shock non-equilibrium plasma flow computations determined on the basis of up-to-date CR models.

The experimental electrical characterization of a shock wave, generated by the acoustic shock tube at University of Bari (Italy), propagating at nearly Mach 1 through a weakly ionized medium generated with a DC discharge, has been performed using laser deflection technique.
Detailed Particle in Cell-Monte Carlo (PIC-MC) investigations have been conducted to evaluate the effect of the resulting self-consistent electric force on the shock wave dynamic.

The characterization in terms of electron density n_e and excitation temperature T_{ex} of the subsonic nitrogen plasma jet produced by DC-Plasmatron facility at Poznan University of Technology (Poland) has demonstrated that the flowing plasma is far from the Saha equilibrium. The observed departure to equilibrium thermodynamic state indicates that the numerical rebuilding of the nitrogen subsonic flow has to be performed with an incompressible fluid model consistently coupled with a critically selected non-equilibrium chemistry description.

Moderately and highly underexpanded supersonic air plasma jets, produced by VKI-Plasmatron facility at von Karman institute (Belgium), have been investigated by uncovering the general features of the local emission, electron density n_e and excitation temperature T_{ex} distributions. The spatial characterization of the first expansion, the Barrel shock regions, the Mach disk and its post-shock area yielded relevant information to enhance the assessment of compressible plasma flow predictions. For instance, for the two considered conditions, the Mach disk location estimated with local emission distribution was found in good agreement with the empirical prediction. Further plasma jet computations have to be carried out with 2D axisymmteric compressible fluid description coupled with a relevant non-equilibrium description to tackle regions where the imbalance kinetic processes are driven by recombining processes (e.g. in the expansion) or dominated by ionizing collisions (e.g. in the post-shock region).

Acknowledgement

The research leading to these results has received funding from the European Communitys Seventh Framework Programme (FP7/2007-2013) under Grant Agreement No. 242311.

References

[1] Cauchon DL, McKee CW, Cornette ES. Radiative Heating Results from the Fire II Flight Experiment at a Reentry Velocity of 11.4 Kilometers per Second. Tech. Rep. NASA TM X-1402, Langley Research Center, 1967.

[2] Keck JC, Camm JC, Kivel B, Wentink T. Radiation from Hot Air Part II. Shock Tube Study of Absolute Intensities. Jr Ann Phys 1959; 7: 1-38.

[3] Thomas GM, Menard WA. Experimental Measurements of Equilibrium and Nonequilibrium Radiation from Planetary Atmospheres. AIAA Journal 1966; 4(2): 227-237.

[4] Grinstead JH, Olejniczak J, Wilder MC, Bogdanoff MW, Allen GA, Lilliar R. Shock-heated air radiation measurements at lunar return conditions: Phase I EAST test report. NASA REPORT, 2007. NASA EG-CAP-07-142. 146

[5] Kozlov PV, Romanenko YuV, Shatalov OP. Radiation intensity measurement in simulated Martian atmospheres on the double diaphragm shock tube. Proc. of 4th International Workshop on Radiation of High Temperature Gases in Atmospheric Entry, Lausanne, Swiss, 2010, ESA SP-689.

[6] Takayanagi H, Fujita K. Absolute Radiation Measurements behind Strong Shock Wave in Carbon Dioxide Flow for Mars Aerocaprure Missions. AIAA 2012-2744.

[7] Cruden DA, Prabhu D, Martinez R, Le H, Bose D, Grinstead JH. Absolute Radiation Measurement in Venus and Mars Entry Conditions. AIAA 2010-4508.
[8] Grinstead JH, Wilder MC ,Wright MJ, Bogdanov DW, Allen DA, Dang K, Forrest MJ. Shock radiation measurements for Mars aerocapture radiative heating analysis. AIAA 2008-1272
[9] Brandis AM, Morgan RG, McIntyre TJ, Jacobs PA. Nonequilibrium Radiation Intensity Measurements in Simulated Titan Atmospheres. J. Thermophys Heat Transfer 2010; 24: 291-300.
[10] Rond C, Boubert P, Félio JM, Chikhaoui A. Radiation Measurements in Shock Tube for Titan Mixtures. J. Thermophys Heat Transfer 2007; 21: 638-646.
[11] Park C, Howe JH, Jaffe RL, GV Candler. Review of chemical-kinetic problems of future NASA missions, I: Earth entries. J. Thermophys Heat Transfer 1993; 7: 385-398.
[12] Park C, Howe JH, Jaffe RL, GV Candler. Review of chemical-kinetic problems of future NASA missions, II: Mars entries. J. Thermophys Heat Transfer 1994; 8: 9-23.
[13] Boubert P, Chaix A, Chikhaoui A, Robin L, Vervisch P. Aerodynamic calibration of TCM2 facility and study of a bow shock layer by emission and laser spectroscopy. Shock Waves 2002; 1: 341-351.
[14] Boubert P, Rond C. Nonequilibrium Radiation in Shocked Martian Mixtures. J. Thermophys Heat Transfer 2010; 24: 40-49.
[15] Panesi M, Magin TE, Bourdon A, Bultel A, Chazot O, Babou Y. Collisional radiative modeling in flow simulation. VKI Lecture Series 2008; RTO-EN-AVT-162 - ISBN 978-92-837-0091-3
[16] Brandis AM, Johnston CO, Cruden BA *et al.* Validation of CO 4th positive radiation for mars entry. J. Quant. Spectrosc. Radiat. Transfer 2013; 121:91-104
[17] Cicala G, Bruno D, Capitelli M, Longo S, Rainò AC. Study of shock waves interacting with Ar and N_2 low pressure dc discharges. Eur. Phys. J. D 2010; 57: 375-385
[18] Ionikh YZ, Chernysheva NV, Meschchanov AV, Yalin AP, Miles RB. Direct evidence for thermal mechanism of plasma influence on shock wave propagation. Phys. Lett. A 1999; 259: 387-392.
[19] Macheret SO, Ionikh YZ, Chernysheva NV, Yalin AP, Martinelli L, Miles RB. Shock wave propagation and dispersion in glow discharge plasmas. Phys. Fluids 2001; 13: 2693-2705.
[20] Aihtal SM and Subramaniam VV. On the characteristics of a spark generated shock wave. Phys. Fluids 2000; 12: 924-935.
[21] White AR and Subramaniam VV. Shock propagation through a low-pressure glow discharge in argon. J. Thermophys. Heat Transfer 2011; 15: 491- 496.
[22] Klimov AI, Koblov AN, Mishin GI, Serov YuL and Yavor IP. Shock wave propagation in a glow discharge Sov. Tech. Phys. Lett. 1982; 8: 192-194.
[23] Bletzinger P, Ganguly BN. Local acoustic shock velocity and shock structure recovery measurements in glow discharges. Phys. Lett. A 1999; 258: 342-348.
[24] Bletzinger P, Ganguly BN and Garscadden A. Electric field and plasma emission responses in a low pressure positive column discharge exposed to a low Mach number shock wave. Phys. Plasmas 2000; 7: 4341-4347
[25] Fischer WPP, Gelhan A, Esser B, Faerber J, Reger N. Plasma-Windtunnel Tests on a New Metallic TPS Material, Hot Structures and Thermal Protection Systems for Space Vehicles. Proceedings of the 4th European Workshop held 26-29 November, 2002 in Palermo, Italy. Edited by A. Wilson. ESA SP-521. Paris: European Space Agency, 2003, p.199
[26] Caristia S, De Filippis D. SCIROCCO project a major plasma wind tunnel for the years 2000. Proceedings of the first International Symposium on Atmospheric Reentry Vehicles and Systems, Arcachon, France, AAAF, March, 1999.
[27] Bottin B, Chazot O, Carbonaro M, Van Der Haagen V, Paris S. Measurement Techniques for High Enthalpy and Plasma Flows. 2000, RTO-EN-8, AC/323(AVT)TP/23, 8
[28] Gordeev AN. Overview of characteristics and experiments in IPM plasmatrons. RTO AVT/VKI Special Course on Measurement Techniques for High Enthalpy Plasma Flows, RTO EN-1, von Karman Institute for Fluid Dynamics, Rhode-Saint-Genèse, Belgium, October.1999
[29] Lequang D, Babou Y, André P. Experimental assessment of local thermodynamic equilibrium in VKI Plasmatron air plasma jet. Journal of Technical Physics 2009; 50: 151-162
[30] Laux CO, Pierrot L, Gessman RJ. State-to-state modeling of a recombining nitrogen plasma experiment. Chem Phys 2012; 398: 46-55.
[31] Van de Sanden MCM, de Regt JM, Schram DC. Recombination of argon in an expanding plasma jet. Phys Rev E 1993; 47: 27922797.
[32] Sember V, Gravelle DV, Boulos MI. Spectroscopic study of a supersonic plasma jet generated by an ICP torch with a convergent- divergent nozzle. J Phys D: Appl Phys 2002; 35: 1350-1361.
[33] Spanier J, Gelbard E M. Monte Carlo Principles and Neutron Transport Problems. Addison Wesley 1969, reprinted Dover 2008
[34] Dupree SA, Fraley SK. Monte Carlo primer: practical approach to radiation transport. Kluwer 2002.
[35] Hockney RW, Eastwood WR. Computer Simulation Using Particles. Adam Hilger 1991.
[36] Drawin HW, Emard F. Optical escape factors for bound-bound and free-bound radiation from plasmas. Beitraege aus der Plasmaphys 1973; 13: 143-68.
[37] Richter J. Plasma Diagnostics. North Holland, Amsterdam: Lochte-Holtgreven 1968.
[38] [Online] Available from: http://www.astronomy.ohio-state.edu/~nahar/nahar_radiativeatomicdata/index.html.
[39] Schluetter D. Gaunt factors for free-free transitions in the fields of positive ions of carbon, nitrogen and oxygen calculated in Scaled Thomas-Fermi approximation. Z. Phys. D - Atoms, Molecules and Clusters 1989; 11: 273-276.
[40] Cabannes F, Chapelle JC. Reactions Under Plasma Conditions. New York: M.Venugopalan, Wiley 1971.
[41] Wilbers ATM, Kroessen GMW, Timmerman CJ, Schramm DC. The continuum emission of an arc plasma. J. Quant. Spectrosc. Radiat. Transfer 1991; 45: 1-10.
[42] Capitelli M, Devoto RS. Transport coefficients of high-temperature nitrogen. Phys. Fluids 1973; 16: 1841-1875.
[43] Lino da Silva M. Simulation des propriétés radiatives du plasma entourant un véhicule traversant une atmosphère planétaire à vitesse hypersonique - application à la planète Mars. Ph.D. diss., Université d'Orléans 2004.
[44] McWhirter RWP. Plasma Diagnostics Techniques. New York: R.H. Huddelstone and S.L. Leonard Academic Press 1965.

[45] [Online] Available from: http://physics.nist.gov/asd2i.
[46] Gigosos MA, Cardenoso V. New plasma diagnosis tables of hydrogen Stark broadening including ions dynamics. J Phys B:At Mol Opt Phys 1996; 29:4795-4838.
[47] Ashkenas H, Sherman FS. The structure and utilization of supersonic free jets in low density wind tunnels. Proc. 4th Int. Symp. on Rarefied Gas Dynamics 1996; 2: 84-105.

Role of State-to-State Kinetics in Determining Transport Coefficients for Hypersonic Flow Simulations

Eswar Josyula, Jonathan M. Burt,

Air Force Research Laboratory

William F. Bailey

Air Force Institute of Technology

Prakash Vedula

University of Oklahoma

A numerical study is performed to assess the influence of thermochemical nonequilibrium on the transport coefficients used in Computational Fluid Dynamics (CFD) simulations of hypersonic external flowfields. An quantitative assessment is made of transport coefficients from simplified methods of Blottner curve fits and Variable Hard Sphere (VHS) model on the numerical solution of a Mach 23 flow past a sphere cone, the RAMC-II test case. The equations derived by Kustova[1] in the state kinetic approach for calculating transport coefficients from the Chapman-Enskog solution of the Wang-Chang Uhlenbeck equation were used to conduct a parametric study for assessment of the effect of the following parameters on the state-specific diffusion coefficients: (1) widely different population distributions, (2) atomic mass concentration, and (3) binary atomic to molecular diffusion coefficient ratio. The present study is a first step to quantify the relative importance of the parameters considered for a future implementation of the computationally expensive state-kinetic transport coefficients in multi-dimensional fluid dynamic flow solvers for flow conditions where the more general state kinetic approach becomes necessary.

Introduction

The design of vehicles for high speed flight, in particular the thermal protection system (TPS) in the highly collisional aerothermal environment, requires development of reliable nonequilib-

rium models for Computational Fluid Dynamics (CFD) solvers. The limitations, development, and use of current and future CFD models for species transport of mass, momentum, and energy with sources and sinks requires a thorough understanding of the physics of nonequilibrium. The three so called transport properties of a fluid are the coefficients of diffusion, viscosity, and thermal conductivity.[2,3] Diffusion is the mass transport through molecular exchange and occurs in a fluid because of random molecular motion. In a macroscopic sense, mass diffusion in a fluid flow occurs due to concentration gradients. In a microscopic sense, the transport of molecules through otherwise identical molecules as a result of concentration gradient is known as self-diffusion. With the idea of momentum transport, viscosity can be stated as the property of the fluid which relates applied stress to the strain rate, where the coefficient of viscosity is directly related to molecular interactions and thus may be considered a thermodynamic property. Thermal conductivity is associated with the transport of mean thermal energy in the flow, where this mean energy consists of random translational energy and internal energy of the molecules.

The Navier-Stokes equations are generally applicable in the study of gaseous systems that are close to the equilibrium state. A primary assumption in dealing with polyatomic and reacting gases is that the volumetric rate terms are negligible compared with those associated with spatial gradients. This implies that the inelastic collisions (those associated with vibrational energy exchange or dissociation) are relatively infrequent and do not significantly influence the transport coefficients. In recent years, however, vibrational excitation and chemical reactions are treated as source terms in fluid dynamic codes, where the sources and sinks necessitate modifications of the equations of motion appropriately. In the absence of information on the cross-sections involved, the use of Blottner curve fits[4] for viscosity, Eucken's relation[5] for thermal conductivity and suitable mixing rules are often used in CFD codes, whereas a variable hard sphere (VHS) model[6] in DSMC provide good estimates for transport properties in air. However, with knowledge of the collision cross section, it is convenient to use the Chapman-Enskog approximation[3] to obtain the transport coefficients for use in hypersonic CFD codes. The Chapman-Enskog approximation is used to find the solution of Wang-Chang Uhlenbeck equation,[7] the transport equation for the phase space distribution function, which includes terms for internal energy exchanges in the collision integral. Considerable work has been carried out on development and tabulation of a database for the collision integral, appearing in the Sonine polynomial expansion of the Boltzmann equation for computing transport coefficients[8–10] for aerthermodynamic analysis; the limitation of the work is the inability to distinguish the different quantum energy states. This limitation is overcome in the approach given in the works of Ref. 1, 11–13 that includes the vibrational energy states in the collision operator of the transport equation, thus providing state to state transport coefficients for calculation of the transport properties in a gas flow. A justification for this more general state kinetic approach for transport coefficients for given sets of flow conditions was provided in earlier work, see for example, Refs. 14, 15.

Although the nonequilibrium effects are inherent to the transport coefficients of Blottner curve fits, which were derived from experimental data, there is no explicit treatment of the different thermal energy modes or the degree of nonequilibrium in deriving them, and this raises questions on the limits of applicability of these curve fits to nonequilibrium flow processes. There is also uncertainty in the limits of applicability of the VHS model, which is based on a power law molecular potential, for flows involving strong vibrational nonequilibrium. In the present study, a quantitative assessment is made of the relative differences in transport coefficients calculated from Blottner curve fits[4] and the VHS model[6] in air mixture of a high temperature hypersonic flow. Then, using the state kinetic approach of Kustova,[1] the role of binary and self diffusion is identified in a gas mixture.

Governing Equations

Consider a multi-species, reacting gas mixture, whose underlying distribution functions corresponding to each species c, (quantized) vibrational energy level i and (quantized) rotational energy level j are represented as $f_{cij}(\mathbf{x}, \mathbf{u}_c, t)$, where $\mathbf{x}$, $\mathbf{u}_c$ and t denote the spatial coordinate, (microscopic) velocity and time instance respectively. The evolution of these distribution functions, based on kinetic theory, can be expressed as[1,7,11–13]

$$\partial_t f_{cij} + \mathbf{u}_c \cdot \partial_{\mathbf{x}} f_{cij} = J_{cij}, \tag{1}$$

where J_{cij} denotes the full collision operator that accounts for interactions not only due to elastic collisions but also due to rotational and vibrational energy exchanges and chemical reactions. While each of these mechanisms can be associated with a characteristic time scale, it was found from experimental data (under certain conditions) that there exists a separation of time scales according to the relation $\tau_{el} < \tau_{rot} << \tau_{vib} < \tau_{react} \sim \theta$, where τ_{el}, τ_{rot}, τ_{vib}, τ_{react} and θ correspond to mean times characterizing collisions resulting in translational, rotational, vibrational energy transfer, chemical reactions and macroscopic time scale respectively. In other words, as translational and rotational energy modes tend to equilibrate much faster in comparison to other modes, the collision operator on the r.h.s of Eqn. (1) can be expressed as $J_{cij} = \frac{1}{\epsilon} J^{rapid}_{cij} + J^{slow}_{cij}$, where $J^{rapid}_{cij} \equiv J^{el}_{cij} + J^{rot}_{cij}$ and $J^{slow}_{cij} \equiv J^{vib}_{cij} + J^{react}_{cij}$ correspond to collision operators of rapid and slow processes and ϵ is a small parameter denoting the ratio of timescales of fast and slow (collisional) processes. Note that the collision operators J^{el}_{cij}, J^{rot}_{cij}, J^{vib}_{cij} and J^{react}_{cij} correspond to elastic collisions, rotational energy exchanges, vibrational energy exchanges and chemical reactions, respectively. While a direct solution of Eqn. (1) can be very computationally expensive, the generalized Chapman-Enskog method can be used to obtain approximate solutions. In this

approach, the distribution functions f_{cij} are expressed in a power series involving the (small) parameter ϵ. The zeroth order solution $f_{cij}^{(0)}$ satisfies the relation $J_{cij}^{el}(f_{cij}^{(0)}, f_{cij}^{(0)}) + J_{cij}^{rot}(f_{cij}^{(0)}, f_{cij}^{(0)}) = 0$. Consideration of collision invariants, leads to the following form for the zeroth order distribution function:

$$f_{cij}^{(0)} = \left(\frac{m_c}{2\pi kT}\right)^{3/2} s_j^{ci} \frac{n_{ci}}{Z_{ci}^{rot}(T)} \exp\left(-\frac{m_c c_c^2}{2kT} - \frac{\epsilon_j^{ci}}{kT}\right), \tag{2}$$

where n_{ci} is the number density of molecules of species c (with molecular mass m_c) in vibrational level i, s_j^{ci} denotes the statistical weight, k is the Boltzmann constant, T is the temperature, $\mathbf{c}_c \equiv \mathbf{u}_c - \mathbf{v}$ is the peculiar velocity, $\mathbf{v}$ is the macroscopic gas velocity and Z_{ci}^{rot} is the rotational partition function. The macroscopic parameters $n_{ci}(\mathbf{x}, t)$, $\mathbf{v}(\mathbf{x}, t)$ and $T(\mathbf{x}, t)$ are defined in terms of the distribution function and satisfy the following relations:

$$n_{ci} = \sum_j \int f_{cij}\, d\mathbf{u}_c = \sum_j \int f_{cij}^{(0)}\, d\mathbf{u}_c \tag{3}$$

$$\rho\mathbf{v} = \sum_{cij} m_c \int \mathbf{u}_c f_{cij}\, d\mathbf{u}_c = \sum_{cij} m_c \int \mathbf{u}_c f_{cij}^{(0)}\, d\mathbf{u}_c \tag{4}$$

$$\rho U = \sum_{cij} \int \left(\frac{1}{2} m_c c_c^2 + \epsilon_i^c + \epsilon_j^{ci} + \epsilon^c\right) f_{cij}\, d\mathbf{u}_c \tag{5}$$

$$= \sum_{cij} \int \left(\frac{1}{2} m_c c_c^2 + \epsilon_i^c + \epsilon_j^{ci} + \epsilon^c\right) f_{cij}^{(0)}\, d\mathbf{u}_c. \tag{6}$$

Note that U denotes the total energy per unit mass defined such that $\rho U \equiv \frac{3}{2} nkT + \rho E_r + \rho E_v + \rho E_f$. For each species c and vibrational level i, the corresponding (mass) density is defined as $\rho_{ci} = m_c n_{ci}$, the vibrational energy of the molecule is given by ϵ_i^c (based on reference minimum of its potential curve, $\epsilon^c = -D_c$, where D_c is the energy of dissociation of the molecular species c). The components of total energy per unit volume due to rotation, vibration and dissociation are given by $\rho E_r = \sum_{cij} \int \epsilon_j^{ci} f_{cij}\, d\mathbf{u}_c$, $\rho E_v = \sum_{ci} \epsilon_i^c n_{ci}$ and $\rho E_f = \sum_c \epsilon^c n_c$ respectively. Also note that the number density of species c is given by $n_c = \sum_i n_{ci}$, the total number of particles is given by $n = \sum_{ci} n_{ci}$ and the density of the gas mixture is given by $\rho = \sum_c m_c \sum_i n_{ci}$.

Based on Eqn. (1)–(6), macroscopic equations governing the evolution of $n_{ci}(\mathbf{x}, t)$, $\mathbf{v}(\mathbf{x}, t)$ and $T(\mathbf{x}, t)$ for a multi-component reacting gas mixture in vibrational and chemical nonequilibrium

can be obtained as

$$\frac{dn_{ci}}{dt} + n_{ci}\nabla\cdot\mathbf{v} + \nabla\cdot(n_{ci}\mathbf{V}_{ci}) = R_{ci} \tag{7}$$

$$\rho\frac{d\mathbf{v}}{dt} + \nabla\cdot\mathbf{P} = 0 \tag{8}$$

$$\rho\frac{dU}{dt} + \nabla\cdot\mathbf{q} + \mathbf{P}\colon\nabla\mathbf{v} = 0, \tag{9}$$

where the production terms are given by $R_{ci} \equiv \sum_j \int J_{cij}^{slow}\ d\mathbf{u}_c$, the diffusion velocity $\mathbf{V}_{ci}$ of the chemical species c at vibrational level i is given by $n_{ci}\mathbf{V}_{ci} \equiv \sum_j \int \mathbf{c}_c f_{cij}\ d\mathbf{u}_c$, the pressure tensor is given by $\mathbf{P} \equiv \sum_{cij} \int m_c \mathbf{c}_c\mathbf{c}_c f_{cij}\ d\mathbf{u}_c$ and the heat flux vector is given by $\mathbf{q} \equiv \sum_{cij} \int \left(m_c c_c^2/2 + \epsilon_j^{ci} + \epsilon_i^c + \epsilon^c\right)\mathbf{c}_c f_{cij}\ d\mathbf{u}_c$. Based on the zeroth order distribution function, the corresponding approximations for the diffusion velocity, pressure tensor and heat flux vector can be obtained as ${\mathbf{V}_{ci}}^{(0)} = 0$, $\mathbf{P}^{(0)} = p\mathbf{I}$ and $\mathbf{q}^{(0)} = 0$, where p denotes the pressure and I denotes the unit tensor. First order corrections to these approximations can be obtained from linear integral equations for the first order distribution functions $f_{cij}^{(1)} \equiv f_{cij}^{(0)}\phi_{cij}$. These linear integral equations result in the following form of the first order distribution function:

$$f_{cij}^{(1)} = \frac{f_{cij}^{(0)}}{n}\left(-\mathbf{A}_{cij}\cdot\nabla\ln T - \sum_{dk}\mathbf{D}_{cij}^{dk}\cdot\mathbf{d}_{dk} - \mathbf{B}_{cij}\colon\nabla\mathbf{v} - F_{cij}\nabla\cdot\mathbf{v} - \mathbf{G}_{cij}\right). \tag{10}$$

The functions $\mathbf{A}_{cij}$, $\mathbf{B}_{cij}$, $\mathbf{D}_{cij}^{dk}$, F_{cij} and $\mathbf{G}_{cij}$, which depend on microscopic velocities $\mathbf{u}_c$ and macroscopic parameters $n_{ci}(\mathbf{x},t)$, $\mathbf{v}(\mathbf{x},t)$ and $T(\mathbf{x},t)$ can be identified as coefficients of the underlying gradient terms in the linear integral equations. Note that the diffusion driving forces for each chemical species c at vibrational level i is given by $\mathbf{d}_{ci} = \nabla(n_{ci}/n) + \{(n_{ci}/n) - (\rho_{ci}/\rho)\}\nabla\ln p$. The above first order distribution functions can be used to obtain expressions for the diffusion velocity, pressure tensor and total heat flux vector as:

$$\mathbf{V}_{ci} = -\sum_{dk} D_{cidk}\mathbf{d}_{dk} - D_{Tci}\nabla\ln T \tag{11}$$

$$\mathbf{P} = (p - p_{rel})\,\mathbf{I} - 2\mu\mathbf{S} - \eta\nabla\cdot\mathbf{v}\mathbf{I} \tag{12}$$

$$\mathbf{q} = -\lambda'\nabla T - p\sum_{ci} D_{Tci}\mathbf{d}_{ci} + \sum_{ci}\left(\frac{5}{2}kT + \langle\epsilon_j^{ci}\rangle_r + \epsilon_i^c + \epsilon^c\right)n_{ci}\mathbf{V}_{ci}. \tag{13}$$

Here D_{cidk} and D_{Tci} denote the diffusion coefficient and thermal diffusion coefficient for each chemical and vibrational species, given in terms of bracket integrals as $D_{cidk} = \frac{1}{3n}[\mathbf{D}^{ci},\ \mathbf{D}^{dk}]$ and $D_{Tci} = \frac{1}{3n}[\mathbf{D}^{ci},\ \mathbf{A}]$. Note that the pressure tensor (based on the first order approximation) depends on the strain rate tensor S, the shear viscosity coefficient $\mu = \frac{kT}{10}[\mathbf{B},\ \mathbf{B}]$, the bulk viscosity coefficient $\eta = kT[F,F]$ and the relaxation pressure $p_{rel} = kT[F,G]$. As a result of inelastic translational and rotational energy transfers in collisions between molecules of different vibrational and

chemical species, additional terms appear in the pressure tensor in the form of relaxation pressure and bulk viscosity. The coefficient of thermal conductivity $\lambda' = \frac{k}{3}[\mathbf{A},\ \mathbf{A}]$ appearing in the total heat flux vector also depends on the elastic and inelastic exchanges between translational and rotational modes. The transport coefficients corresponding to shear viscosity, thermal conductivity, mass diffusion and thermal diffusion coefficients can be obtained using Sonine and Waldmann-Trubenbacher orthogonal polynomials. An important aspect of this approach for obtaining the transport coefficients is that detailed interactions due to vibrational energy transfers and chemical kinetics are carefully considered and could result in more accurate expressions for diffusion velocity, stress tensor and heat flux vector in the presence of thermochemical nonequilibrium.

Simplifications to the above approach are possible when the diffusion velocity is assumed to be given by a Fick's law as

$$\rho_{ci}\mathbf{V}_{ci} = -\rho_{ci}D_{11}\nabla(\rho_{ci}/\rho_c), \tag{14}$$

where D_{11} is the self-diffision coefficient which can be obtained from kinetic theory as $D_{11} = \eta'\mu/\rho$, where η' is 1.2 for hard sphere molecules, is 1.43 for Maxwell molecules and is somewhere in between these two values based on experimental results. The species diffusion velocity $\mathbf{V}_c \equiv \tilde{\mathbf{C}}_c - \mathbf{v}$ defined as the species mass-averaged velocity $\tilde{\mathbf{C}}_c \equiv \frac{1}{\rho_c}\sum_{i,j} m_c \int \mathbf{u}_c f_{cij}\, d\mathbf{u}_c$ relative to the mixture mass-averaged velocity $\mathbf{v}$, can also be approximated by Fick's law as

$$\rho_c\mathbf{V}_c = -\rho_c D_{12}\nabla(\rho_c/\rho), \tag{15}$$

where the binary diffusion coefficient D_{12} is obtained by assuming a constant Lewis number. These simplified approximations for transport coefficients can be used in conjunction with the global conservation equations as:

$$\partial_t\rho_{ci} + \nabla\cdot\left[\rho_{ci}\left(\mathbf{v} + \mathbf{V}_c + \mathbf{V}_{ci}\right)\right] = \dot{\omega}_{ci} \tag{16}$$

$$\partial_t\rho_c + \nabla\cdot\left[\rho_c\left(\mathbf{v} + \mathbf{V}_c\right)\right] = \dot{\omega}_c \tag{17}$$

$$\partial_t(\rho\mathbf{v}) + \nabla\cdot(\rho\mathbf{v}\mathbf{v} + \tilde{\tau}) = 0 \tag{18}$$

$$\partial_t(\rho e_{vib}) + \nabla\cdot\left[\rho e_{vib}(\mathbf{v} + \mathbf{V}_c) + \dot{\mathbf{q}}_{trans} + \dot{\mathbf{q}}_{vib}\right] = \rho\dot{\omega}_{vib} \tag{19}$$

$$\partial_t(\rho e) + \nabla\cdot\left[\rho(e + p/\rho)\mathbf{v} - \sum\dot{\mathbf{q}}_{vib} + \sum(\rho_c h_c\mathbf{V}_c) - \mathbf{v}\cdot\tau\right] = 0 \tag{20}$$

The conservation Eqn. (16) is used in the state to state kinetics code, written for mass density in quantum level i for diatomic molecules. The source term $\dot{\omega}_{ci}$ derived from the vibrational master equations is made up of the relevant energy exchange processes consisting of the V-T and V-V energy exchange mechanisms. The density of molecular species is the sum of population densities

in the various vibrational levels. For diatomic species in the state to state kinetics formulation, a separate vibrational conservation equation was not necessary as the vibrational energy was calculated at each quantum level. The mass conservation of species is represented by Eqn. (17). The production of small amounts of atoms due to dissociation of molecules is included in the source term, $\dot{\omega}_c$. The mixture density, ρ is the sum of the partial species densities,

$$\rho = \rho_{N_2} + \rho_{O_2} + \rho_O + \rho_{NO} + \rho_N \tag{21}$$

Eqn. (18) gives the conservation of total momentum. For diatomic molecules other than those treated with the state-kinetic rates, vibrational relaxation in Eqn. 19 was modeled according to the Landau-Teller[5,16] form. Eqn. 19 also includes terms for the conduction and diffusion of vibrational energy. The conservation of total energy is given by Eqn. (20) with heat conduction and species diffusion terms.

Results and Discussions

Results are presented in two sections. The first section provides comparisons of using two commonly used transport coefficient models for the RAMC-II test case. The second section is a parametric study of binary & self diffusion on an N_2-N gas mixture using a state specific approach.

Relative effects of simplified transport coefficients on RAMC-II test case

In this section, an assessment is made of two simplified transport coefficient models commonly used in current hypersonic CFD codes, based on flow simulation for a RAMC-II test case (Mach 23 air flow at 61 km altitude). A post-processing technique is used to assess the local influence of the transport coefficient model on diffusion coefficient values throughout the flowfield. The dynamic viscosity for each of the five species in the reacting flow hypersonic sphere-cone simulation is calculated as a function of temperature, using the Blottner model[4] employed in a CFD flow simulation that solved Eqns 17-20. This viscosity is given as

$$\mu_{Blottner} = \exp[(A \ln T + B) \ln T + C] \tag{22}$$

where A, B, and C are species specific constants.

For comparison, species viscosities are also computed for the variable hard sphere (VHS) model of Bird[6] through a series of post-processing calculations based on CFD simulation results.

The VHS model is the standard transport coefficient model in the direct simulation Monte Carlo (DSMC) method, and is widely used for a range of gas kinetic schemes due to its ease of implementation and the existence of analytical solutions involving integration over equilibrium velocity distributions. In this model, the cross section for intermolecular collisions scales as a constant power of the relative speed for each collision pair, and the post-collision relative velocity is isotropically distributed. It follows that the viscosity is proportional to a constant power (ω) of temperature, with the allowable range bounded by a value of $\frac{1}{2}$ for a hard sphere gas and 1 for a Maxwell gas. Given a reference temperature T_{ref} and a reference collision diameter d_{ref} at this temperature, the VHS viscosity may be expressed as

$$\mu_{VHS} = \frac{15\sqrt{\pi m k_B T_{ref}}}{2\pi d_{ref}^2 (5-2\omega)(7-2\omega)} \left[\frac{T}{T_{ref}}\right]^{\omega} \tag{23}$$

where m is the molecular mass, T is the gas temperature and k_B is Boltzmann's constant. As with the Blottner model, the species-specific dynamic viscosity in the VHS model is a function of only temperature and species constants. The local ratio of Blottner viscosity to VHS viscosity may therefore be calculated for each species as a function of temperature. Eucken's relation is employed to calculate species thermal conductivities for both Blottner and VHS models. Species thermal conductivities will therefore have the same dependence on internal energy excitation in both models, and the local ratio of thermal conductivities should equal the corresponding viscosity ratio. In the flow simulation, the mixture viscosity and thermal conductivity values are computed as functions of species transport coefficients and concentrations using the mixing rule of Wilke.[5] As part of post-processing calculations, this mixing rule is applied separately to the species-specific VHS viscosities given by Eq 23. The resulting local mixture VHS viscosity, μ_{VHS}, mix may then be compared with the mixture viscosity $\mu_{Blottner}, mix$ employed in the simulation by evaluating the ratio $\mu_{Blottner}, mix/\mu_{VHS}, mix$. Note that, while for individual species, the ratio of Blottner-to-VHS thermal conductivities is equal to the corresponding viscosity ratio, these two ratios are not necessarily equal for the mixture; this follows from the fact that species thermal conductivities depend on the number of internal degrees of freedom, so the relative contributions of each species to summations used in Wilke's mixing rule will be different for thermal conductivity than for viscosity. In order to guarantee that the summation of species diffusive mass fluxes is zero, a single diffusion coefficient is utilized in the simulation through a constant Lewis number approximation. This approximation is equivalent to setting the mixture diffusion coefficient as a function of only the mixture viscosity. The ratio of Blottner to VHS mixture diffusion coefficients is therefore equal to the viscosity ratio $\mu_{Blottner}, mix/\mu_{VHS}, mix$.

Note that the transport coefficient assessment here is inherently approximate, due in part to the following three factors: First, a separate simulation employing the VHS model is not performed, and instead the same local temperature values are used to compute Blottner and VHS viscosities.

Second, in DSMC simulation of a gas mixture, each combination of species involved in a binary collision may be assigned a different reference diameter d_{ref} and temperature exponent (ω) , which makes application of VHS procedures for a mixture not easily amenable to CFD calculations or analysis. Single species viscosity ratios are used in order to avoid consideration of differences associated with mixing rules, and the Wilke mixing rule is employed as a simplified means of relating VHS and Blottner transport coefficients for a five-species air mixture. Finally, due to the approximate nature of the VHS power law temperature dependence, VHS input parameters are generally only valid over a limited temperature range. The temperature range in the calculated flowfield is considerably wider than the appropriate range for a single set of VHS parameters, so a comparison between VHS and Blottner transport coefficients should be performed with an understanding that VHS coefficient values may not be accurate at all points within the simulation domain.

In order to quantify the variation in transport coefficient ratios among the different species, ratio values extracted along the stagnation streamline are presented in Fig 1. The corresponding temperature variation is also shown in the figure. We find a maximum value within the highest temperature shock region for N, a drop in viscosity ratio values across the shock for all other species, and a relatively small range of ratio values for N_2 in comparison with the other species. For all species, very little variation in the viscosity ratio is found over the large temperature range (over 10,000 K) which characterizes the post-shock region; this trend seems to indicate that the relative validity of the Blottner and VHS models and input parameters may be comparable over this temperature range. For the mixture ratio, it is observed in Fig 1 that values are greater than one outside a small region around the shock, with a maximum of 1.20 near the outer edge of the thermal boundary layer.

The strong dependence of the mixture Blottner/VHS transport coefficient ratio on nitrogen dissociation and recombination is illustrated in Fig 2, which shows the variation in mixture ratio along with species mole fractions over the stagnation streamline. In this figure, the maximum ratio value is coincident with the location of highest N concentration, near the outer edge of the boundary layer. Due to comparatively low dissociation energy, O_2 is shown in Fig 2 to almost completely dissociate a short distance downstream of the shock. As a result, the large transport coefficient ratio values for O (in addition to the large ratio for atomic nitrogen) may be assumed to contribute significantly to a post-shock increase in the mixture ratio. Based on general trends in Fig 2, including mixture transport coefficient ratio values which are smaller than one near the shock and greater than one elsewhere along the stagnation streamline, we assume that the use of the VHS model in place of the Blottner model would result in a somewhat reduced shock thickness and a slightly thicker boundary layer.

Due to the inherent difficulty in adjusting the constants in the Blottner model or VHS parameters for thermochemical nonequilibrium gas mixtures of air, the evaluation of transport coefficients

based on state to state kinetic modeling is attractive.

Parametric study of binary and self diffusion in N_2-N gas mixture: state kinetic approach

Having assessed the effects of experimental-based and empirical transport models, in this section we assess the importance of state specific transport coefficients for given flow conditions. The work of Kustova[1] lays the foundation for this extension. Her formalism is recaptured, recast in a parametric form and then evaluated for a molecular/atomic nitrogen mixture with a focus on vibrational state specific coefficients.

Following Kustova[1] the diffusion coefficients - both binary and self - are expressed in terms of mass fractions of the relevant species. The system under consideration is a mixture of molecular nitrogen and atomic nitrogen. A state specific approach is adopted with the relevant molecular states being the vibrational states. Only a single atomic state is considered. The molecular mass fraction for a given molecular state is recast into a fractional vibrational population form and the diffusion coefficients simplified. The fractional population is displayed in Fig 3 as a function of the vibrational states. The vibrational temperature, $T_v = -\Delta/\ln[n2/n1]$, ranges from 1500 to 3000 K with Δ set to $[0.3 \times 11600$ K]. An artificially enhanced population in the high vibrational states is introduced (shown in Eqn.24 below) to simulate effects due to anharmonic pumping and biased recombination.

$$n_i/n_{N2} = \exp[-0.3 \times i/((T_v/11600) \times (1 + 0.0431 \times i))] \qquad i = 0, 1, 2, 3...48 \tag{24}$$

The original form of the self-diffusion coefficient in Ref. 1 given below (Eqn. 25) is cast in a functional form that permits parametric studies.

$$D_{N_{2i},N_{2i}} = \frac{\left(\frac{C_N}{\mathcal{D}_{N_2}} + \frac{2(-1-C_N+1/C_{N_{2i}})}{\mathcal{D}_{NN_2}}\right)\mathcal{D}_{NN_2}m_N^2n^2}{\left(\frac{C_{N_2}}{2\mathcal{D}_{N_2}} + \frac{C_N}{\mathcal{D}_{NN_2}}\right)\rho^2} \qquad i = 0, 1, 2, 3... \tag{25}$$

This form is achieved by expressing the atomic nitrogen mass fraction as $1/f$, the ratio of the binary, atomic nitrogen-molecular nitrogen diffusion coefficients $\mathcal{D}_{NN_2}/\mathcal{D}_{N_2}$ as β and the vibrational state concentrations, ξ, in terms of the fractional populations. The resulting equation,

$$D_{N_{2i},N_{2i}} = \mathcal{D}_{N_2}\frac{(1+f)^2\beta[2f^2(-1+\xi) + \xi(-2+\beta) - f\xi\beta]}{2(-1+f)f^2\xi[2 + (-1+f)\beta]} \tag{26}$$

asymptotically depends inversely on the fractional population. This is made obvious in Fig. 4 by plotting the product of the state concentration and the state-specific self diffusion coefficient. For this and the future comparisons, we have normalized the diffusion coefficients to the molecular

nitrogen self-diffusion coefficient, $\mathcal{D}_{N_2}$. Note that the asymptotic value is insensitive to vibrational temperature and population departures from Boltzmann form.

The state specific vibrational binary diffusion coefficient, $D_{N_{2i}N_{2k}}$ given in Ref. 1,

$$D_{N_{2i}N_{2k}} = D_{N_2N_2} = \frac{(\frac{C_N}{\mathcal{D}_{N_2}} - \frac{2(1+C_N)}{\mathcal{D}_{NN_2}})\mathcal{D}_{NN_2}m_N^2n^2}{(\frac{C_{N_2}}{2\mathcal{D}_{N_2}} + \frac{C_N}{\mathcal{D}_{NN_2}})\rho^2} \qquad i \neq k \tag{27}$$

is also cast into the parametric representation with the result:

$$D_{N_2N_2} = \mathcal{D}_{N_2}\frac{(1+f)^2(2+2f-\beta)\beta}{2f^2[2+(-1+f)\beta]} \tag{28}$$

It is interesting to note that state specific binary diffusion coefficient is directly proportional to the molecular nitrogen binary diffusion coefficient and independent of the states of the collision partners, i and k.

In Fig. 5, we examine the variation of the binary state specific diffusion coefficient with f, the inverse of the atomic mass concentration for β=1. At small concentrations, less than 20% (f >5), the coefficient approaches the molecular nitrogen binary diffusion coefficient, $\mathcal{D}_{N_2}$. This binary state specific diffusion coefficient is less sensitive to the relative values of the atomic and molecular diffusion coefficients, β. We examine this dependence in Fig. 6 for β ranging from 0.5 to 2 with f assigned the value of 10 and note less than a 20% variation.

In Fig. 7, we examine the sensitivity of the state-specific self-diffusion coefficient to the atomic to molecular ratio, β for population distribution at 3000 K with f set to 10. The dependence is weak over the entire range of β from 0.5 to 2.0, with asymptotic value decreasing as β decreases and converging to the state specific binary value. Fixing β at 1 and the population distribution at the 3000 K value, we next examine the variation of the state specific self-diffusion coefficient with respect to atomic concentration, $1/f$. With f = 2, 5 and 10, the state specific self-diffusion coefficient decreases monotonically from values near 3 to those near 1, simultaneously approaching the value of the state specific binary diffusion coefficient, $D_{N_{2i}N_{2k}}$, shown earlier in Fig. 6.

CONCLUDING REMARKS

A numerical study is performed to assess the influence of thermochemical nonequilibrium on the transport coefficients used in Computational Fluid Dynamics (CFD) simulation of hypersonic flows and to introduce a much more rigorous approach to modeling of the nonequilibrium transport process than the current practice. A quantitative assessment is made of transport coefficients from simplified methods of Blottner curve fits and the Variable Hard Sphere (VHS) model for hypersonic external flowfield of a Mach 23 air flow past a sphere cone, the RAMC-II test case. A

parametric study was conducted using a state specific approach to examine the roles of binary and self diffusion in an N_2-N gas mixture.

Comparison of simplified transport coefficient models of Blottner curve fits and VHS model for a Mach 23 air flow past a body showed that use of VHS model would result in reduced shock thickness and a slightly thicker boundary layer. Large transport coefficient ratios between Blottner and VHS models for atomic oxygen and nitrogen contribute significantly to a post-shock increase in the Blottner/VHS ratio for a high temperature air mixture. The ratio of viscosity coefficients of the air mixture from the Blottner curve fits and VHS model has a relatively small variation for the large temperature range. However, significant differences in transport coefficients from both models are expected in mixtures with large oxygen concentration. It should be noted that variation in transport coefficient values associated with model selection is a well established fact, and the existence of the discrepancies discussed here is very much expected. The analysis shown in this work is not intended to demonstrate that such discrepancies exist, but instead to quantify the differences among both species-specific and mixture transport coefficients for a representative hypersonic flow problem. This analysis shows the potential impact of different models for the temperature dependence of transport coefficients on these coefficients themselves, as well as on predicted flowfield characteristics.

A parametric study of assessing the role of binary and self diffusion in a N_2-N gas mixture showed that self diffusion coefficients depend inversely on the population in the quantum energy states. It was found that the asymptotic value for the self diffusion coefficient is insensitive to the vibrational temperature as well as the population distributions, but this value is sensitive to the degree of dissociation. The state specific binary diffusion coefficient is directly proportional to molecular nitrogen binary diffusion coefficient and is independent of the states of the collision partners. For low atomic concentration the state specific binary diffusion coefficient approaches that of diatomic nitrogen. These findings have the potential to significantly impact the implementation and modeling of state-to-state transport coefficients in computational fluid dynamics flow solvers.

ACKNOWLEDGEMENTS

Helpful discussion with E. Kustova of Saint Petersburg University is gratefully acknowledged.

References

[1]E.V. Kustova. On the Simplified State-to-State Transport Coefficients. *Chemical Physics*, 270:177–195, 2001.

[2]R. B. Bird, W. E. Stewart, and E. N. Lightfoot. *Transport Phenomena*. John Wiley & Sons, Inc, New York,

1960.

[3]J.O. Hirschfelder, C.F. Curtiss, and R.B. Bird. *Molecular Theory of Gases and Liquids*. John Wiley & Sons, Inc, New York, 1964.

[4]F. G. Blottner, M. Johnson, and M. Ellis. Chemically Reacting Viscous Flow Program for Multicomponent Gas Mixtures. Technical Report SC-RR-70-754, Sandia Laboratories, 1971.

[5]W. G. Vincenti and C. H. Kruger Jr. *Introduction to Physical Gas Dynamics*. John Wiley & Sons, 1967.

[6]G.A. Bird. *Molecular Gas Dynamics and the Direct Simulation of Gas Flows*. Clarendon Press, Oxford, 1994.

[7]J.H. Ferziger and H.G. Kaper. *Mathematical Theory of Transport Processes in Gases*. North Holland Publishing Compnay, New York, 1972.

[8]G. Palmer. An Assessment of Transport Property Methodologies for Hypersonic Flows. *AIAA Paper 97-0983*, January 1997.

[9]G Palmer and M.J. Wright. A Comprison of Methods to Compute High Temperature Gas Thermal Conductivity. *AIAA Paper 2003-3913*, June 2003.

[10]M.J. Wright, D. Bose, G. Palmer, and E. Levin. Recommended Collision Integrals for Transport Property Computations, Part 1: Air Species. *AIAA Journal*, 43, December 2005.

[11]E.V. Kustova and E.A. Nagnibeda. Strong Nonequilibrium Effects on Specific Heats and Thermal Conductivity of Diatomic Gas. *Chemical Physics*, 208:313–329, 1996.

[12]E.V. Kustova and E.A. Nagnibeda. Transport Properties of a Reacting Gas Mixture with Strong Vibrational and Chemical Nonequilibrium. *Chemical Physics*, 233:57–75, 1998.

[13]A. Chikhaoui, J.P. Dudon, E.V. Kustova, and E.A. Nagnibeda. Transport Properties in Reacting Mixture of Polyatomic Gases. *Physica A*, 247:526–552, 1997.

[14]D. Bruno, M. Capitelli, E. Kustova, and E. Nagnibeda. Non-Equilibrium Vibrational Distributions and Transport Coefficients of $N_2(v)$-N Mixtures. *Chemical Physics Letters*, 308:463–472, 1999.

[15]A. Orsini, P. Rini, V. Taviani, D. Fletcher, E.V. Kustova, and E.A. Nagnibeda. State-to-State Simulation of Nonequilibrium Nitrogen Stagnation-Line Flows: Fluid Dynamics and Vibrational Kinetics. *Journal of Thermophysics and Heat Transfer*, 22:390–398, Julyl-Sept 2008.

[16]L. Landau and E. Teller. Zur Theorie der Schalldispersion. *Physikalische Zeitschrift der Sowjetunion*, 10(1):34–43, 1936.

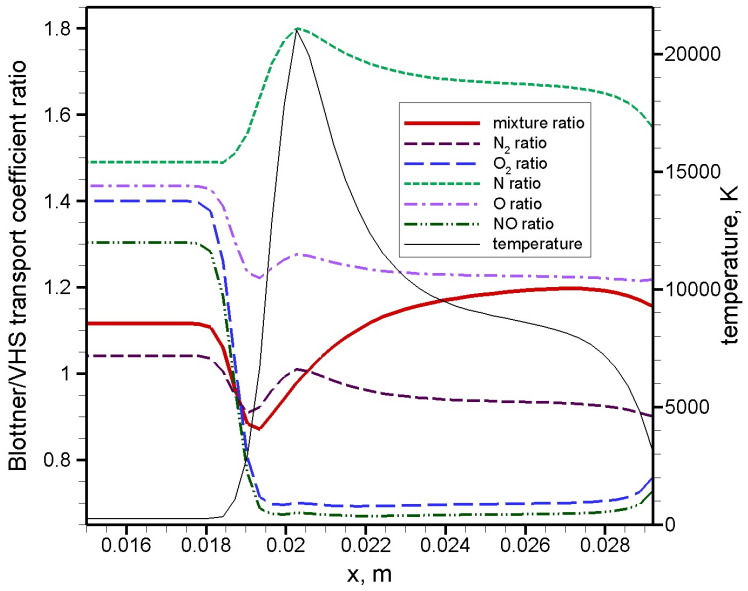

Figure 1. Variation in transport coefficient ratios and temperature along stagnation streamline, RAMC-II test case at 61 km altitude, Medium=Air.

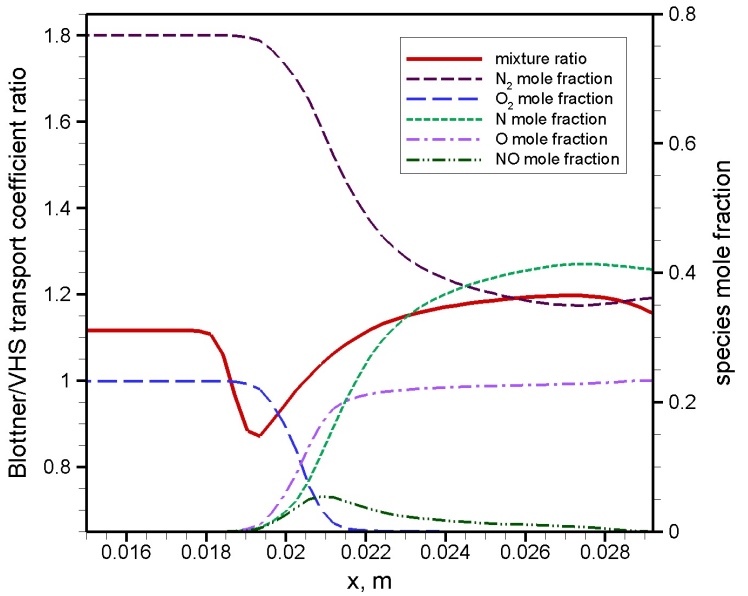

Figure 2. Mixture transport coefficient ratio and species mole fractions along stagnation streamline, RAMC-II test case at 61 km altitude, Medium=Air.

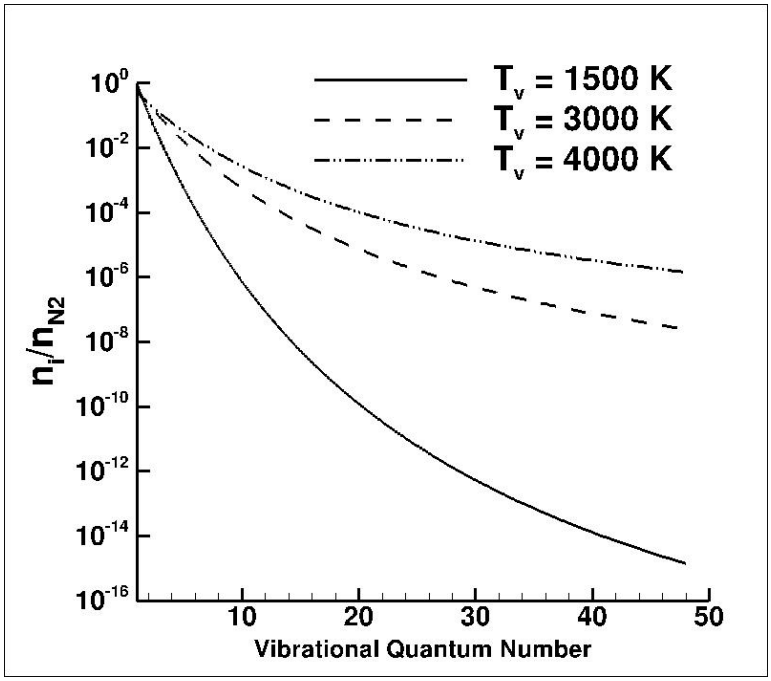

Figure 3. Fractional population distribution in vibrational energy states from 1500 K to 4000 K, Medium=N_2-N gas mixture

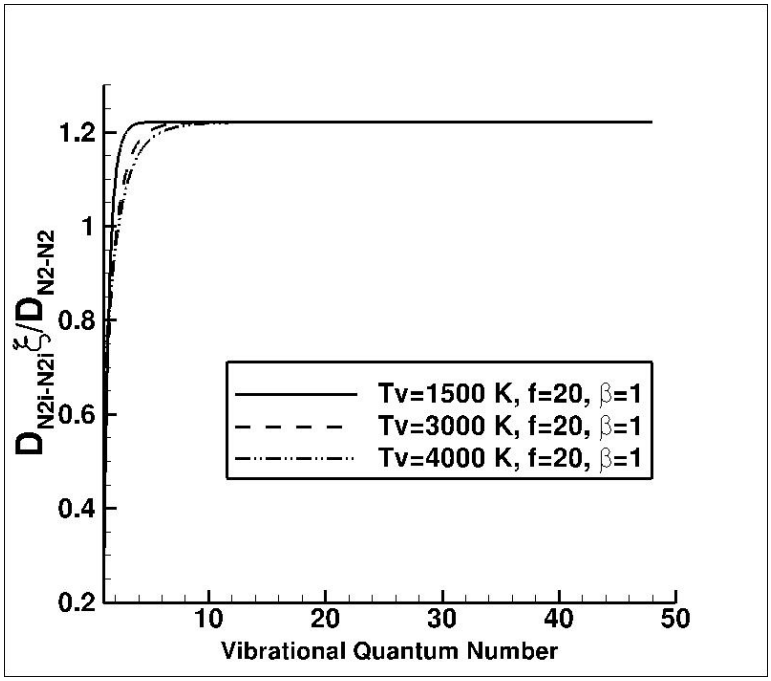

Figure 4. Self-diffusion coefficient from 1500 K to 4000 K, f=20, β=1, Medium=N_2-N gas mixture

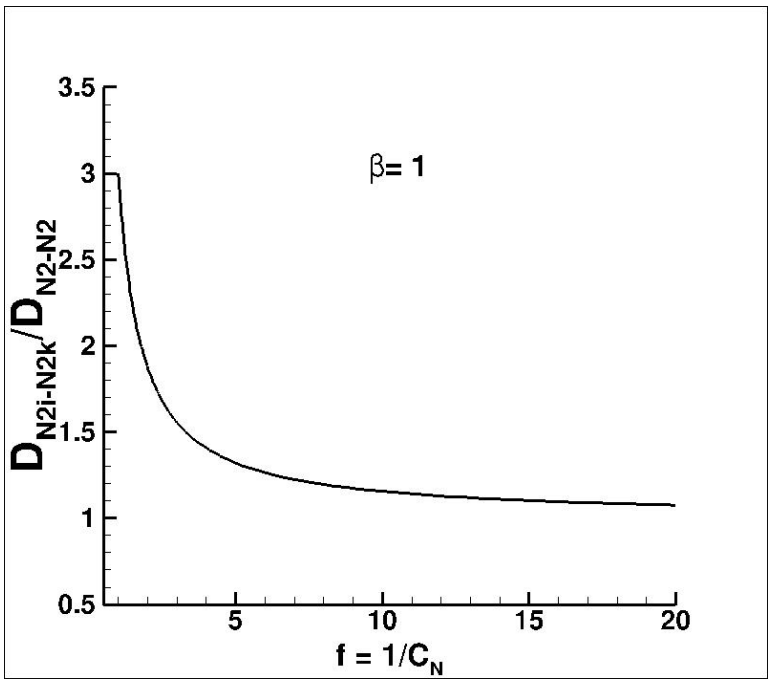

Figure 5. Variation of binary diffusion coefficient with inverse of mass concentration, β=1, Medium=N_2-N gas mixture

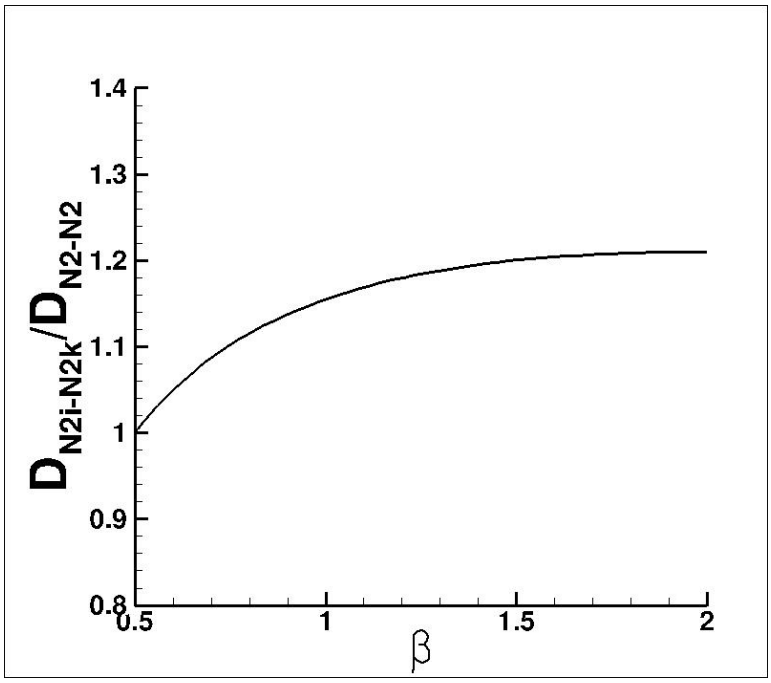

Figure 6. Variation of binary diffusion coefficient with ratio of atomic to molecular diffusion coefficient (β), $f = 10$, Medium=N_2-N gas mixture

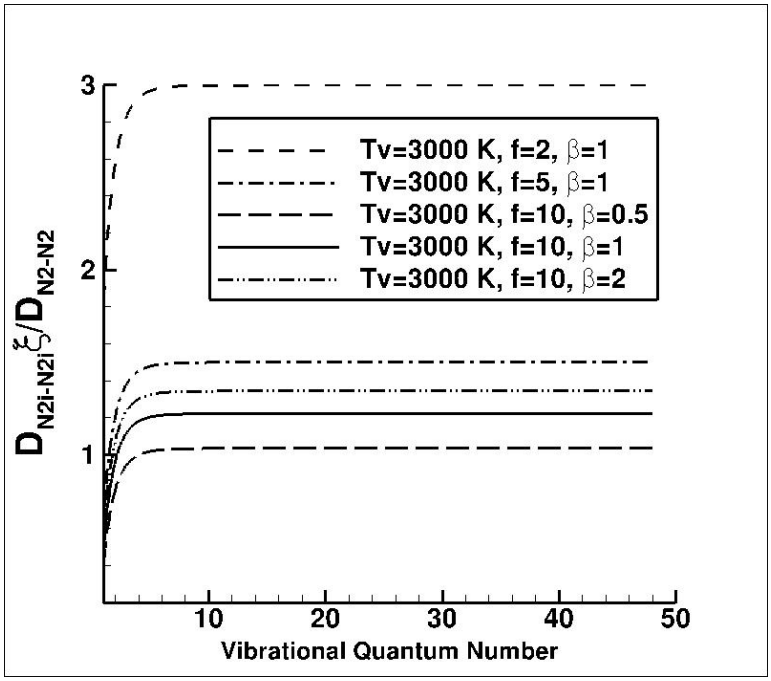

Figure 7. Variation of self diffusion coefficient in the vibrational energy states at 3000 K, Medium=N_2-N gas mixture

Different approximation levels in using CFD for the design of hypersonic vehicles

Antonio Schettino
CIRA Italian Aerospace Research Centre, Capua (CE), 81043, Italy

Domenic D'Ambrosio
Politecnico di Torino, Dipartimento di Ingegneria Meccanica e Aerospaziale, Torino, 10129, Italy

In this paper the importance of using accurate CFD simulations in the design of hypersonic vehicles is stressed. The attention is focused on one side on the necessity to be able to provide to the vehicle designer the estimated error bars together with nominal values of the design parameters. On the other side it is underlined how, in the different design phases, different levels of accuracy can be used, from simple inviscid computations to complex viscous non-equilibrium modellization, depending on the problem that must be solved. Then the attention is focused on the kinetic models, from the classic macroscopic to the advanced models based on state to state approach. Some examples of test cases are then presented, used in the last years to validate CFD codes with respect to the kinetic modeling, emphasizing the potential advantages in using state to state approach. Finally, the wind tunnel test cases that are currently being performed in the frame of Phys4Entry Project for code validation are summarized.

Nomenclature

B = magnetic induction field
C_i = aerodynamic coefficient
H_0 = total enthalpy
n = number density
P_0 = total pressure
T = temperature
x_i = mole fraction of the i-th species
y_i = mass fraction of the i-th species

Greek letters
α = ionization degree
ρ = density
σ = electrical conductivity

Superscript
Nom = Nominal
Tol = Tolerance
Var = Variation

I. Introduction

In the last decades Computational Fluid Dynamics has acquired an important role in hypersonics not only for research activities but also as a practical design tool; depending on the design phase, CFD codes are used with different levels of accuracy. During phase A, where several design loops are necessary to support the definition of the aerodynamic configuration, fast estimates are typically performed by means of engineering tools and inviscid or simplified CFD computations. During phase B, aerodynamic and aerothermodynamic databases are determined by means of more complex CFD computations taking into account viscous and nonequilibrium effects. In this phase also the available experiments are generally simulated, in order to validate the CFD results in representative conditions. Finally, during phase C, detailed computations are normally repeated on the final configuration by using the best available physical modeling, in order to provide the final database, and local effects are numerically studied in more detail.

The data that are typically needed in the design of a hypersonic vehicle can be classified in two main categories:

- the aerodynamic database includes all the aerodynamic coefficients (i.e. lift, drag, momentum) as well as the derivatives of these coefficients with respect to a number of parameters (the so called stability derivatives); the aerodynamic database is a fundamental input for flight mechanics in order to determine and optimize the vehicle trajectory and verify and guarantee its stability; furthermore, it provides mechanical loads for the sizing of the vehicle structure.
- The aerothermodynamic database mainly includes the wall heat fluxes, that are necessary to size the Thermal Protection System (TPS), especially for re-entry vehicles

It must be stressed that for both aerodynamic and aerothermodynamic databases, in order to make the data really useful for design purposes, the CFD specialist must provide not only the nominal values, but also the estimated error bar of each data. This is a fundamental aspect that is often not sufficiently taken into account and makes sometimes difficult to use CFD data for the sizing.

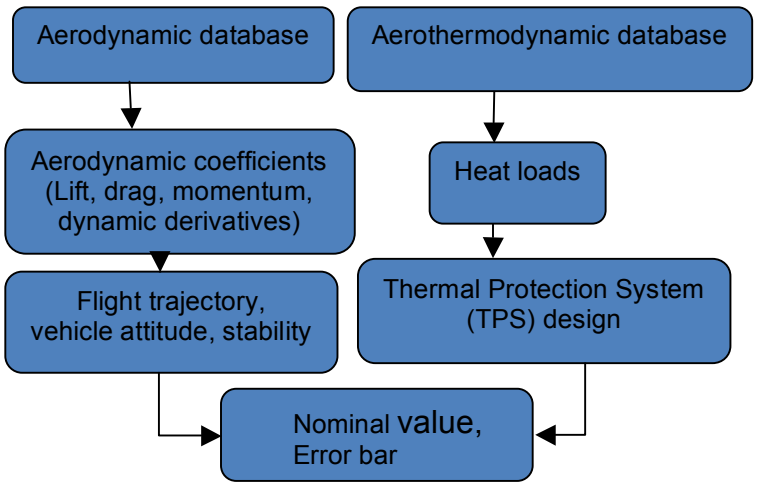

Fig. 1 – Main parameters needed in the design of a hypersonic vehicle

This topic is extensively discussed in [1], where the aerodynamic design of USV vehicle is presented. In this paper the different sources of errors and their effects on aerodynamic and aerothermodynamic databases are dealt with.
In [2] a similar logic has been applied to the design of the Expert capsule; in this paper the nominal mechanical and heat loads and the related error bars are determined by means of CFD computations and experimental data; furthermore, as far as the error bars are concerned, a clear distinction is made between tolerances and variations, that were defined as follows:

- **tolerances**: the error in the determination of the nominal values, due to the approximation of both numerical and experimental methods and modelling;
- **variations**: the error due to the fact that the "real flight" conditions are different from the ones used for the computations and for the experimental tests.

Tolerances are normally defined by the aerodynamic specialist, while variations are added by the designer. The aerodynamic coefficients are finally provided as a combination of nominal values, tolerances and variations.

$$C_i = C_i^{Nom} \pm \Delta C_i^{Tol} \pm \Delta C_i^{Var}$$

An example of the output is shown in Fig. 2, where the momentum coefficient of the Expert capsule is shown; the error bars are emphasized, together with the nominal values. The numerical data were computed by means of different codes of several contributors.

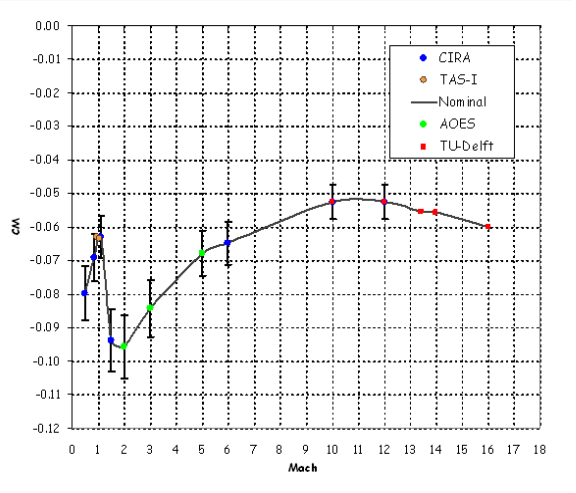

Fig. 2 – Estimated momentum coefficient of the Expert capsule as a function of Mach number [2]

More recently CFD was extensively used, along with ground experiments, for the definition of aerodynamic and aerothermodynamic databases of the ESA Intermediate Experimental Vehicle [3].

In order to estimate tolerances, several methods can be used. The accuracy of the final results, normally depends on numerical and physical modeling. As far as the numerical modeling is concerned, the CFD specialist should carefully verify not only the computation convergence, but also the grid convergence, comparing the results obtained on different grids with increasing number of cells. The grid level that is needed obviously depends on the target parameters, but also on the design phase; in phase A, for example, coarser grid can be used to perform several fast computations and get the aerodynamic coefficients, that depend mainly on wall pressure, provided that at least some computations are performed with fine grids in order to estimate the error and provide the corresponding error bar to the designer. However, from phase B, grid convergence should be always guaranteed comparing the most significant and sensitive parameters, like wall heat flux, on different grid levels.
Also the numerical scheme has normally an effect on the solution accuracy; the most appropriate numerical scheme should be selected, depending on the target parameters.
However the most critical aspect is often the physical modeling; actually both aerodynamic coefficients and mostly the wall heat fluxes can be significantly influenced by the chosen physical models, i.e. turbulence and thermochemical models. To properly define the error bar, on one side the previous experiences made on similar problems can be used, and on the other side it is important to perform and numerically rebuild representative experimental tests to validate the numerical code in similar conditions.

In some cases, most accurate physical models are available in principle, but they are not used because they are computationally too expensive. In these cases the most accurate models can be used at least to estimate the tolerances.

As far as the kinetic model is concerned, for example, different levels can be considered; in phase A, preliminary computations can be performed assuming chemical equilibrium, which

does not increase significantly the computation time and can be suitable to provide the aerodynamic coefficients.

Nevertheless, nonequilibrium modellization is necessary for accurate calculations. Macroscopic kinetic models are typically used (e.g. [4] and Kang-Dunn [5]), but the very sophisticate State-to-State models can also be used for specific problems. In the following sections some examples of applications of macroscopic and state-to-state kinetic models are shown, as well as some results recently obtained by using a novel macroscopic model, whose coefficients have been determined based on state to state approach.

II. Kinetic models

A. Macroscopic models

Thermo-chemical non-equilibrium effects are included in CFD codes adding a number of new balance equations to the usual total mass, momentum and total energy conservation equations. The new balance equations account for changes in the mass of the chemical species and in the different contributions to the internal energy. The commonly used approach is the multi-temperature approach that assigns a different temperature to each degree of freedom in non-equilibrium within the gas and requires the integration of a relaxation equation for each temperature. Usually, in aerospace applications, the rotational energy is assumed to be in equilibrium with the translational energy. These two energies are described by the so-called roto-translational temperature. Conversely, the vibrational energy of multi-atomic species is thought to be in non-equilibrium conditions and a balance equation for the vibrational energy of each multi-atomic species has to be solved. Once the vibrational energy at a given point and instant is known, it can be described by its vibrational temperature. If the gas energy is sufficiently high, species electronic energy can be assumed to be in non-equilibrium also. Therefore, an electronic temperature different from the roto-translational and the vibrational temperature may also be defined. When ionization processes are present, free-electrons may populate the flowfield. The electrons translational energy is typically in non-equilibrium also, so that an electron temperature may be defined. Since the internal energy of atoms or molecules affects the chemical reaction rates, the latter should be considered as functions of the various temperatures that are defined within the used model. The complexity of a thermo-chemical non-equilibrium model depends to what extent the effect of internal energy non-equilibrium is accounted for in the evaluation of chemical reaction rates, and vice-versa.

Using macroscopic models, one assumes that the internal energy of molecules is distributed across the energy levels according to the Boltzmann distribution, even in thermodynamic non-equilibrium conditions. Thus, a single local value of the internal energy is associated to each molecular species. For example, we consider the rotational, vibrational and electronic specific energies of molecular oxygen as single local values, namely $e^r_{O2}(x,t)$, $e^v_{O2}(x,t)$, $e^e_{O2}(x,t)$, without taking into account how these energies are distributed. The distribution is assumed *a priori* and this is why it is possible to define a temperature that pertains to a given energy of a given species. Using macroscopic models, we are interested in calculating the evolution of the concentrations of each molecular species, for example the mass fraction y_{O2}, but not the evolution of the populations of the energy levels. We will also need a model to evaluate the evolution of the internal energies of the single species.

The additional balance equations that are added to the classical governing equations of fluid dynamics are:

$$\frac{\partial \rho_i}{\partial t} + \nabla \cdot (\rho_i v) + \nabla \cdot J_{m_i} = \Omega_i^{ch} \quad i = 1, N_s \quad (1)$$

$$\frac{\partial \rho e_j^v}{\partial t} + \nabla \cdot (\rho e_j^v v) + \nabla \cdot J_{e_j^v} = \Omega_j^v \quad j = 1, N_v \quad (2)$$

In the equations above, the attention was restricted to chemical and vibrational non-equilibrium. Equation (1) is the mass balance equations for a generic i-th chemical species and equation (2) is the vibrational energy balance equation for a generic j-th species. At the left-hand side, time change, convection and diffusion can be recognized, while the source terms at right-hand side contain the chemical rates and the vibrational energy rates, respectively. As an example, the number of additional equations for a gas mixture composed of O_2, N_2, NO, O and N (air without ionization) is eight: five species mass balance equations and three vibrational energy balance equations (assuming the vibrational energy of O_2, N_2, NO are in non-equilibrium conditions).

B. State-to-state models

State-to-state models consist in solving the balance equation for all the internal states of the degree of freedom (usually vibration) that is not in equilibrium. Using state-to-state models, the energy distributions are not assumed and the evolution of the population of the different energy levels must be computed. For example, the global specific vibrational energy of molecular oxygen will be obtained as the sum of the vibrational energies of each level:

$$e_{O_2}^v = \sum_{\ell=1}^{N_{O_2}^{v,\ell}} y_{O_2,\ell}^v e_{O_2,\ell}^v \quad (3)$$

where $y^v_{O2,l}$ is the mass fraction of O_2 that populates the l-th vibrational energy level and $e^v_{O2,l}$ is the specific energy of the l-th vibrational energy level, which is a given quantity. Here, we are interested in calculating the evolution of the populations of the energy levels, $y^v_{O2,l}$.

The internal (vibrational) temperatures obtained by state-to-state calculations and related to the first energy levels reproduce the results obtained by macroscopic models. On the other hand, the chemical rate coefficients, which in the state-to-state approach are calculated as the mean value of the state-to-state rates weighted over the internal distribution, are very different. In multi-temperature models, the rate coefficients are calculated following the Arrhenius trend with a temperature that is the weighted geometrical mean of the temperatures involved in the process (Park model), or using coupling functions that also depend on the involved temperatures (CVD models). In the state-to state approach, rates are influenced by the vibrational distributions; in case of strong departures from the Boltzmann distribution, with strongly overpopulated tails, the rate coefficients do not follow the Arrhenius law, showing in some cases an opposite trend. The most difficult problem in state-to-state modelling is the lack of kinetic data (rates for selected states). To complete the data set, the ladder climbing model is often used that estimates the chemical rates from available data.

When a state-to-state approach is used to model thermo-chemical non-equilibrium, the additional balance equations that are added to the classical governing equations of fluid dynamics are:

$$\frac{\partial \rho_{i,\ell}}{\partial t} + \nabla \cdot \left(\rho_{i,\ell} v\right) + \nabla \cdot J_{m_{i,\ell}} = \Omega_{i,\ell}^{ch} \quad i = 1, N_s, \quad \ell = 1, N_i^{v,\ell} \qquad (4)$$

where l is a generic vibrational level of the i-th species. Thus, vibrational energy balance equations the species are not needed if a state-to-state chemistry approach is adopted, but the number of species mass balance equations dramatically increases. For example, the typical number of vibrational energy levels of O_2 is 34.

Note that, when we adopt a state-to-state approach to simulate thermo-chemical non-equilibrium, we have to model the production term, $\Omega^{v}_{i,l}$ and the diffusive flux, $J_{m\,i,l}$. The latter can be assumed to be the same for each energy level of a given species, while the former depends on the particular energy level and on the processes that influence that energy level. Thus, the chemical reactions scheme for state-to-state models is much more complex than for macroscopic models. To show the difference, in Table 2 we compare the reaction schemes for a gas mixture composed of 5 specie, namely O, N, NO, O_2 and N_2. Only vibrational non-equilbrium processes are accounted for.

r	reaction
1	$O_2 + O \rightleftharpoons 2O + O$
2	$O_2 + N \rightleftharpoons 2O + N$
3	$O_2 + NO \rightleftharpoons 2O + NO$
4	$O_2 + O_2 \rightleftharpoons 2O + O_2$
5	$O_2 + N_2 \rightleftharpoons 2O + N_2$
6	$N_2 + O \rightleftharpoons 2N + O$
7	$N_2 + N \rightleftharpoons 2N + N$
8	$N_2 + NO \rightleftharpoons 2N + NO$
9	$N_2 + O_2 \rightleftharpoons 2N + O_2$
10	$N_2 + N_2 \rightleftharpoons 2N + N_2$
11	$NO + O \rightleftharpoons N + 2O$
12	$NO + N \rightleftharpoons 2N + O$
13	$NO + NO \rightleftharpoons N + O + NO$
14	$NO + O_2 \rightleftharpoons N + O + O_2$
15	$NO + N_2 \rightleftharpoons N + O + N_2$
16	$NO + O \rightleftharpoons N + O_2$
17	$N_2 + O \rightleftharpoons N + NO$

r	reaction		
1	N_2(M) + N_2	$\rightleftharpoons$	2N + N_2
2	N_2(v) + N_2	$\rightleftharpoons$	N_2(v-1) + N_2
3	N_2(v) + N_2(M)	$\rightleftharpoons$	N_2(v-1) + 2N
4	N_2(v) + N_2(w-1)	$\rightleftharpoons$	N_2(v-1) + N_2(w)
5	N_2(v) + N	$\rightleftharpoons$	2N + N
6	N_2(v) + N	$\rightleftharpoons$	N_2(v-dv) + N
7	O_2(v) + O_2(w-1)	$\rightleftharpoons$	O_2(v-1) + O_2(w)
8	O_2(v) + O_2(M)	$\rightleftharpoons$	O_2(v-1) +2O
9	O_2(v) + O_2	$\rightleftharpoons$	O_2(v-1) + O_2
10	O_2(M) + O_2	$\rightleftharpoons$	2O + O_2
11	O_2(v) + O	$\rightleftharpoons$	O_2(v-dv) + O
12	O_2(v) + O	$\rightleftharpoons$	2O + O
13	N_2(v) + O_2	$\rightleftharpoons$	N_2(v-1) + O_2
14	N_2(v) + O_2	$\rightleftharpoons$	2N + O_2
15	N_2(v) + O	$\rightleftharpoons$	N_2(v-1) + O
16	N_2(v) + O	$\rightleftharpoons$	2N + O
17	O_2(v) + N_2	$\rightleftharpoons$	O_2(v-1) + N_2
18	O_2(v) + N_2	$\rightleftharpoons$	2O + N_2
19	O_2(v) + N	$\rightleftharpoons$	NO + O
20	N_2(v) + O	$\rightleftharpoons$	NO + N
21	O_2(v) + N_2(w-1)	$\rightleftharpoons$	O_2(v-2) + N_2(w)
22	NO(0) + O	$\rightleftharpoons$	N + O + O
23	NO(0) + N	$\rightleftharpoons$	N + O + N
24	NO(0) + NO	$\rightleftharpoons$	N + O + NO
25	NO(0) + O_2	$\rightleftharpoons$	N + O + O_2
26	NO(0) + N_2	$\rightleftharpoons$	N + O + N_2

Table 1 – List of chemical processes to be considered using macroscopic (left) and a state-to-state (right) models.

In the state-to-state model we have a list of 26 processes, but note that when ‘v’ or ‘w’ is indicated next to a diatomic species, it varies from 1 to the number of energy levels of that species. Therefore, the total number of processes that are accounted for is definitely larger than 26. A large number of processes implies a large computational cost for each evaluation of non-equilibrium source terms.

III. Examples of test cases simulation

In this section some examples of test cases performed in previous projects for code validation are shown, with the goal to emphasize the importance to design and perform representative experiments for code validation.

The first two tests were used to check the code capability to provide reliable data in case of flow separation; this is a typical problem of practical interest, because the flow separation phenomenon can significantly affect the flap efficieny of a hypersonic vehicle.

Afterwards some examples are shown of simulations inside a hypersonic nozzle; the strong expansion occurring in a nozzle is a typical case where the accuracy of kinetic model is very important, especially when one is interested in an accurate estimate of the ionization level.

These test cases were simulated with classic macroscopic kinetic models, or with a novel macroscopic model based on state to state approach. In subsection C, we show some results that were obtained by directly applying the state-to-state modelling, in order to emphasize the expected differences with respect to macroscopic models.

A. Flow separation test cases

In [5] a double cone test case at Mach 9 was tested and numerically rebuilt. The activity was carried out in the framework of the CAST Project, funded by the Italian Space Agency (ASI) and devoted to the development of a numerical code able to simulate high-enthalpy reacting flows on complex geometries by means of state of the art physical models.

Several experimental tests were performed in the HEAT facility at ALTA and numerical simulations for some representative conditions were carried out using two different numerical codes, developed by CIRA and Politecnico di Torino, respectively, whose main characteristics are described in [5]. In particular, the attention was focused on the experiments corresponding to the freestream conditions listed in Table 1.

ID	p^o [bar]	h^o [MJ/kg]
Run 8 (12-03-2008)	3.11	3.61
Run 3 (13-03-2008)	3.17	4.64

Table 2 – Freestream conditions for the numerical rebuilding of the double-cone experiments [6]

In Fig. 3 the typical flow structure that is expected from the experiment is shown, while in Fig. 4 an example of the Mach number contour is plotted for one of the experimental conditions.

In Fig. 5 and Fig. 6 the comparison is shown between numerical and experimental results, in terms of wall heat flux and pressure.

It can be seen that, with respect to the experimental data, both CFD codes show a good agreement for the heat flux, while the comparison is less satisfactory for the wall pressure. More in detail, CFD computations seemed to predict a stronger interaction than the experiment, with a much higher pressure peak and a well visible effect of the transmitted shock with a consequent second smaller peak of pressure over the 55 degrees cone. In the experiments, conversely, the separation length seemed smaller. Therefore a sensitivity analysis was performed, by changing physical models (wall catalysis) and freestream conditions, that were computed by simulating the nozzle flow also. This last point seemed the most relevant. Actually, in [5] it was shown how the correct modelling of the nozzle flow has a significant effect on the final solution over the double cone, and allows for a better agreement also for wall pressure; this can be seen in Fig. 6, where the green line represents the wall pressure recomputed with updated freestream conditions obtained by means of a more accurate simulation of the nozzle flow.

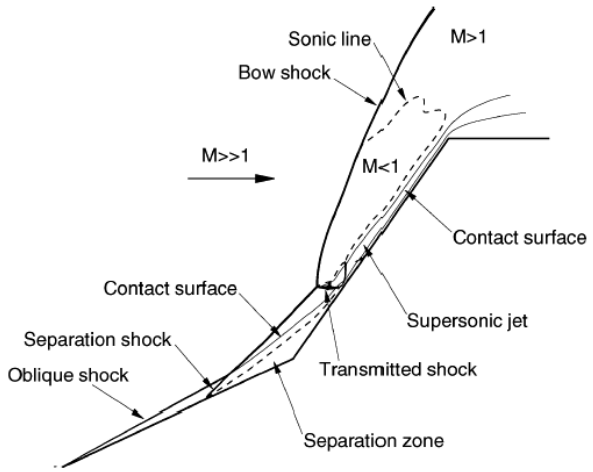

Fig. 3 – Shock interaction pattern [7]

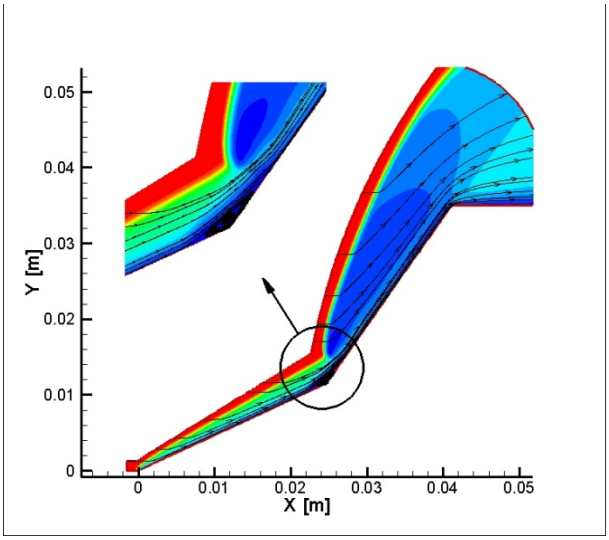

Fig. 4 – Mach number contour (run 3) [6]

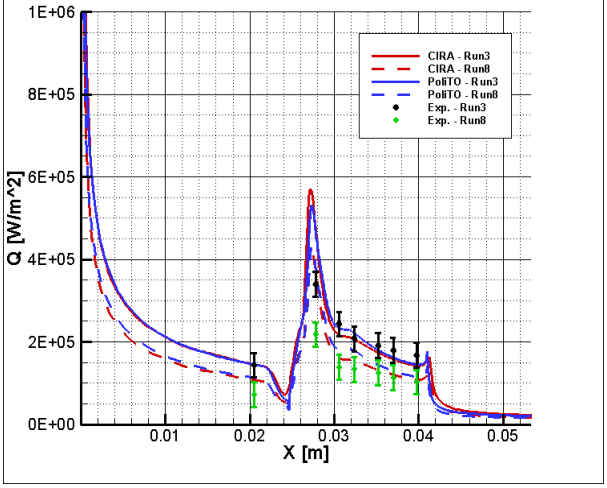

Fig. 5 – Wall heat flux. Comparison between numerical results and experimental data [6].

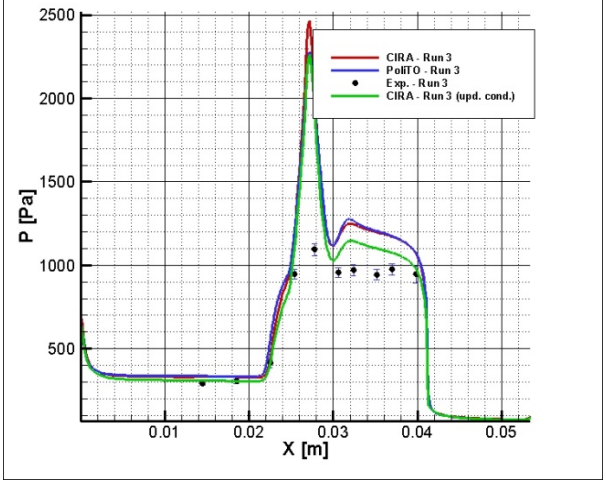

Fig. 6 - Wall pressure. Comparison between numerical results and experimental data [6].

In [8] another experiment devoted to the study of shock wave – boundary layer interaction inducing flow separation is discussed. This experiment was carried out in the Scirocco Plasma Wind Tunnel at CIRA. In [8], some details about the numerical computations are given, while in [9] some experimental results are shown, together with details on the related flight experiment that was designed and set-up by CIRA to be performed on the ESA Expert capsule.

A flap that represents one of those designed and built for the Expert capsule was mounted on a model holder. The goal of the test was to reproduce in a ground experiment freestream conditions similar to real flight conditions in order to obtain a flow separation on the flap similar to the one foreseen in flight.

With respect to the previously described double cone experiment, which is characterized by a total enthalpy of approximately 5 MJ/kg, the energy level is significantly higher here (up to 15

MJ/kg) and the model dimensions are much bigger. Therefore, in this case, real gas effects are much stronger than in the double-cone experiment.

In Fig. 7 the pressure contours over half model are shown, while in Fig. 8 one can see a detail of the flap region. Here, skin friction lines are also plotted, in order to emphasize the separation zone.

Several sensors were embedded in the test article to acquire useful data for code validation. Pressure transducers (PT) and thermocouples (TC) were installed on both the model holder and the flap. A very important measurement was performed by means of a combined pressure/heat flux sensor (CFP) specifically designed for the Expert capsule and qualified in the Scirocco wind tunnel. In Fig. 9, the positions of all the sensors are put in evidence, while in Fig. 10 the comparison between numerical and experimental data is shown. It can be seen that a very good agreement was obtained.

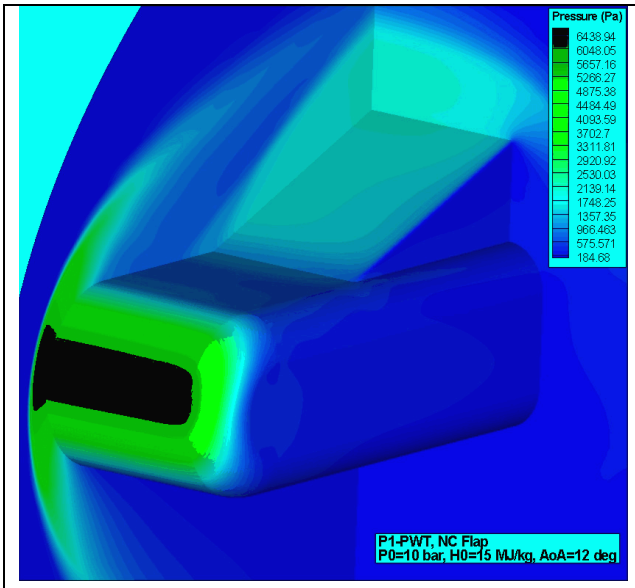

Fig. 7 – CLAE model. Computed pressure contours [8]

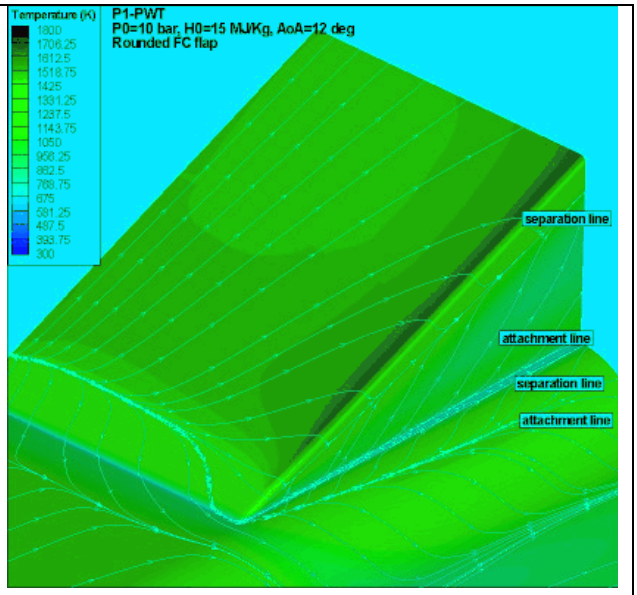

Fig. 8 - CLAE model. Computed temperature contours over the flap and separation zone [8]

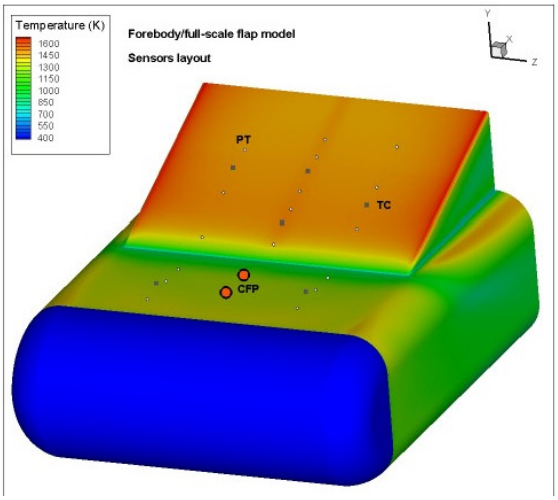

Fig. 9 – CLAE model. Sensors location [8]

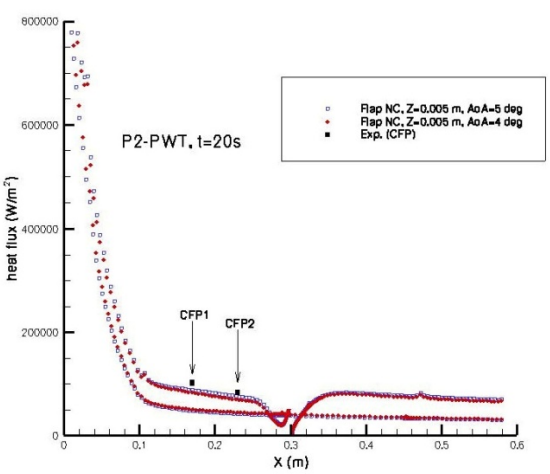

Fig. 10 – CLAE model. Wall heat flux. Comparison between numerical and experimental results [9]

B. Nozzle test cases

The effect of the choice of a given chemical model is particularly important in hypersonic nozzle flows, where the strong expansion is strongly affected by chemical non-equilibrium conditions.

In the framework of the already cited CAST Project, a novel macroscopic model was proposed by CNR-IMIP at Bari, whose coefficients were determined by means of state-to-state computations. Such a model was used, together with a classic Kang-Dunn model, to simulate the flow inside the Scirocco nozzle, whose geometry is shown in Fig. 11.

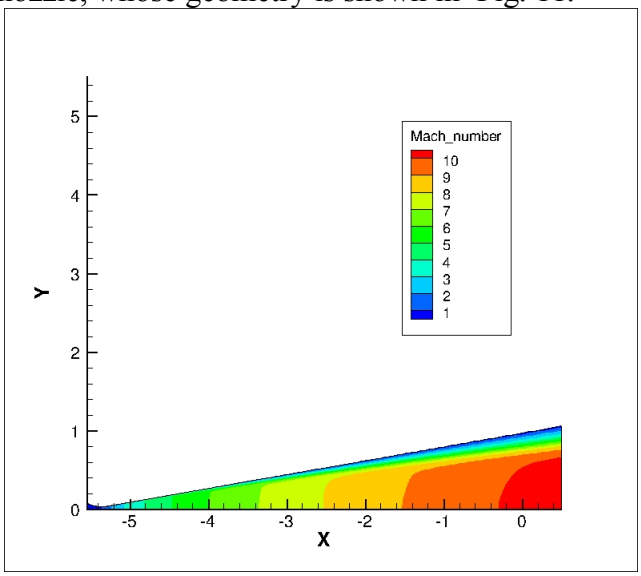

Fig. 11 - Scirocco nozzle. Mach number contour [11]

It is worth to underline that very few data are available to validate CFD codes with respect to the electron number density n_e; on the other hand, this parameter was particularly important within that project, since the freestream n_e plays an important role in the MHD interaction.

In Fig. 12, Mach and temperature distributions along the nozzle axis obtained using the Kang-Dunn and new CAST models are compared. It can be seen that the latter provides a less intense expansion with respect to Kang-Dunn.

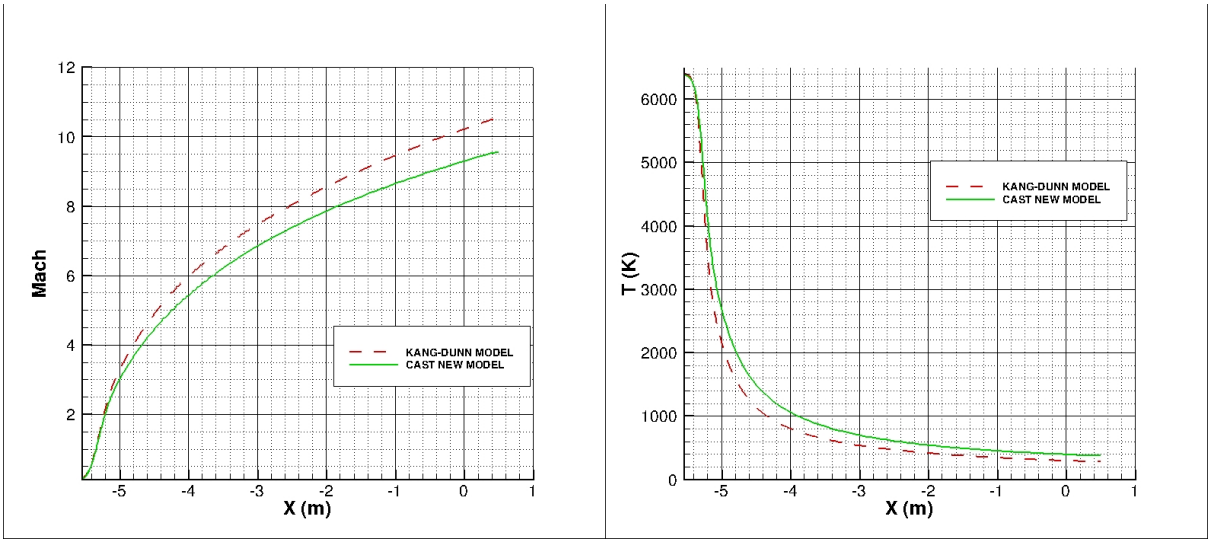

Fig. 12 - Mach and temperature plots along the Scirocco nozzle axis [11]

However, the most important result is shown in Fig. 13, where the computed electron number density, n_e, is plotted and compared with the experimental data measured at the nozzle exit. It can be seen that the new CAST model provides a higher value of n_e with respect to Kang-Dunn, very close to the experimental one.

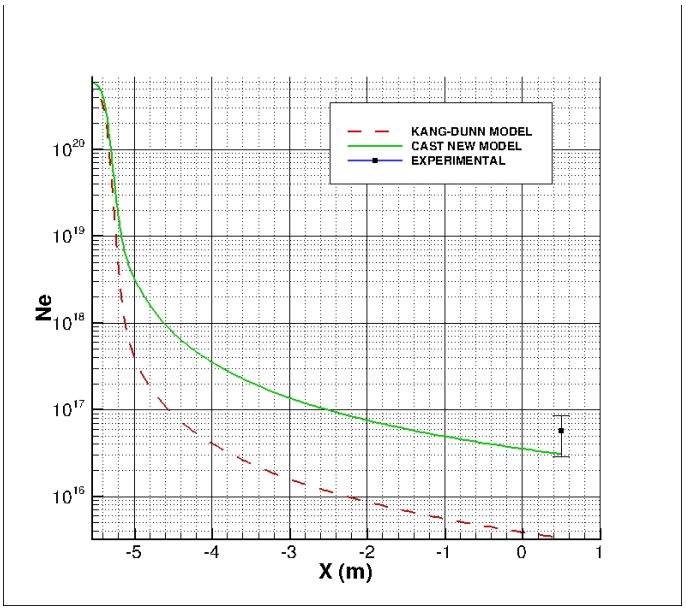

Fig. 13 - Electron density along the Scirocco nozzle; comparison with experimental value measured [11]

A similar result was obtained also in a different test condition, that were characterized by a lower total enthalpy. For this test, some spectroscopic measurements were also available [11], that allowed to estimate the translational temperature and the vibrational temperature of NO at the nozzle exit. The comparison between numerical and experimental results are shown in Fig. 14

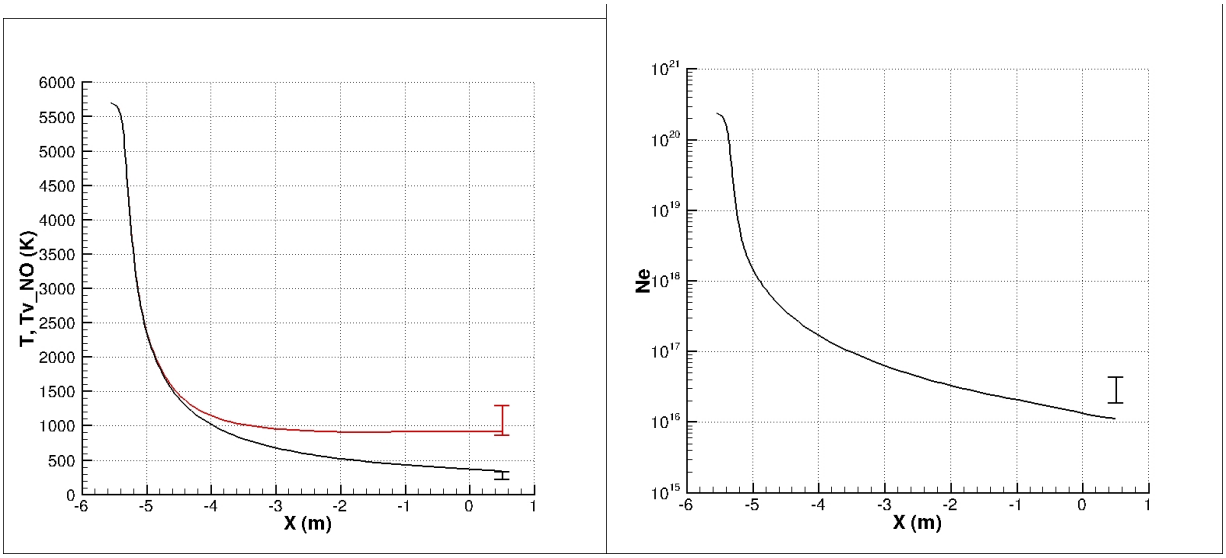

Fig. 14 – Scirocco nozzle. Low enthalpy case. Translational and NO vibrational temperature (left). Electron density (right) [11]

These results confirm a previous similar result obtained in the framework of the CAST project in the smaller research facility GHIBLI, also available at CIRA [12].

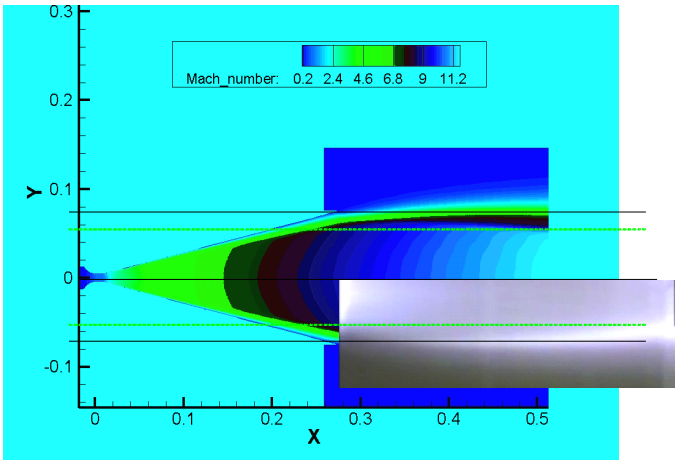

Fig. 15 – Ghibli nozzle. Plume shape compared with experimental data [12]

In this case, nozzle simulations were performed using both the EMC3NS code with a classical kinetic model (i.e. Kang Dunn) and the CAST code.

In Fig. 16, it can be seen that, as it occurred for the Scirocco nozzle experiment, the electron number density obtained with the CAST model is very close to the experimental measurements provided by interferometry, while the results obtained using the Kang Dunn model predict an electron number density about one order of magnitude smaller.

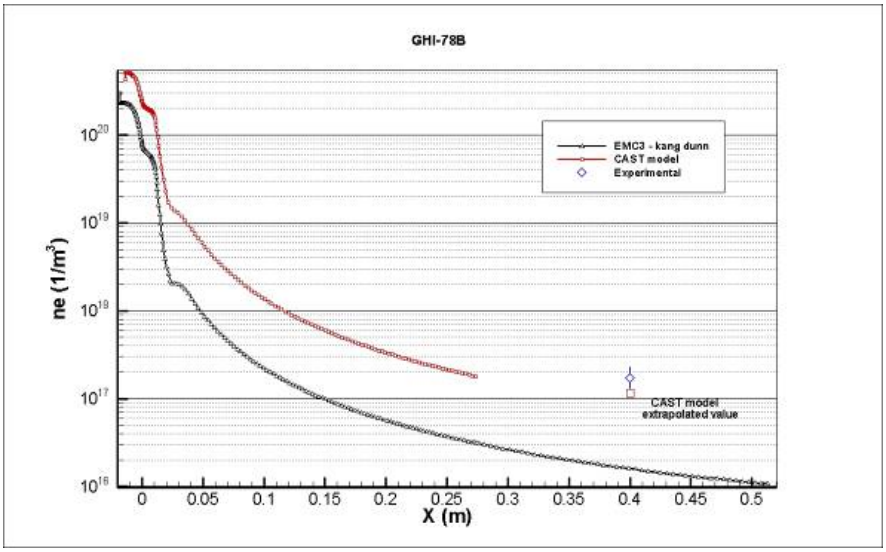

Fig. 16 – Electron density along the Ghibli nozzle; comparison with experimental value measured [12]

C. State-to-state computations

In this section we show an example of a state-to-state simulation in a hypersonic nozzle flow. Details about the used thermochemical models and numerical method can be found in [13]. The numerical prediction aims at reproducing one of the experiments conducted in the NASA Ames EAST facility nozzle by Sharma, Gillespie et alii [14][15]. The working gas is pure nitrogen and the stagnation conditions for the considered experiment are defined in Table 2, which correspond to case B of reference [16]. For the sake of simplicity, quasi-one-dimensional simulations were carried out.

Experiment	h^o [MJ/kg]	p^o [Pa]	T^o [K]	ρ [kg/m^3]	x_{N2}	x_N
Case B [15]	7.60	$1.03352\ 10^7$	5616	6.164	0.9883	0.0117

Table 3 - Stagnation conditions used in the simulation of the EAST nozzle experiments.

As expected, the results of the state-to-state model are characterized by a strong freezing of the distributions tails to values larger than those predicted by the Boltzmann distribution (Fig. 17). The freezing starts before the throat and induces a slightly faster recombination, as shown in Fig. 18 (left). In this particular test case, the differences between the state-to-state and the macroscopic models are quite small. This can be partly due to the consistency that exists between the two models. The only significant difference is in the recombination of the atomic nitrogen N, which may be due to the tails freezing mechanism. Note that the macroscopic model incorporates a chemistry-to-vibration mechanism that should enhance the recombination rate in the present experimental conditions. However, such a model is based on the hypothesis of a Boltzmann distribution for the vibrational energy levels and it does not account for deviation from it. Since the amount of dissociation in the present experiment is very small, further computations should

be carried out considering stagnation conditions capable of producing a larger amount of atomic nitrogen. If, in those cases also, the recombination processes were more pronounced using the state-to-state model rather than the macroscopic model, this would be a proof that macroscopic models should incorporate some mechanism to account for the freezing of the population tails in strongly expanding flows.

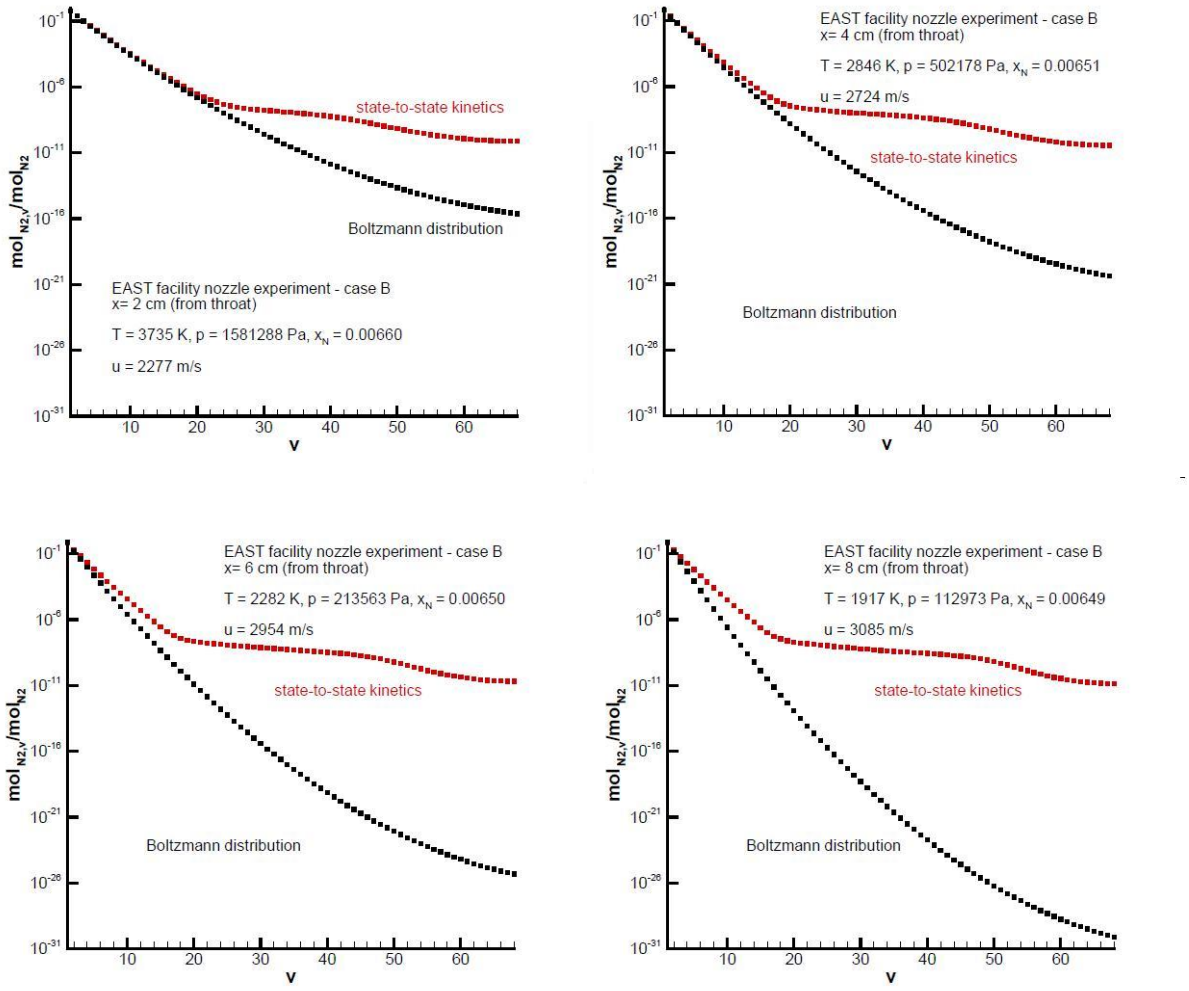

Fig. 17 - Computed vibrational levels distributions at different positions along the EAST nozzle.

With respect to the experimental data, which contain information about the vibrational temperature distribution along the nozzle, the present results are in very good agreement as far as the roto-traslational temperature is concerned, but they underestimate the value of the vibrational temperature. In Fig. 18 (right), we can see a ratio T^{v}_{N2}/T^{o} approximately equal to 0.51-0.52, while experimental data measure values of about 0.58-0.6. Other models, both state-to-state and macroscopic [16], provide a definitely better agreement, though it must be put in evidence that at least part of them was tuned on this particular experiment.

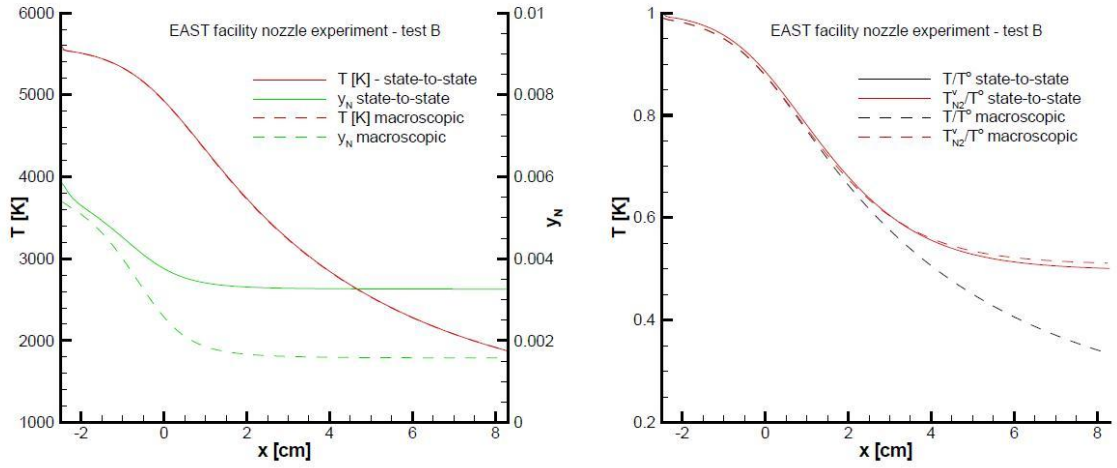

Fig. 18 - Computed temperatures and chemical composition along the EAST nozzle.

IV. Planned test cases to be rebuilt in Phys4Entry Project

In the frame of Phys4Entry Project, funded by the European Community, several test cases are being performed at Von Karman Institute. The test cases will concern different gas mixtures corresponding to the atmosphere of different planets: Earth, Mars and Jupiter. Tests concerning Earth and Mars are being performed in Plasmatron facility, while Jupiter atmosphere will be simulated in the VKI Minitorch. Several experimental data will be available, from standard calorimetric and pressure measurements to non intrusive measurements with conventional and advanced spectroscopic diagnostics to characterize the supersonic expanding plasma jet in terms of internal levels populations, atom number densities, ionization degree and radiation signatures.

Preliminary experimental data, mainly concerning nitrogen and air tests are shown in [17]; in Fig. 17 a preliminary example of the flow field computed by CIRA is shown. It can be seen that the plume inside the test chamber has a typical structure characterized by several oblique waves, depending not only on the flow conditions but also on the test chamber pressure. One of the first goals of the numerical simulation is to correctly reproduce this flow structure and the plume shape.

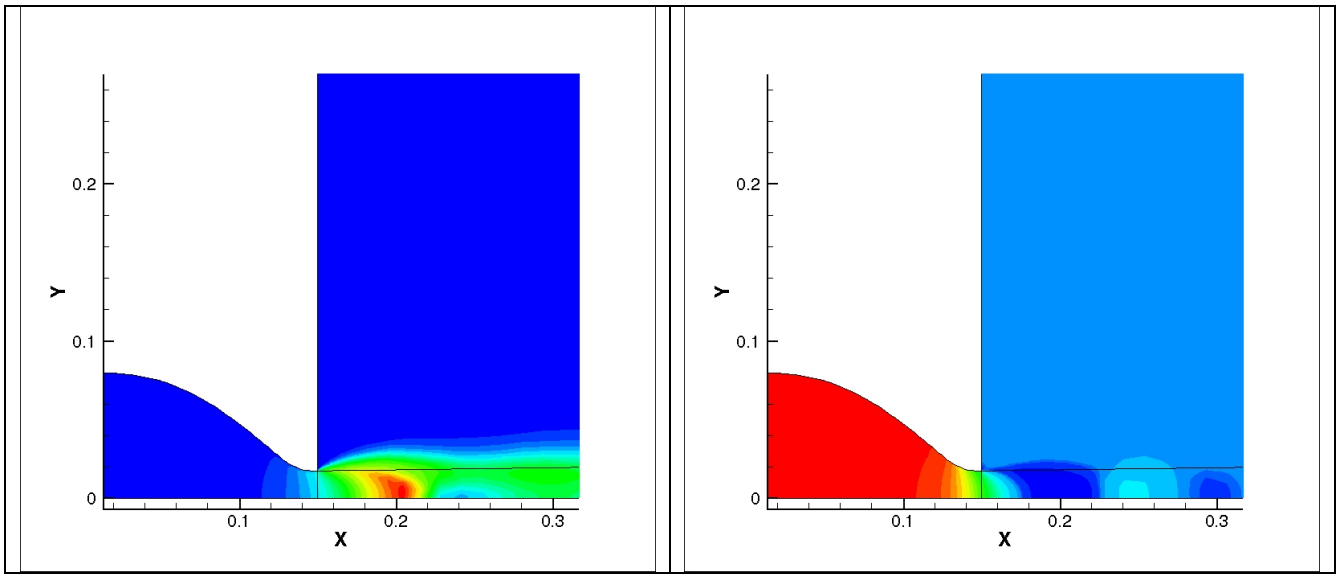

Fig. 17 – CFD rebuilding of Plasmatron test case #1. Mach number (left) and pressure (right) contours

The flow fields are being computed by means of macroscopic models; both the classic and novel models previously described will be used, and the results will be compared with experimental data in terms of electron densities. Furthermore, the computed CFD flow fields will be used as input for one-dimensional computations that will be performed by CNR-IMIP using state to state approach; this will allow to directly compare also the internal levels populations and the excitation temperature.

The Plasmatron conditions that will be simulated with air and nitrogen are summarized in the following table.

TC	Gas	Reservoir pressure [mbar]	Test chamber pressure [mbar]	Mass flow rate [g/s]
#1	Nitrogen	97	10	4
#2	Air	120	6	4.5
#3	Air	120	12	4.5

Similar computations will be performed with different mixtures representative of Mars and Jupiter atmospheres as soon as experimental data will be available.

The final goal of this activity will be to validate the kinetic models developed in Phys4Entry project for the earth, Mars and Jupiter atmospheres, emphasizing the differences between the results obtained with classic and state to state kinetic models.

Acknowledgments

Phys4Entry Project was funded by the European Community's Seventh Framework Program (FP7/2007-2013)

References

1. G.C. Rufolo, P. Roncioni, M. Marini, R. Votta, S. Palazzo "Experimental and Numerical Aerodynamic Data Integration and Aerodatabase Development for the PRORA-USV-FTB_1 Reusable Vehicle", AIAA-2006-8031.
2. Schettino A., Votta R., Roncioni P., Di Clemente M., Gerritsma M., Chiarelli C., Ferrarella D. "Aerodynamic and Aerothermodynamic database of Expert capsule", West-East High Speed Flow Field Conference, Moscow, Nov. 19-22, 2007.
3. G. Pezzella, M. Marini, G. Rufolo "Aerodynamic Characterization of the ESA Intermediate Experimental Vehicle", 17th AIAA International Space Planes and Hypersonic Systems and Technologies Conference, 2011.
4. Park C., "Review of Chemical-kinetic Problems of future NASA Missions, I: Earth Entries", Journal of Thermophysics and Heat Transfer, Vol.7, No.3, July-Sept. 1993.
5. S.W. Kang, W.L. Jones, M.G. Dunn, "Theoretical and measured electron-density distributions at high altitudes", AIAA Journal, Vol.11, No.2, Feb.1973.
6. A. Schettino, F. Battista, G, Ranuzzi, D. D'Ambrosio "Rebuilding of new experimental tests on a double cone at Mach 9", Sixth European Symposium on Aerothermodynamics for Space Vehicles, Versailles, Nov. 3-6, 2008.
7. Nompelis I., Candler G.V, Holden M.S. "Effect of Vibrational Non-equilibrium on Hypersonic Double-Cone Experiments", AIAA Journal, Vol.41, No.11, November 2003.
8. M. Di Clemente, M. Marini, S. Di Benedetto, A. Schettino, G. Ranuzzi "Numerical Prediction of Aerothermodynamic Effects on a Reentry Vehicle Body Flap Configuration", IAC-06-D2.6.08.
9. M. Di Clemente et al. "Shock Wave Boundary Layer Interaction Measurement Assembly on the Expert Capsule", 16th AIAA/DLR/DGLR International Space Planes and Hypersonic Systems and Technologies Conference, Bremen (Germany), October 2009.
10. Cristofolini A., Borghi C.A., Neretti G., Schettino A., et al. "Experimental investigations on the magneto-hydro-dynamic interaction around a blunt body in a hypersonic unseeded air flow", Journal of Applied Physics, 112, 093304 (2012).
11. Cristofolini A., Borghi C.A., Schettino A., Battista F. "Numerical Rebuilding of MHD Tests in an Unseeded Mach 10 Air flow around a Blunt Body", 43rd AIAA Plasmadynamics and Lasers Conference, 25 - 28 June 2012, New Orleans.
12. Trifoni E., Purpura C., Martucci A., Graps E., Schettino A., Battista F. et al. "MHD experiment at CIRA GHIBLI Plasma Wind Tunnel", 7th Aerothermodynamics Symposium, 9-12 May 2011, Bruges (Belgium).

13. Colonna G., D'Ambrosio D., Capitelli M. "Consistent comparison of macroscopic and state-to-state kinetics in hypersonic flows", 39th AIAA Thermophysics Conference, Miami (FL), June 2007, AIAA Paper 2007-3906.
14. Sharma S.P., Ruffin S.M., Gillespie W.D., Meyer S. A. "Vibrational relaxation measurements in an expanding flow using spontaneous Raman scattering", Journal of Thermophysics and Heat Transfer, Vol. 7, No. 4 (1993), pp. 697-703.
15. Gillespie W.D, Bershader D., Sharma S.P., Ruffin S.M. "Raman scattering measurements of vibrational and rotational distributions in expanding nitrogen", 31st Aerospace Sciences Meeting and Exibit, Reno (NV), Jan. 1993, AIAA Paper 1993-0274.
16. Ruffin S.M. "Prediction of Vibrational Relaxation in Hypersonic Expanding Flows Part 2: Results", Journal of Thermophysics and Heat Transfer, Vol. 9, No. 3 (1995), pp. 438-445.
17. Babou Y. et al. "Experimental aspects in hypersonic and supersonic plasma flows", (2013) submitted.